Studying the role of matrix metalloproteinases (MMPs) and their tissue inhibitors in gastric carcinoma under hyperglycemic condition

Thesis submitted for the degree of

Doctor of Philosophy (Science)

of

Jadavpur University

Abhishek Chatterjee, M.Sc.

CSIR–Indian Institute of Chemical Biology

4, Raja S.C. Mullick Road

Kolkata – 700032

2025

सी.एस.आई.आर–भारतीय रासायनिक जीवविज्ञान संस्थान
वैज्ञानिक तथा औद्योगिक अनुसंधान परिषद की एक इकाई
विज्ञान एवं प्रौद्योगिकी मंत्रालय, भारत सरकार
4, राजा एस. सी. मल्लिक रोड, यादवपुर, कोलकाता - 700 032
CSIR - INDIAN INSTITUTE OF CHEMICAL BIOLOGY
A Unit of Council of Scientific & Industrial Research
Ministry of Science & Technology, Government of India
4, Raja S. C. Mullick Road, Jadavpur, Kolkata-700 032

CERTIFICATE FROM THE SUPERVISOR(S)

This is to certify that the thesis entitled "**Studying the role of matrix metalloproteinases (MMPs) and their tissue inhibitors in gastric carcinoma under hyperglycemic condition**" submitted by **Sri ABHISHEK CHATTERJEE** who got his name registered on **11.02.2022** for the award of **Ph. D. (Science) Degree of Jadavpur University**, is absolutely based upon his own work under the supervision of **Dr. SNEHASIKTA SWARNAKAR & Dr. SUJOY K.DAS** and that neither this thesis nor any part of it has been submitted for either any degree / diploma or any other academic award anywhere before.

02/04/25

(Signature of the Supervisor date with official seal)

DR. SNEHASIKTA SWARNAKAR
Ex. Chief Scientist, Ph.D. FNASc., FAScT
Head, Infectious Diseases & Immunology
Head, P&I Division, Professor, AcSIR
CSIR - India Institute of Chemical Biology
Jadavpur, Kolkata - 700 032, India

2/4/25

(Signature of the Supervisor date with official seal)

Dr. Sujoy K. Das, PhD
Principal Scientist
CSIR-Indian Institute of Chemical Biology
Jadavpur, Kolkata 700 032, India

Dedicated to my parents

and

my teachers

ACKNOWLEDGEMENT

As I pen down the final words of this thesis, I find myself overwhelmed with emotions—gratitude, relief, joy, and an indescribable sense of accomplishment. This journey, filled with both challenges and triumphs, would not have been possible without the unwavering support, guidance, and encouragement of many individuals who have played a significant role in shaping my academic and personal growth.

First and foremost, I express my deepest gratitude to my PhD supervisor, Dr Snehasikta Swarnakar. Your invaluable guidance, patience, and belief in my potential have been the pillars of my research journey. Your constructive criticisms pushed me beyond my comfort zone, and your encouragement instilled in me the confidence to strive for excellence. Your mentorship has not only helped me grow as a researcher but has also shaped my perspective on perseverance, discipline, and scientific curiosity. I am forever indebted to you for your support and kindness throughout these years. I extend my sincere gratitude to my co-guide, Dr. Sujoy K Das, for your unwavering support and guidance. I acknowledge Dr. Smrutisanjita Behera for her help. I remain forever grateful to Prof. Samit Chattopadhyay, ex-Director, IICB for allowing me to undertake my doctoral studies at the institute.

I extend my heartfelt thanks to my lab mates and colleagues, especially Tapasi di, Tanaya di, Preety di, and Vineet da, who have been my second family during this journey. The long hours in the lab, the thought-provoking discussions, and the countless moments of frustration and laughter that we shared have created an irreplaceable bond. Each one of you has contributed in some way, whether through scientific insights, moral support, or simply by being there during the difficult days. Thank you for making this journey less daunting and more memorable. I would also like to thank my friends from other labs of CSIR-IICB who have helped me immensely throughout this journey.

To my parents, no words can truly express my gratitude for your unconditional love, patience, and sacrifices. Your unwavering belief in me, even when I doubted myself, has been my greatest source of strength. Every success I achieve reflects your endless support and prayers. Thank you for being my safe haven and my guiding light.

Above all, I bow my head in deep gratitude to the Almighty, whose grace and blessings have given me the strength to overcome challenges, the resilience to keep moving forward, and the wisdom to navigate this journey. Without His divine guidance, none of this would have been possible.

This PhD journey has been a rollercoaster of emotions—marked by sleepless nights, moments of self-doubt, but also by the joy of discoveries, personal growth, and cherished memories. As I reach this milestone, I carry with me not just a degree, but a treasure trove of experiences and relationships that will remain with me for a lifetime

With heartfelt gratitude,

Abhishek Chatterjee
March, 2025

ABBREVIATIONS

AP-1, activator protein-1; **AP-2**, activator protein-2; **ATP**, adenosine triphosphate; **BSA**, bovine serum albumin; **C/EBP-β**, CCAAT/enhancer binding protein-β; **$CaCl_2$**, calcium chloride; **cAMP**, cyclic adenosine monophosphate; **CDK**, cyclin dependent kinase; **cGMP**, cyclic guanosine monophosphate; **ChIP**, chromatin immunoprecipitation; **CO_2**, carbon dioxide; **CTRL**, control; **DAPI**, 4',6-diamidino-2-phenylindole; **DCFH-DA**, 2'-7'-Dichlorodihydrofluorescein diacetate; **DMSO**, dimethyl sulfoxide; **DNA**, deoxyribonucleic acid; **DTT**, dithiothretol; **ECM**, extracellular matrix; **EMT**, epithelial-mesenchymal transition; **ERK**, extracellular signal-regulated kinase; **ERK**, extracellular signal-regulated kinase; **ETC**, electron transport chain; **FACS**, fluorescence-activated cell sorting; **FBS**, fetal bovine serum; **FITC**, fluorescein isothiocyanate; **GAPDH**, glyceraldehyde-3-phosphate dehydrogenase; **GC**, gastric cancer; **GI tract**, gastrointestinal tract; **HBS**, HIF-binding site; **HCl**, hydrochloric acid/hydrogen chloride; **HG**, hyperglycemia / hyperglycemic; **HRP**, horseradish peroxidase; **IgG**, immunoglobulin G; **IP3**, inositol triphosphate; **JNK**, c-Jun N-terminal kinase; **KCl**, potassium chloride; **KRE-M9**, keratinocyte differentiation factor-1 responsive element-4; **LBP-1**, leader-binding protein; **LPS**, lipopolysaccharide; **MAPK**, mitogen-activated protein kinase; **MD**, molecular dynamics; **MELA**, melatonin; **MMP**, matrix metalloproteinase; **MT1-MT3**, melatonin specific receptor 1, 2, 3; **NAC**, N-acetyl-L-cysteine; **NaCl**, sodium chloride; **NF1**, nuclear factor-1; **NF-κB**, nuclear factor-κB; **NG**, normoglycemic; **OSE-2**, osteoblast-specific element-2; **p53/AP-2**, p53/AP-2 composite binding site; **PA**, polyadenylation signal; **PAGE**, polyacrylamide gel electrophoresis; **PBS**, phosphate buffered saline; **PBST**, phosphate buffered saline with 0.1% Tween® 20 detergent; **PCR**, polymerase chain reaction; **PDB**, protein data bank; **PEA3**, polyoma enhancer A binding protein-3; **PI**, propidium iodide; **PIC**, protease inhibitor cocktail; **PLC**, phospholipase C; **PMSF**, phenylmethylsulfonyl fluoride; **p-Rb**, phosphorylated retinoblastoma; **PVDF**, polyvinylidene fluoride; **QR-2**, quinone reductase 2; **RARE**, retinoic acid responsive element; **Rb**, retinoblastoma; **RMSD**, root mean square deviation; **RMSF**, root mean square fluctuation; **RNA**, ribonucleic acid; **ROS**, reactive oxygen species; **ROS**, reactive oxygen species; **RZR/RORα**, retinoid Z receptor/retinoic acid receptor-related orphan receptor; **SAF-1**, serum amyloid A activating factor-1; **SBE**, STAT-binding element; **SDS**, sodium dodecyl sulphate; **SEM**, standard error of the mean; **Si**, silencer sequence; **S-IV**, Shatavarin-IV; **SP-1**, specificity protein 1; **SPRE**, stromelysin-1 PDGF-responsive element; **STED**, stimulated emission depletion; **TATA**, TATA box; **TBST**, Tris-buffered saline with 0.1% Tween® 20 detergent; **Tcf-4**, T-cell factor-4/β-catenin-binding site; **TIE**, TGF-β inhibitory element; **TIMP**, tissue inhibitor of metalloproteinase; **TNF-α**, tumor necrosis factor-alpha; **TRF**, octamer-binding protein; **TUNEL**, terminal deoxynucleotidyl transferase dUTP nick end labeling.

TABLE OF CONTENTS

Chapter 1

Review of Literature

REVIEW OF LITERATURE

1. STOMACH: STRUCTURE AND FUNCTION

The human stomach is an essential organ in the digestive system, serving a pivotal function in the second stage of digestion. It occupies the area between the esophagus and the duodenum, situated in the upper left quadrant of the abdominal cavity. The stomach functions as a temporary reservoir for the storage and mechanical distribution of food before its passage into the intestine. The stomach is a J-shaped, muscular organ segmented into four primary regions: the fundus, body, antrum, and pylorus (Wilson and Stevenson 2019).

1.1. Structure:

The fundus is a dilated region arching over the cardiac orifice (the passage from the esophagus to the stomach). The body, or intermediate area, is located distal to the fundus and constitutes the central and biggest section of the stomach. The antrum is the lowest, rather funnel-shaped section of the stomach. The pylorus transports food into the duodenum via a constricted aperture at the junction of the stomach and small intestine. Both the cardiac and pyloric apertures possess sphincter muscles that maintain closure of the adjacent areas, save during the passage of food. The stomach encases food until it is prepared for digestion.

The stomach walls consist of many layers from innermost to outermost: the mucosa, submucosa, muscularis externa, and serosa (Wilson and Stevenson 2019). The mucosa, the innermost layer, is lined by epithelial tissue and predominantly consists of gastric glands that release gastric juices. The fundus produces stomach secretions. The cardia secretes protective mucus that covers the inner stomach mucosal wall through mucus (Foveolar) cells. The mucus safeguards the stomach lining against degradation by gastric acids secreted by main cells (pepsin) and parietal cells (HCl). The submucosa consists of thick connective tissue and houses blood arteries, lymphatic vessels, and nerves. The submucosa provides support to the mucosal layer. This layer contains many folds, known as "rugae", which facilitate intraluminal expansion upon the introduction of food into the stomach. The muscularis externa encases the submucosa. The serosa is the outermost layer, consisting of many strata of connective tissue that interconnect with the peritoneum.

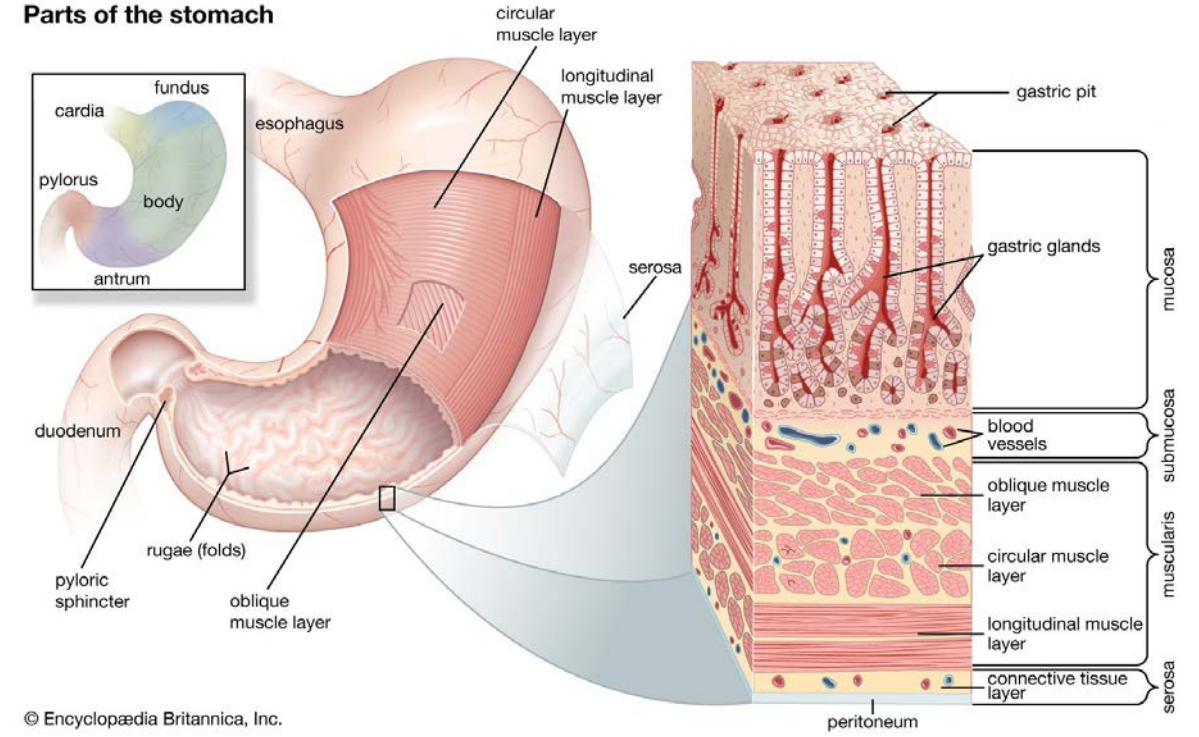

Figure 1. Structure of the human stomach. The human stomach is split into four regions: the fundus, the body, the antrum, and the pylorus. The pyloric sphincter separates the stomach from the duodenum. The stomach comprises three muscular layers: an external longitudinal layer, a middle circular layer, and an internal oblique layer. The inner lining has four layers: the serosa, muscularis, submucosa, and mucosa. The mucosa is highly populated with gastric glands that house cells responsible for the secretion of digesting enzymes, hydrochloric acid, and mucus. (Adapted from Encyclopaedia Britannica, Inc.)

1.2. Function

The main activities of the stomach are the temporary storage and partial chemical and mechanical digestion of food. The superior regions of the stomach (i.e., cardia, fundus, and body) relax with the introduction of food to accommodate larger volumes of intake. The inferior segment of the stomach contracts rhythmically to mechanically disintegrate food. The meal bolus amalgamates with gastric secretions in the inferior gastric area, chemically destroying the food. At this stage of digestion, partially digested food transforms into a mixture known as "chyme." The pyloric sphincter permits little amounts of adequately liquid chyme to enter the small intestine with each wave. Chyme undergoes further digestion in the duodenum.

Gastric juices are fluids naturally produced by the fundic cells to chemically break down meals. Gastric secretions comprise hydrochloric acid (HCl) and the enzyme pepsin. Hydrochloric acid is produced by the stomach parietal cells. This gastric acid secretion creates a very low luminal pH, in the range of 1 and 2. Pepsin is a degradation product of the proenzyme pepsinogen, which is released by the gastric main cells. Pepsinogen is transformed into pepsin upon interaction with hydrochloric acid. In addition to HCl, gastric parietal cells synthesize intrinsic factor, a glycoprotein essential for the transport and absorption of vitamin B12 (cobalamin) in the terminal ileum of the small intestine. The generation of intrinsic factors is crucial, as vitamin B12 is necessary for erythropoiesis and neurological function (Cheng et al., 2016; Fagoonee and Pellicano, 2019).

The stomach may digest food and convey it to the duodenum within 2 to 4 hours. Nevertheless, this rate is significantly influenced by the sort of food ingested. Carbohydrates and proteins are metabolized in the stomach relatively quickly, however, lipids such as triglycerides require a longer duration for processing by the stomach. The stomach does not mainly facilitate nutrition absorption. It also absorbs several chemicals, such as water (during dehydration), and some drugs including aspirin, amino acids, ethanol, caffeine, and water-soluble vitamins. The stomach contains neuroendocrine cells, such as gastrin-secreting G cells, which produce hormones essential for controlling acid secretion and gastric motility. The surface mucous cells secrete a mucus coating that safeguards the stomach wall from its acidic surroundings. Gastric acid can be fatal to certain bacteria and germs ingested, so safeguarding the body from infection and sickness (Gonsalves, 2019; Pimentel et al., 2019).

1.3. Clinical Significance

Clinically, the stomach is vulnerable to many medical conditions that present with analogous symptoms, including epigastric pain, burning, gnawing discomfort, nausea/vomiting (+/– blood), satiety, and distension. Pathologies can be sub-divided into following categories: anatomical pathologies (Hypertrophic Pyloric Stenosis); ulcerative pathologies (Peptic Ulcer Disease, Gastroesophageal Reflux Disease, Dyspepsia); inflammatory conditions (Inflammatory Bowel Disease, Gastritis); gastric cancers (Gastric adenocarcinoma, MALToma, carcinoid tumors, stromal tumors); and other pathologies (Menetrier's disease, Gastric Antral Vascular Ectasia, Gastroparesis) (Hsu et al., 2023). Such pathological manifestations can significantly impair digestion, nutrition, and quality of life. Proper stomach function is essential for maintaining metabolic health and preventing gastrointestinal disorders.

2. OVERVIEW OF GASTRIC CANCER

2.1. Gastric cancer: A brief introduction

Gastric cancer (GC) is a multifaceted disease which involves many factors, including environmental and genetic changes, that may affect its development (Yusefi et al. 2018). According to the estimations of GLOBOCAN 2020, GC is the 5th most common type of cancer and the 4th most prevalent reason for cancer-related mortality on a global scale (Sung et al., 2021) (Figure 2). The median survival rate of GC patients is usually less than 12 months for the advanced stage (Zhang and Zhang, 2017). Due to its heterogeneous nature, GC is a highly aggressive form of malignant cancer that poses a threat to global health (Gao et al. 2018).

Early gastric cancer symptoms may be associated with indigestion or a burning sensation (heartburn), which in most of the cases remains neglected in third-world countries. However, 2% of such cases that are referred for endoscopy are diagnosed with GC. Unfortunately, in most of the cases, GC is diagnosed at a late stage when the symptoms become more pronounced. Treatment of GC in its advanced or metastatic stage has achieved little progress with average survival of less than a year (Zhang and Zhang, 2017). Thus, continued research is needed with regard to early diagnosis, prevention and novel therapy. The current treatment regime for GC is comprised of mainly surgical removal with adjuvant chemotherapy or radiation therapy, in desired cases (Joshi and Badgwell, 2021).

The distribution of GC varies in different parts of the world with highest incidence rates documented in eastern Asia, eastern Europe and South America; while North America and Africa show the lowest recorded rates (Sung et al., 2021) (Figure 2 & 3). This indicates the association of multiple factors with the incidence of this disease. In India, the incidence of GC is higher in the southern and north-eastern states (Dikshit et al. 2011; Sharma and Radhakrishnan, 2011). Although, the etiology of GC is multi-factoral, more than 80% of the cases are associated with *Helicobacter pylori* infection (Khatoon et al. 2016). Other risk factors include high-salt diet, poor hygiene, lifestyle, bad socioeconomic conditions and susceptible genetic factors.

GC patients are often asymptomatic but sometimes there are a few symptoms like indigestion, heartburn, loss of appetite and abdominal discomfort in stage I GC patients; weakness, fatigue and bloating of stomach usually after meal are noticed in stage II GC patients; and stage III

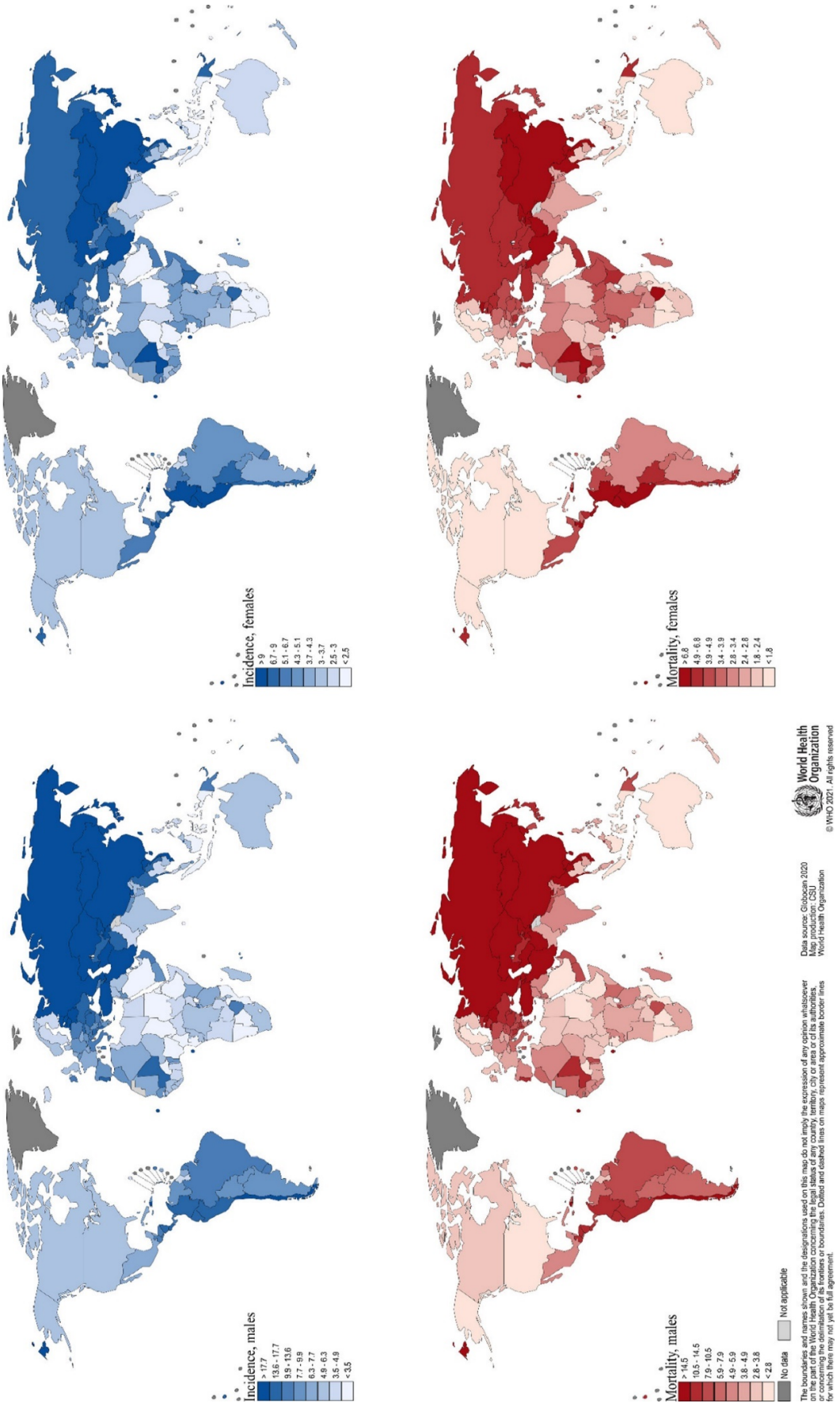

Figure 2. Worldwide gastric cancer incidence and mortality rates (age-adjusted according to the world standard population, per 100 000) in males and females in 2020. Adapted from GLOBOCAN 2020 (Sung et al., 2021)

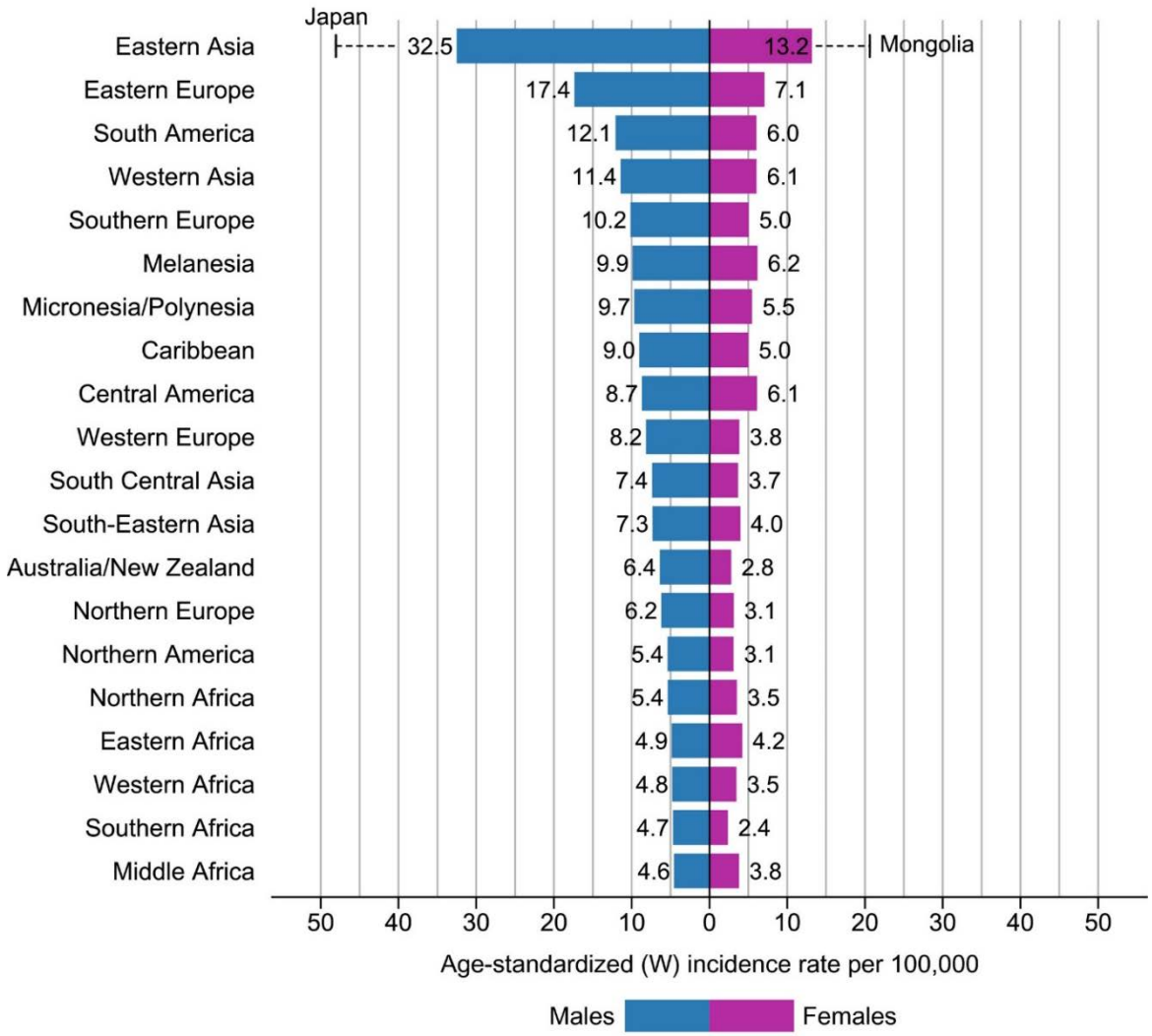

Figure 3. Region-wise occurrence of age-standardized rates according to sex for Gastric Cancer during 2020. The region-wise GC occurrence rate is shown in descending order of the age-standardized rate (per 100,000) among men and women throughout the world. The highest national rate for men and women is superimposed therein. The image is adapted from GLOBOCAN 2020 (Sung et al., 2021).

patients exhibit upper abdominal pain, nausea, occasional vomiting, diarrhoea or constipation, weight loss, bleeding and dysphagia.

2.2. Pathophysiology of gastric cancer

GC is clinically classified as early or advanced stage and histologically into different subtypes based on major morphological changes and further subdivided into various classes based on anatomic location. The widely known classification of GC is the Lauren classification; which,

recognizes two sub-types of GC: intestinal and diffuse type adenocarcinomas; in addition to indeterminate type as an uncommon variant (Lauren, 1965). The clinical symptoms, genetics, morphology, epidemiology, and expansion qualities of these subtypes differ significantly from one another. This division also influences surgical decisions, regarding the range of stomach resections. Tubular and glandular components with varying degrees of differentiation are displayed by the intestinal subtype. Whereas, the diffuse subtype has single cells with poor cohesive properties lacking gland formation (Vogelaar et al. 2017). Furthermore, GC with signet ring cells is rather common and is categorized by the Lauren classification as a "diffuse type" (Lauren, 1965). Presently, signet ring cell carcinoma is identified as a weakly cohesive form of cancer. This type of cancer generally consists of tumor cells with clear cytoplasmic mucin and an eccentrically located crescent-shaped nucleus (Pernot et al. 2015). According to the age of the individual during diagnosis, GC can be classified as either traditional (older than 45) or early-onset (45 years or under) (Milne and Offerhaus, 2010).

Based on anatomic location, the International Gastric Cancer Association separates GCs into type I, type II and type III to represent the tumors at distal esophagus, cardia and stomach distal to cardia, respectively. Most recently, the 7th edition of the TNM classification by the American Joint Committee on Cancer has modified the classification based on the location of tumor epicentre. If the epicentre is >5cm distal to the gastroesophageal junction (GEJ), or within 5cm of GEJ but does not extend into the GEJ or esophagus, then it is called as gastric carcinoma. Most early gastric tumors are small, measuring 2-5cm in size, and often located at lesser curvature around angularis. Grossly, early GC is divided inti Type I for the tumor with protruding growth, Type II with superficial growth, Type III with excavating growth, and Type IV for infiltrating growth with lateral spreading. WHO recognizes four major histologic patterns of GC; viz., tubular, papillary, mucinous and poorly cohesive; plus uncommon histologic variants.

GC does not arise *de novo* from normal epithelium, but occurs through successive changes. These changes are well-characterized for the intestinal type of human GC; where there is a transformation of normal mucosa into a mucosa that resembles intestinal epithelium (intestinal metaplasia). The presence of intestinal metaplasia increases the risk of GC, which is proportional to the extent of surface area involved in metaplasia. Subsequently, such intestinal metaplasia may progress to dysplasia and ultimately to carcinoma. This theoretical sequence of GC development is illustrated in Figure 4.

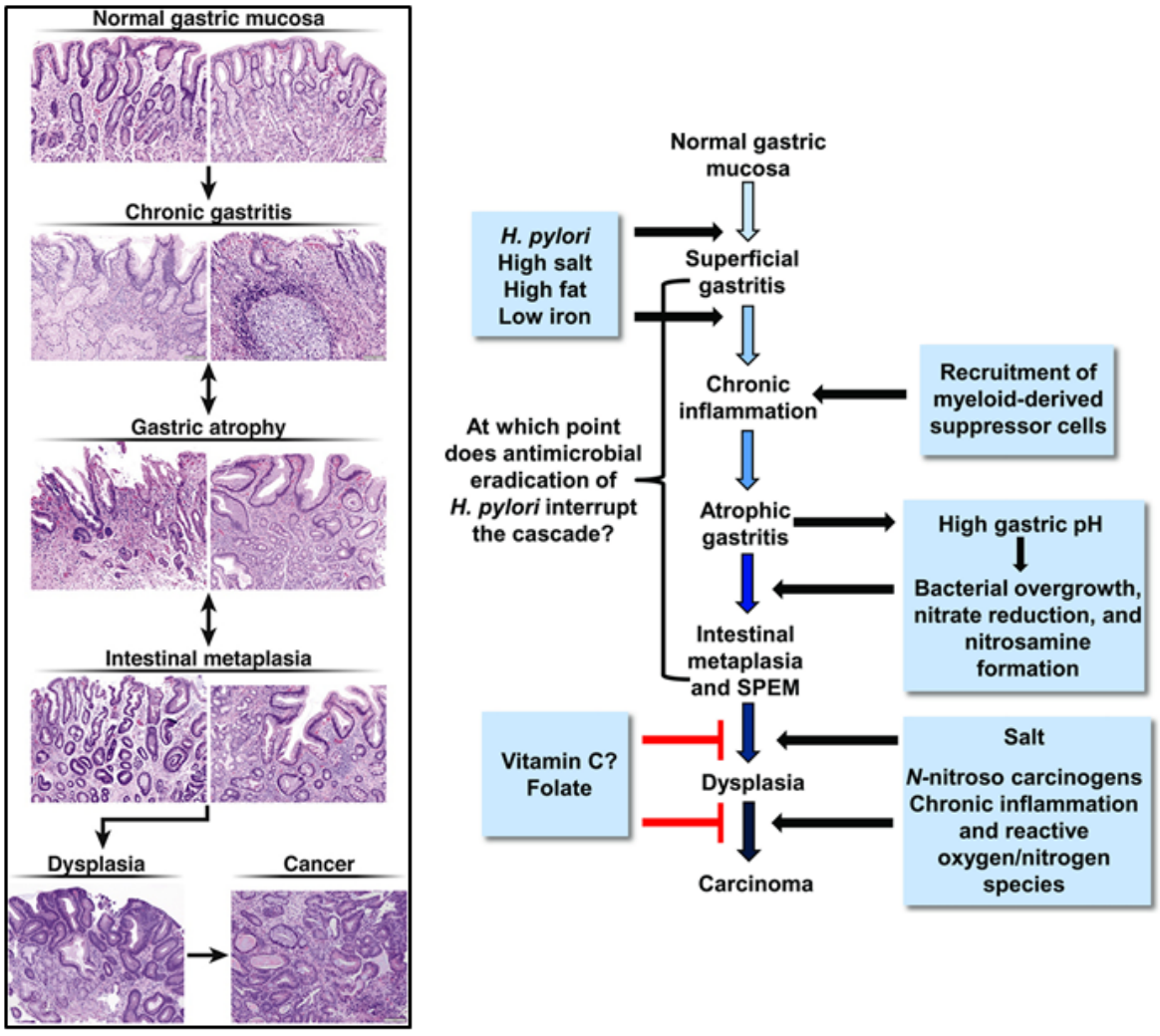

Figure 4. Correa cascade of pathological events in the development of gastric adenocarcinoma. Adapted from Fox and Wang, 2014 & Gawron et al., 2020.

In contrast, the diffuse type GC presumably arises as single cell changes in the mucus neck region of the gastric glands. Then, these cells may proliferate and invade out from the crypt into the lamina propria. A hypothesis about gastric carcinogenesis was proposed in 1975 by Correa et al (Correa et al. 1975). According to this hypothesis, GC is a multistep and multi-factorial process which involves environmental factors as well as other factors like acid secretion, bacterial overgrowth and bacterial production of nitrites or N-nitroso compounds from dietary nitrites (Figure 4). The result of this cascade is the progressive spectrum of histological states ranging from normal gastric epithelium to gastric adenocarcinoma.

2.3. Epidemiology of gastric cancer

During the early 20th century, GC was the most frequent type of cancer. Over the past century, mortality rates have fallen drastically in developed countries. But, till 2020, GC is considered as a significant cancer globally. It is responsible for more than a million new case records and 769,000 proclaimed deaths (or one in every 13 deaths worldwide) (Sung et al. 2021). GC holds fifth position in terms of incidence and fourth position in terms of mortality worldwide (Sung et al. 2021). Men are two times more susceptible in developing GC as compared to women. In a number of South-Central Asian nations, such as Iran, Afghanistan, Turkmenistan, and Kyrgyzstan, GC is the most prevalent cancer diagnosed in men and the primary cause of cancer-related deaths (Sung et al. 2021). The highest incidence rates are reported from Eastern Asia and Eastern Europe. Japan shows highest GC cases in men, whereas, Mongolia has the highest recorded GC cases in women. However, the GC occurrence rate is modest in Northern America and Northern Europe and quite similar to those observed across the African regions.

The incidence of gastric cancer has steadily declined worldwide over the past 50 years. These declines preceded the successful reduction of *H. pylori* infection, and are likely attributable to changes in food preservation, such as less pickling of vegetables, and less smoking and processing of meat. The decline has also been elicited by the greater availability of fresh fruits and vegetables (Balakrishnan et al. 2017). The second major factor in gastric cancer decline has been the success in preventing and treating *H. pylori* infections in much of the developing world. As many as 90% of cases of non-cardia gastric cancer are attributable to *H. pylori*, which explains why the incidence of that subtype of gastric cancer has declined in step with declining infection rates (Plummer et al. 2015; Balakrishnan et al. 2017). Cancers of the gastric cardia due to *H. pylori* infection requires the association with gastric atrophy. However, cancers in the gastric cardia are not generally the outcome of *H. pylori* infection (Kamangar et al. 2006). Present research works suggest a dual etiology for GC of cardia, some related to *H. pylori* infection and others to excess body mass and injury due to gastroesophageal reflux disease, showing similarities with esophageal adenocarcinoma.

GC incidence in India is overall less compared to worldwide incidence (Dikshit et al. 2011; Sharma and Radhakrishnan, 2011). Out of the 10,89,103 cases of GC diagnosed worldwide in 2020, only 60,222 cases were diagnosed in India (Morgan et al. 2022). The age-standardized rate (ASR) per 100,000 population of GC in India is 6.1 for males and 2.9 for females (Morgan et al. 2022). Whereas, the worldwide ASR is 15.8 and 7.0 for males and females, respectively

(Morgan et al. 2022). The incidence of GC in Mizoram has been reported to be the highest in India. Such high prevalence of GC in Mizoram has been attributed to dietary and possibly some unknown genetic factors. Similar to global trends, a decreasing trend of GC incidence has been observed over the last 30 years in India as well (Dikshit et al. 2011; Sharma and Radhakrishnan, 2011).

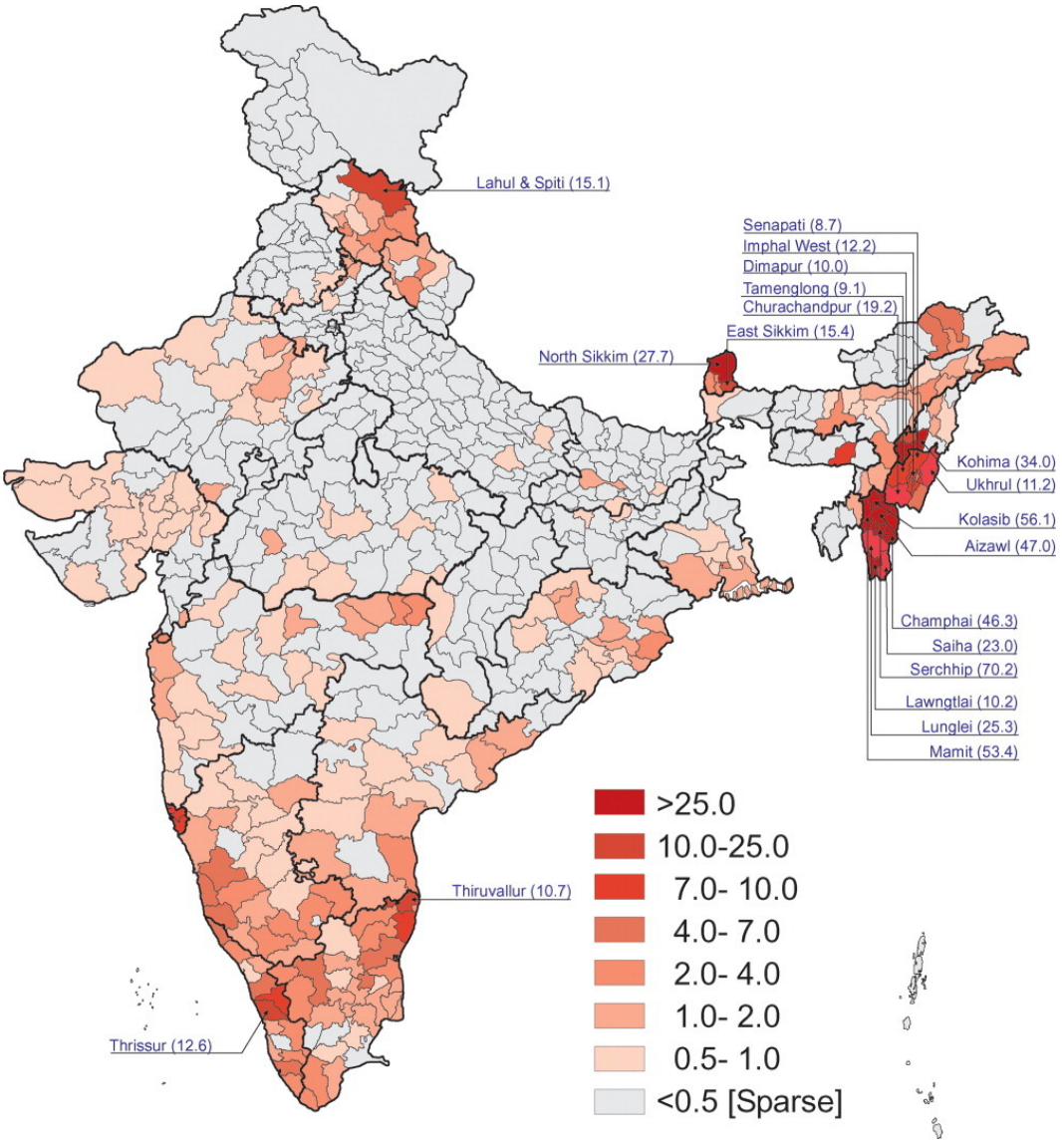

Figure 5. District-wise microscopic age adjusted incidence rates (MAAR) of gastric cancer per 100,000 males in India for the year 2001–2002. Data Source: NCRP database, ICMR. (Adapted from Nandakumar et al. 2005)

2.4. Risk factors for gastric cancer development

Multiple variables markedly elevate the risk of developing gastric cancer, including *Helicobacter pylori* (*H. pylori*) infection, tobacco use, alcohol use, obesity, sedentary lifestyle, and excessive salt intake. The modifiable risk factors, as identified by Poorolajal et al. (2020), can be successfully addressed in gastric cancer prevention initiatives. Besides these risk factors, family history, dietary habits, and Epstein–Barr virus (EBV) infections also play a significant role in GC development.

A family history of GC is also one of the most crucial risk factors (Yaghoobi et al., 2010; Choi and Kim, 2016). However, GCs mostly occur randomly in scattered instances or isolated outbursts, with about 10% showing a familial inheritance pattern. Among the inherited GCs, Mendelian inheritance pattern is observed in less than 3% of all GC cases (Boland and Yurgelun, 2017). The most recognizable form of familial GC, hereditary diffuse gastric cancer (HDGC), is caused by mutations in the cadherin 1 (CDH1) gene (Pinheiro et al., 2014). The World Cancer Research Fund/American Institute for Cancer Research (WCRF/AICR) concluded that fruits and vegetables act as protective agents against gastric cancer (GC) growth, while broiled and charbroiled meats, salt-preserved meals, and smoked foods likely promote GC development (Kim et al., 2014). Carcinogens of food-origin may interfere with gene expression leading to alterations and genetic changes in gastric epithelial cells. Salty taste preference, always using table salt, and a greater high-salt and salt-preserved foods resulting in a high intake of sodium chloride has been shown to damage the gastric mucosa, leading to increased risk of GC (Morais et al., 2022). N-nitroso compounds have been shown to elevate the chance of developing GC, particularly in non-cardia regions (Keszei et al., 2013).

The World Health Organization has recognized *H. pylori*, a gram-negative bacterium, as a class I carcinogen for GC development (Ishaq and Nunn, 2015). *H. pylori* causes oncogenesis through two main mechanisms: an indirect inflammatory response to stomach mucosa infection and a direct epigenetic influence on gastric epithelial cells (Kim and Wang, 2021). In addition to *H. pylori* infection, the Epstein–Barr virus (EBV) is the second factor linked to the development of GC. EBV is a widespread infectious agent. Approximately 10% of GCs are reported as EBV-positive; however, insufficient reports make us unable to establish any definitive etiological relation between EBV and GC development (Nishikawa et al., 2018).

3. OVERVIEW OF DIABETES

3.1. Diabetes: A brief introduction

Diabetes mellitus (DM) or diabetes is a metabolic disorder characterized by elevated blood glucose levels. The term diabetes mellitus is adopted from the Greek word "*diabetes*", which translates to 'siphon' meaning 'to pass through' and the Latin word "*mellitus*", which means 'sweet'. Diabetes encompasses several categories: type 1, type 2, gestational diabetes, neonatal diabetes, and maturity-onset diabetes of the young (MODY). Secondary causes of diabetes are related to endocrinopathies and use of steroids. The primary subtypes of diabetes are Type 1 diabetes mellitus (T1DM) and Type 2 diabetes mellitus (T2DM), characterized by impaired insulin secretion (in T1DM) and/or action (in T2DM). T1DM typically manifests in young adults, whereas T2DM is generally associated with older adults experiencing long-term hyperglycemia resulting from suboptimal lifestyle and food habits. The pathogenesis of T1DM and T2DM differs significantly, resulting in distinct etiologies, clinical presentations, and treatment approaches for each type.

3.2. Types of diabetes

In the year 1889, Mering and Minkowski identified the pancreas's role in the pathogenesis of diabetes. The islets of Langerhans in the pancreas contain two primary subclasses of endocrine cells; viz., the β cells, which produce insulin, and the α cells, which secrete glucagon. β and α cells continuously adjust their hormone secretion levels in response to the blood glucose levels. An imbalance between insulin and glucagon leads to dysregulated glucose levels, resulting in diabetes.

3.2.1. Type 1 diabetes mellitus (T1DM)

The term "type-1 diabetes mellitus" has replaced some former terminologies, including childhood-onset diabetes, juvenile diabetes, and insulin-dependent diabetes mellitus (IDDM). T1DM is characterized by the autoimmune-mediated damage of pancreatic β cells. The outcome is the complete destruction of β cells, resulting in an absence or significant reduction of insulin levels (Sapra and Bhandari, 2023).

3.2.2. Type 2 diabetes mellitus (T2DM)

The term "type-2 diabetes mellitus" has replaced some former terminologies, including adult-onset diabetes, obesity-related diabetes, and non-insulin-dependent diabetes mellitus (NIDDM). T2DM is characterized by a gradual onset, resulting from an altered balance among level of insulin and its sensitivity, leading to a functional insulin deficiency. Resistance to insulin arises from multiple factors, predominantly obesity and aging. T2DM encompasses a complex interaction between genetic factors and lifestyle choices. Evidence indicates that T2DM exhibits a stronger hereditary profile than T1DM. Most individuals with T2DM have at least one parent diagnosed with T2DM (Sapra and Bhandari, 2023).

3.2.3. Maturity-onset diabetes of the young (MODY)

MODY is a heterogeneous condition characterized by diabetic condition which is not dependent on insulin, diagnosed in youth, typically before the age of 25. It exhibits autosomal dominant inheritance and is not associated with autoantibodies, unlike T1DM. Multiple genes are implicated in this condition, notably mutations in hepatocyte nuclear factor-1-alpha (HNF1A) and the glucokinase (GCK) genes (Shields et al., 2010; Sapra and Bhandari, 2023). The genetic basis of this disease remains ambiguous, as certain patients exhibit mutations without manifesting the disease, while others present clinical symptoms of MODY despite lacking identifiable mutations (Sapra and Bhandari, 2023).

3.2.4. Gestational diabetes

Gestational diabetes refers to diabetes that occurs during pregnancy. Excessive proinsulin is believed to contribute to gestational diabetes. Some researchers propose that elevated levels of hormones, including progesterone, cortisol, prolactin, human placental lactogen, and estrogen, may influence beta-cell function and peripheral insulin sensitivity (Sapra and Bhandari, 2023).

3.3. Pathophysiology of diabetes

Diabetes mellitus is a heterogeneous metabolic disorder characterized by various types, each with a unique pathophysiological origin, yet frequently manifests as a disorder with overlapping and challenging-to-differentiate features. The pathophysiology of diabetes is intricate, marked by a lack of insulin (type 1) or peripheral insulin resistance (type 2), disrupted regulation of hepatic glucose production, and deteriorating β-cell function, ultimately resulting in β-cell failure (Banday et al., 2020). Diabetes encompasses various hormones, including

insulin, glucagon, and growth hormone. The interplay of these hormones with the liver and their role in renal function complicates the identification of the pathological mechanisms of this disease, resulting in significant variability among patients. Diabetes is characterized by elevated blood glucose levels, or hyperglycemia, resulting from abnormalities in insulin secretion, insulin action, or both. Hyperglycemia presents in multiple forms, leading to dysfunctions in carbohydrate, fat, and protein metabolism. Chronic hyperglycemia frequently results in multiple microvascular and macrovascular complications related to diabetes, which are primarily accountable for the morbidity and mortality associated with the condition. Hyperglycemia is the principal biomarker utilized for diagnosing diabetes (Banday et al., 2020).

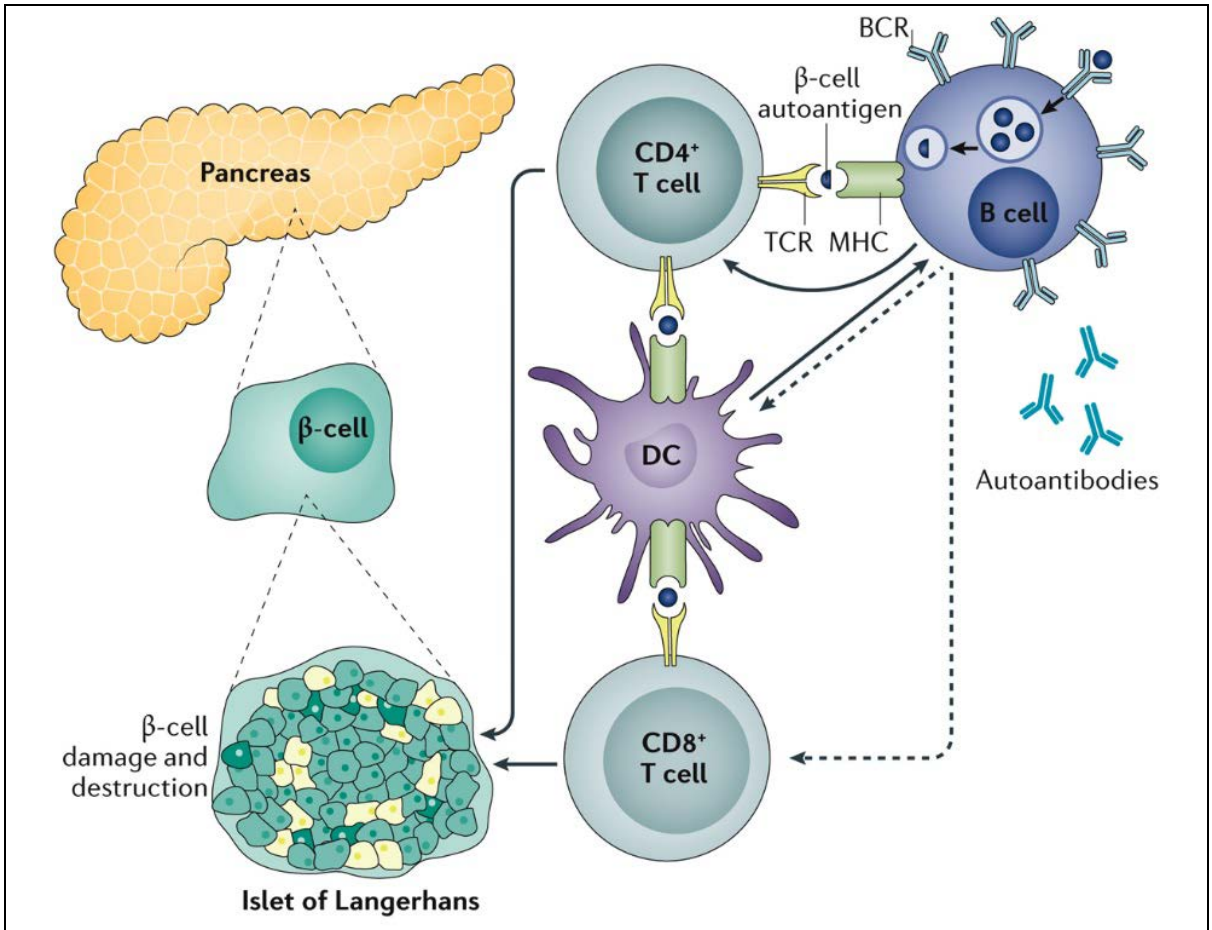

Figure 6. Pathogenesis of T1DM. Type 1 diabetes mellitus (T1DM) is an immunological disorder. Activated B cells engage in interactions with dendritic cells (DCs) as well as $CD4^+$ and $CD8^+$ T cells. Antigen presentation by B cells and dendritic cells facilitates the activation of β-cell-specific T cells. Furthermore, the exposure of B cells to β-cell autoantigens results in the generation of islet-targeting autoantibodies, which act as indicators for asymptomatic illness. Dashed arrows denote the possible interactions between B cells and $CD8^+$ T cells, as

well as between B cells and dendritic cells (DCs). BCR refers to the B cell receptor; TCR denotes the T cell receptor. Adapted from Katsarou et al., 2017.

In this context, blood glucose levels exceeding 180 mg/dL are typically classified as hyperglycemic; however, due to the involvement of diverse pathophysiological mechanisms, a definitive cutoff point is not yet established. Osmotic diuresis occurs in patients when the transporters for glucose in the nephron become saturated at elevated blood glucose levels. Serum glucose levels exceeding 250 mg/dL are associated with the onset of symptoms such as polyuria and polydipsia, though the effect may vary.

Chronic hyperglycemia leads to the nonenzymatic glycosylation of proteins and lipids. The magnitude can be quantified through the glycation hemoglobin (HbA1c) test. Glycation results in damage to small blood vessels in the retina, kidneys, and peripheral nerves. Elevated glucose levels tend to further accelerate this process. Such damage results in the typical complications associated with diabetes, including diabetic retinopathy, nephropathy, and neuropathy, which can lead to preventable outcomes such as blindness, dialysis, and amputation, respectively (Sapra and Bhandari, 2023).

3.4. Epidemiology of diabetes

Diabetes continues to pose a significant public health challenge. T2DM constitutes the majority of diabetes cases and is largely preventable; in certain instances, it may be reversible if detected and managed early in the disease progression. Evidence suggests that the prevalence of diabetes is rising globally, primarily attributed to an increase in obesity driven by various factors. Preventing and controlling T2DM continues to pose significant challenges.

In 2021, the global population of individuals with diabetes reached 529 million (95% uncertainty interval [UI] 500–564), resulting in an age-standardized total diabetes prevalence of 6.1% (5.8–6.5) (GBD 2021 Diabetes Collaborators, 2023). The incidence of T1DM progressively rises from birth, reaching its peak between the ages of 4 to 6 years, and again from 10 to 14 years (Felner et al., 2005). The prevalence among individuals under the age of 20 is approximately 2.3 per 1,000 (Sapra and Bhandari, 2023). The prevalence of T1DM has been rising globallyr, anging from 2% to 5% annual increase in various countries of Europe, Australia, and the Middle Eas (Patterson et al., 2009).

Figure 7. Age-standardized total diabetes prevalence rates in 2021. ATG=Antigua and Barbuda. VCT=Saint Vincent and the Grenadines. LCA=Saint Lucia. TTO=Trinidad and Tobago. Isl=Islands. FSM=Federated States of Micronesia. TLS=Timor-Leste. Adapted from GBD 2021 Diabetes Collaborators, 2023.

The inception of T2DM typically occurs in the later phases of life; however, rising obesity rates among adolescents have contributed to increased diagnosis of T2DM cases in young individuals. The prevalence of T2DM is approximately 9% in the overall population of the United States, while it rises to about 25% among individuals aged 65 and older (Sapra and Bhandari, 2023). The International Diabetes Federation (IDF) estimated that in 2015, 1 in 11 adults aged 20 to 79 years globally had diabetes mellitus (Sapra and Bhandari, 2023). In a recent study, the IDF has predicted that the global burden of diabetes will rise to 783.2 million people by the year 2045 (Sun et al., 2022). The most significant relative increase in diabetes prevalence from 2021 to 2045 is projected in middle-income countries (21.1%), in contrast to high-income (12.2%) and low-income (11.9%) countries (Sun et al., 2022).

3.5. Diabetes in gastric cancer

Diabetes and hyperglycemia significantly influence cancer development and progression through multiple mechanisms. Elevated glucose levels in the bloodstream augment cancer cell metabolism by enhancing the Warburg effect, thereby providing essential energy for enhanced tumor growth. Elevated blood glucose levels increase oxidative stress and result in the production of more reactive oxygen species (ROS) (González et al., 2023). This causes DNA damage, promotes mutations, and increases the likelihood of cancer development (Thonsri et al., 2021). Chronic hyperglycemia and insulin resistance result in elevated insulin levels, activating the insulin and insulin-like growth factor (IGF) signaling pathways, promoting cell proliferation, angiogenesis, and reduced apoptosis (AbdlWhab et al., 2024; Kotsifaki et al., 2024). These pathways create conditions that enhance tumorigenesis, thereby aiding cancer progression (Kotsifaki et al., 2024). Chronic inflammation linked to diabetes generates cytokines that may promote tumor growth and metastasis. Diabetes-associated immune dysfunction reduces the body's ability to recognize and eradicate cancer cells, consequently increasing cancer risk (Berbudi et al., 2020). Several epidemiological studies link diabetes to elevated incidences of several cancers, including gastric cancer (Miao et al., 2017; De la Torre et al., 2024). It has been found that the risk of developing gastric cancer is particularly high during the first decade following diabetes diagnosis (De la Torre et al., 2024). The association between diabetes and cancer highlights the importance of regulating glucose and insulin levels to mitigate cancer risk. Certain cancer therapies may worsen glycemic control, underscoring the necessity for integrated management strategies for both conditions.

4. MATRIX METALLOPROTEINASES (MMPs): AN OVERVIEW OF THEIR STRUCTURE AND FUNCTION

Matrix metalloproteinases (MMPs) are proteases that break extracellular matrix proteins and thereby regulate cellular behaviors such as apoptosis, proliferation, differentiation, migration, and invasion, as well as angiogenesis and immune surveillance. They belong to the metzincin family of proteases, which includes bacterial serralysins and astacins, adamalysins (a disintegrin and metalloproteinase domain or ADAMs), and matrixins and are distinguished by the presence of zinc in the catalytic cleft (matrix metalloproteinases or MMPs) (Verma and Hansch 2007) (Lu et al. 2012). Metzincins harbor three histidine (H) residues to bind the zinc ion at their catalytic site (Gomis-Rüth 2009). MMP was first discovered during the investigation of the tadpole tail undergoing metamorphosis (Brinckerhoff and Matrisian 2002). To date, 27 different vertebrate MMPs have been recognized, of which 24 are found in humans (Freije et al. 2003) (Khokha et al. 2013).

4.1. Structural diversity and classification of MMPs

MMPs have an amino-terminal signal sequence (Pre) that leads them to the endoplasmic reticulum, as well as an 80-amino-acid propeptide (Pro) domain that contains a cysteine-switch motif. Furthermore, the catalytic domain is 170 amino acids long and contains two zinc ions (one catalytic and the other structural) that interact with the zinc-binding motif HEXXHXXGXXH. The catalytic domain also includes a “Met-turn” structure that stabilizes it by containing eight residues from the catalytic zinc ion. The cysteine residue in the pro-peptide domain binds to the catalytic zinc ion, preventing it from being accessed by a water molecule and so inactivating MMP until the pro-peptide domain is cleaved. A linker segment of varied length connects the catalytic and haemopexin domains. The haemopexin domain at the C-terminus is around 200 amino acids long and forms a propeller blade shape. The haemopexin domain is necessary for MMP substrate selectivity (Khokha et al. 2013). A disulfide bond (S–S) connects the first and final of the four repetitions in the hemopexin-like domains. Inserts or patches that mimic collagen-binding type II repetitions of fibronectin make up the gelatin-binding MMPs (Fi). Furin-activated secretory MMPs have a recognition motif for intracellular furin-like serine proteinases (Fu), flanked by their pro-peptide and catalytic domains, which allows these proteases to work intracellularly (Page-McCaw et al. 2007). This motif can also be seen in MMPs that include vitronectin-like inserts (Vn) and membrane-type MMPs (MT-MMPs). The glycosylphosphatidylinositol (GPI)-anchored MMPs are found at the carboxy-

terminal end of MT-MMPs. They have a transmembrane domain (TM), a single-span transmembrane domain, a very short cytoplasmic domain (Cy), and a transmembrane domain (TM). MMP-23 also comprises a third form of membrane-linked MMP, which is a type II transmembrane MMP with an N-terminal signal anchor (SA) that leads it to the cell membrane (Page-McCaw et al. 2007) (Figure 8).

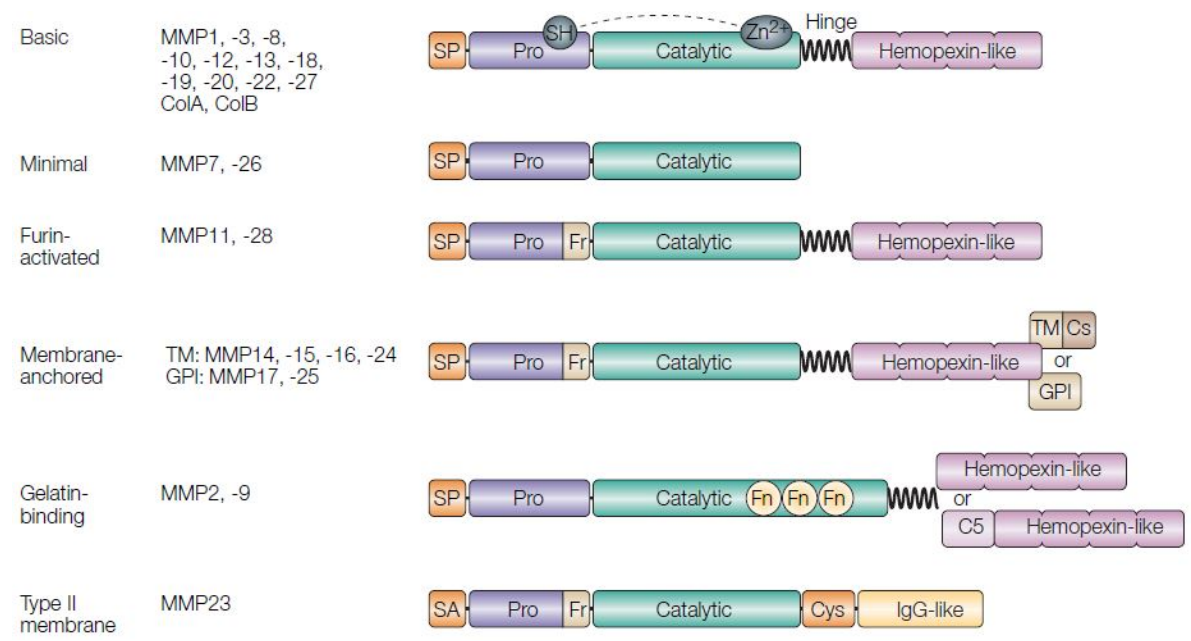

Figure 8. Domain structure of the mammalian MMP family. The important features of matrix metalloproteinases (MMPs) are illustrated, showing the minimal domain structures. C5, type-V-collagen-like domain; Col; collagenase-like protein; Cs, cytosolic; Cys, cysteine array; Fn, fibronectin repeat; Fr, furin-cleavage site; Pro, pro-domain; SH, thiol group; SP, signal peptide; Zn, zinc. Adapted from Parks et al. 2004

MMPs are classified as the matrixin subfamily of the zinc metalloprotease family and the matrixin clan of metalloprotease (Page-McCaw et al. 2007). MMPs are classified as collagenases, gelatinases, stromelysins, matrilysins, membrane-type (MT)-MMPs, and others based on their domain organization and substrate specificities. Though a number nomenclature (e.g., MMP-2, MMP-9, etc.) is now favored due to some overlap with substrate specificities in the many MMPs.

4.2. Transcriptional modulation of MMPs

MMPs are mostly regulated at the steps of transcription, zymogen activation, and inhibition (Figure 9) (Page-McCaw et al. 2007). Additionally, regulations are also implicated in the steps of protein synthesis, at levels of secretion and intracellular trafficking, subcellular or extracellular localization, etc.

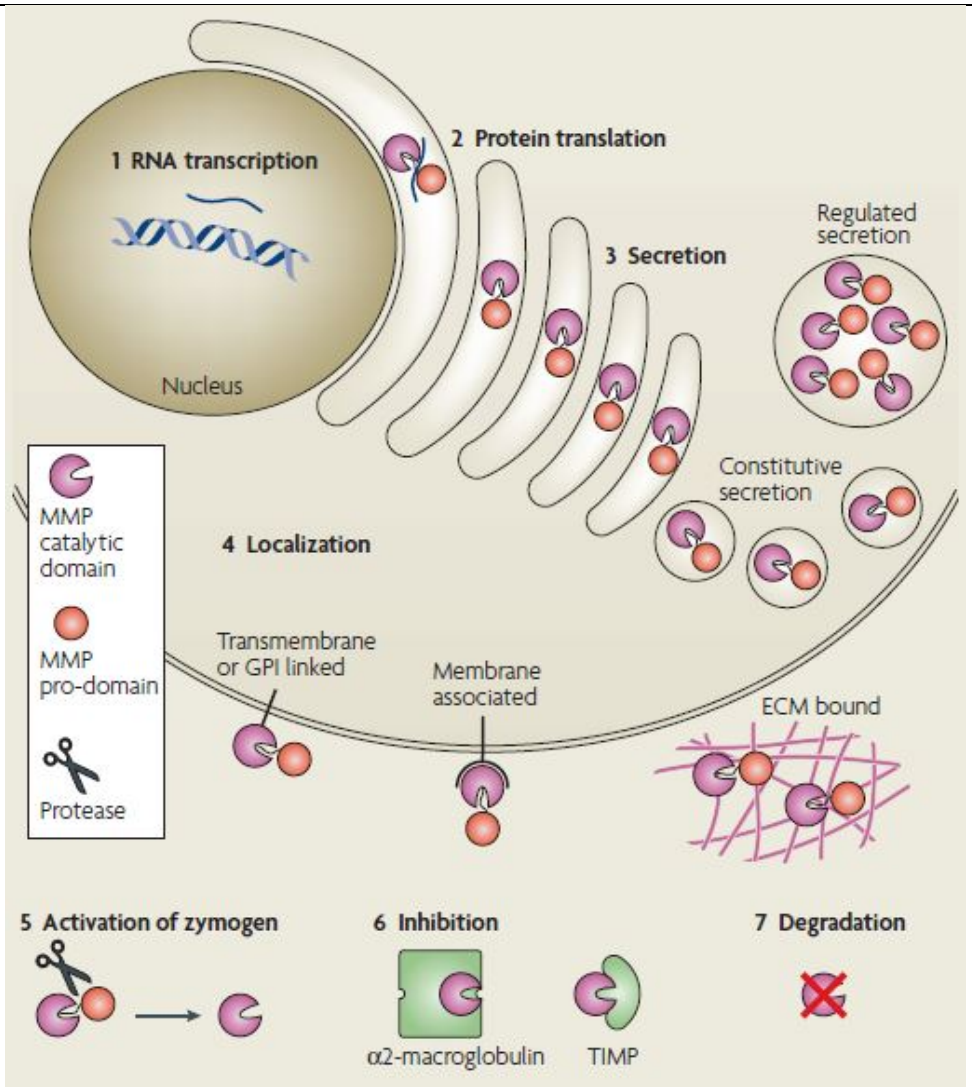

Figure 9. Regulation of extracellular proteolysis. MMP function can be controlled at many levels. In addition to (1) RNA transcription and (2) protein synthesis, MMP function can be regulated at the levels of (3) secretion, intracellular trafficking, (4) subcellular or extracellular localization, (5) activation of the zymogen form, (6) expression of their endogenous protein inhibitors, such as tissue inhibitors of metalloproteinases (TIMPs) and α2-macroglobulin, and (7) protease degradation. GPI, glycosylphosphatidylinositol. (adapted from Page-McCaw et al 2007).

The MMP promoter contains a large number of cis-acting elements that are modulated/regulated by a variety of trans-activators such as AP-1 (activator protein 1), TCF4 (transcription factor 4), NFB (nuclear factor kappa-light-chain-enhancer of activated B cells), SP-1 (specificity protein 1), and PEA3, among others (Yan and Boyd 2007). The JUN, FOS, ATF (activating transcription factor), and MAF (musculoaponeurotic fibrosarcoma) protein families are members of the AP-1 protein family, which may form homodimers and heterodimers via their leucine-zipper domains. Distinct dimers recognize different sequence regions in the promoters and enhancers of target genes depending on the combinations (Eferl and Wagner 2003). Most of MMPs contain the TATA box (-30bp) and the AP-1 site at about bp upstream of the transcriptional start site plays a dominant function in the transcriptional activation of the MMP promoters (Figure 10) (Yan and Boyd 2007).

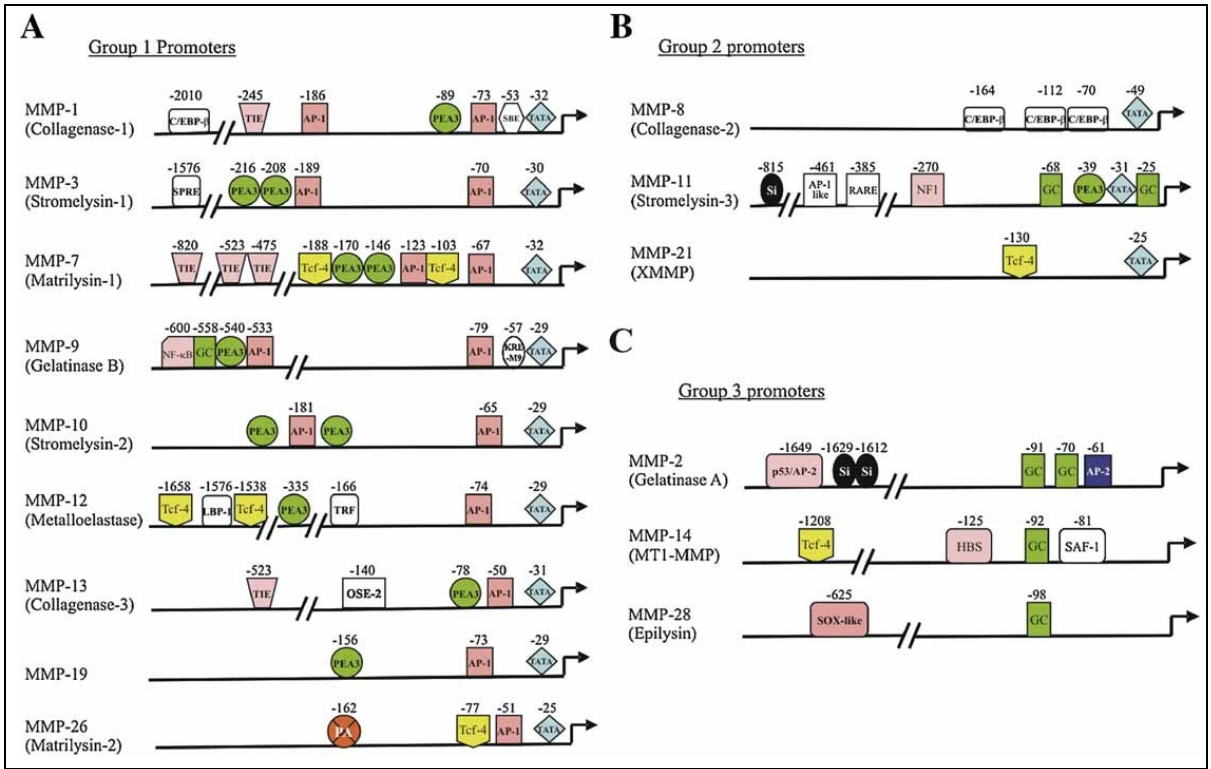

Figure 10. Cis-elements in human MMP promoters. (Abbreviations: AP-1, activator protein-1; AP-2, activator protein-2; C/EBP-β, CCAAT/enhancer binding protein-β; GC, Sp-1-binding site; HBS, HIF-binding site; KRE-M9, keratinocyte differentiation factor-1 responsive element-4; LBP-1, leader-binding protein; NF1, nuclear factor-1; NF-κB, nuclear factor-κB; OSE-2, osteoblast-specific element-2; p53/AP-2, p53/AP-2 composite binding site; PA, polyadenylation signal; PEA3, polyoma enhancer A binding protein-3; RARE,

retinoic acid responsive element; SBE, STAT-binding element; Si, silencer sequence; SPRE, stromelysin-1 PDGF-responsive element; TATA, TATA box; Tcf-4, T-cell factor-4/β-catenin-binding site; TIE, TGF-β inhibitory element; TRF, octamer-binding protein; SAF-1, serum amyloid A activating factor-1). Adapted from Yan and Boyd 2007.

AP-1 is evidenced to regulate different MMPs, including MMP-1, MMP-3, MMP-7, and MMP-9 by several external stimuli like growth factors, cytokines, and cellular stress signals. Additionally, NFκB, PEA3, and TCF-4 are vital regulators for MMP-7,-14,-12,-26 (Yan and Boyd 2007). TCF is mainly documented to control MMP gene expression through Wnt-β-catenin mediated signaling pathway (Ilyas 2005), whereas NFκB mediated signaling pathway regulates MMP-9, -3, and -11 expressions (Overall and López-Otín 2002).

4.3. Regulation of MMPs activity

All MMPs are translated as latent precursors, and activation of the form occurs via the removal of the pro-domain or chemical modification of the cysteine amino acid residue by a mechanism called “cysteine switch mechanism” (Springman et al. 1990) (Strongin et al. 1995) (Figure 11).

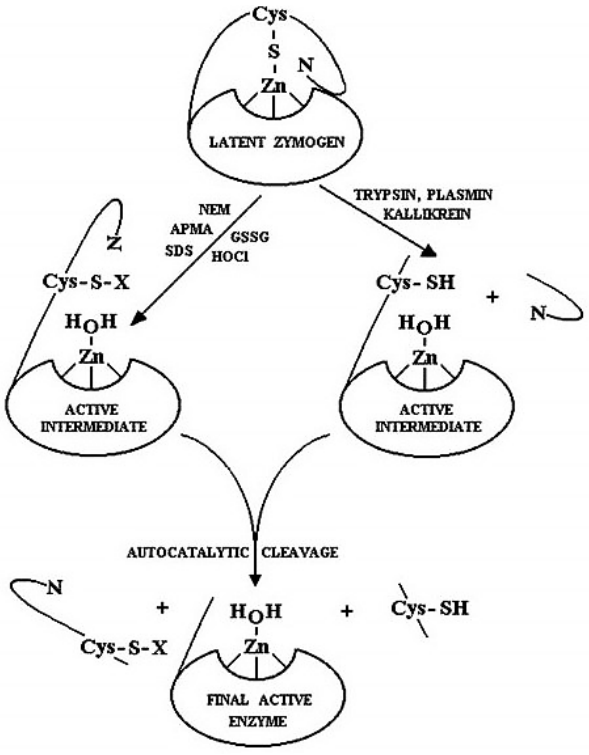

Figure 11. Cysteine switch mechanism for activation of MMP as proposed by Springman et.al. 1990

A conserved unpaired cysteine residue in the pro-domain of MMPs forms a cysteine switch, and this notion has been supported by structural analysis of proMMP-2 and proMMP-3 (Van Wart and Birkedal-Hansen 1990). Additionally, Plasmin and other serine proteases have been implicated in the maturation of pro-MMPs (Monea et al. 2002). Integrins are also reported to form part of this activation complex, thereby being involved in the pericellular activation of specific MMPs (Dumin et al. 2001). Allosteric activation of pro-MMPs occurs through interactions between pro-MMPs and other molecules that induce a conformational change in the pro-MMP disrupting the cysteine switch and allowing autolytic cleavage of the pro-domain (Ra and Parks 2007). The function of MMPs can also be modulated by reactive oxygen species (ROS). These oxidants at low concentrations initially activate MMPs via oxidation of the pro-domain cysteine but eventually inactivate MMPs by modification of amino acids of the catalytic domain by hypochlorous acid which is produced by enzyme myeloperoxidase from inflammatory cells (Fu et al. 2003).

4.4. Inhibitors of MMPs

The activities of MMPs are tightly regulated in vivo by two foremost inhibitors (i) α2-macroglobulin and (ii) TIMP (tissue inhibitor of metalloproteinases1-4). The α2-macroglobulin is a tissue fluid and blood protease inhibitor with a broad scope. By enclosing/entrapping the whole enzyme and clearing it by LDL receptor-related protein-1 driven endocytosis, this homo-tetrameric macromolecule (725 kDa) inhibits approximately all kinds of endopeptidases (Baker et al. 2002). TIMPs, on the other hand, are endogenous MMP inhibitors that interact and bind MMPs in a 1:1 stoichiometry. TIMPs are made up of two distinct domains: a larger N-terminal domain and a smaller C-terminal domain, both of which are stabilized by three conserved disulfide links. The N terminal domain of TIMPs may fold independently and has a wedge-like shape. A disulfide bond from a neighboring ridge slot into the catalytic domain of MMPs connects the N-terminal four amino acid residues Cys1-Thr-Cys-Val4. MMPs' catalytic zinc atom is bidentally coordinated by Cys 1 (Nagase 2016).

4.5. MMPs in gastric cancer and diabetes

MMPs are a group of Zn^{+2}-comprising, Ca^{+2}-requiring enzymes which are essential for the degradation and restructuring of the extracellular matrix (ECM). MMP dysregulation can compromise integrity of ECM thereby promoting cancer cell metastasis and invasion. The degradation of the extracellular matrix facilitates the entry of tumor cells, hence promoting metastasis. MMPs not only breakdown ECM components but also reveal binding sites for additional receptors and release physiologically active compounds (Walker et al., 2018). Invasive cancer cells generate specific F-actin-based protrusions of the plasma membrane, known as invadopodia, to facilitate extracellular matrix breakdown (Paz et al., 2014). In this context, trans-membrane-type 1 MMP (MT1-MMP), also known as MMP-14, aggregates in invadopodia and promotes the localized breakdown of the extracellular matrix during the intra/extravasation process (Jacob and Prekeris, 2015). In 2020, Yan et al. demonstrated that MT4-MMP affects invadopodia production and cellular motility, hence enhancing cell migration and invasion (Yan et al., 2020). Cells that undergo epithelial-mesenchymal transition (EMT) can generate increased levels of matrix metalloproteinases (MMPs), so promoting cell invasion and metastasis; the heightened concentrations of MMPs subsequently augment the EMT process. MMPs −1, −2, −3, −7, −9, −14, and −28 are the principal MMPs involved in epithelial-mesenchymal transition (Mustafa et al., 2022).

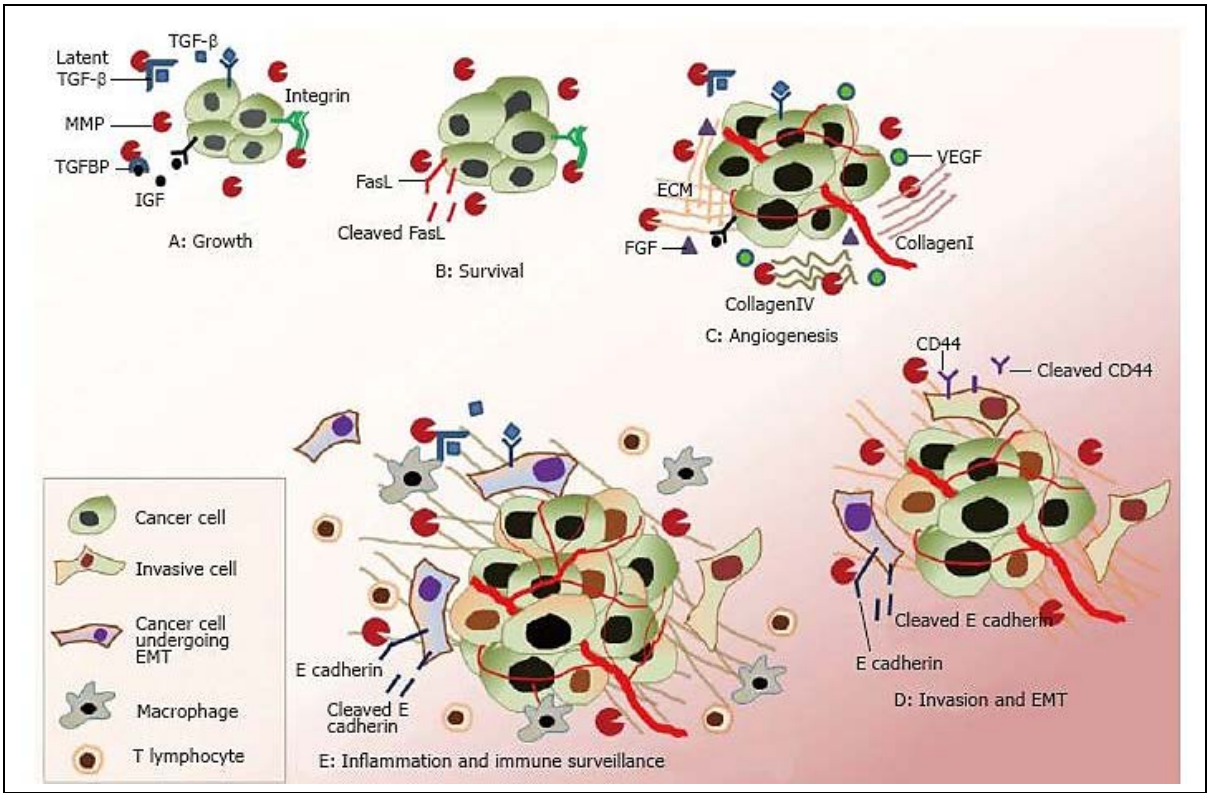

Figure 12. Roles of matrix metalloproteinases in cancer progression. Matrix metalloproteinases (MMPs) have significant and multifaceted roles throughout various stages of cancer progression. **A & B: Growth and survival**. MMP regulates cellular growth through the cleavage of various cellular components; for instance, by releasing IGF from IGF-BP (insulin growth factor-binding protein). MMP-7 enhances cell survival by inhibiting apoptosis via the cleavage of Fas ligand (FasL). MMPs alter integrin signalling via regulating the extracellular matrix (ECM), which in turn influences cellular growth. During tumor development, transforming growth factor-β (TGF-β) is activated from its latent form by MMPs. **C: Angiogenesis**. MMPs facilitate angiogenesis by recruiting VEGF and FGF. Angiogenesis is further enhanced by degradation of ECM components such as collagen -I, -IV, fibrin, etc., that can serve as pro-angiogenic factors. **D: Invasion and EMT**. MMPs regulate invasion by degrading E-cadherin and CD-44. MMPs participate in mesenchymal transition by cleaving E-cadherin and modulating TGF-β signaling. MMP-3 and -9 have specific roles in EMT and cellular differentiation, respectively. **E: Inflammation and immune surveillance**. MMPs also alter immune responses against the cancer cells. MMP-induced TGF-β activation inhibits proliferation of T-lymphocytes. MMPs further regulate sensitivity of cancer cells to NK cells and leukocyte accumulation through the cleavage of various chemokines and cytokines. Adapted from Verma et al., 2014

Hyperglycemic conditions arising from diabetes greatly influence the activity and expression of matrix metalloproteinases (MMPs), especially MMP-2 and MMP-9, which are essential for preserving tissue integrity (Kang et al., 2015; Sun et al., 2017). These MMPs may also participate in pathogenic processes when dysregulated. Hyperglycemia induces the overexpression and activity of MMP by processes including oxidative stress, chronic inflammation, and the accumulation of advanced glycation end-products (AGEs), which interact with receptors (RAGE) and activate signaling pathways that promote MMP synthesis. The dysregulation of MMPs may exacerbate the chronicity of wounds, a common issue observed in diabetes patients (Ayuk et al., 2016). The correlation between diabetes and compromised wound healing, along with other vascular problems, is a significant public health concern. These may ultimately result in chronic foot ulcers and amputation (Ayuk et al., 2016). Increased MMP-9 levels can deteriorate ECM components, facilitating cancer cell invasion into adjacent tissues and fostering angiogenesis to sustain tumor proliferation (Jabłońska-Trypuć et al., 2016). Hyperglycemia promotes invasion and metastasis by elevating MMP-9 levels in lung cancer cells (Kang et al., 2015) and breast cancer cells (Sun et al., 2017), as well as MMP-2 levels in cholangiocarcinoma cells (Saengboonmee et al., 2016) and breast cancer cells (Sun et al., 2017).

Consequently, inhibiting MMP activity or managing hyperglycemia may alleviate the detrimental impacts of diabetes on vascular problems, wound healing, and cancer advancement. Ensuring glycemic control is crucial for mitigating MMP-related diseases, highlighting the interdependent functions of metabolic and enzymatic pathways in diabetes.

5. TISSUE INHIBITORS OF METALLOPROTEINASES (TIMPs): NATURAL INHIBITORS OF MMPs

The tissue inhibitors of metalloproteinases (TIMPs) were first identified as collagenase inhibitors. Later on, it was discovered that TIMPs are endogenous inhibitors of MMPs that bind and inhibit most activated MMPs. TIMPs inhibit MMP activity by forming non-covalent 1:1 stoichiometric complex; i.e. one TIMP molecule can inhibit only one molecule of an active MMP. TIMPs vary greatly in their efficacy with respect to MMP inhibition.

5.1. Structural peculiarities of TIMPs

There are four types of TIMPs, namely TIMP -1, -2, -3, and -4 (Brew and Nagase, 2010). The human genome contains four paralogous genes that encode these TIMPs. All these four TIMPs inhibit MMPs, exhibiting varying affinities towards different inhibitor-protease pairs. TIMP-3 exhibits the most extensive inhibition spectrum. Other than their MMP inhibitory properties, TIMPs can participate in various biological activities like promoting cell proliferation, anti-angiogenic, pro- and anti-apoptotic and synaptic plasticity activities (Brew and Nagase, 2010).

TIMPs usually consist of around 184-194 amino acid residues. They are subdivided into an N-terminal domain (consisting of ~125 aa residues) and a C-terminal domain (consisting of ~65 aa residues). The structural stability of these domains is governed by three di-sulfide bonds (Williamson et al. 1990). The four TIMPs of human origin are ~40% similar in their sequence. The maximum sequence similarity is found between TIMP-2 and -4, showing 50% sequence similarity; while TIMP-1 shows only 37-41% similarity to the rest of the TIMPs (Brew and Nagase, 2010). Interestingly, the N-terminal domain can fold and function as an independent unit. In heterologous systems, the recombinant N-terminal domains of TIMPs show stable native conformation and can independently act as MMP inhibitors (Brew and Nagase, 2010).

5.2. Functional specialization for MMP inhibition

The four TIMPs of human origin with differences in their specificity are broad-spectrum inhibitors of the 23 human MMPs. TIMP-1 shows a more conserved inhibitory range compared to the other three TIMPs.

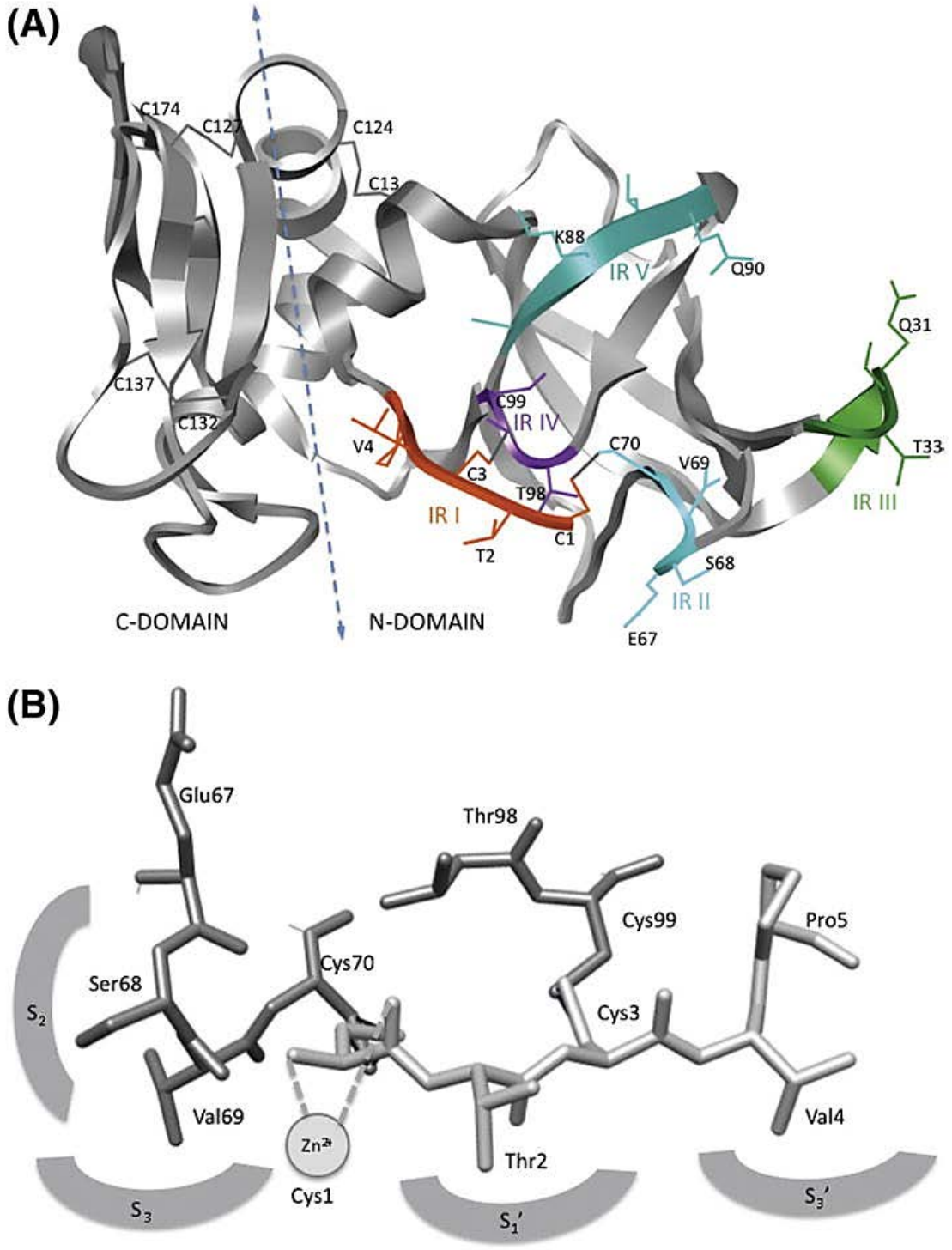

Figure 13. TIMP-1 structure and MMP interaction regions of TIMP-1. (A) A ribbon representation of the 3-D conformation of TIMP-1 depicting the positions of the di-sulfide bonds, the two domains, domain interface and interaction regions (IR I to V) interacting with metzincins and their constituent residues. The image was produced using Chimera. (B) The structure of the TIMP interaction site's core, illustrating interactions with specific subsites within the MMP active site. Adapted from Brew and Nagase, 2010.

There are some relatively subtle differences between the affinities of different TIMPs for other MMPs. For example, TIMPs-2 and -3 are weaker inhibitors than TIMP-1 for MMP-3 and MMP-7, contrasting with their affinities for other MMPs (Hamze et al. 2007).

5.3. 3-D structure of TIMPs and their interaction with MMPs

X-ray crystallography techniques have been employed to determine the 3-D structures of full-length TIMP-1 (PDB ID: 1UEA), TIMP-2 (PDB ID: 1BUV & 2E2D), N-TIMP-1 (PDB ID: 2JOT), and N-TIMP-3 (PDB ID: 3CKI). In most of these structures, TIMPs remain associated with their target MMPs forming inhibitory complexes.

Whole-length TIMPs and N-TIMPs have a "wedge-shaped" structure. The N-terminal domain consists of an oligonucleotide and oligosaccharide binding pocket, characterized by a closed twisted β-barrel composed of five β strands (sA through sF) exhibiting a Greek key topology. This domain comprises of three α-helices, one situated close to the N-terminus (hI) and the other two (hII and hIII) close to the C-terminus. The C-domain contains a pair of parallel β strands (sG and sH) joined with a loop, after which there is a helix (hIV) along with a pair of β-strands (sI and sJ) running in opposite direction to each other linked through a β-hairpin (Figure 13A).

The N-terminal region of all TIMPs exhibit a high degree of conservation, indicating its important role in inhibition of MMPs. Disulfide bonds connecting the cysteines in the Cys1-X-Cys3 sequence with Cys70 and Cys100 (numbering corresponds to the TIMP-1sequence) (Figure 13B). All structurally characterized inhibitory TIMP-MMP complexes exhibit significant similarity in the core of the protein–protein interaction interface. About 60 – 75% of interactions among TIMPs and MMPs are the outcome of the uninterrupted ridge formation by the five residues located at the N-terminal of TIMP-1 (Cys1-Thr-Cys-Val-Pro5), designated here as IR I (interaction region I) along with the loop connecting sC and sD (i.e. CD loop), interaction region II in TIMP-1 (comprising of Met66-Glu-Ser-Val-Cys70 residues), which are covalently joined by the S–S bond between Cys1 and Cys70. This ridge docks itself into the active site of MMPs such that the conserved N-terminal Cys1 of the TIMP remains positioned above the catalytic Zn^{2+} in MMPs. The process of inhibition involves the bi-dentate coordination between the metal ion by the N-terminal α-amino group and carbonyl group of Cys1. This displaces the water molecule needed for peptide bond hydrolysis from the enzyme. (Brew and Nagase, 2010)

6. NATURAL COMPOUNDS IN THE TREATMENT OF GASTRIC CANCER & DIABETES

Compared to conventional chemotherapeutics, natural products and their derivatives exhibit superior efficiency, less toxicity, and a diminished chance of multi-drug resistance compared to chemically manufactured drugs (Atanasov et al., 2021). Polyphenols, flavonoids, alkaloids, and terpenoids are natural substances that have been widely researched for their anti-cancer potential. Curcumin, present in turmeric, has shown considerable anti-tumor properties by promoting apoptosis and suppressing cell growth in gastric cancer cells (Zhou et al., 2017; Wang et al., 2024). Similarly, epigallocatechin gallate (EGCG), a polyphenol present in green tea, inhibits tumor growth by obstructing angiogenesis and metastasis (Zhao et al., 2020). Marine-derived chemicals, such as fucoidan from brown algae, have anti-inflammatory and pro-apoptotic properties in gastric cancer models (Park et al., 2011; Lin et al., 2020). These drugs frequently engage several signaling pathways, rendering them adaptable in addressing cancer development and resistance.

Natural compounds have demonstrated efficacy in diabetes management by enhancing insulin sensitivity, lowering blood glucose levels, and alleviating oxidative stress. Plants like Berberis produce Berberine, an alkaloid that activates AMP-activated protein kinase (AMPK) to promote insulin production and regulate glucose metabolism (Xu et al., 2021). Flavonoids like quercetin, present in onions and apples, demonstrate anti-inflammatory and antioxidant effects, safeguarding pancreatic β-cells from harm (Liu et al., 2022a). Marine sources, such as seaweeds and fish oils, include bioactive elements like omega-3 fatty acids and polysaccharides, which enhance lipid profiles and diminish insulin resistance (Bayram and Kiziltan, 2024). Moreover, chemicals such as resveratrol derived from grapes stimulate sirtuins, improving mitochondrial activity and glucose homeostasis (de Ligt et al., 2018).

Natural compounds embody a potential strategy in the management of gastric cancer and diabetes, providing a supplementary approach to conventional medical treatments. Their incorporation into clinical practice has the potential to enhance patient outcomes and quality of life.

6.1. Melatonin

Melatonin, chemically known as N-acetyl-5-methoxy-tryptamine, is an indoleamine hormone produced by the pineal gland during nocturnal hours. Synthesis also occurs in various other organs, such as the heart, retina, gastrointestinal tract, skin, bone marrow, and lymphocytes. Melatonin plays a crucial role in the regulation of human circadian rhythms and sleep-wake patterns (Salehi et al., 2019).

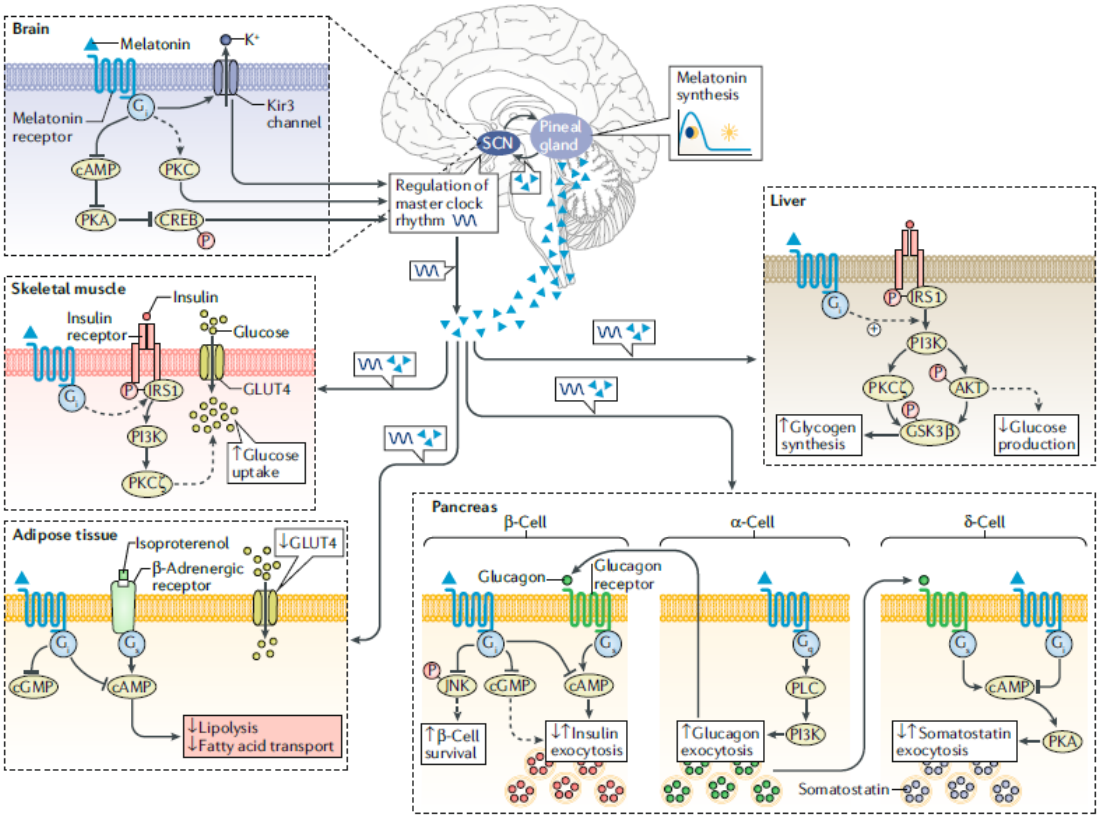

Figure 14. Melatonin signaling regulates the metabolic functioning of both central and peripheral organs. Melatonin receptors are present in central and peripheral locations, where they play a role in regulating metabolism. Melatonin is released in a circadian rhythm from the pineal gland, regulated by the master clock located in the hypothalamic suprachiasmatic nucleus (SCN). Melatonin receptors located in the SCN sequentially suppress the CREB pathway while activating the PKC pathway and Kir3 channels to modulate acute and circadian neuronal firing and expression of clock gene. In the bloodstream of peripheral tissues, melatonin regulates metabolism either by acting directly on peripheral organs or indirectly by influencing the circadian rhythm of the central master clock. In murine liver, melatonin is essential for insulin-stimulated PI3K–AKT activity; in rats, it lowers hepatic glucose production, and in HepG2 cell line, it promotes synthesis of

glycogen, likely through a PKCδ–AKT–GSK3β pathway. In murine skeletal muscle, melatonin stimulates the IRS1–PI3K–PKCδ pathway to upregulate glucose uptake. In inguinal rat adipocytes, melatonin suppresses the cAMP–PKA pathway and, in certain instances, isoproterenol-mediated lipolysis and fatty acid transport. In the human brown adipocyte cell line (PAZ6), melatonin critically suppresses production of cGMP and diminishes expression of GLUT4 and uptake of glucose following prolonged exposure. In pancreatic β-cells of rodents, melatonin acutely diminishes insulin secretion by inhibiting cAMP and cGMP levels, while long-term (physiological) melatonin stimulation enhances the cAMP pathway and stimulates insulin hormone release. Melatonin treatment in human pancreatic islets enhances insulin production and supports β-cell viability by reducing JNK activation. Administration of melatonin in murine pancreatic α-cells and human pancreatic islets enhances glucagon production, potentially through the activation of the Gq/11–PLC–PI3K pathway. Glucagon stimulates secretion of insulin from β-cells and somatostatin from δ-cells through its Gs-coupled glucagon receptor (GCGR). Ultimately, in human pancreatic δ-cells, melatonin secretion affects secretion of somatostatin by modulating cAMP levels. The broken lines represent the assigned functions of melatonin receptors however further clarification of the specific pathways are required. The dark blue wave-patterened lines depict oscillations of circadian clock. Adapted from Karamitri and Jockers, 2019.

6.1.1. Role as an antioxidant

Melatonin is regarded as a highly effective antioxidant found in nature. In contrast to conventional antioxidants like vitamins C and E, each molecule of melatonin can bind up to ten free radicals (Bonomini et al., 2018), influencing ROS/RNS as well as the antioxidant enzymes within cells (Cecon et al., 2018). Two primary mechanisms elucidate the antioxidant and free radical scavenging properties of melatonin, as depicted in Figure 15. The initial method involves the interaction of melatonin with the MT3 receptor, which regulates the transfer of electrons and helps to mitigate oxidative stress. Meanwhile, in the second method, melatonin enters the nucleus of the brain and attaches itself to the transcription factors RZR/RORα (Skarlis and Anagnostouli, 2020).

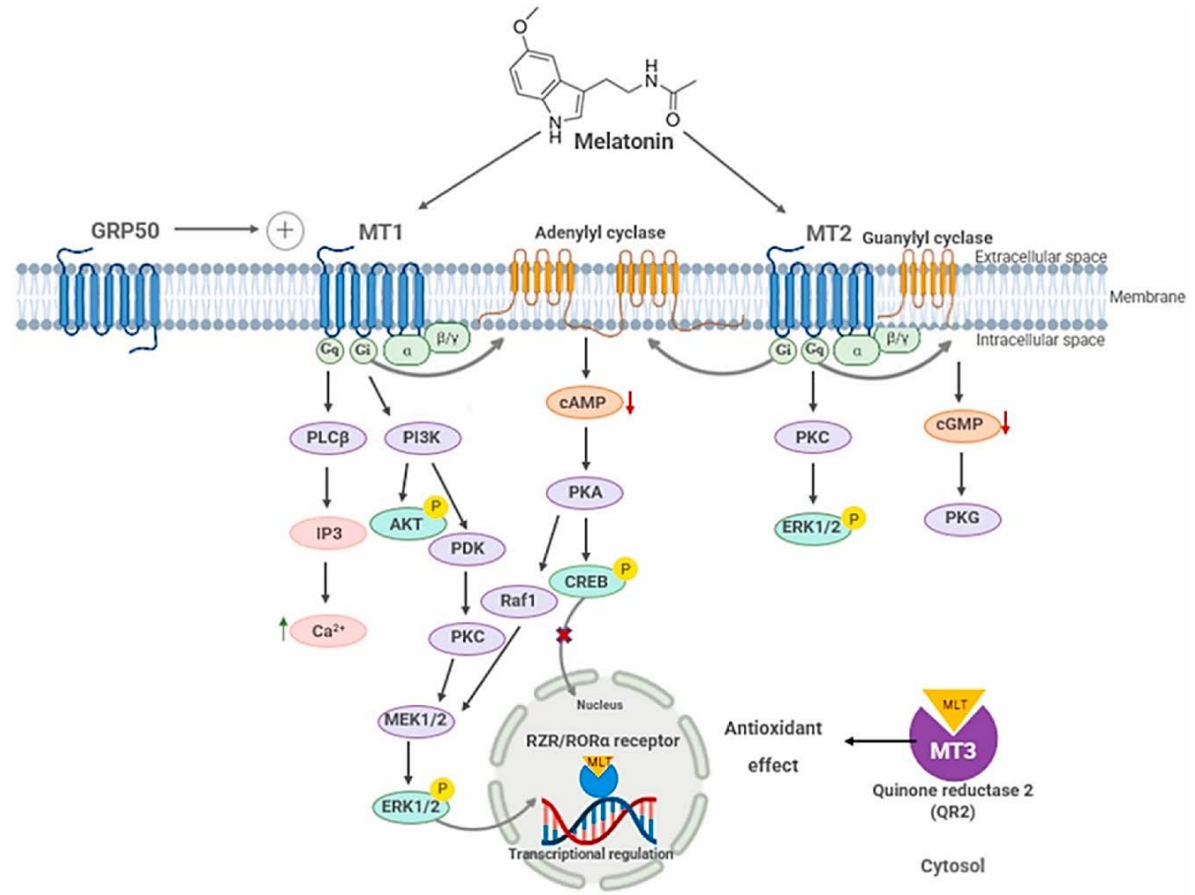

Figure 15. Signaling pathways of melatonin receptors in relation to antioxidant mechanisms. Melatonin works through interactions with the quinone reductase II enzyme (MT3), the G-protein-coupled membrane-bound melatonin receptors MT1 and MT2, and indirectly through the nuclear orphan receptors of the RZR/RORα family. In response to the activation of MT1 receptors by melatonin, Gαi is activated, leading to a reduction in the levels of the secondary messenger cAMP and the activation of PI3K/Akt, PKC, and ERK pathways through Gβγ-dependent mechanisms. The connection of MT1 to Gq leads to the activation of PLC and a rise in intracellular Ca^{2+} levels. Furthermore, as MT2 receptors activated by melatonin, Gαi-dependent signaling is aggravated, leading to a reduction in the cAMP and ERK signaling pathways while also inhibiting cGMP levels. Adapted from Kamfar et al., 2024.

Melatonin indirectly stimulates antioxidative enzymes, including glucose-6-phosphate dehydrogenase, glutathione peroxidase, glutathione reductase, and superoxide dismutase, thereby preventing cellular damage during excessive oxidative stress (Skarlis and Anagnostouli, 2020). Melatonin's high lipophilicity facilitates its passage across cell

membranes, allowing it to access intracellular compartments such as nuclei and mitochondria. Melatonin preserves mitochondrial function at the same time inhibits apoptotic cell death by decreasing mitochondrial ROS (Permuy et al., 2017).

6.1.2. Melatonin in diabetes and gastric cancer

The evaluation of the correlation among diabetes, glucose metabolism, and the effects of melatonin is a topic of significant interest. Recent genetic mapping and genome-wide association studies have identified a significant function for the rs10830963 SNP of the melatonin receptor type 1B (MTNR1B) gene, which encodes the melatonin MT2 receptor, in modulating fasting glucose levels in plasma and the susceptibility to T2DM (Gaulton et al., 2015; Karamitri and Jockers, 2019). Evidence suggests that the stimulation of MT2 receptor signaling enhances pancreatic β-cell survival and reinstates glucose-stimulated insulin production in normal islets subjected to chronic hyperglycemia, as well as in islets from individuals with T2DM (Costes et al., 2015). This indicates that melatonin possesses preventative and therapeutic potential for the preservation of β-cell mass and function in type 2 diabetes mellitus (T2DM).

Melatonin plays a crucial role in tackling gastric carcinogenesis through several mechanisms, including regulating cell lifecycle, modulating immune system function, and targeting oncogenic signaling pathways (Gong et al., 2022). It induces apoptosis in GC cells by regulating critical genes such as cytochrome c, Bax, Bcl-2, and Fas (Song et al., 2018). Simultaneously, melatonin also inhibits the proliferation of GC cells by arresting the cell cycle via regulatory proteins including cyclin D1, cyclin B1, CDK1, and CDK4 (Song et al., 2018; Huang et al., 2021). Alterations in molecules including HIF-1, VEGF, and MMPs inhibit the formation of new blood vessels and metastasis (Wang et al., 2019; Ma et al., 2020). Melatonin enhances immune function by enlarging splenic zones and activating T and B cells (Bondy and Campbell, 2020). Additionally, melatonin suppresses carcinogenesis via several signaling pathways, including as p38/MAPK, NF-κB, PI3K/Akt, and Wnt/β-catenin (Song et al., 2018; Wang et al., 2019; Huang et al., 2021). Melatonin, therefore, represents a promising potential therapeutic agent for treatment of GC.

6.2. Shatavarin-IV

Shatavarin-IV, can be extracted from the roots of *Asparagus racemosus* Willd. (also known as 'Shatavari' in ancient classical Ayurvedic literature) – a well-known plant with medicinal importance that is native to South Asian countries. The name "Shatavari" translates to "a woman who possesses 100 husbands", referring to the Shatavar rejuvenation effect in female reproductive organs (Joshi, 2016). Shatavari is known for its phytoestrogenic properties and is extensively used in combating menopausal symptoms and increasing lactation. Root extract of *A. racemosus* has antiulcer activity (Sairam et al., 2003), antioxidant, anti-diarrheal, anti-diabetic and immuno-modulatory activities (Bopana and Saxena, 2007).

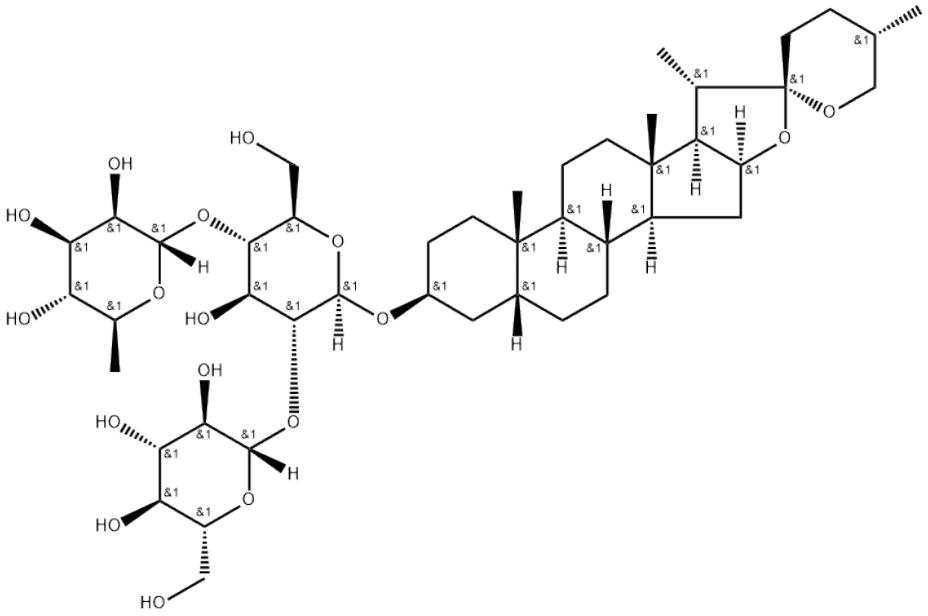

Figure 16. Chemical structure of Shatavarin-IV. Shatavarin-IV, a steroidal saponin, is a major bioactive phytochemical present in the roots of *Asparagus racemosus* (Shatavari).

Shatavarin-IV is the predominant steroidal saponin found in the roots of *A. racemosus*. A prior investigation indicated that the Shatavarin-IV rich fraction (84.69% purity) derived from root of *A. racemosus* demonstrated anti-cancer effects on human colorectal cancer (HCT-29), human breast cancer (MCF-7), and human renal carcinoma (A498) cell lines, in addition to its efficacy in Ehrlich ascites carcinoma (EAC) - bearing mice. (Mitra et al., 2012). Besides this preliminary report on the anti-cancer activity of Shatavarin-IV, there is no other report of its biological activity.

Chapter 2

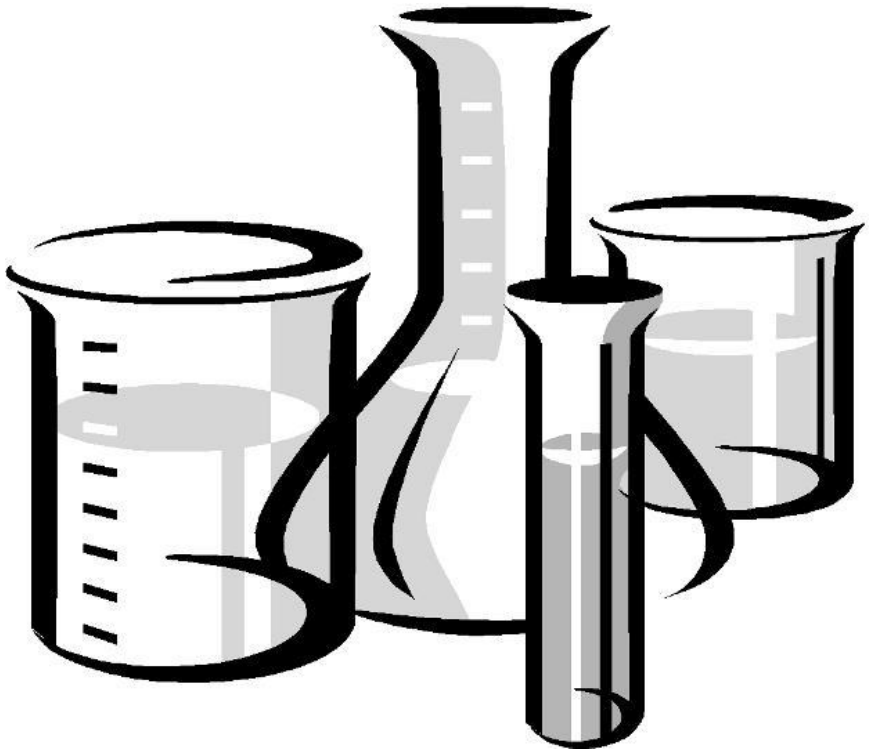

Materials and Methods

MATERIALS AND METHODS

1. Materials

2'-7'-Dichlorodihydrofluorescein diacetate (DCFH-DA), bovine serum albumin (BSA), Bradford reagent, D-glucose, D-mannitol, dithiothreitol (DTT), gelatin, melatonin, Triton-X-100, protease inhibitors, RNase A solution, Shatavarin-IV (≥90% pure), Tween®-20, and Fluoromount Aqueous Mounting Medium were purchased from Sigma Chemical Co, St. Louis, MO, USA. ADP-Glo Kinase Assay kit, CDK2/Cyclin E2 Kinase Enzyme System, CellTiter-Glo luminescent cell viability assay kit, and Luciferase Assay System were purchased from Promega (Madison, WI, United States). Primary antibodies, horseradish peroxidase (HRP) conjugated secondary antibodies, and Texas Red conjugated secondary antibodies for western blotting were purchased from Santa Cruz Biotechnology (Dallas, TX, USA). Clarity™ Western ECL Substrate solution was purchased from Bio-Rad (Hercules, CA, USA). Trans-well chambers and Matrigel were sourced from Corning, USA. Crystal violet was purchased from HiMedia Laboratories, Maharashtra, India. RNAi duplexes corresponding to human siRNAs of NF-κB p65, MMP-9, and control siRNA-A were purchased from Santa Cruz Biotechnology (Dallas, TX, USA). The human MMP-9 promoter plasmid was a kind gift from Etty Benveniste & Douglas Boyd (Addgene plasmid # 53434). Plasmid DNA preparation kits were obtained from QIAGEN (Valencia, CA, USA). Lipofectamine™ RNAiMAX and Lipofectamine™ 2000 transfection reagents were procured from Invitrogen, Thermo Fisher Scientific corporation (Waltham, MA, USA). TRIzol™ Reagent, SuperScript™ IV First-Strand Synthesis System, recombinant Taq DNA Polymerase, and 1 Kb Plus DNA Ladder were purchased from Invitrogen (Waltham, MA, USA). Primers for cloning and conventional RT-PCR were purchased from Integrated DNA Technologies, IDT (Coralville, IA, USA). High-Sensitivity ChIP Kit and Glucose Assay Kit were purchased from Abcam (Cambridge, UK). c-Jun, c-Fos primary antibodies (ChIP grade) and rabbit IgG isotype control antibody were purchased from Cell Signaling Technologies (Danvers, MA, USA). FITC – Annexin V Apoptosis Detection kit I was procured from BD Biosciences (Franklin Lakes, NJ, USA). APO-BRDU (TUNEL) Apoptosis Kit was purchased from Novus Biologicals, USA. AGS cells were purchased from the American Type Culture Collection (ATCC, Manassas, VA, USA). All cell culture-related materials were sourced from Gibco (Thermo Fisher, MA, USA).

2. Cell culture

AGS cells (human gastric adenocarcinoma cells) were cultured in Ham's F12K nutritional medium enriched with 10% FBS and 1% Antibiotic-Antimycotic (100×) solution. The cells were maintained at 37°C in a humidified environment with 5% CO_2 and 95% air. All experiments were performed using AGS cells within 10 passages.

3. Optimization of hyperglycemic treatment conditions

AGS cells were cultured in six-well plates and incubated overnight in normoglycemic media supplemented with 10% FBS. A concentration of 5.5 mM D-glucose was utilized to formulate normoglycemic media, as this level simulates typical blood glucose concentrations (Koobotse et al., 2020). Initially, the effect of high glucose on AGS cell proliferation was determined by incubating them in increasing concentrations of D-glucose or D-mannitol (5.5, 8, 12.5, 25, 35, and 50 mM) for 0, 6, 12, 24, 36, and 48 hours. After the respective incubation periods, cell viability was measured using CellTiter-Glo luminescent cell viability assay kit. Subsequently, the cells were subjected to incomplete Ham's F12K media containing varying concentrations of D-glucose or D-mannitol (5.5, 8, 12.5, 25, 35, and 50 mM) for 24 hours to determine the optimal dosage for enhanced expression and activity of MMP-9. The expression and activity levels of MMP-9 were subsequently assessed at various incubation time points (0, 6, 12, 24, 36, and 48 hours) following the administration of the chosen dose of D-glucose. Luciferase reporter assays and western blotting were conducted. to assess MMP-9 expression at both the transcriptional and translational levels, respectively. The gelatin zymography assay was employed to assess the gelatinolytic activity of MMP-9. AGS cells incubated in D-mannitol, rather than D-glucose, functioned as the osmolarity control.

4. Determining the IC_{50} of melatonin and Shatavarin-IV in hyperglycemic AGS cells

To determine the impact of melatonin and Shatavarin-IV on cell viability, AGS cells cultured in normoglycemic medium were inoculated in a 96-well plate at a density of 1×10^4 cells per well and incubated overnight. Subsequently, the normoglycemic medium was substituted with incomplete hyperglycemic medium including escalating concentrations of melatonin (0.5, 1, 2, 3, 4, and 5 mM) or Shatavarin-IV (1, 2, 3, 4, and 5 µM). Cell vitality was assessed after 24 hours by the CellTiter-Glo luminous cell viability assay. To determine the IC50 values of these two drugs, the cell viability data from three independent experiments were initially expressed as percentages. Drug concentrations were subsequently converted to a

logarithmic scale, and the IC_{50} values were calculated with the help of a non-linear regression model using GraphPad Prism (version 5.01, SD, CA, USA) software.

5. Treatment of AGS cells

D-glucose and D-mannitol were solubilized in culture medium and subsequent dilutions were prepared for the specified concentrations. The MAPK pathway inhibitors (PD98059, SB203580, and SP600125) and Shatavarin-IV were first solubilized in DMSO and subsequently diluted in culture medium prior to administration. Melatonin was originally dissolved in a small quantity of ethanol (5%) and subsequently diluted in culture medium prior to treatment.

In following experiments, AGS cells were seeded in NG medium (5.5 mM glucose) enriched with 10% FBS. Subsequently, cells were incubated for 24 hours in serum-free NG medium, serum-free HG media (25 mM glucose), and serum-free HG media supplemented with 2 mM melatonin or 2.2 µM Shatavarin-IV. These four treatment groups were designated as 'NG', 'HG', 'HG + MELA', and 'HG + S-IV', respectively. This work utilized 50 µM PD98059, 20 µM SB203580, and 50 µM SP600125. The MAPK inhibitors were administered one hour before to hyperglycemic therapy. The maximum concentration of DMSO in the experiments did not surpass 0.1%. The administered inhibitor dosages exhibited no harmful effects on AGS cells, as corroborated by the CellTiter-Glo luminous cell viability test (data not shown).

6. Scratch wound healing assay

A standard scratch wound healing experiment involves creating a "wound gap" in a cell monolayer by scratching, followed by the observation and quantification of the "healing" process as cells migrate and proliferate towards the center of the gap (Lampugnani, 1999). This test is straightforward, cost-effective, and the experimental conditions may be readily modified for various objectives.

Each well of a six-well plate was treated with 50 µg/mL poly-L-lysine by incubating the plates for 2 hours at 37°C. The unbound solution was aspirated, and the wells were rinsed with sterile 1× PBS. AGS cells were inoculated into six-well plates coated with poly-L-lysine and incubated until a monolayer developed. The monolayer was meticulously scraped in a linear fashion using an autoclaved 200 µL pipette tip across the middle of the well. Subsequent to scratching, the wells were rinsed twice with cell culture media to eliminate any

dislodged cells. The wells were subsequently refilled with incomplete media including the appropriate treatments. Following a 24-hour period, the cells were washed with PBS and subsequently fixed with 4% paraformaldehyde for 30 minutes. The fixed cells were subjected to staining with a 0.5% crystal violet solution for an additional 30 minutes. Images of the stained monolayer were captured using an Olympus IX71 inverted microscope in conjunction with Image-Pro Express software. The wound area was determined from these photos with ImageJ software.

7. Invasion Assay

The trans-well invasion experiment consists of two chambers filled with culture medium, separated by a porous membrane coated with an extracellular matrix component (Justus et al., 2023). A medium with the chemotactic agent is introduced into the bottom chamber, after which cells are seeded in the top chamber to create a chemoattractant gradient for directed cellular migration. After incubation, the degree of cell chemotaxis may be evaluated by quantifying the adhering cells that have moved to the basal side of the porous membrane.

An aliquot of Matrigel was frozen overnight at 4°C and subsequently diluted with cold serum-free medium at a 1:3 ratio. 25 µL of the diluted Matrigel solution was employed to cover the inner surface of the trans-well membrane (8 µm pore filter). The trans-well chambers containing Matrigel were incubated at 37°C for 30 minutes to facilitate gel formation. The matrigel-coated chambers were positioned in a 24-well plate, and 1×10^5 AGS cells in 100 µL serum-free media with the corresponding treatments was introduced into the upper chambers of the trans-well insert. To facilitate chemotaxis, the bottom chambers were supplied with 500 µl Ham's F12K medium (supplemented with 20% FBS). Following a 24-hour incubation, the chambers were extracted, rinsed with PBS, and the cells were preserved using 4% PFA for 15 minutes at ambient temperature. Transwell inserts were rinsed twice on both sides of the membrane with sterile 1× PBS to eliminate debris, unattached cells, and surplus fixation solution. The transwell inserts were treated with a 0.5% crystal violet solution for 30 minutes at room temperature to stain the invading cells. The pictures were obtained using an Olympus IX71 inverted microscope in conjunction with Image-Pro Express software, and the quantity of invasive cells was quantified.

8. Colony formation Assay

The clonogenic assay, also known as the colony formation assay, is an in vitro test for cell survival that relies on a single cell's capacity to proliferate into a colony. The colony is defined to consist of at least 50 cells. The assay effectively analyzes every cell in the population for its ability to undertake “unlimited” division. Clonogenic test is the method of choice to evaluate cell reproductive mortality following treatment with ionizing radiation, but may also be used to determine the efficacy of other cytotoxic chemicals. (Franken et al., 2006)

AGS cells (1×10^6 cells) were added to 60 mm culture dishes and incubated for 24 hours with the various treatments. Afterward, cells were trypsinized, pelleted, and resuspended. 1×10^3 cells from every treatment groups were subsequently re-plated into 6-well plates. The 6-well plates were thereafter maintained at 37°C in a humidified environment containing 5% CO_2 until the cells in the control dishes developed adequately sized colonies. Complete fresh media was administered to each well every other day or as necessary. Subsequently, the media in the wells were aspirated and rinsed twice with PBS. The colonies were subsequently incubated in a solution of 6% glutaraldehyde and 0.5% crystal violet for 30 minutes. Subsequent to the removal of this solution, the plates were meticulously cleaned with tap water and allowed to air dry at ambient temperature. The plates were ultimately imaged, and the colonies were enumerated using a stereomicroscope.

9. Gelatin zymography

MMP-9 activity was evaluated through the gelatin zymographic method. 1×10^6 AGS cells were inoculated in a 60 mm dish. Following 24 hours of incubation with the designated treatments, the conditioned media containing 70 µg protein from different groups were subjected to electrophoresis using 8% SDS-PAGE gel containing gelatin (1 mg/ml), under non-reducing conditions. After electrophoresis, the gel was washed twice in wash buffer containing 2.5% Triton-X-100 and incubated in a buffer comprising Tris-HCl (40 mM; pH 7.4), NaCl (0.2 M), and $CaCl_2$ (10 mM) for 18 hours at 37ºC. 0.1% Coomassie blue was next used to stain the gel. After de-staining, the bands were represented as negative stained, and densitometry was conducted using ImageJ software.

10. Reverse zymography

TIMP-1 activity was evaluated utilizing the reverse zymographic method. 1×10^6 AGS cells were inoculated in a 60 mm dish. Following 24 hours of incubation with the designated treatments, the conditioned media was harvested and 70 µg protein was subjected to electrophoresis using 12% SDS-PAGE with gelatin (1 mg/ml) and an MMP source, under non-reducing conditions. For this experiment, conditioned media of MDA-MB-231 cells served as the source of MMP. After electrophoresis, the gel was washed twice in wash buffer containing 2.5% Triton-X-100 and incubated in a buffer comprising Tris-HCl (40 mM; pH 7.4), NaCl (0.2 M), and $CaCl_2$ (10 mM) for 18 hours at 37ºC. 0.1% Coomassie blue was next used to stain the gel. After de-staining, the bands were represented as stained bands in a transparent background and ImageJ software was used to quantify them.

11. Immunofluorescence Assay

AGS cells were grown on sterile coverslips coated with poly-L-lysine and subjected to corresponding treatments for 24 hours. After discarding the culture media, AGS cells were rinsed with PBS and fixed using 4% PFA. Cells were permeabilized for 10 minutes using PBS with 0.25% Triton X-100, followed by a 1-hour blocking with 1% BSA in PBST (137 mM NaCl, 2.7 mM KCl, 10 mM Na_2HPO_4, 1.8 mM KH_2PO_4, and 0.1% Tween-20; pH 7.4). After blocking, overnight incubation of cells was performed with the specified antibodies at 4°C. The coverslips were subsequently washed twice with PBS, and the cells were incubated for 2 hours at room temperature in the dark with a Texas Red-conjugated secondary antibody solution (1:400 dilution in TBS with 1% BSA). The coverslips were rinsed three times in PBS, and counter-staining was performed using DAPI, and affixed with Fluoromount Aqueous Mounting Medium. Images were obtained utilizing a high-resolution STED microscope (Leica TCS SP8). Images were captured in a single session under consistent settings. Localization of various proteins were detected from random fields. The images represented five distinct experiments to eliminate artifacts that could arise during individual trials.

12. Preparation of cell lysate and Immunoblotting

AGS cells were inoculated at a density of 1×10^6 cells in 60 mm plates. Following a 24-hour incubation with the designated treatments, the cells were rinsed with PBS, subjected to trypsinization, and subsequently centrifuged. Cells were lysed using a solution containing

Tris-HCl (20 mM; pH 7.4), NaCl (150 mM), 1% Triton X-100, 1× PIC, and PMSF (1 mM), followed by centrifugation at 12,000 rpm for 10 minutes at 4ºC. Supernatants were taken in a fresh tube, and the concentration of protein in the collected supernatants were determined with the Bradford assay. 50 µg of protein from each treatment group were combined with 1× reducing Laemmli sample loading buffer, subjected to boiling, electrophoresed in a 10% SDS-PAGE, and transferred onto PVDF membranes that have been activated by methanol. PVDF membranes were subsequently blocked with 3% BSA in TBST (137 mM NaCl, 2.7 mM KCl, 50 mM Tris-HCl, and 0.1% Tween-20; pH 7.4) for a period of two hours at ambient temperatures and incubation was carried out overnight with the relevant primary antibodies at 4ºC. After being washed with TBST, incubation with appropriate secondary antibodies tagged with HRP were performed. The blot was generated via a western ECL substrate solution. Images were acquired with the Bio-Rad ChemiDoc MP imager. Quantification of protein expression was performed via densitometry utilizing ImageJ software. GAPDH served as the loading control.

13. Nuclear localization of c-Fos and c-Jun

The nuclei were initially isolated from cultured AGS cells in vitro, resulting in the separation of their nuclear and cytosolic fractions. The fractions were prepared according to a previously documented method (Senichkin et al., 2021). AGS cells were cultured in 10 cm dishes and subjected to their designated treatments. Following a 24-hour period, the culture media was aspirated, and the cells were rinsed twice with ice-cold PBS. The culture dishes were placed on ice, and the cells were detached from the plate using 1 mL of PBS. The resultant cell suspension was pelleted by centrifugation for 5-10 seconds at 10,000 rpm. The supernatant was removed, and the pellet was resuspended in 600 µL of ice-cold PBS with 0.1% NP-40. The cell suspension was triturated five times on ice using a P1000 micropipette tip and subsequently centrifuged at the previously established settings. The supernatant obtained from this centrifugation step was collected and designated as the cytoplasmic fraction. The pellet was resuspended in 1 mL of ice-cold PBS with 0.1% NP-40 and subsequently centrifuged. The supernatant was discarded, and the pelleted nuclei were resuspended in 150 µL of PBS, sonicated, and centrifuged at 12,000 rpm for 10 minutes at 4ºC. The supernatant from this stage was collected and designated as the nuclear fraction.

Protein concentrations of both the cytosolic and nuclear fractions were estimated using Bradford assay. An equal quantity of protein (80 µg) from each group was combined with 1×

reducing Laemmli sample loading buffer (0.0625 M Tris-HCl, pH 6.8; 2% SDS, 10% glycerol, 0.05% β-mercaptoethanol, 0.001% bromophenol blue), heated for 1 minute, and immunoblotted for c-Fos and c-Jun. Histone - H3 and GAPDH used as the loading controls for the nuclear and cytosolic fractions, respectively.

14. RNA isolation and PCR

Total RNA was extracted from AGS cells utilizing TRIzol (Invitrogen, CA), following the manufacturer's guidelines. In order to remove any DNA contamination, the extracted RNA was treated with DNase I; followed by rt-PCR to synthesize the cDNA. Conventional PCR analysis was then conducted for fragments of N-cadherin, E-cadherin, Vimentin, β-catenin, MMP-9, and TIMP-1, utilizing GAPDH as the reference. Table 1 specifies the primer sequences.

Table 1. Primers used for conventional PCR analysis.

Target gene	Forward primer (5'–3')	Reverse primer (5'–3')
GAPDH	GAAGGTGAAGGTCGGAGT	GAAGATGGTGATGGGATTTC
N-Cadherin	CTCCATGTGCCGGATAGC	CGATTTCACCAGAAGCCTCTAC
E-Cadherin	GCCGAGAGCTACACGTTCA	GACCGGTGCAATCTTCAAA
Vimentin	GTTTCCCCTAAACCGCTAGG	AGCGAGAGTGGCAGAGGA
β-catenin	ACAGCACCTTCAGCA CTCT	AAGTTCTTGGCTATTACGACA
MMP-9	CTGTACCGCTATGGTTACACTC	ACTCGTCATCGTCGAAATGG
TIMP-1	TCGTCATCAGGGCCAAGTTC	TCCACAAGCAATGAGTGCCA

15. Generation of MMP-9 promoter deletion constructs

To elucidate the signaling pathway(s) governing hyperglycemia-induced MMP-9 expression, a series of progressive deletion mutants (–580 bp, –461 bp, and –72 bp) from the 5'-end of the human MMP-9 promoter were constructed and cloned into the pGL2Basic plasmid

(Promega). The NF-κB, distal AP-1, and proximal AP-1 binding sites were sequentially removed in the –580 bp, –461 bp, and –72 bp constructs, respectively. PCR amplification was conducted relative to the transcription start site using the primers specified in Table 2. All forward primers included a KpnI restriction site, while the reverse primer incorporated a XhoI restriction site, as indicated in bold font in Table 2.

Table 2. List of primers that target the human MMP-9 promoter.

Target	Forward primer (5'–3')	Reverse primer (5'–3')	References
Primers for Promoter Deletion Constructs			
–580 bp	GC**GGTACC**TAGCAGAGCCC ATTCCTTCC		–
–461 bp	GC**GGTACC**TCAAAGAAGGC TGTCAGC	GC**CTCGAG**TGGTGAGGGC AGAGGTGTCT	Mittelstadt et al., 2012
–72 bp	GC**GGTACC**GCACTTGCCTGT CAAGGAGG		Mittelstadt et al., 2012
Primers for ChIP Assay			
Proximal AP-1	GAGTCAGCACTTGCCTGTCA	CTGCTGTTGTGGGGGCTTT A	Mishra et al., 2016
Distal AP-1	CTTGCCTAGCAGAGCCCATT	TTTTTCCCTCCCTGACAGCC	Mishra et al., 2016

16. Transient transfection of AGS cells and Luciferase activity assays

Transient transfection of siRNAs and luciferase reporter plasmids was conducted using Lipofectamine™ RNAiMAX and Lipofectamine™ 2000 transfection reagents (Invitrogen, Waltham, MA, USA), respectively. The complete MMP-9 promoter and its deletion constructs were generated utilizing QIAGEN plasmid DNA preparation kits, in accordance with the manufacturer's instructions. Transfection of AGS cells were performed with 1 µg of luciferase reporter plasmids, 50 nM of siRNA, or both, following preparation with their respective transfection reagents. Following 48 hours of transfection, cells were cultured in either NG or HG media for subsequent experiments. The silencing effectiveness of siRNAs was validated through western blotting technique employing either an anti-p65 or anti-MMP-9 antibody.

In case of the luciferase assay, transfected AGS cells were lysed using passive lysis buffer (1X) following their respective treatments. The lysates were evaluated for firefly luciferase activity utilizing the Luciferase Assay System (Promega, Madison, WI, USA), in accordance with the manufacturer's instructions. GloMax® 20/20 Luminometer (Promega, WI, USA) was used to measure luminescence of the samples with a 1s integration time. Luminescence values were normalized according to the micrograms of protein in each sample. The normalized values were expressed as fold change relative to the NG cells transfected with the complete MMP-9 promoter. The values denote the means of triplicate samples from five distinct experiments.

17. Chromatin Immunoprecipitation (ChIP) assay

The ChIP assay was performed using 100–120 mg of DNA-protein complex derived from crosslinked samples, following manufacturer's protocol of the High-Sensitivity ChIP Kit (Abcam, Cambridge, UK). Samples were immuno-precipitated using antibodies either c-Fos or c-Jun, and the binding of these proteins to both the distal and proximal AP-1 binding sites of the MMP-9 promoter was measured following 40 cycles of PCR. 1% chromatin that has been obtained prior to the immuno-precipitation step from all samples was utilized as their corresponding input. DNA was collected and amplified by PCR to function as the loading control. Anti-rabbit IgG served as the negative control for immuno-precipitation experiments. The PCR analysis was conducted on 2% agarose gels stained with ethidium bromide. Images were acquired using the Bio-Rad ChemiDoc™ MP imager, and band intensities were

assessed by densitometry with ImageJ software. The primers utilized in this experiment are enumerated in Table 2.

18. Determination of ROS generated within AGS cells

Live cell imaging was conducted to visualize ROS generated within AGS cells following treatment. Cells were cultured in confocal dishes and incubated for 16-18 hours prior to the administration of respective treatments. Following a 24-hour incubation period, cells were rinsed with PBS and subsequently stained with 10 µM DCFH-DA for 30 minutes at 37°C in the dark. Following washing, the cells were visualized with high-resolution STED microscopy (Leica TCS SP8). The images represented five distinct experiments to eliminate artifacts. To quantify ROS generation, the DCFH-DA fluorescence of AGS cells in each treatment group was measured using a F-7 Fluorescence Spectrophotometer (Hitachi High Technologies Corporation). Background fluorescence was appropriately subtracted (Ex/Em: 485/535 nm) and results were normalized to the protein concentration of each sample.

19. Determination of cell cycle and apoptosis by flow cytometry

AGS cells were cultured at a density of 1×10^6 cells in 60 mm plates and incubated overnight to investigate the phases of the cell cycle. Flavopiridol (125 nM) served as the positive control. Following incubation with designated treatments for 24 hours, cells were trypsinized. Afterward cells were rinsed with PBS, and fixation was performed with ice-cold ethanol (70%) maintaining gentle vortexing. Following fixation, cells were maintained for 16 to 18 hours at 4°C. All traces of ethanol were eliminated by rinsing the cells with PBS. The cells were then treated with a staining solution (50 µg/ml PI and 100 µg/ml RNaseA in PBS) for 15 minutes at ambient temperatures. After staining, the cells were examined using the BD LSRFortessa™ Cell Analyzer and the findings were evaluated with Flowing Software (version 2.5.1).

Further, 1×10^6 AGS cells were cultured in 60 mm plates to detect apoptotic cell death. Following 24 hours of designated treatments, cells were trypsinized, rinsed with PBS, and processed utilysing the FITC-Annexin V Apoptosis Detection Kit I, in accordance with the manufacturer's instructions. After staining, the cells were examined using the BD LSRFortessa™ Cell Analyzer and the findings were evaluated with Flowing Software (version 2.5.1).

20. TUNEL assay

AGS cells were cultured on sterile coverslips coated with poly-L-lysine and subjected to a 24-hour incubation with corresponding treatments. Following incubation, cells were stained with an APO-BRDU (TUNEL) Apoptosis kit according to the manufacturer's specifications. AGS cells were fixed using a 4% PFA solution and subsequently permeabilized in PBS with 0.25% Triton X-100 for 10 minutes. The cells were treated with a freshly produced TUNEL reaction mixture for one hour at 37°C, in the absence of light. The cells were then counter-stained with DAPI and affixed on a slide using a drop of Fluoromount Aqueous Mounting Medium (Sigma, USA). Pictures were obtained utilizing a high-resolution STED microscope (Leica TCS SP8). Images were captured in a single session under consistent settings. Various protein localizations were detected from randomly selected areas. The photos represented five distinct studies to eliminate artifacts that may arise from individual trials.

21. Molecular docking

The molecular docking study was conducted using AUTODOCK Vina software (Morris et al., 2009). The 3D atomic coordinates for the CDK-2/Cyclin E enzyme (PDB ID: 7KJS) were utilized as a standard reference (Berman et al., 2000). Docking of the co-crystallized ligand (PF-06873600) was initially conducted to validate the docking protocol. The docked pose exhibited a strong alignment with the crystallized ligand pose, evidenced by an RMSD value of 0.5 Å, and demonstrated standard interactions with Leu83, Asp86, Lys89, and Gln131 (Bell and Zhang, 2019). The docking grid established during the validation process was utilized for the test molecule. The dimensions of the docking grid box were 72 × 84 × 68 Å, with the center located at X = 25.522, Y = 5.261, and Z = -15.164. The exhaustiveness was maintained at 8, with a grid spacing of 1 Å employed for energy calculations. The receptor was generated utilizing PyMol software (Oberhauser et al., 2014). Following the elimination of all non-standard atoms and water molecules, Gasteiger charges and polar hydrogens were incorporated and the structure was subsequently saved in .pdbqt format utilizing MGL Tools (v 1.5.6). Melatonin structure was generated using ChemDraw Ultra (v 10.0) software and saved in .mol format. The 3-D structure of melatonin was optimized utilizing Marvinsketch software (Kaushik, 2014) and subsequently saved in .pdbqt format. The docking of melatonin with the CDK-2/Cyclin E enzyme (PDB ID: 7KJS) was conducted using Autodock Vina software employing a blinded rigid receptor docking approach. The complete protein complex was utilized for docking instead of solely the active site. The final deviations in the

receptor-structure complex were regularized through energy minimization utilizing the GROMOS96 force field via Deep View, employing a 200-step steepest descent algorithm followed by a 200-step conjugate gradients algorithm. The PyMol software was utilized to carry out the visualization and image production of the protein-melatonin complex (Schrödinger, LLC).

22. Molecular Dynamics (MD) simulation

MD simulations for the docked complex of CDK-2/Cyclin E enzyme receptor with melatonin was carried out with the Nanoscale Molecular Dynamics (NAMD) software (Phillips et al., 2020). The VMD software was used to generate a protein structure file (.psf) of CDK-2/Cyclin E enzyme (Yamada et al., 2017). Topology files for melatonin was produced through the CHARM-Gui server (Allouche, 2011; Lee et al., 2016; Kim et al., 2017). The cube-shaped three-point water model (TIP3) was employed to solvate the entire system, subsequently neutralized with sodium or chlorine counter ions. The system was minimized prior to the dynamics study for 2000 steps and subsequently equilibrated under constant particle number, pressure, and temperature (NVT) for 200 pico-seconds (ps) at 300 K. The final run of MD simulations was carried out for 100 ns (nano-seconds) (1,00,000 steps of 1 ps each). The VMD software was used for analysis and plot generation.

23. In-vitro kinase assay

CDK-2/Cyclin E1 kinase activity against increasing concentrations of melatonin was measured using the ADP-Glo Kinase Assay kit (Promega), as per the manufacturer's protocols. A broad-spectrum protein kinase inhibitor, staurosporine, was used as the positive control in this experiment. GloMax® 20/20 Luminometer (Promega, WI, USA) was used to measure luminescence of the samples with a 1s integration time. Luminescence values were normalized according to the micrograms of protein in each sample. The normalized values are expressed in percentage relative to the vehicle control. The IC_{50} values for staurosporine and melatonin were calculated by fitting their respective relative luminescence data from three independent experiments to a quadratic binding model using non-linear regression in GraphPad Prism (version 5.01, San Diego, California, USA).

24. Estimation of protein concentrations

The Bradford assay was employed to measure the protein content in AGS cell samples. This test is based on the observation that the absorbance maxima of an acidic solution of Coomassie Brilliant Blue G-250 moves from 465 nm to 595 nm upon protein binding. Hydrophobic and ionic interactions stabilize the anionic form of the dye, resulting in a noticeable color shift. The experiment is valuable because the extinction coefficient of a dye-albumin complex solution remains constant throughout a 10-fold concentration range (Bradford, 1976).

Five microliters of AGS cell lysate from each treatment group were dispensed into individual microplate wells, followed by the addition of 250 microliters of Bradford reagent (Sigma, USA) to each well. The mixture was incubated for 10 minutes at ambient temperature in the absence of light. Protein concentrations were subsequently quantified using a spectrophotometer at 595 nm. A standard curve was generated by graphing the average blank-corrected data at 595 nm for each BSA standard against its concentration in µg/mL. This standard curve is utilized to ascertain the protein content of each unidentified sample.

25. Statistical analysis

All experiments were conducted independently for five times. The statistical analysis was conducted utilizing GraphPad Prism (version 5.01, SD, CA, USA). The Student's t-test was employed to compare between two groups. Statistical significance relative to the NG control group was shown by an asterisk (*), whereas a hash (#) indicated comparisons with the HG treatment group. In all illustrations, statistically significant differences have been denoted as *$p<0.05$, #$p<0.05$, **$p\leq0.01$, ##$p\leq0.01$, ***$p\leq0.001$, and ###$p\leq0.001$. ns indicates non-significant ($p\geq0.05$). All the data has been provided as mean ± SEM.

Chapter 3

Effect of Hyperglycemia on Gastric Cancer cells

EFFECT OF HYPERGLYCEMIA ON GASTRIC CANCER CELLS

1. Introduction

Gastric cancer (GC) is the 5th most frequently occurring malignancy and the 4th most prominent cause for cancer-related death worldwide, according to the estimations of GLOBOCAN 2020 (Sung et al., 2021). A variety of metabolic syndromes are thought to play an important role in GC and also influence its prognosis in cancer patients (Li et al., 2018). Diabetes mellitus (DM) is one such metabolic syndrome, which has already been recognized as a global epidemic. In 2015, WHO has predicted that the number of diabetic individuals, across the world, will increase from 382 million to 592 million by 2035 (Popkin, 2015). Consequently, DM and GC have become major threats to public health worldwide.

It has also been observed that these two maladies are frequently diagnosed in the same individuals (Onitilo et al., 2012). This suggests that DM and cancer share a significant amount of common risk factors and pathophysiological mechanisms. The underlying mechanics of such an association have not yet been fully uncovered. However, plausible connections may include chronic inflammation (Nigam et al., 2023), oxidative stress (Hayes et al., 2020), insulin resistance (Chiefari et al., 2021), hyperinsulinemia (Gallagher and LeRoith, 2020), and hyperglycemia (Hammer et al., 2019).

Even though hyperglycemia (HG) is among the most widely studied metabolic changes in DM; its effects on cancer progression have received a great deal of negligence. In few studies performed, it has been noted that HG during cancer treatment is associated with a plethora of adverse outcomes like increased risk of infections (Hammer et al., 2016; Storey and Von Ah, 2016), a longer period of hospitalization (Storey and Von Ah, 2015), chemoresistance (Biernacka et al., 2013), cancer recurrence (Wright et al., 2013), metastatic cancer progression (Barua et al., 2018) and decreased overall and disease-free survival (Barua et al., 2018).

Although, HG has started to be seen as a possible risk factor for different forms of malignancy, yet, very few studies have been conducted on the relation of HG with the development and spread of GC. But there remains a difference in opinion. Yamagata and colleagues performed a study that showed that high fasting plasma glucose levels were a risk

factor for GC, in a Japanese cohort (Yamagata et al., 2005). Similar studies on Korean (Jee et al., 2005) and Austrian (Rapp et al., 2006) cohorts were unable to delineate any correlation between HG and GC risk. This suggests that the global scientific community has not yet reached a consensus on the topic. In this chapter, the various effects of hyperglycemia on cancer cells will be investigated.

2. Results

2.1. Standardization of HG treatment in AGS cells

AGS cells were cultured with varying doses of D-glucose and D-mannitol (8, 12.5, 25, 35, and 50 mM) to ascertain the optimal concentration of glucose for HG treatment. The impact of varying concentrations of glucose and mannitol on AGS cell proliferation was assessed at various time intervals (6, 12, 24, and 36 hours) with the CellTiter-Glo luminous cell viability test.

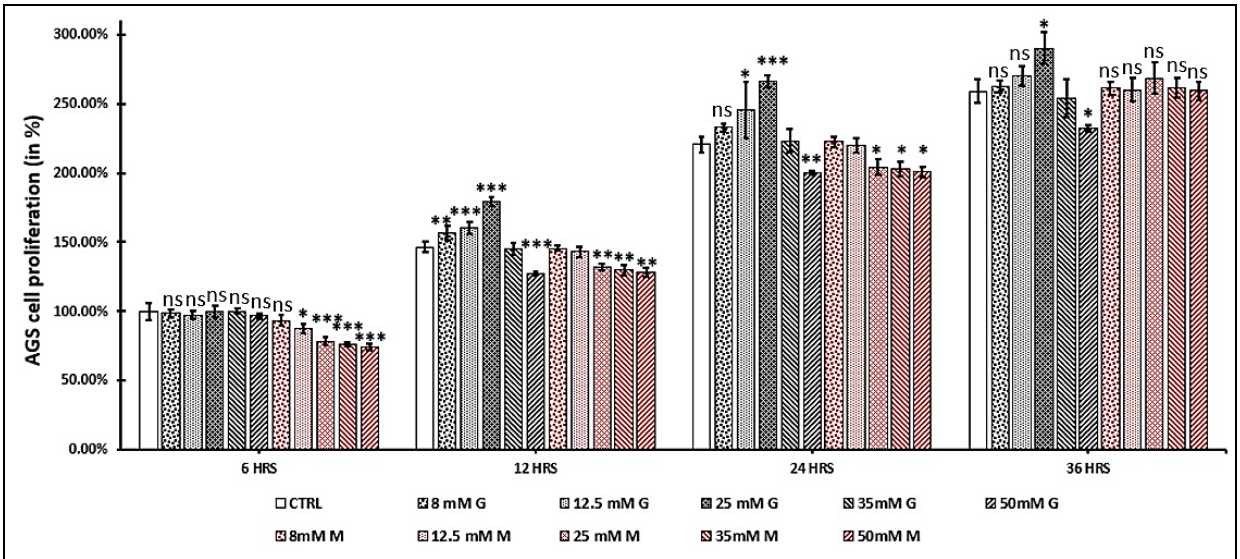

Figure 17. Cell viability of gastric adenocarcinoma (AGS) cells incubated with different glucose (G) and mannitol (M) concentrations at varying time-points. AGS cells were seeded and treated with the denoted concentrations of D-glucose and its osmotic control, D-mannitol. AGS cell proliferation was evaluated using the CellTiter-Glo® Luminescent Cell Viability Assay after 6, 12, 24 and 36 hours. The bars represent percentage of viable cells in each sample and are the means (± SEM) of three independent experiments. All results have been normalized to CTRL-6 hours sample cells. P-values have been calculated against the control samples of respective time-points. Statistical significance was determined using one-way ANOVA followed by Student-Newman-Keuls T-test (*$p<0.05$, **$p<0.01$ and ***$p<0.001$; ns = not significant).

Addition of mannitol in the culture media, as an osmolarity control, does not seem to have any negative effects on AGS cells. Based on the results of this experiment, it can be said that increasing the concentration of glucose in the culture media has significantly upregulated AGS cell proliferation (Figure 17). This effect seems to be dose-dependent, as the cells grown in 25 mM glucose media have greater viability in comparison to its 12.5 mM counterpart. The maximum changes in cell viability between the control and high glucose treatment groups was observed with 25 mM D-glucose after 24 hours of incubation (Fig. 1A). Hence, all the following experiments were performed utilizing 25 mM glucose for a duration of 24 hours.

2.2. Hyperglycemia induces AGS cell proliferation

Ki-67 protein is a widely used marker to ascertain tumor proliferation rate based on its cellular expression during all phases of cell cycle besides G0/G1. For this reason, immunocytochemical technique was used to stain AGS cells incubated in normoglycemic (NG; 5.5 mM D-glucose) and hyperglycemic (HG; 25 mM D-glucose) media with anti-Ki-67 monoclonal antibody.

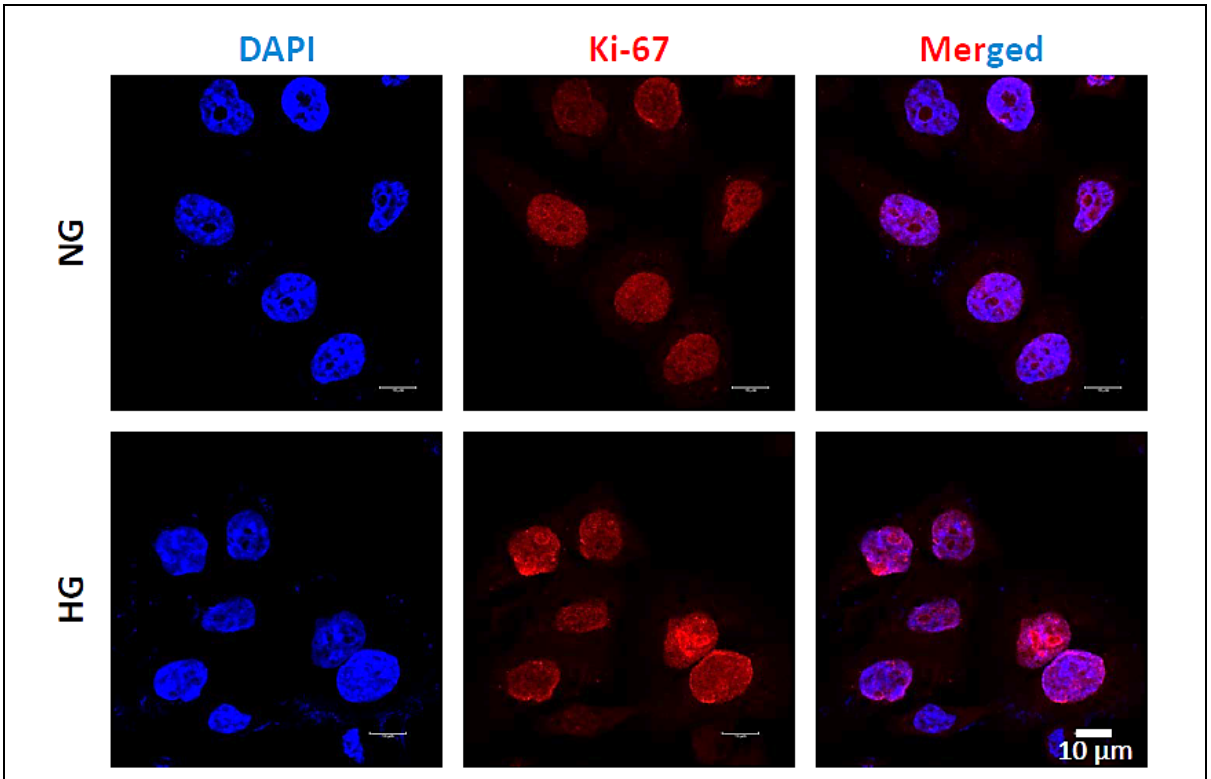

Figure 18. Hyperglycemia induces AGS cell proliferation. AGS cells incubated in NG (5.5 mM D-glucose) and HG (25 mM D-glucose) media were stained with fluorophore-conjugated anti-Ki-67 monoclonal antibody.

The expression of Ki-67 is significantly higher in AGS cells incubated with HG media as compared to NG (Figure 18). This experiment further proves that hyperglycemic condition induces AGS cell proliferation.

2.3. Hyperglycemia induces ROS generation in AGS cells

2′− 7′- dichlorodihydrofluorescein diacetate (DCFH-DA) dye was used to quantify ROS in normoglycemic and hyperglycemic AGS cells. Live cell imaging utilizing high-resolution STED microscopy showed that cells maintained under HG conditions had the highest DCFH-DA fluorescence; in comparison to the normoglycemic and osmolarity control cells (Figure 19).

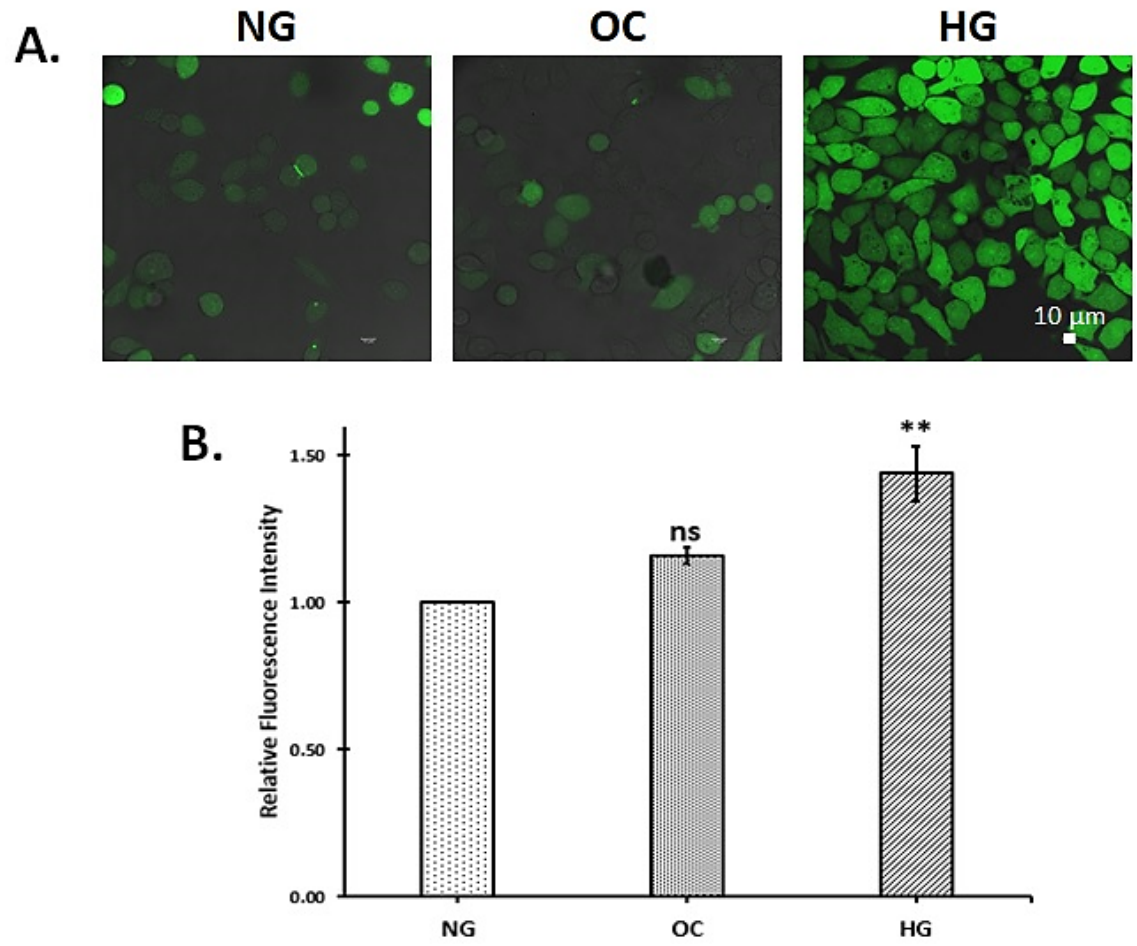

Figure 19. Hyperglycemia induces ROS generation in AGS cells. AGS cells were seeded and given the denoted treatments. Cells were harvested after 24 hours and DCF-DA fluorescence was measured by STED microscopy (A) and fluorometry (B). Values are expressed as mean ± SEM. A Student's t-test was performed for group comparisons. **p<0.01 (vs. 'NG') and ns represents non-significant.

2.4. Hyperglycemia promotes AGS cell migration

The *in vitro* scratch wound healing assay is a simple, cost-effective, and established technique for assessing cell migration *in vitro*. The fundamental processes entail establishing a "scratch" in a cell monolayer, collecting photos at the outset and at consistent intervals throughout cell migration, and analyzing the images to estimate the cellular migration rate.

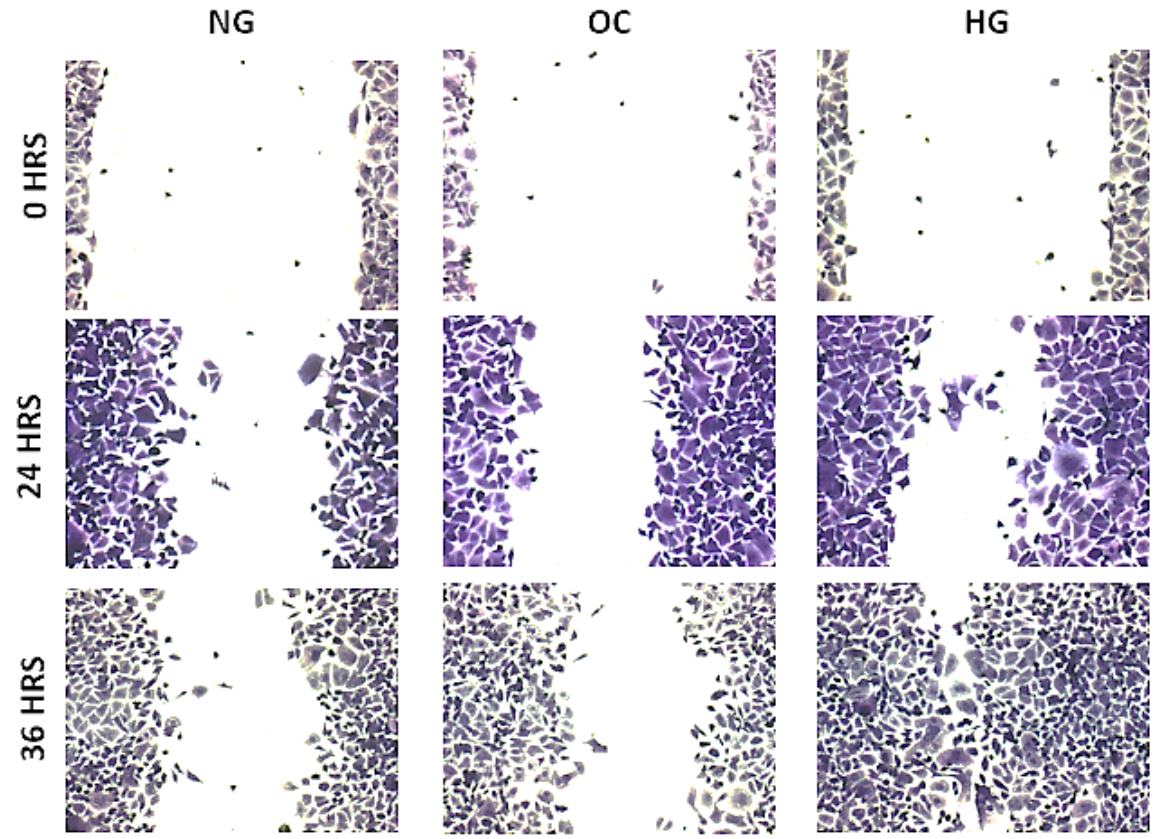

Figure 20. Hyperglycemia promotes AGS cell migration. AGS cells were cultured in six-well plates and grown till confluence, wounded at 0 hours and supplemented with the appropriate incomplete media containing either 25 mM mannitol (OC) or 25 mM glucose (HG). The wounded area was photographed after 24 and 36 hours.

In this scratch wound healing assay, AGS cells have shown a higher rate of migration under hyperglycemic conditions compared to normoglycemic conditions. This effect of hyperglycemia on AGS cell migration is most evident after 36 hours of incubation. The normoglycemic and osmolarity control groups showed similar rate of AGS cell migration.

2.5. Identifying the MMP(s) and TIMP(s) that are affected by hyperglycemia

Hyperglycemia upregulates the expression and activity of MMP-9 and -2 in most cases. Therefore, this study focused on only these two gelatinolytic MMPs. To identify the gelatinase that is affected, AGS cells were incubated in HG media for 0, 6, 12, 24, 36 and 48 hours. Conditioned media was collected and it was used to determine the respective activities of MMP-9 and -2 via gelatin zymography

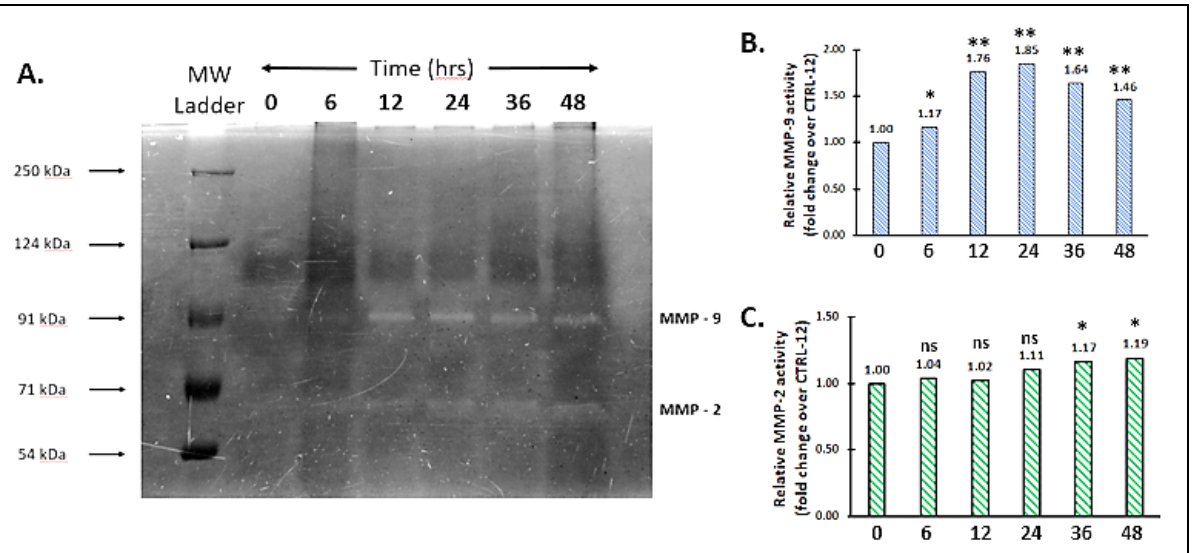

Figure 21. Determination of MMP-9 and -2 activities in hyperglycemic AGS cells using gelatin zymography. (A) After culturing AGS cells in HG media for 0, 6, 12, 24, 36 and 48 hours; conditioned media was collected and it was used to determine the respective activities of MMP-9 and -2 via gelatin zymography. Quantitation of MMP-9 (B) and -2 (C) activities showed that hyperglycemia has a pronounced time-dependent effect on MMP-9 activity only. Values are expressed as mean ± SEM. Statistical significance was determined using Student's t-test (*$p<0.05$ and **$p<0.01$ vs. 0 hr. control; ns = not significant).

The gelatinolytic activity of MMP-9 was upregulated under hyperglycemic conditions; whereas, MMP-2 remained mostly unaffected. An incremental change in MMP-9 activity was observed up to 24 hours of incubation, after which the activity slowly decreased. Upregulation of MMP-9 activity, in turn, indicates a decreased expression of its specific tissue inhibitor, TIMP-1 under hyperglycemic conditions. This was confirmed via western immunoblotting technique in Figure 22.

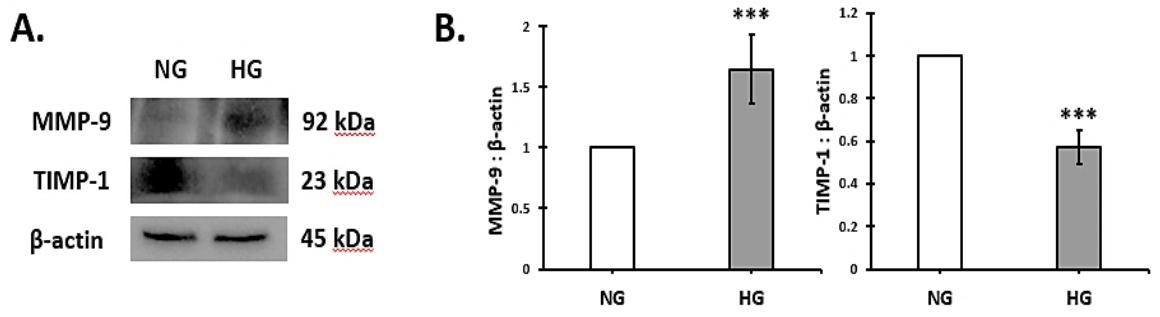

Figure 22. Hyperglycemia is associated with upregulation of MMP-9 and downregulation of TIMP-1 expression. The representative western blots (A) and its consecutive graphical representations (B) show that the expression level of MMP-9 is upregulated and that of TIMP-1 is downregulated under hyperglycemic conditions. Values are mean ± SEM. Statistical significance was determined using Student's t-test (***p-value<0.001 vs.NG).

2.6. Hyperglycemia-induced MMP-9 facilitates the migration and invasion of AGS cells.

The scratch-wound healing assay and transwell invasion assay were employed to investigate AGS cell migration and invasion, respectively. AGS cells were treated with 10 µM hydroxyurea to prevent interference with cell proliferation.

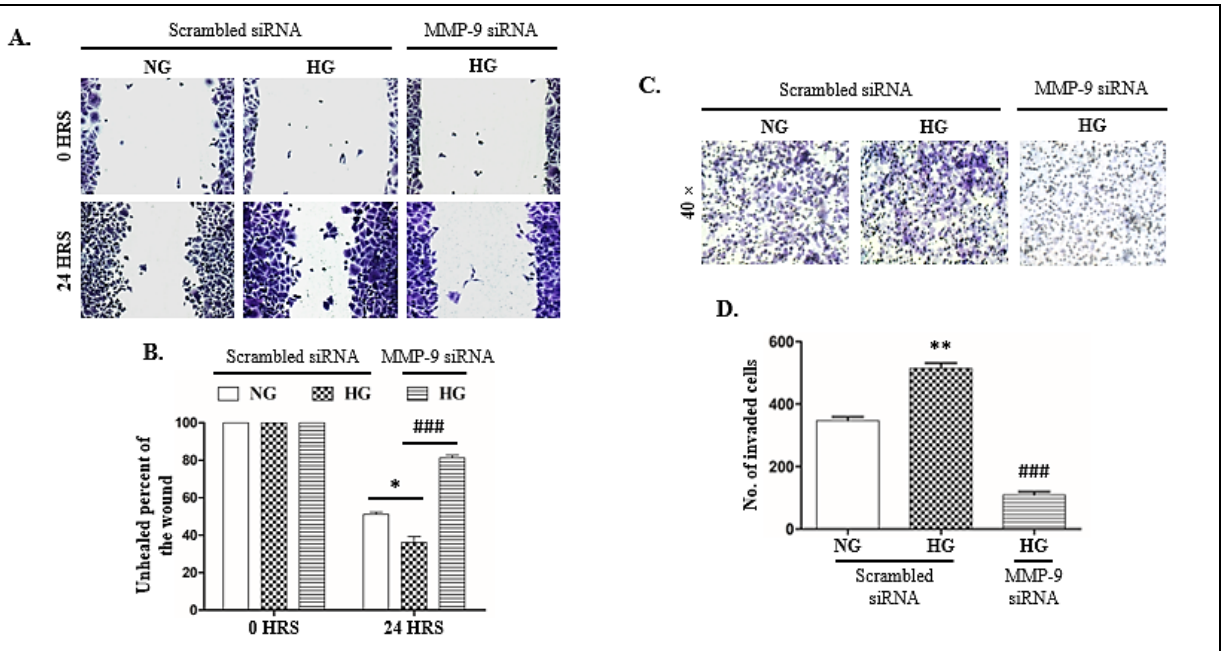

Figure 23. Hyperglycemia-induced migration and invasion of AGS cells is mediated by MMP-9. (A–B) Wound-healing assays were conducted on AGS cells transfected with either scrambled or MMP-9 specific siRNA, evaluated under NG and HG conditions at 0 hours and 24 hours post-

incubation. (C–D) Images depicting the number of transfected AGS cells that traversed the Matrigel-coated membrane of trans-well inserts under NG and HG conditions after 24 hours of incubation. All images represent five separate experiments. Values were expressed as mean ± SEM. A Student's t-test was performed for group comparisons. *p<0.05, **p<0.01 (vs. 'NG') and ###p<0.001 (vs. 'HG'). Adapted from Chatterjee et al., 2024a.

AGS cell migration and invasion were significantly elevated under HG conditions relative to NG control. However, transfection of AGS cells with MMP-9 siRNA resulted in a significant reduction of HG-induced cell migration and invasion. This observation directly links the HG-induced aggressive nature of AGS cells to the elevated MMP-9 levels.

3. Discussion

In this chapter, the influence of hyperglycemia—a hallmark of diabetes mellitus—on gastric cancer (GC) progression, was explored using the AGS cell line as a model. AGS cell line was used because it was derived from gastric adenocarcinoma (the predominant type of gastric malignancy) of a patient. Considering that GC is among the most prevalent and lethal malignancies globally, and that diabetes is rapidly increasing in prevalence, it is essential to understand the molecular interactions between elevated blood glucose levels and GC progression.

To mimic the hyperglycemic environment in an in vitro setting, extra amounts of D-glucose was added in the cell culture medium. D-mannitol was included in these experiments as an osmolarity control to strengthen the conclusion that the observed effects are glucose-specific rather than osmotic artifacts. A significant increase in AGS cell proliferation was observed under HG conditions (25 mM glucose). This observation aligns with prior studies linking hyperglycemia to enhanced tumor growth in other malignancies, such as human epithelial lung cancer (Alisson-Silva et al., 2013; Kang et al., 2015), breast cancer (Sun et al., 2017), and cholangiocarcinoma (Saengboonmee et al., 2016). Immunocytochemical analysis using anti-Ki-67, a nuclear protein marker present during all active phases of the cell cycle (except G0/G1), revealed that AGS cells in a hyperglycemic environment exhibit a significantly higher proliferation rate compared to those in normoglycemic conditions.

Utilizing DCFH-DA dye and high-resolution STED microscopy, it was observed that hyperglycemic AGS cells produced significantly higher ROS levels compared to

normoglycemic and osmolarity-controlled conditions. This elevation of ROS in hyperglycemic AGS cells supports the hypothesis that oxidative stress is a key mechanistic link between hyperglycemia and cancer progression. Chronic HG is known to promote mitochondrial dysfunction and NADPH oxidase activation (González et al., 2023). It also increases ROS generation by O-GlcNAcylating the four main enzyme complexes of the mitochondrial ETC (Kaludercic and Di Lisa, 2020).

Such an increased level of ROS production can induce oxidative stress, which activates various signaling pathways associated with cell proliferation, apoptosis prevention, migration, and may even induce the expression of oncogenes including some MMPs (Mori et al., 2019; Arfin et al., 2021). The HG-induced increase in MMP-9 activity, along with decreased TIMP-1 expression, indicates a transition toward extracellular matrix (ECM) degradation, which is characteristic of metastatic invasion. The siRNA-mediated knockdown of MMP-9, which reduced migration and invasion, offers causal evidence for its involvement in HG-induced aggressiveness.

Overall, the findings of this chapter underscore the potential link between HG and GC progression and also highlights the importance of metabolic control in cancer therapy. Moreover, reversing MMP-9 overexpression could offer new avenues for therapeutic intervention, especially in patients with concurrent diabetes and gastric cancer. However, in order to do so, the signaling pathway(s) responsible for the HG-induced upregulation of MMP-9 must be identified.

Chapter 4

Delineating the signaling pathway accountable for Hyperglycemia-induced excessive MMP-9 transcription

DELINEATING THE SIGNALING PATHWAY ACCOUNTABLE FOR HYPERGLYCEMIA-INDUCED EXCESSIVE MMP-9 TRANSCRIPTION

1. Introduction

Hyperglycemia might exacerbate the progression of cancer by enhancing inflammation, angiogenesis, proliferation of tumor cell, and metastasis. Elevated glucose levels contribute to tumorigenesis and EMT in human epithelial lung cancer cells (Alisson-Silva et al., 2013; Kang et al., 2015), breast cancer cells (Sun et al., 2017), and cholangiocarcinoma cells (Saengboonmee et al., 2016).

Several researchers have investigated the correlation between hyperglycemia and metastasis, emphasizing the role of MMPs. MMPs constitutes a family of enzymes that are zinc dependent and calcium requiring and are essential for the degradation and reorganization of the ECM. MMP dysregulation can compromise integrity of ECM and promote metastasis. HG can influence the expression and activity of many MMPs, including MMP-9, which is linked to cancer cell motility, invasion, and angiogenesis (Kang et al., 2015; Sun et al., 2017). Elevated MMP-9 levels can destroy ECM components, facilitating cancer cell invasion into adjacent tissues and promoting angiogenesis to sustain tumor development (Jabłońska-Trypuć et al., 2016). Nonetheless, the precise biochemical mechanism by which the hyperglycemic milieu promotes MMP-9 production remains unclear, especially in GC.

Moreover, comprehending the complex interaction among hyperglycemia, MMP-9, and metastasis is essential for formulating tailored treatment strategies. Strategies designed to regulate glucose levels, modulate MMP-9 activity, and impede metastatic processes show potential to alleviate the adverse impacts of HG on cancer advancement. This chapter seeks to elucidate the molecular signaling mechanisms responsible for the hyperglycemia-induced overexpression of MMP-9 in gastric cancer cells, which may facilitate the designing of targeted therapeutics for GC-HG co-morbidity.

2. Results

2.1. MMP-9 expression and activity increase in response to glucose in a dose- and time-dependent manner in AGS cells

A substantial increase of MMP-9 was observed after incubating AGS cells in culture media with various concentrations of glucose (5.5, 8, 12.5, 25, 35, and 50 mM D-glucose). MMP-9 levels demonstrated a dose-dependent response, with elevated glucose concentration (up to 25mM) resulting in a more significant rise in MMP-9 levels (Figure 24A–24E). Any subsequent elevation in media glucose concentration, beyond 25 mM, resulted in a dose-dependent reduction of MMP-9 levels (Figure 24A–24E).

Subsequently, AGS cells were cultured in HG media with 25 mM D-glucose for various time-points (0, 6, 12, 24, 36, and 48 hours). The elevation of MMP-9 occurs progressively, peaking at 24 hours; subsequent incubation does not provide significant changes, showing a time-dependent influence of glucose concentration on MMP-9 levels (Figure 24F–24J). The results indicate that elevated glucose levels enhance the activity and expression of MMP-9 in a dose- and time-dependent fashion in AGS cells. Consequently, in the following studies, HG induction was done by treating AGS cells for 24 hours with 25 mM glucose.

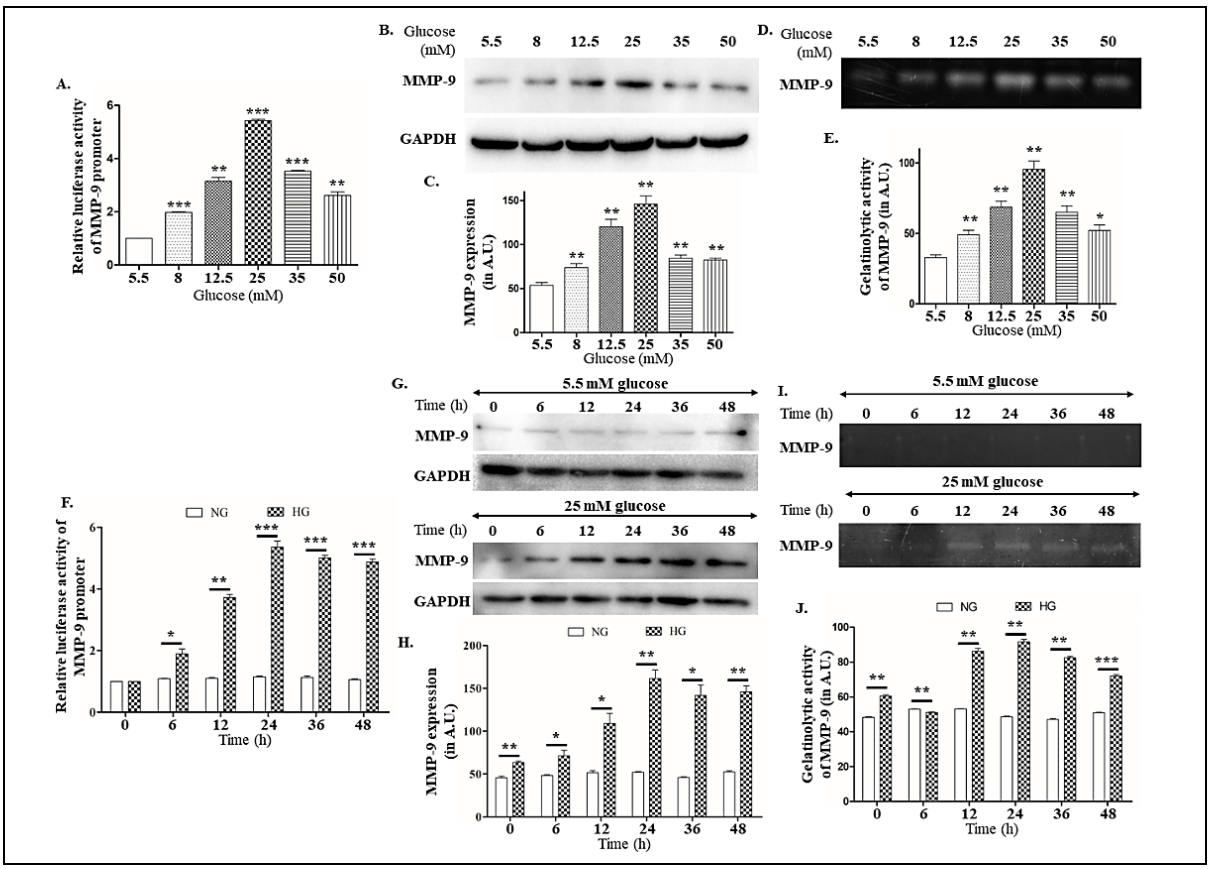

Figure 24. Elevated glucose levels promote the excessive expression and activity of MMP-9 in AGS cells. (A–E) The impact of elevated glucose concentrations on the activity of promoter (A), expression of MMP-9 (B, C), and MMP-9 activity (D, E). AGS cells that were transfected with complete MMP-9 luciferase reporter constructs, along with un-transfected AGS cells, were subjected to treatment with escalating concentrations of D-glucose (5.5, 8, 12.5, 25, 35, and 50 mM) for a duration of 24 hours. Subsequently, luciferase reporter assays, immunoblotting, and gelatin zymography assays were conducted to assess activity of promoter, expression of MMP-9, and MMP-9 activity, respectively. (F–J) The time-dependent influence of 5.5 mM and 25 mM D-glucose on the activity of promoter (F), expression of MMP-9 (G, H), and MMP-9 activity (I, J). AGS cells that were transfected with complete MMP-9 luciferase reporter constructs, along with un-transfected AGS cells, were maintained in NG (5.5 mM) and HG media (25 mM) for the durations of 0, 6, 12, 24, 36, and 48 hours. Subsequently, luciferase reporter assays, immunoblotting, and gelatin zymography were conducted to assess activity of promoter, expression of MMP-9, and MMP-9 activity respectively. Values were expressed as mean ± SEM. The Student's t-test was employed to compare between groups (***p<0.001, **p<0.01, and *p<0.05). Adapted from Chatterjee et al., 2024a.

In analogous tests utilizing D-mannitol (non-metabolizable; serves as an osmolarity control for D-glucose), luciferase activity of the MMP-9 promoter exhibited no significant alteration relative to NG cells (Figure 25). This indicates that the detected elevation in MMP-9 levels under HG conditions was likely attributable to the metabolic effects of glucose rather than alterations in cell culture medium osmolarity.

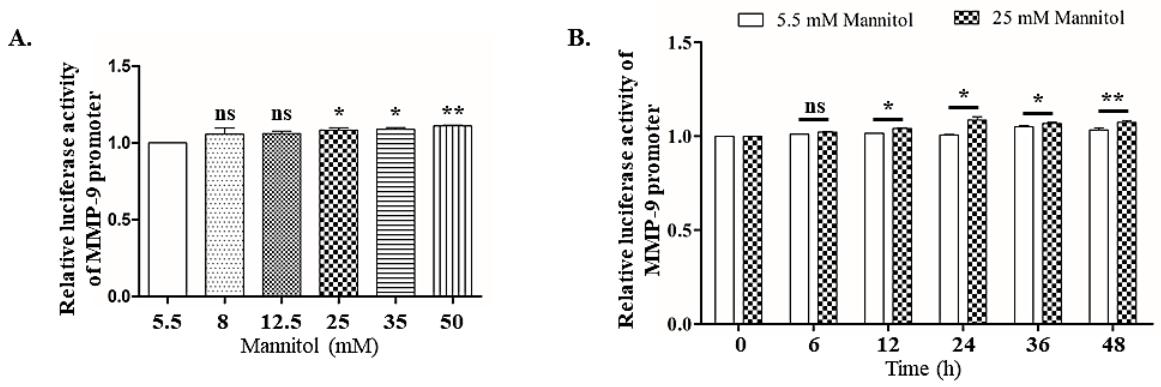

Figure 25. Dose and time-dependent effect of D-mannitol on MMP-9 promoter activity. (A) Effect of increasing concentrations of D-mannitol on the promoter activity of MMP-9. AGS cells that were transfected with full-length MMP-9 luciferase reporter plasmids were subjected to

treatment with different concentrations of D-mannitol (5.5, 8, 12.5, 25, 35, and 50 mM) for duration of 24 hours. Subsequently, luciferase reporter assay was used to measure MMP-9promoter activity. (B) The time-dependent influence of 5.5 mM and 25 mM D-mannitol on the MMP-9 promoter activity. AGS cells that were transfected with complete MMP-9 luciferase reporter construct, along with un-transfected AGS cells, were incubated in NG (5.5 mM) and HG media (25 mM) for durations of 0, 6, 12, 24, 36, and 48 hours. Subsequently, luciferase reporter assay was used to measure the promoter activity of MMP-9. Values were expressed as mean ± SEM. The Student's t-test was employed to compare between groups (**p<0.01, *p<0.05, and "ns" denotes non-significant). Adapted from Chatterjee et al., 2024a.

2.2. HG-induced expression of MMP-9 is independent of the NF-κB (p65) signaling pathway

An increase in the expression (~1.91-fold; p<0.01) and phosphorylation (~3.83-fold; p<0.01) of p65 was observed under HG conditions (Figure 26A, 26B & 26C). In order to understand the role that increased levels of p65 and p-p65 play in controlling MMP-9 production, AGS cells were transfected with either p65-specific siRNA or non-specific scrambled siRNA and complete MMP-9 luciferase reporter construct. Transfected cells were then grown for 24 hours under both NG and HG conditions. Western blot analysis and Luciferase assay were then used to assess MMP-9 levels. These findings indicate that p65 silencing did not produce a statistically significant effect on the protein levels (Figure 26E–26G) and promoter activity (Figure 26H) of MMP-9. The Luciferase reporter assay further demonstrated that MMP-9 expression was not suppressed when the NF-κB binding sequence was removed from the MMP-9 promoter (Figure 26I & 26J). These findings suggest that the p65-NF-κB signaling pathway is not substantially involved in HG-induced MMP-9 synthesis.

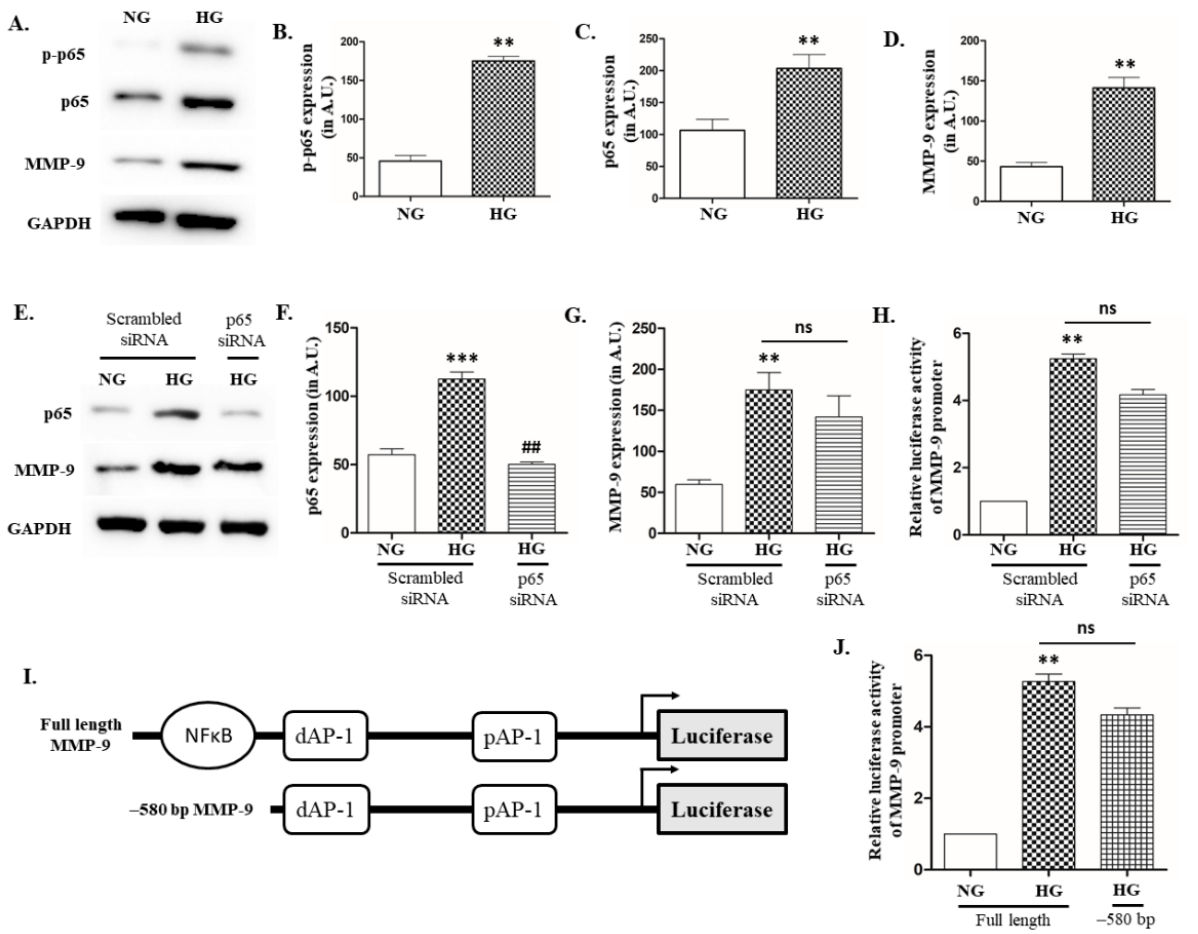

Figure 26. HG-induced expression of MMP-9 is independent of the NF-κB (p65) signaling pathway. (A) Immunoblot analysis was conducted to assess the expression patterns of p-p65, p65, and MMP-9 in AGS cells under both NG and HG conditions, keeping GAPDH as the loading control. (B–D) Histographic representation showing the densitometric analysis of the expression patterns of p-p65, p65, and MMP-9 respectively. (E) Immunoblot analysis demonstrating p65 and MMP-9 protein expression following transfection of AGS cells with either the non-specific or the p65-specific siRNA, in both NG and HG conditions. GAPDH was used as the loading control. (F–G) Histographic representation showing the densitometric analysis of the expression patterns of p65 and MMP-9, respectively. (H) Relative luciferase activity of the MMP-9 promoter following the transfection of AGS cells with either the non-specific or p65-specific siRNA, in both NG and HG conditions. (I) Schematic representation of the complete and –580 bp deletion construct of the human MMP-9 promoter. (J) Relative luciferase activity of MMP-9 promoter following the transfection of AGS cells with both the complete and –580 bp deletion construct of the human MMP-9 promoter, under both NG and HG conditions. Values were expressed as mean ± SEM. Student's t-test was employed to compare between groups. ***p<0.001, **p<0.01 (vs. 'NG'); ##p<0.01, (vs. 'HG'); and "ns" denotes non-significant. Adapted from Chatterjee et al., 2024a.

2.3. HG-induced overexpression of MMP-9 is controlled through the MAPK pathway

Analysis of protein expression and phosphorylation levels of key signaling components within the MAPK pathway was conducted. Immunoblot analyses indicated a significant upregulation of p-ERK 1 (~2.13 fold; $p<0.05$), p-ERK 2 (~2.03 fold; $p<0.01$), and c-Fos (~1.94 fold; $p<0.01$). Under hyperglycemic conditions, p-JNK 1 exhibited an increase of approximately 2.53 fold ($p<0.05$), p-JNK 2 showed a rise of about 2 fold ($p<0.05$), c-Jun increased by roughly 1.38 fold ($p<0.01$), and p-p38 demonstrated an increase of approximately 1.74 fold ($p<0.05$) (Figure 27).

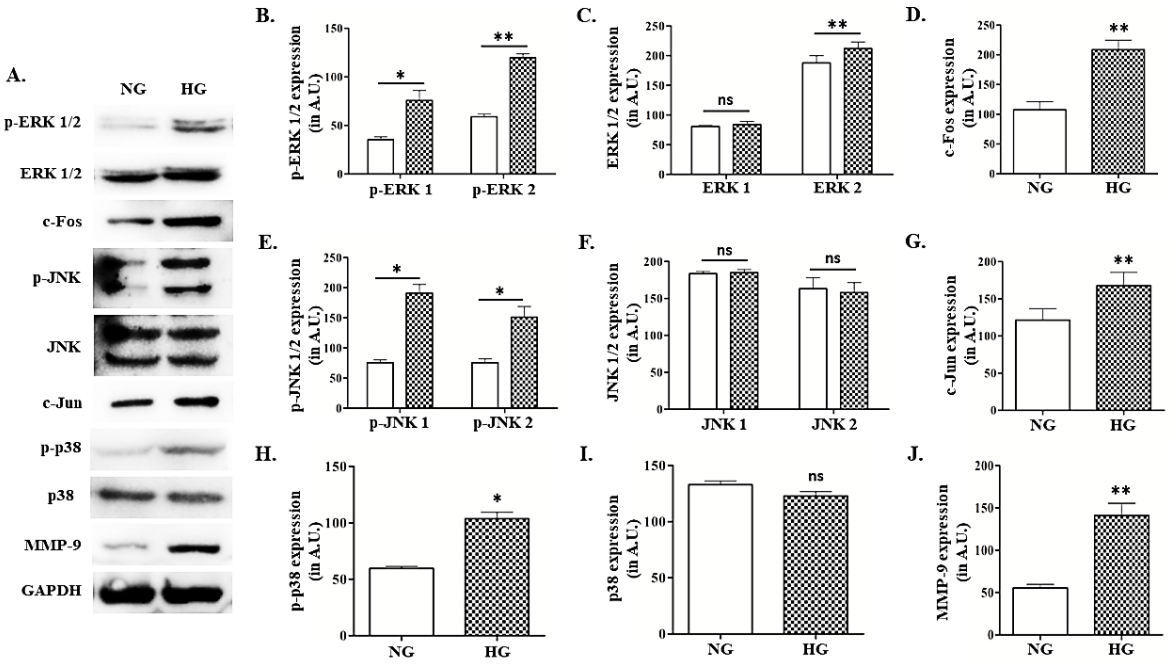

Figure 27. The impact of HG on various elements of the MAPK pathway. (A) Immunoblot analysis was conducted to assess the expression patterns of various MAPK pathway regulators in AGS cells under both NG and HG conditions. GAPDH was used as the loading control. (B–J) Histographic representation showing the densitometric analysis of the expression patterns of p-ERK 1/2, ERK 1/2, c-Fos, p-JNK, JNK, c-Jun, p-p38, p38, and MMP-9, respectively. Values were expressed as mean ± SEM. The Student's t-test was employed to compare between groups (**p<0.01, *p<0.05, and "ns" denotes non-significant). Adapted from Chatterjee et al., 2024a.

To ascertain the involvement of these elevated proteins in the modulation of MMP-9 production, AGS cells were pre-treated with SP 600125, which is a JNK inhibitor at a concentration of 50 µM; PD 98059, which is an ERK 1/2 inhibitor at a concentration of 50 µM; and SB 203580, which is a p38 MAPK inhibitor at a concentration of 20 µM. These MAPK inhibitors were added one hour prior to the induction of hyperglycemia (Figure 28A–28E). AGS cells subjected to either of these inhibitors were unable to synthesize MMP-9 in hyperglycemic conditions (Figure 28A, 28F & 28G). This established that the HG-induced increase of MMP-9 relies on the MAPK pathway.

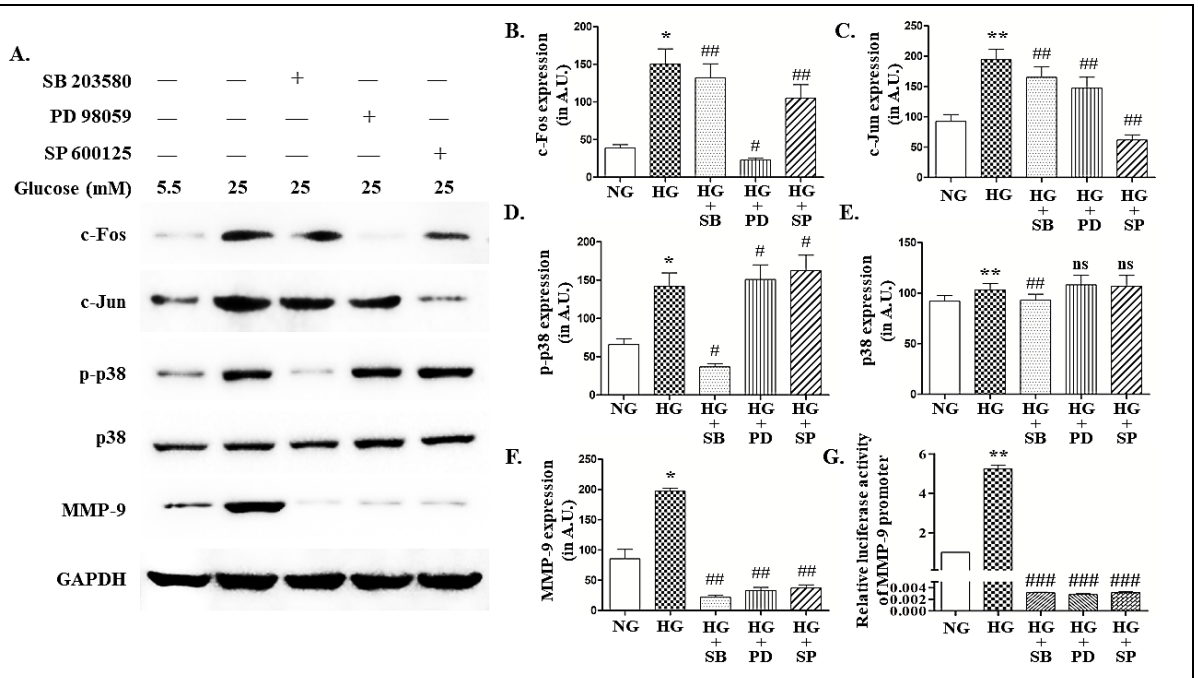

Figure 28. HG-induced expression of MMP-9 is contingent upon the MAPK signaling pathway. (A) Immunoblot analysis was conducted to assess the expressions of key MAPK pathway proteins in AGS cells following pre-treatment with or without SB203580, PD98059, and SP600125, under both NG and HG conditions. GAPDH was used as the loading control. (B–F) Histographic representation showing the densitometric analysis of the protein expressions of c-Fos, c-Jun, p-p38, p38, and MMP-9, respectively. (G) Relative luciferase activity of MMP-9 promoter in AGS cells pre-treated with or without SB203580, PD98059, and SP600125, under both NG and HG conditions. Values were expressed as mean ± SEM. The Student's t-test was employed to compare between groups. **p<0.01, *p<0.05 (vs. 'NG'); ###p<0.001, ##p<0.01, #p<0.05 (vs. 'HG') and "ns" represents non-significant. Adapted from Chatterjee et al., 2024a.

2.4. Hyperglycemia induces the nuclear translocation of both c-Fos and c-Jun

Nuclear proteins from AGS cells cultivated under normoglycemic and hyperglycemic conditions were extracted, followed by western blot analysis. An increase of approximately 1.45-fold ($p<0.05$) in the nuclear localization of c-Fos was observed under HG circumstances (Figure 29A & 29B). The cytoplasmic levels of c-Fos had also undergone significant increase (~1.65 fold; $p<0.001$) (Figure 29A & 29B). c-Jun exhibited approximately ~1.96-fold increase ($p<0.05$) in its nuclear localization, while a ~1.58-fold amplification ($p<0.05$) was seen in the cytosolic fraction (Figure 29A & 29C). The immunofluorescence pictures exhibit a comparable pattern of c-Jun and c-Fos localization (Figure 29D & 29E). The findings indicate that c-Jun and c-Fos, triggered by the JNK and ERK pathways, translocate to the nucleus and forms hetero-dimer to generate the AP-1 transcription factor, that subsequently activates MMP-9 transcription.

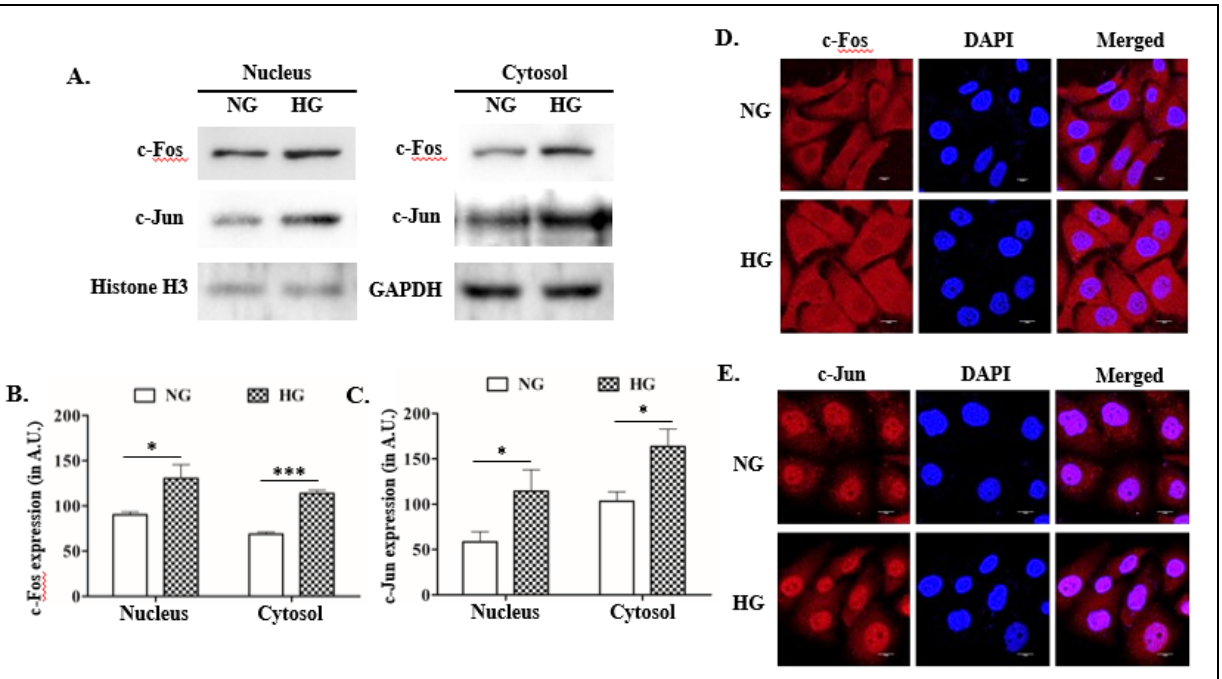

Figure 29. HG induces the nuclear translocation of both c-Jun and c-Fos. (A) Immunoblot analysis was conducted to examine the expressions of c-Jun and c-Fos in the nuclear and cytoplasmic fractions of AGS cells under both NG and HG conditions. Histone H3 and GAPDH functioned as the loading controls for nuclear and cytoplasmic fractions, respectively. (B–C) Histographic representation showing the densitometric analysis of the expressions of c-Jun and c-Fos in the nuclear and cytoplasmic fractions. (D) Images of c-Fos immunostaining in AGS cells under both NG and HG conditions. The red fluorescence (Texas Red) indicates the presence of c-Fos protein while the blue fluorescence (DAPI) marks the nucleus. (E) Images of c-Jun immune-staining in AGS cells under

both NG and HG conditions The red fluorescence of Texas Red indicates the presence of c-Jun protein while the blue fluorescence of DAPI marks the nucleus. All the images represent five separate experiments. Values were expressed as mean ± SEM. The Student's t-test was employed to compare the groups (***p<0.001 and *p<0.05). Adapted from Chatterjee et al., 2024a.

2.5. AP-1 heterodimer binding to both distal and proximal sites of the MMP-9 promoter are upregulated under HG conditions

Two different AP-1 binding sites are present in the MMP-9 promoter: the distal site (dAP-1) located from –514 to –507 and the proximal site (pAP-1) from –80 to –71. The binding efficiency of the AP-1 hetero-dimer frequently differs between the above mentioned two locations. The Luciferase Reporter Assay with MMP-9 promoter deletion constructs demonstrated that deletion of the dAP-1 binding site (in the –461 bp deletion construct) resulted in a reduction of approximately ~2.92 fold ($p<0.05$) in MMP-9 promoter activity relative to the full-length promoter (Figure 30A & 30B). The –72 bp deletion construct exhibited a total loss of MMP-9 promoter activity due to the lack of both the dAP-1 and pAP-1 binding sites, which are critical for MMP-9 transcription (Figure 30A & 30B). This experiment's results indicate that both the dAP-1 and pAP-1 binding sites are crucial for modulating MMP-9 production in HG circumstances.

A ChIP test was conducted to ascertain which of the two AP-1 binding sites plays a greater role in regulating HG-induced MMP-9 production. This was measured by comparing the fold change in c-Fos and c-Jun proteins associated with the dAP-1 and pAP-1 binding sites, relative to NG conditions. Hyperglycemia enhanced the binding of c-Jun (~2.47-fold; $p<0.01$) and c-Fos (~4.23-fold; $p<0.01$) to the pAP-1 binding region of the MMP-9 promoter (Figure 30C, 30E, 30F & 30H). The binding of c-Jun and c-Fos to the dAP-1 binding site increased by approximately 17.12-fold ($p<0.001$) and 7.44-fold ($p<0.01$), respectively (Figure 30C, 30D, 30F & 30G). Furthermore, immune-precipitated samples, with IgG control antibodies never produced discernible PCR result. The findings of this experiment verify that both the dAP-1 and pAP-1 binding sites are simultaneously active in HG conditions and accountable for HG-induced MMP-9 production.

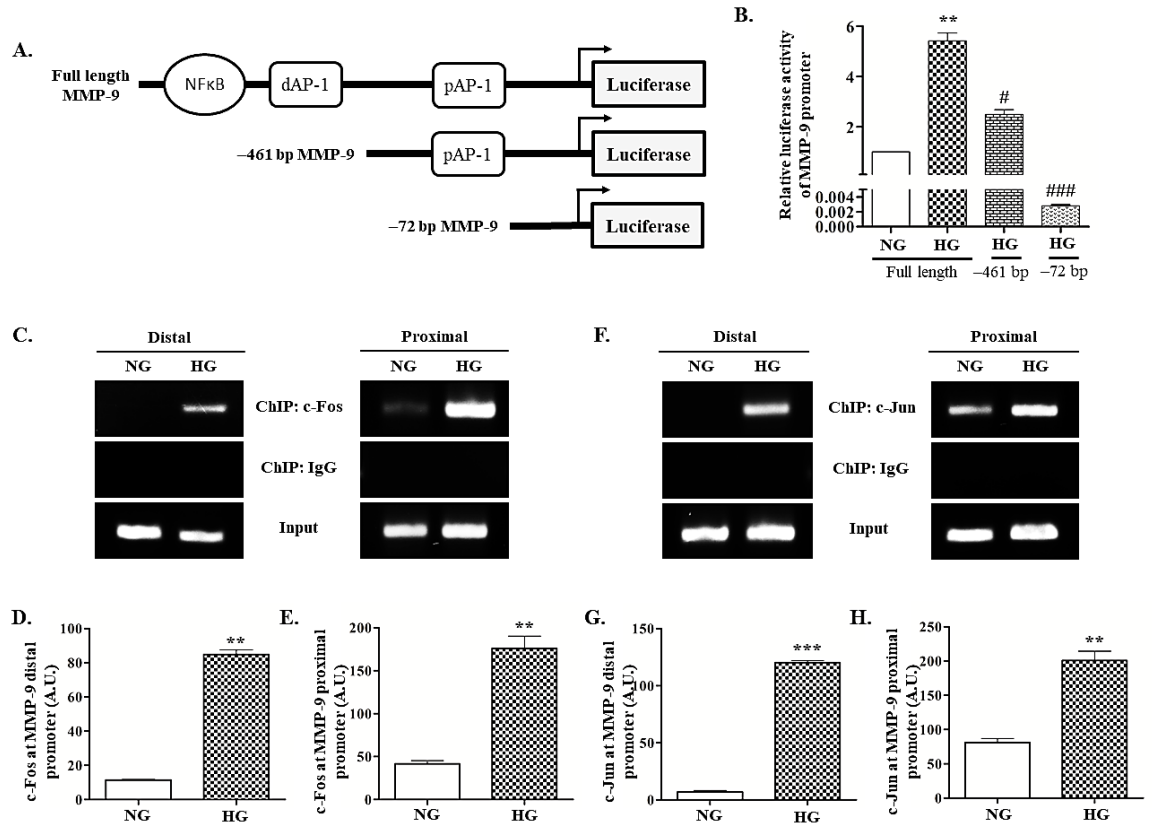

Figure 30. Both the dAP-1 and pAP-1 binding sites of the MMP-9 promoter are concurrently activated under HG conditions. (A) Schematic representation of the complete, –461 bp and –72 bp deletion constructs of the human MMP-9 promoter. (B) Histographic representation of the relative luciferase activity of MMP-9 promoter was assessed in AGS cells after transfection with complete, –461 bp and –72 bp deletion constructs, under both NG and HG conditions. The association of c-Fos (C–E) and c-Jun (F–H) at the dAP-1 and pAP-1 binding sites of MMP-9 promoter was measured using a ChIP assay. DNA precipitated with the IgG isotype served as the negative control. Values were expressed as mean ± SEM. The Student's t-test was employed to compare between groups. ***p<0.001, **p<0.01 (vs. 'NG'); ###p<0.001, #p<0.05 (vs. 'HG'). Adapted from Chatterjee et al., 2024a.

3. Discussion

Both diabetes and cancer have consistently posed a global challenge to human health, primarily due to the rising incidence and death rates linked to both conditions. As of 2021, about 536.6 million individuals globally are afflicted with diabetes (Sun et al., 2022). By the year 2045, it is anticipated that 9.9% of the global human population would get diabetes (Standl et al., 2019). The GLOBOCAN 2020 figures estimate the annual incidence of all

types of cancer (excluding melanoma) to be around 20 million (Sung et al., 2021). Patients over the age of 65 make up approximately 60% of those who have just been diagnosed with cancer (Yancik and Ries, 2000), and around 25% of individuals over 65 also have diabetes (Kirkman et al., 2012). Consequently, almost 3 million new instances of people with co-morbid cancer and diabetes are diagnosed annually.

Hyperglycemia, which occurs in diabetes, creates an environment that facilitates cancer growth and markedly increases the spreading potential of cancer cells (Wu et al., 2018). These effects have been previously described in lung cancer (Kang et al., 2015), breast cancer (Sun et al., 2017), and cholangiocarcinoma (Saengboonmee et al., 2016). Metastasis is significantly affected by the role of matrix metalloproteinases (MMPs) (Niland et al., 2021). MMP-9 is particularly noteworthy among other MMPs, as hyperglycemia has been shown to promote invasion and metastasis by increasing MMP-9 levels in breast and lung cancer cells.

MMP-9 expression in AGS cells has similarly been demonstrated to increase with varying concentrations of glucose up to 25 mM, resulting in a bell-shaped response curve. Such a response is likely due to the cytotoxic effects of glucose concentrations (>25 mM) on AGS cells (Figure 17). Incubation of AGS cells in HG media (with 25 mM D-glucose) for varying durations results in an increased expression of MMP-9 upto 24 hours, followed by a subtle decline at 36 hours, and a significant decline at 48 hours compared to its expression level at 24 hours. The reduction in the expression of MMP-9 may be ascribed to a corresponding decline in medium glucose content beyond 48 hours of incubation.

The migratory and invasive characteristics of AGS cells were amplified under HG conditions. The aggressive behavior of AGS cells caused by hyperglycemia was diminished following the silencing of MMP-9. Consequently, the augmented invasive potential of AGS cells under HG conditions is linked to the elevated expression of MMP-9. Determining the factors accountable for the HG-induced MMP-9 overexpression is essential for developing targeted therapeutics for GC-HG co-morbidity.

The MMP-9 promoter is recognized for possessing many functional cis-regulatory domains containing binding sites for NF-κB, SP-1, and AP-1 (Chakraborti et al., 2003; Farina et al., 2014). These transcription factors govern both basal and inducible transcriptional responses (Yan and Boyd, 2007). Prior research has indicated significant roles for NF-κB and AP-1 transcription factors in regulating the expression of MMP-9 (Park et al., 2018). Given that

both NF-κB and AP-1 possess binding sites on the MMP-9 promoter region, they should presumably be active during the overexpression of MMP-9. Nonetheless, it remains uncertain whether they are similarly active in GC under HG circumstances and equally accountable for the overexpression of MMP-9.

This study indicates that while the NF-κB (p65) pathway was activated in HG settings, it had no significant influence the regulation of hyperglycemia-induced MMP-9 expression. However, previous investigations demonstrated that NF-κB plays a crucial role in regulating MMP-9 expression (Li et al., 2013; Wang et al., 2014; Al-Roub et al., 2023). This substantial discrepancy may arise from the fact that these research articles investigate the more conventional type of MMP-9 transcriptional regulation, mostly linked to inflammatory indicators (such as TNF-α and interleukins) or inflammation-inducing substances (such as LPS). Despite hyperglycemia triggering inflammatory signals, the signaling molecules appear to possess a diminished potential to promote transcription of MMP-9 under HG conditions. This situation is particularly accurate in the early hours of HG onset (till 24 hours).

Additionally, MMP-9 may be activated through mechanisms that are not reliant on NF-κB signaling in gastric cancer (Yoon et al., 2013). The MAPK pathway is significantly implicated in regulating the expression of MMP-9. Amidst the three families of MAPK, the p38 MAPK activates MMP-9 transcription. p38 MAPK elevation in turn elevate the expression of MMP-9, hence facilitating invasion in cervical and hepatic cancer cell lines (Liu et al., 2022). On the other hand, p38 MAPK downregulation results in decreased MMP-9 activity and expression (Mao et al., 2010). Additionally, p38γ MAPK was shown to collaborate with c-Jun in the trans-activation of MMP-9 (Loesch et al., 2010). Huang et al. establish a correlation between the elevation of phospho-p38 and MMP-9 production in human GC tissues (Huang et al., 2014). Consequently, MMP-9 expression was significantly reduced following the incubation of AGS cells in HG conditions with SB203580–an inhibitor of the p38 MAPK pathway.

Moreover, the production of the AP-1 transcription factor is the culmination of the JNK and ERK pathways, often accomplished by the hetero-dimerization of the c-Jun and c-Fos proteins. While the hetero-dimerization of c-Jun and c-Fos is predominant, c-Jun can, in rare instances, homodimerize and attach to the AP-1 binding site as a homodimer (Halazonetis et al., 1988; Ozanne et al., 2007). AP-1 binds to the promoter region of the target gene in a

sequence-specific way (Hess et al., 2004), and depending on the circumstances and composition of the bound subunits, it regulates the transcription of MMP-9.

This work demonstrated that the interaction of c-Jun and c-Fos with the AP-1 binding site is essential for HG-induced overexpression of MMP-9, as the inhibition of ERK or JNK pathways significantly reduced MMP-9 production. Both c-Jun and c-Fos experience nuclear translocation in HG circumstances, suggesting the development of the AP-1 hetero-dimer. The ChIP experiment demonstrated that c-Jun and c-Fos were exclusively associated to the pAP-1 binding site on the MMP-9 promoter in NG circumstances. This indicates that the pAP-1 binding site is essential for sustaining a baseline level of MMP-9 transcription. However, under HG circumstances, the dAP-1 exhibited a more pronounced reaction for AP-1 binding than pAP-1. Such disparity in reaction between them may be ascribed to the observation that, in contrast to pAP-1, the dAP-1 binding site remained predominantly dormant under NG circumstances. Consequently, it was evident that the dAP-1 binding site governs the HG-inducible transcription of MMP-9, while the pAP-1 binding site facilitates both HG-inducible as well as basal transcription of MMP-9.

A comparable function of AP-1 in the control of MMP-9 transcription has been previously linked to diabetic retinopathy (Mishra et al., 2016). These findings validate their results and emphasize the significance of the dAP-1 binding site in modulating the HG-induced MMP-9 transcription. The dAP-1 binding site may be included into future pharmacological developmental efforts, as its inhibition may significantly diminish the HG-induced production of MMP-9 while leaving its basal levels unaffected. This technique may enhance the quality of life for people with co-morbid GC and diabetes.

Chapter 5

Therapeutic effects of natural compounds (Melatonin & Shatavarin-IV) in Gastric Cancer cells under Hyperglycemic conditions

THERAPEUTIC EFFECTS OF NATURAL COMPOUNDS (MELATONIN & SHATAVARIN-IV) IN GASTRIC CANCER CELLS UNDER HYPERGLYCEMIC CONDITIONS

1. Introduction

Although hyperglycemia is known to promote the survival and progression of cancer cells, no distinct treatment protocol has been established for co-morbid patients with GC and HG. Numerous chemo-therapeutic molecules have been produced and assessed as of late; however, the median overall survival of metastatic gastric cancer patients has not surpassed one year (Liang et al., 2020). Consequently, it is highly pertinent to identify superior anti-cancer agents that exhibit enhanced effectiveness and reduced side effects for treating GC-HG co-morbidity. This chapter will concentrate on two such alternative therapeutic agents: Melatonin and Shatavarin-IV.

Given that ROS significantly contributes to the increased metastatic nature of GC cells under HG conditions, it is plausible to consider that an antioxidant could potentially ameliorate this condition. Melatonin is a naturally occurring antioxidant hormone synthesized and released by the pineal gland and the enterochromaffin cells of the GI tract. Melatonin, produced by enterochromaffin cells, exhibits considerable stability in the gastric environment, with its concentration being 10-100 times greater in the gastrointestinal tract than that in plasma (Bubenik, 2008). Recent studies indicate that melatonin protects several cancer cell lines against neoplastic proliferation, including breast cancer (Martínez-Campa et al., 2017), colorectal cancer (Kvietkauskas et al., 2020), non-small cell lung cancer (Ma et al., 2019), and prostate cancer (Zharinov et al., 2020; Wang et al., 2021), among others. Nonetheless, the therapeutic efficacy of melatonin in the context of hyperglycemia-gastric cancer comorbidity has yet to be assessed.

Shatavarin-IV is a steroidal saponin present in the roots of *Asparagus racemosus* Willd., a medicinal plant utilized in traditional Indian Ayurvedic medicine for the treatment of stomach ulcers and diabetes (Bopana and Saxena, 2007). The effects of Shatavarin-IV was investigated in this study primarily due to the anti-diabetic properties of its source plant.

2. Results

2.1. Melatonin and Shatavarin-IV induce hyperglycemic AGS cell death in a dose-dependent manner

To determine the impact that melatonin and Shatavarin-IV have on AGS cell viability under HG conditions (25 mM D-glucose), the cells were incubated with different doses of melatonin (0, 0.5, 1, 2, 3, 4, and 5 mM) or Shatavarin-IV (0, 1, 2, 3, 4, and 5 µM) for 24 hours. The results of the CellTiter-Glo luminescent cell viability experiment demonstrated that vitality of hyperglycemic AGS cells steadily reduced upon increased dose of melatonin and Shatavarin-IV (Figure 31). The IC_{50} values of melatonin and Shatavarin-IV were calculated to be 3.843 mM and 2.463 µM, respectively under HG conditions. However, a less toxic dose of both compounds was chosen for conducting experiments. A concentration of 2 mM melatonin and 2.2 µM Shatavarin-IV was used for all further experiments.

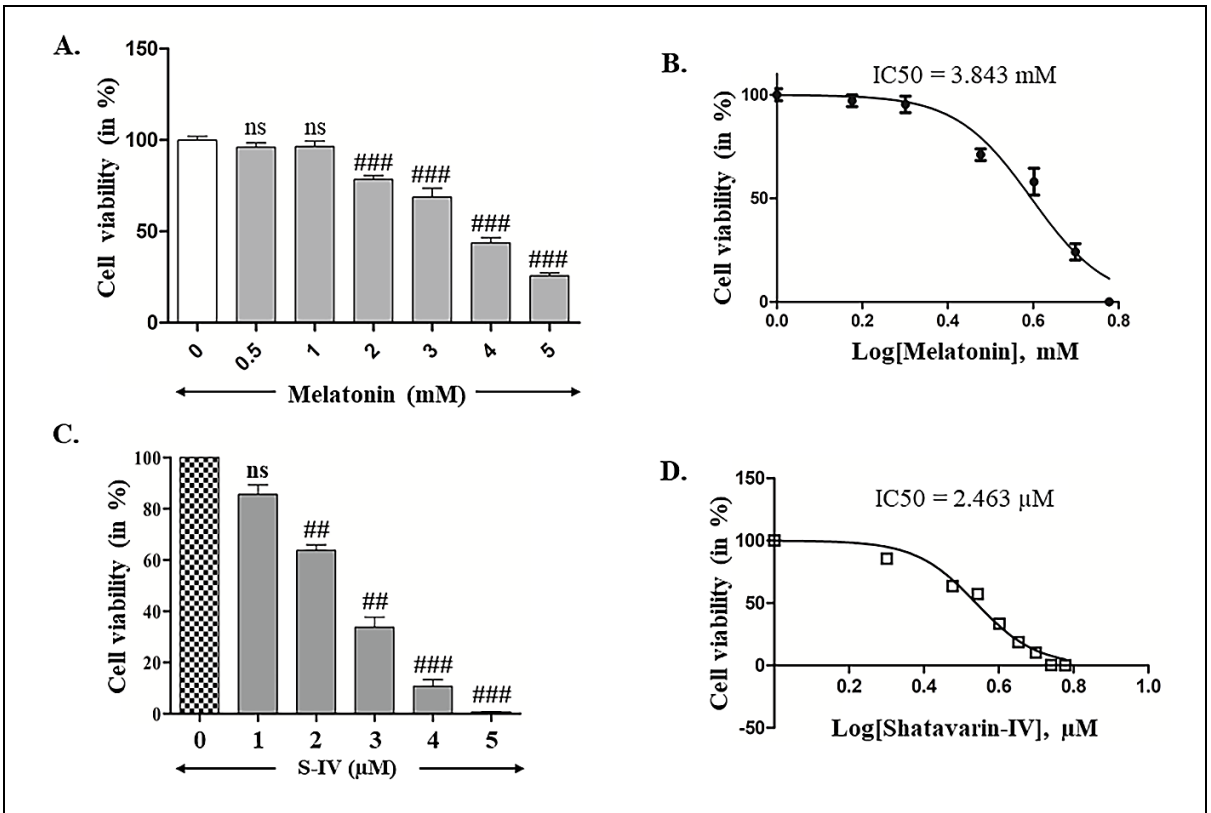

Figure 31. Dose-dependent response of AGS cells maintained in hyperglycemic conditions to increasing concentrations of Melatonin (A, B) and Shatavarin-IV (C, D). Values are expressed as mean ± SEM. Student's t-test was employed to compare groups. ###p<0.001, ##p<0.01, ns = not significant. Adapted from Chatterjee et al., 2024b & Chatterjee et al., 2024c.

2.2. Melatonin inhibits HG-induced ROS production in AGS cells

To observe and measure the production of reactive oxygen species in AGS cells under HG conditions, the cell-permeable ROS-sensing dye, DCFH-DA was employed. H_2O_2 (50 µM) served as the positive control for ROS production, while 2.5 mM N-acetyl cysteine (NAC) functioned as the negative control due to its ROS scavenging property. High-resolution STED microscopy of live cells demonstrated that H_2O_2-treated AGS cells exhibited the maximum fluorescence of DCFH-DA relative to NG cells (control), followed by those maintained under HG conditions; while pre-incubation of cells with NAC inhibited ROS production. Additionally, melatonin administration demonstrated a significant decrease in the ROS level (Figure 32A).

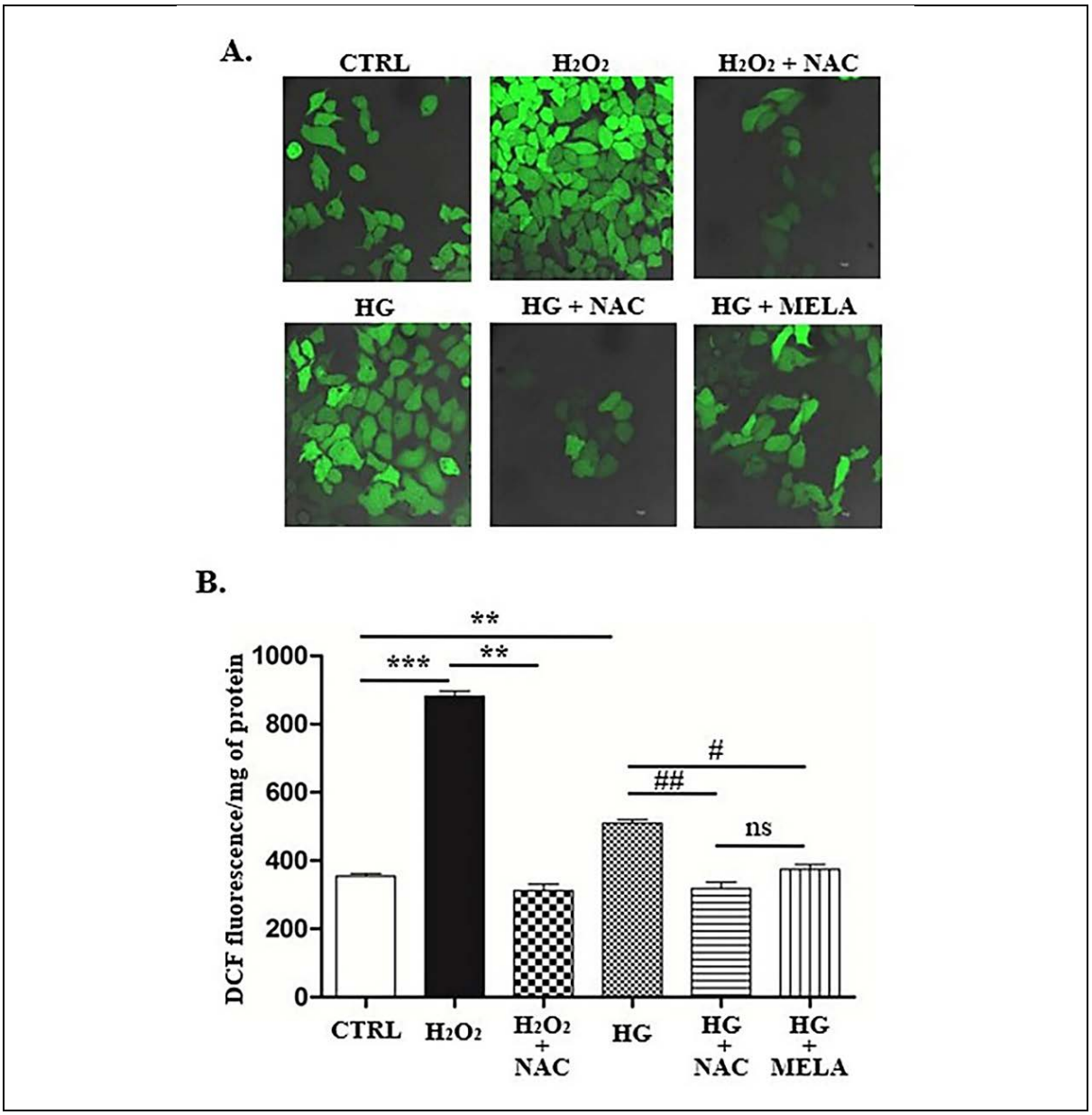

Figure 32. Melatonin mitigates HG-induced ROS production. (A) After 24 hours of respective treatments, AGS cells were stained with DCFH-DA, a fluorogenic dye that reports intracellular ROS. Images were obtained utilizing a high-resolution STED microscope at a magnification of 63X. Each image represents five separate experiments. (B) After 24 hours of respective treatments, AGS cells were stained with DCFH-DA, and the fluorescence was measured using an F-7 Fluorescence Spectrophotometer ensuring appropriate background fluorescence subtraction. Values were expressed as mean ± SEM. Group comparisons were conducted utilizing the Student's t-test. ***p<0.001, **p<0.01, *p<0.05 (vs. 'CTRL'); ##p<0.01, #p<0.05 (vs. 'HG'), and "ns" represent non-significant. Adapted from Chatterjee et al., 2024b.

Fluorometric analysis revealed that H_2O_2 exposure resulted in approximately 2.49-fold increase in DCFH-DA fluorescence, compared to the control. AGS cells cultured in high glucose medium exhibited ~1.44-fold increase in DCF fluorescence. No increases in ROS levels were detected in the groups pre-treated with NAC. They exhibited decreased DCF fluorescence relative to the NG control cells (Figure 32B). These findings demonstrate the role of ROS in AGS cells under HG circumstances. Melatonin significantly reduced the ROS generated (1.36-fold drop in DCF-DA fluorescence) in AGS cells under HG conditions (Figure 32B).

2.3. Melatonin and Shatavarin-IV inhibit hyperglycemia-induced aggressive nature of AGS cells by altering the expression and activity of MMP-9 and TIMP-1

Immunoblotting and gelatin zymography procedures were utilized to determine the effects of HG on the expression and activity profile of MMP-9, respectively. This study revealed a significant augmentation (~2.15-fold; $p<0.01$) of MMP-9 activity (Figure 33A) as well as its expression (~2.04-fold; $p<0.001$) (Figure 33C & 33D) in AGS cells sustained in HG conditions. Furthermore, melatonin administration reduced the activity (Figure 33A) and expression (Figure 33C & 33D) of MMP-9 by approximately 1.55-fold and 1.22-fold, respectively. The HG-induced elevation in MMP-9 levels was associated with a corresponding reduction in the activity (approximately 1.4-fold) and expression (approximately 2.97-fold) of TIMP-1. The activity (Fig. 33B) and expression (Fig. 33C & 33E) of TIMP-1 were nearly completely restored following melatonin treatment.

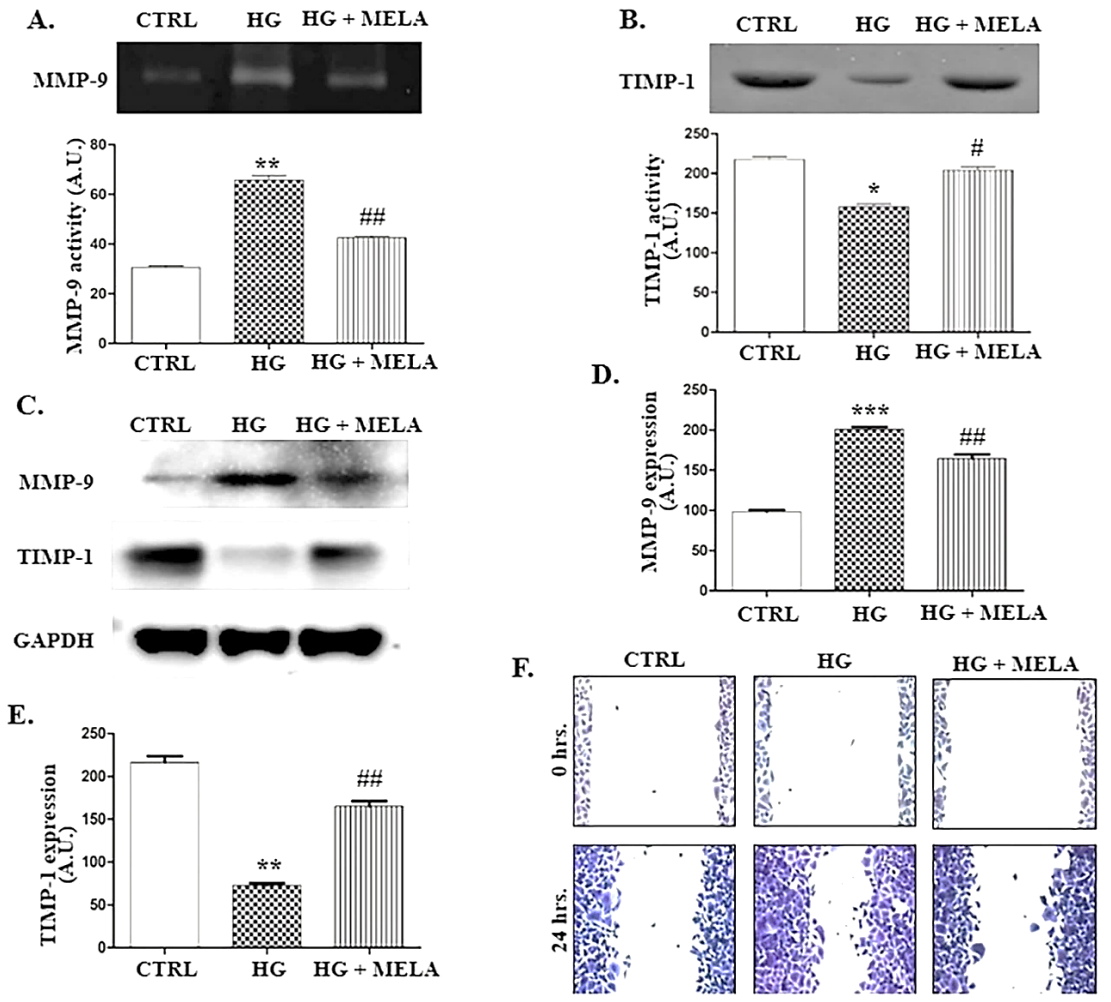

Figure 33. Melatonin reduces AGS cell migration under HG conditions by altering the expression and activity of MMP-9 and TIMP-1. (A) Gelatin zymography and densitometric analysis demonstrate the suppression of MMP-9 activity in AGS cells under HG conditions following melatonin treatment. (B) Reverse zymography and densitometric analysis indicate the restitution of TIMP-1 activity in AGS cells under HG conditions following melatonin treatment (C) Immunoblots showing the expression of MMP-9 and TIMP-1 utilizing GAPDH as the loading control. Every blot represents the results of five separate experiments (D–E) Histographic representation of the densitometric analysis of MMP-9 and TIMP-1 expressions, respectively. (F) Wound healing assay demonstrating the suppression of HG-induced cell migration following melatonin treatment. Every image represents the results of five separate experiments. Quantification of the zymographs and blots was conducted through densitometry utilizing the ImageJ software. Values were expressed as mean ± SEM. The Student's t-test was utilized for the comparison between groups. ***p<0.001, **p<0.01, *p<0.05 (vs. 'CTRL'); ##p<0.01, #p<0.05 (vs. 'HG'). Adapted from Chatterjee et al., 2024b.

Shatavarin-IV treatment reduced transcription, protein expression, and enzymatic activity of MMP-9 by about 2.67-fold ($p<0.05$; Figure 34A and 34B), 2.63-fold ($p<0.05$; Figure 34D and 34E), and 1.88-fold ($p<0.001$; Figure 34G), respectively, in comparison to the HG state. An immunocytochemistry examination to elucidate MMP-9 expression pattern (stained with Texas Red) demonstrated a comparable trend (Figure 34I). The transcription, protein expression, and enzymatic activity of TIMP-1 increased by about 1.94-fold ($p<0.05$; Figure 34A and 34C), 1.44-fold ($p<0.01$; Figure 34D and 34F), and 2.63-fold ($p<0.001$; Figure 34H), respectively, following Shatavarin-IV treatment compared to hyperglycemic cells.

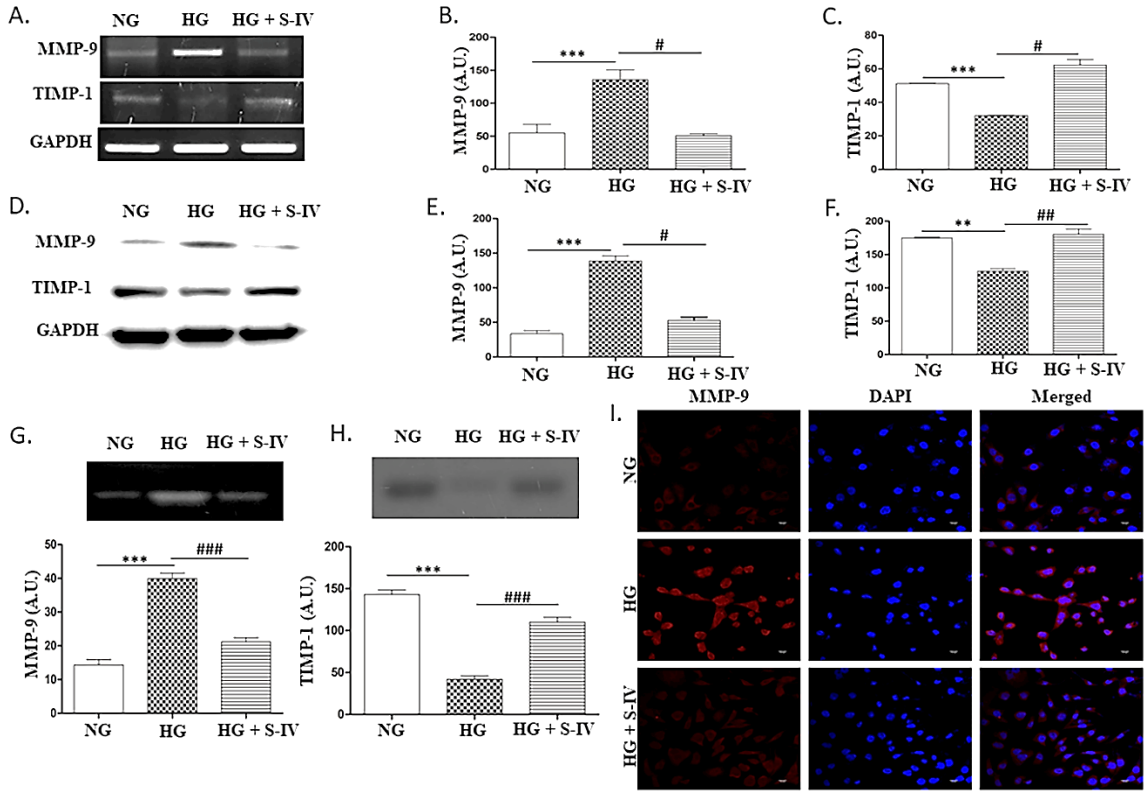

Figure 34. Shatavarin-IV counteracts alterations of MMP-9 and TIMP-1 levels caused by hyperglycemia. (A) Standard RT-PCR analysis of the expression levels of MMP-9 and TIMP-1 after incubating AGS cells with their respective treatments for 24 hours. GAPDH served as the loading control. Every image represents the outcomes of five separate experiments. (B–C) Histographic representation of the densitometric analysis of MMP-9 and TIMP-1 mRNA expressions, respectively. (D) Immunoblots showing the expression of MMP-9 and TIMP-1 across the three treatment groups. GAPDH served as the loading control. Every blot represents the outcomes of five separate experiments. (E–F) Histographic representation of the densitometric analysis of MMP-9 and TIMP-1 protein expression, respectively. (G) Gelatin zymography accompanied by densitometric analysis of MMP-9 activity. (H) Reverse zymography accompanied

by densitometric analysis of TIMP-1 activity. (I) Images of MMP-9 immunostaining across the three treatment groups. The red fluorescence of Texas Red indicates the presence of MMP-9 protein; whereas the blue fluorescence of DAPI signifies the nucleus. Every image reflects the outcomes of five distinct experiments. Values were expressed as mean ± SEM. The Student's t-test was utilized for the comparison of groups. ***p<0.001, **p<0.01 (vs. 'NG'); ###p<0.001, ##p<0.01, #p<0.05 (vs. 'HG'). Adapted from Chatterjee et al., 2024c.

MMP-9 is recognized as a pivotal enzyme that significantly facilitates tumor cell motility. Subsequently, the impact of Melatonin and Shatavarin-IV was examined on the migratory characteristics of AGS cells in high glucose circumstances, employing the scratch wound-healing assay. Melatonin therapy reduced the migratory rate of AGS cells under high glucose conditions (Figure 33F). Treatment with 2.2 µM Shatavarin-IV considerably decreased the HG-induced migration of AGS cells (Figure 35A). This finding indicates that Shatavarin-IV effectively inhibits AGS cell motility. The trans-well invasion assay findings indicate that Shatavarin-IV therapy significantly decreased the number of invading cells (Figure 35B).

The ability of AGS cells to proliferate was assessed through the colony formation experiment and an immunofluorescence assay was used to evaluate the expression of Ki-67, a proliferation marker. The colony formation test revealed a considerable increase in the number of colonies under HG circumstances (Figure 35C). Following Shatavarin-IV therapy, a significant reduction in AGS cells growth rate was observed by the reduced number of colonies (Figure 35C). A same pattern was observed in the Ki-67 immunofluorescence pictures stained with Texas Red. Ki-67expression, a hallmark of actively proliferating cells, was markedly elevated (enhanced red fluorescence) in AGS cells subjected to HG conditions, but dramatically diminished following Shatavarin-IV therapy (Figure 35D).

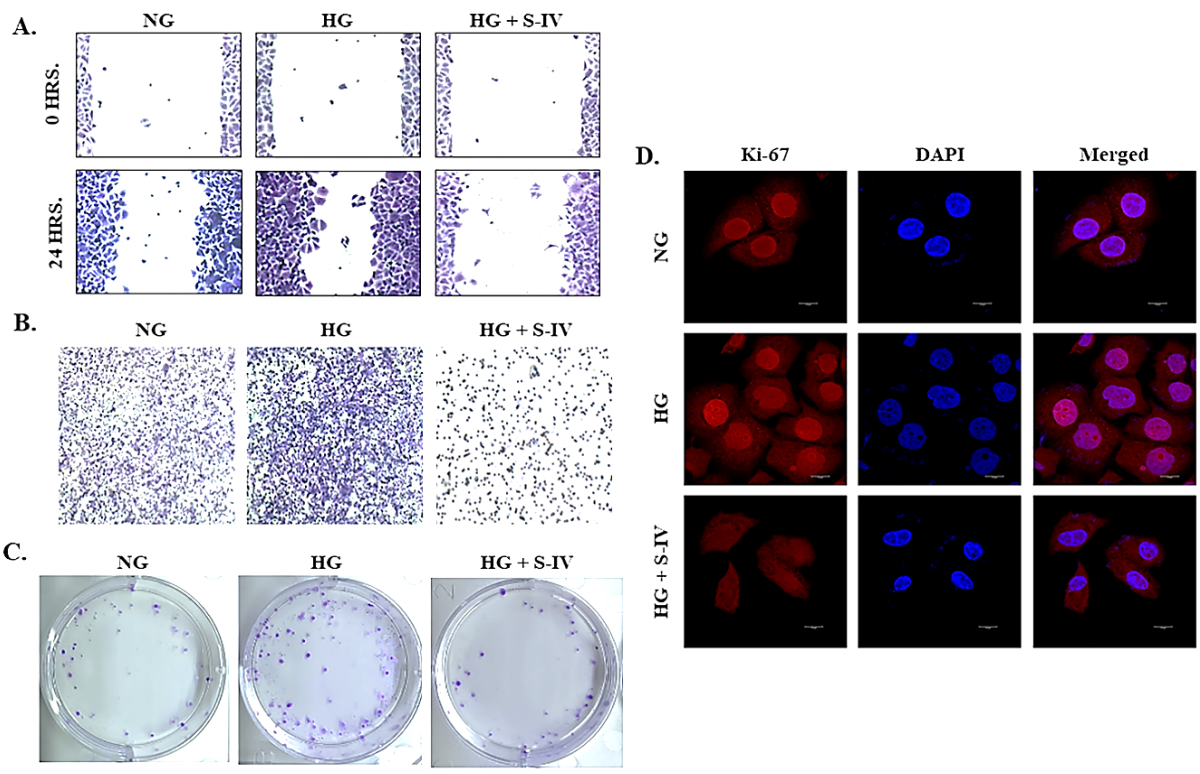

Figure 35. Shatavarin-IV effectively suppresses the HG-induced migration, invasion, and proliferation of AGS cells. (A) Images of scratch wound-healing experiment after incubating AGS cells with their respective treatments for 24 hours. (B) Images of AGS cells after passing through the Matrigel-coated membrane of the trans-well insert during 24 hours of incubation with their respective treatments. (C) Images of the colony formation experiment after incubating AGS cells with their respective treatments for 24 hours. Prior to imaging, the migrated cells, invaded cells, and colonies underwent staining with crystal violet. (D) Images showcasing Ki-67 immunostaining across the three treatment groups. The red fluorescence from Texas Red, indicates the presence of Ki-67 protein, while the blue fluorescence of DAPI, signifies the nucleus. Every image reflects the results of five separate experiments. Adapted from Chatterjee et al., 2024c.

2.4. Melatonin and Shatavarin-IV induce cell cycle arrest at G0/G1 phase under hyperglycemic conditions

The distribution of cell cycle phases was analyzed by flow cytometry to determine the impact of melatonin and Shatavarin-IV on cell cycle progression in hyperglycemic circumstances. A little change in the proportion of cells belonging to the Synthesis phase (decreasing from 29.7% in the NG group to 26.3% in the HG group) and G2/M phase (increasing from 14.7% in the NG group to 22.7% in the HG group) after maintaining AGS cells in HG medium (Figure 36A & 36B). This was followed by a modest reduction in the proportion of cells in the G0/G1 phase (from 55.6% in the NG group to 50.9% in the HG group).

A significant rise in the proportion of cells in the G0/G1 phase (from about 50.9% to 76.8%) following melatonin administration. Additionally, a consequent reduction in the proportion of cells in the Synthesis phase (from 26.3% to 10.6%) and G2/M phase (from 22.7% to 12.6%) was noted following melatonin therapy (Figure 36A & 36B). Further, the expressions of proteins relevant in cell cycle regulation critical for the progression of the G1 phase and S phase transition was evaluated, employing the western blotting approach. AGS cells subjected to HG circumstances exhibited around a 1.23-fold elevation in Cyclin D1 expression and a comparable rise of around 1.25-fold in Cyclin E expression (Figure 36C, 36D & 36F) relative to the NG control. CDK-2 and CDK-4 expression were elevated by approximately 1.67-fold and 1.25-fold, respectively (Figure 36C, 36E & 36G). The amount of phosphorylated retinoblastoma (p-Rb) rose by approximately 1.55-fold, but total Rb levels stayed relatively stable (Figure 36C, 36H & 36I) compared to the NG control. Melatonin therapy, however, markedly decreased the levels of CDK-4 (~1.38-fold) and cyclin D1 (~1.52-fold) expression (Figure 36C, 36D & 36E). A significant reduction in CDK-2 (~4.15-fold) and cyclin E (~3.64-fold) expression was noted following melatonin administration (Figure 36C, 36F & 36G). Melatonin reduced the amount of phosphorylated Rb by approximately 1.2-fold (Figure 36C, 36H & 36I). The data clearly indicate that melatonin triggers cell cycle arrest during the G0/G1 phase in AGS cells under hyperglycemic circumstances.

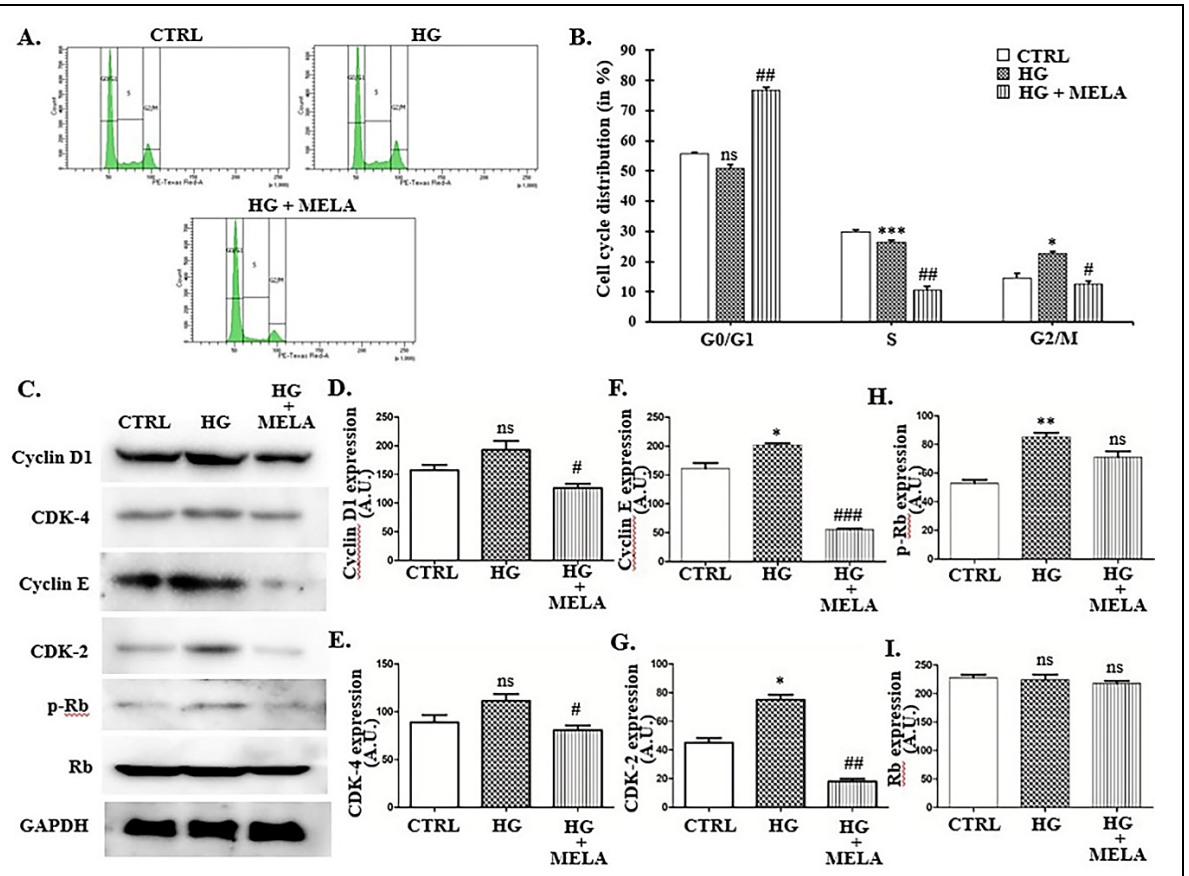

Figure 36. Melatonin induces cell cycle arrest at G0/G1 phase in AGS cells maintained under hyperglycemic condition. (A) Following 24-hours of treatment, AGS cells were harvested, fixed, and stained with PI. Flow cytometric method was employed to analyze the phases of the cell cycle. (B) Histograms representing the proportion of cells in each phase of the cell cycle across the three treatment groups. (C) Immunoblot analysis was conducted to assess the expressions of the proteins relevant to cell cycle regulation, utilizing GAPDH as the loading control. (D-I) Histographic representation of the densitometric analyses of Cyclin D1, CDK-4, Cyclin E, CDK-2, p-Rb, and total Rb expression patterns, respectively. Densitometry was conducted utilizing ImageJ software. Values were expressed as mean ± SEM. The Student's t-test was utilized for the comparison between groups. ***p<0.001, **p<0.01, *p<0.05 (vs. 'CTRL'); ###p<0.001, ##p<0.01, #p<0.05 (vs. 'HG'), and "ns" represent non-significant. Adapted from Chatterjee et al., 2024b.

Incubation of AGS cells (sustained under hyperglycemic conditions) with Shatavarin-IV (2.2 µM) led to an increase in cell population in the G0/G1 phase (from about 49.13% in 'HG' to 67.27% in 'HG + S-IV'; $p<0.05$) (Figure 37A & 37B). A subsequent reduction was noted in the proportion of cells in the G2/M phase (from approximately 18.57% in 'HG' to about 9.05% in 'HG + S-IV'; $p<0.05$). Nonetheless, no significant alteration ($p>0.05$) in the proportion of cells in the S phase was observed (Figure 37A & 37B). Treatment with 125 nM

Flavopiridol (positive control) resulted in a substantial rise ($p<0.01$) in the G0/G1 phase cells, accompanied by a reduction in number of cells present in S phase and G2/M phase (Figure 37A & 37B). The results demonstrated that Shatavarin-IV, at a concentration of 2.2 µM, may induce cell cycle arrest during the G0/G1 phase under HG circumstances.

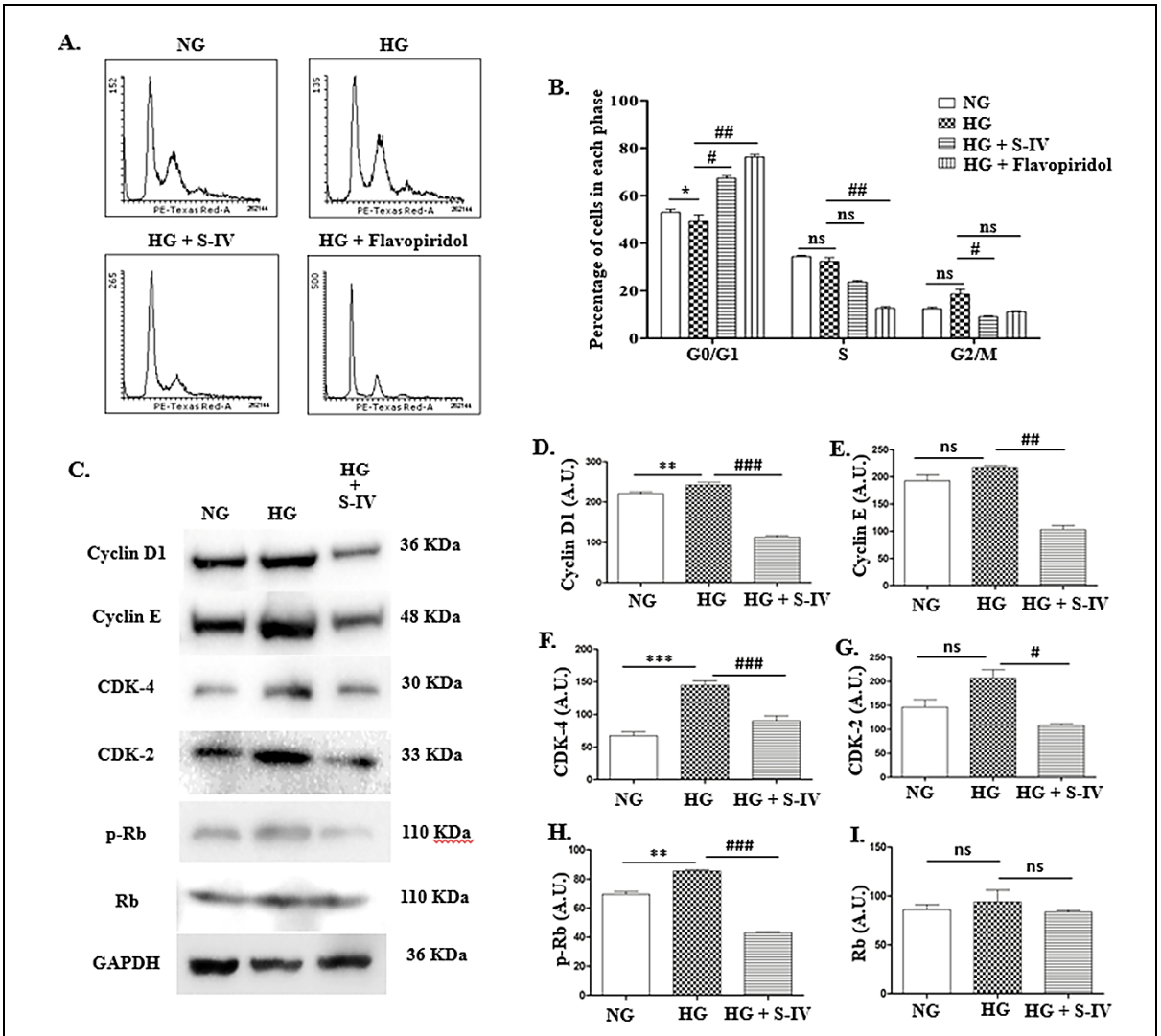

Figure 37. Shatavarin-IV causes cell cycle arrest in hyperglycemic AGS cells. (A) Cell cycle profiles after incubating AGS cells with their respective treatments for 24 hours (B) Histograms representing the proportion of cells in each phase of the cell cycle across the four treatment groups. (C) Immunoblot analysis was conducted to assess the expressions of proteins regulating the cell cycle, utilizing GAPDH as the loading control. (D–I) Histograms representing the densitometric analysis of Cyclin D1, Cyclin E, CDK-4, CDK-2, p-Rb, and total Rb expression patterns, respectively. Densitometric analyses were conducted utilizing ImageJ software. Each result represents the findings from five separate experiments. The values were expressed as mean ± SEM. The Student's t-test was utilized for the comparison between groups. ***$p<0.001$, **$p<0.01$,

*p<0.05 (vs. 'NG'); ###p<0.001, ##p<0.01, #p<0.05 (vs. 'HG') and "ns" represents non-significant. Adapted from Chatterjee et al., 2024c.

This observation was subsequently verified using western blotting technique. The expression patterns of many cell cycle regulatory proteins critical for cell progression through the G0/G1 phase and the initiation of the S phase were assessed (Figure 37C-37I). A significant elevation in cyclin D1 (~1.1-fold increase; p<0.01; Figure 37C & 37D), cyclin E (~1.13-fold increase; p>0.05; Figure 37C & 37E), CDK-4 (~2.15-fold increase; p<0.001; Figure 37C & 37F), and CDK-2 (~1.41-fold increase; p>0.05; Figure 37C & 37G) expression levels was observed in AGS cells subjected to HG conditions. Moreover, the phosphorylation status of the Rb protein was similarly raised (~1.23-fold increase; p<0.01; Figure 37C & 37H) under HG conditions. Following Shatavarin-IV treatment, the expression levels of cyclin D1 (~2.15-fold reduction; p<0.001; Figure 37C & 37D), cyclin E (~2.11-fold reduction; p<0.01; Figure 37C & 37E), CDK-4 (~1.6-fold reduction; p<0.001; Figure 37C & 37F), CDK-2 (~1.91-fold reduction; p<0.05; Figure 37C & 37G), and p-Rb (~1.98-fold reduction; p<0.001; Figure 37C & 37H) exhibited a significant decline in comparison to the HG group. The reduced levels of cyclin E and CDK-2 primarily contribute to the increased number of cells in the G0/G1 phase following Shatavarin-IV application. Furthermore, reduced concentration of cyclin D1 in cells halted in the G0/G1 phase signifies a shift to a dormant G0 phase. In summary, Shatavarin-IV therapy promotes cell cycle arrest at the G0/G1 phase.

2.5. Shatavarin-IV promotes apoptosis in AGS cells under HG conditions

A TUNEL test and flow cytometry analysis was conducted with Annexin V-FITC/PI to ascertain if the application of Shatavarin-IV may trigger apoptosis in AGS cells subjected to HG conditions. A minor alteration in the proportion of apoptotic cells (from ~0.98% in 'HG' to ~9.34% in 'HG + S-IV') (Figure 38A & 38B) and TUNEL-positive cells (Figure 38C) was noted following 24 hours of Shatavarin-IV administration. Extending the incubation time to 36 hours significantly affected the rate of AGS cell apoptosis. The quantity of TUNEL-positive cells surged significantly from 24 hours to 36 hours (Figure 38C). The overall proportion of apoptotic cells rose from ~9.34% at 24 hours to ~33.75% at 36 hours (Figure 38A & 38B).

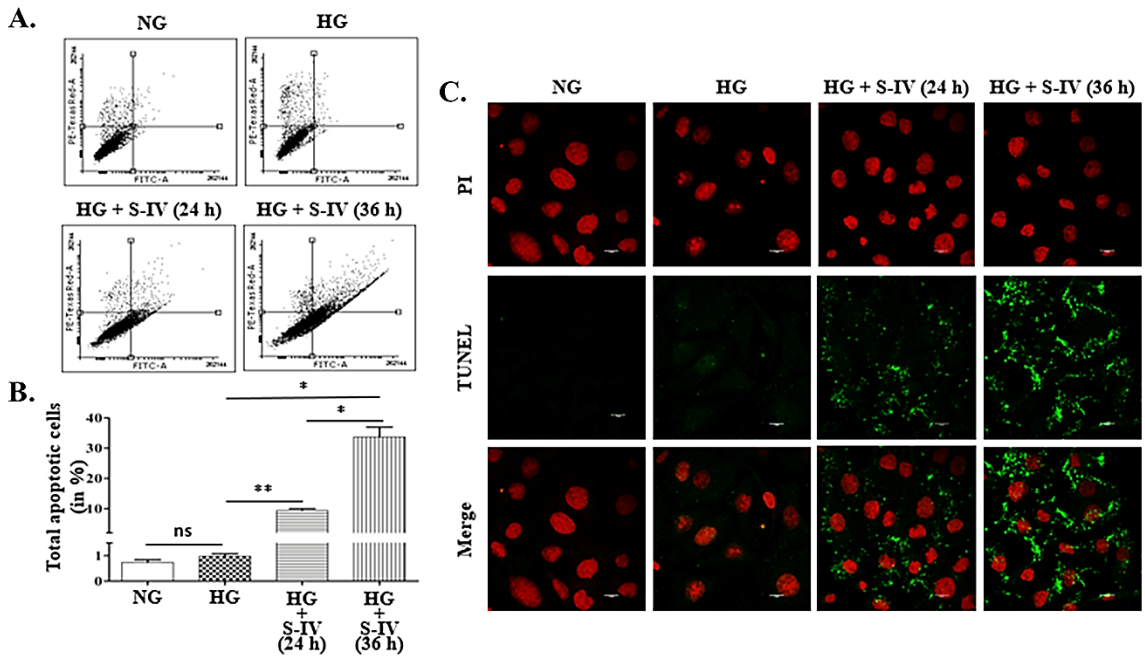

Figure 38. Shatavarin-IV promotes apoptosis in AGS cells under HG conditions. (A) Flow cytometric scatter-grams illustrating the number of apoptotic cells across the four treatment groups. (B) Histographic representation illustrating the percentage of total apoptotic cells (both early and late) across the treatment groups. (C) TUNEL staining images acquired after incubating AGS cells with their respective treatments for the mentioned time durations. The green fluorescence from FITC indictes TUNEL-positive cells and the red fluorescence of PI denotes the nucleus. Every image represents the outcomes of five separate experiments. Values were expressed as mean ± SEM. The Student's t-test was utilized to compare between groups. ***p<0.001, **p<0.01, *p<0.05 (vs. 'NG'); ###p<0.001, ##p<0.01, #p<0.05 (vs. 'HG') and "ns" represents non-significant. Adapted from Chatterjee et al., 2024c.

2.6. Melatonin inhibits CDK-2/Cyclin E kinase activity by binding with its ATP binding site

Blind molecular docking was conducted to investigate the potential interactions among melatonin and the CDK-2/Cyclin E complex. PF-06873600–the positive control was effectively docked in the active site (ATP binding domain) of CDK-2, yielding the optimal posture with a binding energy of –10.2 kcal/mol. The docked conformation resembled that of the co-crystallized structure (PDB ID: 7KJS), exhibiting a RMSD of 0.5 Å. The ATP binding pocket of CDK-2 comprises the critical amino acid residues Phe80, Glu81, Phe82, Leu83, Asp86, Lys89, and Gln131. The results indicated that melatonin may attach to the active domain of CDK-2 (ATP binding site), with –6.3 kcal/mol binding affinity, interacting with the Lys33 and Leu83 amino acid residues (Figure 39A & 39B). The binding energy indicates that melatonin may suppress the activity of CDK-2/Cyclin E.

Subsequently, molecular dynamics simulations was conducted to assess the stability of the docked conformation of melatonin and its dynamic interactions with the CDK-2/Cyclin E complex. Melatonin remained constant in the active site over the 100 ns simulation period. The RMSD of the protein backbone was approximately 2.5 Å, while the RMSD of melatonin was roughly 1.95 Å (Figure 39C). Figure 39D illustrates the RMSF. The first 1-298 amino acids of CDK-2 exhibit reduced mobility (lower RMSF), indicating less variations in the 3D structure of CDK-2 relative to Cyclin E. The mean number of hydrogen bonds of melatonin during the molecular dynamics simulation run is around 1, as seen in Figure 39E. The Asp86 and Leu83 residues in the hinge region of CDK-2 are crucial for stabilizing melatonin in the active site, exhibiting H-bond occupancies of 55% and 11% throughout productive MD run time (65 ns to 100 ns), respectively (Figure 39F). The docking and molecular dynamics simulation studies indicate that melatonin effectively binds to the CDK-2/Cyclin E complex at the ATP binding pocket, hence reducing its activity.

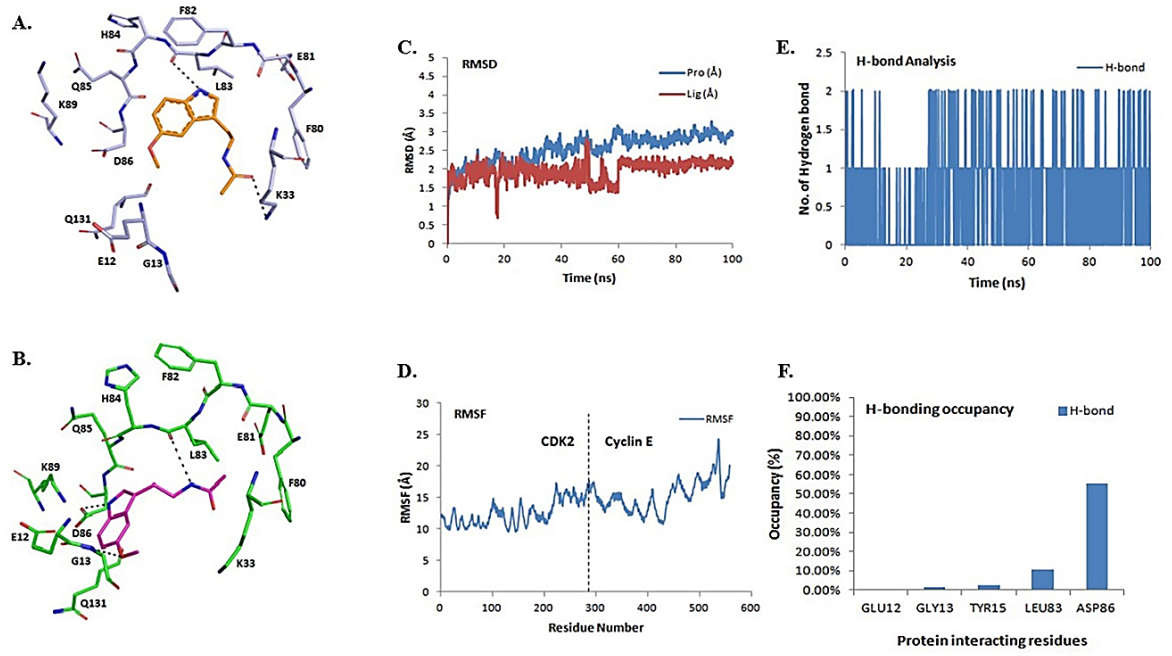

Figure 39. An in-silico investigation of the interaction among melatonin and the CDK-2/Cyclin E complex. (A) The docked pose of melatonin, depicted with orange color, is situated within the active site of CDK-2 (ATP binding pocket), shown in light blue color. (B) The binding pose of melatonin (depicted in magenta color) with the CDK-2/Cyclin E complex (CDK-2 shown in green color) through the most stable productive phase (between 65-100 ns) of molecular dynamics simulation. The stick model illustrates only the amino acid residues located within 5 Å of melatonin that are part of the active site. The proposed hydrogen bonds are illustrated as broken lines. (C) The RMSD plot illustrates the trajectory of melatonin, represented in maroon color, alongside the CDK-2/Cyclin E protein backbone, depicted by blue color, over the course of 100 ns of molecular dynamics simulation. (D) The RMSF plot of protein residues in CDK-2/Cyclin E-melatonin complex. (E) Variation in the number of hydrogen-bonds between melatonin and CDK-2/Cyclin E protein over time throughout molecular dynamics simulation. (F) Hydrogen bond interaction occupancy of melatonin with various amino acid residues in the CDK-2/Cyclin E complex active site. Adapted from Chatterjee et al., 2024b.

An *in-vitro* ADP-Glo Kinase Assay was conducted to corroborate the findings of the *in-silico* interaction analysis. Melatonin was shown to inhibit CDK-2 kinase activity with an IC_{50} value of 367.1 ± 84 µM (Figure 40B). Staurosporine, the positive control, exhibited a significantly lower IC_{50} value of 7.288 ± 2.7 nM. This value is in close agreement with IC_{50} values published previously, for the inhibition of CDK-2 kinase activity induced by

Staurosporine. The outcomes of this study indicate that melatonin influences the kinase activity of the CDK-2/Cyclin E1 complex.

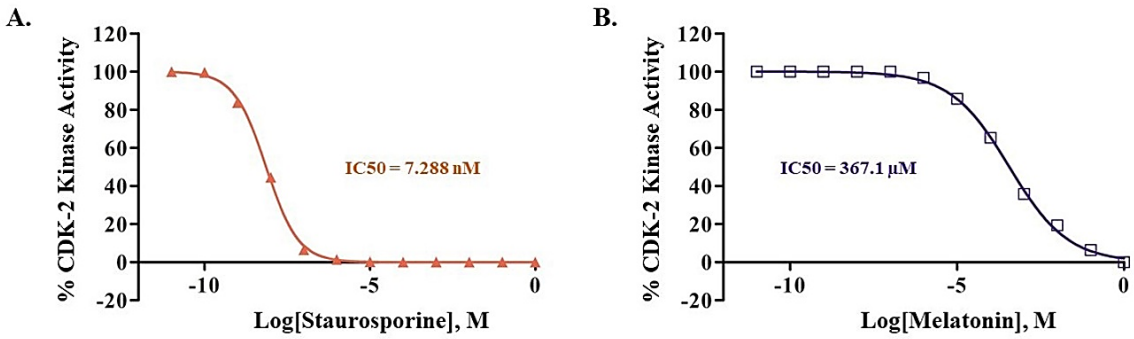

Figure 40. Impact of varying concentrations of (A) staurosporine and (B) melatonin on the kinase activity CDK-2/Cyclin E1 complex. Adapted from Chatterjee et al., 2024b.

3. Discussion

Gastric cancer ranks as the fifth foremost cause of cancer-related mortality, notwithstanding recent advancements in cancer treatment (Sung et al., 2021). Concurrently, the incidence of diabetes is increasing worldwide, attributed to alterations in human lifestyle (Standl et al., 2019). Cancer cells primarily rely on glucose for their metabolism; hence, HG conditions in diabetic individuals create a favorable milieu for cancer growth and markedly increase metastatic potential (Wu et al., 2018). These effects have been previously observed in lung cancer (Kang et al., 2015), cholangiocarcinoma (Saengboonmee et al., 2016), and breast cancer (Sun et al., 2017). Cancer metastasis is widely recognized as the principal cause of cancer morbidity and mortality, responsible for around 90% of cancer-related fatalities (Fares et al., 2020). Metastasis is a multifaceted, multi-step process including components such as cell proliferation, motility, invasion, and adhesion (Lambert et al., 2017). To successfully address cancer spread, prospective pharmaceuticals must be assessed for their capacity to inhibit these essential metastatic mechanisms.

Hyperglycemia significantly exacerbates the proliferative, migratory, and invasive capacities of AGS cells. Hyperglycemia results in the generation and accumulation of reactive oxygen species in cancer cells. Consistent with other results (Burgos-Morón et al., 2019), a considerable increase in ROS generation and accumulation in AGS cells was also noted under HG circumstances. The increased concentration of ROS is fundamental to nearly all

detrimental impacts of hyperglycemia on AGS cells. Melatonin, owing to its robust antioxidant properties, efficiently neutralizes the surplus reactive oxygen species generated by AGS cells in a hyperglycemic setting. Shatavarin-IV therapy did not diminish ROS generation in hyperglycemic AGS cells (data not shown).

Following treatment with Shatavarin-IV, the quantity of AGS cell colonies developed under HG conditions was significantly decreased. The administration of Shatavarin-IV also decreased the migratory and invasive nature of AGS cells under HG conditions. Melatonin therapy also inhibited the migratory capacity of hyperglycemic AGS cells. They restore epithelial integrity by enhancing E-cadherin expression and diminishing mesenchymal markers such as N-cadherin, β-catenin, and vimentin, thereby reversing epithelial-to-mesenchymal transition (EMT). Melatonin and Shatavarin-IV diminish MMP-9 activity while enhancing TIMP-1 expression, therefore stabilizing extracellular matrix turnover and inhibiting metastasis.

Additionally, both drugs cause cell cycle arrest at the G0/G1 phase by downregulating Cyclin D1/CDK-4 expression. This action inhibits cells from advancing to the S phase, hence diminishing cell growth. In silico analyses and kinase experiments indicate that melatonin binds to the ATP-binding pocket of CDK-2, exhibiting a low binding free energy of –6.3 kcal/mol, hence reducing its kinase activity and obstructing cell cycle advancement. In contrast to Shatavarin-IV, melatonin does not markedly impede Rb phosphorylation, highlighting disparities in their methods of action. Moreover, Shatavarin-IV, in contrast to melatonin, may trigger apoptosis in hyperglycemic AGS cells; however, this impact is delayed, perhaps due to hyperglycemia's protective function in suppressing apoptosis (Kopeć et al., 2022).

Previous reports suggest that a few natural compounds such as resveratrol, sulforaphane, quercetin, and curcumin have anti-gastric cancer activity via apoptosis induction, inhibition of cell proliferation, and reducing metastasis (Zhao et al., 2023). Interestingly, both melatonin and Shatavarin-IV work in a similar manner through the inhibition of cell proliferation by inducing cell cycle arrest at the G0/G1 phase, stabilization of the dysregulated MMP-9/TIMP-1 axis, and the prevention of metastasis. Nonetheless, additional investigation is required to achieve a comprehensive understanding of the mechanism of action of these two compounds in addition to evaluate the clinical potential of these two promising natural products.

Chapter 6

Conclusion

CONCLUSION

Gastric cancer (GC) continues to be a predominant cause of cancer-related death globally. The increasing incidence of diabetes and related hyperglycemia (HG) has been demonstrated to accelerate the advancement of GC. HG stimulates cancer cell metabolism, increases the formation of ROS, and fosters a more aggressive cancer phenotype by affecting critical molecular pathways related to cell proliferation, migration, invasion, and metastasis.

HG-induced ROS buildup significantly contributes to cancer development by activating signaling pathways that modulate the production of MMP-9 and TIMP-1. The increase of MMP-9 in HG circumstances enhances extracellular matrix breakdown, hence aiding tumor cell movement and invasion. The downregulation of TIMP-1, which inherently reduces MMP-9 activity, exacerbates the aggressive characteristics of AGS cells. This indicates that targeting the MMP-9/TIMP-1 axis may serve as an effective treatment strategy for GC in HG circumstances.

Utilizing an in vitro model of GC-HG co-morbidity, a unique mechanism behind the HG-induced MMP-9 over-expression was identified. The p65 NF-κB pathway has no control over the HG-induced transcriptional activation of MMP-9. Rather it is primarily regulated by the MAPK pathway. The assembly of the AP-1 hetero-dimer is essential for the MMP-9 transcription in HG circumstances. Additionally, AP-1 binding at pAP-1 and dAP-1 sites on the MMP-9 promoter region is essential for HG-induced expression of MMP-9. The pAP-1 binding site is functional in both NG and HG states, while the dAP-1 binding site became functional solely upon the induction of hyperglycemia. Consequently, the problems arising from the co-morbidity of gastric cancer and hyperglycemia may be mitigated by obstructing the interaction of the AP-1 hetero-dimer with the dAP-1 binding site on the MMP-9 promoter. Subsequent research including a drug particularly formulated to obstruct this interaction may significantly aid in managing metastases in GC patients with HG co-morbidity.

Furthermore, the dysregulated MMP-9/TIMP-1 axis under HG conditions was attempted to be therapeutically stabilized. For this reason, melatonin, a potent antioxidant as well as a regulator of several cellular processes, and Shatavarin-IV, a natural steroidal saponin with previously reported anti-cancer activity, were chosen.

Melatonin has shown potential anti-cancer benefits in reducing the advancement of GC induced by HG. It significantly diminishes ROS levels, counteracting HG-induced MMP-9 overexpression while augmenting TIMP-1 expression. Moreover, melatonin has been shown to inhibit HG-induced AGS cell growth by causing G0/G1 cell cycle arrest. Melatonin mechanistically targets CDK-2 and its regulatory partner, cyclin E, which are crucial for S-phase entrance. In silico docking and kinase activity experiments shown that melatonin binds to the ATP-binding pocket of CDK-2, resulting in the inhibition of CDK-2/cyclin E1 kinase activity. This obstructs AGS cells from advancing in the cell cycle, thereby diminishing HG-induced cell proliferation. Contrary to earlier results indicating that melatonin triggers apoptosis in GC cells, its principal mechanism of action under HG conditions seems to involve cell cycle arrest rather than apoptosis.

Besides melatonin, Shatavarin-IV has also surfaced as a potential anti-cancer agent against GC, especially in HG environments. Shatavarin-IV markedly diminishes the proliferative, migratory, and invasive properties of AGS cells via regulating EMT markers. It enhances the expression of E-cadherin, a crucial epithelial marker that facilitates cell-cell adhesion, while diminishing the mesenchymal markers' expression like β-catenin, N-cadherin, and vimentin. This reversal of EMT is essential for inhibiting metastasis. Moreover, Shatavarin-IV inhibits MMP-9 production and activity while augmenting TIMP-1 levels, therefore obstructing the extracellular matrix remodeling necessary for tumor advancement. It also affects the cell cycle by downregulating cyclin D1 and CDK-4 expression, diminishing Rb phosphorylation, and finally resulting in G0/G1 phase arrest. In contrast to melatonin, Shatavarin-IV promotes apoptosis in hyperglycemic AGS cells, albeit this occurs with a delay, since apoptotic effects manifest after 36 hours of treatment. Due to its effectiveness in impeding GC progression in HG environments, Shatavarin-IV also has considerable promise as a new therapeutic agent for patients with GC and diabetes comorbidity. However, further research is necessary to evaluate the clinical potential of these two promising natural products.

References

AbdlWhab, H. M., Al-Saffar, A., Mahdi, O. A., & Alameri, R. B. (2024). The impact of insulin resistance and glycaemic control on insulin-like growth factor-1 in patients with type 2 diabetes: a cross-sectional study. Clinical diabetes and endocrinology, 10(1), 36. https://doi.org/10.1186/s40842-024-00202-8

Alisson-Silva, F., Freire-de-Lima, L., Donadio, J. L., Lucena, M. C., Penha, L., Sá-Diniz, J. N., Dias, W. B., & Todeschini, A. R. (2013). Increase of O-glycosylated oncofetal fibronectin in high glucose-induced epithelial-mesenchymal transition of cultured human epithelial cells. PloS one, 8(4), e60471. https://doi.org/10.1371/journal.pone.0060471

Allouche A. R. (2011). Gabedit–a graphical user interface for computational chemistry softwares. Journal of Computational Chemistry, 32(1), 174–182. https://doi.org/10.1002/jcc.21600

Al-Roub, A., Akhter, N., Al-Rashed, F., Wilson, A., Alzaid, F., Al-Mulla, F., Sindhu, S., & Ahmad, R. (2023). TNFα induces matrix metalloproteinase-9 expression in monocytic cells through ACSL1/JNK/ERK/NF-kB signaling pathways. Scientific reports, 13(1), 14351. https://doi.org/10.1038/s41598-023-41514-6

Arfin, S., Jha, N. K., Jha, S. K., Kesari, K. K., Ruokolainen, J., Roychoudhury, S., Rathi, B., & Kumar, D. (2021). Oxidative Stress in Cancer Cell Metabolism. Antioxidants (Basel, Switzerland), 10(5), 642. https://doi.org/10.3390/antiox10050642

ASGE Standards of Practice Committee, Evans, J. A., Chandrasekhara, V., Chathadi, K. V., Decker, G. A., Early, D. S., Fisher, D. A., Foley, K., Hwang, J. H., Jue, T. L., Lightdale, J. R., Pasha, S. F., Sharaf, R., Shergill, A. K., Cash, B. D., & DeWitt, J. M. (2015). The role of endoscopy in the management of premalignant and malignant conditions of the stomach. Gastrointestinal endoscopy, 82(1), 1–8. https://doi.org/10.1016/j.gie.2015.03.1967

Atanasov, A. G., Zotchev, S. B., Dirsch, V. M., International Natural Product Sciences Taskforce, & Supuran, C. T. (2021). Natural products in drug discovery: advances and opportunities. Nature reviews. Drug discovery, 20(3), 200–216. https://doi.org/10.1038/s41573-020-00114-z

Ayuk, S. M., Abrahamse, H., & Houreld, N. N. (2016). The Role of Matrix Metalloproteinases in Diabetic Wound Healing in relation to Photobiomodulation. Journal of diabetes research, 2016, 2897656. https://doi.org/10.1155/2016/2897656

Baker, A. H., Edwards, D. R., & Murphy, G. (2002). Metalloproteinase inhibitors: biological actions and therapeutic opportunities. Journal of cell science, 115(Pt 19), 3719–3727. https://doi.org/10.1242/jcs.00063

Balakrishnan, M., George, R., Sharma, A., & Graham, D. Y. (2017). Changing Trends in Stomach Cancer Throughout the World. Current gastroenterology reports, 19(8), 36. https://doi.org/10.1007/s11894-017-0575-8

Banday, M. Z., Sameer, A. S., & Nissar, S. (2020). Pathophysiology of diabetes: An overview. Avicenna journal of medicine, 10(4), 174–188. https://doi.org/10.4103/ajm.ajm_53_20

Barua, R., Templeton, A. J., Seruga, B., Ocana, A., Amir, E., & Ethier, J. L. (2018). Hyperglycaemia and Survival in Solid Tumours: A Systematic Review and Meta-analysis. Clinical Oncology, 30(4), 215–224. https://doi.org/10.1016/j.clon.2018.01.003

Bayram, S. Ş., & Kızıltan, G. (2024). The Role of Omega- 3 Polyunsaturated Fatty Acids in Diabetes Mellitus Management: A Narrative Review. Current nutrition reports, 13(3), 527–551. https://doi.org/10.1007/s13668-024-00561-9

Bell, E. W., & Zhang, Y. (2019). DockRMSD: an open-source tool for atom mapping and RMSD calculation of symmetric molecules through graph isomorphism. Journal of Cheminformatics, 11(1), 40. https://doi.org/10.1186/s13321-019-0362-7

Berbudi, A., Rahmadika, N., Tjahjadi, A. I., & Ruslami, R. (2020). Type 2 Diabetes and its Impact on the Immune System. Current diabetes reviews, 16(5), 442–449. https://doi.org/10.2174/1573399815666191024085838

Berman, H. M., Westbrook, J., Feng, Z., Gilliland, G., Bhat, T. N., Weissig, H., Shindyalov, I. N., & Bourne, P. E. (2000). The Protein Data Bank. Nucleic Acids Research, 28(1), 235–242. https://doi.org/10.1093/nar/28.1.235

Biernacka, K. M., Uzoh, C. C., Zeng, L., Persad, R. A., Bahl, A., Gillatt, D., Perks, C. M., & Holly, J. M. (2013). Hyperglycaemia-induced chemoresistance of prostate cancer cells due to IGFBP2. Endocrine-related cancer, 20(5), 741–751. https://doi.org/10.1530/ERC-13-0077

Boland, C. R., & Yurgelun, M. B. (2017). Historical Perspective on Familial Gastric Cancer. Cellular and molecular gastroenterology and hepatology, 3(2), 192–200. https://doi.org/10.1016/j.jcmgh.2016.12.003

Bondy, S. C., & Campbell, A. (2020). Melatonin and Regulation of Immune Function: Impact on Numerous Diseases. Current aging science, 13(2), 92–101. https://doi.org/10.2174/1874609813666200711153223

Bonomini, F., Borsani, E., Favero, G., Rodella, L. F., & Rezzani, R. (2018). Dietary Melatonin Supplementation Could Be a Promising Preventing/Therapeutic Approach for a Variety of Liver Diseases. Nutrients, 10(9), 1135. https://doi.org/10.3390/nu10091135

Bopana, N., & Saxena, S. (2007). Asparagus racemosus--ethnopharmacological evaluation and conservation needs. Journal of ethnopharmacology, 110(1), 1–15. https://doi.org/10.1016/j.jep.2007.01.001

Bradford M. M. (1976). A rapid and sensitive method for the quantitation of microgram quantities of protein utilizing the principle of protein-dye binding. Analytical biochemistry, 72, 248–254. https://doi.org/10.1016/0003-2697(76)90527-3

Brew, K., & Nagase, H. (2010). The tissue inhibitors of metalloproteinases (TIMPs): an ancient family with structural and functional diversity. Biochimica et biophysica acta, 1803(1), 55–71. https://doi.org/10.1016/j.bbamcr.2010.01.003

Brinckerhoff, C. E., & Matrisian, L. M. (2002). Matrix metalloproteinases: a tail of a frog that became a prince. Nature reviews. Molecular cell biology, 3(3), 207–214. https://doi.org/10.1038/nrm763

Bubenik G. A. (2008). Thirty four years since the discovery of gastrointestinal melatonin. Journal of physiology and pharmacology, 59 Suppl 2, 33–51.

Burgos-Morón, E., Abad-Jiménez, Z., Marañón, A. M., Iannantuoni, F., Escribano-López, I., López-Domènech, S., Salom, C., Jover, A., Mora, V., Roldan, I., Solá, E., Rocha, M., & Víctor, V. M. (2019). Relationship Between Oxidative Stress, ER Stress, and Inflammation in Type 2 Diabetes: The Battle Continues. Journal of clinical medicine, 8(9), 1385. https://doi.org/10.3390/jcm8091385

Cecon, E., Oishi, A., & Jockers, R. (2018). Melatonin receptors: molecular pharmacology and signalling in the context of system bias. British journal of pharmacology, 175(16), 3263–3280. https://doi.org/10.1111/bph.13950

Chakraborti, S., Mandal, M., Das, S., Mandal, A., & Chakraborti, T. (2003). Regulation of matrix metalloproteinases: an overview. Molecular and cellular biochemistry, 253(1-2), 269–285. https://doi.org/10.1023/a:1026028303196

Chatterjee, A., Roy, T., & Swarnakar, S. (2024a). Transcriptional upregulation of MMP-9 gene under hyperglycemic conditions in AGS cells: Role of AP-1 transcription factor. Cellular signalling, 124, 111435. https://doi.org/10.1016/j.cellsig.2024.111435

Chatterjee, A., Roy, T., Jyothi, D., Mishra, V. K., Singh, U. P., & Swarnakar, S. (2024b). Melatonin Inhibits AGS Cell Proliferation by Binding to the ATP Binding Site of CDK2 Under Hyperglycemic Conditions. Cell biochemistry and biophysics, 82(2), 895–908. https://doi.org/10.1007/s12013-024-01241-9

Chatterjee, A., Roy, T., Kumar Mishra, V., & Swarnakar, S. (2024c). Shatavarin-IV, a steroidal saponin from Asparagus racemosus, inhibits cell cycle progression and epithelial-to-mesenchymal transition in AGS cells under hyperglycemic conditions. Steroids, 210, 109487. https://doi.org/10.1016/j.steroids.2024.109487

Cheng, J., Wu, J., Ye, Y., Zhang, C., Zhang, Y., & Wang, Y. (2016). The prognostic significance of extramural venous invasion detected by multiple-row detector computed tomography in stage III gastric cancer. Abdominal radiology (New York), 41(7), 1219–1226. https://doi.org/10.1007/s00261-015-0627-1

Chiefari, E., Mirabelli, M., La Vignera, S., Tanyolaç, S., Foti, D. P., Aversa, A., & Brunetti, A. (2021). Insulin Resistance and Cancer: In Search for a Causal Link. International journal of molecular sciences, 22(20), 11137. https://doi.org/10.3390/ijms222011137

Choi, Y. J., & Kim, N. (2016). Gastric cancer and family history. The Korean journal of internal medicine, 31(6), 1042–1053. https://doi.org/10.3904/kjim.2016.147

Correa, P., Haenszel, W., Cuello, C., Tannenbaum, S., & Archer, M. (1975). A model for gastric cancer epidemiology. Lancet (London, England), 2(7924), 58–60. https://doi.org/10.1016/s0140-6736(75)90498-5

Costes, S., Boss, M., Thomas, A. P., & Matveyenko, A. V. (2015). Activation of Melatonin Signaling Promotes β-Cell Survival and Function. Molecular endocrinology (Baltimore, Md.), 29(5), 682–692. https://doi.org/10.1210/me.2014-1293

De la Torre, K., Song, M., Abe, S. K., Rahman, M. S., Islam, M. R., Saito, E., Min, S., Huang, D., Chen, Y., Gupta, P. C., Sawada, N., Tamakoshi, A., Shu, X. O., Wen, W., Sakata, R., Kim, J., Nagata, C., Ito, H., Park, S. K., Shin, M. H., … Kang, D. (2024). Diabetes and gastric cancer incidence and mortality in the Asia Cohort Consortium: A pooled analysis of more than a half million participants. Journal of diabetes, 16(6), e13561. https://doi.org/10.1111/1753-0407.13561

de Ligt, M., Bruls, Y. M. H., Hansen, J., Habets, M. F., Havekes, B., Nascimento, E. B. M., Moonen-Kornips, E., Schaart, G., Schrauwen-Hinderling, V. B., van Marken Lichtenbelt, W., & Schrauwen, P. (2018). Resveratrol improves ex vivo mitochondrial function but does not affect insulin sensitivity or brown adipose tissue in first degree relatives of patients with type 2 diabetes. Molecular metabolism, 12, 39–47. https://doi.org/10.1016/j.molmet.2018.04.004

Dikshit, R. P., Mathur, G., Mhatre, S., & Yeole, B. B. (2011). Epidemiological review of gastric cancer in India. Indian journal of medical and paediatric oncology : official journal of Indian Society of Medical & Paediatric Oncology, 32(1), 3–11. https://doi.org/10.4103/0971-5851.81883

Dumin, J. A., Dickeson, S. K., Stricker, T. P., Bhattacharyya-Pakrasi, M., Roby, J. D., Santoro, S. A., & Parks, W. C. (2001). Pro-collagenase-1 (matrix metalloproteinase-1) binds the alpha(2)beta(1) integrin upon release from keratinocytes migrating on type I collagen. Journal of biological chemistry, 276(31), 29368–29374. https://doi.org/10.1074/jbc.M104179200

Eferl, R., & Wagner, E. F. (2003). AP-1: a double-edged sword in tumorigenesis. Nature reviews. Cancer, 3(11), 859–868. https://doi.org/10.1038/nrc1209

Fagoonee, S., & Pellicano, R. (2019). Helicobacter pylori: molecular basis for colonization and survival in gastric environment and resistance to antibiotics. A short review. Infectious diseases (London, England), 51(6), 399–408. https://doi.org/10.1080/23744235.2019.1588472

Fares, J., Fares, M. Y., Khachfe, H. H., Salhab, H. A., & Fares, Y. (2020). Molecular principles of metastasis: a hallmark of cancer revisited. Signal transduction and targeted therapy, 5(1), 28. https://doi.org/10.1038/s41392-020-0134-x

Farina, A. R., & Mackay, A. R. (2014). Gelatinase B/MMP-9 in Tumour Pathogenesis and Progression. Cancers, 6(1), 240–296. https://doi.org/10.3390/cancers6010240

Felner, E. I., Klitz, W., Ham, M., Lazaro, A. M., Stastny, P., Dupont, B., & White, P. C. (2005). Genetic interaction among three genomic regions creates distinct contributions to early- and late-onset type 1 diabetes mellitus. Pediatric diabetes, 6(4), 213–220. https://doi.org/10.1111/j.1399-543X.2005.00132.x

Finan, K. M., Hodge, G., Reynolds, A. M., Hodge, S., Holmes, M. D., Baker, A. H., & Reynolds, P. N. (2006). In vitro susceptibility to the pro-apoptotic effects of TIMP-3 gene delivery translates to greater in vivo efficacy versus gene delivery for TIMPs-1 or -2. Lung cancer (Amsterdam, Netherlands), 53(3), 273–284. https://doi.org/10.1016/j.lungcan.2006.06.006

Fox, J. G., & Wang, T. C. (2014). Dietary factors modulate Helicobacter-associated gastric cancer in rodent models. Toxicologic pathology, 42(1), 162–181. https://doi.org/10.1177/0192623313512564

Franken, N. A., Rodermond, H. M., Stap, J., Haveman, J., & van Bree, C. (2006). Clonogenic assay of cells in vitro. Nature protocols, 1(5), 2315–2319. https://doi.org/10.1038/nprot.2006.339

Freije, J. M., M. Balbín, et al. (2003). Matrix metalloproteinases and tumor progression. New Trends in Cancer for the 21st Century, Springer: 91-107.

Fu, X., Kassim, S. Y., Parks, W. C., & Heinecke, J. W. (2003). Hypochlorous acid generated by myeloperoxidase modifies adjacent tryptophan and glycine residues in the catalytic domain of matrix metalloproteinase-7 (matrilysin): an oxidative mechanism for restraining proteolytic activity during inflammation. The Journal of biological chemistry, 278(31), 28403–28409. https://doi.org/10.1074/jbc.M304739200

Gallagher, E. J., & LeRoith, D. (2020). Hyperinsulinaemia in cancer. Nature reviews. Cancer, 20(11), 629–644. https://doi.org/10.1038/s41568-020-0295-5

Gao, J. P., Xu, W., Liu, W. T., Yan, M., & Zhu, Z. G. (2018). Tumor heterogeneity of gastric cancer: From the perspective of tumor-initiating cell. World journal of gastroenterology, 24(24), 2567–2581. https://doi.org/10.3748/wjg.v24.i24.2567

Gaulton, K. J., Ferreira, T., Lee, Y., Raimondo, A., Mägi, R., Reschen, M. E., Mahajan, A., Locke, A., Rayner, N. W., Robertson, N., Scott, R. A., Prokopenko, I., Scott, L. J., Green, T.,

Sparso, T., Thuillier, D., Yengo, L., Grallert, H., Wahl, S., Frånberg, M., … DIAbetes Genetics Replication And Meta-analysis (DIAGRAM) Consortium (2015). Genetic fine mapping and genomic annotation defines causal mechanisms at type 2 diabetes susceptibility loci. Nature genetics, 47(12), 1415–1425. https://doi.org/10.1038/ng.3437

Gawron, A. J., Shah, S. C., Altayar, O., Davitkov, P., Morgan, D., Turner, K., & Mustafa, R. A. (2020). AGA Technical Review on Gastric Intestinal Metaplasia-Natural History and Clinical Outcomes. Gastroenterology, 158(3), 705–731.e5. https://doi.org/10.1053/j.gastro.2019.12.001

GBD 2021 Diabetes Collaborators (2023). Global, regional, and national burden of diabetes from 1990 to 2021, with projections of prevalence to 2050: a systematic analysis for the Global Burden of Disease Study 2021. Lancet (London, England), 402(10397), 203–234. https://doi.org/10.1016/S0140-6736(23)01301-6

Gomis-Rüth F. X. (2009). Catalytic domain architecture of metzincin metalloproteases. The Journal of biological chemistry, 284(23), 15353–15357. https://doi.org/10.1074/jbc.R800069200

Gong, Y. Q., Hou, F. T., Xiang, C. L., Li, C. L., Hu, G. H., & Chen, C. W. (2022). The mechanisms and roles of melatonin in gastrointestinal cancer. Frontiers in oncology, 12, 1066698. https://doi.org/10.3389/fonc.2022.1066698

Gonsalves N. (2019). Eosinophilic Gastrointestinal Disorders. Clinical reviews in allergy & immunology, 57(2), 272–285. https://doi.org/10.1007/s12016-019-08732-1

González, P., Lozano, P., Ros, G., & Solano, F. (2023). Hyperglycemia and Oxidative Stress: An Integral, Updated and Critical Overview of Their Metabolic Interconnections. International journal of molecular sciences, 24(11), 9352. https://doi.org/10.3390/ijms24119352

Halazonetis, T. D., Georgopoulos, K., Greenberg, M. E., & Leder, P. (1988). c-Jun dimerizes with itself and with c-Fos, forming complexes of different DNA binding affinities. Cell, 55(5), 917–924. https://doi.org/10.1016/0092-8674(88)90147-x

Hammer, M. J., D'Eramo Melkus, G., Knobf, M. T., Casper, C., Fletcher, J., & Cleland, C. M. (2016). Glycemic Status and Infection Risk in Nondiabetic Autologous Hematopoietic Cell

Transplantation Recipients. Biological research for nursing, 18(3), 344–350. https://doi.org/10.1177/1099800415619227

Hammer, M., Storey, S., Hershey, D. S., Brady, V. J., Davis, E., Mandolfo, N., Bryant, A. L., & Olausson, J. (2019). Hyperglycemia and Cancer: A State-of-the-Science Review. Oncology nursing forum, 46(4), 459–472. https://doi.org/10.1188/19.ONF.459-472

Hamze, A. B., Wei, S., Bahudhanapati, H., Kota, S., Acharya, K. R., & Brew, K. (2007). Constraining specificity in the N-domain of tissue inhibitor of metalloproteinases-1; gelatinase-selective inhibitors. Protein science : a publication of the Protein Society, 16(9), 1905–1913. https://doi.org/10.1110/ps.072978507

Hayes, J. D., Dinkova-Kostova, A. T., & Tew, K. D. (2020). Oxidative Stress in Cancer. Cancer cell, 38(2), 167–197. https://doi.org/10.1016/j.ccell.2020.06.001

Hess, J., Angel, P., & Schorpp-Kistner, M. (2004). AP-1 subunits: quarrel and harmony among siblings. Journal of cell science, 117(Pt 25), 5965–5973. https://doi.org/10.1242/jcs.01589

Hsu M, Safadi AO, Lui F. Physiology, Stomach. [Updated 2023 Jul 17]. In: StatPearls [Internet]. Treasure Island (FL): StatPearls Publishing; 2024 Jan-. Available from: https://www.ncbi.nlm.nih.gov/books/NBK535425/

Huang, Q., Lan, F., Wang, X., Yu, Y., Ouyang, X., Zheng, F., Han, J., Lin, Y., Xie, Y., Xie, F., Liu, W., Yang, X., Wang, H., Dong, L., Wang, L., & Tan, J. (2014). IL-1β-induced activation of p38 promotes metastasis in gastric adenocarcinoma via upregulation of AP-1/c-fos, MMP2 and MMP9. Molecular cancer, 13, 18. https://doi.org/10.1186/1476-4598-13-18

Huang, Y., Yuan, K., Tang, M., Yue, J., Bao, L., Wu, S., Zhang, Y., Li, Y., Wang, Y., Ou, X., Gou, J., Zhao, Q., & Yuan, L. (2021). Melatonin inhibiting the survival of human gastric cancer cells under ER stress involving autophagy and Ras-Raf-MAPK signalling. Journal of cellular and molecular medicine, 25(3), 1480–1492. https://doi.org/10.1111/jcmm.16237

Ilyas M. (2005). Wnt signalling and the mechanistic basis of tumour development. The Journal of pathology, 205(2), 130–144. https://doi.org/10.1002/path.1692

Ishaq, S., & Nunn, L. (2015). Helicobacter pylori and gastric cancer: a state of the art review. Gastroenterology and hepatology from bed to bench, 8(Suppl 1), S6–S14.

Jabłońska-Trypuć, A., Matejczyk, M., & Rosochacki, S. (2016). Matrix metalloproteinases (MMPs), the main extracellular matrix (ECM) enzymes in collagen degradation, as a target for anticancer drugs. Journal of enzyme inhibition and medicinal chemistry, 31(sup1), 177–183. https://doi.org/10.3109/14756366.2016.1161620

Jacob, A., & Prekeris, R. (2015). The regulation of MMP targeting to invadopodia during cancer metastasis. Frontiers in cell and developmental biology, 3, 4. https://doi.org/10.3389/fcell.2015.00004

Jee, S. H., Ohrr, H., Sull, J. W., Yun, J. E., Ji, M., & Samet, J. M. (2005). Fasting serum glucose level and cancer risk in Korean men and women. JAMA, 293(2), 194–202. https://doi.org/10.1001/jama.293.2.194

Joshi, R. K. (2016). Asparagus racemosus (Shatawari), phytoconstituents and medicinal importance, future source of economy by cultivation in Uttrakhand: A review. International Journal of Herbal Medicine, 4(4), 18–21.

Joshi, S. S., & Badgwell, B. D. (2021). Current treatment and recent progress in gastric cancer. CA: a cancer journal for clinicians, 71(3), 264–279. https://doi.org/10.3322/caac.21657

Justus, C. R., Marie, M. A., Sanderlin, E. J., & Yang, L. V. (2023). Transwell In Vitro Cell Migration and Invasion Assays. Methods in molecular biology (Clifton, N.J.), 2644, 349–359. https://doi.org/10.1007/978-1-0716-3052-5_22

Kaludercic, N., & Di Lisa, F. (2020). Mitochondrial ROS Formation in the Pathogenesis of Diabetic Cardiomyopathy. Frontiers in cardiovascular medicine, 7, 12. https://doi.org/10.3389/fcvm.2020.00012

Kamangar, F., Dawsey, S. M., Blaser, M. J., Perez-Perez, G. I., Pietinen, P., Newschaffer, C. J., Abnet, C. C., Albanes, D., Virtamo, J., & Taylor, P. R. (2006). Opposing risks of gastric cardia and noncardia gastric adenocarcinomas associated with Helicobacter pylori seropositivity. Journal of the National Cancer Institute, 98(20), 1445–1452. https://doi.org/10.1093/jnci/djj393

Kamfar, W. W., Khraiwesh, H. M., Ibrahim, M. O., Qadhi, A. H., Azhar, W. F., Ghafouri, K. J., Alhussain, M. H., Aldairi, A. F., AlShahrani, A. M., Alghannam, A. F., Abdulal, R. H., Al-Slaihat, A. H., Qutob, M. S., Elrggal, M. E., Ghaith, M. M., & Azzeh, F. S. (2024).

Comprehensive review of melatonin as a promising nutritional and nutraceutical supplement. Heliyon, 10(2), e24266. https://doi.org/10.1016/j.heliyon.2024.e24266

Kang, X., Kong, F., Wu, X., Ren, Y., Wu, S., Wu, K., Jiang, Z., & Zhang, W. (2015). High glucose promotes tumor invasion and increases metastasis-associated protein expression in human lung epithelial cells by upregulating heme oxygenase-1 via reactive oxygen species or the TGF-β1/PI3K/Akt signaling pathway. Cellular Physiology and Biochemistry, 35(3), 1008–1022. https://doi.org/10.1159/000373928

Karamitri, A., & Jockers, R. (2019). Melatonin in type 2 diabetes mellitus and obesity. Nature reviews. Endocrinology, 15(2), 105–125. https://doi.org/10.1038/s41574-018-0130-1

Katsarou, A., Gudbjörnsdottir, S., Rawshani, A., Dabelea, D., Bonifacio, E., Anderson, B. J., Jacobsen, L. M., Schatz, D. A., & Lernmark, Å. (2017). Type 1 diabetes mellitus. Nature reviews. Disease primers, 3, 17016. https://doi.org/10.1038/nrdp.2017.16

Kaushik, M. (2014). A review of innovative chemical drawing and spectra prediction computer software. Mediterranean Journal of Chemistry, 3:759–766. https://doi.org/10.13171/mjc.3.1.2014.04.04.16

Keszei, A. P., Goldbohm, R. A., Schouten, L. J., Jakszyn, P., & van den Brandt, P. A. (2013). Dietary N-nitroso compounds, endogenous nitrosation, and the risk of esophageal and gastric cancer subtypes in the Netherlands Cohort Study. The American journal of clinical nutrition, 97(1), 135–146. https://doi.org/10.3945/ajcn.112.043885

Khatoon, J., Rai, R. P., & Prasad, K. N. (2016). Role of Helicobacter pylori in gastric cancer: Updates. World journal of gastrointestinal oncology, 8(2), 147–158. https://doi.org/10.4251/wjgo.v8.i2.147

Khokha, R., Murthy, A., & Weiss, A. (2013). Metalloproteinases and their natural inhibitors in inflammation and immunity. Nature reviews. Immunology, 13(9), 649–665. https://doi.org/10.1038/nri3499

Kim, J., & Wang, T. C. (2021). Helicobacter pylori and Gastric Cancer. Gastrointestinal endoscopy clinics of North America, 31(3), 451–465. https://doi.org/10.1016/j.giec.2021.03.003

Kim, J., Cho, Y. A., Choi, W. J., & Jeong, S. H. (2014). Gene-diet interactions in gastric cancer risk: a systematic review. World journal of gastroenterology, 20(28), 9600–9610. https://doi.org/10.3748/wjg.v20.i28.9600

Kim, S., Lee, J., Jo, S., Brooks, C. L., 3rd, Lee, H. S., & Im, W. (2017). CHARMM-GUI ligand reader and modeler for CHARMM force field generation of small molecules. Journal of Computational Chemistry, 38(21), 1879–1886. https://doi.org/10.1002/jcc.24829

Kirkman, M. S., Briscoe, V. J., Clark, N., Florez, H., Haas, L. B., Halter, J. B., Huang, E. S., Korytkowski, M. T., Munshi, M. N., Odegard, P. S., Pratley, R. E., Swift, C. S., & Consensus Development Conference on Diabetes and Older Adults (2012). Diabetes in older adults: a consensus report. Journal of the American Geriatrics Society, 60(12), 2342–2356. https://doi.org/10.1111/jgs.12035

Koobotse, M. O., Schmidt, D., Holly, J. M. P., & Perks, C. M. (2020). Glucose Concentration in Cell Culture Medium Influences the BRCA1-Mediated Regulation of the Lipogenic Action of IGF-I in Breast Cancer Cells. International journal of molecular sciences, 21(22), 8674. https://doi.org/10.3390/ijms21228674

Kopeć, M., Beton, K., Jarczewska, K., & Abramczyk, H. (2022). Hyperglycemia and cancer in human lung carcinoma by means of Raman spectroscopy and imaging. Scientific reports, 12(1), 18561. https://doi.org/10.1038/s41598-022-21483-y

Kotsifaki, A., Maroulaki, S., Karalexis, E., Stathaki, M., & Armakolas, A. (2024). Decoding the Role of Insulin-like Growth Factor 1 and Its Isoforms in Breast Cancer. International journal of molecular sciences, 25(17), 9302. https://doi.org/10.3390/ijms25179302

Kvietkauskas, M., Zitkute, V., Leber, B., Strupas, K., Stiegler, P., & Schemmer, P. (2020). The role of melatonin in colorectal cancer treatment: a comprehensive review. Therapeutic advances in medical oncology, 12, 1758835920931714. https://doi.org/10.1177/1758835920931714

Lambert, A. W., Pattabiraman, D. R., & Weinberg, R. A. (2017). Emerging Biological Principles of Metastasis. Cell, 168(4), 670–691. https://doi.org/10.1016/j.cell.2016.11.037

Lampugnani M. G. (1999). Cell migration into a wounded area in vitro. Methods in molecular biology (Clifton, N.J.), 96, 177–182. https://doi.org/10.1385/1-59259-258-9:177

Lauren P. (1965). The two histological main types of gastric carcinoma: Diffuse and so-called intestinal-type carcinoma. An attempt at a histo-clinical classification. Acta Pathologica et Microbiologica Scandinavica, 64, 31–49. https://doi.org/10.1111/apm.1965.64.1.31

Lee, J., Cheng, X., Swails, J. M., Yeom, M. S., Eastman, P. K., Lemkul, J. A., et al. (2016). CHARMM-GUI Input Generator for NAMD, GROMACS, AMBER, OpenMM, and CHARMM/OpenMM Simulations Using the CHARMM36 Additive Force Field. Journal of Chemical Theory and Computation, 12(1), 405–413. https://doi.org/10.1021/acs.jctc.5b00935

Li, F., Du, H., Li, S., & Liu, J. (2018). The Association Between Metabolic Syndrome and Gastric Cancer in Chinese. Frontiers in oncology, 8, 326. https://doi.org/10.3389/fonc.2018.00326

Li, Y. Q., Yan, J. P., Xu, W. L., Wang, H., Xia, Y. J., Wang, H. J., Zhu, Y. Y., & Huang, X. J. (2013). ADAM17 mediates MMP9 expression in lung epithelial cells. PloS one, 8(1), e51701. https://doi.org/10.1371/journal.pone.0051701

Liang, X., Zhu, J., Li, Y., Xu, Y., Chen, K., Lv, L., & Mao, W. (2020). Treatment strategies for metastatic gastric cancer: chemotherapy, palliative surgery or radiotherapy?. Future oncology (London, England), 16(5), 91–102. https://doi.org/10.2217/fon-2019-0495

Lin, Y., Qi, X., Liu, H., Xue, K., Xu, S., & Tian, Z. (2020). The anti-cancer effects of fucoidan: a review of both in vivo and in vitro investigations. Cancer cell international, 20, 154. https://doi.org/10.1186/s12935-020-01233-8

Liu, H., Zhou, W., Guo, L., Zhang, H., Guan, L., Yan, X., Zhai, Y., Qiao, Y., Wang, Z., Zhao, J., Lyu, K., Li, P., Wang, H., & Peng, L. (2022a). Quercetin protects against palmitate-induced pancreatic β-cell apoptosis by restoring lysosomal function and autophagic flux. The Journal of nutritional biochemistry, 107, 109060. https://doi.org/10.1016/j.jnutbio.2022.109060

Liu, J., Shao, T., Zhang, J., Liu, Q., Hua, H., Zhang, H., Wang, J., Luo, T., Shi, Y. E., & Jiang, Y. (2022b). Gamma synuclein promotes cancer metastasis through the MKK3/6-p38MAPK cascade. International journal of biological sciences, 18(8), 3167–3177. https://doi.org/10.7150/ijbs.69155

Loesch, M., Zhi, H. Y., Hou, S. W., Qi, X. M., Li, R. S., Basir, Z., Iftner, T., Cuenda, A., & Chen, G. (2010). p38gamma MAPK cooperates with c-Jun in trans-activating matrix

metalloproteinase 9. The Journal of biological chemistry, 285(20), 15149–15158. https://doi.org/10.1074/jbc.M110.105429

Lu, P., Weaver, V. M., & Werb, Z. (2012). The extracellular matrix: a dynamic niche in cancer progression. The Journal of cell biology, 196(4), 395–406. https://doi.org/10.1083/jcb.201102147

Ma, Q., Reiter, R. J., & Chen, Y. (2020). Role of melatonin in controlling angiogenesis under physiological and pathological conditions. Angiogenesis, 23(2), 91–104. https://doi.org/10.1007/s10456-019-09689-7

Ma, Z., Liu, D., Di, S., Zhang, Z., Li, W., Zhang, J., Xu, L., Guo, K., Zhu, Y., Li, X., Han, J., & Yan, X. (2019). Histone deacetylase 9 downregulation decreases tumor growth and promotes apoptosis in non-small cell lung cancer after melatonin treatment. Journal of Pineal Research, 67(2), e12587. https://doi.org/10.1111/jpi.12587

Mao, L., Yuan, L., Slakey, L. M., Jones, F. E., Burow, M. E., & Hill, S. M. (2010). Inhibition of breast cancer cell invasion by melatonin is mediated through regulation of the p38 mitogen-activated protein kinase signaling pathway. Breast cancer research, 12(6), R107. https://doi.org/10.1186/bcr2794

Martínez-Campa, C., Menéndez-Menéndez, J., Alonso-González, C., González, A., Álvarez-García, V., & Cos, S. (2017). What is known about melatonin, chemotherapy and altered gene expression in breast cancer. Oncology letters, 13(4), 2003–2014. https://doi.org/10.3892/ol.2017.5712

Mayo, J. C., Hevia, D., Quiros-Gonzalez, I., Rodriguez-Garcia, A., Gonzalez-Menendez, P., Cepas, V., Gonzalez-Pola, I., & Sainz, R. M. (2017). IGFBP3 and MAPK/ERK signaling mediates melatonin-induced antitumor activity in prostate cancer. Journal of pineal research, 62(1), 10.1111/jpi.12373. https://doi.org/10.1111/jpi.12373

Miao, Z. F., Xu, H., Xu, Y. Y., Wang, Z. N., Zhao, T. T., Song, Y. X., & Xu, H. M. (2017). Diabetes mellitus and the risk of gastric cancer: a meta-analysis of cohort studies. Oncotarget, 8(27), 44881–44892. https://doi.org/10.18632/oncotarget.16487

Milne, A. N., & Offerhaus, G. J. (2010). Early-onset gastric cancer: Learning lessons from the young. World journal of gastrointestinal oncology, 2(2), 59–64. https://doi.org/10.4251/wjgo.v2.i2.59

Mishra, M., Flaga, J., & Kowluru, R. A. (2016). Molecular Mechanism of Transcriptional Regulation of Matrix Metalloproteinase-9 in Diabetic Retinopathy. Journal of cellular physiology, 231(8), 1709–1718. https://doi.org/10.1002/jcp.25268

Mitra, S. K., Prakash, N. S., & Sundaram, R. (2012). Shatavarins (containing Shatavarin IV) with anticancer activity from the roots of Asparagus racemosus. Indian journal of pharmacology, 44(6), 732–736. https://doi.org/10.4103/0253-7613.103273

Mittelstadt, M. L., & Patel, R. C. (2012). AP-1 mediated transcriptional repression of matrix metalloproteinase-9 by recruitment of histone deacetylase 1 in response to interferon β. PloS one, 7(8), e42152. https://doi.org/10.1371/journal.pone.0042152

Monea, S., Lehti, K., Keski-Oja, J., & Mignatti, P. (2002). Plasmin activates pro-matrix metalloproteinase-2 with a membrane-type 1 matrix metalloproteinase-dependent mechanism. Journal of cellular physiology, 192(2), 160–170. https://doi.org/10.1002/jcp.10126

Morais, S., Costa, A., Albuquerque, G., Araújo, N., Pelucchi, C., Rabkin, C. S., Liao, L. M., Sinha, R., Zhang, Z. F., Hu, J., Johnson, K. C., Palli, D., Ferraroni, M., Bonzi, R., Yu, G. P., López-Carrillo, L., Malekzadeh, R., Tsugane, S., Hidaka, A., Hamada, G. S., … Lunet, N. (2022). Salt intake and gastric cancer: a pooled analysis within the Stomach cancer Pooling (StoP) Project. Cancer causes & control, 33(5), 779–791. https://doi.org/10.1007/s10552-022-01565-y

Morgan, E., Arnold, M., Camargo, M. C., Gini, A., Kunzmann, A. T., Matsuda, T., Meheus, F., Verhoeven, R. H. A., Vignat, J., Laversanne, M., Ferlay, J., & Soerjomataram, I. (2022). The current and future incidence and mortality of gastric cancer in 185 countries, 2020-40: A population-based modelling study. EClinicalMedicine, 47, 101404. https://doi.org/10.1016/j.eclinm.2022.101404

Mori, K., Uchida, T., Yoshie, T., Mizote, Y., Ishikawa, F., Katsuyama, M., & Shibanuma, M. (2019). A mitochondrial ROS pathway controls matrix metalloproteinase 9 levels and invasive properties in RAS-activated cancer cells. The FEBS journal, 286(3), 459–478. https://doi.org/10.1111/febs.14671

Morris, G. M., Huey, R., Lindstrom, W., Sanner, M. F., Belew, R. K., Goodsell, D. S., & Olson, A. J. (2009). AutoDock4 and AutoDockTools4: Automated docking with selective receptor flexibility. Journal of Computational Chemistry, 30(16), 2785–2791. https://doi.org/10.1002/jcc.21256

Mustafa, S., Koran, S., & AlOmair, L. (2022). Insights Into the Role of Matrix Metalloproteinases in Cancer and its Various Therapeutic Aspects: A Review. Frontiers in molecular biosciences, 9, 896099. https://doi.org/10.3389/fmolb.2022.896099

Nagase H. (2016). A personal journey with matrix metalloproteinases. Biological chemistry, 397(9), 805–813. https://doi.org/10.1515/hsz-2016-0169

Nandakumar, A., Gupta, P. C., Gangadharan, P., Visweswara, R. N., & Parkin, D. M. (2005). Geographic pathology revisited: development of an atlas of cancer in India. International journal of cancer, 116(5), 740–754. https://doi.org/10.1002/ijc.21109

Nigam, M., Mishra, A. P., Deb, V. K., Dimri, D. B., Tiwari, V., Bungau, S. G., Bungau, A. F., & Radu, A. F. (2023). Evaluation of the association of chronic inflammation and cancer: Insights and implications. Biomedicine & pharmacotherapy, 164, 115015. https://doi.org/10.1016/j.biopha.2023.115015

Niland, S., Riscanevo, A. X., & Eble, J. A. (2021). Matrix Metalloproteinases Shape the Tumor Microenvironment in Cancer Progression. International journal of molecular sciences, 23(1), 146. https://doi.org/10.3390/ijms23010146

Nishikawa, J., Iizasa, H., Yoshiyama, H., Shimokuri, K., Kobayashi, Y., Sasaki, S., Nakamura, M., Yanai, H., Sakai, K., Suehiro, Y., Yamasaki, T., & Sakaida, I. (2018). Clinical Importance of Epstein–Barr Virus-Associated Gastric Cancer. Cancers, 10(6), 167. https://doi.org/10.3390/cancers10060167

Oberhauser, N., Nurisso, A., & Carrupt, P. A. (2014). MLP Tools: a PyMOL plugin for using the molecular lipophilicity potential in computer-aided drug design. Journal of Computer-aided Molecular Design, 28(5), 587–596. https://doi.org/10.1007/s10822-014-9744-0

Onitilo, A. A., Engel, J. M., Glurich, I., Stankowski, R. V., Williams, G. M., & Doi, S. A. (2012). Diabetes and cancer I: risk, survival, and implications for screening. Cancer causes & control : CCC, 23(6), 967–981. https://doi.org/10.1007/s10552-012-9972-3

Overall, C. M., & López-Otín, C. (2002). Strategies for MMP inhibition in cancer: innovations for the post-trial era. Nature reviews. Cancer, 2(9), 657–672. https://doi.org/10.1038/nrc884

Ozanne, B. W., Spence, H. J., McGarry, L. C., & Hennigan, R. F. (2007). Transcription factors control invasion: AP-1 the first among equals. Oncogene, 26(1), 1–10. https://doi.org/10.1038/sj.onc.1209759

Page-McCaw, A., Ewald, A. J., & Werb, Z. (2007). Matrix metalloproteinases and the regulation of tissue remodelling. Nature reviews. Molecular cell biology, 8(3), 221–233. https://doi.org/10.1038/nrm2125

Park, H. S., Kim, G. Y., Nam, T. J., Deuk Kim, N., & Hyun Choi, Y. (2011). Antiproliferative activity of fucoidan was associated with the induction of apoptosis and autophagy in AGS human gastric cancer cells. Journal of food science, 76(3), T77–T83. https://doi.org/10.1111/j.1750-3841.2011.02099.x

Park, J., Kwak, C. H., Ha, S. H., Kwon, K. M., Abekura, F., Cho, S. H., Chang, Y. C., Lee, Y. C., Ha, K. T., Chung, T. W., & Kim, C. H. (2018). Ganglioside GM3 suppresses lipopolysaccharide-induced inflammatory responses in rAW 264.7 macrophage cells through NF-κB, AP-1, and MAPKs signaling. Journal of cellular biochemistry, 119(1), 1173–1182. https://doi.org/10.1002/jcb.26287

Patterson, C. C., Dahlquist, G. G., Gyürüs, E., Green, A., Soltész, G., & EURODIAB Study Group (2009). Incidence trends for childhood type 1 diabetes in Europe during 1989-2003 and predicted new cases 2005-20: a multicentre prospective registration study. Lancet (London, England), 373(9680), 2027–2033. https://doi.org/10.1016/S0140-6736(09)60568-7

Paz, H., Pathak, N., & Yang, J. (2014). Invading one step at a time: the role of invadopodia in tumor metastasis. Oncogene, 33(33), 4193–4202. https://doi.org/10.1038/onc.2013.393

Permuy, M., López-Peña, M., González-Cantalapiedra, A., & Muñoz, F. (2017). Melatonin: A Review of Its Potential Functions and Effects on Dental Diseases. International journal of molecular sciences, 18(4), 865. https://doi.org/10.3390/ijms18040865

Pernot, S., Voron, T., Perkins, G., Lagorce-Pages, C., Berger, A., & Taieb, J. (2015). Signet-ring cell carcinoma of the stomach: Impact on prognosis and specific therapeutic challenge.

World journal of gastroenterology, 21(40), 11428–11438. https://doi.org/10.3748/wjg.v21.i40.11428

Phillips, J. C., Hardy, D. J., Maia, J. D. C., Stone, J. E., Ribeiro, J. V., Bernardi, R. C., et al. (2020). Scalable molecular dynamics on CPU and GPU architectures with NAMD. The Journal of Chemical Physics, 153(4), 044130. https://doi.org/10.1063/5.0014475

Phoomak, C., Vaeteewoottacharn, K., Silsirivanit, A., Saengboonmee, C., Seubwai, W., Sawanyawisuth, K., Wongkham, C., & Wongkham, S. (2017). High glucose levels boost the aggressiveness of highly metastatic cholangiocarcinoma cells via O-GlcNAcylation. Scientific reports, 7, 43842. https://doi.org/10.1038/srep43842

Pimentel, A. M., Rocha, R., & Santana, G. O. (2019). Crohn's disease of esophagus, stomach and duodenum. World journal of gastrointestinal pharmacology and therapeutics, 10(2), 35–49. https://doi.org/10.4292/wjgpt.v10.i2.35

Pinheiro, H., Oliveira, C., Seruca, R., & Carneiro, F. (2014). Hereditary diffuse gastric cancer - pathophysiology and clinical management. Best practice & research. Clinical gastroenterology, 28(6), 1055–1068. https://doi.org/10.1016/j.bpg.2014.09.007

Plummer, M., Franceschi, S., Vignat, J., Forman, D., & de Martel, C. (2015). Global burden of gastric cancer attributable to Helicobacter pylori. International journal of cancer, 136(2), 487–490. https://doi.org/10.1002/ijc.28999

Poorolajal, J., Moradi, L., Mohammadi, Y., Cheraghi, Z., & Gohari-Ensaf, F. (2020). Risk factors for stomach cancer: a systematic review and meta-analysis. Epidemiology and health, 42, e2020004. https://doi.org/10.4178/epih.e2020004

Popkin B. M. (2015). Nutrition Transition and the Global Diabetes Epidemic. Current diabetes reports, 15(9), 64. https://doi.org/10.1007/s11892-015-0631-4

Ra, H. J., & Parks, W. C. (2007). Control of matrix metalloproteinase catalytic activity. Matrix biology : journal of the International Society for Matrix Biology, 26(8), 587–596. https://doi.org/10.1016/j.matbio.2007.07.001

Rapp, K., Schroeder, J., Klenk, J., Ulmer, H., Concin, H., Diem, G., Oberaigner, W., & Weiland, S. K. (2006). Fasting blood glucose and cancer risk in a cohort of more than 140,000 adults in Austria. Diabetologia, 49(5), 945–952. https://doi.org/10.1007/s00125-006-0207-6

Saengboonmee, C., Seubwai, W., Pairojkul, C., & Wongkham, S. (2016). High glucose enhances progression of cholangiocarcinoma cells via STAT3 activation. Scientific reports, 6, 18995. https://doi.org/10.1038/srep18995

Sairam, K., Priyambada, S., Aryya, N. C., & Goel, R. K. (2003). Gastroduodenal ulcer protective activity of Asparagus racemosus: an experimental, biochemical and histological study. Journal of ethnopharmacology, 86(1), 1–10. https://doi.org/10.1016/s0378-8741(02)00342-2

Salehi, B., Sharopov, F., Fokou, P. V. T., Kobylinska, A., Jonge, L., Tadio, K., Sharifi-Rad, J., Posmyk, M. M., Martorell, M., Martins, N., & Iriti, M. (2019). Melatonin in Medicinal and Food Plants: Occurrence, Bioavailability, and Health Potential for Humans. Cells, 8(7), 681. https://doi.org/10.3390/cells8070681

Sapra, A., & Bhandari, P. Diabetes. [Updated 2023 Jun 21]. In: StatPearls [Internet]. Treasure Island (FL): StatPearls Publishing; 2024 Jan-. Available from: https://www.ncbi.nlm.nih.gov/books/NBK551501/

Senichkin, V. V., Prokhorova, E. A., Zhivotovsky, B., & Kopeina, G. S. (2021). Simple and Efficient Protocol for Subcellular Fractionation of Normal and Apoptotic Cells. Cells, 10(4), 852. https://doi.org/10.3390/cells10040852

Sharma, A., & Radhakrishnan, V. (2011). Gastric cancer in India. Indian journal of medical and paediatric oncology : official journal of Indian Society of Medical & Paediatric Oncology, 32(1), 12–16. https://doi.org/10.4103/0971-5851.81884

Shields, B. M., Hicks, S., Shepherd, M. H., Colclough, K., Hattersley, A. T., & Ellard, S. (2010). Maturity-onset diabetes of the young (MODY): how many cases are we missing?. Diabetologia, 53(12), 2504–2508. https://doi.org/10.1007/s00125-010-1799-4

Skarlis, C., & Anagnostouli, M. (2020). The role of melatonin in Multiple Sclerosis. Neurological sciences : official journal of the Italian Neurological Society and of the Italian Society of Clinical Neurophysiology, 41(4), 769–781. https://doi.org/10.1007/s10072-019-04137-2

Song, J., Ma, S. J., Luo, J. H., Zhang, H., Wang, R. X., Liu, H., Li, L., Zhang, Z. G., & Zhou, R. X. (2018). Melatonin induces the apoptosis and inhibits the proliferation of human gastric

cancer cells via blockade of the AKT/MDM2 pathway. Oncology reports, 39(4), 1975–1983. https://doi.org/10.3892/or.2018.6282

Springman, E. B., Angleton, E. L., Birkedal-Hansen, H., & Van Wart, H. E. (1990). Multiple modes of activation of latent human fibroblast collagenase: evidence for the role of a Cys73 active-site zinc complex in latency and a "cysteine switch" mechanism for activation. Proceedings of the National Academy of Sciences of the United States of America, 87(1), 364–368. https://doi.org/10.1073/pnas.87.1.364

Standl, E., Khunti, K., Hansen, T. B., & Schnell, O. (2019). The global epidemics of diabetes in the 21st century: Current situation and perspectives. European journal of preventive cardiology, 26(2_suppl), 7–14. https://doi.org/10.1177/2047487319881021

Storey, S., & Von Ah, D. (2015). Prevalence and impact of hyperglycemia on hospitalized leukemia patients. European Journal of Oncology Nursing, 19(1), 13–17. https://doi.org/10.1016/j.ejon.2014.08.005

Storey, S., & Von Ah, D. (2016). Impact of Hyperglycemia and Age on Outcomes in Patients With Acute Myeloid Leukemia. Oncology Nursing Forum, 43(5), 595–601. https://doi.org/10.1188/16.ONF.595-601

Strongin, A. Y., Collier, I., Bannikov, G., Marmer, B. L., Grant, G. A., & Goldberg, G. I. (1995). Mechanism of cell surface activation of 72-kDa type IV collagenase. Isolation of the activated form of the membrane metalloprotease. The Journal of biological chemistry, 270(10), 5331–5338. https://doi.org/10.1074/jbc.270.10.5331

Sun, H., Saeedi, P., Karuranga, S., Pinkepank, M., Ogurtsova, K., Duncan, B. B., Stein, C., Basit, A., Chan, J. C. N., Mbanya, J. C., Pavkov, M. E., Ramachandaran, A., Wild, S. H., James, S., Herman, W. H., Zhang, P., Bommer, C., Kuo, S., Boyko, E. J., & Magliano, D. J. (2022). IDF Diabetes Atlas: Global, regional and country-level diabetes prevalence estimates for 2021 and projections for 2045. Diabetes research and clinical practice, 183, 109119. https://doi.org/10.1016/j.diabres.2021.109119

Sun, X. F., Shao, Y. B., Liu, M. G., Chen, Q., Liu, Z. J., Xu, B., Luo, S. X., & Liu, H. (2017). High-concentration glucose enhances invasion in invasive ductal breast carcinoma by promoting Glut1/MMP2/MMP9 axis expression. Oncology letters, 13(5), 2989–2995. https://doi.org/10.3892/ol.2017.5843

Sung, H., Ferlay, J., Siegel, R. L., Laversanne, M., Soerjomataram, I., Jemal, A., & Bray, F. (2021). Global Cancer Statistics 2020: GLOBOCAN Estimates of Incidence and Mortality Worldwide for 36 Cancers in 185 Countries. CA: ACancerJournal for Clinicians, 71(3), 209–249. https://doi.org/10.3322/caac.21660

Thonsri, U., Wongkham, S., Wongkham, C., Hino, S., Nakao, M., Roytrakul, S., Koga, T., & Seubwai, W. (2021). High glucose-ROS conditions enhance the progression in cholangiocarcinoma via upregulation of MAN2A2 and CHD8. Cancer science, 112(1), 254–264. https://doi.org/10.1111/cas.14719

Van Wart, H. E., & Birkedal-Hansen, H. (1990). The cysteine switch: a principle of regulation of metalloproteinase activity with potential applicability to the entire matrix metalloproteinase gene family. Proceedings of the National Academy of Sciences of the United States of America, 87(14), 5578–5582. https://doi.org/10.1073/pnas.87.14.5578

Verma, R. P., & Hansch, C. (2007). Matrix metalloproteinases (MMPs): chemical-biological functions and (Q)SARs. Bioorganic & medicinal chemistry, 15(6), 2223–2268. https://doi.org/10.1016/j.bmc.2007.01.011

Verma, S., Kesh, K., Ganguly, N., Jana, S., & Swarnakar, S. (2014). Matrix metalloproteinases and gastrointestinal cancers: Impacts of dietary antioxidants. World journal of biological chemistry, 5(3), 355–376. https://doi.org/10.4331/wjbc.v5.i3.355

Vogelaar, I. P., van der Post, R. S., van Krieken, J. H. J., Spruijt, L., van Zelst-Stams, W. A., Kets, C. M., Lubinski, J., Jakubowska, A., Teodorczyk, U., Aalfs, C. M., van Hest, L. P., Pinheiro, H., Oliveira, C., Jhangiani, S. N., Muzny, D. M., Gibbs, R. A., Lupski, J. R., de Ligt, J., Vissers, L. E. L. M., Hoischen, A., … Hoogerbrugge, N. (2017). Unraveling genetic predisposition to familial or early onset gastric cancer using germline whole-exome sequencing. European journal of human genetics : EJHG, 25(11), 1246–1252. https://doi.org/10.1038/ejhg.2017.138

Walker, C., Mojares, E., & Del Río Hernández, A. (2018). Role of Extracellular Matrix in Development and Cancer Progression. International journal of molecular sciences, 19(10), 3028. https://doi.org/10.3390/ijms19103028

Wang, B. S., Zhang, C. L., Cui, X., Li, Q., Yang, L., He, Z. Y., Yang, Z., Zeng, M. M., & Cao, N. (2024). Curcumin inhibits the growth and invasion of gastric cancer by regulating long

noncoding RNA AC022424.2. World journal of gastrointestinal oncology, 16(4), 1437–1452. https://doi.org/10.4251/wjgo.v16.i4.1437

Wang, S. W., Tai, H. C., Tang, C. H., Lin, L. W., Lin, T. H., Chang, A. C., Chen, P. C., Chen, Y. H., Wang, P. C., Lai, Y. W., & Chen, S. S. (2021). Melatonin impedes prostate cancer metastasis by suppressing MMP-13 expression. Journal of cellular physiology, 236(5), 3979–3990. https://doi.org/10.1002/jcp.30150

Wang, X., Wang, B., Zhan, W., Kang, L., Zhang, S., Chen, C., Hou, D., You, R., & Huang, H. (2019). Melatonin inhibits lung metastasis of gastric cancer in vivo. Biomedicine & pharmacotherapy, 117, 109018. https://doi.org/10.1016/j.biopha.2019.109018

Wang, Y., Wu, H., Wu, X., Bian, Z., & Gao, Q. (2014). Interleukin 17A promotes gastric cancer invasiveness via NF-κB mediated matrix metalloproteinases 2 and 9 expression. PloS one, 9(6), e96678. https://doi.org/10.1371/journal.pone.0096678

Williamson, R. A., Marston, F. A., Angal, S., Koklitis, P., Panico, M., Morris, H. R., Carne, A. F., Smith, B. J., Harris, T. J., & Freedman, R. B. (1990). Disulphide bond assignment in human tissue inhibitor of metalloproteinases (TIMP). The Biochemical journal, 268(2), 267–274. https://doi.org/10.1042/bj2680267

Wilson, R. L. & Stevenson, C. E. Anatomy and Physiology of the Stomach, Editor(s): Yeo C. J., Shackelford's Surgery of the Alimentary Tract, 2 Volume Set (Eighth Edition), Elsevier, 2019, pages 634–646.

Wright, J. L., Plymate, S. R., Porter, M. P., Gore, J. L., Lin, D. W., Hu, E., & Zeliadt, S. B. (2013). Hyperglycemia and prostate cancer recurrence in men treated for localized prostate cancer. Prostate cancer and prostatic diseases, 16(2), 204–208. https://doi.org/10.1038/pcan.2013.5

Wu, J., Chen, J., Xi, Y., Wang, F., Sha, H., Luo, L., Zhu, Y., Hong, X., & Bu, S. (2018a). High glucose induces epithelial-mesenchymal transition and results in the migration and invasion of colorectal cancer cells. Experimental and therapeutic medicine, 16(1), 222–230. https://doi.org/10.3892/etm.2018.6189

Xu, X., Yi, H., Wu, J., Kuang, T., Zhang, J., Li, Q., Du, H., Xu, T., Jiang, G., & Fan, G. (2021). Therapeutic effect of berberine on metabolic diseases: Both pharmacological data and clinical

evidence. Biomedicine & pharmacotherapy, 133, 110984. https://doi.org/10.1016/j.biopha.2020.110984

Yaghoobi, M., Bijarchi, R., & Narod, S. A. (2010). Family history and the risk of gastric cancer. British journal of cancer, 102(2), 237–242. https://doi.org/10.1038/sj.bjc.6605380

Yamada, Y., Gohda, S., Abe, K., Togo, T., Shimano, N., Sasaki, T., et al. (2017). Carbon materials with controlled edge structures. Carbon, 122, 694–701. https://doi.org/10.1016/j.carbon.2017.07.012

Yamagata, H., Kiyohara, Y., Nakamura, S., Kubo, M., Tanizaki, Y., Matsumoto, T., Tanaka, K., Kato, I., Shirota, T., & Iida, M. (2005). Impact of fasting plasma glucose levels on gastric cancer incidence in a general Japanese population: the Hisayama study. Diabetes care, 28(4), 789–794. https://doi.org/10.2337/diacare.28.4.789

Yan, C., & Boyd, D. D. (2007). Regulation of matrix metalloproteinase gene expression. Journal of cellular physiology, 211(1), 19–26. https://doi.org/10.1002/jcp.20948

Yan, X., Cao, N., Chen, Y., Lan, H. Y., Cha, J. H., Yang, W. H., & Yang, M. H. (2020). MT4-MMP promotes invadopodia formation and cell motility in FaDu head and neck cancer cells. Biochemical and biophysical research communications, 522(4), 1009–1014. https://doi.org/10.1016/j.bbrc.2019.12.009

Yancik, R., & Ries, L. A. (2000). Aging and cancer in America. Demographic and epidemiologic perspectives. Hematology/oncology clinics of North America, 14(1), 17–23. https://doi.org/10.1016/s0889-8588(05)70275-6

Yoon, J., Cho, S. J., Ko, Y. S., Park, J., Shin, D. H., Hwang, I. C., Han, S. Y., Nam, S. Y., Kim, M. A., Chang, M. S., Lee, H. S., Kim, W. H., & Lee, B. L. (2013). A synergistic interaction between transcription factors nuclear factor-κB and signal transducers and activators of transcription 3 promotes gastric cancer cell migration and invasion. BMC gastroenterology, 13, 29. https://doi.org/10.1186/1471-230X-13-29

Yusefi, A. R., Bagheri Lankarani, K., Bastani, P., Radinmanesh, M., & Kavosi, Z. (2018). Risk Factors for Gastric Cancer: A Systematic Review. Asian Pacific journal of cancer prevention : APJCP, 19(3), 591–603. https://doi.org/10.22034/APJCP.2018.19.3.591

Zhang, X. Y., & Zhang, P. Y. (2017). Gastric cancer: somatic genetics as a guide to therapy. Journal of medical genetics, 54(5), 305–312. https://doi.org/10.1136/jmedgenet-2016-104171

Zhao, N., Wang, W., Jiang, H., Qiao, Z., Sun, S., Wei, Y., Xie, X., Li, H., Bi, X., & Yang, Z. (2023). Natural Products and Gastric Cancer: Cellular Mechanisms and Effects to Change Cancer Progression. Anti-cancer agents in medicinal chemistry, 23(13), 1506–1518. https://doi.org/10.2174/1871520623666230407082955

Zhao, Y., Chen, X., Jiang, J., Wan, X., Wang, Y., & Xu, P. (2020). Epigallocatechin gallate reverses gastric cancer by regulating the long noncoding RNA LINC00511/miR-29b/KDM2A axis. Biochimica et biophysica acta. Molecular basis of disease, 1866(10), 165856. https://doi.org/10.1016/j.bbadis.2020.165856

Zharinov, G. M., Bogomolov, O. A., Chepurnaya, I. V., Neklasova, N. Y., & Anisimov, V. N. (2020). Melatonin increases overall survival of prostate cancer patients with poor prognosis after combined hormone radiation treatment. Oncotarget, 11(41), 3723–3729. https://doi.org/10.18632/oncotarget.27757

Zhou, S., Yao, D., Guo, L., & Teng, L. (2017). Curcumin suppresses gastric cancer by inhibiting gastrin-mediated acid secretion. FEBS open bio, 7(8), 1078–1084. https://doi.org/10.1002/2211-5463.12237

PUBLICATIONS

&

PRESENTATIONS

LIST OF PUBLICATIONS

Research articles published in peer-reviewed journals

1. **Chatterjee, A.**, Roy, T., & Swarnakar, S. (2024). Transcriptional upregulation of MMP-9 gene under hyperglycemic conditions in AGS cells: Role of AP-1 transcription factor. ***Cellular Signalling***, 124, 111435. https://doi.org/10.1016/j.cellsig.2024.111435

2. **Chatterjee, A.**, Roy, T., Kumar Mishra, V., & Swarnakar, S. (2024). Shatavarin-IV, a steroidal saponin from Asparagus racemosus, inhibits cell cycle progression and epithelial-to-mesenchymal transition in AGS cells under hyperglycemic conditions. ***Steroids***, 210, 109487. https://doi.org/10.1016/j.steroids.2024.109487

3. **Chatterjee, A.**, Roy, T., Jyothi, D., Mishra, V. K., Singh, U. P., & Swarnakar, S. (2024). Melatonin Inhibits AGS Cell Proliferation by Binding to the ATP Binding Site of CDK2 Under Hyperglycemic Conditions. ***Cell Biochemistry and Biophysics***, 82(2), 895–908. https://doi.org/10.1007/s12013-024-01241-9

4. Roy, T., **Chatterjee, A.**, & Swarnakar, S. (2023). Rotenone induced neurodegeneration is mediated via cytoskeleton degradation and necroptosis. ***BBA Molecular Cell Research***, 1870(3), 119417. https://doi.org/10.1016/j.bbamcr.2022.119417

5. Choudhary, P., Roy, T., **Chatterjee, A.**, Mishra, V. K., Pant, S., & Swarnakar, S. (2022). Melatonin rescues swim stress induced gastric ulceration by inhibiting matrix metalloproteinase-3 via down-regulation of inflammatory signaling cascade. ***Life Sciences***, 297, 120426. https://doi.org/10.1016/j.lfs.2022.120426

6. Choudhary, P., Biswas, S., Kandoth, N., Tayde, D., **Chatterjee, A.**, Chattopadhyay, S., Das, A., Swarnakar, S., & Pramanik, S. K. (2022). Graphene quantum dots alleviate ROS-mediated gastric damage. ***iScience***, 25(4), 104062. https://doi.org/10.1016/j.isci.2022.104062

Research article accepted for publication

7. Roy, T., Benerjee, R., **Chatterjee, A.**, Swarnakar, S. (2025). Dopamine toxicity induces ROS-dependent death of murine neuroblastoma cells: Impact on the interactions of Cofilin with UCHL1 and MMP9. ***Neurochemical Research***. Accepted for publication.

Book Chapters

Published

1. **Chatterjee, A.**, Mishra, V. K., Saha, S., & Swarnakar, S. (2022). An Insight into Targeted Therapy for Ovarian Cancer. In: Chakraborti, S. (eds) ***Handbook of Oxidative Stress in Cancer: Therapeutic Aspects.*** Springer, Singapore. https://doi.org/10.1007/978-981-16-1247-3_230-1

Accepted for publication

2. Roy, T., **Chatterjee, A.**, & Swarnakar, S. (2025). Necroptosis in neurodegenerative disorders. In: Mansour, H. M. & El-Khatib, A. S. (eds) ***Regulated Cell Death in Neurodegenerative Disorders***. Academic Press, Elsevier, Amsterdam, Netherlands. eBook ISBN: 9780443328534.

Cellular Signalling 124 (2024) 111435

Contents lists available at ScienceDirect

Cellular Signalling

journal homepage: www.elsevier.com/locate/cellsig

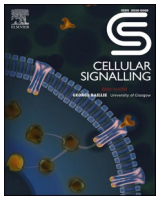

Transcriptional upregulation of MMP-9 gene under hyperglycemic conditions in AGS cells: Role of AP-1 transcription factor

Abhishek Chatterjee, Tapasi Roy, Snehasikta Swarnakar *

Infectious Diseases and Immunology division, CSIR-Indian Institute of Chemical Biology, 4, Raja S.C. Mullick Road, Kolkata 700032, West Bengal, India

ARTICLE INFO

Keywords:
AGS cells
Hyperglycemia
MMP-9
AP-1
Transcription
Gastric Cancer

ABSTRACT

Gastric cancer and diabetes are two complex and interrelated diseases having significant impact on global health. Hyperglycemic condition notably exacerbates cancer by promoting inflammation, angiogenesis, and metastasis. Elevated glucose levels can also upregulate the expression of specific matrix metalloproteinases (MMPs), especially MMP-9, which is associated with cancer cell migration and invasion. However, the molecular mechanism behind such upregulation remains unexplored. In the present study, we have identified the mechanism for hyperglycemia-induced transcriptional activation of MMP-9, in gastric adenocarcinoma (AGS) cells. Using various tools like luciferase-reporter assays with promoter deletion constructs, siRNAs, pharmacological inhibitors, and nuclear translocation experiments, we have identified that the transcriptional activation of MMP-9 under hyperglycemic conditions is predominantly governed by the MAPK pathway, via formation of the AP-1 heterodimer. The p65 NF-κB signaling pathway, although activated, plays no significant role in regulating hyperglycemia-induced MMP-9 expression. Chromatin immunoprecipitation studies indicate that the distal AP-1 binding site is responsible for hyperglycemia-induced MMP-9 transcription; whereas the proximal one accounts for both hyperglycemia-induced and basal MMP-9 transcription. Therefore, binding of AP-1 at both the proximal and distal binding sites on the MMP-9 promoter region is required for hyperglycemia-induced MMP-9 expression. Overall, our study unveils a novel mechanism of MMP-9 transcription under hyperglycemic conditions and also suggests that inhibiting the binding of the AP-1 heterodimer with its distal binding site can potentially reduce the complications developed during gastric cancer-hyperglycemia co-morbidity. A drug designed specifically to inhibit this interaction may prevent hyperglycemia-induced tumor aggressiveness to a considerable extent by impeding MMP-9 transcription.

1. Introduction

Gastric cancer (GC) is the fifth most common cancer worldwide and the fourth leading cause of cancer-associated mortality globally [1]. The development of GC is influenced by many environmental and behavioral factors including unhealthy diet, consumption of high-salt foods and alcohols, *Helicobacter pylori* infection, and obesity [2]. Genetic factors like loss of PTEN, activation of SOX and STAT proteins, can promote GC tumorigenesis [3–5]. Different metabolic syndromes like diabetes are also implicated in GC progression [6,7]. It is predicted that 9.9 % of the world's human population will become diabetic by the year 2045 [8]. Epidemiological studies have shown that persons with diabetes are vulnerable to developing liver, pancreatic, and breast cancer, regardless of their body mass index and other factors [9–13]. Additional reports also suggest that diabetes can increase the risk of early GC development [14,15] and negatively affect its prognosis [7]; thereby leading to a growing number of cases of GC and diabetes co-morbidity.

Among the multitudes of symptoms developed during diabetes, hyperglycemia has received special attention. Hyperglycemia may aggravate cancer progression by increasing inflammation, angiogenesis, tumor cell proliferation, and metastases in patients. High glucose is responsible for tumor development and epithelial-to-mesenchymal transition (EMT) in cultured human epithelial lung cancer cells [16,17], breast cancer cells [18], and cholangiocarcinoma cells [19]. Recently, our group has reported that hyperglycemia can also increase the rate of migration in gastric cancer cells [20,21].

Several studies have explored the association between hyperglycemia and metastasis, with a focus on the involvement of matrix metalloproteinases (MMPs). MMPs are a family of zinc-containing, calcium-dependent enzymes that play a key role in the breakdown and

* Corresponding author.
E-mail address: snehasiktaiicbidi@gmail.com (S. Swarnakar).

https://doi.org/10.1016/j.cellsig.2024.111435
Received 24 May 2024; Received in revised form 6 September 2024; Accepted 23 September 2024
Available online 25 September 2024

remodeling of the extracellular matrix (ECM). Dysregulation of MMPs can disrupt the ECM integrity and facilitate cancer cell invasion and metastasis. Hyperglycemia has been shown to modulate the expression and activity of several MMPs, especially MMP-9 [17,18,20,21], which is associated with cancer cell migration, invasion, and angiogenesis. Such elevated levels of MMP-9 can degrade the ECM components, allowing cancer cells to invade surrounding tissues and promote the formation of new blood vessels to support tumor growth [22]. However, the exact molecular mechanism by which the hyperglycemic environment facilitates MMP-9 expression has not been explored to date.

Therefore, understanding the intricate interplay between hyperglycemia, MMP-9, and metastasis is critical for developing targeted therapeutic interventions. Strategies aimed at controlling glucose levels, regulating MMP-9 activity, and inhibiting metastatic processes hold promise for mitigating the detrimental effects of hyperglycemia on cancer progression. The present study aims to achieve a better understanding of the molecular signaling pathways behind the hyperglycemia-induced upregulation of MMP-9 in gastric cancer cells, which would be helpful for the development of targeted therapeutic strategies against GC-hyperglycemia co-morbidity.

2. Materials and methods

2.1. Materials

Gelatin, Triton-X-100, protease inhibitors, dithiothreitol (DTT), D-glucose, D-mannitol RNase A solution, Tween®-20, Bradford reagent, bovine serum albumin (BSA), and Fluoromount Aqueous Mounting Medium were purchased from Sigma Chemical Co, St. Louis, MO, USA. CellTiter-Glo luminescent cell viability assay kit and Luciferase Assay System were purchased from Promega (Madison, WI, United States). Primary antibodies, horseradish peroxidase (HRP) conjugated secondary antibodies, and Texas Red conjugated secondary antibodies for western blotting were purchased from Santa Cruz Biotechnology (Dallas, TX, USA). Clarity™ Western ECL Substrate solution was purchased from Bio-Rad (Hercules, CA, USA). *Trans*-well chambers and Matrigel were sourced from Corning, USA. Crystal violet was purchased from HiMedia Laboratories, Maharashtra, India. RNAi duplexes corresponding to human siRNAs of NF-κB p65, MMP-9, and control siRNA-A were purchased from Santa Cruz Biotechnology (Dallas, TX, USA). The human MMP-9 promoter plasmid was a kind gift from Etty Benveniste & Douglas Boyd (Addgene plasmid # 53434). Plasmid DNA preparation kits were obtained from QIAGEN (Valencia, CA, USA). Lipofectamine™ RNAiMAX and Lipofectamine™ 2000 transfection reagents were procured from Invitrogen, Thermo Fisher Scientific corporation (Waltham, MA, USA). High-Sensitivity ChIP Kit and Glucose Assay Kit were purchased from Abcam (Cambridge, UK). c-Jun, c-Fos primary antibodies and rabbit IgG isotype control antibody were purchased from Cell Signaling Technologies (Danvers, MA, USA). AGS cells were purchased from the American Type Culture Collection (ATCC, Manassas, VA, USA). All cell culture-related materials were sourced from Gibco (Thermo Fisher, MA, USA).

2.2. Cell culture

AGS cells (human gastric adenocarcinoma cells) were maintained in Ham's F12K nutrient media supplemented with 10 % FBS and 1 % Antibiotic-Antimycotic (100×) mixture. The cells were kept at 37 °C in a humidified atmosphere containing 5 % CO_2 and 95 % air. All experiments were conducted with AGS cells within 10 passage numbers.

2.3. Optimization of hyperglycemic treatment conditions

AGS cells were seeded in six-well plates and maintained overnight in normoglycemic media containing 10 % FBS. 5.5 mM D-glucose was used to prepare normoglycemic media, as this concentration mimics normal blood glucose levels [23]. Afterward, the cells were exposed to incomplete Ham's F12K media with various concentrations of D-glucose or D-mannitol (5.5, 8, 12.5, 25, 35, and 50 mM) for 24 h to optimize the dose at which the expression and activity of MMP-9 is higher. With the selected dose of D-glucose, the expression and activity levels of MMP-9 were further monitored at different time points of incubation (0, 6, 12, 24, 36, and 48 h.). The concentrations of D-glucose and D-mannitol used in these experiments had no toxic effect on AGS cells up to 48 h of incubation, as confirmed by CellTiter-Glo luminescent cell viability assay (data not shown). AGS cells incubated in D-mannitol, instead of D-glucose, served as the osmolarity control. Luciferase-based reporter assay and western blotting were performed. to monitor MMP-9 expression at the transcriptional and translational level, respectively. Gelatin zymography assay was used to detect the gelatinolytic activity of MMP-9.

2.4. Treatment with MAPK inhibitors

D-glucose and D-mannitol were directly dissolved into liquid culture media and further diluted to the desired concentration. The MAPK pathway inhibitors PD98059, SB203580, and SP600125 were initially dissolved in dimethyl sulfoxide (DMSO) and further diluted in media before treatment. 50 μM PD98059, 20 μM SB203580 and 50 μM SP600125 were used in this study. The final concentration of DMSO in the experiments never exceeded 0.1 %. These inhibitors were added 1 h before hyperglycemic treatment. The used inhibitor doses had no toxic effect on AGS cells, as confirmed by CellTiter-Glo luminescent cell viability assay (data not shown).

2.5. Gelatin zymography

The gelatin zymography technique was used to assay the gelatinolytic activity of MMP-9. In brief, 70 μg total protein of conditioned experimental media from AGS cells were electrophoresed, under non-reducing conditions. 8 % SDS-polyacrylamide (PAGE) gel containing 1 mg/ml gelatin was used for this purpose. The gels were washed in Triton-X-100 (2.5 %) and then incubated at 37 °C in assay buffer containing Tris-HCl (40 mM, pH 7.4), NaCl (0.2 M), and $CaCl_2$ (10 mM) for 18 h. The gel was stained with Coomassie blue (0.1 %) followed by destaining. MMP-9 activity was visualized as negatively stained bands and the ImageJ software was used to quantify them.

2.6. Scratch wound healing assay

AGS cells were seeded into six-well plates and the monolayer of cells was then scratched maintaining a sterile condition. The wells were washed with PBS and incubated with their respective treatments. After 0 h. and 24 h., the conditioned media were collected, the cells were rinsed with PBS, fixed with 4 % paraformaldehyde, and stained using 0.5 % crystal violet solution. Images were taken with an Olympus I × 71 inverted microscope using the Image-Pro Express software. The area of the wound was calculated from these images using the ImageJ software.

2.7. Invasion assay

The ability of cell invasion under normoglycemic or hyperglycemic conditions was measured using trans-well chambers having an 8 μm pore filter, after coating them with Matrigel. The coated chambers were placed into the wells of a 24-well plate and AGS cells suspended in serum-free medium containing the respective treatments were seeded into the upper trans-well chambers. To induce chemotaxis, the lower chambers were filled with Ham's F12K media containing 20 % FBS. After incubating for 24 h, the trans-well chambers were removed, washed with PBS, fixed with 4 % paraformaldehyde, and stained with 0.5 % crystal violet solution. Finally, the images were captured with an Olympus I × 71 inverted microscope using the Image-Pro Express

software and the number of invaded cells were counted.

2.8. Preparation of cell lysate and immunoblotting

After 24 h of incubation with the respective treatments, AGS cells were washed with PBS, trypsinized, and pelleted down. Cells were lysed using lysis buffer containing Tris-HCl (pH 7.4, 20 mM), NaCl (150 mM), Triton X-100 (1 %), 1× PIC, and PMSF (1 mM). The cell lysate was centrifuged at 12000 rpm for 10 min at 4 °C and supernatants were collected. Protein concentrations were estimated through Bradford assay. 50 μg of protein from each group were electrophoresed using 10 % SDS-PAGE followed by transferring onto PVDF membranes. The membranes were then blocked at room temperature for 2 h with 3 % BSA in TBST buffer containing NaCl (137 mM), KCl (2.7 mM), Tris-HCl (50 mM, pH 7.4), and Tween-20 (0.1 %). The blocked membranes were next incubated overnight with respective primary antibodies at 4 °C. After washing in TBST, membranes were incubated with HRP-conjugated secondary antibodies. The blot was then developed using a western ECL substrate solution (Bio-Rad Laboratories, USA) Images were taken using the Bio-Rad ChemiDoc™ MP imaging system. Quantification of protein expression was performed using the ImageJ software keeping GAPDH as the loading control.

2.9. Nuclear localization of c-Fos and c-Jun

Nuclear localization of c-Fos and c-Jun was performed by immunofluorescence technique using an anti-rabbit secondary antibody conjugated with Texas red. AGS cells were grown on sterile poly-L-lysine coated coverslips and incubated with respective treatments for 24 h. The slides were prepared using the methods previously reported by us [24]. Images were captured using a high-resolution Stimulated Emission Depletion (STED) microscope (Leica TCS SP8) in a single session while maintaining the same settings. Different protein localizations were identified from randomly selected fields. The images were representative of five individual experiments to exclude artifacts that may result from individual experiments.

Western blotting for c-Jun and c-Fos in the nuclear and cytosolic fractions further confirmed their nuclear localization. The fractions were prepared using a previously reported method [25]. Histone H3 and GAPDH were used as the loading controls for the nuclear and cytosolic fractions, respectively.

2.10. Construction of MMP-9 promoter deletion plasmids

To identify the signaling pathway(s) regulating hyperglycemia-induced MMP-9 expression, a series of progressive deletion mutants (−580 bp, −461 bp, and − 72 bp) from the 5′-end of the human MMP-9 promoter were generated and cloned into pGL2Basic plasmid (Promega). The NF-κB, distal AP-1, and proximal AP-1 binding sites were progressively deleted in the −580 bp, −461 bp, and − 72 bp constructs, respectively. PCR amplification of deleted endpoints was created to the locations relative to the transcription start site using the primers listed in Table 1. Each of the forward primers contained a *Kpn*I restriction site and the reverse primer contained an *Xho*I restriction site (shown in bold font in Table 1).

2.11. Transient transfection of AGS cells and luciferase activity assays

Transient transfection of siRNAs and luciferase reporter plasmids was performed with Lipofectamine™ RNAiMAX and Lipofectamine™ 2000 transfection reagents (Invitrogen, Waltham, MA, USA), respectively. The full-length MMP-9 promoter and its deletion plasmids were prepared using QIAGEN plasmid DNA preparation kits, as per the manufacturer's protocol. AGS cells were transfected with the luciferase reporter plasmids (1 μg) or siRNA (50 nM) or both after formulation with their respective transfection reagent. After 48 h of transfection, the cells were incubated in either normoglycemic or hyperglycemic media for further experimentations. The silencing efficacy of siRNAs was confirmed by immunoblotting analyses using an anti-p65 or MMP-9 antibody.

In the case of luciferase assay, the transfected AGS cells were lysed in passive lysis buffer (supplied along with the kit from Promega) after receiving their respective treatments. These lysates were assayed for firefly luciferase activity using the Luciferase Assay System (Promega, Madison, WI, USA), according to the manufacturer's protocol. The luminescence values were normalized as per microgram protein present in each sample. The values obtained after normalization have been represented as fold change over the normoglycemic control cells transfected with the full-length MMP-9 promoter. The reported values represent averages of triplicate samples from five independent experiments.

2.12. Chromatin immunoprecipitation (ChIP) assay

ChIP assay was executed with 100–120 mg protein-DNA complex obtained from crosslinked samples using the High-Sensitivity ChIP Kit (Abcam, Cambridge, UK), according to the manufacturer's protocol. Samples were immunoprecipitated with either c-Fos or c-Jun antibodies and their binding at the proximal or distal AP-1 binding site of the MMP-9 promoter was quantified after PCR amplification for 40 cycles. We used 1 % chromatin collected before immunoprecipitation from all samples as their respective input. DNA from these inputs was extracted and amplified by PCR to serve as the loading control. Anti-rabbit IgG antibody was used as the negative control in each independent immunoprecipitation experiment. Analysis of PCR products was performed using ethidium bromide-stained agarose gels (2 %). Images were taken using the Bio-Rad ChemiDoc™ MP imaging system and the band intensities were quantified by densitometry using the ImageJ software. The primers used in this experiment are listed in Table 1.

2.13. Estimation of protein concentration

Bradford reagent (Sigma, USA) was used to quantify the protein concentration of AGS cell samples, as per the manufacturer's protocol.

Table 1
List of primers targeting the human MMP-9 promoter region.

Target	Forward primer (5′–3′)	Reverse primer (5′–3′)	Reference
Promoter Deletion Constructs			
–580 bp	GC**GGTACC**TAGCAGAGCCCATTCCTTCC		
−461 bp	GC**GGTACC**TCAAAGAAGGCTGTCAGC	GC**CTCGAG**TGGTGAGGGCAGAGGTGTCT	[26]
−72 bp	GC**GGTACC**GCACTTGCCTGTCAAGGAGG		[26]
ChIP Assay			
Proximal AP-1	GAGTCAGCACTTGCCTGTCA	CTGCTGTTGTGGGGGCTTTA	[27]
Distal AP-1	CTTGCCTAGCAGAGCCCATT	TTTTTCCCTCCCTGACAGCC	[27]

2.14. Statistical analysis

Data is provided as the mean ± SEM of five separate experiments. GraphPad Prism (version 5.01, San Diego, California, USA) was used to perform all statistical analyses. Student's *t*-test was used to compare between groups. Statistically significant differences are indicated as $*p < 0.05$, #p < 0.05, $**p \leq 0.01$, ##p ≤ 0.01, $***p \leq 0.001$ and $###p \leq 0.001$. ns = not significant ($p \geq 0.05$).

3. Results

3.1. High glucose induces a dose- and time-dependent increase in MMP-9 activity and expression

We noticed a significant upregulation in MMP-9 levels following the incubation of AGS cells in a series of high glucose media (5.5, 8, 12.5, 25, 35, and 50 mM). Interestingly, this increase in MMP-9 expression exhibited a dose-dependent response, with higher concentrations of glucose (up to 25 mM) leading to a more pronounced elevation in MMP-9 levels (Fig. 1A–1E). Whereas, a further increase in glucose concentration led to a dose-dependent decrease in MMP-9 levels (Fig. 1A–1E).

Next, AGS cells were incubated in hyperglycemic media containing 25 mM D-glucose for different periods of time (0, 6, 12, 24, 36, and 48 h.). We observed that the upregulation of MMP-9 takes place progressively over time, reaching its peak at 24 h; afterward, no significant change was observed with increasing time of incubation, indicating a time-dependent effect of glucose concentration on MMP-9 levels (Fig. 1F–1J). These results demonstrate that high glucose induces upregulation of MMP-9 activity and expression in AGS cells in a dose- and time-dependent manner. Therefore, in all the subsequent experiments, the hyperglycemic condition was induced by incubating AGS cells with 25 mM glucose for 24 h.

In similar experiments conducted with D-mannitol (osmolarity control for D-glucose; not metabolized), the MMP-9 promoter activity did not undergo any significant change in comparison to normoglycemic control cells (Fig. S1). This shows that the observed increase in MMP-9 levels under hyperglycemic conditions was not in response to the changed media osmolarity, but most likely due to the metabolic action of glucose.

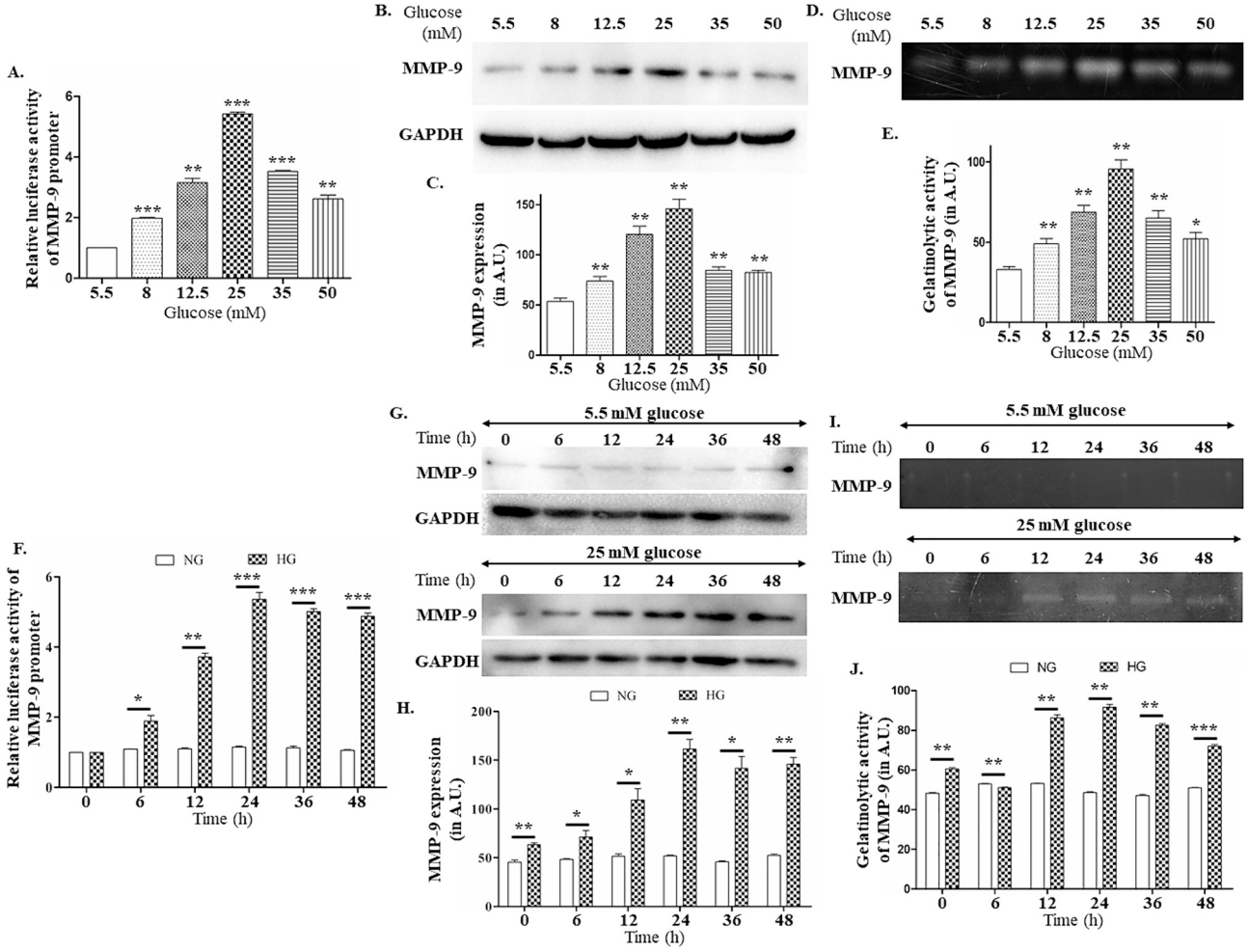

Fig. 1. High glucose induces MMP-9 expression and activity in AGS cells. (A–E) Effect of increasing glucose concentrations on the promoter activity (A), protein expression (B, C), and gelatinolytic activity (D, E) of MMP-9. AGS cells transfected with full-length MMP-9 luciferase reporter plasmids and un-transfected AGS cells were treated with increasing concentrations of D-glucose (5.5, 8, 12.5, 25, 35, and 50 mM) for 24 h. Afterward, luciferase reporter assay, western blotting, and gelatin zymography assays were performed to measure the promoter activity, protein expression, and gelatinolytic activity of MMP-9, respectively. (F–J) Time-dependent effect of 5.5 mM and 25 mM glucose on the promoter activity (F), protein expression (G, H), and gelatinolytic activity (I, J) of MMP-9. AGS cells transfected with full-length MMP-9 luciferase reporter plasmids and un-transfected AGS cells were incubated with normoglycemic (5.5 mM) and hyperglycemic media (25 mM) for 0, 6, 12, 24, 36, and 48 h. Afterward, luciferase reporter assay, western blotting, and gelatin zymography assays were performed to measure the promoter activity, protein expression, and gelatinolytic activity of MMP-9, respectively. Values are mean ± SEM. Student's *t*-test was used to compare between groups ($***p < 0.001$, $**p < 0.01$, and $*p < 0.05$).

3.2. Hyperglycemia-induced MMP-9 is responsible for AGS cell migration and invasion

The functional response of AGS cells to the increased activity and expression of MMP-9 was examined using the scratch wound healing assay and trans-well invasion assay. To eliminate any interference with cell proliferation, AGS cells were treated with 10 μM hydroxyurea (proliferation inhibitor). We observed that the rate of AGS cell migration and invasion was significantly higher under hyperglycemic conditions compared to normoglycemic control (Fig. 2A–2D). We also observed that when MMP-9 was silenced by transfecting AGS cells with MMP-9 siRNA (Fig. 2E–2H), the high glucose-induced cell migration and invasion were significantly reduced (Fig. 2I–2L). Analyzing the whole cell protein lysate and conditioned media confirmed that MMP-9 protein expression and activity were attenuated upon siRNA transfection (Fig. 2E–2H).

These experiments showed that MMP-9 is crucial for the induction of AGS cell migration and invasion, under high glucose conditions. Therefore, proper elucidation of the underlying signaling pathway(s) responsible for hyperglycemia-induced MMP-9 expression is of great interest.

3.3. p65 NF-κB signaling pathway is not significantly responsible for hyperglycemia-induced MMP-9 expression

We observed an increased expression of p65 (~1.91fold; $p < 0.01$) and phosphorylated p65 (~3.83 fold; $p < 0.01$) under hyperglycemic conditions (Fig. 3A, 3B & 3C). These upregulations in the total and phosphorylated p65 protein levels correlated with the hyperglycemia-induced upregulation in MMP-9 levels (Fig. 3A & 3D).

To evaluate whether the upregulated p65 has any role in the regulation of MMP-9 expression, we transfected AGS cells with a p65-specific siRNA and a non-specific siRNA. The transfected cells were further incubated in normoglycemic and hyperglycemic conditions for 24 h. MMP-9 levels were then estimated by Luciferase assay and western blotting. Surprisingly, we observed that p65 silencing had no significant effect ($p > 0.05$) on the protein levels (Fig. 3E–3G) and promoter activity (Fig. 3H) of MMP-9. It has also been observed through the Luciferase reporter assay, that even after deleting the NF-κB binding site from the MMP-9 promoter region, the expression of MMP-9 remained unhindered (Fig. 3I & 3J). From these results, we can say that the p65 NF-κB signaling pathway is not significantly responsible for hyperglycemia-induced MMP-9 expression.

3.4. Hyperglycemia-induced MMP-9 expression is regulated by the MAPK pathway

We analyzed the protein expression and phosphorylation level of some key signaling elements in the MAPK pathway. Western blot analyses showed that there was a significant upregulation of p-ERK 1 (~2.13 fold; $p < 0.05$), p-ERK 2 (~2.03 fold; $p < 0.01$), c-Fos (~1.94 fold; $p < 0.01$) p-JNK 1 (~2.53 fold; $p < 0.05$), p-JNK 2 (~2 fold; $p < 0.05$), c-Jun (~1.38 fold; $p < 0.01$) and p-p38 (~1.74 fold; $p < 0.05$), under hyperglycemic conditions (Fig. 4). To determine whether these upregulated proteins played any role in regulating MMP-9 expression, we pre-treated AGS cells with SP 600125 (JNK inhibitor, 50 μM), PD 98059 (ERK 1/2 inhibitor, 50 μM) and SB 203580 (p38 MAPK inhibitor, 20 μM); 1 h before inducing hyperglycemia (Fig. 5A–5E). AGS cells treated with either of these inhibitors could not produce MMP-9 under hyperglycemic conditions (Fig. 5A, 5F & 5G). This confirmed that the hyperglycemia-induced upregulation of MMP-9 is dependent on the MAPK pathway.

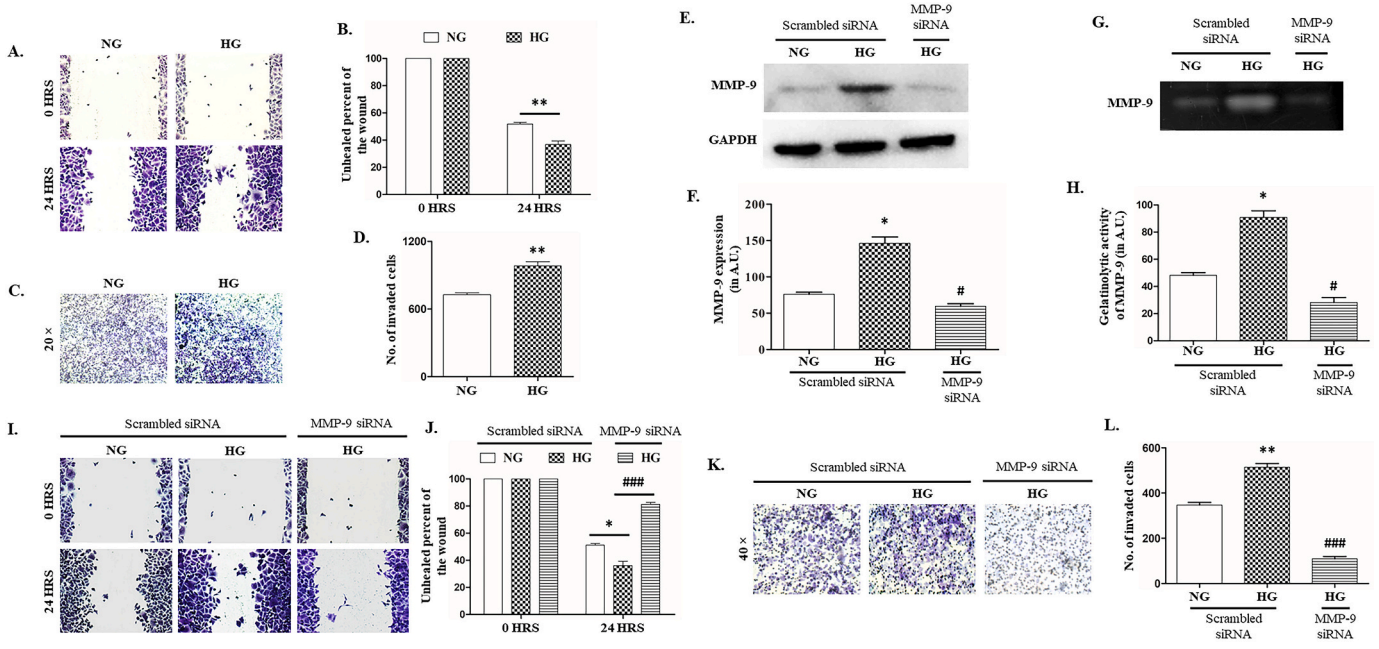

Fig. 2. Hyperglycemia-induced AGS cell migration and invasion is dependent on MMP-9. (A–B) Wound-healing assay with AGS cells under normoglycemic and hyperglycemic conditions after 0 h and 24 h of incubation. (C–D) Representative images showing the number of AGS cells that passed through the Matrigel-coated trans-well chamber under normoglycemic and hyperglycemic conditions after 24 h of incubation. (E–F) Western blot analysis showing MMP-9 expression after AGS cells were transfected with scrambled or MMP-9 specific siRNA, under normoglycemic and hyperglycemic conditions. GAPDH served as a loading control. (G–H) Gelatin zymography analysis showing MMP-9 activity after AGS cells were transfected with scrambled or MMP-9 specific siRNA, under normoglycemic and hyperglycemic conditions. (I–J) Wound-healing in AGS cells transfected with scrambled or MMP-9 specific siRNA, under normoglycemic and hyperglycemic conditions after 0 h and 24 h of incubation. (K–L) Images showing the number of transfected AGS cells (scrambled or MMP-9 specific siRNA) that passed through the Matrigel-coated trans-well chamber under normoglycemic and hyperglycemic conditions after 24 h of incubation. All images used in this figure are representative of five independent experiments. Values are mean ± SEM. Student's *t*-test was used to compare between groups. *$p < 0.05$, **$p < 0.01$ (vs. 'NG') and #$p < 0.05$, ###$p < 0.001$ (vs. 'HG').

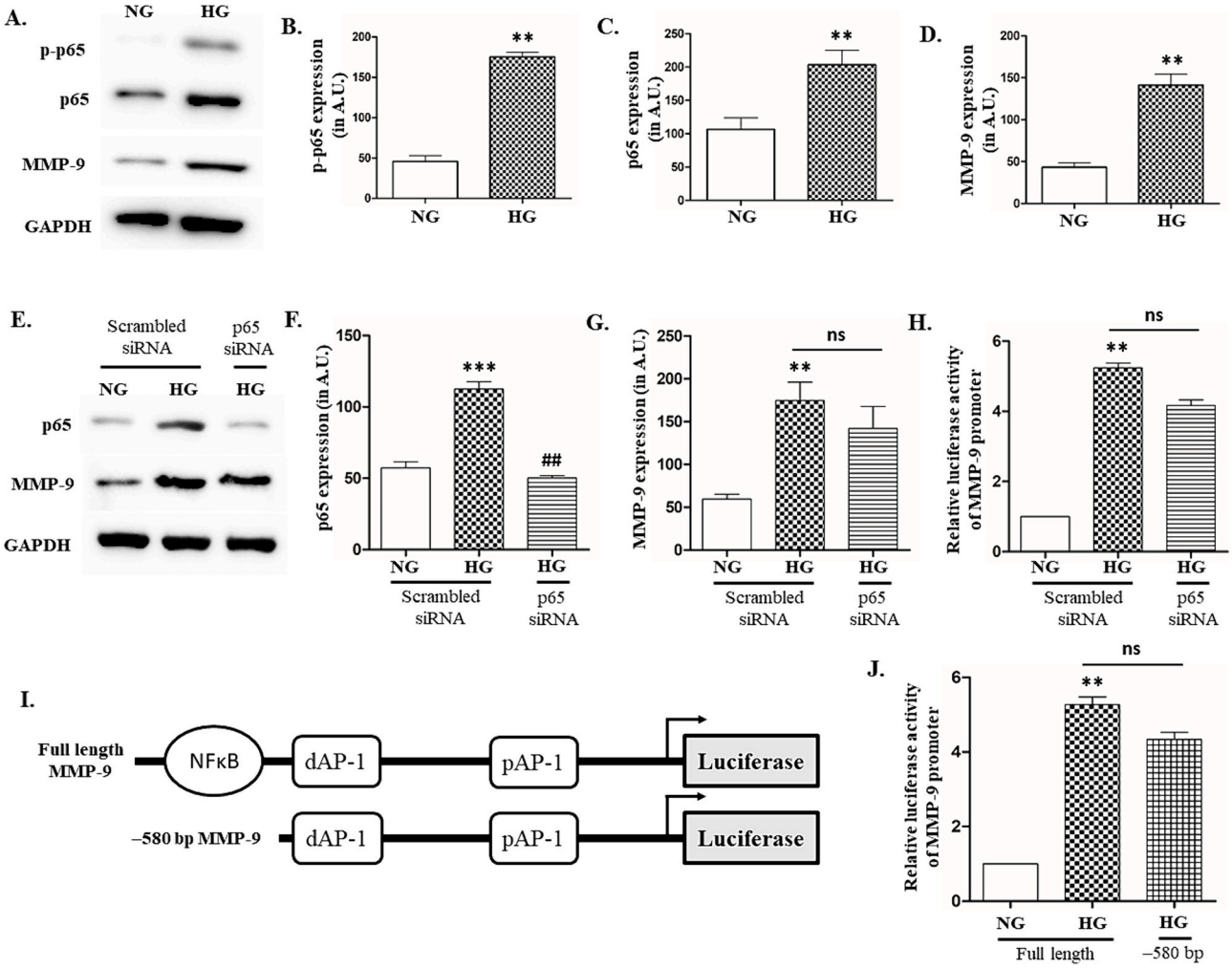

Fig. 3. Hyperglycemia-induced MMP-9 expression is not dependent on the p65 NF-κB signaling pathway. (A) Western blot analysis of the expression patterns of p-p65, p65, and MMP-9 in AGS cells under normoglycemic and hyperglycemic conditions. GAPDH served as a loading control. (B–D) Densitometric analysis of the expression pattern of p-p65, p65, and MMP-9, respectively. (E) Western blot analysis showing p65 and MMP-9 expression after AGS cells were transfected with scrambled or p65-specific siRNA, under normoglycemic and hyperglycemic conditions. GAPDH served as a loading control. (F–G) Densitometric analysis of the expression pattern of p65 and MMP-9, respectively. (H) Relative luciferase activity of MMP-9 promoter after AGS cells were transfected with scrambled or p65 specific siRNA, under normoglycemic and hyperglycemic conditions. (I) Schematic diagram of the full-length and − 580 bp deletion construct of the human MMP-9 promoter. (J) Relative luciferase activity of MMP-9 promoter after AGS cells were transfected with full-length and − 580 bp deletion construct of the human MMP-9 promoter, under normoglycemic and hyperglycemic conditions. Values are mean ± SEM. Student's *t*-test was used to compare between groups. ***$p < 0.001$, **$p < 0.01$ (vs. 'NG'); ##$p < 0.01$, (vs. 'HG'); and "ns" represents non-significant.

Next, we isolated the nuclear proteins of AGS cells grown in normoglycemic and hyperglycemic conditions, and western blot analysis was performed. We observed a significant increase (~1.45 fold; $p < 0.05$) in the nuclear localization of c-Fos under hyperglycemic conditions (Fig. 6A & 6B). Whereas, the cytoplasmic reserves of c-Fos also underwent a drastic upregulation (~1.65 fold; $p < 0.001$) (Fig. 6A & 6B). However, in the case of c-Jun, we observed a ~ 1.96 fold upregulation ($p < 0.05$) in the nuclear fraction; whereas a ~ 1.58 fold upregulation ($p < 0.05$) was observed in its cytoplasmic counterpart (Fig. 6A & 6C). The immunofluorescence images show a similar trend in the localization of c-Fos and c-Jun (Fig. 6D & 6E). These findings suggest that c-Fos and c-Jun activated by the ERK and JNK pathways undergo nuclear translocation and heterodimerize to form the AP-1 transcription factor which in turn is responsible for activating MMP-9 transcription.

3.5. Both the AP-1 binding sites on the MMP-9 promoter are required for MMP-9 expression under hyperglycemic conditions

The MMP-9 promoter has two AP-1 binding sites; the distal site (−514 to −507) and the proximal site (−80 to −71). The binding efficacy of the AP-1 heterodimer often varies between these two sites. The results of the Luciferase Reporter Assay with MMP-9 promoter deletion constructs revealed that the MMP-9 promoter activity was drastically lowered (~2.92 fold; $p < 0.05$) in the −461 bp deletion construct (containing only the proximal AP-1 binding site), compared to the full-length promoter (Fig. 7A & 7B). Whereas, the −72 bp deletion construct had completely lost all MMP-9 promoter activity (Fig. 7A & 7B). This loss of promoter activity in the −72 bp deletion construct was expected since this construct does not retain either the distal AP-1 or proximal AP-1 binding sites which are known to be essential for MMP-9 transcription. From the results of this experiment, it seems that both the distal and proximal AP-1 binding sites are important for regulating MMP-9 expression under hyperglycemic conditions.

ChIP assay was performed to further confirm which of the two AP-1 binding sites is responsible for regulating hyperglycemia-induced MMP-9 expression. We quantified this by the fold change in c-Fos and c-Jun proteins bound to the two AP-1 binding sites, with respect to normoglycemic condition. We observed that, in the proximal AP-1 binding site

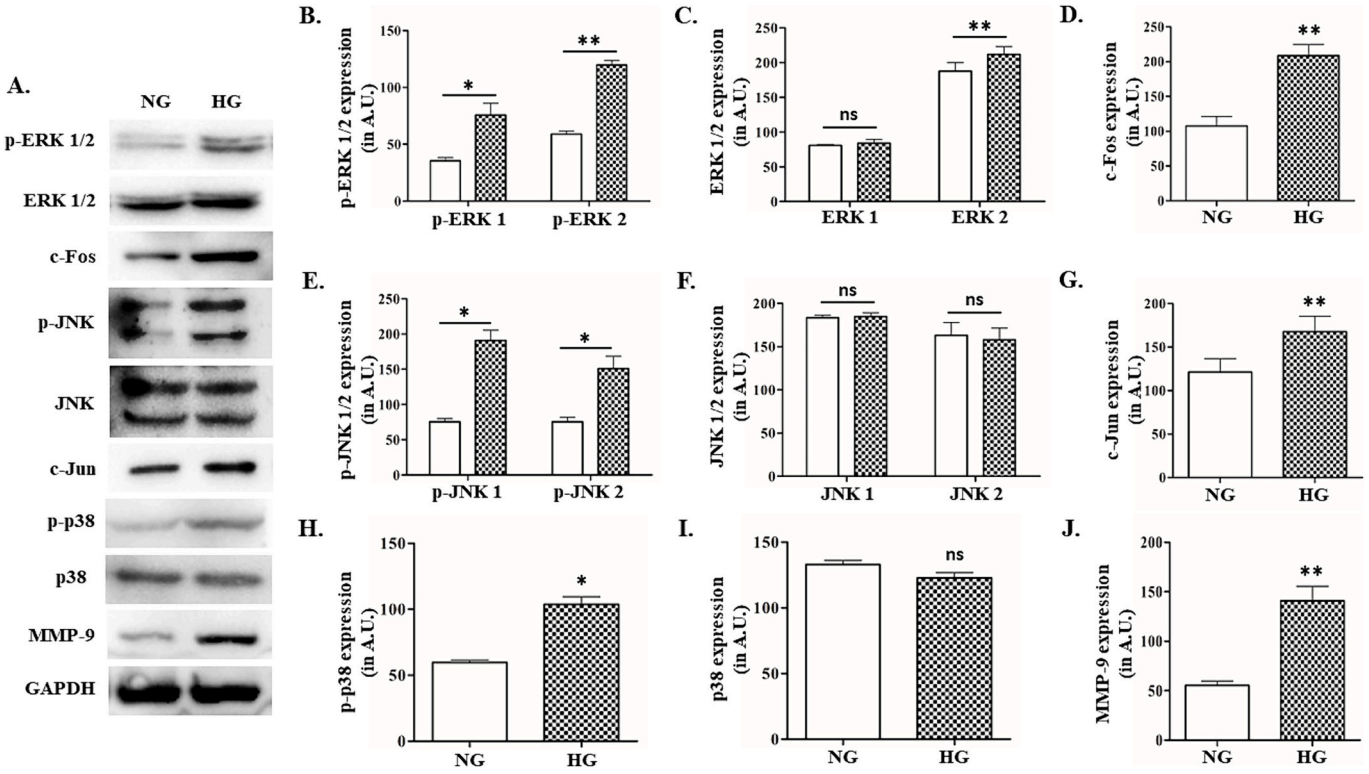

Fig. 4. Effect of hyperglycemia on different components of the MAPK pathway. (A) Western blot analysis of the expression patterns of p-ERK 1/2, ERK 1/2, c-Fos, p-JNK, JNK, c-Jun, p-p38, p38, and MMP-9 in AGS cells under normoglycemic and hyperglycemic conditions. GAPDH served as a loading control. (B–J) Densitometric analysis of the expression pattern of p-ERK 1/2, ERK 1/2, c-Fos, p-JNK, JNK, c-Jun, p-p38, p38, and MMP-9, respectively. Values are mean ± SEM. Student's *t*-test was used to compare between groups (**$p < 0.01$, *$p < 0.05$, and "ns" represents non-significant).

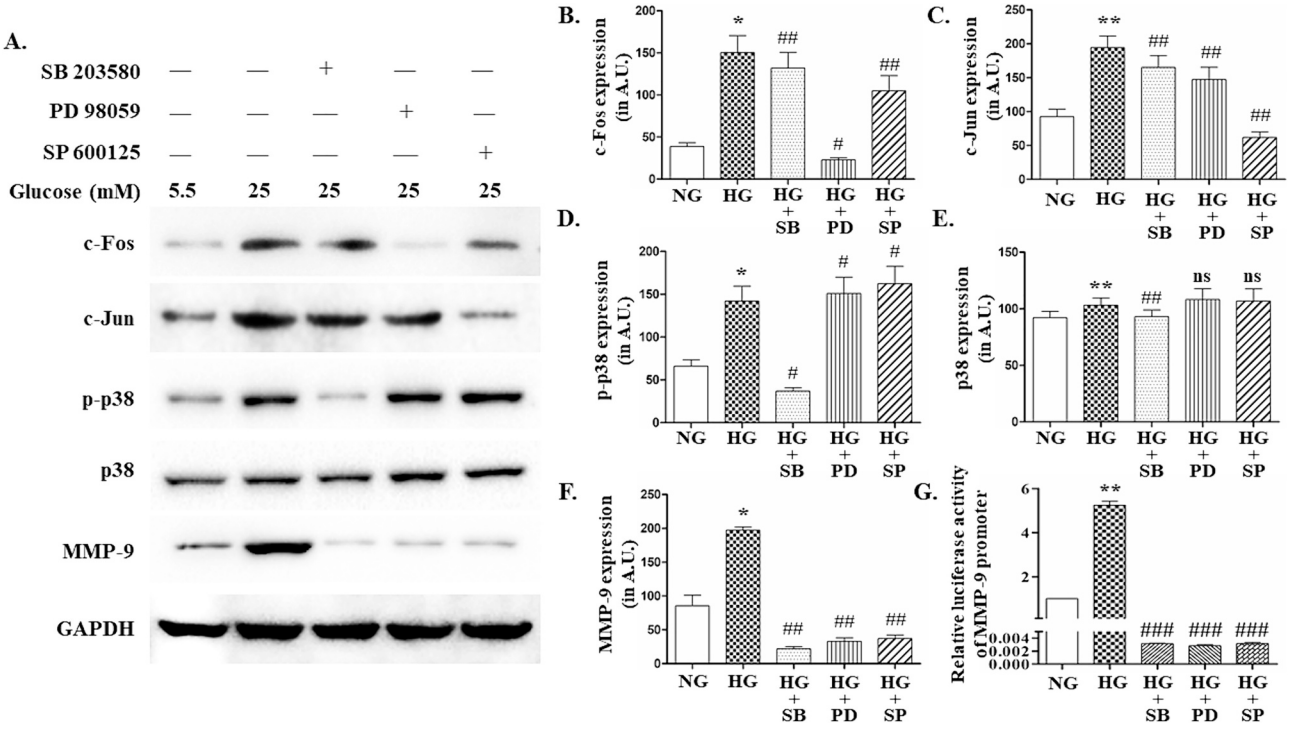

Fig. 5. Hyperglycemia-induced MMP-9 expression is dependent on the MAPK signaling pathway. (A) Western blot analysis of the expression patterns of c-Fos, c-Jun, p-p38, p38, and MMP-9 in AGS cells after pre-treatment with or without SB203580, PD98059, and SP600125, under normoglycemic and hyperglycemic conditions. GAPDH served as a loading control. (B–F) Densitometric analysis of the expression patterns of c-Fos, c-Jun, p-p38, p38, and MMP-9, respectively. (G) Relative luciferase activity of MMP-9 promoter after AGS cells were pre-treated with or without SB203580, PD98059, and SP600125, under normoglycemic and hyperglycemic conditions. Values are mean ± SEM. Student's *t*-test was used to compare between groups. **p < 0.01, *$p < 0.05$ (vs. 'NG'); ###$p < 0.001$, ##p < 0.01, #p < 0.05 (vs. 'HG') and "ns" represents non-significant.

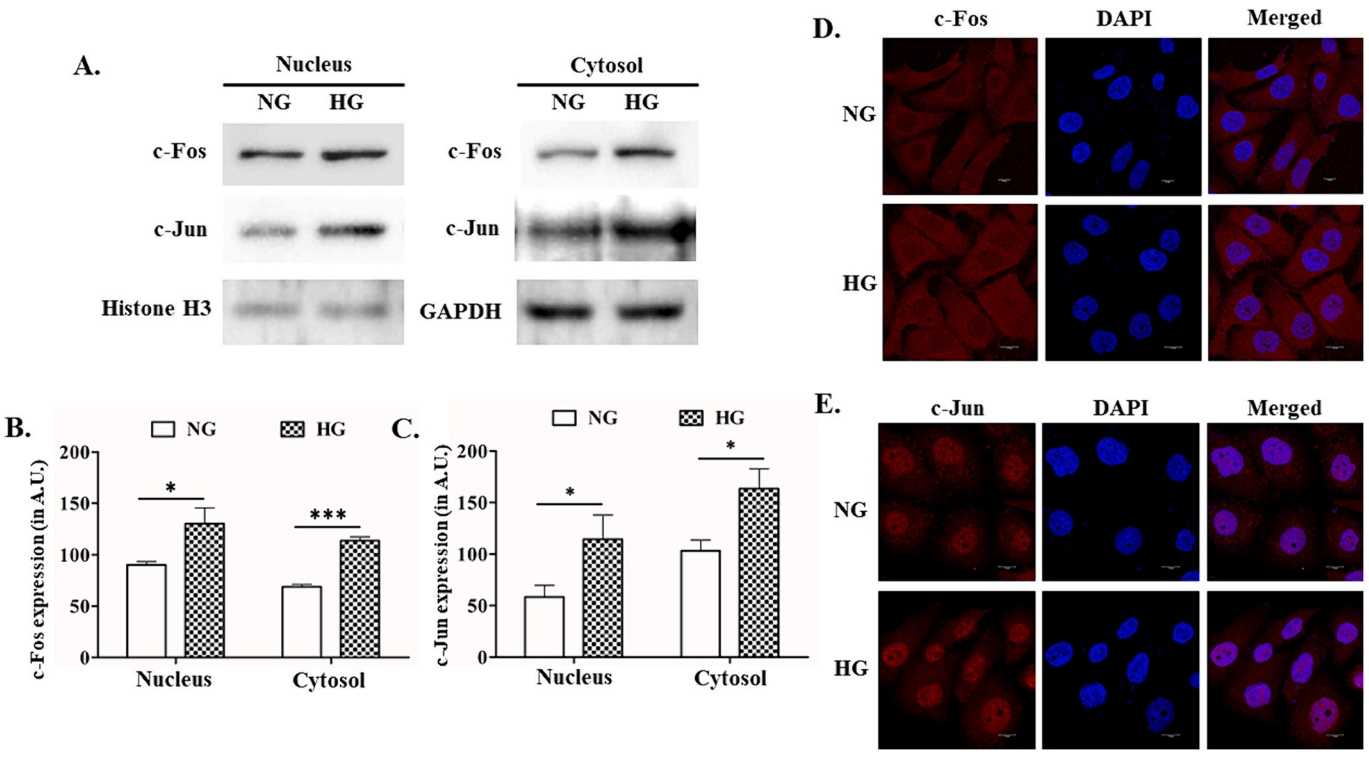

Fig. 6. Nuclear translocation of c-Fos and c-Jun under hyperglycemic conditions. (A) Western blot analysis of the expression patterns of c-Fos and c-Jun in the nuclear and cytosolic fractions of AGS cells under normoglycemic and hyperglycemic conditions. Histone H3 and GAPDH served as loading controls for the nuclear and cytosolic fractions, respectively. (B–C) Densitometric analysis of the expression patterns of c-Fos and c-Jun, respectively in the nuclear and cytosolic fractions. (D) Representative images of c-Fos immunostaining in AGS cells under normoglycemic and hyperglycemic conditions. The red fluorescence (Texas Red) represents the c-Fos protein and the blue fluorescence (DAPI) represents the nucleus. (E) Representative images of c-Jun immunostaining in AGS cells under normoglycemic and hyperglycemic conditions. The red fluorescence (Texas Red) represents the c-Jun protein and the blue fluorescence (DAPI) represents the nucleus. All images used in this figure are representative of five independent experiments. Values are mean ± SEM. Student's t-test was used to compare between groups (***$p < 0.001$ and *$p < 0.05$). (For interpretation of the references to colour in this figure legend, the reader is referred to the web version of this article.)

of the MMP-9 promoter, hyperglycemia increased the binding of c-Jun and c-Fos by ~2.47 fold ($p < 0.01$) and ~ 4.23 fold ($p < 0.01$), respectively (Fig. 7C, E, F & 7H). In the distal AP-1 binding site, binding of c-Jun and c-Fos was increased consistently by ~17.12 fold ($p < 0.001$) and ~ 7.44 fold ($p < 0.01$), respectively (Fig. 7C, D, F & 7G). Moreover, samples immunoprecipitated with IgG control antibodies did not yield any noticeable PCR product. The results of this ChIP assay confirm that both the proximal and distal AP-1 binding sites are concomitantly activated under hyperglycemic conditions. We can now conclude that both of these AP-1 binding sites are responsible for hyperglycemia-induced MMP-9 expression.

4. Discussion

Diabetes and cancer have remained an international concern for human healthcare for a long time, mainly due to the increasing incidence and mortality associated with these diseases. As of 2021, just over half a billion people (536.6 million people) are living with diabetes worldwide [28]. It is predicted that 9.9 % of the world's human population will become diabetic by the year 2045 [8]. The GLOBOCAN 2020 statistics have estimated the rate of cancer incidence (excluding melanoma) to be ~20 million new cases per year [1]. About 60 % of newly diagnosed cancer patients are above the age of 65 years [29] and ~ 25 % of people above 65 years also have diabetes [30]. Therefore, approximately 3 million new cases of cancer-diabetes co-morbid patients are diagnosed every year.

Hyperglycemic condition, developed during diabetes, provides a conducive environment for cancer progression and can significantly enhance the metastatic capabilities of cancer cells [31]. Such effects have been documented previously in lung cancer [17], breast cancer [18], cholangiocarcinoma [19], and gastric cancer [20,21]. The process of metastasis is greatly influenced by the involvement of matrix metalloproteinases (MMPs) [32]. Among various MMPs, MMP-9 is of particular interest as hyperglycemia is reported to induce invasion and metastasis by enhancing the levels of MMP-9 in lung cancer cells [17] and breast cancer cells [18].

Similarly, we have also observed that the expression of MMP-9 in AGS cells increases with increasing concentration of glucose (up to 25 mM). This bell-shaped response curve of MMP-9 expression to glucose concentration may most likely be attributed to the fact that glucose concentrations beyond 25 mM have a cytotoxic effect on AGS cells [20,21]. We have also observed that upon incubating AGS cells in hyperglycemic media (containing 25 mM D-glucose) for different lengths of time, MMP-9 expression increases until 24 h, then undergoes a slight decrease at 36 h, and finally drops significantly at 48 h, compared to the level of expression at 24 h. This drop in MMP-9 expression may be attributed to a similar decrease in the media glucose concentration, after 48 h of incubation (Fig. S2).

Corroborating with the previous studies [17–21,31], we also observed that the migration and invasive nature of AGS cells were heightened under hyperglycemic conditions. Interestingly, this hyperglycemia-induced aggressive nature of AGS cells was attenuated after silencing MMP-9. Therefore, the enhanced invasive capability of AGS cells under hyperglycemic conditions can be directly associated with the increase in MMP-9 expression. Identifying the factor(s) responsible for the hyperglycemia-induced upregulation of MMP-9 could be crucial for the development of targeted therapies against GC-hyperglycemia co-morbidity.

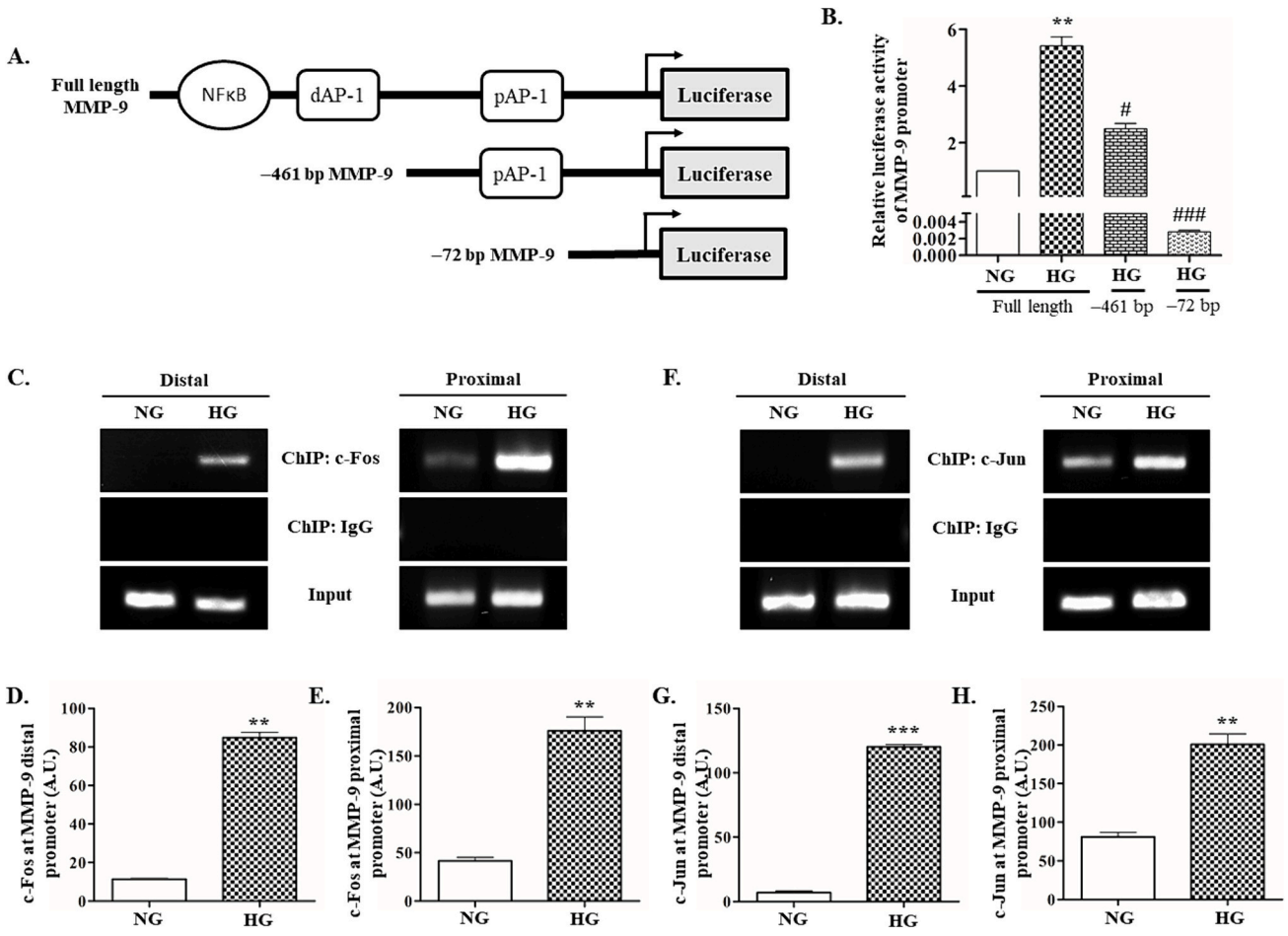

Fig. 7. Both the proximal and distal AP-1 binding sites are concomitantly activated under hyperglycemic conditions. (A) Schematic diagram of the full-length, −461 bp and − 72 bp deletion constructs of the human MMP-9 promoter. (B) Relative luciferase activity of MMP-9 promoter after AGS cells were transfected with full-length, −461 bp and − 72 bp deletion constructs of the human MMP-9 promoter, under normoglycemic and hyperglycemic conditions. Binding of c-Fos (C–E) and c-Jun (F—H) at the proximal and distal sites of the MMP-9 promoter as quantified by ChIP assay. IgG isotype precipitated DNA was used as the negative control. Values are mean ± SEM. Student's *t*-test was used to compare between groups. ***p < 0.001, **p < 0.01 (vs. NG); ###p < 0.001, #*p* < 0.05 (vs. 'HG').

It is well known that the MMP-9 promoter has multiple functional cis-regulatory regions with NF-κB, SP-1, and AP-1 binding sites [33,34]. These transcription factors are responsible for both basal and inducible transcriptional responses [35]. Previous studies have suggested crucial roles for NF-κB and AP-1 transcription factors in controlling MMP-9 expression [36]. Since both these transcription factors have binding sites in the MMP-9 promoter, they should be activated during MMP-9 over-expression. However, it is unclear, if they are likewise active in GC under hyperglycemic conditions and similarly responsible for the MMP-9 over-expression.

Our results showed that although the p65 NF-κB pathway was activated under hyperglycemic conditions; it did not play a significant role in regulating hyperglycemia-induced MMP-9 expression. However, in previous studies, NF-κB was shown to play a pivotal role in regulating the expression of MMP-9 [37–39]. Such a stark contradiction in our observation may be because these studies explore the more canonical form of MMP-9 transcriptional regulation which is mostly associated with inflammatory markers (like TNF-α, interleukins) or inflammation-inducing agents (like LPS). Even though hyperglycemia leads to the activation of inflammatory signals; these signaling moieties seem to have lost their capability to induce MMP-9 transcription under hyperglycemic conditions. This scenario is especially true during the initial hours of hyperglycemia induction (up to 24 h).

Further, MMP-9 can also be induced by other pathways independent of the NF-κB signaling in gastric cancer [40]. The MAPK pathway is well involved in the regulation of MMP-9 expression. Among the three families of MAP kinases, p38 MAPK is an activator of MMP-9 transcription. The upregulation of p38 MAPK was reported to increase MMP-9 expression, enhancing cancer cell invasion in hepatic cancer and cervical cancer cell lines [41]. Whereas, the downregulation of p38 MAPK leads to suppressed expression and activity of MMP-9 [42]. Further, p38γ MAPK has been reported to cooperate with c-Jun in transactivating MMP-9 [43]. Huang et al. correlated the upregulation of phospho-p38 with the expression of MMP-9 in human gastric adenocarcinoma tissues [44]. Correspondingly, we observed that MMP-9 expression was severely down-regulated after incubating hyperglycemic AGS cells with SB203580, a potent p38 MAPK inhibitor.

Further, the ERK and JNK pathways culminate in the formation of the AP-1 transcription factor, usually through heterodimerization of c-Fos and c-Jun proteins. Although heterodimerization of c-Fos and c-Jun is favored, in some rare cases, c-Jun can dimerize with itself and get recruited as a homodimer onto the AP-1 binding site [45,46]. The binding of AP-1 at the target gene's promoter region occurs in a sequence-specific manner [47], and based on the conditions and composition of the bound subunits, they regulate MMP-9 transcription.

In this study, we observed that the association of both c-Fos and c-Jun to the AP-1 binding site is crucial for hyperglycemia-induced MMP-9 transcription, as inhibiting either of the two pathways (ERK or JNK) severely down-regulated MMP-9 expression. We also observed that both c-Fos and c-Jun undergo nuclear translocation under hyperglycemic

conditions; implying the formation of the AP-1 heterodimer. ChIP assay revealed that both c-Fos and c-Jun remained bound only to the proximal AP-1 binding site on the MMP-9 promoter, under normoglycemic conditions. This suggests that the proximal AP-1 binding site is most likely involved in maintaining a basal transcription level of MMP-9. However, under hyperglycemic conditions, the distal promoter showed a greater response for AP-1 binding compared to the proximal one. This difference in response between the two AP-1 binding sites could be attributed to the fact that, unlike the proximal site, the distal AP-1 binding site was mostly inactive under normoglycemic conditions. Therefore, we suggest that the distal AP-1 binding site is responsible for the inducible MMP-9 transcription only; whereas the proximal AP-1 binding site accounts for both inducible and basal transcription of MMP-9.

A similar role of AP-1 in the transcriptional regulation of MMP-9 was previously associated with diabetic retinopathy [27]. Our results corroborate their findings and further highlight the role of the distal AP-1 binding site in regulating the hyperglycemia-induced transcription of MMP-9. The distal AP-1 binding site can be included in future drug development strategies as inhibiting its function can greatly reduce the inducible expression of MMP-9, without affecting its basal levels. Such an approach could help to elevate the quality of life of gastric cancer-diabetes co-morbid patients.

5. Conclusion

In summary, by using an in vitro model of gastric cancer-hyperglycemia co-morbidity, we have discovered a novel mechanism responsible for hyperglycemia-induced transcriptional upregulation of MMP-9. We have shown for the first time that the hyperglycemia-induced transcriptional activation of MMP-9 is not regulated by the p65 NF-κB pathway. Instead, it is predominantly governed by the MAPK pathway. Formation of the AP-1 heterodimer is crucial for the transcriptional activation of MMP-9 under hyperglycemic conditions. Furthermore, AP-1 binding at both the proximal and distal binding sites on the MMP-9 promoter region is required for hyperglycemia-induced MMP-9 expression. The proximal AP-1 binding site remains active under both normoglycemic and hyperglycemic conditions; whereas the distal AP-1 binding site is activated only after inducing hyperglycemia. Therefore, we can potentially reduce the complications developed during gastric cancer-hyperglycemia co-morbidity by inhibiting the binding of the AP-1 heterodimer with its distal binding site on the MMP-9 promoter region. Future studies with a drug specifically designed to inhibit this interaction may prove to be greatly helpful for controlling metastasis in gastric cancer-hyperglycemia co-morbidity.

Funding

This study was supported by institutional grant no. P-07 from CSIR-Indian Institute of Chemical Biology, Kolkata, India.

CRediT authorship contribution statement

Abhishek Chatterjee: Writing – original draft, Methodology, Investigation, Formal analysis, Data curation, Conceptualization. **Tapasi Roy:** Writing – original draft, Validation, Investigation, Formal analysis. **Snehasikta Swarnakar:** Writing – review & editing, Visualization, Validation, Supervision, Funding acquisition, Conceptualization.

Declaration of competing interest

The authors declare that they have no known competing financial interests or personal relationships that could have appeared to influence the work reported in this paper.

Data availability

Data will be made available on request.

Acknowledgments

A.C. is thankful to the University Grants Commission (UGC), India for providing financial support. T.R. acknowledges the receipt of the National Post Doctoral Fellowship from SERB. We acknowledge Director, CSIR-IICB for her kind support.

Appendix A. Supplementary data

Supplementary data to this article can be found online at https://doi.org/10.1016/j.cellsig.2024.111435.

References

[1] H. Sung, J. Ferlay, R.L. Siegel, et al., Global cancer statistics 2020: GLOBOCAN estimates of incidence and mortality worldwide for 36 cancers in 185 countries, CA Cancer J. Clin. 71 (3) (2021) 209–249, https://doi.org/10.3322/caac.21660.
[2] Y. Hui, C. Tu, D. Liu, et al., Risk factors for gastric cancer: a comprehensive analysis of observational studies, Front. Public Health 10 (2023) 892468, https://doi.org/10.3389/fpubh.2022.892468.
[3] M. Ashrafizadeh, M. Najafi, H.L. Ang, et al., PTEN, a barrier for proliferation and metastasis of gastric cancer cells: from molecular pathways to targeting and regulation, Biomedicines 8 (8) (2020) 264, https://doi.org/10.3390/biomedicines8080264.
[4] M. Ashrafizadeh, A. Zarrabi, S. Orouei, et al., STAT3 pathway in gastric cancer: signaling, therapeutic targeting and future prospects, Biology 9 (6) (2020) 126, https://doi.org/10.3390/biology9060126.
[5] A.J. Abadi, A. Zarrabi, F. Hashemi, et al., The role of SOX family transcription factors in gastric cancer, Int. J. Biol. Macromol. 180 (2021) 608–624, https://doi.org/10.1016/j.ijbiomac.2021.02.202.
[6] S. Sen, Y. He, D. Koya, et al., Cancer biology in diabetes, J. Diabetes Investig. 5 (3) (2014) 251–264, https://doi.org/10.1111/jdi.12208.
[7] F. Li, H. Du, S. Li, J. Liu, The association between metabolic syndrome and gastric cancer in Chinese, Front. Oncol. 8 (2018) 326, https://doi.org/10.3389/fonc.2018.00326.
[8] E. Standl, K. Khunti, T.B. Hansen, et al., The global epidemics of diabetes in the 21st century: current situation and perspectives, Eur. J. Prev. Cardiol. 26 (2_suppl) (2019) 7–14, https://doi.org/10.1177/2047487319881021.
[9] S.S. Coughlin, E.E. Calle, L.R. Teras, et al., Diabetes mellitus as a predictor of cancer mortality in a large cohort of US adults, Am. J. Epidemiol. 159 (12) (2004) 1160–1167, https://doi.org/10.1093/aje/kwh161.
[10] E. Friberg, N. Orsini, C.S. Mantzoros, et al., Diabetes mellitus and risk of endometrial cancer: a meta-analysis, Diabetologia 50 (7) (2007) 1365–1374, https://doi.org/10.1007/s00125-007-0681-5.
[11] S.C. Larsson, C.S. Mantzoros, A. Wolk, Diabetes mellitus and risk of breast cancer: a meta-analysis, Int. J. Cancer 121 (4) (2007) 856–862, https://doi.org/10.1002/ijc.22717.
[12] E. Giovannucci, D.M. Harlan, M.C. Archer, et al., Diabetes and cancer: a consensus report, Diabetes Care 33 (7) (2010) 1674–1685, https://doi.org/10.2337/dc10-0666.
[13] B. Carstensen, S.H. Read, S. Friis, et al., Cancer incidence in persons with type 1 diabetes: a five-country study of 9,000 cancers in type 1 diabetic individuals, Diabetologia 59 (5) (2016) 980–988, https://doi.org/10.1007/s00125-016-3884-9.
[14] J.M. Yoon, K.Y. Son, C.S. Eom, et al., Pre-existing diabetes mellitus increases the risk of gastric cancer: a meta-analysis, World J. Gastroenterol. 19 (6) (2013) 936–945, https://doi.org/10.3748/wjg.v19.i6.936.
[15] A. Sekikawa, H. Fukui, T. Maruo, et al., Diabetes mellitus increases the risk of early gastric cancer development, Eur. J. Cancer 50 (12) (2014) 2065–2071, https://doi.org/10.1016/j.ejca.2014.05.020.
[16] F. Alisson-Silva, L. Freire-de-Lima, J.L. Donadio, et al., Increase of O-glycosylated oncofetal fibronectin in high glucose-induced epithelial-mesenchymal transition of cultured human epithelial cells, PloS One 8 (4) (2013) e60471, https://doi.org/10.1371/journal.pone.0060471.
[17] X. Kang, F. Kong, X. Wu, et al., High glucose promotes tumor invasion and increases metastasis-associated protein expression in human lung epithelial cells by upregulating heme oxygenase-1 via reactive oxygen species or the TGF-β1/PI3K/Akt signaling pathway, Cell. Physiol. Biochem. 35 (3) (2015) 1008–1022, https://doi.org/10.1159/000373928.
[18] X.F. Sun, Y.B. Shao, M.G. Liu, et al., High-concentration glucose enhances invasion in invasive ductal breast carcinoma by promoting Glut1/MMP2/MMP9 axis expression, Oncol. Lett. 13 (5) (2017) 2989–2995, https://doi.org/10.3892/ol.2017.5843.
[19] C. Saengboonmee, W. Seubwai, C. Pairojkul, et al., High glucose enhances progression of cholangiocarcinoma cells via STAT3 activation, Sci. Rep. 6 (2016) 18995, https://doi.org/10.1038/srep18995.

[20] A. Chatterjee, T. Roy, D. Jyothi, et al., Melatonin inhibits AGS cell proliferation by binding to the ATP binding site of CDK2 under hyperglycemic conditions, Cell Biochem. Biophys. 82 (2) (2024) 895–908, https://doi.org/10.1007/s12013-024-01241-9.
[21] A. Chatterjee, T. Roy, V.K. Mishra, et al., Shatavarin-IV, a steroidal saponin from Asparagus racemosus, inhibits cell cycle progression and epithelial-to-mesenchymal transition in AGS cells under hyperglycemic conditions, Steroids 210 (2024) 109487, https://doi.org/10.1016/j.steroids.2024.109487.
[22] A. Jabłońska-Trypuć, M. Matejczyk, S. Rosochacki, Matrix metalloproteinases (MMPs), the main extracellular matrix (ECM) enzymes in collagen degradation, as a target for anticancer drugs, J. Enzyme Inhib. Med. Chem. 31 (sup1) (2016) 177–183, https://doi.org/10.3109/14756366.2016.1161620.
[23] M.O. Koobotse, D. Schmidt, J.M.P. Holly, et al., Glucose concentration in cell culture medium influences the BRCA1-mediated regulation of the lipogenic action of IGF-I in breast cancer cells, Int. J. Mol. Sci. 21 (22) (2020) 8674, https://doi.org/10.3390/ijms21228674.
[24] T. Roy, A. Chatterjee, S. Swarnakar, Rotenone induced neurodegeneration is mediated via cytoskeleton degradation and necroptosis, Biochim. Biophys. Acta Mol. Cell Res. 1870 (3) (2023) 119417, https://doi.org/10.1016/j.bbamcr.2022.119417.
[25] V.V. Senichkin, E.A. Prokhorova, B. Zhivotovsky, et al., Simple and efficient protocol for subcellular fractionation of normal and apoptotic cells, Cells 10 (4) (2021) 852, https://doi.org/10.3390/cells10040852.
[26] M.L. Mittelstadt, R.C. Patel, AP-1 mediated transcriptional repression of matrix metalloproteinase-9 by recruitment of histone deacetylase 1 in response to interferon β, PloS One 7 (8) (2012) e42152 https://doi.org/10.1371/journal.pone.0042152.
[27] M. Mishra, J. Flaga, R.A. Kowluru, Molecular mechanism of transcriptional regulation of matrix metalloproteinase-9 in diabetic retinopathy, J. Cell. Physiol. 231 (8) (2016) 1709–1718, https://doi.org/10.1002/jcp.25268.
[28] H. Sun, P. Saeedi, S. Karuranga, et al., IDF diabetes atlas: global, regional and country-level diabetes prevalence estimates for 2021 and projections for 2045, Diabetes Res. Clin. Pract. 183 (2022) 109119, https://doi.org/10.1016/j.diabres.2021.109119.
[29] R. Yancik, L.A. Ries, Aging and cancer in America. Demographic and epidemiologic perspectives, Hematol. Oncol. Clin. North Am. 14 (1) (2000) 17–23, https://doi.org/10.1016/s0889-8588(05)70275-6.
[30] M.S. Kirkman, V.J. Briscoe, N. Clark, et al., Diabetes in older adults: a consensus report, J. Am. Geriatr. Soc. 60 (12) (2012) 2342–2356, https://doi.org/10.1111/jgs.12035.
[31] J. Wu, J. Chen, Y. Xi, et al., High glucose induces epithelial-mesenchymal transition and results in the migration and invasion of colorectal cancer cells, Exp. Ther. Med. 16 (1) (2018) 222–230, https://doi.org/10.3892/etm.2018.6189.
[32] S. Niland, A.X. Riscanevo, J.A. Eble, Matrix metalloproteinases shape the tumor microenvironment in cancer progression, Int. J. Mol. Sci. 23 (1) (2021) 146, https://doi.org/10.3390/ijms23010146.
[33] S. Chakraborti, M. Mandal, S. Das, et al., Regulation of matrix metalloproteinases: an overview, Mol. Cell. Biochem. 253 (1–2) (2003) 269–285, https://doi.org/10.1023/a:1026028303196.
[34] A.R. Farina, A.R. Mackay, Gelatinase B/MMP-9 in tumour pathogenesis and progression, Cancers 6 (1) (2014) 240–296, https://doi.org/10.3390/cancers6010240.
[35] C. Yan, D.D. Boyd, Regulation of matrix metalloproteinase gene expression, J. Cell. Physiol. 211 (1) (2007) 19–26, https://doi.org/10.1002/jcp.20948.
[36] J. Park, C.H. Kwak, S.H. Ha, et al., Ganglioside GM3 suppresses lipopolysaccharide-induced inflammatory responses in rAW 264.7 macrophage cells through NF-κB, AP-1, and MAPKs signaling, J. Cell. Biochem. 119 (1) (2018) 1173–1182, https://doi.org/10.1002/jcb.26287.
[37] Y.Q. Li, J.P. Yan, W.L. Xu, et al., ADAM17 mediates MMP9 expression in lung epithelial cells, PloS One 8 (1) (2013) e51701, https://doi.org/10.1371/journal.pone.0051701.
[38] Y. Wang, H. Wu, X. Wu, et al., Interleukin 17A promotes gastric cancer invasiveness via NF-κB mediated matrix metalloproteinases 2 and 9 expression, PloS One 9 (6) (2014) e96678, https://doi.org/10.1371/journal.pone.0096678.
[39] A. Al-Roub, N. Akhter, F. Al-Rashed, et al., TNFα induces matrix metalloproteinase-9 expression in monocytic cells through ACSL1/JNK/ERK/NF-kB signaling pathways, Sci. Rep. 13 (1) (2023) 14351, https://doi.org/10.1038/s41598-023-41514-6.
[40] J. Yoon, S.J. Cho, Y.S. Ko, et al., A synergistic interaction between transcription factors nuclear factor-κB and signal transducers and activators of transcription 3 promotes gastric cancer cell migration and invasion, BMC Gastroenterol. 13 (2013) 29, https://doi.org/10.1186/1471-230X-13-29.
[41] J. Liu, T. Shao, J. Zhang, et al., Gamma synuclein promotes cancer metastasis through the MKK3/6-p38MAPK cascade, Int. J. Biol. Sci. 18 (8) (2022) 3167–3177, https://doi.org/10.7150/ijbs.69155.
[42] L. Mao, L. Yuan, L.M. Slakey, et al., Inhibition of breast cancer cell invasion by melatonin is mediated through regulation of the p38 mitogen-activated protein kinase signaling pathway, Breast Cancer Res. 12 (6) (2010) R107, https://doi.org/10.1186/bcr2794.
[43] M. Loesch, H.Y. Zhi, S.W. Hou, et al., p38gamma MAPK cooperates with c-Jun in trans-activating matrix metalloproteinase 9, J. Biol. Chem. 285 (20) (2010) 15149–15158, https://doi.org/10.1074/jbc.M110.105429.
[44] Q. Huang, F. Lan, X. Wang, et al., IL-1β-induced activation of p38 promotes metastasis in gastric adenocarcinoma via upregulation of AP-1/c-Fos, MMP2 and MMP9, Mol. Cancer 13 (2014) 18, https://doi.org/10.1186/1476-4598-13-18.
[45] T.D. Halazonetis, K. Georgopoulos, M.E. Greenberg, et al., C-Jun dimerizes with itself and with c-Fos forming complexes of different DNA binding affinities, Cell 55 (5) (1988) 917–924, https://doi.org/10.1016/0092-8674(88)90147-x.
[46] B.W. Ozanne, H.J. Spence, L.C. McGarry, et al., Transcription factors control invasion: AP-1 the first among equals, Oncogene 26 (1) (2007) 1–10, https://doi.org/10.1038/sj.onc.1209759.
[47] J. Hess, P. Angel, M. Schorpp-Kistner, AP-1 subunits: quarrel and harmony among siblings, J. Cell Sci. 117 (Pt 25) (2004) 5965–5973, https://doi.org/10.1242/jcs.01589.

Steroids 210 (2024) 109487

Contents lists available at ScienceDirect

Steroids

journal homepage: www.elsevier.com/locate/steroids

Shatavarin-IV, a steroidal saponin from *Asparagus racemosus*, inhibits cell cycle progression and epithelial-to-mesenchymal transition in AGS cells under hyperglycemic conditions

Abhishek Chatterjee, Tapasi Roy, Vineet Kumar Mishra, Snehasikta Swarnakar *

Infectious Diseases and Immunology division, CSIR-Indian Institute of Chemical Biology, 4, Raja S.C. Mullick Road, Kolkata 700032, West Bengal, India

ARTICLE INFO

Keywords:
Shatavarin-IV
AGS
Hyperglycemia
Epithelial-Mesenchymal Transition
Cell Cycle Regulation
MMP-9

ABSTRACT

Gastric cancer (GC)-diabetes co-morbidity is nowadays growing into a rising concern. However, no separate treatment procedures have been outlined for such patients. Phytochemicals and their derivatives can therefore be used as therapeutics as they have greater effectiveness, reduced toxicity, and a reduced likelihood of developing multi-drug resistance in cancer treatments. The present study intended to assess the therapeutic efficacy of Shatavarin-IV – a major steroidal saponin from the roots of *Asparagus racemosus,* in human gastric adenocarcinoma cell line under hyperglycemic conditions and explore its mechanism of action in controlling GC progression. For the present study, AGS cells were incubated in high glucose-containing media and the effects of Shatavarin-IV therein have been evaluated. Cell proliferation, confocal microscopic imaging, flow-cytometric analysis for cell cycle and apoptosis, immunoblotting, zymography, reverse zymography, wound-healing, colony formation, and invasion assays were performed. Shatavarin-IV has a prominent effect on AGS cell proliferation; with IC50 of 2.463 μ M under hyperglycemic conditions. Shatavarin-IV induces cell cycle arrest at the G0/G1 phase, thereby preventing hyperglycemia-induced excessive cell proliferation that later on leads to apoptotic cell death at 36 h of incubation. Shatavarin-IV further inhibits the migratory and invasive potential of AGS cells by altering the expression patterns of different EMT markers. It also inhibits MMP-9 while promoting TIMP-1 activity and expression; thereby regulating ECM turnover. This is the first report demonstrating the therapeutic efficacy of Shatavarin-IV against AGS cells grown in hyperglycemic conditions, implicating new insights into the treatment paradigm of patients with GC-diabetes co-morbidity.

1. Introduction

Gastric cancer (GC) is the fifth most common cancer worldwide and the fourth leading cause of cancer-associated mortality globally [1]. The development of GC is influenced by many environmental and behavioral factors including unhealthy diet, consumption of high-salt foods and alcohols, *Helicobacter pylori* infection, obesity, and different metabolic syndromes like diabetes [2]. The number of diabetic cases is increasing rapidly due to current human lifestyle. It is predicted that 9.9 % of the world's human population will become diabetic by the year 2045 [3]. It is well known that cancer cells consume more glucose than the surrounding normal cells [4] and diabetes greatly increases the amount of glucose in the cancer microenvironment. According to previous reports, hyperglycemia promotes epithelial-mesenchymal transition (EMT), which in turn stimulates cancer cell invasiveness and motility [5,6]. Reports also suggest that diabetes can increase the risk of early GC

Abbreviations: BSA, bovine serum albumin; CDK, cyclin dependent kinase; DAPI, 4′,6-diamidino-2-phenylindole; DNA, deoxyribonucleic acid; DTT, dithiothretol; EMT, epithelial-mesenchymal transition; FACS, fluorescence-activated cell sorting; FBS, fetal bovine serum; FITC, fluorescein isothiocyanate; GAPDH, glyceraldehyde-3-phosphate dehydrogenase; GC, gastric cancer; HG, hyperglycemic; HRP, horseradish peroxidase; MMP, matrix metalloproteinase; NG, normoglycemic; PAGE, polyacrylamide gel electrophoresis; PBS, phosphate buffered saline; PBST, phosphate buffered saline with 0.1% Tween® 20 detergent; PCR, polymerase chain reaction; PI, propidium iodide; PIC, protease inhibitor cocktail; PMSF, phenylmethylsulfonyl fluoride; p-Rb, phosphorylated retinoblastoma; PVDF, polyvinylidene fluoride; Rb, retinoblastoma; RNA, ribonucleic acid; S-IV, Shatavarin-IV; SDS, sodium dodecyl sulphate; STED, stimulated emission depletion; TBST, Tris-buffered saline with 0.1% Tween® 20 detergent; TIMP, tissue inhibitor of metalloproteinase; TUNEL, terminal deoxynucleotidyl transferase dUTP nick end labeling.

* Corresponding author at: Infectious Diseases and Immunology Division, CSIR-Indian Institute of Chemical Biology, 4, Raja S. C. Mullick Road, Jadavpur, Kolkata 700032, West Bengal, India.

E-mail addresses: snehasiktaiicbidi@gmail.com, sikta@iicb.res.in (S. Swarnakar).

https://doi.org/10.1016/j.steroids.2024.109487
Received 6 February 2024; Received in revised form 3 August 2024; Accepted 3 August 2024
Available online 4 August 2024

development [7,8] and negatively affect its prognosis [2] as most patients remain asymptomatic in the early stage, leading to a growing number of cases with GC and diabetes co-morbidity.

Despite the knowledge that hyperglycemic condition enhances cancer cell survival and progression; no separate treatment protocol has yet been outlined for the patients with GC-hyperglycemia co-morbidity. Many chemotherapeutic agents have been developed and evaluated in recent years, but the median overall survival of patients with metastatic GC could not be extended beyond a year [9]. Therefore, it is of great interest to find better anti-cancer agents with greater efficacy and fewer adverse effects for treating patients with GC-hyperglycemia co-morbidity.

Natural products and their derivatives have greater efficacy, reduced toxicity, and a lesser risk of developing multi-drug resistance than chemically synthesized drugs [10]. One such potent phytochemical, Shatavarin-IV, has been found in the roots of *Asparagus racemosus* Willd. – an important medicinal plant of Asparagaceae family that is native to South Asian countries. This plant is used in traditional Indian Ayurvedic medicine to treat diarrhea, dysentery, constipation, stomach ulcers, and diabetes [11]. Shatavarin-IV is the major steroidal saponin present in *Asparagus racemosus*, having defined estrogen-like activity. This phytochemical may have a pivotal part to play in the medicinal value of this plant. A previous study reported that Shatavarin-IV rich fraction (84.69 % pure) of *Asparagus racemosus* root extract exhibited anti-cancer activity against human breast cancer (MCF-7), human colorectal cancer (HCT-29), and human renal carcinoma (A-498) cell lines as well as in Ehrlich ascites carcinoma (EAC) tumor-bearing mice [12]. However, there is no report suggesting the anti-gastric cancer efficacy of Shatavarin-IV. In the present study, we incubated AGS cells under hyperglycemic conditions to mimic the physiological conditions of a patient suffering from GC and hyperglycemia co-morbidity, intending to evaluate the protective efficacy of Shatavarin-IV (>90 % pure) therein. To the best of our knowledge, we are the first to report the anti-cancer effect of Shatavarin-IV in AGS cells (gastric cancer cell line) through inhibition of EMT and G0/G1 phase cell cycle arrest.

2. Materials and methods

2.1. Materials

Shatavarin-IV (≥90 % pure) was purchased from Merck. Gelatin, Triton-X-100, protease inhibitors, dithiothreitol (DTT), D-glucose, 5-Fluorouracil (5-FU), RNase A solution, Tween-20, Bradford reagent, bovine serum albumin (BSA), and Fluoromount Aqueous Mounting Medium were procured from Sigma (St. Louis, MO, USA). CellTiter-Glo luminescent cell viability assay kit was obtained from Promega (Madison, WI, United States). A protease inhibitor cocktail was procured from Calbiochem. Primary antibodies, horseradish peroxidase (HRP) conjugated secondary antibodies, and Texas Red conjugated secondary antibodies were sourced from Santa Cruz Biotechnology, TX, USA. Clarity™ Western ECL Substrate solution was purchased from Bio-Rad (Hercules, CA, USA). Trans-well chambers and Matrigel were sourced from Corning, USA. Crystal violet was purchased from HiMedia Laboratories, Maharashtra, India. FITC – Annexin V Apoptosis Detection kit I was procured from BD Biosciences (Franklin Lakes, NJ, USA). APO-BRDU (TUNEL) Apoptosis Kit was purchased from Novus Biologicals, USA. AGS cells were purchased from American Type Culture Collection (ATCC). All materials used in cell culture were purchased from Gibco (Thermo Fisher, MA, USA).

2.2. AGS cell culture and treatment paradigm

The human gastric adenocarcinoma cell line (AGS), was maintained in Ham's F12K nutrient media containing 10 % fetal bovine serum (FBS) and 1 % Antibiotic-Antimycotic (100 ×) mixture. The cells were kept at 37 °C in a humidified incubator maintaining 5 % CO_2 and 95 % air.

For subsequent experiments, AGS cells were seeded in normoglycemic media (5.5 mM glucose) supplemented with 10 % FBS. Afterward, cells were incubated with serum-free normoglycemic media, serum-free hyperglycemic media (25 mM glucose), and serum-free hyperglycemic media containing 2.2 μ M Shatavarin-IV for 24 h. These three treatment groups were labeled 'NG', 'HG', and 'HG+S-IV', respectively. These treatment groups were kept constant in all the subsequent experiments. Before all experiments, Shatavarin-IV was prepared freshly by dissolving it in DMSO.

2.3. Cell viability assay

To establish the effect of Shatavarin-IV on cell viability, AGS cells grown in normoglycemic and hyperglycemic media were seeded in a 96-well plate at a density of 1×10^4 cells/well and kept overnight. AGS cells were incubated with increasing concentrations of Shatavarin-IV (1-, 2-, 3-, 4- and 5 μ M) or 5-FU (50-, 100-, 150-, 200-, 250- and 300 μ M) for 24 h and the CellTiter-Glo luminescent cell viability assay was performed to monitor the cell viability. 5-FU was used as a positive control. Furthermore, a non-cancerous cell line, HEK-293, was used to determine the cytotoxicity of Shatavarin-IV. To calculate the IC50 values of these two drugs, their respective cell viability data from three independent experiments were first calculated in percentage, drug concentrations were then transformed into logarithmic scale and IC50 values were computed using a non-linear regression model in GraphPad Prism (ver 5.01, San Diego, California, USA).

2.4. Determination of cell cycle and apoptosis by flow cytometry

To analyze the phases of the cell cycle, AGS cells were plated at a density of 1×10^6 cells per 60 mm dishes and kept for 24 h. Flavopiridol (125 nM) was used as the positive control. After another 24 h of incubation with the respective treatments, the cells were trypsinized, washed with PBS, and fixed using ice-cold 70 % ethanol with gentle vortexing. After fixation, cells were kept at 4 °C for 16–18 h. Any trace of ethanol was removed by washing the cells with PBS. The fixed cells were incubated in a staining solution containing 50 μg/ml propidium iodide and 100 μg/ml RNaseA for 15 min at room temperature. Analysis of the stained cells was performed by BD LSRFortessa™ Cell Analyzer and the results were analyzed using Flowing Software (ver 2.5.1).

For the analysis of apoptosis, AGS cells were seeded at a density of 1×10^6 cells in 60 mm dishes. After 24 h of respective treatments, the cells were trypsinized, washed with PBS, and processed using FITC – AnnexinV Apoptosis Detection Kit I, as per the manufacturer's protocol. Analysis of the stained cells was performed by BD LSRFortessa™ Cell Analyzer and the results were analyzed using Flowing Software (ver 2.5.1).

2.5. Monitoring apoptosis by TUNEL assay

AGS cells were grown on sterile poly-L-lysine coated coverslips and incubated with respective treatments for 24 h. After incubation, the cells were stained using a TUNEL assay kit [13]. Briefly, AGS cells were fixed with 4 % paraformaldehyde solution and then permeabilized in PBS containing 0.25 % Triton X-100 for 10 min. Next, the cells were stained for 1 h using freshly prepared TUNEL reaction mixture at 37 °C, in the dark. Then the cells were counter-stained with DAPI and mounted with Fluoromount Aqueous Mounting Medium (Sigma, USA). Finally, images were captured using a high-resolution Stimulated Emission Depletion (STED) microscope (Leica TCS SP8). Images were taken in a single session while maintaining the same settings. Different protein localizations were identified from randomly selected fields. The images were representative of five individual experiments to exclude artifacts that may result from individual experiments.

2.6. Gelatin zymography

The gelatinolytic activity of MMP-9 was assayed using gelatin zymography [14]. Briefly, the conditioned media (70 μg total protein) from the three treatment groups were electrophoresed in 1 mg/ml gelatin containing 8 % SDS- PAGE, under non-reducing conditions; washed in 2.5 % Triton-X-100, and incubated in buffer containing 40 mM Tris-HCl (pH 7.4), 0.2 M NaCl and 10 mM $CaCl_2$ for 18 hrs. at 37 °C. The staining of the gel was performed with 0.1 % Coomassie blue followed by de-staining. The bands were visualized as negative staining and densitometric quantification was performed using the ImageJ software.

2.7. Reverse zymography

TIMP-1 was enzymatically assayed by using the reverse zymography technique [14]. In brief, AGS cells were seeded at a density of 1×10^6 cells in 60 mm. After a 24-hour incubation with the respective treatments, conditioned media was collected and 70 μg total protein was electrophoresed in 12 % SDS-PAGE containing 1 mg/ml gelatin and an MMP source, under non-reducing conditions. The conditioned media from MDA-MB-231 cells was used as an MMP source for this assay. After electrophoresis, the gels were washed in 2.5 % Triton-X-100 and incubated in buffer containing 40 mM Tris-HCl (pH 7.4), 0.2 M NaCl, and 10 mM $CaCl_2$ for 18 hrs. at 37 °C. After staining with 0.1 % Coomassie blue, the gel was de-stained. The bands were visualized as colored bands and quantified by densitometry using the ImageJ software.

2.8. Wound healing assay

AGS cells were seeded into six-well plates and incubated until a monolayer was formed. The monolayer was scratched, washed with PBS, and incubated with their respective treatments. After 24 h, the cells were rinsed with PBS, fixed with 4 % paraformaldehyde, and stained using 0.5 % crystal violet solution. Images were taken with an Olympus I×71 inverted microscope using the Image-Pro Express software.

2.9. Invasion assay

The ability of cell invasion with or without Shatavarin-IV treatment was measured using *trans*-well chambers having 8 μm pore filter after coating them with Matrigel. The coated chambers were placed into the wells of a 24-well plate and AGS cells suspended in serum-free medium containing the respective treatments were seeded into the upper *trans*-well chambers. To induce chemotaxis, the lower chambers were filled with 500 μl Ham's F12K media (containing 20 % FBS). After incubating for 24 h, the *trans*-well chambers were removed, washed with PBS and the cells were fixed with 4 % paraformaldehyde and stained with 0.5 % crystal violet solution. Finally, the images were captured with an Olympus I×71 inverted microscope using the Image-Pro Express software.

2.10. Colony formation assay

AGS cells were seeded in 60 mm dishes. After 24 h of incubation with the respective treatments, the cells were trypsinized, pelleted, and single-cell suspensions were obtained from each treatment. 1×10^3 cells from each treatment group were then seeded into 6-well plates and incubated in a humidified incubator maintaining 5 % CO_2 at 37 °C for colony formation. Fresh complete media was added to each well on every alternate day or as often required. After 10 days, the colonies were fixed with 4 % paraformaldehyde, washed with PBS, and stained using 0.5 % crystal violet solution. Afterward, the plates were washed with ddH_2O several times, dried, and photographed.

2.11. Immunofluorescence assay

AGS cells were grown on sterile poly-L-lysine coated coverslips and incubated with respective treatments for 24 h. The cells were washed with PBS and fixed with 4 % paraformaldehyde. Permeabilization was performed for 10 min by incubating the cells with PBS containing 0.25 % Triton X-100 and subsequently blocked with 1 % BSA in PBST (137 mM NaCl, 2.7 mM KCl, 10 mM Na_2HPO_4, 1.8 mM KH_2PO_4, and 0.1 % Tween-20; pH 7.4) for 1 h. Cells were incubated overnight at 4 °C with anti-Ki-67 antibody and anti-MMP-9 antibody. Next, the cells were incubated for 2 h with Texas Red conjugated secondary antibody solution (1:400 dilutions in TBS containing 1 % BSA) in the dark, at room temperature. The coverslips were washed thrice with PBS, counter-stained with DAPI, and mounted with a drop of Fluoromount Aqueous Mounting Medium. Finally, images were captured using a high-resolution Stimulated Emission Depletion (STED) microscope (Leica TCS SP8). Images were taken in a single session while maintaining the same settings. Different protein localizations were identified from randomly selected fields. The images were representative of five individual experiments to exclude artifacts that may result from individual experiments.

2.12. Immunoblotting

AGS cells were seeded at a density of 1×10^6 cells in 60 mm dishes. After a 24-hour incubation with respective treatments, the cells were washed with PBS, trypsinized, and pelleted down. Cell pellets were lysed (20 mM Tris-HCl, 150 mM NaCl, 1 % Triton X-100, 1 × PIC, and 1 mM PMSF; pH 7.4) and then centrifuged at 12000 rpm for 10 min at 4 °C. Supernatants were collected in a separate vial and their protein concentrations were estimated using Bradford assay. Same amount of protein (50 μg) from each group was electrophoresed using 10 % SDS-PAGE and transferred onto methanol-activated PVDF membranes. The PVDF membranes were then blocked with 3 % BSA in TBST (137 mM NaCl, 2.7 mM KCl, 50 mM Tris-HCl, and 0.1 % Tween-20; pH 7.4) for 2 h at room temperature and incubated with appropriate primary antibodies overnight at 4 °C. The membrane was washed with TBST and incubated with the corresponding HRP-conjugated secondary antibodies. The blot was developed using a western ECL substrate solution. Images were collected using the Bio-Rad ChemiDoc MP imaging system. Protein expression levels were quantified by densitometry using the ImageJ software. GAPDH was kept as the loading control.

2.13. RNA isolation and PCR analyses

Total RNA was isolated from AGS cells using TRIzol (Invitrogen, CA), as per the manufacturer's instructions. Afterward, RNA was incubated with DNase I in order to remove any contaminating DNA, and then reverse transcription was performed using Oligo(dT) primers. The conventional PCR analysis for a fragment of MMP-9, TIMP-1, *N*-cadherin, E-cadherin, β-catenin, and Vimentin was performed keeping GAPDH as the reference gene. Table 1 lists the primer sets used in this study.

2.14. Protein estimation

AGS cell pellets were lysed (20 mM Tris-HCl, 150 mM NaCl, 1 % Triton X-100, 1 × PIC, and 1 mM PMSF; pH 7.4) and centrifuged at 12000 rpm for 10 min at 4 °C. Supernatants were collected in a separate vial and their protein concentrations were estimated using Bradford assay.

2.15. Statistical analysis

All the experiments were repeated five times independently. The statistical analysis was performed using GraphPad Prism (ver 5.01, San Diego, California, USA). Student's *t*-test was used to compare between two groups. The statistical significance was compared against the

Table 1
List of primers used for semi-quantitative PCR detection of respective genes.

Target gene	Forward primer sequence (5′–3′)	Reverse primer sequence (5′–3′)
GAPDH	GAAGGTGAAGGTCGGAGT	GAAGATGGTGATGGGATTTC
***N*-Cadherin**	CTCCATGTGCCGGATAGC	CGATTTCACCAGAAGCCTCTAC
E-Cadherin	GCCGAGAGCTACACGTTCA	GACCGGTGCAATCTTCAAA
Vimentin	GTTTCCCCTAAACCGCTAGG	AGCGAGAGTGGCAGAGGA
β-catenin	ACAGCACCTTCAGCA CTCT	AAGTTCTTGGCTATTACGACA
MMP-9	CTGTACCGCTATGGTTACACTC	ACTCGTCATCGTCGAAATGG
TIMP-1	TCGTCATCAGGGCCAAGTTC	TCCACAAGCAATGAGTGCCA

control group, was represented with a '*' mark, and '#' was used for comparisons against the hyperglycemic treatment group. In all representations, statistically significant differences are indicated as *p ≤ 0.05, #p ≤ 0.05, **p ≤ 0.01, ##p ≤ 0.01, ***p ≤ 0.001 and ###p ≤ 0.001. ns = not significant (p > 0.05). All data has been represented as mean ± SEM.

3. Results

3.1. Shatavarin-IV promotes AGS cell death under hyperglycemic condition

AGS cells were incubated with different concentrations of D-glucose (8, 12.5, 25, 35, and 50 mM) to determine the optimum glucose concentration for hyperglycemic treatment. We observed that cell viability increased proportionally with glucose concentration up to 25 mM (Fig. 1A). Higher glucose concentrations negatively affected AGS cell viability (Fig. 1A). Hence, 25 mM glucose was decided to be the optimum concentration for AGS cell proliferation and all the following experiments were performed using 25 mM glucose thereon.

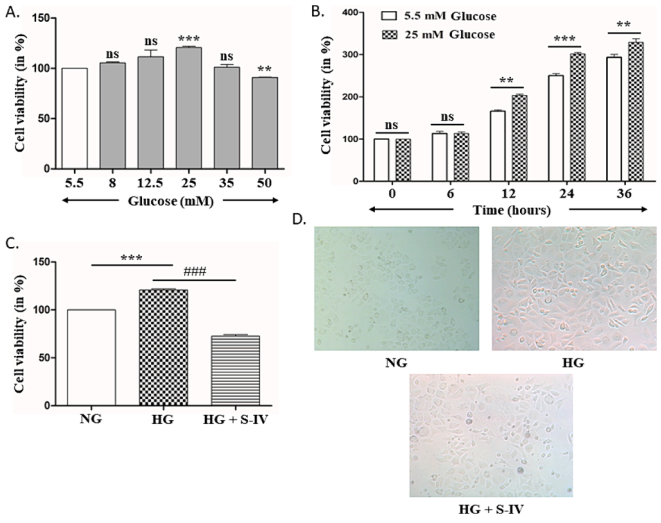

Fig. 1. Shatavarin-IV induces cell death in AGS cells under hyperglycemic conditions. (A) Dose-dependent response of AGS cells against increasing concentration of glucose. AGS cells cultured in normoglycemic media were plated into 96-well plates and treated with incomplete media containing increasing concentrations of D-glucose (5.5, 8, 12.5, 25, 35, and 50 mM). After 24 h of incubation, CellTiter-Glo luminescent cell viability assay kit was used to measure cell viability. (B) Time-dependent response of AGS cells against 5.5 mM and 25 mM glucose. AGS cells cultured in normoglycemic media were seeded into 96-well plates and treated with incomplete media containing 25 mM D-glucose. After respective incubation periods of 0, 6, 12, 24, and 36 h, CellTiter-Glo luminescent cell viability assay kit was used to measure cell viability. (C) Protective efficacy of Shatavarin – IV. AGS cells were seeded into 96-well plates and treated with 5.5 mM D-glucose (NG), 25 mM D-glucose (HG), and 2.2 μ M Shatavarin-IV in HG media (HG+S-IV) for 24 h. CellTiter-Glo luminescent cell viability assay kit was used to measure cell viability. (D) Light microscopic images of AGS cells after incubation with respective treatments for 24 h. Values are mean ± SEM. Comparison between groups was done using the Student's *t*-test. ***p < 0.001, **p < 0.01, *p < 0.05 (vs. 'NG'); ###p < 0.001 (vs. 'HG') and "ns" represents non-significant.

Next, to determine the optimal time point for the experimental designs, we incubated AGS cells with 25 mM D-glucose for 6 h to 36 h. We observed that the difference in viability between AGS cells growing under normoglycemic (5.5 mM glucose) and hyperglycemic (25 mM glucose) conditions was the highest as well as most statistically significant (p < 0.001) after 24 h of incubation (Fig. 1B). Therefore, the hyperglycemic condition was induced in all further experiments by incubating AGS cells in 25 mM D-glucose containing media for 24 h.

CellTiter-Glo luminescent cell viability assay showed that the viability of hyperglycemic AGS cells gradually decreased with increasing concentrations of Shatavarin-IV (0, 1, 2, 3, 4, and 5 μ M); suggesting its dose-dependent effect (Fig. S1). There was no statistically significant difference between the hyperglycemic and 1 μ M Shatavarin-IV treatment groups (p > 0.05); whereas the 5 μ M Shatavarin-IV treatment group had the highest inhibition with ~ 0.43 % cell viability. The IC50 value of Shatavarin-IV in AGS cells grown under hyperglycemic conditions was calculated to be 2.463 μ M (Fig. S1-A & B). We also conducted a similar experiment to determine the IC50 value of Shatavarin-IV under normoglycemic conditions, which was calculated to be 1.517 μ M (Fig. S1-C & D). Comparatively, 5-FU (a known anti-cancer drug) had a much higher IC50 value of 100.7 μ M (Fig. S2). This difference in IC50 values of the two compounds clearly shows that Shatavarin-IV is a much more potent alternative.

Since, the IC50 value of Shatavarin-IV under hyperglycemic conditions is 2.463 μM, hence we have used a concentration of 2.2 μ M for all further experiments. Cytotoxicity assay in HEK-293, a non-cancerous cell line, revealed that the dose of 2.2 μ M Shatavarin-IV has negligible harmful effects on adjacent normal cells (Fig. S3). At this dose, the hyperglycemia-induced increase in AGS cell viability is brought down from ~ 120.65 % to ~ 72.6 % of normoglycemic control; thereby effectively reversing the effect of hyperglycemia on AGS cell proliferation (Fig. 1C). We observed notable abscission and distinct morphological changes in cells treated with 2.2 μ M Shatavarin-IV for 24 h (Fig. 1D). Therefore, it can be concluded that Shatavarin-IV can negate hyperglycemia-induced AGS cell proliferation.

3.2. Shatavarin-IV induces cell cycle arrest at G0/G1 phase and apoptosis

Cell cycle phase distribution was studied using flow cytometry to understand whether Shatavarin-IV has any effect on cell cycle progression under hyperglycemic conditions. We observed that AGS cells grown in hyperglycemic conditions have a lower percentage of cells in the G0/G1 phase (from ~ 53.05 % in 'NG' to ~ 49.13 % in 'HG'; p < 0.05), compared to normoglycemic ones (Fig. 2A & B). Whereas, changes in the percentage of cells in the S- and G2/M−phases were not statistically significant (p > 0.05). Further, incubating AGS cells (maintained in hyperglycemic condition) with Shatavarin-IV (2.2 μ M), resulted in an accumulation of cells in the G0/G1 phase (from ~ 49.13 % in 'HG' to 67.27 % in 'HG+S-IV'; p < 0.05). A consequent depletion is observed in the percentage of cells in the G2/M phase (from ~ 18.57 % in 'HG' to ~ 9.05 % in 'HG+S-IV'; p < 0.05). However, there was no substantial change in the percentage of cells in the S phase (p > 0.05). Upon

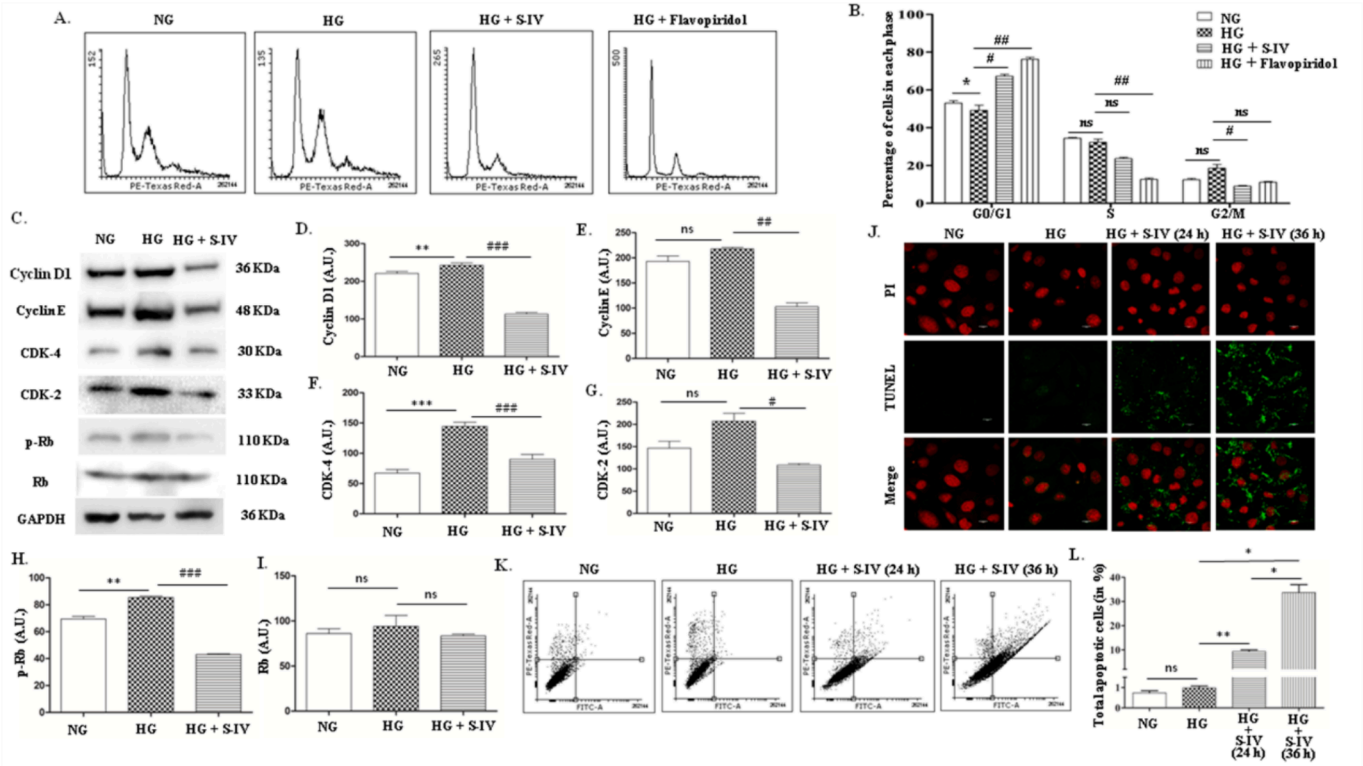

Fig. 2. Shatavarin-IV induces cell cycle arrest and apoptosis in AGS cells under hyperglycemic conditions. (A) Representative cell cycle distribution profiles of normoglycemic, hyperglycemic, Shatavarin-IV (2.2 μM) treated and Flavopiridol (125 nM) treated hyperglycemic AGS cells for 24 h. The X-axis represents the intensity of propidium iodide staining and the Y-axis represents cell count. (B) Graphical representation of the percentage of cells present in each phase of the cell cycle in normoglycemic, hyperglycemic, Shatavarin-IV (2.2 μM) treated and Flavopiridol (125 nM) treated hyperglycemic AGS cells for 24 h. (C) Western blot analysis of the expression patterns of Cyclin D1, Cyclin E, CDK-4, CDK-2, p-Rb, and Rb in normoglycemic, hyperglycemic, and 2.2 μM Shatavarin-IV treated hyperglycemic AGS cells for 24 h. GAPDH was used as a loading control. Each blot is representative of five individual experiments. (D–I) Densitometric analysis of the expression pattern of Cyclin D1, Cyclin E, CDK-4, CDK-2, p-Rb, and Rb, respectively. (J) Representative TUNEL staining images of normoglycemic, hyperglycemic, and 2.2 μM Shatavarin-IV treated hyperglycemic AGS cells for 24 h and 36 h. The green fluorescence (FITC) represents TUNEL-positive cells and the red fluorescence (PI) represents nucleus. Each image is representative of five individual experiments. (K) Representative flow cytometric scatter-gram of normoglycemic, hyperglycemic, and 2.2 μM Shatavarin-IV treated hyperglycemic AGS cells for 24 h and 36 h generated after Annexin V-FITC/PI staining for the detection of apoptosis. (L) Graphical representation of the percentage of total apoptotic cells (both early and late) in each treatment group. Values are mean ± SEM. Comparison between groups was done using the Student's *t*-test. ***$p < 0.001$, **$p < 0.01$, *$p < 0.05$ (vs. 'NG'); ###$p < 0.001$, ##$p < 0.01$, #$p < 0.05$ (vs. 'HG') and "ns" represents non-significant.

treatment of hyperglycemic AGS cells with 125 nM Flavopiridol (positive control), we observed a significant increase ($p < 0.01$) in G0/G1 population with a consequent decrease in S-phase and G2/M−phase cells (Fig. 2A & B). These results indicated that Shatavarin-IV, at a dose of 2.2 μ M, could be inducing cell cycle arrest at the G0/G1 phase under hyperglycemic conditions.

We further validated this finding by immunoblotting. We evaluated the expression patterns of various cell cycle regulatory proteins that are important in the progression of cells through the G0/G1 phase (cyclin D1 and CDK-4) as well as regulate the entry into the S phase (cyclin E and CDK-2) (Fig. 2C–G). We observed a marked increase in the expressions of cyclin D1 (~1.1-fold increase; $p < 0.01$; Fig. 2C & D), cyclin E (~1.13-fold increase; $p > 0.05$; Fig. 2C & E), CDK-4 (~2.15-fold increase; $p < 0.001$; Fig. 2C & F) and CDK-2 (~1.41-fold increase; $p > 0.05$; Fig. 2C & G) in AGS cells that were maintained under hyperglycemic conditions. Furthermore, the phosphorylation level of the retinoblastoma (Rb) protein was also increased in these cells (~1.23-fold increase; $p < 0.01$; Fig. 2C & H). After treatment with Shatavarin-IV, the expression of cyclin D1 (~2.15-fold decrease; $p < 0.001$; Fig. 2C & D), cyclin E (~2.11-fold decrease; $p < 0.01$; Fig. 2C & E), CDK-4 (~1.6-fold decrease; $p < 0.001$; Fig. 2C & F), CDK-2 (~1.91-fold decrease; $p < 0.05$; Fig. 2C & G) and p-Rb (~1.98-fold decrease; $p < 0.001$; Fig. 2C & H) underwent a sharp fall, compared to the hyperglycemic group. This decreased expression of cyclin E and CDK-2 is primarily responsible for the accumulation of cells in the G0/G1 phase after Shatavarin-IV treatment. Moreover, a low level of cyclin D1 within cells arrested at the G0/G1 phase indicates a transition to a quiescent G0 phase. Overall, we can conclude that Shatavarin-IV treatment induces cell cycle arrest at the G0/G1 phase.

Next, we performed TUNEL assay and FACS analysis with Annexin V-FITC/PI to determine whether Shatavarin-IV treatment can induce apoptosis in AGS cells maintained under hyperglycemic condition. It was observed that there was a slight change in the number of TUNEL-positive (Fig. 2J) and Annexin V-FITC/PI-stained cells (from 0.98 ± 0.17 % in HG to 9.34 ± 1.17 % in HG+S-IV), after 24 h of Shatavarin-IV treatment (Fig. 2K & L). Increasing the incubation period to 36 h had a profound impact on the apoptosis rate. The number of TUNEL-positive cells increased drastically from 24 h to 36 h (Fig. 2J). Similarly, the total percentage of apoptotic cells also increased from 9.34 ± 1.17 % (in 24 h) to 33.75 ± 5.61 % (in 36 h) (Fig. 2K & L).

3.3. *Shatavarin-IV inhibits hyperglycemia-induced migration, invasion, and proliferation of AGS cells*

The migratory capability of AGS cells was measured using the wound-healing assay. We observed that AGS cells grown in hyperglycemic conditions migrated a greater distance as compared to their normoglycemic counterpart (Fig. 3A) after 24 hrs. After treating

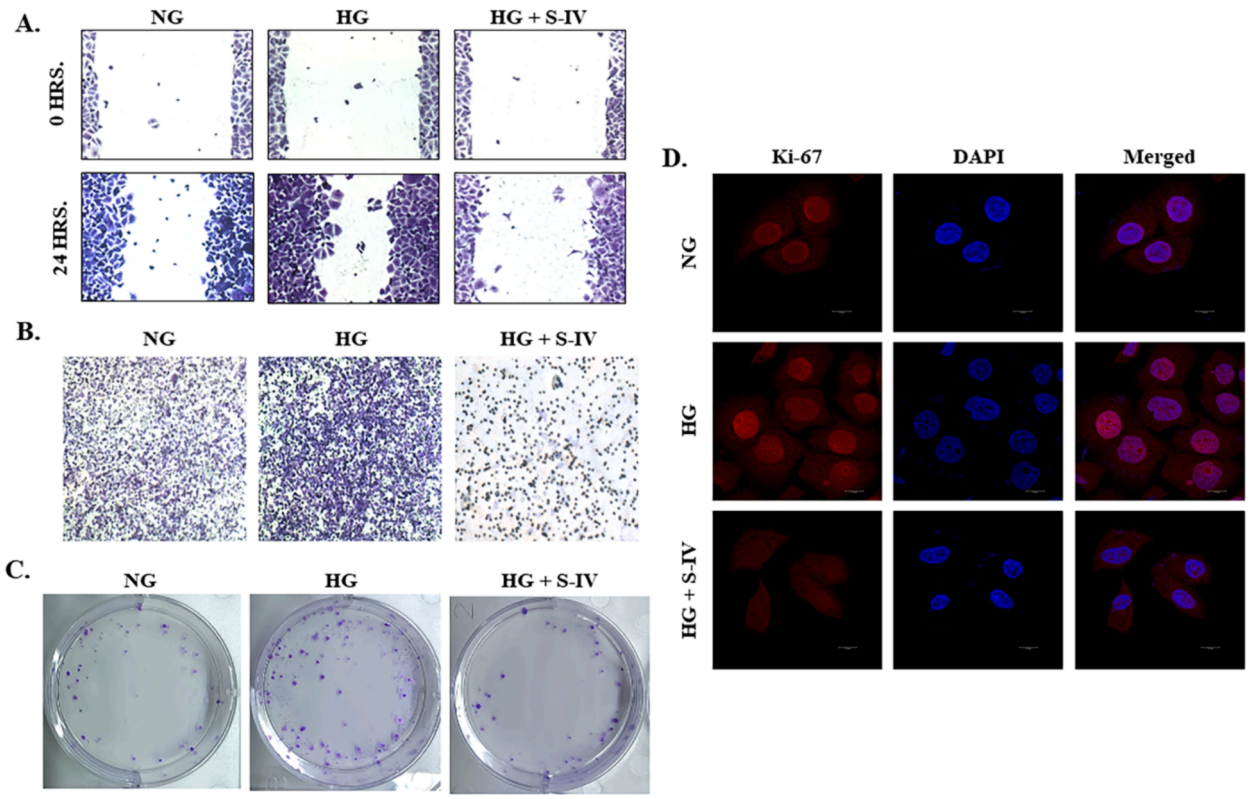

Fig. 3. Shatavarin-IV inhibits hyperglycemia-induced migration, invasion, and proliferation of AGS cells. (A) Representative images of wound-healing assay with normoglycemic, hyperglycemic, and 2.2 μM Shatavarin-IV treated hyperglycemic AGS cells for 24 h. (B) Representative images of AGS cells that passed through the *trans*-well chamber in each of the three treatment groups. Cells were stained with crystal violet before imaging. (C) Representative images of the colony formation assay with normoglycemic, hyperglycemic, and 2.2 μM Shatavarin-IV treated hyperglycemic AGS cells. (D) Representative images of Ki-67 immunostaining in normoglycemic, hyperglycemic, and 2.2 μM Shatavarin-IV treated hyperglycemic AGS cells for 24 h. The red fluorescence (Texas Red) represents Ki-67 protein and the blue fluorescence (DAPI) represents nucleus. Each image is representative of five individual experiments.

hyperglycemic AGS cells with 2.2 μ M Shatavarin-IV, the migrated distance was significantly reduced (Fig. 3A). This result demonstrates that Shatavarin-IV is a good inhibitor of AGS cell migration.

According to the *trans*-well invasion assay, the number of invasive AGS cells increased under hyperglycemic conditions. Shatavarin-IV treatment effectively reduced the number of invaded cells by a large margin (Fig. 3B).

The proliferative potential of AGS cells was measured using the colony formation assay and immunofluorescence to determine the expression of the proliferation marker antigen, Ki-67. From the colony formation assay, it was observed that the number of colonies formed increased significantly when maintained under hyperglycemic conditions (Fig. 3C). Whereas, after Shatavarin-IV treatment there was a steep decline in the growth rate of AGS cells, as can be deduced from the decreased number of colonies (Fig. 3C). A similar trend was noticed in the Ki-67 (stained with Texas Red) immunofluorescence images. We observed that the expression of Ki-67, an active cell proliferation marker, was greatly increased (red fluorescence increased) in cells under hyperglycemic conditions, but decreased significantly upon Shatavarin-IV treatment (Fig. 3D).

3.4. Shatavarin-IV inhibits hyperglycemia-induced epithelial-mesenchymal transition (EMT) in AGS cells

To understand the molecular mechanism behind the observed changes in AGS cell migration and invasion, we analyzed the transcription and expression patterns of various EMT markers like E-cadherin, *N*-cadherin, β-catenin and Vimentin using qualitative PCR and immunoblotting techniques.

We observed that under hyperglycemic conditions, the transcription and protein expression of E-cadherin was decreased by ~ 2.32-fold ($p < 0.01$; Fig. 4A and B), and ~ 1.27-fold ($p > 0.05$; Fig. 4F and G) respectively compared to normoglycemic condition. Whereas, the transcription and expression of the other EMT markers were up-regulated, under hyperglycemic conditions. The transcription and protein expression of *N*-cadherin was increased by ~ 1.1-fold ($p < 0.05$; Fig. 4A and C), and ~ 1.39-fold ($p < 0.05$; Fig. 4F and H), respectively. The transcription and protein expression of β-catenin was increased by ~ 1.35-fold ($p < 0.001$; Fig. 4A and D), and ~ 1.42-fold ($p > 0.05$; Fig. 4F and I), respectively. The transcription and protein expression of Vimentin was increased by ~ 1.5-fold ($p < 0.01$; Fig. 4A and E), and ~ 1.08-fold ($p > 0.05$; Fig. 4F and J) respectively.

After Shatavarin-IV treatment, the transcription and expression of E-cadherin was increased by ~ 4.3-fold ($p < 0.01$; Fig. 4A and B), and ~ 1.09-fold ($p > 0.05$; Fig. 4F and G) respectively compared to hyperglycemic condition. Shatavarin-IV treatment also down-regulated the transcription and expression of the other EMT markers. The transcription and protein expression of *N*-cadherin was decreased by ~ 1.7-fold ($p < 0.01$; Fig. 4A and C), and ~ 1.78-fold ($p < 0.01$; Fig. 4F and H), respectively. The transcription and protein expression of β-catenin was decreased by ~ 1.45-fold ($p < 0.01$; Fig. 4A and D), and ~ 1.49-fold ($p < 0.05$; Fig. 4F and I) respectively. The transcription and protein expression of Vimentin was decreased by ~ 1.78-fold ($p < 0.01$; Fig. 4A and E), and ~ 1.85-fold ($p < 0.05$; Fig. 4F and J), respectively.

3.5. Alteration of hyperglycemia-induced MMP-9 and TIMP-1 transcription, expression, and activity upon Shatavarin-IV treatment in AGS cells

MMP-9 is known to be a key enzyme playing a crucial role in

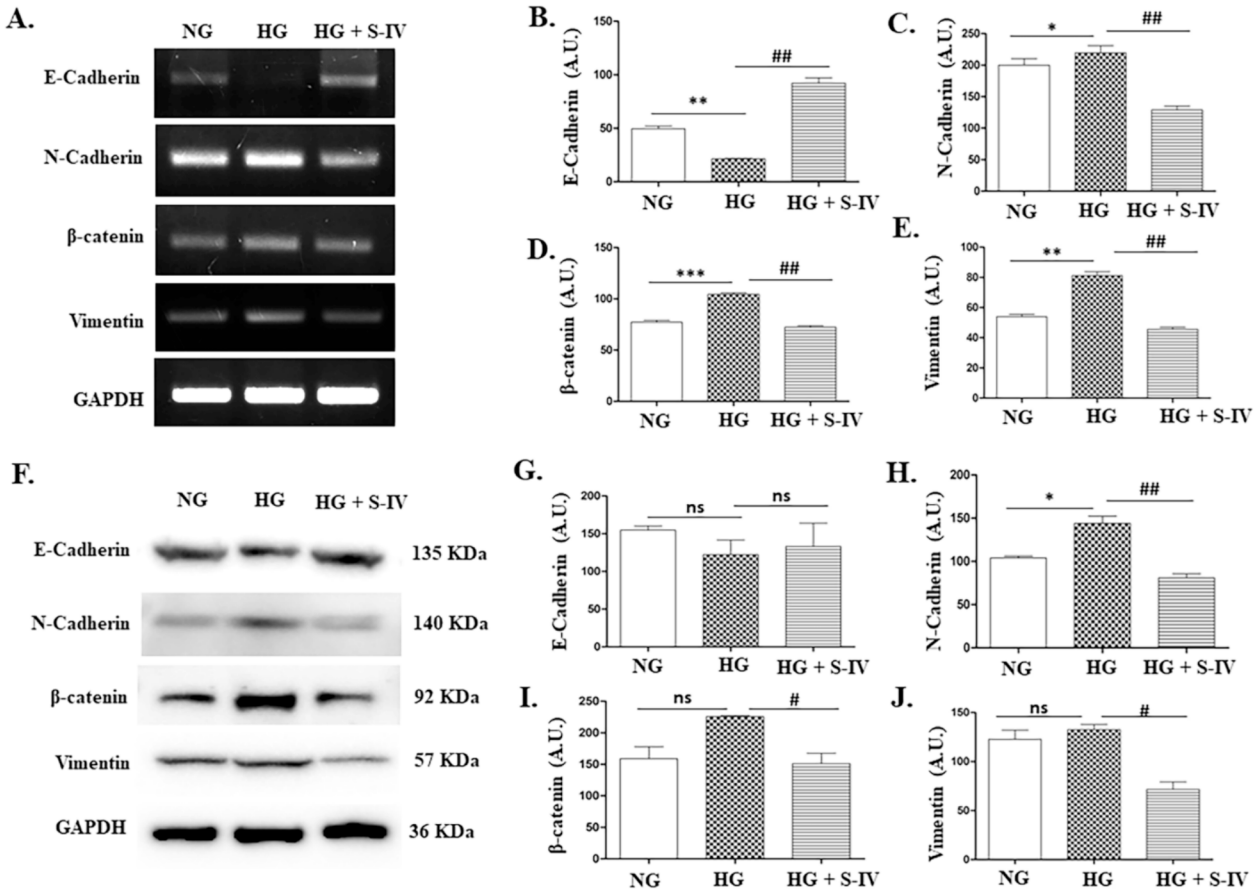

Fig. 4. Shatavarin-IV inhibits hyperglycemia-induced metastasis by down-regulating EMT markers. (A) Conventional RT-PCR analysis of the expression patterns of E-cadherin, *N*-cadherin, β-catenin, and Vimentin in normoglycemic, hyperglycemic, and 2.2 μM Shatavarin-IV treated hyperglycemic AGS cells for 24 h. GAPDH was used as a loading control. Each image is representative of five individual experiments. (B–E) Densitometric analysis of the expression pattern of E-cadherin, *N*-cadherin, β-catenin, and Vimentin, respectively, at the mRNA level. (F) Western blot analysis of the expression patterns of E-cadherin, *N*-cadherin, β-catenin, and Vimentin in normoglycemic, hyperglycemic, and 2.2 μM Shatavarin-IV treated hyperglycemic AGS cells for 24 h. GAPDH was used as a loading control. Each blot is representative of five individual experiments. (G–J) Densitometric analysis of the protein expression pattern of E-cadherin, *N*-cadherin, β-catenin, and Vimentin, respectively. Values are mean ± SEM. Comparison between groups was done using the Student's *t*-test. ***p < 0.001, **p < 0.01, *p < 0.05 (vs. 'NG'); ##p < 0.01, #p < 0.05 (vs. 'HG') and "ns" represents non-significant.

enhancing tumor cell migration and TIMP-1 is its natural inhibitor. Therefore, we studied the transcription and expression profile of MMP-9 and TIMP-1 using qualitative PCR and immunoblotting techniques. Gelatin zymography and reverse zymography techniques were also employed to ascertain the activity of MMP-9 and TIMP-1, respectively.

We observed that under hyperglycemic conditions, the transcription, expression as well as activity of MMP-9 increased by ~ 2.46-fold ($p < 0.001$; Fig. 5A and B), ~4.14-fold ($p < 0.001$; Fig. 5D and E), and ~ 2.78-fold ($p < 0.001$; Fig. 5G) respectively compared to cells maintained in normoglycemic conditions. Consequently, TIMP-1 transcription, expression and activity decreased by ~ 1.59-fold ($p < 0.001$; Fig. 5A and C), ~1.4-fold ($p < 0.01$; Fig. 5D and F), and ~ 3.41-fold ($p < 0.001$; Fig. 5H) respectively, compared to normoglycemic condition.

Treatment with Shatavarin-IV reverted these changes. The transcription, expression, and activity of MMP-9 decreased by ~ 2.67-fold ($p < 0.05$; Fig. 5A and B), ~2.63-fold ($p < 0.05$; Fig. 5D and E), and ~ 1.88-fold ($p < 0.001$; Fig. 5G), respectively compared to hyperglycemic condition. Whereas, transcription, expression and activity of TIMP-1 increased by ~ 1.94-fold ($p < 0.05$; Fig. 5A and C), ~1.44-fold ($p < 0.01$; Fig. 5D and F), and ~ 2.63-fold ($p < 0.001$; Fig. 5H) respectively compared to hyperglycemic cells.

We further performed an immunocytochemistry analysis to visualize the expression pattern of MMP-9 (stained with Texas Red). The images showed that MMP-9 expression was enhanced in cells maintained under hyperglycemic conditions; whereas Shatavarin-IV treatment reverses the expression of MMP-9 as shown by the decrease in Texas red fluorescence (Fig. 5I).

4. Discussion

Gastric cancer is the fifth leading cause of cancer-associated death, in spite of recent advances in cancer therapy [1]. At the same time, the number of diabetic cases is also on a global rise, due to the changed human lifestyle [3]. Since cancer cells are mostly dependent on glucose for their metabolic needs; hyperglycemic condition in patients with diabetes provides a conducive environment for cancer progression and significantly enhances their metastatic capabilities [6]. Such effects have been documented previously in lung cancer [15], cholangiocarcinoma [16], and breast cancer [17]. It is common knowledge that the primary factor behind cancer morbidity and mortality is cancer metastasis, accounting for about ≥ 90 % of cancer deaths [18]. Metastasis is a complex multi-step process that includes various factors like cell proliferation, motility, invasion, and adhesion [19]. To treat cancer metastasis effectively, potential drugs should be evaluated based on their capability to counter these fundamental metastatic processes.

We observed that hyperglycemia does indeed aggravate the proliferative, migratory and invasive capabilities of AGS cells. After being treated with Shatavarin-IV, the number of AGS cell colonies formed

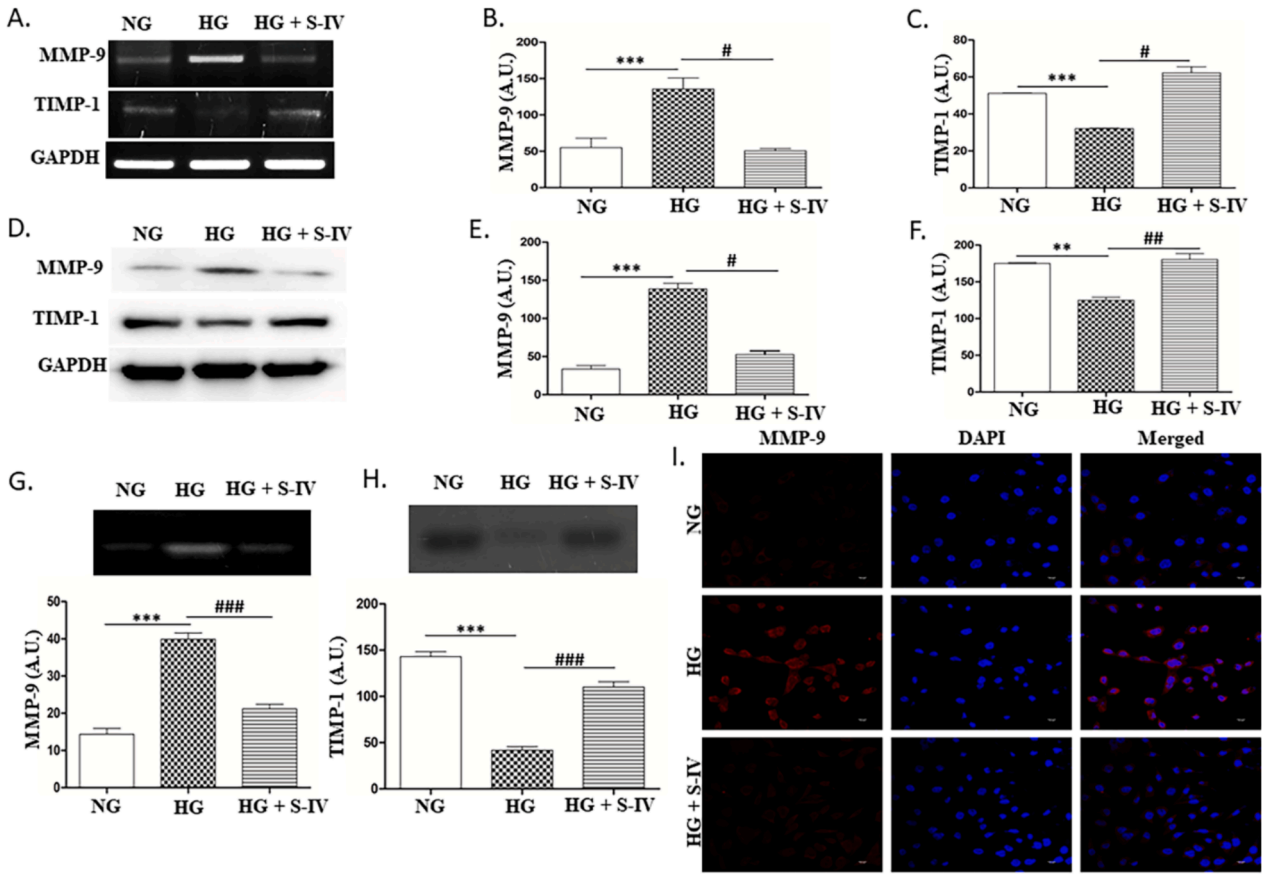

Fig. 5. Shatavarin-IV reverses hyperglycemia-induced changes in MMP-9 and TIMP-1 levels. (A) Conventional RT-PCR of the expression patterns of MMP-9 and TIMP-1 in normoglycemic, hyperglycemic, and 2.2 μM Shatavarin-IV treated hyperglycemic AGS cells for 24 h. GAPDH was used as a loading control. Each image is representative of five individual experiments. (B–C) Densitometric analysis of the expression pattern of MMP-9 and TIMP-1, respectively, at the mRNA level in the three treatment groups. (D) Western blot analysis of the expression patterns of MMP-9 and TIMP-1 in normoglycemic, hyperglycemic, and 2.2 μM Shatavarin-IV treated hyperglycemic AGS cells for 24 h. GAPDH was used as a loading control. Each blot is representative of five individual experiments. (E–F) Densitometric analysis of the expression pattern of MMP-9 and TIMP-1, respectively, at the protein level in the three treatment groups. (G) Gelatin zymography along with densitometric analysis of MMP-9 activity in the three treatment groups. (H) Reverse zymography along with densitometric analysis of TIMP-1 activity in the three treatment groups. (I) Representative images of MMP-9 immunostaining in normoglycemic, hyperglycemic, and 2.2 μM Shatavarin-IV treated hyperglycemic AGS cells for 24 h. The red fluorescence (Texas Red) represents MMP-9 protein and the blue fluorescence (DAPI) represents nucleus. Each image is representative of five individual experiments. Values are mean ± SEM. Comparison between groups was done using the Student's *t*-test. ***p < 0.001, **p < 0.01 (vs. 'NG'); ###p < 0.001, ##p < 0.01, #p < 0.05 (vs. 'HG').

under hyperglycemic conditions was greatly reduced. Shatavarin-IV treatment further reduced the rate of migration and invasion of hyperglycemic AGS cells to a significant extent. PCR and western blot analyses suggest that such changes may be due to a significant increase in the expression pattern of the epithelial marker E-cadherin accompanied by a decrease in the expression pattern of mesenchymal markers like *N*-cadherin, β-catenin, and vimentin.

E-cadherin is the main component responsible for cell–cell and cell-matrix adhesion and is essential for maintaining and establishing the epithelial integrity of the extracellular matrix (ECM) [20]. A decrease in E-cadherin expression under hyperglycemic conditions, as shown by our study, will therefore disrupt cell–cell and cell-matrix adhesion, promoting invasion and metastasis of AGS cells. Further, E-cadherin cleavage during EMT leads to the release of β-catenin, which acts as a transcriptional activator for AGS cell proliferation. It was reported that the β-catenin/*T*-Cell Factor (TCF) pathway, in turn, induces *N*-cadherin expression by regulating the expression of WNT-7A [21]. The switch from the epithelial E-cadherin to the mesenchymal *N*-cadherin is associated with enhanced migratory and invasive traits [22].

Cleavage of E-cadherin can be induced by matrix metalloproteinases (MMPs), which are mostly responsible for tumor cell migration. MMP-9 is crucial for the breakdown of the basement membrane and extracellular matrix, thereby creating a favorable milieu for cancer metastasis [23]. Almost all types of cancer have elevated MMP-9 levels, which are linked to advanced tumors, greater invasion and metastasis, and decreased survival times [24,25]. Furthermore, hyperglycemia is reported to enhance the levels of MMP-9 in lung cancer cells [15] and breast cancer cells [17]. Our results also corroborate with these reports. Further, our results revealed that treatment with Shatavarin-IV reversed this hyperglycemia-induced upregulation of MMP-9. The gelatinolytic activity of MMP-9 was also reduced significantly after Shatavarin-IV treatment. In contrast, the activity and expression of TIMP-1 was significantly increased upon Shatavarin-IV treatment. These results demonstrate that MMP-9 and TIMP-1 mediated ECM turnover is a monumental aspect in the mechanisms of action of Shatavarin-IV on AGS cells.

Furthermore, AGS cells grown in hyperglycemic conditions had a slightly higher expression of Cyclin D1 and CDK-4 which in turn is responsible for the observed increase in Rb phosphorylation as well as E2F-induced Cyclin E and CDK-2 expression. The result is concomitant with the fact that the progression of the cell cycle from G1 to S phase is dependent on the activation of the Rb/E2F complex which in turn is regulated by the Cyclin D1/CDK-4 complex. It is known that under normal conditions, hypo-phosphorylated Rb remains complexed with

E2F, thereby causing its inactivation [26]. Cyclin D combines with CDK4/6 and hyper-phosphorylates Rb, leading to its dissociation from the E2F complex. All these events lead to the transcription of key S phase-promoting genes. In corroboration with the study by Kim et al. [27], our findings also suggest that hyperglycemia significantly increases cell proliferation by accelerating the cell cycle progression. Additionally, the downregulation of Cyclin D1 upon Shatavarin-IV treatment indicates the decreased activity of the Cyclin D1-CDK4 complex. The reduced phosphorylation of Rb after Shatavarin-IV treatment suggests the repressed E2F activity by the inhibition of Rb hyper-phosphorylation. This inhibition of E2F activity is, in turn, leading to the observed cell cycle arrest at G0/G1 phase. Shatavarin-IV treatment, therefore, inhibits the AGS cell's ability to progress through the cell cycle and forces it to enter into a quiescent state. However, a majority of contemporary anti-cancer drugs achieve their anti-cancer effect by activating the apoptotic pathway but we observed that Shatavarin-IV at 2.2 μM concentration was not sufficient to activate the apoptotic pathway after 24 h. Flow cytometry and TUNEL assays showed that apoptotic death of hyperglycemic AGS cells occurs at 36 h of incubation with Shatavarin-IV. Such a delayed induction of apoptosis may be attributed to the fact that hyperglycemia is known to contribute to a more malignant phenotype by inhibiting apoptosis [28].

Treatment of GC has remained a clinically challenging endeavor for a long time. It is mostly limited to two different approaches involving neoadjuvant chemotherapy followed by gastrectomy or primary surgical resection followed by chemotherapy [29]. Standard chemotherapy, therefore, has been the cornerstone of gastric cancer treatment for decades. Drugs like 5-fluorouracil, leucovorin, cisplatin, carboplatin, nivolumab, trifluridine, ramucirumab, paclitaxel, and trastuzumab deruxtecan are usually administered as first-, second-, or third-line treatments for GC [30]. However, such chemotherapeutic agents show varying degrees of effectiveness and are often accompanied by severe side effects which greatly affect the quality-of-life of GC patients. Upon comparing the efficacy of Shatavarin-IV with one such chemotherapeutic agent, 5-Fluorouracil, we have observed that Shatavarin-IV can induce GC cell death at far lower concentrations than 5-Fluorouracil. Additionally, comparing the efficacy of Shatavarin-IV with other natural products that have shown promise in GC treatment is also essential to help position Shatavarin-IV within the broader landscape of GC therapies. For instance, the anti-gastric cancer effects of compounds like curcumin, quercetin, resveratrol and sulforaphane have been well-established. Previous reports suggest that these natural compounds can induce apoptosis, inhibit cell proliferation, and reduce metastasis in GC cells [31]. Interestingly, Shatavarin-IV also works in the same way by inhibiting AGS cell proliferation via G0/G1 phase cell cycle arrest leading to apoptotic cell death as well as metastatic inhibition. While Shatavarin-IV demonstrated such results in vitro at micromolar concentrations, further study is needed to have an in-depth understanding of the mechanism of its action as well as to assess the clinical validity of this promising natural product.

5. Conclusion

Taken together, our results showed that a hyperglycemic environment can induce AGS cell proliferation and metastasis by modulating MMP-9 expression. Shatavarin-IV inhibits metastasis by altering the expression of different EMT markers as well as MMP-9, which regulates tumor cell migration. It also increases the expression of TIMP-1; thereby regulating MMP-9 activity as well. Shatavarin-IV also prevents hyperglycemia-induced excessive cell proliferation via cell cycle arrest at the G0/G1 phase in the early hours and induces apoptosis in the later hours. To the best of our knowledge, we are the first to document the anti-cancer effects of Shatavarin-IV in AGS cell line. Our results suggest that Shatavarin-IV has the potential to be developed as an anti-gastric cancer drug. By demonstrating the efficacy of Shatavarin-IV on AGS cells grown in hyperglycemic conditions, our study gives new insights into the treatment of patients with GC-diabetes co-morbidity.

Funding

This study was supported by institutional grant no. P-07 from CSIR-Indian Institute of Chemical Biology, Kolkata, India.

CRediT authorship contribution statement

Abhishek Chatterjee: Writing – original draft, Investigation, Formal analysis, Data curation, Conceptualization. **Tapasi Roy:** Writing – review & editing, Validation, Investigation. **Vineet Kumar Mishra:** Writing – review & editing, Investigation. **Snehasikta Swarnakar:** Writing – review & editing, Supervision, Resources, Funding acquisition, Conceptualization.

Declaration of Competing Interest

The authors declare that they have no known competing financial interests or personal relationships that could have appeared to influence the work reported in this paper.

Data availability

Data will be made available on request.

Acknowledgments

A.C. is thankful to the University Grants Commission (UGC), India for providing financial support. T.R. acknowledges the receipt of National Post-Doctoral Fellowship from SERB. V.K.M. acknowledges the receipt of Research Associate fellowship from the Department of Biotechnology (DBT), Ministry of Science & Technology, Government of India. We acknowledge Director, CSIR-IICB for his kind support.

Appendix A. Supplementary data

Supplementary data to this article can be found online at https://doi.org/10.1016/j.steroids.2024.109487.

References

[1] H. Sung, J. Ferlay, R.L. Siegel, M. Laversanne, I. Soerjomataram, A. Jemal, F. Bray, Global cancer statistics 2020: GLOBOCAN estimates of incidence and mortality worldwide for 36 cancers in 185 countries, CA Cancer J. Clin. 71 (3) (2021) 209–249, https://doi.org/10.3322/caac.21660.
[2] F., Li, H. Du, S. Li, J. Liu, The association between metabolic syndrome and gastric cancer in Chinese, Front. Oncol. 8 (2018) 326, https://doi.org/10.3389/fonc.2018.00326.
[3] E. Standl, K. Khunti, T.B. Hansen, O. Schnell, The global epidemics of diabetes in the 21st century: Current situation and perspectives, Eur. J. Prev. Cardiol. 26 (2_suppl) (2019) 7–14, https://doi.org/10.1177/2047487319881021.
[4] D. Hanahan, R.A. Weinberg, Hallmarks of cancer: The next generation, Cell 144 (5) (2011) 646–674, https://doi.org/10.1016/j.cell.2011.02.013.
[5] C. Phoomak, K. Vaeteewoottacharn, A. Silsirivanit, C. Saengboonmee, W. Seubwai, K. Sawanyawisuth, C. Wongkham, S. Wongkham, High glucose levels boost the aggressiveness of highly metastatic cholangiocarcinoma cells via O-GlcNAcylation, Sci. Rep. 7 (2017) 43842, https://doi.org/10.1038/srep43842.
[6] J. Wu, J. Chen, Y. Xi, F. Wang, H. Sha, L. Luo, Y. Zhu, X. Hong, S. Bu, High glucose induces epithelial-mesenchymal transition and results in the migration and invasion of colorectal cancer cells, Exp. Ther. Med. 16 (1) (2018) 222–230, https://doi.org/10.3892/etm.2018.6189.
[7] J.M. Yoon, K.Y. Son, C.S. Eom, D. Durrance, S.M. Park, Pre-existing diabetes mellitus increases the risk of gastric cancer: A meta-analysis, World J. Gastroenterol. 19 (6) (2013) 936–945, https://doi.org/10.3748/wjg.v19.i6.936.
[8] A. Sekikawa, H. Fukui, T. Maruo, T. Tsumura, Y. Okabe, Y. Osaki, Diabetes mellitus increases the risk of early gastric cancer development, Eur. J. Cancer 50 (12) (2014) 2065–2071, https://doi.org/10.1016/j.ejca.2014.05.020.
[9] X. Liang, J. Zhu, Y. Li, Y. Xu, K. Chen, L. Lv, W. Mao, Treatment strategies for metastatic gastric cancer: Chemotherapy, palliative surgery or radiotherapy? Future Oncol. 16 (5) (2020) 91–102, https://doi.org/10.2217/fon-2019-0495.
[10] A.G. Atanasov, S.B. Zotchev, V.M. Dirsch, International Natural Product Sciences Taskforce, C.T. Supuran, Natural products in drug discovery: advances and

opportunities, Nat. Rev. Drug Discov. 20 (3) (2021) 200–216, https://doi.org/10.1038/s41573-020-00114-z.
[11] N. Bopana, S. Saxena, Asparagus racemosus—ethnopharmacological evaluation and conservation needs, J. Ethnopharmacol. 110 (1) (2007) 1–15, https://doi.org/10.1016/j.jep.2007.01.001.
[12] S.K. Mitra, N.S. Prakash, R. Sundaram, Shatavarins (containing Shatavarin IV) with anticancer activity from the roots of Asparagus racemosus, Indian J. Pharmacol. 44 (6) (2012) 732–736, https://doi.org/10.4103/0253-7613.103273.
[13] P. Choudhary, T. Roy, A. Chatterjee, V.K. Mishra, S. Pant, S. Swarnakar, Melatonin rescues swim stress induced gastric ulceration by inhibiting matrix metalloproteinase-3 via down-regulation of inflammatory signaling cascade, Life Sci. 297 (2022) 120426, https://doi.org/10.1016/j.lfs.2022.120426.
[14] T. Roy, A. Chatterjee, S. Swarnakar, Rotenone induced neurodegeneration is mediated via cytoskeleton degradation and necroptosis, Biochim. Biophys. Acta Mol. Cell. Res. 1870 (3) (2023) 119417, https://doi.org/10.1016/j.bbamcr.2022.119417.
[15] X. Kang, F. Kong, X. Wu, Y. Ren, S. Wu, K. Wu, Z. Jiang, W. Zhang, High glucose promotes tumor invasion and increases metastasis-associated protein expression in human lung epithelial cells by upregulating heme oxygenase-1 via reactive oxygen species or the TGF-β1/PI3K/AKT signaling pathway, Cell Physiol. Biochem. 35 (3) (2015) 1008–1022, https://doi.org/10.1159/000373928.
[16] C. Saengboonmee, W. Seubwai, C. Pairojkul, S. Wongkham, High glucose enhances progression of cholangiocarcinoma cells via STAT3 activation, Sci. Rep. 6 (2016) 18995, https://doi.org/10.1038/srep18995.
[17] X.F. Sun, Y.B. Shao, M.G. Liu, Q. Chen, Z.J. Liu, B. Xu, S.X. Luo, H. Liu, High-concentration glucose enhances invasion in invasive ductal breast carcinoma by promoting Glut1/MMP2/MMP9 axis expression, Oncol. Lett. 13 (5) (2017) 2989–2995, https://doi.org/10.3892/ol.2017.5843.
[18] J. Fares, M.Y. Fares, H.H. Khachfe, H.A. Salhab, Y. Fares, Molecular principles of metastasis: A hallmark of cancer revisited, Signal Transduct. Target Ther. 5 (1) (2020) 28, https://doi.org/10.1038/s41392-020-0134-x.
[19] A.W. Lambert, D.R. Pattabiraman, R.A. Weinberg, Emerging biological principles of metastasis, Cell 168 (4) (2017) 670–691, https://doi.org/10.1016/j.cell.2016.11.037.
[20] H. Gao X. Lan S. Li Y. Xue Relationships of MMP-9, E-cadherin, and VEGF expression with clinicopathological features and response to chemosensitivity in gastric cancer Tumour Biol. 39 5 2017 101042831769836 10.1177/1010428317698368.
[21] R. Tuli, S. Tuli, S. Nandi, X. Huang, P.A. Manner, W.J. Hozack, K.G. Danielson, D. J. Hall, R.S. Tuan, Transforming growth factor-beta-mediated chondrogenesis of human mesenchymal progenitor cells involves N-cadherin and mitogen-activated protein kinase and Wnt signaling cross-talk, J. Biol. Chem. 278 (42) (2003) 41227–41236, https://doi.org/10.1074/jbc.m305312200.
[22] K.M. Mrozik, O.W. Blaschuk, C.M. Cheong, A.C. Zannettino, K. Vandyke, N-cadherin in cancer metastasis, its emerging role in haematological malignancies and potential as a therapeutic target in cancer, BMC Cancer 18 (1) (2018) 939, https://doi.org/10.1186/s12885-018-4845-0.
[23] K. Augoff, A. Hryniewicz-Jankowska, R. Tabola, K. Stach, MMP9: A tough target for targeted therapy for cancer, Cancers 14 (7) (2022) 1847, https://doi.org/10.3390/cancers14071847.
[24] E. Gobin, K. Bagwell, J. Wagner, D. Mysona, S. Sandirasegarane, N. Smith, S. Bai, A. Sharma, R. Schleifer, J.X. She, A pan-cancer perspective of matrix metalloproteases (MMP) gene expression profile and their diagnostic/prognostic potential, BMC Cancer 19 (1) (2019) 581, https://doi.org/10.1186/s12885-019-5768-0.
[25] C. Joseph, M. Alsaleem, N. Orah, P.L. Narasimha, I.M. Miligy, S. Kurozumi, I. O. Ellis, N.P. Mongan, A.R. Green, E.A. Rakha, Elevated MMP9 expression in breast cancer is a predictor of shorter patient survival, Breast Cancer Res. Treat. 182 (2) (2020) 267–282, https://doi.org/10.1007/s10549-020-05670-x.
[26] S. van den Heuvel, N.J. Dyson, Conserved functions of the pRB and E2F families, Nat. Rev. Mol. Cell Biol. 9 (9) (2008) 713–724, https://doi.org/10.1038/nrm2469.
[27] D. Kim, B.-N. Ahn, Y. Kim, D.Y. Hur, J.W. Yang, G.B. Park, J.E. Jang, E.J. Lee, M. J. Kwon, T.N. Kim, M.K. Kim, J.H. Park, B.D. Rhee, S.H. Lee, High glucose with insulin induces cell cycle progression and activation of oncogenic signaling of bladder epithelial cells cotreated with metformin and pioglitazone, J. Diabetes Res. 2019 (2019) 2376512, https://doi.org/10.1155/2019/2376512.
[28] M. Kopeć, K. Beton, K. Jarczewska, H. Abramczyk, Hyperglycemia and cancer in human lung carcinoma by means of Raman spectroscopy and imaging, Sci. Rep. 12 (1) (2022) 18561, https://doi.org/10.1038/s41598-022-21483-y.
[29] L. Mocan, Surgical Management of Gastric Cancer: A Systematic Review, J. Clin. Med. 10 (12) (2021) 2557, https://doi.org/10.3390/jcm10122557.
[30] Y. Sato, K. Okamoto, Y. Kida, Y. Mitsui, Y. Kawano, M. Sogabe, H. Miyamoto, T. Takayama, Overview of Chemotherapy for Gastric Cancer, J. Clin. Med. 12 (4) (2023) 1336, https://doi.org/10.3390/jcm12041336.
[31] N. Zhao, W. Wang, H. Jiang, Z. Qiao, S. Sun, Y. Wei, X. Xie, H. Li, X. Bi, Z. Yang, 2023. Natural Products and Gastric Cancer: Cellular Mechanisms and Effects to Change Cancer Progression, Anticancer Agents Med. Chem. 23 (13) (2023) 1506–1518, https://doi.org/10.2174/1871520623666230407082955.

Cell Biochemistry and Biophysics
https://doi.org/10.1007/s12013-024-01241-9

ORIGINAL PAPER

Melatonin Inhibits AGS Cell Proliferation by Binding to the ATP Binding Site of CDK2 Under Hyperglycemic Conditions

Abhishek Chatterjee[1] · Tapasi Roy[1] · Deeti Jyothi[1] · Vineet Kumar Mishra[1] · Umesh Prasad Singh[1] · Snehasikta Swarnakar[1]

Received: 24 January 2024 / Accepted: 21 February 2024

Abstract

Cancer cells utilize glucose as their primary energy source. The aggressive nature of cancer cells is therefore enhanced in hyperglycemic conditions. This study has been adopted to investigate the therapeutic potential of melatonin against such aggressive proliferation of AGS cells–a human gastric cancer cell line, under hyperglycemic conditions. AGS cells were incubated with high glucose-containing media, and the effects of melatonin have been evaluated, therein. Cell proliferation, ROS generation, flow-cytometric analysis for cell cycle and apoptosis, wound healing, immunoblotting, zymography, reverse zymography assays, in-silico analysis, and kinase activity assays were performed to evaluate the effects of melatonin. We observed that melatonin inhibited the hyperglycemia-induced cell proliferation in a dose-dependent manner. It further altered the expression and activity of MMP-9 and TIMP-1. Moreover, melatonin inhibited AGS cell proliferation by arresting AGS cells in the G_0/G_1 phase after binding in the ATP binding site of CDK-2, thereby inhibiting its kinase activity. In association, a significant decrease in the expression of cyclin D1, cyclin E, CDK-4, and CDK-2 were observed. In conclusion, these findings suggest that melatonin has anti-gastric cancer potential. Melatonin could therefore be included in future drug designs for gastric cancer-hyperglycemia co-morbidity treatment.

✉ Snehasikta Swarnakar
snehasiktaiicbidi@gmail.com

[1] Infectious Diseases and Immunology division, CSIR-Indian Institute of Chemical Biology, 4, Raja S.C. Mullick Road, Kolkata 700032 West Bengal, India

Graphical Abstract

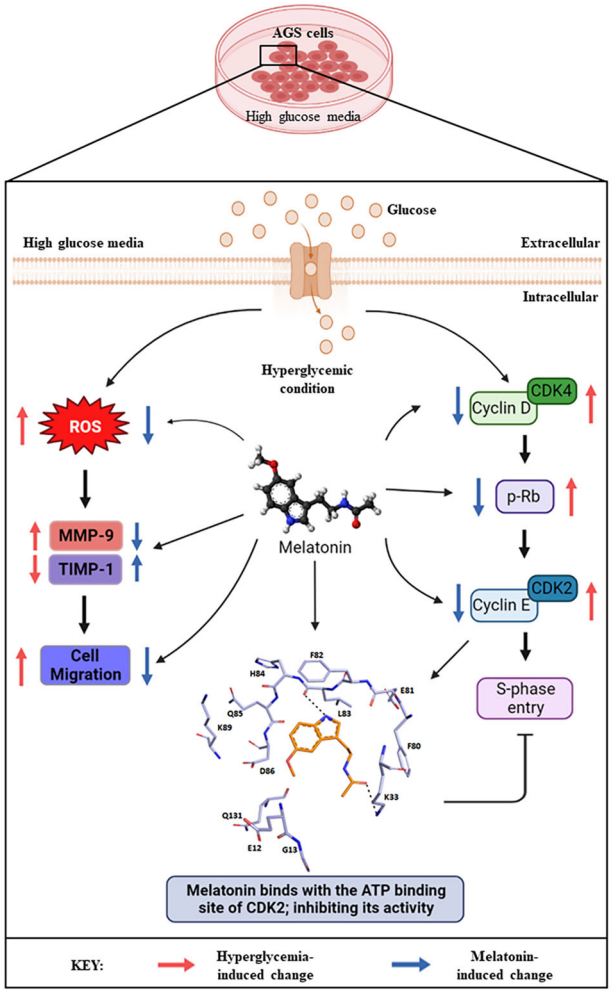

Keywords AGS cells · Hyperglycemia · Melatonin · CDK-2 · MMP-9 · Gastric Cancer

Introduction

Cancer cells consume glucose at a much higher rate than surrounding normal cells [1, 2]. Hyperglycemic condition greatly increases the amount of glucose in the cancer microenvironment; thereby making the situation far more concerning. Hyperglycemia also enhances the production of reactive oxygen species (ROS) through the O-GlcNAcylation of mitochondrial respiratory chain complexes [3]. ROS in turn can stimulate various growth factors and transcription factors, induce cell cycle progression, prevent apoptosis, and induce the expression of various oncogenes including some matrix metalloproteinases (MMPs) [4–7]. MMPs regulate cancer cells' migratory and invasive nature by degrading extracellular matrix proteins [8]. It is reported that hyperglycemia enhances the levels of MMP-9 in lung cancer cells [9] and breast cancer cells [10] and MMP-2 in cholangiocarcinoma cells [11] and breast cancer cells [10]. But, to date, no report has shed light on whether any MMPs are upregulated in gastric cancer (AGS) cells under hyperglycemic conditions.

Since ROS is one of the key factors for the enhanced aggressiveness of cancer cells under hyperglycemic conditions, it is reasonable to think that an antioxidant may be able to reverse this situation. Melatonin is one such naturally occurring antioxidant hormone that is produced and secreted by the pineal gland as well as the enterochromaffin cells of the gastrointestinal tract. By virtue of being produced by the enterochromaffin cells, melatonin is quite stable within the gastric milieu. Although the half-life of melatonin within the gastrointestinal tract is unknown, it has a half-life of ~40 min in the plasma [12]. It is reported to play an important role in inhibiting the growth of different types of cancers by diverse mechanisms [13–16]. Melatonin

is known to enhance the sensitivity of cancer cells to different chemo- or radiotherapy [17]. It is also known to exert its anti-cancer activity through its well-established antioxidant properties [18]. Recent studies suggest that melatonin shows protective effects against cancerous growth in various cancer cell lines, like breast cancer [19], colorectal cancer [20], non-small cell lung cancer [21, 22], prostate cancer [23–25], and many more. It has been reported that melatonin negatively affects the survivability of breast cancer cells by inhibiting their telomerase activity [13], enhancing DNA repairing capability [14], and increasing the susceptibility of different cancer cells to death mechanisms like apoptosis and autophagy [15, 16]. The concentration of melatonin in the gastrointestinal tract is known to be 10–100 times higher than in the plasma [26]; however, under hyperglycemia-gastric cancer comorbidity, the therapeutic potential of melatonin remains to be evaluated.

The present study was adopted to evaluate the therapeutic potential of melatonin and to identify the mechanism through which it performs its anti-cancer activity. The study was performed under hyperglycemic conditions using AGS cells that were established from a patient with gastric adenocarcinoma–the most common form of gastric malignancy.

Material and Methods

Materials

Melatonin, gelatin, casein, Triton-X-100, protease inhibitors, dithiothreitol (DTT), glucose, Tween®-20, Bradford reagent, bovine serum albumin (BSA), and 2'-7'-Dichlorodihydrofluorescein diacetate (DCFH-DA) were purchased from Sigma Chemical Co, St. Louis, MO, USA. CellTiter-Glo luminescent cell viability assay kit, ADP-Glo Kinase Assay kit, and CDK2/Cyclin E2 Kinase Enzyme System were purchased from Promega (Madison, WI, United States). A protease inhibitor cocktail was procured from Calbiochem. Primary antibodies for western blotting were purchased from Santa Cruz Biotechnology (Dallas, TX, USA). The horseradish peroxidase (HRP)-conjugated secondary antibodies were also purchased from Santa Cruz Biotechnology. HRP luminescent substrate solution was purchased from Bio-Rad (Hercules, CA, USA). AGS cells were purchased from the American Type Culture Collection (ATCC, Manassas, VA, USA). All cell culture-related materials were sourced from Gibco (Thermo Fisher, MA, USA).

Cell Culture and Treatment Procedure

AGS cells were grown in Ham's F12K nutrient media supplemented with 10% FBS and 1% Antibiotic-Antimycotic (100×) mixture. The cells were kept at 37 °C in a humidified atmosphere of 5% CO_2 and 95% air. All experiments were performed on AGS cells up to 10 passage numbers.

For experimental purposes, AGS cells were seeded and maintained for 24 h in normoglycemic media supplemented with 10% FBS. Normoglycemic media was prepared with 5.5 mM D-glucose, as this concentration of glucose closely resembles normal blood sugar levels [27]. Afterward, cells were either incubated with serum-free normoglycemic media, serum-free hyperglycemic media (containing 25 mM D-glucose), or hyperglycemic media containing 2 mM melatonin. These three treatment groups were kept constant in all the subsequent experiments and have been designated as control, HG, and HG + MELA, respectively. For each experiment, freshly prepared melatonin was used.

Cell Viability Assay

To determine the effect of high glucose on gastric cancer cell proliferation, AGS cells cultured in normoglycemic media were seeded into 96-well plates. After 24 h, the media was replaced with incomplete media containing increasing concentrations of glucose or mannitol (5.5, 8, 12.5, 25, 35, and 50 mM). Dose- and time-dependent effects of glucose and its osmolarity control, D-mannitol were assayed after 6, 12, 24, and 36 h of incubation. After the respective incubation periods, cell viability was measured using CellTiter-Glo luminescent cell viability assay kit.

To determine the effect of melatonin on cell viability, AGS cells were seeded in a 96-well plate and kept overnight. AGS cells were treated with increasing concentrations of melatonin (0.5-, 1-, 2-, 3-, 4-, and 5 mM) dissolved in HG media. After 24 h, cell viability was determined using the CellTiter-Glo luminescent cell viability assay.

Evaluation of Intracellular ROS Production

We next performed live cell imaging to visualize ROS generated in AGS cells after receiving the treatments. Cells were seeded in confocal dishes and allowed to grow overnight before they received their respective treatments. After 24 h of incubation, cells were washed with PBS and stained with 10 µM DCFH-DA for 30 min at 37 °C, under dark conditions. After washing the cells were visualized using a high-resolution Stimulated Emission Depletion (STED) Microscopy (Leica TCS SP8). The images were representative of five individual experiments to eliminate any artifacts. Further to quantitate ROS, the fluorescence of DCFH-DA from each treatment groups were measured in an F-7 Fluorescence Spectro Photometer (Hitachi High Technologies Corporation) with proper subtraction of background fluorescence (Ex/Em: 485/535 nm) and the results

were represented as fluorescence intensity per microgram of protein.

Flow Cytometric Analysis of Cell Cycle and Apoptosis

To understand the changes in cell cycle progression, AGS cells were plated in 60 mm dishes and kept for 24 h. After incubation with the respective treatments, the cells were trypsinized, washed with PBS, and fixed using ice-cold 70% ethanol with gentle vortexing. Fixed cells were kept at 4 °C for 16–18 h. Any trace of ethanol was removed by washing the cells with PBS. The fixed cells were resuspended in 100 µL of a staining solution containing 50 µg/ml propidium iodide and 100 µg/ml RNaseA. After 15 min of incubation at room temperature, the stained cells were analyzed by BD LSRFortessa™ Cell Analyzer equipped with BD FACSDiva Software.

For the analysis of apoptosis, AGS cells were plated in 60 mm dishes. After 24 h of incubation with the respective treatments, the cells were trypsinized, washed with PBS, and processed using the FITC Annexin V Apoptosis Detection kit I (BD Pharmingen, BD Biosciences, Franklin Lakes, NJ, USA), as per the manufacturer's protocol. The stained cells were analyzed by BD LSRFortessa™ Cell Analyzer equipped with BD FACSDiva Software.

Gelatin Zymography

The gelatinolytic activity of MMP-9 was assayed by the gelatin zymography technique. Briefly, conditioned media (70 µg total protein) from AGS cells were electrophoresed in 8% SDS-polyacrylamide (PAGE) gel containing 1 mg/ml gelatin, under non-reducing conditions. The gels were washed in 2.5% Triton-X-100 and incubated in assay buffer (40 mM Tris-HCl, pH 7.4; 0.2 M NaCl; 10 mM $CaCl_2$) for 18 h at 37 °C. The gel was stained with 0.1% Coomassie blue followed by de-staining. The gelatinolytic activity was visualized as negatively stained bands and quantified by densitometry using the ImageJ software.

Reverse Zymography

The enzymatic activity of TIMP-1 was assayed by reverse zymography technique. Briefly, after 24 h of incubation with the respective treatments, conditioned media was collected and 70 µg total protein was electrophoresed in 12% SDS-PAGE containing 1 mg/ml gelatin and an MMP source, under non-reducing conditions. The conditioned media from MDA-MB-231 cells was used as the MMP source for this assay. After electrophoresis, the gels were processed similarly, as mentioned for gelatin zymography. The bands of TIMP-1 activity were visualized as colored bands and quantified by densitometry using the ImageJ software.

Wound Healing Assay

AGS cells were seeded into six-well plates and after reaching 90% confluency, the monolayer of cells was scratched while maintaining a sterile condition. Scratched cells were washed off with PBS and given their respective treatments. Images were captured at 0 h. and 24 h. time-points with an Olympus I×71 inverted microscope.

Immunoblotting

After a 24 h incubation with the respective treatments, the cells were washed with PBS, trypsinized, and pelleted down. Cell pellets were lysed (Lysis buffer: 20 mM Tris-HCl, 150 mM NaCl, 1% Triton X-100, 1× PIC, and 1 mM PMSF; pH 7.4) and centrifuged at 12,000 rpm for 10 min at 4 °C. Supernatants were collected and the protein concentrations were estimated using the Bradford assay. An equal amount of protein (50 µg) from each group was subjected to 10% SDS-PAGE and transferred onto PVDF membranes. The PVDF membranes were then blocked with 3% BSA in TBST (137 mM NaCl, 2.7 mM KCl, 50 mM Tris-HCl, and 0.1% Tween-20; pH 7.4) for 2 h at room temperature, and incubated with appropriate primary antibodies overnight at 4 °C. The membrane was washed in TBST and incubated with the corresponding HRP-conjugated secondary antibodies. The blot was developed using a western ECL substrate solution (Bio-Rad Laboratories, USA) Images were taken using the Bio-Rad ChemiDoc™ MP imaging system. Protein expression levels were quantified by densitometry using the ImageJ software. GAPDH was used as the loading control.

Molecular Docking

An AUTODOCK Vina software was used for the molecular docking study [28]. The co-crystallized three-dimensional (3D) atomic coordinate for the Cyclin Dependent Kinase-2 (CDK-2)/Cyclin E enzyme (PDB ID: 7KJS) was used as a standard reference which was retrieved from the PDB database (https://www.rcsb.org/) [29]. Initially, we performed docking of the co-crystallized ligand (PF-06873600) for validation of our docking protocol. Our docked pose matched well with the crystallized ligand pose, with an RMSD value of 0.5 Å, showing standard interactions with Leu83, Asp86, Lys89, and Gln131 [30]. The same docking grid, created during docking validation, was used for our test molecules. The docking grid box size was $72 \times 84 \times 68$ Å with centre at X = 25.522 Å; Y = 5.261 Å; Z = −15.164 Å. The exhaustiveness was kept at 8, and 1 Å grid spacing was used for energy calculations. The receptor was prepared by using PyMol software [31]. After removal of all non-standard atoms and water molecules, the gasteiger charges and polar hydrogens were added and the

structure was saved in .pdbqt format by using MGL Tools 1.5.6. The structure of melatonin was drawn in ChemDraw Ultra 10.0 software and saved in .mol format. Then the 3-D structure of melatonin was optimized using Marvinsketch software [32] and saved in .pdbqt format. Docking of melatonin with the receptor (PDB ID: 7KJS) was also performed using Autodock Vina software in a blinded rigid receptor docking method. The entire protein was used for docking rather than just the active site. The final deviations in the receptor-structure-complex were regularized by energy minimization with the GROMOS96 force field using Deep View, by applying the 200-steps steepest descent algorithm and 200-step conjugate gradients algorithm. The visualization and image generation of the protein-melatonin complex was performed using the PyMol software (Schrödinger, LLC).

MD Simulations

Nanoscale Molecular Dynamics (NAMD) software (http://www.ks.uiuc.edu/Research/namd/) was used to carry our Molecular Dynamics (MD) simulations for the docked complex of CDK-2/Cyclin E enzyme receptor with melatonin [33]. The VMD software (https://www.ks.uiuc.edu/Research/vmd/) [34] and CHARM-Gui server (https://www.charmm-gui.org) [35–37] were used to generate a protein structure file (.psf) of CDK-2/Cyclin E enzyme and topology files for melatonin respectively. The cube-shaped three-point water model (TIP3) system was used to solvate the entire system followed by neutralization using Sodium or Chlorine counter ions. The system minimization before the dynamics study was carried out for 2000 steps and then equilibrated using a constant number of particles, pressure, and temperature (NVT) for 200 ps (pico-seconds) at 300 K. The final run of MD simulations was carried out for 100 ns (nano-seconds) (1,00,000 steps of 1 ps each). The analysis and plot generation were done using VMD software.

In Vitro Kinase Assay

The kinase activity of CDK-2/Cyclin E1 with varying concentrations of melatonin was measured using the ADP-Glo Kinase Assay kit (Promega), as per the manufacturer's protocols. Staurosporine, a broad-spectrum protein kinase inhibitor, was used as a positive control for this experiment. Luminescence was measured with Glomax, 20/20 Luminometer, USA using a 1 s integration time and normalized to the vehicle control. The IC50 values for staurosporine and melatonin were determined by fitting their respective relative luminescence data from three independent experiments to a quadratic binding model using non-linear regression in GraphPad Prism.

Protein Estimation

The protein concentration of AGS cell pellets was estimated using Bradford assay (Sigma, USA) after solubilization of the cell membranes in cell lysis buffer.

Statistical Analysis

All data has been represented as mean ± SEM of five independent experiments. The statistical analysis was done using GraphPad Prism (version 5.01, San Diego, California, USA) software. Student's t-test was used to compare the two groups. In all representations, statistically significant differences are indicated as $^{*}p \le 0.05$, $^{\#}p \le 0.05$, $^{**}p \le 0.01$, $^{\#\#}p \le 0.01$, $^{***}p \le 0.001$ and $^{\#\#\#}p \le 0.001$, ns = not significant ($p > 0.05$).

Results

Melatonin Alters Hyperglycemia-induced AGS Cell Proliferation

We have incubated AGS cells with varying concentrations of D-glucose (5.5, 8, 12.5, 25, 35, and 50 mM) to ascertain the dose to induce hyperglycemic (HG) condition (Fig. 1A). The effect of different glucose concentrations on AGS cell proliferation has also been monitored at different time-points (6, 12, 24, and 36 h) using the CellTiter-Glo luminescent cell viability assay (Fig. 1A). We observed significantly enhanced proliferation rate in cells incubated with up to 25 mM glucose, compared to the normoglycemic control (Fig. 1A). We have also used different concentrations of D-mannitol (5.5, 8, 12.5, 25, 35, and 50 mM) as osmolarity control, to help negate any effects brought about by the change in media osmolarity. AGS cell proliferation has also been monitored thereafter at different time points (6, 12, 24, and 36 h) using the CellTiter-Glo luminescent cell viability assay (Fig. 1A). We found that mannitol has almost no effect on AGS cell proliferation (Fig. 1A), whereas the difference in cell viability between control and HG treatment groups was observed to be maximum at 24 h of incubation with 25 mM D-glucose (Fig. 1A). Therefore, all subsequent experiments were performed using 25 mM glucose for 24 h.

To investigate the effect of melatonin on the viability of AGS cells under HG condition (with 25 mM D-glucose), cells were treated with or without varying concentrations of melatonin (0.5-, 1-, 2-, 3-, 4-, and 5 mM) for 24 h. We observed that melatonin inhibited AGS cell viability in a dose-dependent manner (Fig. S1). The IC_{50} value of melatonin was found to be ~3.8 mM in HG conditions. In the subsequent experiments, we used 2 mM melatonin since this concentration was able to counter the effect of

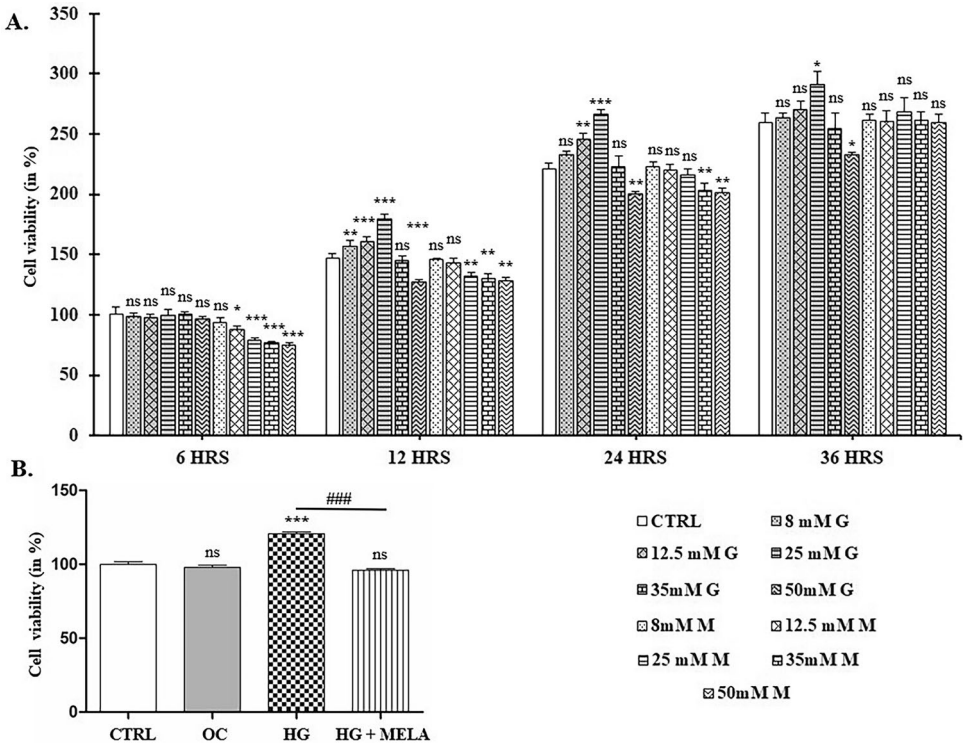

Fig. 1 Melatonin reverses hyperglycemia-induced AGS cell proliferation. **A** AGS cells were treated with increasing concentrations of D-glucose or D-mannitol (5.5, 8, 12.5, 25, 35, and 50 mM). After respective incubation periods of 6, 12, 24, and 36 h, cell viability was measured using CellTiter-Glo luminescent cell viability assay kit according to the manufacturer's instructions. Values are mean ± SEM. Comparison between groups was done using the Student's t-test. $^{***}p < 0.001$, $^{**}p < 0.01$, $^{*}p < 0.05$ (vs. respective 'CTRL' group of each time-point), and "ns" represent non-significant. **B** AGS cells were treated with 25 mM D-mannitol (OC), 25 mM D-glucose (HG), and 2 mM melatonin in HG media (HG + MELA) for 24 h. Cell viability was measured using a CellTiter-Glo luminescent cell viability assay kit according to the manufacturer's instructions. Values are mean ± SEM. Comparison between groups was done using the Student's t-test. $^{***}p < 0.001$ (vs. 'CTRL'); $^{\#\#\#}p < 0.001$ (vs. 'HG'), and "ns" represent non-significant

hyperglycemia on AGS cells by bringing the viability down to near normoglycemic control levels (Fig. 1B).

Melatonin Counters Hyperglycemia-induced ROS Generation in AGS Cells

To visualize and quantify the amount of ROS produced within AGS cells under HG conditions, we used a cell-permeable ROS-detecting dye, DCFH-DA. 50 µM H_2O_2 was used as a positive control for ROS generation and 2.5 mM NAC was used as a negative control for its ROS quenching activity. Live cell imaging using high-resolution STED microscopy revealed that H_2O_2-treated cells had the highest DCFH-DA fluorescence; followed by cells maintained under HG conditions in comparison to the control cells, whereas NAC pre-treatment prevented ROS production. Further, melatonin treatment showed a marked reduction in the ROS level (Fig. 2A).

A similar trend was observed in the quantitative analysis for ROS using the F-7 Fluorescence Spectro Photometer. Upon fluorometric analysis, it was observed that H_2O_2 insult induced a ~ 2.49-fold increase in DCFH-DA fluorescence, compared to the control. Whereas, AGS cells grown in HG media showed a ~ 1.44-fold increase in DCFH-DA fluorescence. Such elevations in DCFH-DA fluorescence were not observed in NAC pre-treated groups which had lower DCF fluorescence values compared to the control AGS cells (Fig. 2B). These results indicate the involvement of ROS in AGS cells under hyperglycemic conditions. Melatonin effectively quenched the ROS produced (1.36-fold decrease in DCF fluorescence) within AGS cells under HG conditions (Fig. 2B).

Melatonin Inhibits the Migration Ability of AGS Cells Under Hyperglycemic Conditions by Reversing the Activity and Expression of MMP-9 and TIMP-1

Gelatin zymography and immunoblotting techniques were employed to ascertain the impact of hyperglycemia on MMP-9 activity and expression profile respectively. We observed a ~ 2.15-fold increase in MMP-9 activity (Fig. 3A) and a ~ 2.04-fold increase in its expression (Fig. 3C, D) in cells maintained under HG conditions. Moreover, treatment with melatonin brought down the activity (Fig. 3A) and

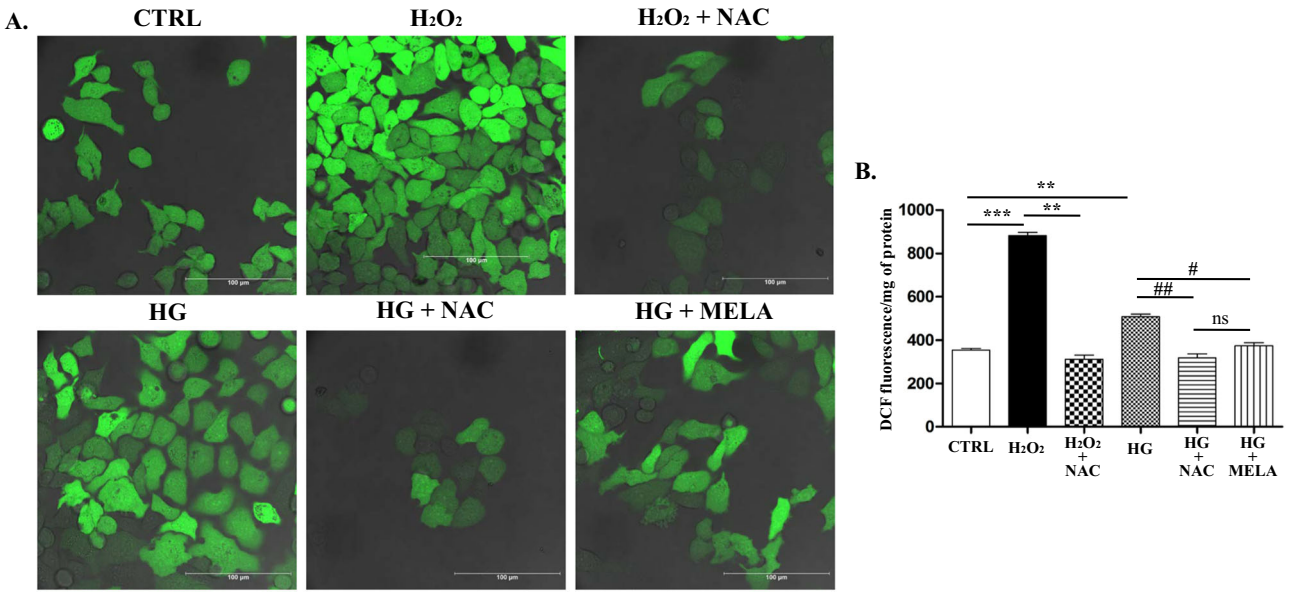

Fig. 2 Melatonin counters hyperglycemia-induced ROS generation. **A** After 24 h of respective treatments, AGS cells were stained with DCFH-DA, an intracellular ROS-reporting fluorogenic dye. Images were captured using a high-resolution STED microscope at 63× magnification. Each image is representative of five individual experiments. **B** After 24 h of incubation with the respective treatments, AGS cells were stained with DCFH-DA, and their fluorescence was measured in an F-7 Fluorescence Spectrophotometer with proper subtraction of background fluorescence. The bars represent fluorescence intensity per microgram of protein. Values are mean ± SEM. Comparison between groups was done using the Student's t-test. $^{***}p < 0.001$, $^{**}p < 0.01$, $^{*}p < 0.05$ (vs. 'CTRL'); $^{\#\#}p < 0.01$, $^{\#}p < 0.05$ (vs. 'HG'), and "ns" represent non-significant

expression (Fig. 3C, D) of MMP-9 by ~1.55-fold and ~1.22-fold, respectively. HG-induced increase in MMP-9 level was accompanied by a concomitant decrease in TIMP-1 activity (~1.4-fold) (Fig. 3B) and expression (~2.97-fold) (Fig. 3C, E). TIMP-1 activity (Fig. 3B) and expression (Fig. 3C, E) were almost fully recovered after melatonin treatment.

MMP-9 is also known to be a key enzyme playing a crucial role in enhancing tumor cell migration. Therefore, we next analyzed the migratory properties of AGS cells, under HG conditions and treated them with or without melatonin. We observed a higher rate of migration in cells maintained under HG conditions in comparison to the control. Melatonin treatment decreased the rate of migration of AGS cells under HG conditions (Fig. 3F).

Melatonin Arrests Cell Cycle Progression at G_0/G_1 Phase Under Hyperglycemic Conditions

Flow-cytometric analysis was performed to ascertain whether melatonin affects the cell cycle progression of AGS cells grown in HG condition. We noticed a slight alteration in the number of cells in the S phase (from 29.7% in control to 26.3% in HG) and G_2/M-phase (from 14.7% in control to 22.7% in HG) upon incubating AGS cells in HG media (Fig. 4A, B). This was accompanied by a slight decrease in the percentage of cells in the G_0/G_1 phase (from 55.6% in control to 50.9% in HG). We observed a considerable increase in the percentage of cells in the G_0/G_1 phase (from 50.9 to 76.8%) upon melatonin treatment. Furthermore, a decrease in the percentage of cells in the S phase (from 26.3 to 10.6%) and G_2/M phase (from 22.7 to 12.6%) were also observed (Fig. 4A, B) after melatonin treatment.

To further validate this observation, we analyzed the expression patterns of cell cycle regulatory proteins that are important in the continuation of the G_1 phase and transition into the S phase, using the immunoblotting technique. AGS cells under HG conditions showed a ~ 1.23-fold increase in the expression of Cyclin D1 and a similar increase (~1.25-fold) in that of Cyclin E (Fig. 4C, D, F) compared to their normoglycemic control. The expressions of CDK-4 and CDK-2 were increased by ~1.25- and ~1.67-fold, respectively (Fig. 4C, E, G). Additionally, the level of phosphorylated retinoblastoma (p-Rb) was increased by ~1.55-fold, whereas total Rb levels remained almost unchanged (Fig. 4, H, I) in comparison to the normoglycemic control. Melatonin treatment on the other hand significantly reduced CDK-4 (~1.38-fold) and cyclin D1 (~1.52-fold) expression levels (Fig. 4C, D, E). A remarkable decrease in the expression levels of CDK-2 (~4.15-fold) and cyclin E (~3.64-fold) was also observed (Fig. 4C, F, G) upon melatonin treatment. Melatonin further decreased the level of phosphorylated Rb by ~1.2-fold (Fig. 4C, H, I). From these results, it is evident that melatonin induces a cell cycle arrest at the G_0/G_1 phase in AGS cells, under hyperglycemic conditions.

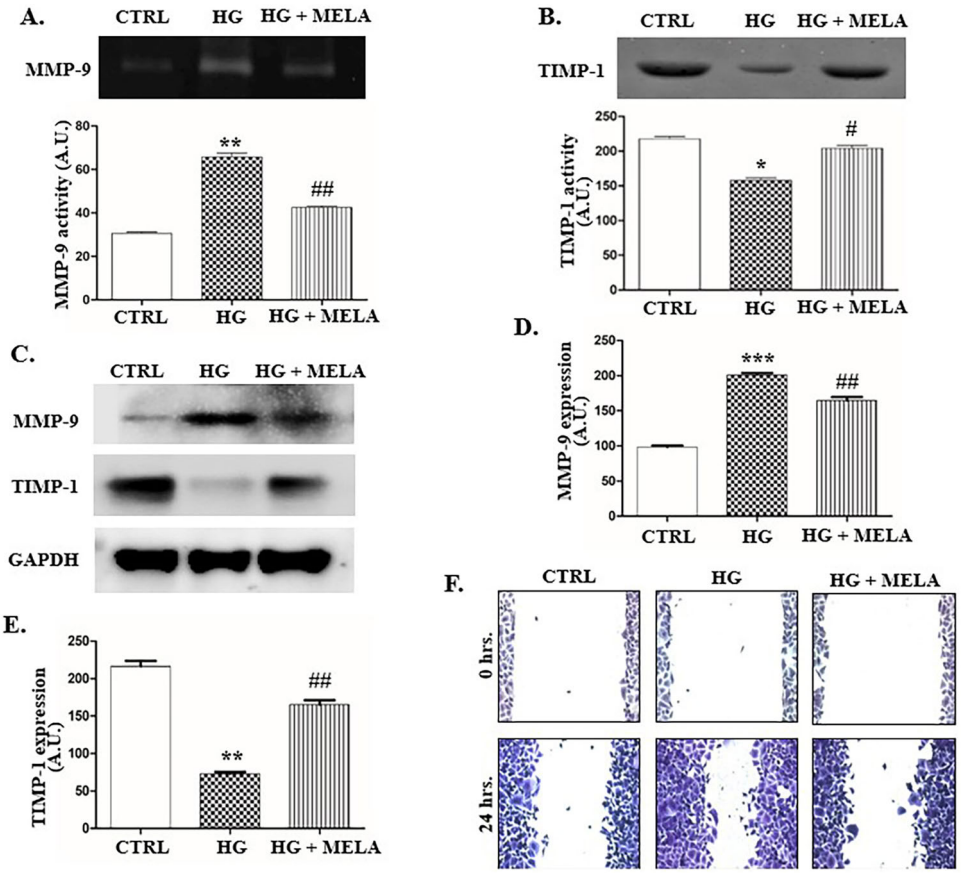

Fig. 3 Melatonin inhibits the migration ability of hyperglycemic AGS cells by reversing the activity and expression of MMP-9 and TIMP-1. **A** Gelatin zymography and densitometric analysis showing the inhibition of MMP-9 activity in hyperglycemic AGS cells after treatment with melatonin. **B** Reverse zymography and densitometric analysis showing the restoration of TIMP-1 activity in hyperglycemic AGS cells after treatment with melatonin. **C** Western blot analysis of the expression patterns of MMP-9 and TIMP-1 using GAPDH as a loading control. Each blot is representative of five individual experiments. **D** Densitometric analysis of the expression pattern of MMP-9. **E** Densitometric analysis of the expression pattern of TIMP-1. **F** Wound healing assay showing the inhibition of hyperglycemic AGS cell migration after treatment with melatonin. Each image is representative of five individual experiments. Densitometric analysis of the zymograms and blots was performed using ImageJ software. Values are mean ± SEM. Comparison between groups was done using the Student's t-test. $^{***}p < 0.001$, $^{**}p < 0.01$, $^{*}p < 0.05$ (vs. 'CTRL'); $^{\#\#}p < 0.01$, $^{\#}p < 0.05$ (vs. 'HG')

Molecular Docking, Dynamics, and MD Simulations of Melatonin with CDK-2/Cyclin E Complex

To find out the possible interactions of melatonin with the CDK-2/Cyclin E complex blind molecular docking was performed. The positive control (PF-06873600) was docked successfully in the ATP binding pocket (active site) of CDK-2, which produced the best pose with a binding energy of −10.2 kcal/mol. The docked pose was similar to that observed in the co-crystallized structure (PDB ID: 7KJS) with Root Mean Square Deviation (RMSD) of 0.5 Å (Fig. S2). The ATP binding site of CDK-2 is formed by the Phe80, Glu81, Phe82, Leu83, Asp86, Lys89, and Gln131 key amino acid residues. The docking results suggested that melatonin can bind in the active site of CDK-2 (ATP binding site) with a binding affinity of −6.3 kcal/mol and interacts with Lys33 and Leu83 residues (Figs. 5A, B & S2). The binding energy suggests that melatonin may be an inhibitor of CDK-2/Cyclin E activity.

Next, we performed the molecular dynamic (MD) simulation to understand the stability of the docked pose of melatonin and its dynamic interactions with the CDK-2/Cyclin E enzyme complex. Melatonin was stable in the active site throughout the simulation time of 100 ns. The RMSD of the protein backbone was around 2.5 Å and the RMSD of melatonin was about 1.95 Å (Fig. 5C). The Root Mean Square Fluctuation (RMSF) was shown in Fig. 5D. The first 1-298 amino acid residues belonging to CDK-2 show less movement (lower RMSF) suggesting lower fluctuations in the 3-D structure of CDK-2 compared to Cyclin E. The average number of H-bonds of melatonin during the MD production run is about 1 as shown in Fig. 5E. The Asp86 and Leu83 residues

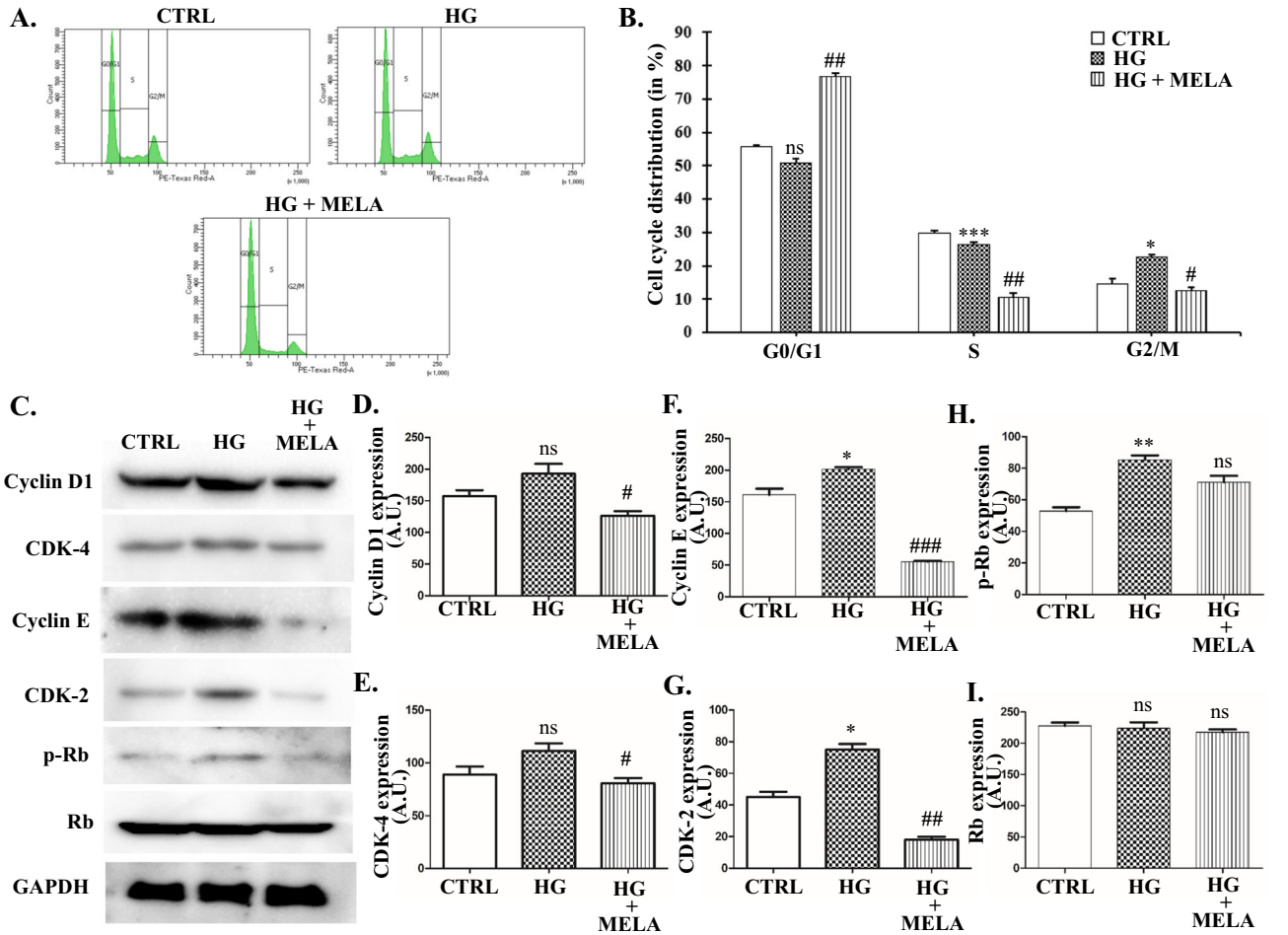

Fig. 4 Melatonin induces cell cycle arrest at G_0/G_1 phase in hyperglycemic AGS cells. **A** After incubating AGS cells for 24 h in the respective treatment media, cells were collected, fixed, and stained with PI. Cell cycle phases were analyzed by flow cytometry. **B** Graphical representation of the percentage of cells present in each phase of the cell cycle. **C** Western blot analysis to detect the expression pattern of cell cycle regulatory proteins using GAPDH as a loading control. **D–I** Densitometric analyses of the expression patterns of Cyclin D1, CDK-4, Cyclin E, CDK-2, p-Rb, and total Rb, respectively. Densitometric analyses of the blots were performed using ImageJ software. Values are mean ± SEM. Comparison between groups was done using the Student's *t*-test. $^{***}p < 0.001$, $^{**}p < 0.01$, $^{*}p < 0.05$ (vs. 'CTRL'); $^{###}p < 0.001$, $^{##}p < 0.01$, $^{#}p < 0.05$ (vs. 'HG'), and "ns" represent non-significant

belonging to the hinge region of CDK-2 play a key role in stabilizing melatonin at the active site with high degrees of H-bond occupancies of 55 and 11% of productive MD run time (65 ns to 100 ns), respectively (Fig. 5F).

During the MD simulation, melatonin was observed to be reoriented around 90° compared to its docked pose. This was attributed to the presence of solvent (water) which is generally removed for docking experiments. During MD simulation partial melting of β-strands close to the active site was observed, involving Gly11-Val18 and His84-Asp86 residues together with a short alpha-helical region (residues Gln131 and Asn132); suggesting movements in the protein to fit with melatonin. Overall, the docking and MD simulation studies show that melatonin binds well with the CDK-2/Cyclin E enzyme complex at the ATP binding site; thereby inhibiting its activity.

Melatonin Inhibits CDK-2/Cyclin E1 Kinase Activity

An in-vitro ADP-Glo Kinase Assay was performed to further validate the results of the in-silico interaction study. We observed that melatonin inhibits CDK-2 kinase activity with an IC_{50} value of 367.1 ± 84 μM (Fig. 6). The positive control, Staurosporine, had a much lower IC_{50} value of 7.288 ± 2.7 nM. This value matches closely with previously reported IC_{50} values of Staurosporine-mediated inhibition of CDK-2 kinase activity. From the results of this experiment, we can conclude that melatonin can indeed affect the kinase activity of the CDK-2/Cyclin E1 complex.

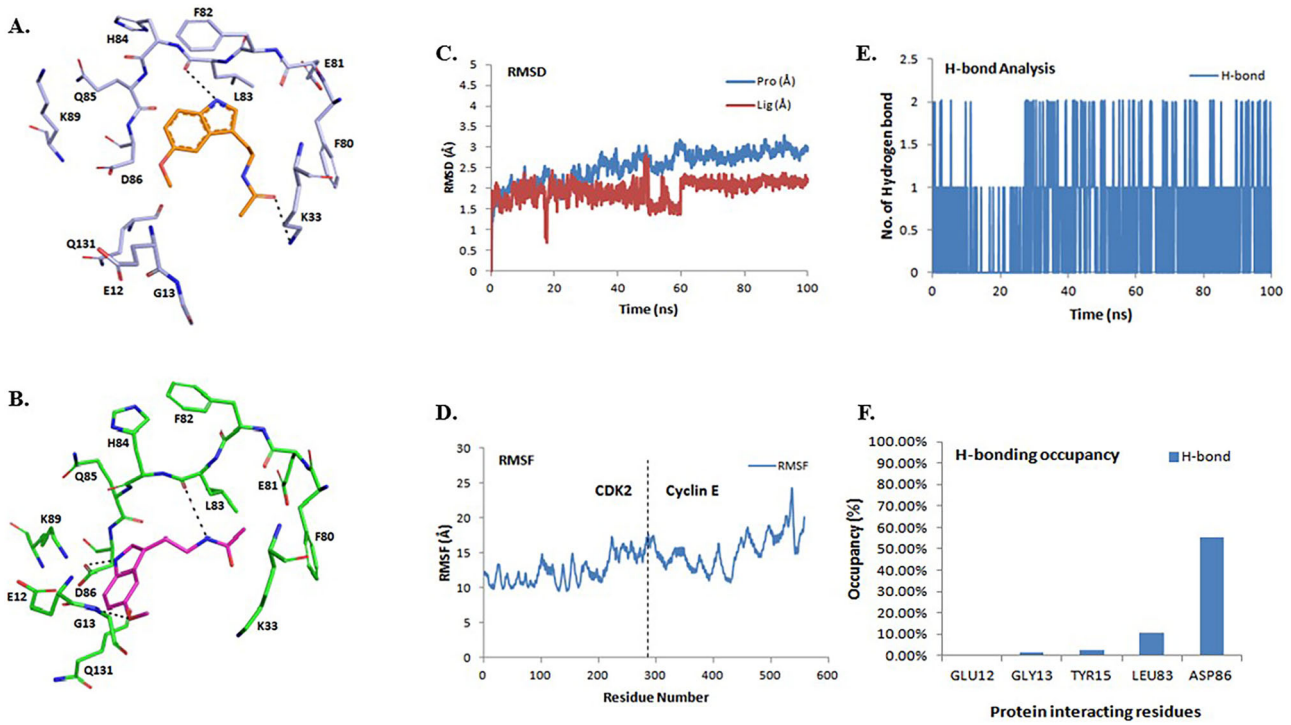

Fig. 5 In-silico interaction study between melatonin and the CDK-2/Cyclin E enzyme complex. **A** Docked pose of melatonin (colored in orange) in the ATP binding site (active site) of CDK-2 (colored in light blue). **B** The binding pose of melatonin (colored in magenta) with CDK-2/Cyclin E complex (CDK-2 colored in green) during the most stable productive phase (between 65 and 100 ns) of MD simulation. Only the amino acid residues belonging to the active site within 5 Å of melatonin were shown in the stick model. The putative H-bonds are shown as dashed lines. **C** Root Mean Square Deviation (RMSD) plot of melatonin (colored in maroon) and CDK-2/Cyclin **E** protein backbone (colored in blue) during 100 ns of MD simulation. **D** Root Mean Square Fluctuation (RMSF) plot of protein residues in CDK-2/Cyclin E-melatonin complex. **E** Variation in the number of hydrogen bonds between melatonin and CDK-2/Cyclin E protein with time during MD simulation. **F** Hydrogen bond interaction occupancy of melatonin with different amino acid residues in the active site of CDK-2/Cyclin E complex

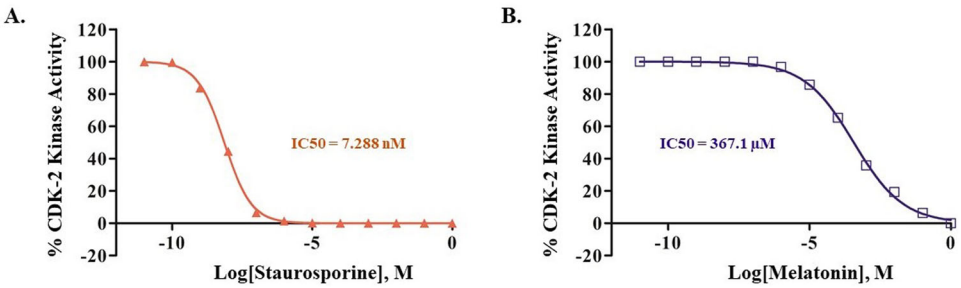

Fig. 6 Effect of different concentrations of staurosporine (**A**) and melatonin (**B**) on CDK-2/Cyclin E1 kinase activity

Discussion

Gastric cancer is a leading cause of cancer-associated mortality and a major public health concern worldwide [38]. Since glucose is the primary energy source for cancer cells; hyperglycemic condition contributes to a more aggressive nature of cancer cells. Hyperglycemic condition leads to increased ROS production as well as its accumulation in cancer cells. In correspondence with the previous reports [3, 39], we also observed that the levels of ROS formation and its accumulation within AGS cells are significantly increased under hyperglycemic conditions. This heightened level of ROS is central to almost every adverse effect that hyperglycemia has on AGS cells. ROS, thus produced, may stimulate various signaling pathways and transcription factors [40–44]. The expression of MMP-9, which regulates the aggressive nature of cancer cells, is also affected by this hyperglycemia-induced increase in ROS [8, 45] Corroborating with this fact, we have noticed an increase in the activity and expression of MMP-9 under hyperglycemic conditions. This up-regulation of MMP-9 is accompanied by a simultaneous decrease in TIMP-1 activity and

expression. Such interplay between MMP-9 and TIMP-1 is expected since TIMP-1 is a naturally occurring enzyme that can bind strongly with MMP-9 and regulate its activity. Altered expressions and activities of MMP-9 and TIMP-1 have led to an altered rate of migration of AGS cells maintained in hyperglycemic conditions. This result shows that hyperglycemia is associated with the aggressive progression of AGS cells by regulating MMP-9 and TIMP-1.

Treatment with melatonin brought down the hyperglycemia-induced elevated ROS to a basal level. Previous reports from our group showed that melatonin binds to the active site of MMP-9 and interacts with a few key amino acid residues as well as the catalytic zinc ion; thereby inhibiting MMP-9 activity [46]. Another study reported that melatonin also inhibits the expression of MMP-9 [47]. Following those previous findings, we observed that the gelatinolytic activity and expression of MMP-9 are indeed reduced significantly after melatonin treatment. This shows that the inhibitory potential of melatonin towards reducing MMP-9 expression and activity remains unhindered even under hyperglycemic conditions. Reports suggest that melatonin also enhances the expression and activity of TIMP-1 [48]. We have also observed a similar trend in TIMP-1 activity and expression patterns after melatonin treatment, under hyperglycemic conditions. This result demonstrates that melatonin inhibits the aggressive progression of AGS cells by modulating the expression and activity of MMP-9 and TIMP-1.

Further, it has been reported that prolonged exposure to high glucose enhances the expression of Cyclin D, CDK-4, and CDK-2 in human bladder epithelial cells [49]. We also found a similar expression pattern for Cyclin D, Cyclin E, CDK-4, and CDK-2 in AGS cells under hyperglycemic conditions. We also observed a significant increase in the phosphorylation status of Rb protein, under similar conditions. These results suggest that hyperglycemia significantly increases cell proliferation by accelerating the cell cycle progression. This hyperglycemia-induced proliferation of AGS cells was markedly reduced upon treatment with melatonin. Melatonin may be achieving this effect by targeting the major cell cycle regulators or by inducing apoptosis [50, 51]. Previous studies have reported that melatonin can induce G_2/M phase cell cycle arrest in the HepG2 cell line [52]. Ovarian cancer cell lines (OVCAR-429 and PA-1) can be arrested in the G_1 phase upon melatonin treatment [50]. Song et al have reported that melatonin can induce both G_1/S phase cell cycle arrest as well as apoptosis in the SGC-7901 gastric cancer cell line [15]. AGS cells were also reported to undergo apoptosis after melatonin treatment [53]. However, we have observed that melatonin did not produce any change in the apoptotic rate of AGS cells (Fig. S3), under hyperglycemic conditions. Instead it induced G_0/G_1 phase cell cycle arrest; thereby preventing AGS cells from entering the S-phase and effectively countering hyperglycemia-induced cell proliferation. This contrast may be attributed to the higher concentration of glucose present in our experimental media.

Again, we observed a significant suppression of Cyclin D1, CDK-4, Cyclin E, and CDK-2 expression after treatment with melatonin upon western blot analysis. This suggests that these major cell cycle regulator proteins could most likely be the main intracellular targets of melatonin-mediated G_0/G_1 arrest in AGS cells under hyperglycemic conditions. The CDK-4/Cyclin D1 complex is a master regulator of the cell cycle and is known to predominantly exert its effects by phosphorylating the Rb protein. But, we observed that melatonin treatment could only slightly reduce (~1.2-fold; $p > 0.05$) the level of p-Rb protein. This shows that melatonin could not significantly affect the kinase activity of the CDK-4/Cyclin D1 complex.

On the other hand, the main function of the CDK-2/Cyclin E1 complex is to activate downstream signaling factors that regulate S-phase entry and progression. Melatonin being able to induce G_0/G_1 phase arrest hints that it may be doing so by inhibiting the activity of the CDK-2/Cyclin E complex. Preliminary evidence towards this assumption was obtained from the in silico study, where it was revealed that melatonin interacts strongly with the ATP-binding site of CDK-2 protein, with a low binding free energy of −6.3 kcal/mol. Melatonin forms hydrogen bonds with two key residues within the ATP binding site identified as Lys33 and Leu83. Further confirmation of such interaction was obtained from the ADP-Glo Kinase Assay, which showed clearly that melatonin can undoubtedly inhibit CDK-2/Cyclin E1 kinase activity, thereby inducing cell cycle arrest. Therefore, it can be concluded that melatonin induces cell cycle arrest by downregulating the expression as well as the kinase activity of the CDK-2/Cyclin E complex.

Conclusion

A hyperglycemic environment can induce AGS cell proliferation and MMP-9 expression by modulating intracellular ROS levels. Melatonin, by virtue of its antioxidant properties, significantly reduces the ROS upregulation brought about by hyperglycemia. It reverses the hyperglycemia-induced changes in the expression and activity of MMP-9 and TIMP-1. Further, melatonin combats hyperglycemia-induced excessive AGS cell proliferation by arresting AGS cells in the G_0/G_1 phase by binding with the ATP binding site of CDK-2 and consequently, inhibiting its kinase activity. To the best of our knowledge, we are the first to document the physiological condition of gastric cancer-hyperglycemia comorbidity and have tried to

replicate the same in an in vitro perspective. Overall, our results suggest that melatonin may be included as a potent therapeutic agent and used for future drug design in the treatment of gastric cancer-hyperglycemia co-morbidity.

Data availability

No datasets were generated or analysed during the current study.

Supplementary information The online version contains supplementary material available at https://doi.org/10.1007/s12013-024-01241-9.

Acknowledgements A.C. is thankful to the University Grants Commission (UGC), India for providing financial support. T.R. acknowledges the receipt of the National Post Doctoral Fellowship from SERB. V.K.M. acknowledges the receipt of a Research Associate fellowship from the Department of Biotechnology (DBT), Ministry of Science & Technology, Government of India. D.J. is thankful to the Council of Scientific and Industrial Research (CSIR), India for her fellowship. We acknowledge Director, CSIR-IICB for his kind support.

Author Contributions Conception and design of the study: A.C., S.S. Acquisition of data: A.C., T.R., V.K.M., D.J. Analysis and/or interpretation of data: A.C., T.R., V.K.M., D.J., U.P.S. Drafting the manuscript: A.C., T.R., D.J. Revising the manuscript critically for important intellectual content: T.R., V.K.M., S.S. All authors have read the manuscript and agreed to its submission in the journal.

Funding This study was supported by institutional grant no. P-07 from CSIR-Indian Institute of Chemical Biology, Kolkata, India.

Compliance with Ethical Standards

Conflict of Interest The authors declare no competing interests.

Abbreviations

ATP	adenosine triphosphate
BSA	bovine serum albumin
CDK	cyclin dependent kinase
CTRL	control
DCFH-DA	2'-7'-Dichlorodihydrofluorescein diacetate
DNA	deoxyribonucleic acid
DTT	dithiothretol
FBS	fetal bovine serum
GAPDH	glyceraldehyde-3-phosphate dehydrogenase
HG	hyperglycemic
HRP	horseradish peroxidase
MD	molecular dynamic
MELA	melatonin
MMP	matrix metalloproteinase
NAC	N-acetyl-L-cysteine
PAGE	polyacrylamide gel electrophoresis
PBS	phosphate buffered saline
PDB	protein data bank
PIC	protease inhibitor cocktail
PMSF	phenylmethylsulfonyl fluoride
p-Rb	phosphorylated retinoblastoma
PVDF	polyvinylidene fluoride
Rb	retinoblastoma
RMSD	root mean square deviation
RMSF	root mean square fluctuation
ROS	reactive oxygen species
SDS	sodium dodecyl sulphate
STED	stimulated emission depletion
TBST	Tris-buffered saline with 0.1% Tween® 20 detergent
TIMP	tissue inhibitor of metalloproteinase.

References

1. Romero-Garcia, S., Lopez-Gonzalez, J. S., Báez-Viveros, J. L., Aguilar-Cazares, D., & Prado-Garcia, H. (2011). Tumor cell metabolism: an integral view. *Cancer Biology & Therapy*, *12*(11), 939–948. https://doi.org/10.4161/cbt.12.11.18140.
2. Warburg, O. (1956). On the origin of Cancer Cells. *Science*, *123*(3191), 309–314. https://doi.org/10.1126/science.123.3191.309.
3. Kaludercic, N., & Di Lisa, F. (2020). Mitochondrial ROS Formation in the Pathogenesis of Diabetic Cardiomyopathy. *Frontiers in Cardiovascular Medicine*, *7*, 12 https://doi.org/10.3389/fcvm.2020.00012.
4. Ushio-Fukai, M. (2007). VEGF signaling through NADPH oxidase-derived ROS. *Antioxidants & Redox Signaling*, *9*(6), 731–739. https://doi.org/10.1089/ars.2007.1556.
5. Kirova, D. G., Judasova, K., Vorhauser, J., Zerjatke, T., Leung, J. K., Glauche, I., & Mansfeld, J. (2022). A ROS-dependent mechanism promotes CDK2 phosphorylation to drive progression through S phase. *Developmental Cell*, *57*(14), 1712–1727.e9. https://doi.org/10.1016/j.devcel.2022.06.008.
6. Redza-Dutordoir, M., & Averill-Bates, D. A. (2016). Activation of apoptosis signalling pathways by reactive oxygen species. *Biochimica et Biophysica Acta*, *1863*(12), 2977–2992. https://doi.org/10.1016/j.bbamcr.2016.09.012.
7. Mori, K., Uchida, T., Yoshie, T., Mizote, Y., Ishikawa, F., Katsuyama, M., & Shibanuma, M. (2019). A mitochondrial ROS pathway controls matrix metalloproteinase 9 levels and invasive properties in RAS-activated cancer cells. *The FEBS Journal*, *286*(3), 459–478. https://doi.org/10.1111/febs.14671.
8. Page-McCaw, A., Ewald, A. J., & Werb, Z. (2007). Matrix metalloproteinases and the regulation of tissue remodelling. *Nature Reviews Molecular Cell Biology*, *8*(3), 221–233. https://doi.org/10.1038/nrm2125.
9. Kang, X., Kong, F., Wu, X., Ren, Y., Wu, S., Wu, K., Jiang, Z., & Zhang, W. (2015). High glucose promotes tumor invasion and increases metastasis-associated protein expression in human lung epithelial cells by upregulating heme oxygenase-1 via reactive oxygen species or the TGF-β1/PI3K/AKT signaling pathway. *Cellular Physiology and Biochemistry*, *35*(3), 1008–1022. https://doi.org/10.1159/000373928.
10. Sun, X. F., Shao, Y. B., Liu, M. G., Chen, Q., Liu, Z. J., Xu, B., Luo, S. X., & Liu, H. (2017). High-concentration glucose enhances invasion in invasive ductal breast carcinoma by promoting Glut1/MMP2/MMP9 axis expression. *Oncology Letters*, *13*(5), 2989–2995. https://doi.org/10.3892/ol.2017.5843.
11. Saengboonmee, C., Seubwai, W., Pairojkul, C., & Wongkham, S. (2016). High glucose enhances progression of cholangiocarcinoma cells via STAT3 activation. *Scientific Reports*, *6*, 18995 https://doi.org/10.1038/srep18995.
12. Andersen, L. P., Werner, M. U., Rosenkilde, M. M., Harpsøe, N. G., Fuglsang, H., Rosenberg, J., & Gögenur, I. (2016). Pharmacokinetics of oral and intravenous melatonin in healthy volunteers. *BMC Pharmacology & Toxicology*, *17*, 8 https://doi.org/10.1186/s40360-016-0052-2.

13. Leon-Blanco, M. M., Guerrero, J. M., Reiter, R. J., Calvo, J. R., & Pozo, D. (2003). Melatonin inhibits telomerase activity in the MCF-7 tumor cell line both in vivo and in vitro. *Journal of Pineal Research*, *35*(3), 204–211. https://doi.org/10.1034/j.1600-079x.2003.00077.x.
14. Liu, R., Fu, A., Hoffman, A. E., Zheng, T., & Zhu, Y. (2013). Melatonin enhances DNA repair capacity possibly by affecting genes involved in DNA damage responsive pathways. *BMC Cell Biology*, *14*, 1 https://doi.org/10.1186/1471-2121-14-1.
15. Song, J., Ma, S. J., Luo, J. H., Zhang, H., Wang, R. X., Liu, H., Li, L., Zhang, Z. G., & Zhou, R. X. (2018). Melatonin induces the apoptosis and inhibits the proliferation of human gastric cancer cells via blockade of the AKT/MDM2 pathway. *Oncology Reports*, *39*(4), 1975–1983. https://doi.org/10.3892/or.2018.6282.
16. Chok, K. C., Koh, R. Y., Ng, M. G., Ng, P. Y., & Chye, S. M. (2021). Melatonin induces autophagy via reactive oxygen species-mediated endoplasmic reticulum stress pathway in colorectal cancer cells. *Molecules*, *26*(16), 5038 https://doi.org/10.3390/molecules26165038.
17. Talib, W. H., Alsayed, A. R., Abuawad, A., Daoud, S., & Mahmod, A. I. (2021). Melatonin in cancer treatment: current knowledge and future opportunities. *Molecules*, *26*(9), 2506 https://doi.org/10.3390/molecules26092506.
18. Hardeland, R. (2017). Melatonin and the electron transport chain. *Cellular and Molecular Life Sciences*, *74*(21), 3883–3896. https://doi.org/10.1007/s00018-017-2615-9.
19. Martínez-Campa, C., Menéndez-Menéndez, J., Alonso-González, C., González, A., Álvarez-García, V., & Cos, S. (2017). What is known about melatonin, chemotherapy and altered gene expression in breast cancer. *Oncology Letters*, *13*(4), 2003–2014. https://doi.org/10.3892/ol.2017.5712.
20. Kvietkauskas, M., Zitkute, V., Leber, B., Strupas, K., Stiegler, P., & Schemmer, P. (2020). The role of melatonin in colorectal cancer treatment: a comprehensive review. *Therapeutic Advances in Medical Oncology*, *12*, 1758835920931714 https://doi.org/10.1177/1758835920931714.
21. Ma, Z., Yang, Y., Fan, C., Han, J., Wang, D., Di, S., Hu, W., Liu, D., Li, X., Reiter, R. J., & Yan, X. (2016). Melatonin as a potential anticarcinogen for non-small-cell lung cancer. *Oncotarget*, *7*(29), 46768–46784. https://doi.org/10.18632/oncotarget.8776.
22. Ma, Z., Liu, D., Di, S., Zhang, Z., Li, W., Zhang, J., Xu, L., Guo, K., Zhu, Y., Li, X., Han, J., & Yan, X. (2019). Histone deacetylase 9 downregulation decreases tumor growth and promotes apoptosis in non-small cell lung cancer after melatonin treatment. *Journal of Pineal Research*, *67*(2), e12587 https://doi.org/10.1111/jpi.12587.
23. Mayo, J. C., Hevia, D., Quiros-Gonzalez, I., Rodriguez-Garcia, A., Gonzalez-Menendez, P., Cepas, V., Gonzalez-Pola, I., & Sainz, R. M. (2017). IGFBP3 and MAPK/ERK signaling mediates melatonin-induced antitumor activity in prostate cancer. *Journal of Pineal Research*, *62*(1), 12373 https://doi.org/10.1111/jpi.12373.
24. Zharinov, G. M., Bogomolov, O. A., Chepurnaya, I. V., Neklasova, N. Y., & Anisimov, V. N. (2020). Melatonin increases overall survival of prostate cancer patients with poor prognosis after combined hormone radiation treatment. *Oncotarget*, *11*(41), 3723–3729. https://doi.org/10.18632/oncotarget.27757.
25. Wang, S. W., Tai, H. C., Tang, C. H., Lin, L. W., Lin, T. H., Chang, A. C., Chen, P. C., Chen, Y. H., Wang, P. C., Lai, Y. W., & Chen, S. S. (2021). Melatonin impedes prostate cancer metastasis by suppressing MMP-13 expression. *Journal of Cellular Physiology*, *236*(5), 3979–3990. https://doi.org/10.1002/jcp.30150.
26. Bubenik, G. A. (2008). Thirty four years since the discovery of gastrointestinal melatonin. *Journal of Physiology and Pharmacology*, *59*(Suppl 2), 33–51.
27. Koobotse, M. O., Schmidt, D., Holly, J. M. P., & Perks, C. M. (2020). Glucose Concentration in Cell Culture Medium Influences the BRCA1-Mediated Regulation of the Lipogenic Action of IGF-I in Breast Cancer Cells. *International Journal of Molecular Sciences*, *21*(22), 8674 https://doi.org/10.3390/ijms21228674.
28. Morris, G. M., Huey, R., Lindstrom, W., Sanner, M. F., Belew, R. K., Goodsell, D. S., & Olson, A. J. (2009). AutoDock4 and AutoDockTools4: Automated docking with selective receptor flexibility. *Journal of Computational Chemistry*, *30*(16), 2785–2791. https://doi.org/10.1002/jcc.21256.
29. Berman, H. M., Westbrook, J., Feng, Z., Gilliland, G., Bhat, T. N., Weissig, H., Shindyalov, I. N., & Bourne, P. E. (2000). The Protein Data Bank. *Nucleic Acids Research*, *28*(1), 235–242. https://doi.org/10.1093/nar/28.1.235.
30. Bell, E. W., & Zhang, Y. (2019). DockRMSD: an open-source tool for atom mapping and RMSD calculation of symmetric molecules through graph isomorphism. *Journal of Cheminformatics*, *11*(1), 40 https://doi.org/10.1186/s13321-019-0362-7.
31. Oberhauser, N., Nurisso, A., & Carrupt, P. A. (2014). MLP Tools: a PyMOL plugin for using the molecular lipophilicity potential in computer-aided drug design. *Journal of Computer-aided Molecular Design*, *28*(5), 587–596. https://doi.org/10.1007/s10822-014-9744-0.
32. Kaushik, M. (2014). A review of innovative chemical drawing and spectra prediction computer software. *Mediterranean Journal of Chemistry*, *3*, 759–766. https://doi.org/10.13171/mjc.3.1.2014.04.04.16.
33. Phillips, J. C., Hardy, D. J., Maia, J. D. C., Stone, J. E., Ribeiro, J. V., & Bernardi, R. C., et al. (2020). Scalable molecular dynamics on CPU and GPU architectures with NAMD. *The Journal of Chemical Physics*, *153*(4), 044130 https://doi.org/10.1063/5.0014475.
34. Yamada, Y., Gohda, S., Abe, K., Togo, T., Shimano, N., & Sasaki, T., et al. (2017). Carbon materials with controlled edge structures. *Carbon*, *122*, 694–701. https://doi.org/10.1016/j.carbon.2017.07.012.
35. Allouche, A. R. (2011). Gabedit–a graphical user interface for computational chemistry softwares. *Journal of Computational Chemistry*, *32*(1), 174–182. https://doi.org/10.1002/jcc.21600.
36. Kim, S., Lee, J., Jo, S., Brooks, 3rd, C. L., Lee, H. S., & Im, W. (2017). CHARMM-GUI ligand reader and modeler for CHARMM force field generation of small molecules. *Journal of Computational Chemistry*, *38*(21), 1879–1886. https://doi.org/10.1002/jcc.24829.
37. Lee, J., Cheng, X., Swails, J. M., Yeom, M. S., Eastman, P. K., & Lemkul, J. A., et al. (2016). CHARMM-GUI Input Generator for NAMD, GROMACS, AMBER, OpenMM, and CHARMM/OpenMM Simulations Using the CHARMM36 Additive Force Field. *Journal of Chemical Theory and Computation*, *12*(1), 405–413. https://doi.org/10.1021/acs.jctc.5b00935.
38. Sung, H., Ferlay, J., Siegel, R. L., Laversanne, M., Soerjomataram, I., Jemal, A., & Bray, F. (2021). Global Cancer Statistics 2020: GLOBOCAN estimates of incidence and mortality worldwide for 36 cancers in 185 countries. *CA: a cancer journal for clinicians*, *71*(3), 209–249. https://doi.org/10.3322/caac.21660.
39. Burgos-Morón, E., Abad-Jiménez, Z., Marañón, A. M., Iannantuoni, F., Escribano-López, I., & López-Domènech, S., et al. (2019). Relationship between oxidative stress, ER stress, and inflammation in type 2 diabetes: the battle continues. *Journal of Clinical Medicine*, *8*(9), 1385 https://doi.org/10.3390/jcm8091385.
40. Son, Y., Cheong, Y. K., Kim, N. H., Chung, H. T., Kang, D. G., & Pae, H. O. (2011). Mitogen-Activated Protein Kinases and Reactive Oxygen Species: How Can ROS Activate MAPK Pathways? *Journal of Signal Transduction*, *2011*, 792639 https://doi.org/10.1155/2011/792639.

41. Lopez, R., Arumugam, A., Joseph, R., Monga, K., Boopalan, T., & Agullo, P., et al. (2013). Hyperglycemia enhances the proliferation of non-tumorigenic and malignant mammary epithelial cells through increased leptin/IGF1R signaling and activation of AKT/mTOR. *PloS One*, *8*(11), e79708 https://doi.org/10.1371/journal.pone.0079708.
42. Schieber, M., & Chandel, N. S. (2014). ROS function in redox signaling and oxidative stress. *Current Biology*, *24*(10), R453–R462. https://doi.org/10.1016/j.cub.2014.03.034.
43. Wu, D., Hu, D., Chen, H., Shi, G., Fetahu, I. S., & Wu, F., et al. (2018). Glucose-regulated phosphorylation of TET2 by AMPK reveals a pathway linking diabetes to cancer. *Nature*, *559*(7715), 637–641. https://doi.org/10.1038/s41586-018-0350-5.
44. Faubert, B., Solmonson, A., & DeBerardinis, R. J. (2020). Metabolic reprogramming and cancer progression. *Science*, *368*(6487), eaaw5473 https://doi.org/10.1126/science.aaw5473.
45. Lee, G. H., Jin, S. W., Kim, S. J., Pham, T. H., Choi, J. H., & Jeong, H. G. (2019). Tetrabromobisphenol A induces MMP-9 expression via NADPH Oxidase and the activation of ROS, MAPK, and AKT pathways in human breast cancer MCF-7 cells. *Toxicological Research*, *35*(1), 93–101. https://doi.org/10.5487/TR.2019.35.1.093.
46. Rudra, D. S., Pal, U., Maiti, N. C., Reiter, R. J., & Swarnakar, S. (2013). Melatonin inhibits matrix metalloproteinase-9 activity by binding to its active site. *Journal of Pineal Research*, *54*(4), 398–405. https://doi.org/10.1111/jpi.12034.
47. Qin, W., Lu, W., Li, H., Yuan, X., Li, B., Zhang, Q., & Xiu, R. (2012). Melatonin inhibits IL1β-induced MMP9 expression and activity in human umbilical vein endothelial cells by suppressing NF-κB activation. *The Journal of Endocrinology*, *214*(2), 145–153. https://doi.org/10.1530/JOE-12-0147.
48. Ates, G., Tamer, S., Yorulmaz, H., Mutlu, S., Olgac, V., Aksu, A., Caglar, N. B., & Özkök, E. (2022). Melatonin pretreatment modulates anti-inflammatory, antioxidant, YKL-40, and matrix metalloproteinases in endotoxemic rat lung tissue. *Experimental Biology and Medicine*, *247*(12), 1080–1089. https://doi.org/10.1177/15353702221084933.
49. Kim, D., Ahn, B. N., Kim, Y., Hur, D. Y., Yang, J. W., & Park, G. B., et al. (2019). High glucose with insulin induces cell cycle progression and activation of oncogenic signaling of bladder epithelial cells cotreated with metformin and pioglitazone. *Journal of Diabetes Research*, *2019*, 2376512 https://doi.org/10.1155/2019/2376512.
50. Shen, C. J., Chang, C. C., Chen, Y. T., Lai, C. S., & Hsu, Y. C. (2016). Melatonin suppresses the growth of ovarian cancer cell lines (OVCAR-429 and PA-1) and potentiates the effect of G1 arrest by targeting CDKs. *International Journal of Molecular Sciences*, *17*(2), 176 https://doi.org/10.3390/ijms17020176.
51. Liu, R., Wang, H. L., Deng, M. J., Wen, X. J., Mo, Y. Y., & Chen, F. M., et al. (2018). Melatonin inhibits reactive oxygen species-driven proliferation, epithelial-mesenchymal transition, and vasculogenic mimicry in oral cancer. *Oxidative Medicine and Cellular Longevity*, *2018*, 3510970 https://doi.org/10.1155/2018/3510970.
52. Martín-Renedo, J., Mauriz, J. L., Jorquera, F., Ruiz-Andrés, O., González, P., & González-Gallego, J. (2008). Melatonin induces cell cycle arrest and apoptosis in hepatocarcinoma HepG2 cell line. *Journal of Pineal Research*, *45*(4), 532–540. https://doi.org/10.1111/j.1600-079X.2008.00641.x.
53. Li, W., Fan, M., Chen, Y., Zhao, Q., Song, C., Yan, Y., Jin, Y., Huang, Z., Lin, C., & Wu, J. (2015). Melatonin Induces Cell Apoptosis in AGS Cells Through the Activation of JNK and P38 MAPK and the Suppression of Nuclear Factor-Kappa B: a Novel Therapeutic Implication for Gastric Cancer. *Cellular Physiology and Biochemistry*, *37*(6), 2323–2338. https://doi.org/10.1159/000438587.

BBA - Molecular Cell Research 1870 (2023) 119417

Contents lists available at ScienceDirect

BBA - Molecular Cell Research

journal homepage: www.elsevier.com/locate/bbamcr

Rotenone induced neurodegeneration is mediated via cytoskeleton degradation and necroptosis

Tapasi Roy, Abhishek Chatterjee, Snehasikta Swarnakar *

CSIR-Indian Institute of Chemical Biology, Infectious Diseases and Immunology Division, Kolkata, West Bengal, India

ARTICLE INFO

Keywords:
Rotenone
Parkinson's disease
Necroptosis
RIPK1
ROS

ABSTRACT

Rotenone has widespread beneficial effects in agriculture, fisheries and animal husbandries; however prolonged exposure causes a detrimental effect on the health of personnel working in such industries. Rotenone during its extraction, formulation or usage may cross the blood brain barrier leading to neurodegeneration and the development of Parkinson's disease like symptoms. It is a known inhibitor of the mitochondrial ETC complex I and responsible for impairing the OXPHOS system. Our study showed that rotenone exposure results in an increased production of ROS and decreased ATP level along with a conspicuous loss of mitochondrial membrane potential in N2A cells. The transcription and expression pattern of cofilin, a key component of actin cytoskeleton, was also altered after rotenone exposure; leading to the actin cytoskeleton degradation. We further observed an increased expression, as well as activity of matrix metalloproteinase9 (MMP9) in rotenone exposed N2A cells; suggesting the involvement of inflammation upon rotenone exposure. Simultaneously, an opposite pattern was noticed for the tissue inhibitors of metalloproteinases-1 (TIMP-1) protein, which is a known modulator of MMP9 activity. Additionally, the localization of MMP9 along with alpha-synuclein, UCHL1 and cofilin suggested their close proximity and cross interaction upon rotenone treatment. Furthermore, we observed significant increase in the level of TNF-α upon rotenone exposure along with the phosphorylation of RIPK1, RIPK3 and MLKL that has been identified as the necroptosis markers leading to programmed necroptotic death.

1. Introduction

Rotenone is widely used as a selective, non-systemic insecticide in agriculture [1]. Moreover, emulsifiable concentrates of rotenone are extensively used in freshwater fisheries before seeding water bodies with fishes of economic interest [1,2]. Despite being irreplaceably beneficial to different aspects of agriculture, animal husbandry, parasite control and freshwater fishery, rotenone is detrimental to human health upon prolonged exposure [3]. Being an extremely lipophilic compound, rotenone can easily cross the blood-brain barrier. It impairs oxidative phosphorylation by inhibiting mitochondrial electron transport chain (ETC), complex I (reduced nicotinamide adenine dinucleotideubiquinone reductase), affecting ATP synthesis along with the reactive oxygen species (ROS) production; leading to the induction of oxidative stress [4,5]. Neurons rely on oxidative phosphorylation (OXPHOS) that uses oxygen and glucose to generate energy-storing ATP to fulfil the energy requirements [6]. This procedure depends on electron flow through ETC in mitochondrial inner compartment, terminating the lowering of oxygen in the mitochondrial matrix, and produce membrane potential across the mitochondrial inner membrane that is required for the synthesis of ATP from ADP [7]. The brain, in particular, is very vulnerable to free radical exposure and oxidative stress together with mitochondrial dysfunction which plays a critical role in the pathogenesis of neurodegenerative disorders [8,9]. Further rotenone is known to induce the formation of α-synuclein-positive cytoplasmic inclusions in nigral neurons mimicking Lewy bodies (LBs) [10] and progressive neurodegeneration accompanied by Parkinson's disease (PD) like motor and non-motor symptoms [11]. Additionally, components of the ubiquitin proteasome system (UPS) and chaperones, have also been noticed in LBs [8], representing the futile attempt of UPS to eliminate the proteinaceous aggregates. Although the molecular machinery responsible for PD pathogenesis has not yet been completely clarified, it is commonly accepted that an amalgamation of genetic and environmental factors are considerably responsible for the neurodegenerative process and the death of dopaminergic neurons. Cumulating evidence implies that rotenone during its extraction, formulation or use as pesticide may cross

* Corresponding author at: Infectious Diseases and Immunology Division, CSIR-Indian Institute of Chemical Biology, 4, Raja S. C. Mullick Road, Jadavpur, Kolkata 700032, West Bengal, India.
E-mail address: snehasiktaiicbidi@gmail.com (S. Swarnakar).

https://doi.org/10.1016/j.bbamcr.2022.119417
Received 9 September 2022; Received in revised form 7 December 2022; Accepted 16 December 2022
Available online 27 December 2022

the blood-brain barrier of exposed personnel and long-term exposure may lead to the development of neurodegenerative disorders like PD [12,13].

In this present study, we investigated the molecular process that may be involved in rotenone toxicity induced degradation of neuronal cells that mimics PD pathogenesis.

2. Results

2.1. Changes in cell viability, ROS level, intracellular ATP content and mitochondrial membrane potential upon rotenone exposure

The exposure of neuroblastoma cells (N2A cells) to 100 μM rotenone for 24 h has led to a significant loss of cell viability which was quantified by CellTiter-Glo reagent solution. It was observed that nearly 50 % cells died after 24 h of 100 μM rotenone exposure (Fig. 1A).

Moreover, a considerable increase in ROS production (~2.04 fold) was noticed (Fig. 1B) when the cells were exposed to rotenone and probed with DCFHDA. Again, probing with mitochondrial ROS specific dye (MitoSOX Red) also revealed an increase in ROS level of about 2.03 folds (Fig. 1C) through spectrofluorimetric analysis. We also performed live cell imaging with MitoSOX Red and high fluorescence intensity was observed in the rotenone exposed cells when monitored under confocal microscope (Fig. 1D). Further, ROS production and ATP level in a cell showed an antagonistic relation. The calculated amount of intracellular ATP in rotenone exposed cells being 63.8 nmol/mg protein whereas the control cells showed a high concentration of ATP level (393.7 nmol/mg protein). (Fig.1E). Another important observation was a striking loss of mitochondrial membrane potential, evident from a significant (~58 %) decline in the ratio of JC-1 fluorescence emitted at 590 nm and at 527 nm respectively (Fig. 1F).

2.2. Alteration of gene transcription and expression patterns of co-localized proteins in N2A cells after rotenone exposure

The transcription patterns of alpha-synuclein, UCHL1 and cofilin genes were analysed by qualitative RT-PCR after 100 μM rotenone exposure for 24 h (Fig. 2A). Densitometric analysis revealed that the transcription level of alpha-synuclein gene was increased by ~1.3 folds (Fig. 2B) and of UCHL1 decreased by ~1.5 fold (Fig. 2C) as compared to the unexposed ones. However, insignificant changes in the transcription pattern was observed in cofilin-1 gene (Fig. 2D) while transcription of cofilin-2 increased by ~1.75 fold (Fig. 2E).

It is known that, alpha synuclein is linked to PD, UCHL-1 is to deubiquitination while cofilin and MMP are associated with cytoskeletal degradation and neuroinflammation, respectively. Therefore, we studied the co-localization of MMP9 with alpha synuclein (Sup. Fig. 1A), UCHL1 (Sup. Fig. 1B) and Cofilin (Sup. Fig. 1C). N2A cells were treated without (I) or with 100 μM rotenone (II) for 24 h and confocal imaging was performed. We observed that MMP9 (green for FITC) and alpha synuclein (red for Texas Red) are localized in the cytoplasm (Sup. Fig. 1A.I & 1A.II) together with UCHL1 (red for Texas Red) (Sup. Fig. 1B). However, UCHL-1 showed a marked reduction in its expression upon rotenone exposure (Sup. Fig. 1B.I & 1B.II). Cofilin (red for Texas Red) remained distributed throughout the cytoplasm in normal and healthy cells but after rotenone exposure cells lost their normal structure and most of the fluorescence for cofilin was observed towards the periphery of the cell (Sup. Fig. 1C.I & 1C.II).

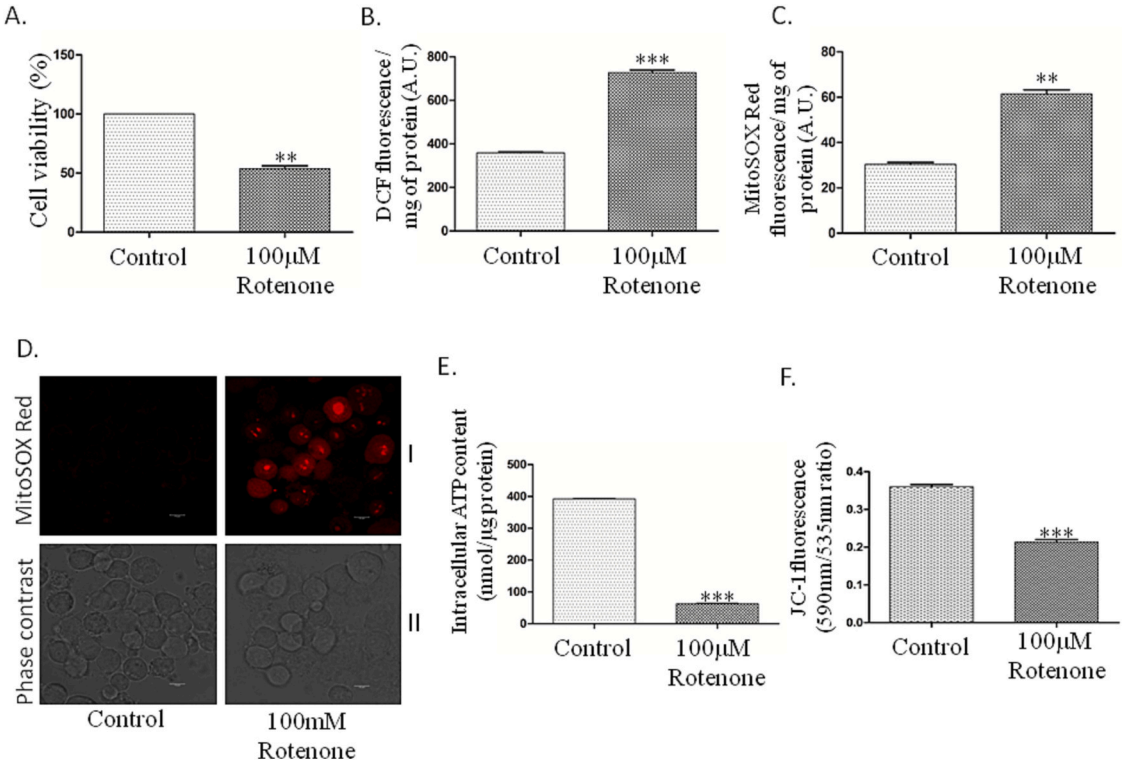

Fig. 1. Rotenone exposure alters cell viability, ROS Level, intracellular ATP content and mitochondrial membrane potential (A) Effect of rotenone on cell viability. N2A cells were treated without (control) or with rotenone (100 μM) for 24 h. At the end of the incubation period, the degree of viability was assayed by CytoTox-Glo cytotoxicity assay kit (**$P = 0.0024$ vs control, Student's *t*-test, paired, two-tailed) (B) ROS generation in N2A cells after rotenone exposure was measured using H2DCFDA (***$P < 0.0001$ vs control, Student's *t*-test, paired, two-tailed) (C) ROS generation in N2A cells after rotenone exposure was measured using MitoSOX Red (**$P = 0.0014$ vs control, Student's t-test, paired, two-tailed) (D) Live cell imaging of rotenone exposed and unexposed cells with MitoSOX Red. Row I represents the fluorescence view and row II represents the respective phase contrast view (E) Alteration in intracellular ATP content in N2A cells treated without (control) or with rotenone (100 μM) for 24 h (***P < 0.0001 vs control, Student's t-test, paired, two-tailed) (F) Alteration in Mitochondrial transmembrane potential in intact N2A cells after rotenone exposure, measured by JC-1 (***$P = 0.0005$ vs control, Student's t-test, paired, two-tailed).

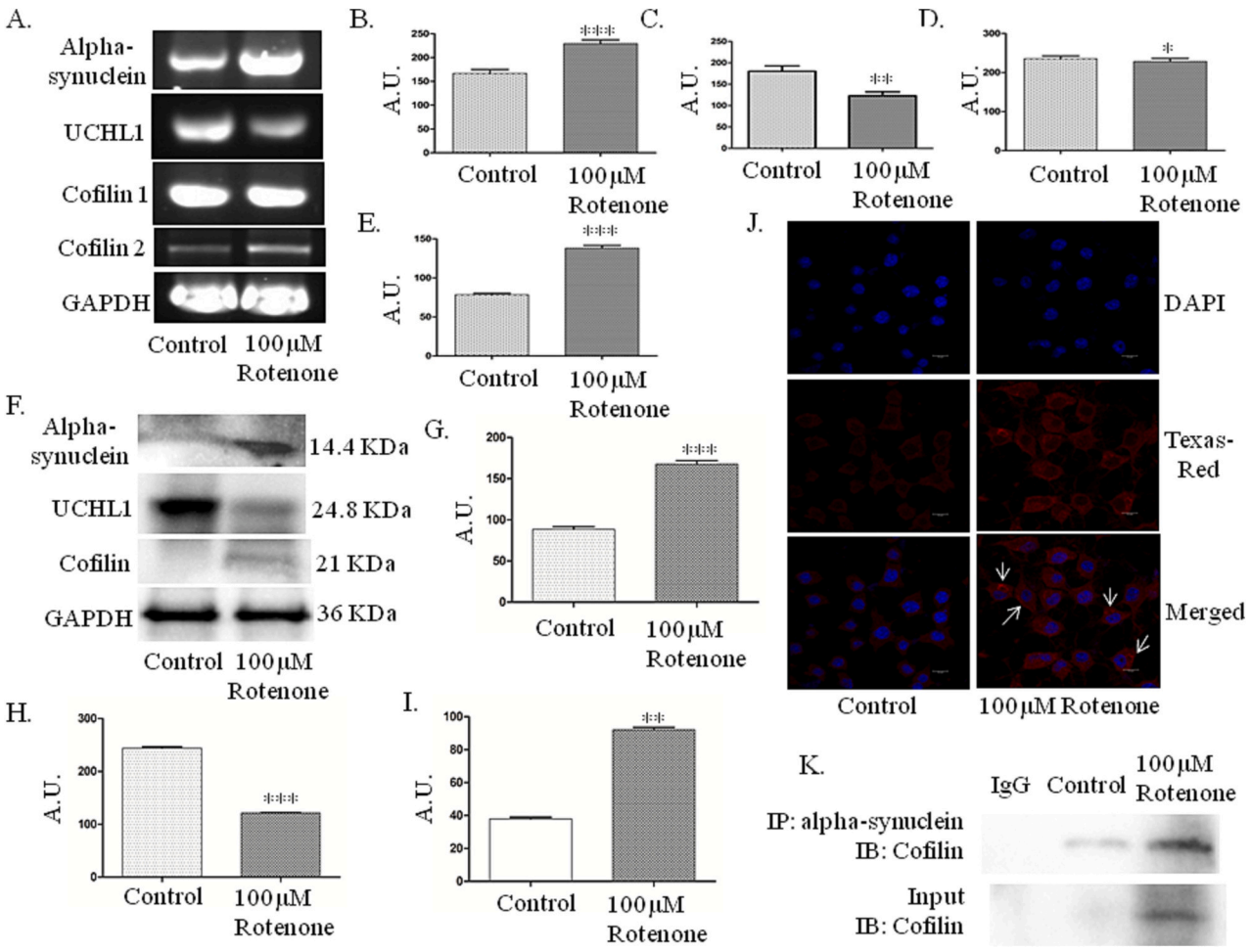

Fig. 2. Effect of rotenone on gene and protein expressions in N2A cells. N2A cells were treated without (control) or with rotenone (100 μM) for 24 h and the expression of different genes and proteins were studied by RT-PCR and immunoblotting respectively. (A) Gene expression pattern by Agarose gel electrophoresis (B) Densitometric analysis of alpha synuclein gene expression (***$P = 0.0001$ vs control, Student's *t*-test, paired, two-tailed)
(C) Densitometric analysis of UCHL1 gene expression (**$P = 0.0042$ vs control, Student's t-test, paired, two-tailed) (D) Densitometric analysis of cofilin1 gene expression (*$P = 0.0186$ vs control, Student's t-test, paired, two-tailed) (E) Densitometric analysis of cofilin 2 gene expression (***$P = 0.0007$ vs control, Student's t-test, paired, two-tailed) (F) Protein expression pattern by Western immunoblotting (G) Densitometric analysis of alpha synuclein expression (***$P = 0.0006$ vs control, Student's t-test, paired, two-tailed) (H) Densitometric analysis of UCHL1 expression (***$P = 0.0003$ vs control, Student's t-test, paired, two-tailed) (I) Densitometric analysis of cofilin expression (**$P = 0.0009$ vs control, Student's *t*-test, paired, two-tailed) (J) Immunocytochemistry using anti alpha synuclein antibody and Texas red (red) conjugated secondary antibody. Nuclei were stained with DAPI (blue) (K) Co-immunoprecipitation was performed using alpha synuclein antibody and interaction of alpha synuclein with cofilin was studied by western blotting.

Moreover, the western immunoblotting (Fig. 2F) revealed a marked increase (~1.8 fold) in alpha-synuclein expression in rotenone treated cells (Fig. 2G). The expression of UCHL1, a deubiquitinating enzyme, diminished ~2.3 folds upon rotenone exposure (Fig. 2H). Furthermore, cofilin - the actin binding protein showed ~2.3 fold increase in its expression upon rotenone exposure (Fig. 2I).

We also investigated the expression and aggregation of alpha synuclein upon 100 μM rotenone exposure for 24 h by immunocytochemistry. The changed patterns of expressions observed using high resolution Stimulated Emission Depletion Microscopy (STED) has been marked with arrowheads. (Fig. 2J).Next we performed co-immunoprcipitation study, where immunoprecipitation was performed using anti alpha-synuclein antibody and the immunoblotting was performed using anti cofilin antibody. We observed that alpha synuclein and cofilin interacts with each other and the interactivity increases upon rotenone exposure (Fig. 2K).

2.3. Rotenone exposure alters the activity and expression of MMP9 and TIMP-1

To understand how rotenone exposure affects MMP9 activity and expression we performed gelatine zymography and immunoblotting respectively. We treated N2A cells with 100 μM rotenone for 24 h. Our result showed that the activity of active MMP9 level increased by ~4.1 fold upon rotenone exposure (Fig. 3A & 3B), while the expression of MMP9 increased by ~1.2 fold as compared to untreated cells (Fig. 3E & 3F).

We further analysed the role of the TIMP-1 in rotenone induced toxicity. To understand the role of TIMP-1 in rotenone mediated damage we performed reverse zymography. We observed ~1.3 fold decrease in the activity of TIMP-1 in rotenone exposed cells in comparison to that of control cells (Fig. 3C & D); whereas, the expression of TIMP-1 after rotenone exposure decreased by ~1.2 times as observed by western immunoblotting (Fig. 3E & G).

Additionally, we performed co-immunoprecipitation study, where immunoprecipitation was performed using anti alpha-synuclein antibody and the immunoblotting was performed using anti MMP9

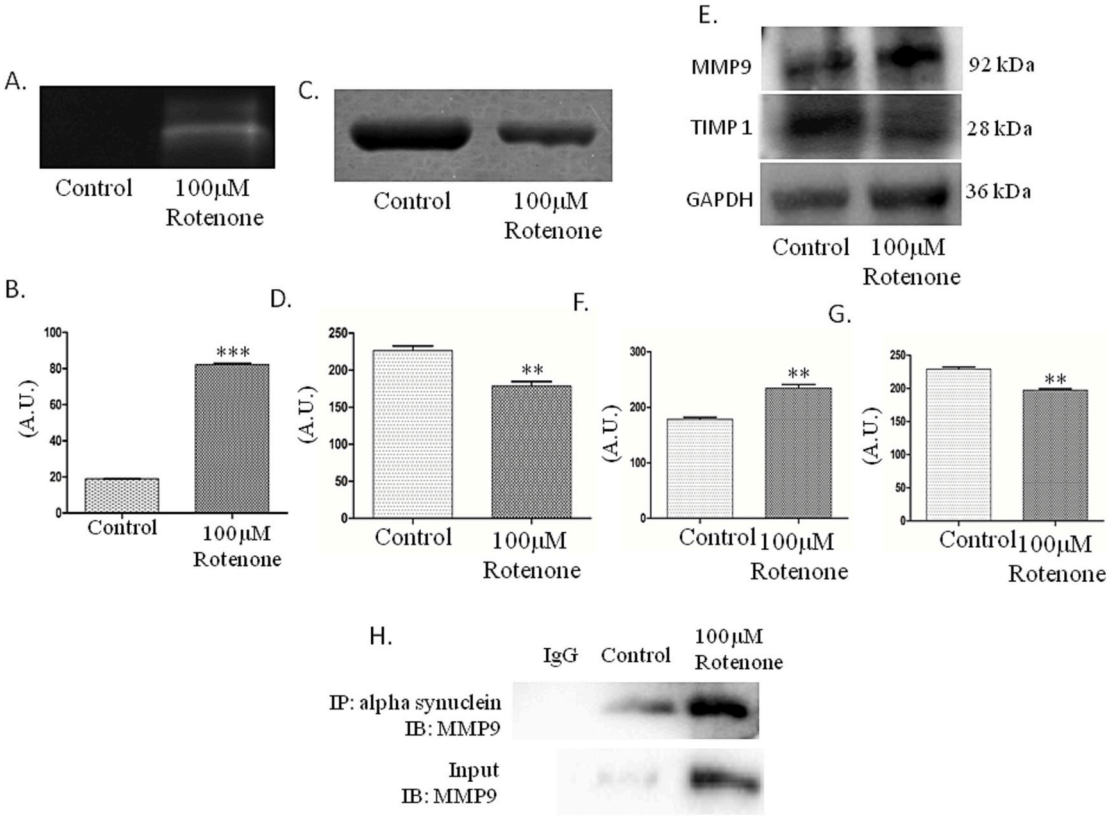

Fig. 3. Activities and expressions of MMP9 and TIMP-1 after rotenone exposure. N2A cells were incubated for 24 h without (control) or with rotenone (100 μM). (A) Activity of MMP9 was observed by Gelatin zymography. (B) Densitometric analysis of MMP9 activity (***$P = 0.0002$ vs control). (C) Reverse zymography showing the activity of TIMP-1 after rotenone exposure. (D) Densitometric analysis of TIMP-1 activity (**$P = 0.0011$ vs control). (E) Western immunoblots for MMP9 and TIMP-1. (F) Densitometric analysis of MMP9 expression (**$P = 0.0035$ vs control). (G) Densitometric analysis of TIMP-1 expression (**$P = 0.0021$ vs control). Student's *t*-test, paired, two-tailed. (H) Co-immunoprecipitation was performed using alpha synuclein antibody and interaction of alpha synuclein with MMP9 was studied by western blotting.

antibody. We observed that alpha-synuclein and MMP9 interacts with each other and the interactivity increases upon rotenone exposure (Fig. 2H).

2.4. Rotenone exposure destabilizes cell cytoskeleton

Cell morphology is usually maintained by the arrangements of cytoskeletal architecture; and the actin filaments play most important roles in different cellular activities. As rotenone alters the expression levels of cofilin, the G actin binding protein, we also investigated the organization of actin filaments upon rotenone exposure. The disruption and destabilization of the actin cytoskeleton of N2A cells were visualized by staining the cells with TRITC-phalloidin. The changed structures upon 100 μM rotenone exposure for 24 h have been shown by the arrowheads (Fig. 4).

2.5. Rotenone exposure induces necroptosis in N2A cells without affecting cell cycle

We studied the effects of rotenone on the cell cycle progression in N2A cells by flow cytometry. Our data revealed that rotenone does not affect cell cycle progression (Fig. 5A-C).

Cells generally die through two most commonly known death pathways i.e. apoptosis and necrosis. We examined which pathway is involved in rotenone mediated toxicity. The results of flow cytometry revealed that rotenone has no effect on early apoptosis and has nominal effect on late apoptosis after 24 h of exposure (Fig. 5D-G). We also examined the expression patterns of Bax, Bcl2 and Caspase 9 in cells after rotenone exposure and no observable changes in expression patterns were observed (Sup. Fig. 2). Hence, it could be concluded that rotenone induced cell death was not dependent on apoptosis. We further analysed whether programmed necroptosis was involved in this process. As necroptotic cells undergo organelle breakdown, leading to the leakage of intracellular contents and subsequently triggering inflammation, we next check the expressions of proteins that are related to necroptosis (Fig. 5H). Our results demonstrate an upregulation of TNF-α of ~3.7 fold (Fig. 5I). The RIPK1 signaling has also been implicated in the induction of necroptosis. Therefore we studied the expression of phospho-RIPK1 and observed ~4 fold enhancement of its expression (Fig. 5J) along with ~3 fold upregulation in the expression of RIPK1 upon rotenone exposure (Fig. 5K); another protein that involved in necroptosis induction is RIPK3, thus we next look into the expression pattern of RIPK3 and its phosphorylated form. We noticed ~2 fold increase in phospho-RIPK3 and ~ 1.2 fold increase in RIPK3 expression (Fig. 5L and M respectively). We further analysed the expression of MLKL-the necroptosis effector protein. We observed ~2.42 fold increase in the expression of phopho-MLKL (Fig. 5N) after rotenone exposure with more or less no change in expression of MLKL (Fig. 5O). Further, we observed no detectable change in caspase 8 expression during the study (Fig. 5P), in addition, caspase 3 expression increased ~1.3 times upon rotenone exposure (Fig. 5Q).

3. Discussion

Most of the neurodegenerative disorders can be described as dynamic and separated processes involving interrelated features influencing each other, such as protein aggregation, mitochondrial dysfunction, cytoskeleton destabilization and subsequently death of

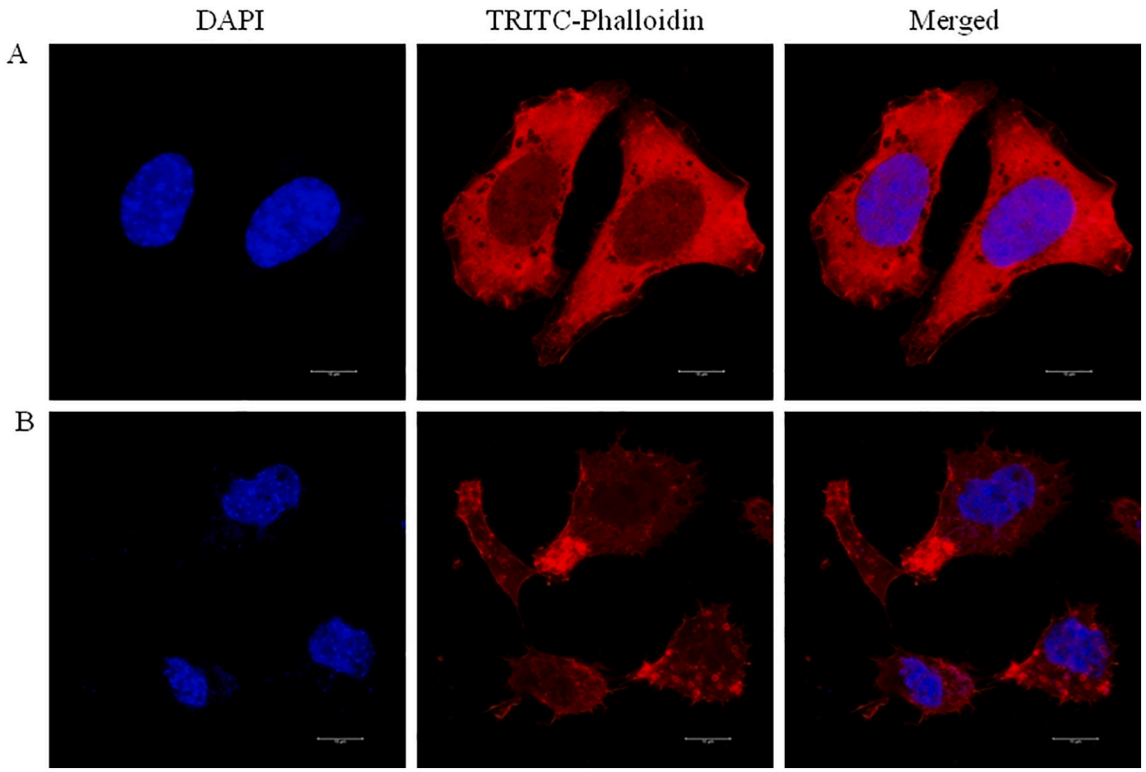

Fig. 4. Degradation of actin cytoskeleton in cultured N2A cells by rotenone. N2A cells were treated without (A) or with 100 μM rotenone (B) for 24 h followed by double staining with TRITC-Phalloidin for actin cytoskeleton and DAPI for nucleus. Condensed and fragmented nuclei and discontinuous and distorted staining for actin cytoskeleton are indicated by arrows.

neurons. In recent years necroptosis is considered as another type of programmed cell death other than apoptosis and necrosis. Necroptosis is also recognized as programmed necrosis or caspase-independent cell death and is assumed to activate an immense inflammatory response that can trigger significant collateral damage to the adjoining cells. Herein, the effect of a range of rotenone concentrations (10–100 μM) on cell viability was tested by CellTiter-Glo reagent, indicating a significant cytotoxic effect of rotenone on murine neuroblastoma (N2A) cells.. In this study RIPK1/RIPK3/MLKL was identified as the necroptosis controllers which supported the work of Wang et al., 2021 [14]. Activated RIPK1 phosphorylates RIPK3 providing a scaffold for RIPK3 autophosphorylation. [15]. In addition, RIPK3 was also shown to be activated independently of RIPK1 [16], which then phosphorylates MLKL at multiple sites [17]. Therefore, we assessed the expressions of phosphorylated and nonphosphorylated forms of RIPK1, RIPK3 and MLKL along with TNF-α by western blot analysis and observed significant upregulation in their expressions, confirming the involvement of necroptosis in rotenone mediated cytotoxicity in neuronal cells. Rotenone, a known inhibitor of the mitochondrial ETC complex I, is responsible for impairing the OXPHOS system and is responsible for increased ROS generation [18]. It has been implicated as the principal factor in activating mPTP opening upon upregulation of RIPK1/RIPK3 expressions [19], thereby accelerating the process of necroptosis. Increased level of ROS has been demonstrated to stabilize RIPK1/RIPK3 necrosome while RIPK1, RIPK3 and MLKL stimulate ROS production and further contribute to necrosome stabilization [20]. Thus provide a positive feedback loop to augment necroptosis [21]. RIPK3 interacts with key enzymes and thereby increases glucose metabolism, which in turn, increases mitochondrial oxidative phosphorylation and hence mtROS production [22]. Moreover, intracellular ROS, particularly the mitochondrial ROS produced in response to TNF/TNFR1 engagement significantly affects necroptosis. [23]. Altogether, mitochondrial dysfunction may be a consequence of the TNF-α mediated signaling and dispensable during necroptosis [24].

Reports suggest that the neurotoxic effects of rotenone are most likely due to oxidative stress rather than metabolic changes. The rate of ROS produced by mitochondria, mitochondrial membrane potential and the activity of ETC are highly interdependent; where mitochondrial membrane potential and ROS generation are inversely related [25]. We also observed a notable loss of mitochondrial transmembrane potential along with increased ROS production in N2A cells following rotenone exposure. Such alterations in mitochondrial functioning may lead to dysregulation of actin dynamics. Further, cofilin is a key component of actin cytoskeleton; hence an alteration in its expression was expected. The disruption and destabilization of the actin cytoskeleton of N2A cells were visualized by confocal microscopy as the loss of actin fibres that may be a result of altered expression of cofilin. Further by inhibiting the mitochondrial respiratory chain at the complex I, rotenone decreases the cellular ATP level. ATP can perform as a switch between apoptosis and necrosis [26]. It was reported that, reduced intracellular ATP level in comparison to normal inhibits apoptosis [27]. In accordance, we observed a significant loss in intracellular ATP content in rotenone treated cells as compared to control suggesting programmed death via the necroptotic pathway.

Furthermore, intracellular proteins like alpha-synuclein are very much linked with aggregation, and synchronized by a balance between synthesis and degradation. Its over-expression may lead to the death of dopaminergic neurons demonstrating the crucial role of alpha-synuclein in familial and sporadic cases of PD [28]. We observed enhanced alpha-synuclein protein levels along with its transcription in rotenone exposed cells, suggesting the impaired degradation of the protein leading the cells to enter the death pathways. The co-IP experiments depicts that necroptotic death induced by rotenone is not dependent on the interaction between alpha synuclein and the terminal necroptosis executor protein (Sup. Fig. 3). Another protein UCHL-1 is located throughout the cytoplasm along with alpha synuclein. But the expression patterns of

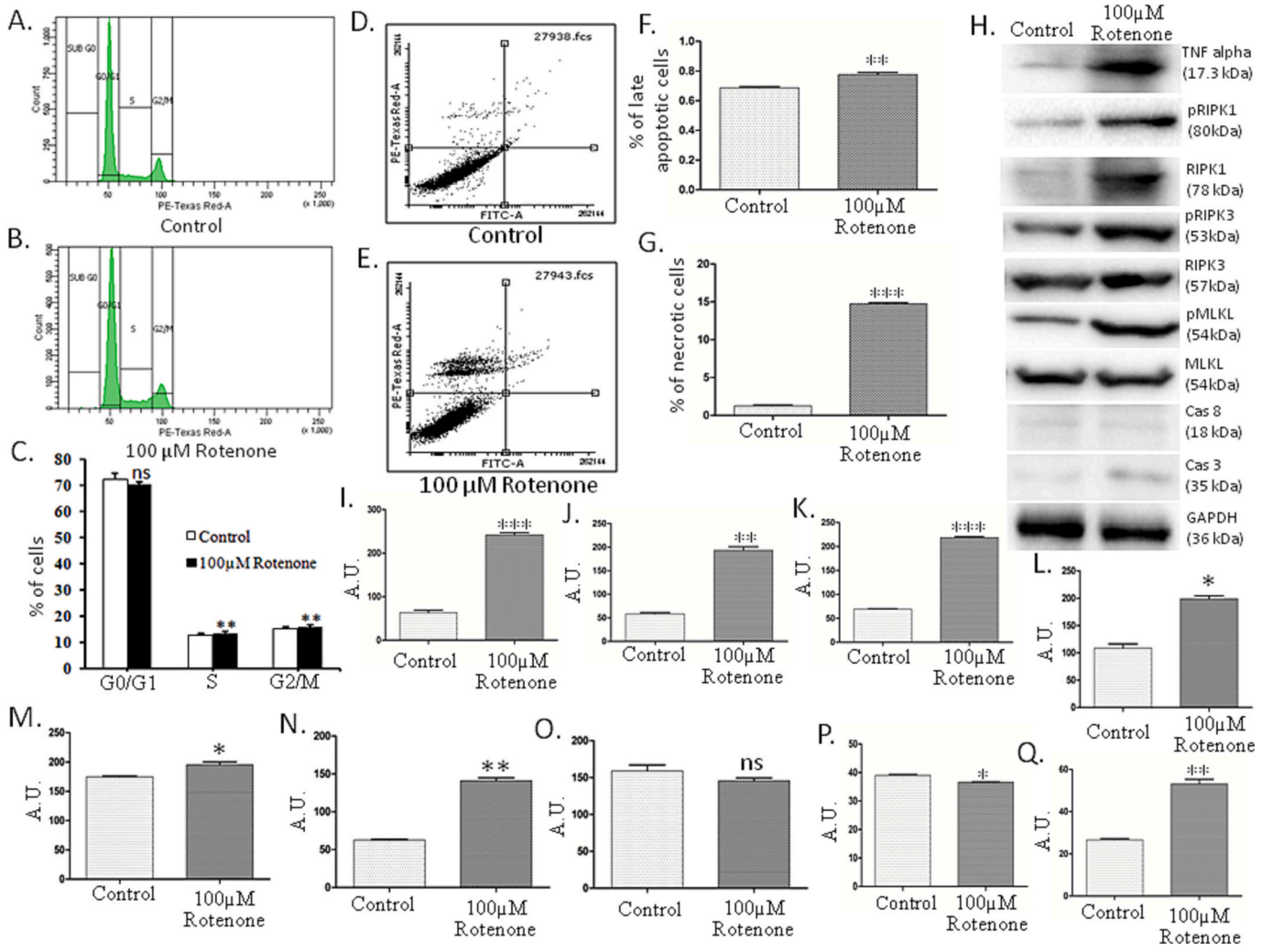

Fig. 5. N2A cells undergo necroptosis upon rotenone exposure. (A, B) Cell cycle analysis of control and rotenone exposed cells respectively. (C) Percentage of cell present in each phases of cell cycle. (D, E) Annexin V-FITC apoptosis detection method wasused to evaluate apoptotic and necroptotic cells respectively. (F) Densitometric analysis of percentage of apoptotic cells (**$P < 0.01$ vs control Student's *t*-test, paired, two-tailed).
(G) Densitometric analysis of percentage of necroptotic cells (***$P < 0.001$ vs control). Student's t-test, paired, two-tailed. (H) Protein expression patterns by Western immunoblotting (I) Densitometric analysis of TNF alpha expression (***$P < 0.0001$ vs control, Student's t-test, paired, two-tailed) (J) Densitometric analysis of phospho-RIPK1 expression (**$P = 0.0014$ vs control, Student's t-test, paired, two-tailed) (K) Densitometric analysis of RIPK1 expression (***P < 0.0001 vs control, Student's t-test, paired, two-tailed) (L) Densitometric analysis of phospho-RIPK3 (*$P = 0.0208$ vs control, Student's t-test, paired, two-tailed) (M) Densitometric analysis of RIPK3 (*$P = 0.0155$ vs control, Student's t-test, paired, two-tailed) (N) Densitometric analysis of phospho-MLKL (**$P = 0.0013$ vs control, Student's t-test, paired, two-tailed) (O) Densitometric analysis of MLKL ($^{ns}P = 0.1147$ vs control, Student's t-test, paired, two-tailed) (P) Densitometric analysis of caspase 8 expression (*$P = 0.0239$ vs control, Student's t-test, paired, two-tailed). (Q) Densitometric analysis of caspase 3 expression (**$P = 0.0038$ vs control, Student's t-test, paired, two-tailed).

these two proteins are inversely related. Although, the fundamental mechanism by which alpha synuclein and UCHL1 modulate each other's expression pattern remains a mystery; one possibility may be a direct interaction between these two proteins. Additionally, it is thought that conformation of alpha synuclein protein has been altered by the proteolytic activity of MMPs [29]. MMPs are the member of a family of extracellular soluble or membrane-bound endopeptidases; predominantly synthesized by microglia, astrocytes and neurons and are involved in remodeling the extracellular matrix as well the neuroinflammatory responses, suggesting role of MMPs in neurodegenerative disorders [30]. We observed an increased level of expression as well as activity of MMP9 in rotenone treated cells and its activity is modulated by tissue inhibitors of metalloproteinases-1 (TIMP-1), suggesting the role of altered MMP9 expression in rotenone induced PD like pathogenesis although the molecular mechanisms behind the reduction of TIMP-1 remain unclear. Further, the localization of MMP9 along with alpha-synuclein, UCHL1 and cofilin suggested their close proximity and possible interaction upon rotenone exposure for cellular death. Our study revealed that alpha synuclein interacts with MMP9 as well all cofilin as confirmed by the Co-IP experiments, thereby inducing neuroinflammation and cytoskeleton degradation.

4. Materials and methods

4.1. Materials

Chemicals were mostly obtained from Sigma (St. Louis, MO, USA). Protease inhibitor cocktail was acquired from Calbiochem (Calbiochem-539137). Bradford reagent and HRP luminescent substrate solution were purchased from Bio-Rad (Hercules, CA, USA). Alpha-synuclein (sc-53955), UCHL1 (sc-271639), Cofilin (sc-376476), MMP9 (sc-393859), TIMP-1 (sc-21734), Caspase 3 (sc-56053), RIPK1 (sc-133102), RIPK3

(sc-374639) and GAPDH (sc-365062) antibodies were procured from Santa Cruz Biotechnology (CA, USA). p-RIPK3 antibody (ab195117) was purchased from Abcam. MLKL (37705S) and p-MLKL (37333S) were procured from Cell Signaling Technology (MA, USA). The phalloidin stain was obtained from Merck Millipore (P1951). Mitosox Red (M36008), p-RIPK1 antibody (PA5-117250), ATP kit (A22066) and TRIzol (15596-018) were purchased from Invitrogen, CA. CellTiter-Glo kit was obtained from Promega (G7570). N2A cells were procured from American Type Culture Collection (ATCC). All cell culture related materials were sourced from Gibco (Thermo Fisher, MA, USA).

4.2. N2A cell culture, differentiation and treatment paradigm

Mouse Neuroblastoma (N2A) cells were grown in DMEM medium (Gibco, Invitrogen, USA) containing 10 % heat-inactivated fetal bovine serum, 2 mM glutamine, 100 units/ml penicillin, 100 μg/ml streptomycin (Gibco, Invitrogen, USA) in a humidified settings having 5 % CO_2 and 95 % air at 37 °C. For neuron-like differentiation the N2A cells were grown in serum deprived condition for 12 h in DMEM medium [31]. All experiments were executed with the differentiated N2A cells. Sterile tissue-culture flasks (25cm^2) were used to maintain the cells in culture and maximum 5 cell passages were used for this study.

4.3. Assessment of cell viability

Cell survival was assessed after the completion of the incubation time. 50 μl of CellTiter-Glo reagent solution was added into each well and mixed thoroughly with the culture medium. The reaction was carried for 15mins. Luminescent signal was then measured in a microplate luminometer (Glomax, 20/20 Luminometer, USA). The experiment was performed five times keeping triplicate for each set.

4.4. Quantifying ROS in N2A cells upon rotenone exposure

ROS sensitive and cell permeable fluorescent dye (DCF-DA, Sigma-Aldrich, USA) was used to measure intracellular ROS and Mitosox Red was used to measure intracellular superoxide production. In the intracellular space DCF-DA was oxidized to DCF (2′,7′-dichlorofluorescein) in presence of ROS. DCF is an extremely fluorescent compound with excitation 475 nm and emission 525 nm [32]. Whereas, Mitosox Red oxidizes by mitochondrial superoxides and produce bright red fluorescence with excitation 561 nm and emission 610 nm [33]. Cells were incubated with 100 μM rotenone for 24 h. Afterwards cells were carefully washed in pre-warmed PBS and incubated with either DCF-DA (20 μM) or Mitosox Red (5 μM) for 30 min at 37 °C in Krebs–Ringer's buffer (130 mM NaCl, 5 mM KCl, 10 mM glucose, 2 mM MgCl2, 1 mM CaCl2, 20 mM HEPES) maintaining dark condition. The dye laden cells were washed two times before the measurement of fluorescence. The fluorescence intensity was measured in an F-7 Fluorescence Spectro Photometer (Hitachi High Technologies Corporation) with proper subtraction of the background fluorescence.

4.5. Live cell imaging with Mitosox Red

Cells were incubated with or without 100 μM rotenone for 24 h. Afterwards cells were carefully washed in pre-warmed PBS and incubated with Mitosox Red (5 μM) for 30 min in Krebs–Ringer's buffer (130 mM NaCl, 5 mM KCl, 10 mM glucose, 2 mM MgCl2, 1 mM CaCl2, 20 mM HEPES) maintaining dark condition. The dye laden cells were washed twice before live cell imaging with an excitation of 561 nm and emission 610 nm [33]. The cells were viewed under a high resolution Stimulated Emission Depletion Microscopy (STED) (Leica TCS SP8). For imaging, 63 × 1.4 a numerical aperture oil immersion objective was used. Images were collected during a single session keeping identical settings with randomly selected fields. The images were representative of five complete sets of experiments.

4.6. Quantification of mitochondrial transmembrane potential

Mitochondrial transmembrane potential was evaluated by using JC-1 [34]. Depending on the negative mitochondrial membrane potential JC-1 accumulates within mitochondria forming J-aggregates, while the monomeric type of the dye remains dispersed in the cytoplasm. The monomeric form has its excitation at 490 nm and emission at 527 nm whereas the aggregate has its excitation at 490 nm and emits at 590 nm. Mitochondrial membrane potential within intact cells was calculated as the ratio of fluorescence intensities at 590 nm and 535 nm [34]. The control and rotenone exposed cells were washed two times with pre-warmed PBS, re-suspended in 1 ml of incomplete media containing JC-1 (final concentration, 10 μM) and incubated at 37 °C for half an hour maintaining dark condition. The dye-contained cells were again washed twice with pre-warmed incomplete media to get rid of the excess dye before the measurement of fluorescence intensities in an F-7 Fluorescence Spectro-photometer (Hitachi High Technologies Corporation).

4.7. Measurement of intracellular ATP concentration

The intracellular ATP level was evaluated in non-treated and rotenone exposed N2A cells using a commercial kit relied on luciferin–luciferase reaction (Invitrogen, USA). Briefly, following rotenone exposure for 24 h the treated and untreated cells were washed with PBS, lysed by an ice-cold lysis-buffer containing 10 mM Tris, 1 mM EDTA, 0.5 % Triton X-100, pH 7.6 and then instantly used for measurement of ATP content [35]. The luminescence thus generated was monitored immediately in a microplate luminometer (Glomax, 20/20 Luminometer, USA) according to the manufacturer's protocol. An ATP-standard curve of known concentration was used to calculate intracellular ATP content and the values were represented as nmol of ATP/mg of protein [35].

4.8. Gelatin zymography

The gelatinase activity in control and rotenone treated N2A cells were assessed by gelatin zymography. In brief, equal volume of experimental media (70 μg of total protein) was loaded in the lanes and electrophoresed in 8 % SDS-poly acrylamide gel containing 1.2 mg/ml gelatin under non-reducing condition [32]. The gel was washed in 2.5 % Triton X-100 and then kept for 18 h at 37 °C in calcium assay buffer containing 40 mm Tris–HCl, pH 7.4, 0.2 M NaCl, 10 mM $CaCl_2$. Staining of gels was then performed by 0.1 % Coomassie blue. The gelatinolytic activity has shown as negative staining. The of band intensities was quantified by densitometry using ImageJ software.

4.9. Reverse zymography

The activity of TIMP-1 was analysed by reverse zymography [32]. Briefly, culture media from treated and untreated N2A cells (70 μg protein) were electrophoresed in 1 mg/ml gelatin containing 12 % SDS-PAGE under non-reducing conditions. As MMP source we used conditioned media of MDA-MB-231 cells. After electrophoresis, the gels were washed, incubated in calcium assay buffer and stained by 0.1 % Coomassie blue. The regions of TIMP-1 activity have shown as coloured bands and the band intensities were quantified densitometrically by ImageJ software.

4.10. Effect of rotenone on gene expression

Total RNA extraction was performed from control and rotenone treated cells using TRIzol (Invitrogen, CA). After extraction, RNA was treated with DNase I, to eliminate contaminating DNA followed by reverse transcription utilizing random primers. The conventional PCR analysis for a fragment of alpha-synuclein, UCHL1, Cofilin 1 and 2 genes was performed using GAPDH as the reference gene (Sigma, USA) Primer sets are available in Table 1.

Table 1
Showing the primer sequences used in this study.

Gene	Primer Sequence
UCHL1-F	5′- ATG CAG CTG AAA CCG ATG -3′
UCHL1-R	5′- TTA GGC TGC TTT GCA GAG A-3′
cofilin 1-F	5′- AAC ATG GCC TCT GGT GTG -3′
cofilin 1-R	5′ - TCA CAA AGG CTT GCC CTC- 3′
cofilin 2-F	5′- ATG GCA TCT GGA GTT ACA GT -3′
cofilin 2-R	5′-TTA TAG TGG CTT TCC TTC AAG G-3′
α-synuclein-F	5′- ATG GAT GTG TTC ATG AAA GGA C-3′
α-synuclein-R	5′-TTA GGC TTC AGG CTC ATA GT-3′
GAPDH-F	5′-ATGGTGAAGGTCGGTGT-3′
GAPDH-R	5′-CTCCTTGGAGGCCATGTA-3′

4.11. Western blot analysis

N2A cells were treated with or without rotenone for 24 h. Afterwards, cells were lysed (composition of lysis buffer: 1 % Triton X-100, 150 mM NaCl, and 10 mM Tris-HCL-pH 8.0, containing a protease inhibitor cocktail from calbiochem) by repeated freeze-thaw cycle and centrifuged at 12,000 rpm for 10 min at 4 °C. SDS-PAGE was performed using 50 μg of total protein followed by immunoblotting [32] and then incubated at 4 °C using respective primary antibodies at 1:500 dilutions in 0.3 % BSA. The blots were then washed with TBST, incubated with HRP-conjugated secondary antibody and visualization of bands was performed using western ECL substrate solution (Bio-rad laboratories, USA). GAPDH was used as the loading control.

4.12. Co-immunoprecipitation

Cell lysates from both rotenone treated and untreated cells were prepared by adding cell lysis buffer (1 % Triton X-100, 137 mM NaCl, 20 mM Tris-HCL-pH 8.0, 2 mM EDTA and protease inhibitor cocktail). In between 50 μl of A/G agarose beads were prepared by washing with lysis buffer and blocked in 0.1 % BSA. 10 μl of primary antibody was next added to the beads and incubated for 4 h at 4 °C on a shaker. Beads were centrifuged at 1500 *g* for 5mins at 4 °C and the supernatant was discarded. These antibody coated beads were washed and 150 μg of cell lysate was added to it. The sample loaded beads were incubated overnight at 4 °C, centrifuged and the supernatant was removed. The beads were again washed before the beads were finally eluted by heating at 50 °C for 10mins in 50 μl of SDS-PAGE loading buffer without DTT. Beads were pelleted and 100 mM DTT was added to the supernatant [36]. The immunoprecipitated samples, thus obtained, were analysed by western blotting.

4.13. Studying co-localization of proteins

Untreated and treated N2A cells were washed twice with ice cold PBS before fixation with 4 % paraformaldehyde for 10 min, then permeabilized with 0.1 % Triton X-100 for 10 min, blocked with 5 % BSA for 30 min at room temperature and then incubated with primary antibodies overnight at 4 °C using different combinations of primary antibodies (1:200 dilutions in TBS with 1 % BSA). Unbound primary antibodies were washed with PBS (three times) following incubation with Texas Red or FITC-conjugated secondary antibody (Santa Cruz Biotechnology, USA) solutions (1:400 dilutions in TBS containing 1 % BSA) respectively [37] for 2 h at room temperature, washed five times in PBS, mounted with Fluoromount Aqueous Mounting Medium (Sigma, USA) and analysed using a high resolution Stimulated Emission Depletion Microscopy (STED) (Leica TCS SP8). A 63 × 1.4 numerical aperture oil immersion objective was used for all imaging. Images were collected during a single session keeping identical settings. Randomly selected fields were used to identify localization of different proteins. The images were representative of five individual experiments to eliminate any artefacts that may arise from individual experiments.

4.14. TRITC-Phalloidin staining of actin cytoskeleton

Fixed control and rotenone treated N2A cells were incubated with DAPI to stain the nucleus for 5 min followed by incubation with TRITC-Phalloidin (1 mg/ml in PBS) for 30 min at 37 °C. Mounting of cells were performed with Fluoromount Aqueous Mounting Medium (Sigma, USA) and viewed by a high resolution Stimulated Emission Depletion Microscopy (STED) (Leica TCS SP8). For imaging, 63 × 1.4 a numerical aperture oil immersion objective was used. Images were collected during a single session keeping identical settings with randomly selected fields. The images were representative of five complete sets of experiments.

4.15. Cell cycle analysis

N2A cells plated at a density of 1×10^6 cells per 60 mm dish were treated with or without rotenone for 24 h. After completion of the incubation, cells were trypsinized, washed, fixed using chilled ethanol (70 %) and kept at 4 °C for 16–18 h. Staining was performed with a solution containing 50 μg/ml propidium iodide and 100 μg/ml RNase, incubated at room temperature for 15 min and analysed immediately by flow cytometry.

4.16. Analyzing the cell death procedures by FACS

FITC Annexin V apoptosis detection kit I (BD Pharmingen; BD Biosciences, Franklin Lakes, NJ, USA, 556547) was used to analyze the cell death, following the manufacturer's instructions. Briefly, N2A cells were exposed to 100 μM rotenone for 24 h, trypsinized, washed and stained according to the manufacturer's guideline. The stained cells were then analysed by BD LSRFortessa™ Cell Analyzer-Flow Cytometers and data was processed using Flowing Software 2. Each sample was analysed using 10,000 events.

4.17. Protein quantification

The protein content was quantified after solubilising the cell membranes in lysis buffer by using Bradford reagent (Sigma, USA) according to the manufacturer's protocol.

4.18. Statistics

Statistical analyses for every experiment were executed using Prism software, version 5 (GraphPad). Differences between groups were analysed by two-tailed, paired, Student's *t*-test. Data are expressed as mean ± SEM for at least five independent experimentations, and significance was considered when $p \leq 0.05$.

Supplementary data to this article can be found online at https://doi.org/10.1016/j.bbamcr.2022.119417.

CRediT authorship contribution statement

Conception and design of study was performed by *T. Roy* and S. Swarnakar, acquisition of data was performed by *T. Roy* and A. Chatterjee, analysis and/or interpretation of data was performed by *T. Roy* and A. Chatterjee. The manuscript was initially drafted by *T. Roy* and A. Chatterjee. *T. Roy* and S. Swarnakar have revised the manuscript critically. All the authors have read and approve the final manuscript.

Declaration of competing interest

We wish to confirm that there are no known conflicts of interest associated with this publication and there has been no significant financial support for this work that could have influenced its outcome. We confirm that the manuscript has been read and approved by all named authors and that there are no other persons who satisfied the

criteria for authorship but are not listed. We further confirm that the order of authors listed in the manuscript has been approved by all of us. We confirm that we have given due consideration to the protection of intellectual property associated with this work. We confirm that we have followed the regulations of our institutions concerning intellectual property.

We understand that the Corresponding Author is the sole contact for the Editorial process (including Editorial Manager and direct communications with the office). She is responsible for communicating with the other authors about progress, submissions of revisions and final approval of proofs. We confirm that we have provided a current, correct email address which is accessible by the Corresponding Author.

Data availability

Data will be made available on request.

Acknowledgments

This research was supported by grants from Science and Engineering Research Board (SERB), Department of Science & Technology, Government of India. Tapasi Roy acknowledges the receipt of National Post Doctoral Fellowship from SERB. Abhishek Chatterjee would like to acknowledge the University Grants Commission (UGC), India for providing financial support.

References

[1] N. Ling, Rotenone - a review of its toxicity and use for fisheries management, Sci. Conserv. 211 (2003) 1–40.
[2] W. McClay, Rotenone use in North America (1988–1997), Fisheries 25 (2000) 15–21.
[3] S. Murakami, I. Miyazaki, K. Miyoshi, M. Asanuma, Long-term systemic exposure to rotenone induces central and peripheral pathology of Parkinson's disease in mice, Neurochem. Res. 40 (2015) 1165–1178, https://doi.org/10.1007/s11064-015-1577-2.
[4] S. Duty, P. Jenner, Animal models of Parkinson's disease: a source of novel treatments and clues to the cause of the disease, Br. J. Pharmacol. 164 (2011) 1357–1391, https://doi.org/10.1111/j.1476-5381.2011.01426.x.
[5] T.N. Martinez, J.T. Greenamyre, Toxin models of mitochondrial dysfunction in Parkinson's disease, Antioxid. Redox Signal. 16 (2012) 920–934, https://doi.org/10.1089/ars.2011.4033.
[6] P.P. Hsu, D.M. Sabatini, Cancer cell metabolism: Warburg and beyond, Cell 134 (2008) 703–707, https://doi.org/10.1016/j.cell.2008.08.021.
[7] A.J. Whitworth, L.J. Pallanck, PINK1/Parkin mitophagy and neurodegeneration-what do we really know in vivo? Curr. Opin. Genet. Dev. 44 (2017) 47–53, https://doi.org/10.1016/j.gde.2017.01.016.
[8] S. Buratta, E. Chiaradia, A. Tognoloni, A. Gambelunghe, C. Meschini, L. Palmieri, G. Muzi, L. Urbanelli, C. Emiliani, B. Tancini, Effect of curcumin on protein damage induced by rotenone in dopaminergic PC12 cells, Int. J. Mol. Sci. 21 (2020) 2761, https://doi.org/10.3390/ijms21082761.
[9] J.D. Guo, X. Zhao, Y. Li, G.R. Li, X.L. Liu, Damage to dopaminergic neurons by oxidative stress in Parkinson's disease, Int. J. Mol. Med. 41 (2018) 1817–1825.
[10] R. Betarbet, T.B. Sherer, G. Mackenzie, M. Garcia-Osuna, A.V. Panov, J. T. Greenamyre, Chronic systemic pesticide exposure reproduces features of Parkinson's disease, Nat. Neurosci. 3 (2000) 1301–1306, https://doi.org/10.1038/81834.
[11] M.E. Johnson, L. Bobrovskaya, An update on the rotenone models of Parkinson's disease: their ability to reproduce the features of clinical disease and model gene–environment interactions, Neurotoxicology 46 (2015) 101–116, https://doi.org/10.1016/j.neuro.2014.12.002.
[12] T. Chen, J. Tan, Z. Wan, Y. Zou, H.K. Afewerky, Z.E. Zhang, Effects of commonly used pesticides in China on the mitochondria and ubiquitin-proteasome system in Parkinson's disease, Int. J. Mol. Sci. 18 (2017), E2507.
[13] L.H. Sanders, T.J. Greenamyre, Oxidative damage to macromolecules in human parkinson disease and the rotenone model, Free Radic. Biol. Med. 62 (2013) 111–120.
[14] F. Wang, L. Tang, B. Liang, C. Jin, L. Gao, Y. Li, Z. Li, J. Shao, Z. Zhang, S. Tan, F. Zhang, S. Zheng, Yi-qi-Jian-pi formula suppresses RIPK1/RIPK3-complex-dependent necroptosis of hepatocytes through ROS signaling and attenuates liver injury in vivo and in vitro, Front. Pharmacol. 12 (2021), 658811, https://doi.org/10.3389/fphar.2021.658811.
[15] M.I. Faizan, T. Ahmad, Altered mitochondrial calcium handling and cell death by necroptosis: an emerging paradigm, Mitochondrion 57 (2021) 47–62, https://doi.org/10.1016/j.mito.2020.12.004.
[16] L. Wang, X. Chang, J. Feng, J. Yu, G. Chen, TRADD mediates RIPK1- independent necroptosis induced by tumor necrosis factor, Front. Cell Dev. Biol. 7 (2019), https://doi.org/10.3389/fcell.2019.00393.
[17] E.J. Petrie, P.E. Czabotar, J.M. Murphy, The structural basis of necroptotic cell death signalling, Trends Biochem. Sci. 44 (2019) 53–63, https://doi.org/10.1016/j.tibs.2018.11.002.
[18] K. Radad, W.D. Rausch, G. Gille, Rotenone induces cell death in primary dopaminergic culture by increasing ROS production and inhibiting mitochondrial respiration, Neurochem. Int. 49 (2006) 379–386, https://doi.org/10.1016/j.neuint.2006.02.003.
[19] S. He, Y. Liang, F. Shao, X. Wang, Toll-like receptors activate programmed necrosis in macrophages through a receptor-interacting Kinase-3-mediated pathway, Proc. Natl. Acad. Sci. 108 (2011) 20054–20059, https://doi.org/10.1073/pnas.1116302108.
[20] F. Basit, L.M. van Oppen, L. Schöckel, H.M. Bossenbroek, S.E. van Emst-de Vries, J. C. Hermeling, S. Grefte, C. Kopitz, M. Heroult, P. Hgm Willems, W.J. Koopman, Mitochondrial complex I inhibition triggers a mitophagy-dependent ROS increase leading to necroptosis and ferroptosis in melanoma cells, Cell Death Dis. 8 (2017), e2716, https://doi.org/10.1038/cddis.2017.133.
[21] B. Schenk, S. Fulda, Reactive oxygen species regulate smac mimetic/TNFa-induced necroptotic signaling and cell death, Oncogene 34 (2015) (2015) 5796–5806, https://doi.org/10.1038/onc.2015.35.
[22] Z. Yang, Y. Wang, Y. Zhang, X. He, C.Q. Zhong, H. Ni, X. Chen, Y. Liang, J. Wu, S. Zhao, D. Zhou, J. Han, RIP3 targets pyruvate dehydrogenase complex to increase aerobic respiration in TNF-induced necroptosis, Nat. Cell Biol. 20 (2018) 186–197, https://doi.org/10.1038/s41556-017-0022-y.
[23] P. Zhu, S. Hu, Q. Jin, D. Li, F. Tian, S. Toan, Y. Li, H. Zhou, Y. Chen, Ripk3 promotes ER stress-induced necroptosis in cardiac IR injury: a mechanism involving calcium overload/XO/ROS/mPTP pathway, Redox Biol. 16 (2018) 157–168, https://doi.org/10.1016/j.redox.2018.02.019.
[24] L. Galluzzi, J.M. Bravo-San Pedro, O. Kepp, G. Kroemer, Regulated cell death and adaptive stress responses, CMLS 73 (2016) 2405–2410, https://doi.org/10.1007/s00018-016-2209-y.
[25] P.R. Angelova, A.Y. Abramov, Role of mitochondrial ROS in the brain: from physiology to neurodegeneration, FEBS Lett. 592 (2018) 692–702, https://doi.org/10.1002/1873-3468.12964.
[26] N. Li, K. Ragheb, G. Lawler, J. Sturgis, B. Rajwa, J.A. Melendez, J.P. Robinson, Mitochondrial complex I inhibitor rotenone induces apoptosis through enhancing mitochondrial reactive oxygen species production, J. Biol. Chem. 278 (2003) 8516–8525, https://doi.org/10.1074/jbc.M210432200.
[27] N. Li, K. Ragheb, G. Lawler, J. Sturgis, B. Rajwa, J.A. Melendez, J.P. Robinson, Mitochondrial complex I inhibitor rotenone induces apoptosis through enhancing mitochondrial reactive oxygen species production, J. Biol. Chem. 278 (2003) 8516–8525, https://doi.org/10.1074/jbc.M210432200. Epub 2002 Dec 20 PMID: 12496265.
[28] Y.H. Yuan, W.F. Yan, J.D. Sun, J.Y. Huang, Z. Mu, N.H. Chen, The molecular mechanism of rotenone-induced α-synuclein aggregation: emphasizing the role of the calcium/GSK3β pathway, Toxicol. Lett. 233 (2015) 163–171, https://doi.org/10.1016/j.toxlet.2014.11.029.
[29] B. Marjana, B. Sriram, L. Claude, V.E. Roosmarijn, Friends or foes: matrix metalloproteinases and their multifaceted roles in neurodegenerative diseases, Mediat. Inflamm. (2015), https://doi.org/10.1155/2015/620581.
[30] H.J. Sung, C.E. Johnson, S.M. Lessner, R. Magid, D.N. Drury, Z.S. Galis, Matrix metalloproteinase 9 facilitates collagen remodeling and angiogenesis for vascular constructs, Tissue Eng. 11 (2005) 267–276, https://doi.org/10.1089/ten.2005.11.267.
[31] E. Lekholm, M.M. Ceder, E.C. Forsberg, H.B. Schiöth, R. Fredriksson, Differentiation of two human neuroblastoma cell lines alters SV2 expression patterns, Cell Mol Biol Lett. 26 (2021) 5, https://doi.org/10.1186/s11658-020-00243-8.
[32] P. Choudhary, T. Roy, A. Chatterjee, V.K. Mishra, S. Pant, S. Swarnakar, Melatonin rescues swim stress induced gastric ulceration by inhibiting matrix metalloproteinase-3 via down-regulation of inflammatory signaling cascade, Life Sci. 297 (2022), 120426, https://doi.org/10.1016/j.lfs.2022.120426.
[33] M.L. Wheeler, A.L. Defranco, Prolonged production of reactive oxygen species in response to B cell receptor stimulation promotes B cell activation and proliferation, J. Immunol. 189 (2012) 4405–4416, https://doi.org/10.4049/jimmunol.1201433.
[34] D. Harshkova, E. Zielińska, A. Aksmann, Optimization of a microplate reader method for the analysis of changes in mitochondrial membrane potential in Chlamydomonas reinhardtii cells using the fluorochrome JC-1, J. Appl. Phycol. 31 (2019) 3691–3697, https://doi.org/10.1007/s10811-019-01860-3.
[35] G. Morciano, A.C. Sarti, S. Marchi, S. Missiroli, S. Falzoni, L. Raffaghello, V. Pistoia, C. Giorgi, F. Di-Virgilio, P. Pinton, Use of luciferase probes to measure ATP in living cells and animals, Nat. Protoc. 12 (2017) 1542–1562, https://doi.org/10.1038/nprot.2017.052.
[36] H. Iqbal, D.R. Akins, M.R. Kenedy, Co-immunoprecipitation for identifying protein-protein interactions in borrelia burgdorferi, Methods Mol. Biol. 1690 (2018) 47–55, https://doi.org/10.1007/978-1-4939-7383-5_4.
[37] W. Qin, J. Li, R. Zhu, S. Gao, J. Fan, M. Xia, R.C. Zhao, J. Zhang, Melatonin protects blood-brain barrier integrity and permeability by inhibiting matrix metalloproteinase-9 via the NOTCH3/NF-κB pathway, Aging 11 (2019) 11391–11415, https://doi.org/10.18632/aging.102537.

Life Sciences 297 (2022) 120426

Contents lists available at ScienceDirect

Life Sciences

journal homepage: www.elsevier.com/locate/lifescie

Melatonin rescues swim stress induced gastric ulceration by inhibiting matrix metalloproteinase-3 via down-regulation of inflammatory signaling cascade

Preety Choudhary [a], Tapasi Roy [a], Abhishek Chatterjee [a], Vineet Kumar Mishra [a], Suyash Pant [b], Snehasikta Swarnakar [a,*]

[a] Inflammatory Diseases and Immunology division, CSIR-Indian Institute of Chemical Biology, 4, Raja S.C. Mallick Road, Jadavpur, Kolkata 700032, West Bengal, India
[b] Department of Pharmacoinformatics, National Institute of Pharmaceutical Education and Research, Kolkata, West Bengal, India

ARTICLE INFO

Keywords:
Stress
Gastric ulcer
Matrix metalloproteinase
Extracellular matrix
Melatonin

ABSTRACT

Aim: This study investigated the link between forced swim induced acute gastric ulceration, inflammation and MMP-3 along with the possible mechanism of protective efficacy of melatonin.
Main methods: We distributed Balb/c mice into four different groups. Group 1 and 2 were given PBS gavage. Group 3 and 4 were given melatonin (60 mg/kg b.wt.) and omeprazole (25 mg/kg b.wt.), respectively, an hour prior to forced swim. Ulcer index, tissue histology, immunohistochemistry, protein carbonylation, lipid peroxidation, Myeloperoxidase, Zymography, Western blotting, reactive oxygen species (ROS), mitochondrial dehydrogenase, mitochondrial transmembrane potential and bioinformatical analysis were performed.
Key findings: Our data revealed that gastric ulceration due to forced swim stress is responsible for overproduction of ROS, which may be a prime reason for mitochondrial dysfunction and induction of apoptosis via activation of Caspase-3. ROS is also responsible for p38 phosphorylation which in turn increases the activity of MMP-3 in ulcerated milieu, along with the oxidation of proteins, peroxidation of lipids and altered expression patterns of heat shock protein (HSP)-70. Melatonin is shown to reduce the inflammatory burden in gastric milieu and offers gastroprotection by binding to the active site of MMP-3; thereby inhibiting its activity, as suggested by in silico studies. Melatonin also inhibits the downregulation of HSP-70 and activates p38 dephosphorylation and thereby, it rescues gastric mucosal cells from stress-induced ulceration.
Significance: Our findings suggest that, melatonin imparts its gastroprotective effect by down-regulating the activation of MAPK-ERK pathway along with binding to the active site of MMP-3.

1. Introduction

Stress is one of the modulators of inflammation and ulcer formation [1], leading to moderate or acute mucosal bleeding and its associated high mortality [2]. Persistent mental ailments often perturb normal gastrophysiology and morphology [3]. Other than *Helicobacter pylori* infection and excess consumption of non-steroidal anti-inflammatory drugs (NSAIDs), mucosal hypoxic-ischemia has been identified as another main reason for stomach injury [4]. Hypoxic-ischemia is known to induce oxidative stress by producing superoxide anions (O_2^-), hydrogen peroxide (H_2O_2), and hydroxyl radicals (·OH), resulting in the development of mucosal ulceration and subsequent cell death [5]. It is also associated with acute inflammatory response, marked by production of inflammatory mediators and infiltration of inflammatory cells. The recruited active neutrophils affects stress mediated pathophysiological processes occurring in the later stages of gastric inflammation [6]. Moreover, the neutrophils, monocytes, and macrophages are responsible for production of myeloperoxidase, a major source of reactive oxygen species (ROS) [7]. Myeloperoxidase produces hypochlorous acid (HOCl), a cytotoxic oxidant which cleaves several matrix metalloproteinases (MMPs) into their proteolytically active forms [8]. MMPs perform key function for extracellular matrix remodeling during gastric ulceration [9]. Their activity could be regulated at transcription level during synthesis of proenzyme or by the inhibition of enzyme activity [10].

The involvement of MMPs on gastric ulcers were mostly studied in

* Corresponding author.
E-mail address: sikta@iicb.res.in (S. Swarnakar).

https://doi.org/10.1016/j.lfs.2022.120426
Received 5 January 2022; Received in revised form 11 February 2022; Accepted 18 February 2022
Available online 23 February 2022

ethanol and NSAIDs induced gastropathy [11,9], but less is known about swim stress induced acute gastric mucosal injury. It has already been documented that numerous external stimuli including stress, growth factors and cytokines affects the expression of MMPs [12]. Additionally, TNF-α, IL-1β, and IL-18 have recently been identified as significant determining factors for stress mediated inflammation and gastric injury [13,14].

On the other hand, ROS activates various redox-sensitive signal transduction cascades [15], including the mitogen-activated protein (MAP) kinase, thereby regulating expression of several pro-inflammatory molecules [16]. The MAPK family member - p38 is recognized to perform a significant role in stress-mediated immune and inflammatory responses, apoptosis and cell survival processes [17]. Stress is also known to activate extracellular signal-regulated kinase (ERK)-1/2 and c-Jun N-terminal *kinases (*JNK) [18,19]. The phosphorylated products of JNK and ERK after dimerization, enters into the nucleus and increase the transcription of many MMPs and other inflammatory genes [20].

Moreover, it is well known that stress is responsible for ROS production and melatonin regulate the homeostasis of the gastro-intestinal tract. [21]. It has potent anti-inflammatory and antioxidant activity which provide protection to cells and tissues from adverse effects of ROS via diminishing glutathione reductase activity, myeloperoxidase (MPO) activity and lipid peroxidation [22]. Several studies on cancer metastasis and gastric ulcer have demonstrated the regulatory mechanism of melatonin on cell-matrix interaction and remodeling of ECM by MMPs [23,24]. Melatonin is also known to inhibit MMP-9 activity by directly interacting to its active site cleft [25]. The present study is designed to demonstrate the link between forced swim induced acute gastric ulceration, inflammation and MMP-3, along with the possible mechanism of protective efficacy of melatonin.

2. Material and methods

2.1. Materials

All the chemicals used in this present study were purchased from Sigma (St. Louis, MO, USA). Protease inhibitors cocktail was purchased from Calbiochem (Calbiochem-539,137). Bradford reagent and HRP luminescent substrate solution were obtained from Bio-Rad (Hercules, CA, USA). MMP-3 (sc-21,732), TIMP-1 (sc-21,734), phospho-p38 (sc-7973), p38 (sc-7972), HSP-70 (sc-24), Caspase-3 (sc-56,053), TNF-α (sc-52,746), IL-1β (sc-52,012), p-p65 NFκB (sc-166,748), ERK 1/2 (sc-135,900) and GAPDH (sc-365,062) antibodies were procured from Santa Cruz Biotechnology (CA, USA). The phospho-ERK1/2 (05-797R) antibody was obtained from Merck Millipore.

2.2. Experimental design

6 to 8 weeks old mice (Balb/c; male) were bred in-house and kept in an air-conditioned chamber, maintained at 22 °C with 12 h light/dark cycle. The mice were fed with regular chow diet and autoclaved tap water. A total of 40 mice were alienated blindly keeping 10 animals each in four randomly-assigned groups. All mice in the four groups were fasted for 18 h, before the beginning of this experiment. The control group (Group 1) and Group 2 were given PBS gavage. Group 3 mice were given melatonin (60 mg/kg b.wt.), which was administered via oral gavages. Group 4 was the positive control; where a potent antioxidant drug - omeprazole, was fed orally to the mice at a dose of 25 mg/kg b.wt. An hour after drug treatment, the three groups (Group 2, 3 and 4) were subjected to swim stress to induce gastric ulceration. The experimental procedures were conducted with approval of the animal ethical committee of the institute (IICB/AEC/Meeting/September 2019).

2.3. Induction of gastric ulcer

Gastric ulceration was induced by forcing the mice to swim in a half water filled vertical cylinder (height 40 cm and diameter 20 cm), maintaining the temperature at 22 ± 2 °C [26]. After 4 h, the mice were sacrificed and their stomachs were harvested for scoring the ulcer index [9]. Lesions were calculated as: '0' signifies no pathology; '10' scored for a pinhead ulcer and '20'–'50'represents lesions of 2–5 mm length according to standard protocol [9]. The mean was represented by the total scores divided by the number of animals.

2.4. Tissue histology

For histological studies, stomach tissues from each experimental group were fixed in 4% paraformaldehyde after being sectioned into 2–3 mm^2 pieces. Fixed and paraffin embedded tissue blocks were sliced into 5 μm thick sections and transferred onto glass slides. These sections were either counter-stained with hematoxylin and eosin [27], or subjected to TUNEL assay using commercially available kit (Novus Biologicals; Colorado, USA). Collagen fibers of the gastric tissue sections were stained using the Masson's Trichrome Staining kit as per manufacturer's protocol. The processed slides were mounted using DPX. An Olympus microscope, loaded with Camedia software (E-20P 5.0 Megapixel), was used to capture images.

2.5. Immunohistochemistry

Immunohistochemical staining of tissue sections were performed as previously described [25]. Briefly, tissue sections were deparaffinized in xylene and hydrated through a decreasing percentage of ethanol. For better detection, sections were incubated in antigen retrieval buffer (0.03% trypsin, 0.1% $CaCl_2$, pH 7.8) for 30 min at 37 °C. The tissue sections were incubated with anti-MMP-3 antibody (diluted 1:200) overnight at 4 °C, washed and incubated with Texas Red conjugated secondary antibody. The slides were washed twice before counter staining the nuclei with DAPI. The processed slides were mounted using fluoro-Mount mounting medium. An Olympus microscope, loaded with Camedia software (E-20P 5.0 Megapixel), was used to capture images.

2.6. Extraction and estimation of tissue protein

The stomach tissue sample was homogenized in 10 mM phosphate buffered saline (PBS) added with protease inhibitor cocktail (PIC), followed by incubation for 10 min., then centrifuged for 15 min at 12,000*g*. The resulting supernatant was labeled as "PBS extract". The residual pellet was resuspended in lysis buffer containing 10 mM Tris-HCl pH 8.0, 150 mM NaCl, 1% Triton X-100 and PIC, followed by another round of centrifugation at the same settings. The supernatant obtained after this step was collected and labeled as "TX extract". Both the extracts were kept at −80 °C till further use. Lowry assay was performed for tissue protein estimation [28].

2.7. Determination of protein carbonyl content

The gastric tissue from each experimental group were homogenized in 50 mM sodium phosphate buffer (pH 7.4) and centrifuged for 10 min at 600 *g*. 10% trichloroacetic acid (TCA) was used to precipitate the obtained supernatant and then 10 mM 2, 4-dinitrophenyl hydrazine (DNPH) was added to the obtained precipitate and incubated for 1 h. This solution was again precipitated with 20% TCA; washed for three times using 1:1 mixture of ethanol and ethyl acetate. 6 M guanidine HCl in 20 mM potassium phosphate (pH 2.3) was then used to dissolve the obtained pellet. After a final centrifugation, the supernatant was used to measure the carbonyl content at 362 nm (ϵ = 22,000/M/cm) [29].

2.8. Measurement of lipid peroxide

The PBS extract was used to measure lipid peroxide content. Briefly, TCA-TBA-HCl (15% TCA, 0.375% TBA, 0.25 N HCl) reagent was allowed to react with the PBS extract of gastric tissues in 2:1 ratio. This solution was heated at 100 °C for 15 min, cooled and centrifuged for 10 min at 600 *g*. The nano moles of thiobarbituric acid reactive species (TBARS) was measured at the absorbance of 535 nm ($\epsilon = 1.5 \times 10^5$/ M/cm) [29].

2.9. Myeloperoxidase assay

The Myeloperoxidase (MPO) activity was calculated via an assay with guaiacol as substrate. In brief, after homogenizing the respective tissue in 5 mM phosphate buffer; 1 ml of reaction buffer containing 0.4 M guaiacol and 0.5 mM H_2O_2 in 50 mM phosphate buffer (pH 7.4) was added to the tissue homogenate. The generation of tetraguaiacol was measured kinetically at 470 nm ($\epsilon = 26.6$/mM/cm) [29].

2.10. Casein zymography

The PBS extract of gastric tissues were used for zymographic studies. We have performed casein zymography in order to identify caseinolytic MMPs. For casein zymography, 100 μg protein was electrophoresed in 10% SDS-PAGE added with casein (1 mg/ml), washed and incubated for 21 h. at 37 °C in buffer containing 100 mM Tris-HCl, 5 mM $CaCl_2$, 0.001% (*w/v*) sodium azide and 0.005% (*v*/v) Brij-35 (pH 7.4). The gels were then stained with 0.1% coomassie blue solution. The caseinolytic activities of MMPs were observed as negatively stained bands after de-staining. The bands were visualized using software and quantified densitometrically (Image Lab, Bio-Rad Laboratories, Germany) [30].

2.11. Reverse zymography

For reverse zymographic analysis of TIMP-1, the PBS extracts (100-μg protein) were electrophoresed in 1 mg/ml gelatin containing 12% SDS-PAGE under nonreducing conditions. As MMP source, PBS tissue extracts of control mice with high expression of MMP-2 was copolymerized with the gelatin-SDS-PAGE gel. Tissue samples from all the experimental groups were loaded equally in all the lanes. The gels were washed and incubated as described in the previous section [30].

2.12. Western blotting

100 μg of total protein from the TX extracts were resolved by 10% reducing SDS-PAGE, transferred to nitrocellulose membranes, blocked for 2 h at room temperature in 3% bovine serum albumin (BSA) prepared in TBST (20 mM Tris-HCl, pH 7.4 containing 150 mM NaCl and 0.02% Tween 20), incubated overnight at 4 °C with primary antibodies against MMP-3, TIMP-1, phospho-p38, p38, HSP-70, Caspase-3, TNF-α, IL-1β, phospho-p65 NFκB, phospho-ERK 1/2, ERK 1/2 and GAPDH. Finally the blots were washed with TBST and incubated with HRP-conjugated secondary antibodies and visualized using HRP luminescent substrate solution [31].

2.13. Measurement of total ROS

Gastric tissue extracts from all four experimental groups, were incubated for 30 min. With 2′, 7′-Dichlorofluorescin diacetate (DCFDA), washed three times and the emitted fluorescence was measured in F-7000 Fluorescence Spectrophotometer (Hitachi High-Technologies Corporation).

2.14. Studying mitochondrial dehydrogenase activity

Mitochondria were isolated from gastric tissues using differential centrifugation procedures [32], protein content was calculated following Lowry method [28], incubated for 4 h at 37 °C in 5% CO_2 chamber with MTT solution. The purple-colored solution thus developed after addition of DMSO was measured at 570 nm [33].

2.15. Measurement of mitochondrial transmembrane potential ($\Delta\psi m$)

Mitochondria were incubated for 15 min in dark with 300 nM JC-1. The fluorescence intensities were measured at excitation, 490 nm; emission, 530 nm for JC-1 monomer and 590 nm for JC-1 aggregates [33].

2.16. In silico study

2.16.1. System preparation for bioinformatics study using computational methodology

X-ray structures of the MMP-3 (PDB ID: 1HY7) protein, bound to inhibitors were extracted from protein data bank. The catalytic Zn^{2+} ion bound to the active site of MMP-3 was considered during the docking procedure and molecular dynamics simulation. The three-dimensional structures were drawn in Marvin sketch and minimized in ligprep module of Schrodinger suite. OPLS2005 force field was employed for minimization and geometry optimization at pH 7.4, consequently the minimized structures was subjected for molecule docking.

2.16.2. Molecular docking

Docking of melatonin into the active site of MMP-3 was carried out by using the Glide program. Docking was performed at two different modes, SP (standard precision) and XP (extra precision). Binding site was defined by choosing the co-crystallized ligand as a grid centre and then forms a 20 Å box from the centre to define the boundary for docking. Posts docking the poses were rescored by calculating binding free energy by performing MMGBSA free energy calculation. Glide score, glide e-model score was considered to find the suitable complex for molecular dynamics simulation. To validate whether the above docking protocol can reproduce experimentally observed binding modes, the co-crystallized inhibitors were docked into the binding site of receptive proteins.

2.16.3. Molecular dynamics

Based on our docking result, one pose for MMP-3 was selected for 50 ns of MD simulation. All the calculations were performed at Desmond package, using OPLS3e force field. The system was created by inserting the protein-ligand complex solvated in explicit water molecule with periodic boundary conditions. The overall charge of the system was neutralized and 0.15 M of salt was added. Subsequently, the system was minimized for 2000 steps by using steepest descent method, followed by minimization of another 2000 steps by using conjugate gradient method. The NPT ensemble was used with a constant temperature of 298.15 K. Hydrogen positions were constrained by the M-SHAKE algorithm. Long-range electrostatics were computed every third time step by using Smooth particle mesh (Ewald method). A 9 Å radius cut-off was set for columbic short-range interaction cut-off method. The frames were recorded after every 4.8 ps time step. After successful completion of 50 ns of simulation, the trajectory was clustered and last 100 frames were subjected for MMGBSA free energy calculations.

2.17. Statistical analysis

All the experiments were repeated five times, independently. GraphPad PRISM 5 (v. 5.04) software was used for statistical analyses. Data was compared by Student's *t*-test. Data were represented as means ± SEM [$^{***}p < 0.001$; $^{**}p < 0.01$, $^{*}p < 0.05$ (vs. 'Control'); ###p < 0.001; ##p < 0.01, #p < 0.05 (vs. 'Stress') and "ns" represents non-significant].

3. Results

3.1. Melatonin protects mice gastric mucosa from forced swim induced oxidative stress, inflammation and injury

Forced swim for 4 h at 22 ± 2 °C caused severe injury (ulcer index~70) and bleeding all over the mice gastric epithelium, whereas such damage was not found in melatonin (60 mg/kg b.w.) or conventional anti-ulcer drug- omeprazole (25 mg/kg b.w.) pretreated groups (Fig. 1A & B). Histological inspection of tissue sections indicated that stress resulted in disruption of the gastric epithelial-mucosal layer compared with that of control. Such an indication of ulcer was also absent in melatonin or omeprazole-pretreated groups (Fig. 1C).

Moreover, myeloperoxidase (MPO) activity was significantly increased in the gastric mucosa of mice (Group 2), which were forced to swim and were not pretreated with either of the drugs. MPO activity in per gram tissue was reduced to normal level, when those groups were pretreated with melatonin; demonstrating the anti-inflammatory property of melatonin (Table 1).

In addition, the TUNEL assay (Fig. 1D) and Masson's trichrome staining (Fig. 1E) clearly indicated that, stress caused gastric mucosal cell death and ECM degradation in vivo, whereas pretreatment with melatonin protect the cells against the damage and collagen degradation. The localization of end labeling within the nucleus and extensive fragmentation of DNA was specified by the green fluorescence from gastric cells after the induction of acute ulcer due to forced swim

Table 1
Effect of melatonin and standard anti-ulcer drug omeprazole on murine forced swim induced ulceration.

Assays	Control	Stress	Stress + Melatonin	Stress + Omeprazole
Lipid peroxidation (nmol TBARS/mg protein)	0.15 ± 0.007	0.31 ± 0.032**	0.235 ± 0.02$^{\#\#}$	0.17 ± 0.039$^{\#\#}$
Protein Carbonylation (nmol/mg protein)	1.22 ± 0.082	2.84 ± 0.29**	1.93 ± 0.189$^{\#\#}$	1.57 ± 0.077$^{\#\#}$
Myeloperoxidase (units/g tissue)	3.82 ± 0.4	30.58 ± 0.18***	5.22 ± 0.36$^{\#\#\#}$	6.47 ± 0.52$^{\#\#\#}$

Forced swim induced gastric ulceration produced oxidative damage as assessed by increasing lipid peroxidation and protein oxidation. Lipid peroxidation, protein carbonylation and myeloperoxidase activity were measured as described in method section. The results were expressed as mean ± SEM. ***$p < 0.001$, ** $p < 0.01$ (vs. 'Control'); ###p < 0.001 and ##p < 0.01 (vs. 'Stress').

(Fig. 1D).

3.2. Melatonin alters stress induced ROS accumulation, and mitochondrial function while protecting against acute gastropathy

ROS is a primary conducive agent for the development of gastric ulcers which engenders oxidative damage by enhancing protein oxidation and lipid peroxidation. In this connection we evaluated total ROS accumulation in mice gastric mucosa of all experimental groups. Results

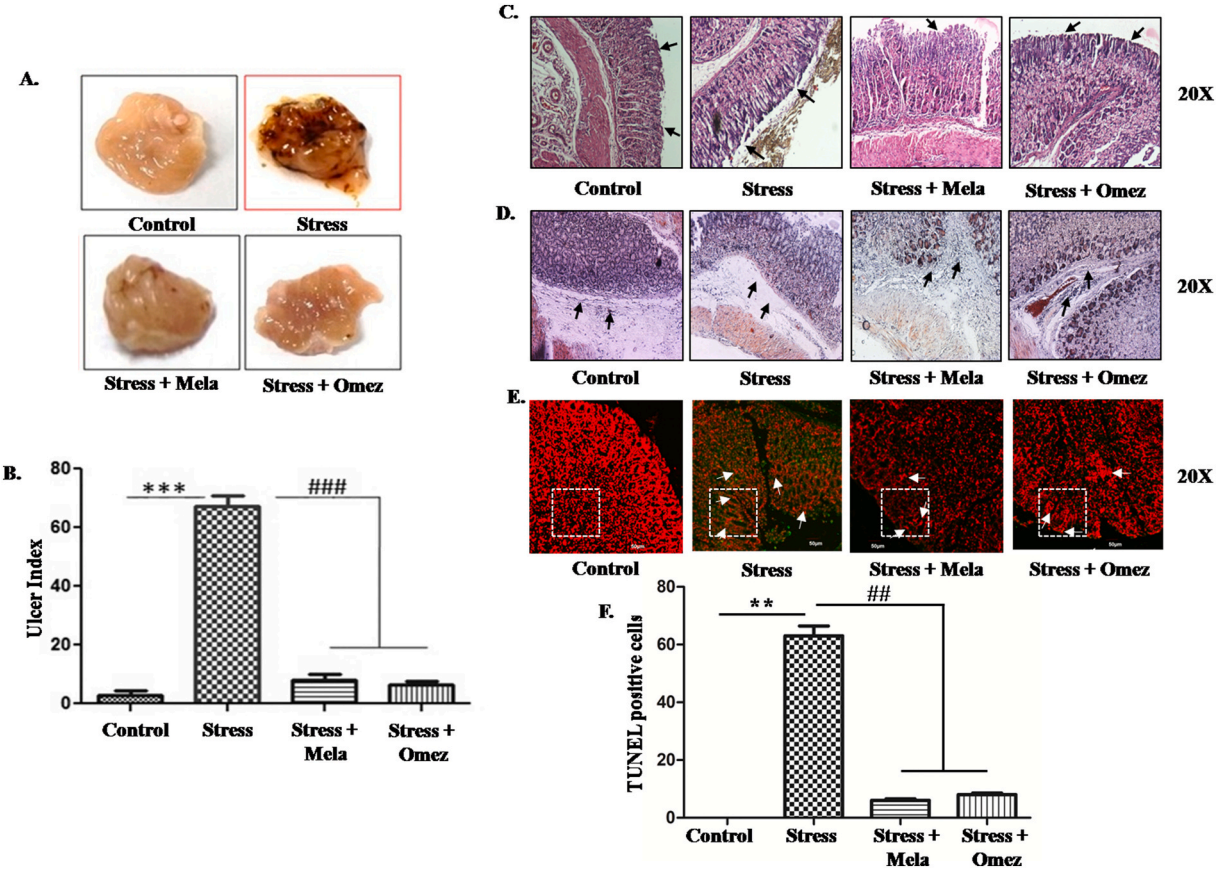

Fig. 1. Acute gastric ulceration in adult Balb/c mice caused due to forced swim stress and effect of melatonin thereon. (A) Macroscopic images of gastric tissues of the four experimental groups (B) Graphical representation of the ulcer index of gastric mucosa. Values are mean ± SEM. ***$p < 0.001$ (vs. 'Control'), ###p < 0.001 (vs. 'Stress'). (C) Histological inspection of tissue sections showing stress mediated disruption of the gastric epithelial-mucosal layer compared with that of control, melatonin or omeprazole pre-treated tissues (D) Collagen fibers were stained with Masson's trichrome stain (blue) for mice gastric tissue sections from control, forced swim stress ulcerated and melatonin or omeprazole-pretreated groups. (E) TUNEL staining of mice gastric mucosal sections. The nuclei were PI-stained (red) while the nick end label was stained with FITC (green). (F) Graphical representation of the TUNEL positive cells. Values are mean ± SEM. **$p < 0.01$ (vs. 'Control'), ##p < 0.01 (vs. 'Stress'). (For interpretation of the references to colour in this figure legend, the reader is referred to the web version of this article.)

showed that melatonin significantly inhibited ROS generation in mice gastric mucosa (Fig. 2A). Table 1 shows the significant antioxidant property of melatonin and omeprazole. The antioxidant property of melatonin is responsible for blocking stress-induced elevation of protein oxidation and lipid peroxidation; thereby protecting gastric mucosal damage.

Further, in order to understand the bioenergetic crisis, we assessed mitochondrial functional integrity by quantifying the mitochondrial dehydrogenase activity (Fig. 2B). Data showed significant reduction in dehydrogenase activity in ulcerated gastric tissue compared with that of control. The reduction in activity was rescued by melatonin (Fig. 2B). Additionally, significant depolarization of membrane potential (Δψm) was observed in mitochondria extracted from ulcerated gastric tissue, however the condition was averted by melatonin (Fig. 2C).

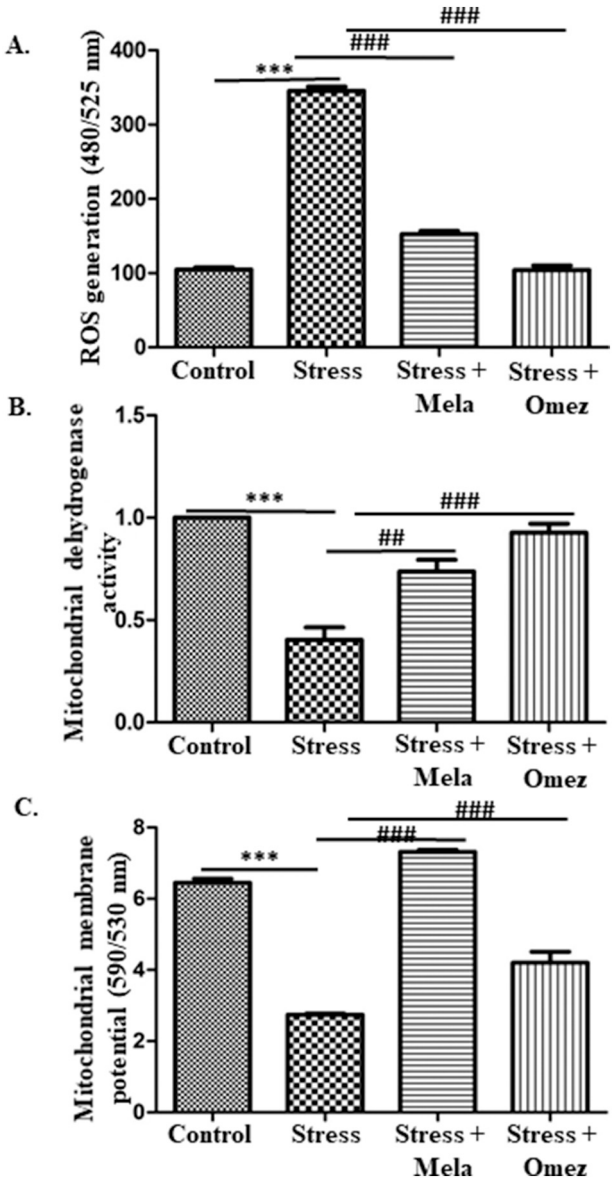

Fig. 2. Reversal of acute gastropathy mediators by melatonin. (A) Measurement of ROS in mice gastric tissue extract in all experimental groups using 2′, 7′-Dichlorofluorescin diacetate. (B) Mitochondrial dehydrogenase activity in mice gastric mitochondria (C) Mitochondrial trans- membrane potential measurement from gastric tissue (ΔΨm). Values are mean ± SEM. ***$p < 0.001$ (vs. 'Control'); ###$p < 0.001$ and ##$p < 0.01$ (vs. 'Stress').

3.3. Melatonin prevents gastric ulceration by altering the activity and expression of MMP-3 and TIMP-1

MMP-3 is well known for its inflammatory action in gastric tissues; hence, its inhibition may ameliorate the pathogenic condition. To check this possibility, tissue extracts from all experimental groups were used to analyze MMP-3 activity by casein zymography (Fig. 3A). The densitometric analysis revealed that stress increased the pro MMP-3 activity with respect to that of control, whereas, melatonin and omeprazole inhibited its activity and thereby offers gastro-protection (Fig. 3B). Further, to check the activity of TIMP-1, we performed reverse zymography (Fig. 3C). The densitometric analysis revealed that stress significantly decreased the TIMP-1 activity with respect to that of control, whereas, melatonin and omeprazole reinstated its activity (Fig. 3D).

To define the effect that melatonin has on the expression of MMP-3 and its tissue inhibitor (TIMP-1), western blotting was performed using the TX extracts of all experimental groups (Fig. 3E). Our data revealed that stress-induced gastric ulceration causes significant enhancement of MMP-3 expression (~3 fold) and downregulation of TIMP-1 (~1.4 fold), whereas pretreatment with melatonin significantly altered their expression patterns (Fig. 3F & G).

Additionally, tissues from all experimental groups were processed for in vivo analysis of MMP-3 expression by staining with fluorescent dyes (Fig. 3H). Enhanced expression of MMP-3 was observed in ulcerated tissue compared to control (red fluorescence). Both, melatonin (60 mg/kg b.w.) and omeprazole (25 mg/kg b.w.) pretreated sections have shown inhibited MMP-3 signals (Fig. 3H). The nuclei were counter stained with DAPI.

3.4. Melatonin inhibits activation of inflammatory signaling molecules in ulcerated milieu of stomach

Immunoblotting technique was adopted to study the changes in the expression level of the inflammatory signaling molecules. To examine p38 activation, the phosphorylated form of p38 was monitored, which showed ~5.5 fold increase in its expression (Fig. 4A & B). However, total p38 level remained more or less constant in different experimental groups (Fig. 4A & C). Additionally, we studied ERK1/2 (Fig. 4A & J) and its phophorylated form (Fig. 4A & I) along with expressions of apoptotic and inflammatory markers. Among them caspase-3 shows ~2.5 fold increase (Fig. 4A & E), HSP-70 shows ~1.2 fold decrease (Fig. 4A & D), TNF-α shows ~2 fold increase (Fig. 4A & F), IL-1β shows ~1.5 fold increase (Fig. 4A & G) and phosphorylated p-65 subunit of NF-κB shows ~7 fold increase (Fig. 4A & H) using GAPDH as the loading control (Fig. 4A). Interestingly, melatonin showed significant effect as a gastroprotectant as evident from the graphical representation of densitometric values.

3.5. Melatonin binds with high specificity to the active sites of pro-MMP-3

Direct interaction of melatonin with pro-MMP-3 as revealed by computational method suggests a strong binding affinity (low binding free energy) and high specificity (Table 2, Fig. 5A & B). Binding site of MMP-3 consist of a Zn metal ion complexes with three biologically relevant histidine residues (Fig. 5A). Melatonin was able to form pi-pi stacking interaction with His201- one of the three histidines complexed with Zn ion. Melatonin also forms a hydrogen bond with His224 and Ala217 and an aromatic hydrogen bond with Tyr220. From all the generated poses, one pose with a feasible interaction with His201 was considered for molecular dynamics simulations (Fig. 5B). To understand the specificity, conformational changes and stability of melatonin toward MMP-3 was performed 50 ns of molecular dynamics simulation. The same simulation was run to analyze the root-mean square deviation (RMSD), root-mean square fluctuation (RMSF) and protein-ligand contact map during the simulation for MMP-3 (Fig. S1). MMP-3-melatonin complex shows a better performance, which provides an insight of

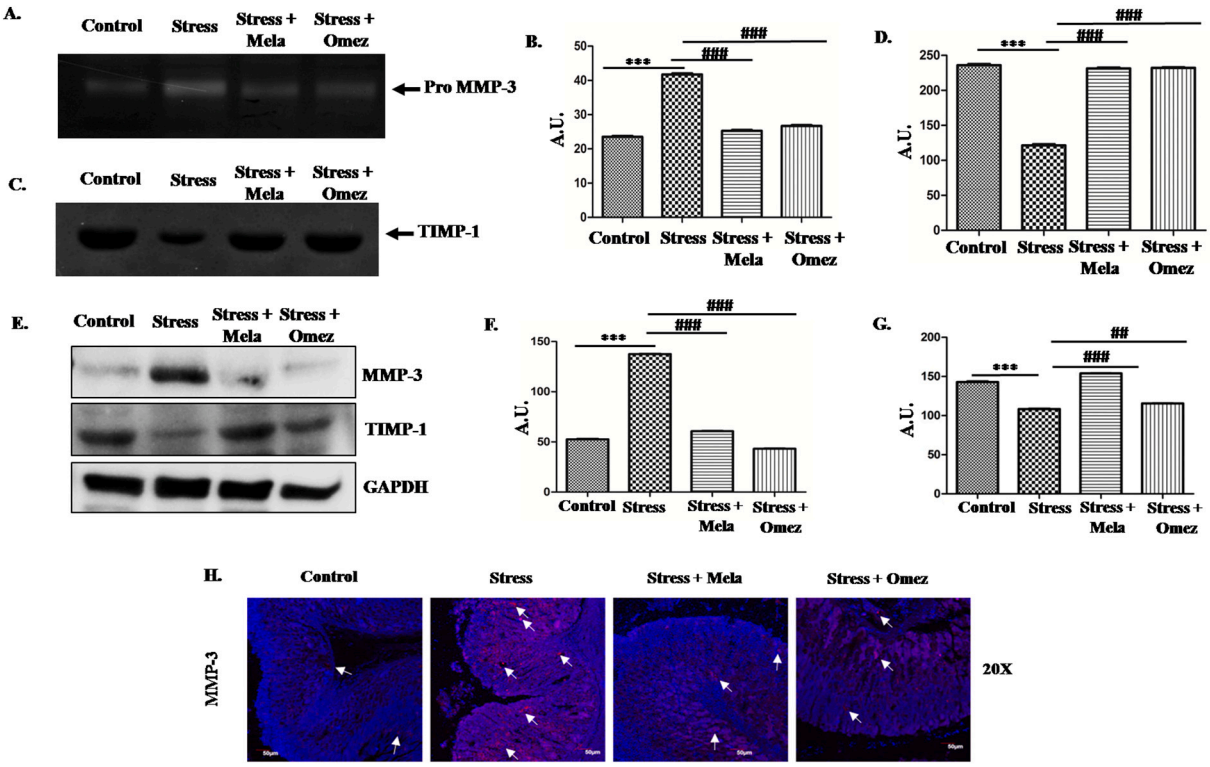

Fig. 3. Studying the activity and expression of MMP-3 and TIMP-1. (A) Casein zymography showing inhibition of MMP-3 activity by melatonin during forced swim-stress induced gastric ulceration in mice (B) Densitometric analysis of MMP-3 activity in all experimental groups. (C) Reverse zymography showing restoration of TIMP-1 activity by melatonin during forced swim-stress induced gastric ulceration in mice (D) Densitometric analysis of TIMP-1 activity in all experimental groups. (E) Equal amounts of protein from the PBS extracts of four different groups of gastric tissues were analyzed by western blotting for MMP-3 and TIMP-1 using GAPDH as a loading control. (F) Graphical representation of expression pattern of MMP-3. (G) Graphical representation of expression pattern of TIMP-1. (H) MMP-3 was immuno-stained with anti-MMP-3 antibody and Texas Red conjugated secondary antibody for control, stress, melatonin and omeprazole pre-treated tissues. The nuclei were stained with DAPI (blue). Values are mean ± SEM. Comparison between groups was performed using Student−Newman−Keuls *t*-test. ***$p < 0.001$ (vs. 'Control'); ###p < 0.001 (vs. 'Stress'); ##$p < 0.01$ (vs. 'Stress'). Densitometric analysis was measured by Image J software from the zymograms and blots. (For interpretation of the references to colour in this figure legend, the reader is referred to the web version of this article.)

selectivity of melatonin toward MMP-3 (Fig. 5C & D). This complex was stable throughout the simulation and shows least fluctuation in the RMSD and protein got stabilize before 10 ns. A minor fluctuation can be observed in the ligand RMSD that could be the free movement of alkyl chain of melatonin. Protein RMSF was also stable, a major fluctuation was observed near binding site and in the loops region. Most of the interactions were last for more than 70% and two interactions, H-bonding Tyr223 and pi-pi stacking His201 were for more than 95% (Fig. 5C & D).

4. Discussion

Exposure to physical and psychological stresses induced by forced swim can cause a variety of pathophysiological disorders. It is also a well-known risk factor for gastritis and gastric ulcer development; leading to inflammation [34]. Extracellular matrix (ECM) disruption and hemorrhage in stomach due to stress-induced gastric ulcer in critically ill patients remains an important clinical management issue. Interestingly, matrix metalloproteinases (MMPs) family of enzyme are known for ECM remodeling in human tissues [9,35]. In support MMP-9 upregulation in gastric injury has been well documented in several studies [9,29]. The involvement of MMP -2, -3 and -9 has previously been suggested by our group for the onset of NSAID and *Helicobacter pylori* induced gastric ulcers [36,37]. Moreover, several studies on gastric cancer have also shown that the expression of MMP-9, -2, -3, -7 and -14 either at transcription or translation level are well linked with the severity of the disease [38,39,40]. However, the role of MMP-3 in gastric ulcer is poorly understood and not known yet in stress mediated ulcer, which prompted us to address the involvement of MMP-3 in stress induced gastric ulcer. Indeed, we have found positive correlation of MMP-3 expression in gastric ulceration induced by stress. In the present study, we are addressing this gap of information by experimenting with an in vivo model of forced swim stress induced acute gastric ulceration.

Previous study has reported that stress is responsible for localized ROS production [6]. The increase in lipid peroxidation and protein carbonylation levels have proved that forced swim stress does indeed lead to the production of ROS (Table- 1, Fig. 2A) which in turn induces the development of acute gastric ulceration. The extent of tissue damage and inflammation caused due to forced swim stress has been well documented through an almost ten-fold rise in myeloperoxidase titers. Further, significantly higher levels of TNF-α, IL-1β and NF-κB also testify to the extent of inflammation instigated by forced swim stress (Fig. 4A). Such an excessive damage to the gastric tissue along with protein and lipid oxidation has played a pivotal role in inducing mitochondrial dysfunction and subsequent apoptosis.

Additionally, ROS is involved in several signal transduction pathways, including p38 (MAPK family member) and its associated downstream transcription factors like NF-κB. A recent study on rat gastric ulcer model showed that ulcerogen treatment activated the protein kinase C zeta (PKCζ)-p38 MAP kinase (P38)-dynamin-related protein 1 (DRP1) cascade and correspondingly altered the mitochondrial dynamics leading to apoptosis [41]. An upregulation of ERK1/2, and its phosphorylated counterpart in the ulcerated gastric milieu is also noted after forced swimming (Fig. 4A, I & J). These proteins are part of a signaling cascade that is known to affect the transcription and consequent expression of various MMPs [42].

Following the upregulation of these signaling moieties, the

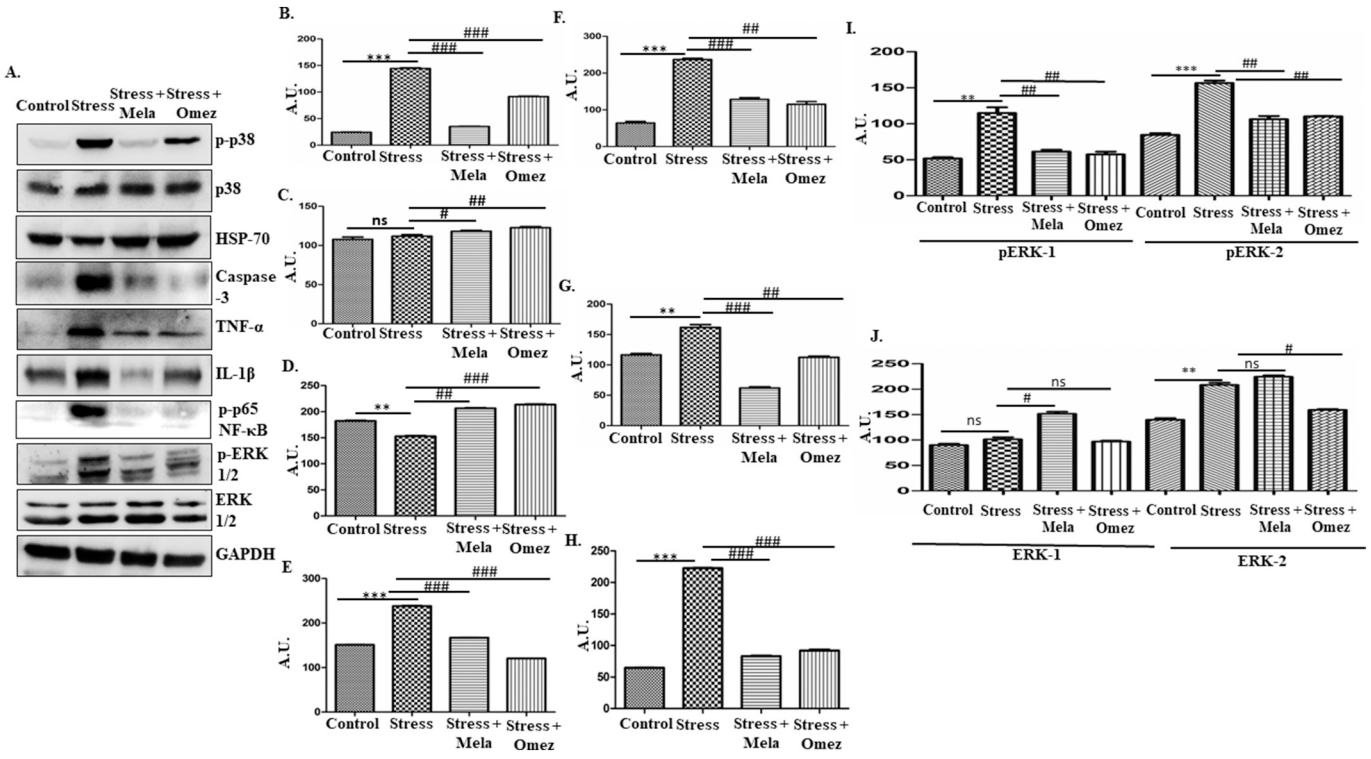

Fig. 4. Melatonin reversed redox-sensitive stress signaling and expression pattern of MMPs in ulcerated milieu of stomach (A) Western Blotting was performed for different signaling molecules, inflammatory and apoptotic markers using GAPDH as a loading control. (B-J) Graphical representations of expression pattern of p-p38, p38, HSP-70, Caspase-3, TNF-α, IL-1β, p-p65-NFκB, pERK 1/2 and ERK 1/2 respectively. Data were presented as mean ± SEM. ***$p < 0.001$; ** $p < 0.01$ (vs. 'Control'); ###p < 0.001; ##p < 0.01, #$p < 0.05$ (vs. 'Stress') and "ns" represents non-significant.

Table 2
Docking results for MMP-3.

Complex	Glide score	Glide emodel
MMP 3 – Melatonin	−6.625	−54.666

expression profile of MMP -3 has undergone significant changes; as is evident from zymographic (Fig. 3A & B), immunohistochemical (Fig. 3H) and western blot (Fig. 3E & F) analyses of the respective tissue samples. Whereas, reverse zymography (Fig. 3C & D) and western blot (Fig. 3E & G) analysis of TIMP-1 shows an opposite pattern of expression in comparison to MMP-3. These results re-establish the role of TIMP-1 as the tissue inhibitor of MMP-3 [43].

All these changes seem to have been originated by the disturbance in the delicate anti-oxidant and oxidant balance due to forced swim stress. In order to prevent the manifestation of such physiological changes generated by oxidative stress, we decided to check the preventive efficacy of melatonin [44] having diverse physiological roles including regulation of antioxidative defense, body temperature and blood pressure etc., apart from major role in balancing circadian rhythm. Although, synthetic melatonin is not FDA-approved for treatment of GI diseases so far, however, in many European countries it is prescribed as a drug for the treatment of insomnia in elderly patients [45]. As a sleeping aid, the single dose of 1–10 mg melatonin is considered safe, whereas, in animal models, melatonin has been administered safely at a dose upto 800 mg/kg b.wt. [46]. Moreover, 200/mg/kg/day of melatonin administered into Sprague-Dawley rats during gestation period (6th day-19th day) showed no effect on the prenatal mortality [47]. Thereby, we have used melatonin at a dose of 60 mg/kg b.wt. corresponding to 4.87 mg/kg b.wt. (Human equivalent dose) according to the FDA Guidelines, 2005, which is considered safe to use. As we are investigating the preventive efficacy of melatonin in acute ulceration, all mice in treatment groups were administered with melatonin or omeprazole (the positive control drug) an hour prior to swim stress. Interestingly, melatonin has been able to counter the increase in ulcer index, lipid peroxidation, protein carbonylation and myeloperoxidase titers in forced swim stress induced gastric ulcerated tissue. Melatonin also prevented the onset of swim stress-induced apoptosis in the gastric milieu by regulating the production of pro-apoptotic proteins like Caspase-3. The expression of various pro-inflammatory proteins (TNF-α, IL-1β and NF-κB) were brought down to near control levels in melatonin treated groups, indicating that melatonin pre-treatment successfully prevented the inflammation developed due to forced swim stress. This result is very much corroborated with our previous findings [48]. The expression and phosphorylation patterns of ERK1/2 and p38 MAPK were significantly altered in melatonin pre-treated groups. As a result, the elevated titer of MMP -3 that occur in forced swim stress induced ulceration was returned back to its original state. Further, In silico studies revealed that melatonin can interact directly with MMP-3, as suggested by low binding free energy between the two. Melatonin interacts with zinc ion linked His201 which in turn interacts with MMP-3. MMP-3-melatonin complex provides an insight of selectivity of melatonin toward MMP-3. Taken together, our results demonstrate that forced swim stress induces gastric ulcers elicit a plethora of inflammatory responses and signaling cascades. We are the first to report the involvement of MMP-3 in the process of forced swim stress induced acute gastric ulceration. This model will be a new addition to the few models that are currently employed by the global scientific community to study gastric ulcers. Pre-treatment with melatonin prevents synthesis of MMP -3, due to its antioxidant and anti-inflammatory properties. Melatonin also inhibits the activity of any existing MMP-3 in the system by tightly binding to its active site, near the catalytic cleft. From the results of this study, it can be said that melatonin, a naturally produced anti-oxidant, can be used as a potential pharmacological drug to prevent acute gastric ulcerogenesis.

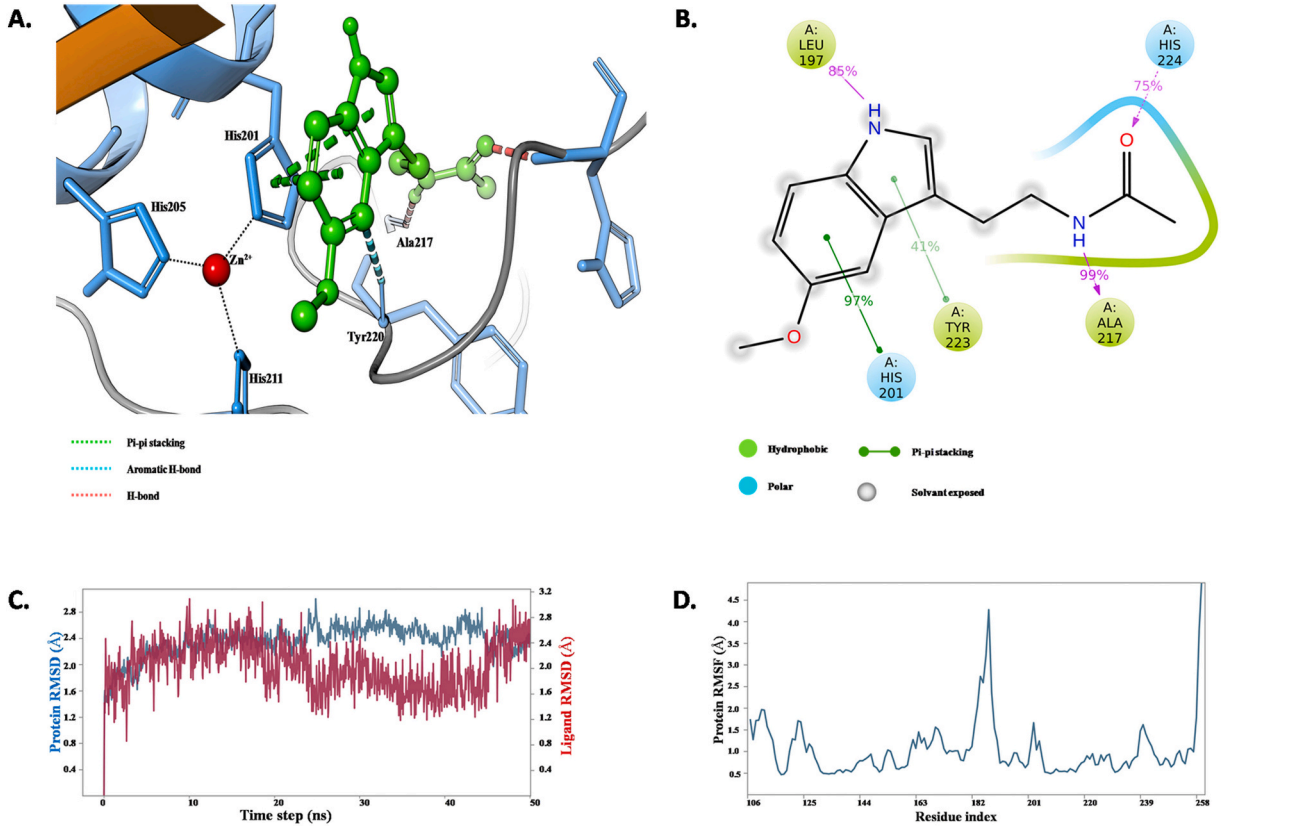

Fig. 5. Interaction study between melatonin and MMP-3. (A) Binding mode of melatonin to MMP-3. (B) Interaction map of melatonin during the simulation (C) Root-mean square deviation of protein-ligand (red colour) and ligand (blue colour). (D) Root-mean square fluctuation of protein. (For interpretation of the references to colour in this figure legend, the reader is referred to the web version of this article.)

5. Conclusion

It is evident from the present study that MMP-3 plays a key role in forced swim stress mediated acute gastric ulceration. The observed up-regulation of MMP-3 is in turn regulated by MAPK-ERK signaling pathways. In this experimental condition, melatonin plays a dual role in preventing gastric ulceration by down-regulating the activation of MAPK-ERK pathway along with binding to the active site of MMP-3, thereby imparting its gastroprotective effect.

Supplementary data to this article can be found online at https://doi.org/10.1016/j.lfs.2022.120426.

CRediT authorship contribution statement

Conception and design of study: P. Choudhary, S. Swarnakar.

Acquisition of data: P. Choudhary, T. Roy, A. Chatterjee, V. K. Mishra, S. Pant.

Analysis and/or interpretation of data: P. Choudhary, T. Roy, A. Chatterjee, V. K. Mishra, S. Pant

Drafting the manuscript: P. Choudhary, T. Roy, A. Chatterjee, S. Pant

Revising the manuscript critically for important intellectual content: T. Roy, A. Chatterjee, V. K. Mishra, S. Swarnakar

Approval of the version of the manuscript to be published (the names of all authors must be listed): P. Choudhary, T. Roy, A. Chatterjee, V. K. Mishra, S. Pant, S. Swarnakar

Declaration of competing interest

We wish to confirm that there are no known conflicts of interest associated with this publication and there has been no significant financial support for this work that could have influenced its outcome.

Acknowledgement

This research work was supported by DRDO, India (Project Code: LSRB-287). Preety Choudhary received fellowship from DRDO (Project Code: LSRB-287). Tapasi Roy, Abhishek Chatterjee, Vineet Kumar Mishra and Suyash Pant would like to acknowledge the receipt of their fellowships from SERB-NPDF (Project Code: PDF/2017/001918), UGC-Junior Research Fellowship, DBT-RA and NIPER-Kolkata, respectively.

References

[1] K.V. Kudryavtsev, A.O. Markevich, O.V. Virchenko, T.M. Falalyeyeva, T. V. Beregova, L.I. Ostapchenko, D.V. Zabolotnev, N.S. Zefirov, Pharmacological correction of stress-induced gastric ulceration by novel small-molecule agents with antioxidant profile, Sci. World J. 2014 (2014), 217039, https://doi.org/10.1155/2014/217039.

[2] M. Krag, A. Perner, J. Wetterslev, M.P. Wise, M. Borthwick, S. Bendel, C. McArthur, D. Cook, N. Nielsen, P. Pelosi, F. Keus, A.B. Guttormsen, A.D. Moller, M.H. Møller, SUP-ICU collaborators, stress ulcer prophylaxis in the intensive care unit: an international survey of 97 units in 11 countries, Acta Anaesthesiol. Scand. 59 (2015) 576–585, https://doi.org/10.1111/aas.12508.

[3] A. Tawakol, A. Ishai, R.A. Takx, A.L. Figueroa, A. Ali, Y. Kaiser, Q.A. Truong, C. J. Solomon, C. Calcagno, V. Mani, C.Y. Tang, W.J. Mulder, J.W. Murrough, U. Hoffmann, M. Nahrendorf, L.M. Shin, Z.A. Fayad, R.K. Pitman, Relation between resting amygdalar activity and cardiovascular events: a longitudinal and cohort study, Lancet 389 (2017) 834–845, https://doi.org/10.1016/S0140-6736(16)31714-7.

[4] A.F. Syam, M. Simadibrata, S.I. Wanandi, B.S. Hernowo, M. Sadikin, A.A. Rani, Gastric ulcers induced by systemic hypoxia, Acta Med. Indones. 43 (2011) 243–248.

[5] K. Biswas, U. Bandyopadhyay, I. Chattopadhyay, A. Varadaraj, E. Ali, R. K. Banerjee, A novel antioxidant and antiapoptotic role of omeprazole to block gastric ulcer through scavenging of hydroxyl radical, J. Biol. Chem. 278 (2003) 10993–11001, https://doi.org/10.1074/jbc.M210328200.

[6] Y.T. Jia, W. Wei, B. Ma, Y. Xu, W.J. Liu, Y. Wang, K.Y. Lv, H.T. Tang, D. Wei, Z. F. Xia, Activation of p38 MAPK by reactive oxygen species is essential in a rat model of stress- induced gastric mucosal injury, J. Immunol. 179 (2007) 7808–7819, https://doi.org/10.4049/jimmunol.179.11.7808.

[7] A. Daugherty, J.L. Dunn, D.L. Rateri, J.W. Heinecke, Myeloperoxidase, a catalyst for lipoprotein oxidation, is expressed in human atherosclerotic lesions, J. Clin. Invest. 94 (1994) 437–444, https://doi.org/10.1172/JCI117342.

[8] X. Fu, S.Y. Kassim, W.C. Parks, J.W. Heinecke, Hypochlorous acid generated by myeloperoxidase modifies adjacent tryptophan and glycine residues in the catalytic domain of matrix Metalloproteinase-7 (Matrilysin) an oxidative mechanism for restraining proteolytic activity during inflammation, J. Biol. Chem. 278 (2003) 28403–28409, https://doi.org/10.1074/jbc.M304739200.

[9] S. Swarnakar, K. Ganguly, P. Kundu, A. Banerjee, P. Maity, A.V. Sharma, Curcumin regulates expression and activity of matrix metalloproteinases 9 and 2 during prevention and healing of indomethacin-induced gastric ulcer, J. Biol. Chem. 280 (2005) 9409–9415, https://doi.org/10.1074/jbc.M413398200.

[10] W.C. Parks, R.P. Mecham, Matrix Metalloproteinases, Academic Press, Elsevier, San Diego, 1998.

[11] L.P. Singh, A. Mishra, D. Saha, S. Swarnakar, Doxycycline blocks gastric ulcer by regulating matrix metalloproteinase-2 activity and oxidative stress, World J. Gastroenterol. 17 (2011) 3310–3321, https://doi.org/10.3748/wjg.v17.i28.3310.

[12] C. Yan, D.D. Boyd, Regulation of matrix metalloproteinase gene expression, J. Cell. Physiol. 211 (2007) 19–26, https://doi.org/10.1002/jcp.20948.

[13] I. Chauhan, S. Agrawal, R.K. Goel, Status of inflammatory markers and growth factor in gastric ulcer protective effects of Punica granatum L. peel extract in rat, Natl. J. Physiol. Pharm. Pharmacol. 8 (2018) 12–17, https://doi.org/10.5455/njppp.2018.8.0309317072017.

[14] H. Seino, H. Ueda, M. Kokai, N.M. Tsuji, S. Kashiwamura, Y. Morita, H. Okamura, IL-18 mediates the formation of stress-induced, histamine-dependent gastric lesions, Am. J. Physiol. Gastrointest. Liver Physiol. 292 (2007) G262–G267, https://doi.org/10.1152/ajpgi.00588.2005.

[15] M. Schieber, N.S. Chandel, ROS function in redox signaling and oxidative stress, Curr. Biol. 24 (2014) R453–R462, https://doi.org/10.1016/j.cub.2014.03.034.

[16] S.J. Forrester, D.S. Kikuchi, M.S. Hernandes, Q. Xu, K.K. Griendling, Reactive oxygen species in metabolic and inflammatory signaling, Circ. Res. 122 (2018) 877–902, https://doi.org/10.1161/CIRCRESAHA.117.311401.

[17] Y. Yang, S.C. Kim, T. Yu, Y.S. Yi, M.H. Rhee, G.H. Sung, B.C. Yoo, J.Y. Cho, Functional roles of p38 mitogen-activated protein kinase in macrophage-mediated inflammatory responses, Mediat. Inflamm. 2014 (2014), 352371, https://doi.org/10.1155/2014/352371.

[18] A. Verlande, M. Krafčíková, D. Potěšil, L. Trantírek, Z. Zdráhal, M. Elkalaf, J. Trnka, K. Souček, N. Rauch, J. Rauch, W. Kolch, S. Uldrijan, Metabolic stress regulates ERK activity by controlling KSR-RAF heterodimerization, EMBO Rep. 19 (2018) 320–336, https://doi.org/10.15252/embr.201744524.

[19] K. Mitsuyama, O. Tsuruta, Y. Matsui, K. Harada, N. Tomiyasu, A. Suzuki, K. Takaki, J. Masuda, K. Handa, Y. Satoh, B.L. Bennett, A. Toyonaga, M. Sata, Activation of c-Jun N-terminal kinase (JNK) signalling in experimentally induced gastric lesions in rats, Clin. Exp. Immunol. 143 (2006) 24–29, https://doi.org/10.1111/j.1365-2249.2005.02959.x.

[20] M. Yao, X. Wang, Y. Zhao, X. Wang, F. Gao, Expression of MMPs is dependent on the activity of mitogen-activated protein kinase in chondrosarcoma, Mol. Med. Rep. 15 (2017) 915–921, https://doi.org/10.3892/mmr.2016.6077.

[21] K. Ganguly, P. Maity, R.J. Reiter, S. Swarnakar, Effect of melatonin on secreted and induced matrix metalloproteinase-9 and-2 activity during prevention of indomethacin-induced gastric ulcer, J. Pineal Res. 39 (2005) 307–315, https://doi.org/10.1111/j.1600-079X.2005.00250.x.

[22] D. Bilici, H. Süleyman, Z.N. Banoğlu, A. Kiziltunç, B. Avci, A. Ciftçioğlu, S. Bilici, Melatonin prevents ethanol-induced gastric mucosal damage possibly due to its antioxidant effect, Dig. Dis. Sci. 47 (2002) 856–861, https://doi.org/10.1023/a:1014764705864.

[23] S.C. Su, M.J. Hsieh, W.E. Yang, W.H. Chung, R.J. Reiter, S.F. Yang, Cancer metastasis: mechanisms of inhibition by melatonin, J. Pineal Res. 62 (2017), https://doi.org/10.1111/jpi.12370. 10.1111/jpi.12370.

[24] R.J. Reiter, S.A. Rosales-Corral, D.X. Tan, D. Acuna-Castroviejo, L. Qin, S.F. Yang, K. Xu, Melatonin, a full service anti-cancer agent: inhibition of initiation, progression and metastasis, Int. J. Mol. Sci. 18 (2017) 843, https://doi.org/10.3390/ijms18040843.

[25] D.S. Rudra, U. Pal, N.C. Maiti, R.J. Reiter, S. Swarnakar, Melatonin inhibits matrix metalloproteinase-9 activity by binding to its active site, J. Pineal Res. 54 (2013) 398–405, https://doi.org/10.1111/jpi.12034.

[26] S.K. Pramanik, U. Pal, P. Choudhary, H. Singh, R.J. Reiter, A. Ethirajan, S. Swarnakar, A. Das, Stimuli-responsive nanocapsules for the spatiotemporal release of melatonin: protection against gastric inflammation, ACS Appl. Bio Mater. 2 (2019) 5218–5226, https://doi.org/10.1021/acsabm.9b00236.

[27] D.K. Yadav, Y.P. Bharitkar, A. Hazra, U. Pal, S. Verma, S. Jana, U.P. Singh, N. C. Maiti, N.B. Mondal, S. Swarnakar, Tamarixetin 3-O-β-d-glucopyranoside from Azadirachta indica leaves: gastroprotective role through inhibition of matrix metalloproteinase-9 activity in mice, J. Nat. Prod. 80 (2017) 1347–1353, https://doi.org/10.1021/acs.jnatprod.6b00957.

[28] O.H. Lowry, N.J. Rosebrough, A.L. Farr, R.J. Randall, Protein measurement with the folin phenol reagent, J. Biol. Chem. 193 (1951) 265–275, https://doi.org/10.1016/S0021-9258(19)52451-6.

[29] L.P. Singh, P. Kundu, K. Ganguly, A. Mishra, S. Swarnakar, Novel role of famotidine in downregulation of matrix metalloproteinase-9 during protection of ethanol-induced acute gastric ulcer, Free Radic. Biol. Med. 43 (2007) 289–299, https://doi.org/10.1016/j.freeradbiomed.2007.04.027.

[30] P.A.Snoek-van Beurden, J.W.Von den Hoff, Zymographic techniques for the analysis of matrix metalloproteinases and their inhibitors, Biotechniques 38 (2005) 73–83, https://doi.org/10.2144/05381RV01.

[31] S. Jana, S. Paul, S. Swarnakar, Curcumin as anti-endometriotic agent: implication of MMP- 3 and intrinsic apoptotic pathway, Biochem. Pharmacol. 83 (2012) 797–804, https://doi.org/10.1016/j.bcp.2011.12.030.

[32] T. Micakovic, W.Z. Banczyk, E. Clark, B. Kränzlin, J. Peters, S.C. Hoffmann, Isolation of pure mitochondria from rat kidneys and western blot of mitochondrial respiratory chain complexes, Bio-Protoc. 9 (2019), e3379, https://doi.org/10.21769/BioProtoc.3379.

[33] S. Mazumder, R. De, S. Sarkar, A.A. Siddiqui, S.J. Saha, C. Banerjee, M.S. Iqbal, S. Nag, S. Debsharma, U. Bandyopadhyay, Selective scavenging of intra-mitochondrial superoxide corrects diclofenac-induced mitochondrial dysfunction and gastric injury: a novel gastroprotective mechanism independent of gastric acid suppression, Biochem. Pharmacol. 121 (2016) 33–51, https://doi.org/10.1016/j.bcp.2016.09.027.

[34] S. Levenstein, S. Rosenstock, R.K. Jacobsen, T. Jorgensen, Psychological stress increases risk for peptic ulcer, regardless of helicobacter pylori infection or use of nonsteroidal anti-inflammatory drugs, Clin. Gastroenterol. Hepatol. 13 (2015) 498–506.e1, https://doi.org/10.1016/j.cgh.2014.07.052.

[35] R.E. Vandenbroucke, C. Libert, Is there new hope for therapeutic matrix metalloproteinase inhibition? Nat. Rev. Drug Discov. 13 (2014) 904–927, https://doi.org/10.1038/nrd4390.

[36] A.V. Sharma, K. Ganguly, S. Paul, N. Maulik, S. Swarnakar, Curcumin heals indomethacin-induced gastric ulceration by stimulation of angiogenesis and restitution of collagen fibers via VEGF and MMP-2 mediated signaling, Antioxid. Redox Signal. 16 (2012) 351–362, https://doi.org/10.1089/ars.2011.4232.

[37] P. Kundu, R. De, I. Pal, A.K. Mukhopadhyay, D.R. Saha, S. Swarnakar, Curcumin alleviates matrix metalloproteinase-3 and-9 activities during eradication of helicobacter pylori infection in cultured cells and mice, PLoS One 6 (2011), e16306, https://doi.org/10.1371/journal.pone.0016306.

[38] G.I. Murray, M.E. Duncan, E. Arbuckle, W.T. Melvin, J.E. Fothergill, Matrix metalloproteinases and their inhibitors in gastric cancer, Gut 43 (1998) 791–797, https://doi.org/10.1136/gut.43.6.791.

[39] Y.Q. Shan, R.C. Ying, C.H. Zhou, A.K. Zhu, J. Ye, W. Zhu, T.F. Ju, H.C. Jin, MMP-9 is increased in the pathogenesis of gastric cancer by the mediation of HER2, Cancer Gene Ther. 22 (2015) 101–107, https://doi.org/10.1038/cgt.2014.61.

[40] A. Kasurinen, T. Tervahartiala, A. Laitinen, A. Kokkola, T. Sorsa, C. Böckelman, C. Haglund, High serum MMP-14 predicts worse survival in gastric cancer, PLoS One 13 (2018), e0208800, https://doi.org/10.1371/journal.pone.0208800.

[41] S. Mazumder, R. De, S. Debsharma, S. Bindu, P. Maity, S. Sarkar, S.J. Saha, A. A. Siddiqui, C. Banerjee, S. Nag, D. Saha, S. Pramanik, K. Mitra, U. Bandyopadhyay, Indomethacin impairs mitochondrial dynamics by activating the PKCζ–p38–DRP1 pathway and inducing apoptosis in gastric cancer and normal mucosal cells, J. Biol. Chem. 294 (2019) 8238–8258, https://doi.org/10.1074/jbc.RA118.004415.

[42] L. Fan, Y. Wu, J. Wang, J. He, X. Han, Sevoflurane inhibits the migration and invasion of colorectal cancer cells through regulating ERK/MMP-9 pathway by up-regulating miR-203, Eur. J. Pharmacol. 850 (2019) 43–52, https://doi.org/10.1016/j.ejphar.2019.01.025.

[43] F.X. Gomis-Rüth, K. Maskos, M. Betz, A. Bergner, R. Huber, K. Suzuki, N. Yoshida, H. Nagase, K. Brew, G.P. Bourenkov, H. Bartunik, W. Bode, Mechanism of inhibition of the human matrix metalloproteinase stromelysin-1 by TIMP-1, Nature 389 (1997) 77–81, https://doi.org/10.1038/37995.

[44] R.J. Reiter, J.C. Mayo, D.X. Tan, R.M. Sainz, M. Alatorre-Jimenez, L. Qin, Melatonin as an antioxidant: under promises but over delivers, J. Pineal Res. 61 (2016) 253–278, https://doi.org/10.1111/jpi.12360.

[45] L.P. Andersen, I. Gögenur, J. Rosenberg, R.J. Reiter, The safety of melatonin in humans, Clin. Drug Investig. 36 (2016) 169–175, https://doi.org/10.1007/s40261-015-0368-5.

[46] J. Barchas, F. DaCosta, S. Spector, Acute pharmacology of melatonin, Nature 214 (1967), 919920, https://doi.org/10.1038/214919a0.

[47] G. Jahnke, M. Marr, C. Myers, R. Wilson, G. Travlos, C. Price, Maternal and developmental toxicity evaluation of melatonin administered orally to pregnant Sprague-dawley rats, Toxicol. Sci. 50 (1999) 271–279, https://doi.org/10.1093/toxsci/50.2.271.

[48] K. Ganguly, S. Swarnakar, Induction of matrix metalloproteinase-9 and -3 in nonsteroidal anti-inflammatory drug-induced acute gastric ulcers in mice: regulation by melatonin. (2009), J. Pineal Res. 47 (2009) 43–55, https://doi.org/10.1111/j.1600-079X.2009.00687.x.

iScience

CellPress
OPEN ACCESS

Article

Graphene quantum dots alleviate ROS-mediated gastric damage

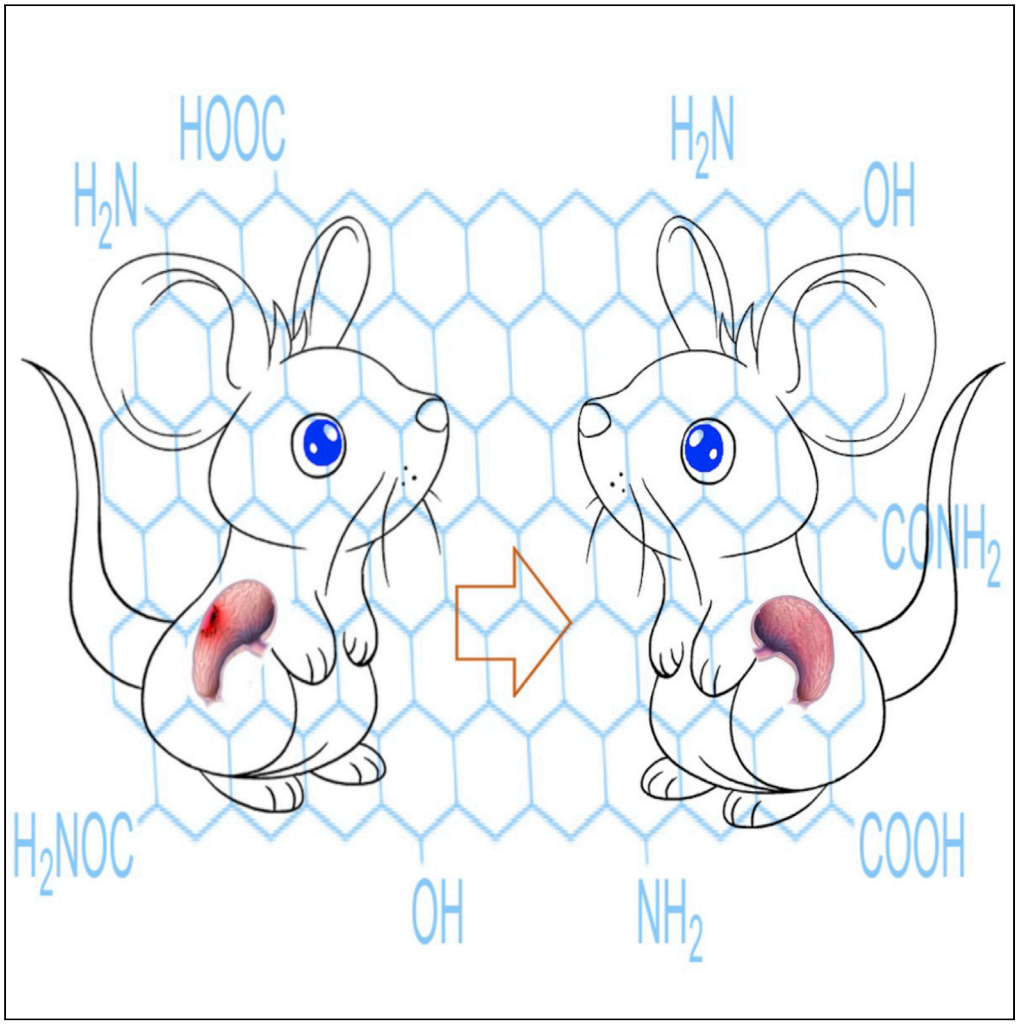

Preety Choudhary, Sushama Biswas, Noufal Kandoth, ..., Amitava Das, Snehasikta Swarnakar, Sumit Kumar Pramanik

amitava@iiserkol.ac.in (A.D.)
sikta@iicb.res.in (S.S.)
samitc@goa.bits-pilani.ac.in (S.C.)
sumitpramanik@csmcri.res.in (S.K.P.)

Highlights

The gastrointestinal tract is one of the major sites for ROS generation•

Graphene quantum dots (GQDs) have broad-spectrum antioxidant properties•

GQDs scavenge the ROS and suppress gastric ulcers by targeting the MMP-9 pathway

Choudhary et al., iScience *25*, 104062
April 15, 2022
https://doi.org/10.1016/j.isci.2022.104062

iScience

CellPress
OPEN ACCESS

Article

Graphene quantum dots alleviate ROS-mediated gastric damage

Preety Choudhary,[1] Sushama Biswas,[2] Noufal Kandoth,[3] Deepak Tayde,[2,4] Abhishek Chatterjee,[1] Samit Chattopadhyay,[5,*] Amitava Das,[3,*] Snehasikta Swarnakar,[1,*] and Sumit Kumar Pramanik[2,4,6,*]

SUMMARY

The gastrointestinal (GI) tract is one of the major sites for reactive oxygen species generation (ROS). Physiological ROS, lower than the threshold concentration, is beneficial for human physiology to preserve gut functional integrity. However, ROS generated in large quantities in presence of external stimuli overwhelms the cellular antioxidant defense mechanism and results in oxidative damage and associated physiological disorder. Graphene quantum dots (GQDs) are a class of carbon-based nanomaterials that have attracted tremendous attention not only for their tunable optical properties but also for their broad-spectrum antioxidant properties. In this report we have shown that GQDs are highly efficient in scavenging ROS and suppressing stress-induced gastric ulcers by targeting the MMP-9 pathway and reducing the inflammatory burden by suppressing excessive oxidative stress by inducing high caspase activity, overproduction of Bax, and downregulation of BCL2.

INTRODUCTION

The significance of keeping up physiological degrees of ROS in the gastrointestinal (GI) tract is critical for persistent intestinal inflammatory disorders. However, the specific role of the tightly regulated redox balance on multifactorial gastrointestinal inflammation generation is a subject of intense debate and is still not well understood (Aviello and Knaus, 2017). Lower ROS level due to impaired NADPH oxidase activity is linked to Crohn disease and pancolitis (Aviello and Knaus, 2017; Patlevič et al., 2016), whereas higher ROS level caused by overexpression of oxidases or mitochondrial function alteration is associated with ulcerative colitis and ileitis(Aviello and Knaus, 2018). Ulcers and ulcerative colitis are the most prevalent diseases, accounting for ~5% of the world's population(Ungaro et al., 2017). The hydroxyl or/and superoxide radicals ($^{\bullet}OH/^{\bullet}O^{2-}$) are among the most prevalent ROS species that cause gastric ulceration and lesions. The higher level of $^{\bullet}O^{2-}$ and inactivation of superoxide dismutase are linked to the pathogenesis of Barrett esophagus and its transformation to adenocarcinoma(Bandyopadhyay et al., 1999; Bhattacharyya et al., 2014; Pérez et al., 2017; Taylor and Colgan, 2017). Certain prescription drugs are developed over the last few decades and are proven effective in controlling such disease states. However, their long-term maintenance use is not recommended because of their side effects such as swelling, headache, myalgia, nausea, weight gain, growth problems, osteoporosis, problems associated with bone marrow, etc. (Kinoshita et al., 2018; Strand et al., 2017). Such limitations imposed by the intrinsic properties of the materials employed offer a distinct scope for developing alternate efficient therapeutic agents for prolonged use for treating gastric hyperacidity and ulcers. As an elevated level of $^{\bullet}OH/^{\bullet}O^{2-}$ accounts for these disease states, an efficient antioxidant is expected to scavenge such ROS species and inhibit the damage. Recent reports also reveal that graphene quantum dots (GQDs) exhibit radical scavenging activity, which varied with the changes in the nature of ROS species via different radical inhibition mechanisms. Graphene and GQDs have come out as important materials for various biomedical applications due to their biocompatibility, unique optical, chemical, and physicochemical properties. GQDs are a member of zero-dimensional nano-structured materials with a lateral size of less than 100 nm having a few layers of sp^2-hybridized along with some sp^3-hybridized carbon atoms linked to certain oxygen-containing functional groups(Zhang et al., 2012). All these allow GQDs to a delicate balance between hydrophobicity and hydrophilicity, unique dispersibility in an aqueous medium, and cell membrane permeance. Importantly, synthetic methodologies enable us to synthesize GDQs with desired reproducibility and repeatability from relatively inexpensive carbon precursors, as well as to achieve the chosen functionalization and large-scale production (Middha and Liu, 2020; Patel et al., 2019; Sandler et al., 2019; Yang et al., 2020). An earlier report also reveals that

[1]CSIR-Indian Institute of Chemical Biology, 4, Raja S. C. Mullick Road, Kolkata 700 032, India

[2]CSIR-Central Salt and Marine Chemicals Research Institute, Bhavnagar, Gujarat, India

[3]Department of Chemical Sciences, Indian Institute of Science Education and Research, Kolkata 741246, India

[4]Academy of Scientific and Innovative Research (AcSIR), Ghaziabad 201002, India

[5]BITS Pilani K K Birla Goa Campus, NH 17B, Bypass, Road, Zuarinagar, Sancoale, Goa 403726, India

[6]Lead contact

*Correspondence: amitava@iiserkol.ac.in (A.D.), sikta@iicb.res.in (S.S.), samitc@goa.bits-pilani.ac.in (S.C.), sumitpramanik@csmcri.res.in (S.K.P.)

https://doi.org/10.1016/j.isci.2022.104062

GQDs derived from neem root extract exhibit excellent cellular internalization with minimal cell toxicity (Singh et al., 2019). Neem plant extracts are also known to be a rich source of antioxidants (Islas et al., 2020; Saleh Al-Hashemi and Hossain, 2016). A recent report suggests that the relative distribution of C and N in different plant tissue (leaf and root) is expected to vary, and extracts of several parts of neem plants are a rich source of antioxidants (Tang et al., 2018; Yan et al., 2019). These extracts are chemo-preventive and show very good antitumor properties. The *in vivo* administration of GQDs had no toxic effects on blood biochemistry and caused no histopathological abnormality (Patel et al., 2019). In addition, GQDs administered in human physiology via intravenous/intramuscular/subcutaneous injection are excreted efficiently and rapidly (Li et al., 2020).

Earlier studies have shown that GQDs could differ in chemical composition, electron density, and sp^2-hybridized carbon content depending on the synthetic methodologies adopted and carbon precursor used. Such variations account for the different mechanistic pathways of the respective GQDs for ROS-scavenging activity(Chong et al., 2016; Ruiz et al., 2017). Literature reports also reveal that the presence of a relatively higher distribution of sp^2 hybrid carbon domains, hydrogen donor functionality, and unpaired electrons caused by defects and vacancies are some of the important factors that contribute to the antioxidant activity of GQDs (Chong et al., 2016; Wang et al., 2014; Yoo et al., 2009; Zheng et al., 2015).

To date, there have been several reports that reveal that aqueous extract of neem bark and neem leaf successfully blocks ROS-induced gastric lesions in rats (Saleem et al., 2018). Bandyopadhyay et al. had reported that more than 90% of the rats treated with neem bark extract showed no evidence of gastric lesions and mucosa. These rats appeared as healthy as that of the control (Bandyopadhyay et al., 2002). It was also observed that the neem bark extract effectively inhibited pylorus-ligation-induced gastric damage in rats (85% inhibition at 20 mg/kg dose) and histamine-induced gastric lesions in guinea pigs (80% inhibition at 40 mg/kg dose) (Bandyopadhyay et al., 2002), thereby utilizing the neem bark extract as the precursor for GQDs; presumably, one can combine the advantages of both the neem bark extract and GQDs, which could be meaningful for the development of nano-antioxidants for gastric lesions. In this work, we report the synthesis of GQDs from neem bark extract following a hydrothermal procedure. Efficacy of these GQDs in scavenging intracellular ROS and anti-inflammatory effects were examined in the model of stress-induced gastric ulcer by maintaining tissue integrity. These GQDs could scavenge $^{\bullet}OH$, $^{\bullet}O^{2-}$ and 1,1-diphenyl-2- picrylhydrazyl ($DPPH^{\bullet}$), and the half-maximal effective concentration (EC_{50}) of GQDs against these three radicals were evaluated as 0.21, 0.24, and 0.19 mg/mL, respectively. GQDs are typically benign to the environment and nontoxic to human physiology (Facure et al., 2020; Tian et al., 2018). This, along with the ability of GQDs to act as a free radical scavenger, impelled us to explore the possibility of using GQDs for antioxidant therapy. Successive experiments reveal that GQD derived from Neem bark following a hydrothermal synthesis process is an efficient therapeutic candidate for ROS scavenging in the experimental swim-stress-induced gastric ulcer model. As the ROS production by macrophages is regulated via the inflammatory MMP-9-mediated pathway, evidence suggests that GQDs limit the expression of MMP-9 signaling. Therefore, these studies reveal the possibility of GQDs as a proficient scavenger for ROS and associated stress-induced gastric ulceration. This work offers a new therapeutic strategy and use of GQDs as an agent for treating gastric and intestinal dysfunctions.

RESULTS AND DISCUSSION

The GQDs were synthesized from neem bark extract following a solvothermal synthesis at 200°C temperature with a reaction time of 6 h (see details in supporting information), which were optimized based on previous works (Singh et al., 2019). Following centrifugation at 10k rpm for 10 min, the GQDs in the supernatant were isolated and purified by dialysis against deionized water for 12 h. Deionized water used for dialysis was periodically replaced after every hour. The pH of the resultant solution of GQDs was found to be 7.9 ± 0.1 ($n = 3$).

The transmission electron microscopic (TEM) images (Figure 1A) reveal that GQDS are nearly monodisperse, having average particle sizes of 5 ± 1 nm (Figure 1C). The high-resolution TEM image (Figure 1A, inset) reveals an identical well-resolved lattice fringe with a spacing of 0.30 nm, which is characteristic of the (100) in-plane lattice of graphene(Ding et al., 2016). As shown by AFM images (Figure S1A), the height of the GQDs are in the range of 4–6 nm, which indicates that the synthesized GQDs consist of 6–9 graphene layers. From TEM images, we calculated that the aspect ratio (ratio of length-to-width) of GQDs is 1–1.05, which confirms spherical morphology. The Raman spectra of GQDs show a D band at 1353 cm^{-1} and a G

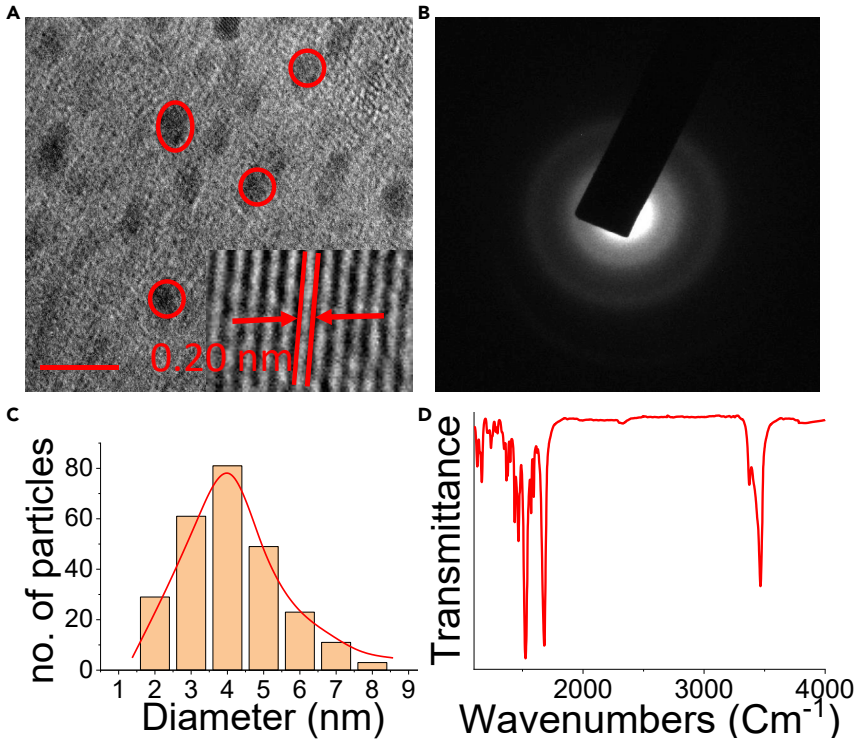

Figure 1. Morphological characterizations of GQDs

(A–D) (A) TEM image of the GQDs, in the inset HRTEM image of the GQDs; (B) FFT or SAED pattern of the GQDs; (C) size distribution of the GQDs; (D) FT-IR spectra of the GQDs. Scale bar: 6 nm.

band at 1596 cm^{-1} with a I_D/I_G intensity ratio of 0.89, which is higher than the ID/IG ratio of graphite powder (0.255) (Figure S1B). This indicates that the GQDs have more disordered structure than the constituent graphite powder, and this could also be due to the presence of more oxygen- and nitrogen-containing functional groups in the prepared (Li et al., 2012). Moreover, the DLS studies (in triplicate) with freshly sonicated GQD-dispersion reveal a hydrodynamic diameter of ~7 ± 2 nm. The powder X-ray diffraction (pXRD) patterns of the GQDs show a broad diffraction peak at 2Θ = 23.9 of the (002) plane with the "d" spacing of 0.29 nm (Figure S2). This indicates that the formed GQDs consist of very few layers of graphene sheets. In addition, the increased interlayer spacing value could be attributed to the intercalation of base between the graphene sheets and further insertion of oxygen-containing functional groups, which is consistent with previous reports on GQDs.

The Fourier transform infrared spectrum (FT-IR) of GQDs reveals a significant distribution of hydrophilic functionalities, such as O−H (3450 cm^{-1}), N−H (3230 cm^{-1}), C−O (1251 cm^{-1}), and COOH (175. cm^{-1}) on their surfaces (Figure 1D) (Ding et al., 2016); this also attributes to its good water solubility. Furthermore, the stretching vibrations of C−N= (1420 cm^{-1}), C=C (1521 cm^{-1}), and C=N (1640 cm^{-1}) bonds confirm the creation of polyaromatic structures in the GQDs during the hydrothermal reaction (Wang et al., 2012; Zhou et al., 2013).

The X-ray photoelectron spectroscopic (XPS) measurements were performed to examine the surface functionalities of the GQDs. The full spectrum is presented in Figure S3, and this shows three characteristic peaks: C 1s (285 eV), N 1s (400 eV), and O 1s (531 eV); this confirms the presence of these elements in the GQDs (Singh et al., 2019). For the high-resolution XPS spectra (Figure 2), the C 1s band can be deconvoluted into four peaks that correspond to sp^2 carbons (C=C, 284.5 eV), sp^3 carbons (C−O/C−N, 286.1 eV), carbonyl carbons (C=O, 288.5 eV), and carboxyl carbons (COOH, 290.8 eV) (Figure 2A) (Ding et al., 2016). The N 1s band can be deconvoluted into three peaks at 400.1, 401.7, and 403.3 eV, which represent pyrrolic N, Graphitic N, and amino N, respectively (Figure 2B). The O 1s band is deconvoluted into three peaks at 531.6 532.8 and 533.5 eV for C=O, C−O, and carboxylate hydroxyl oxygen, respectively (Ding et al., 2016; Singh et al., 2019). In addition, XPS spectra suggest the distribution of the three elements present

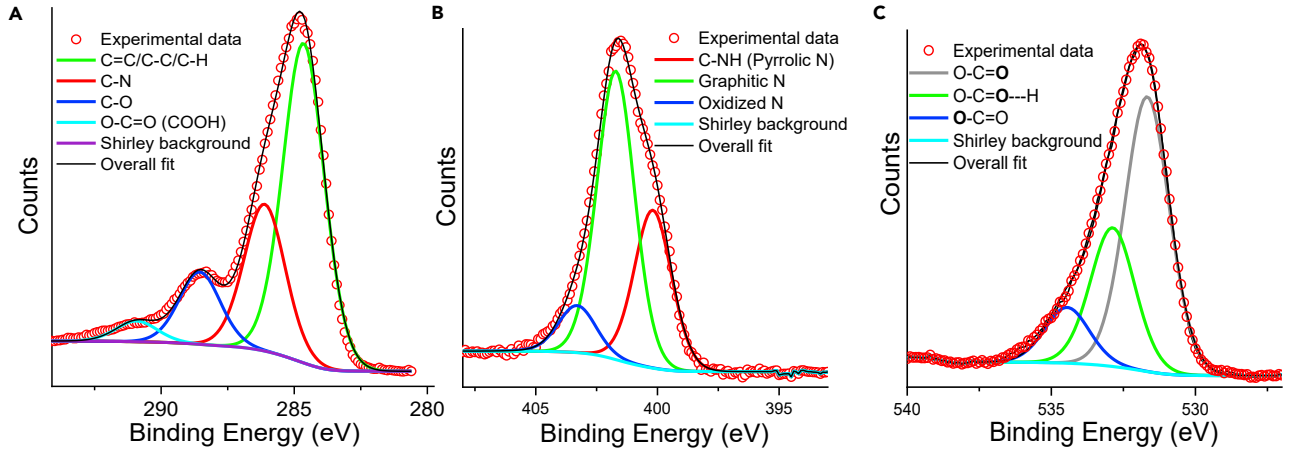

Figure 2. XPS analysis of GQDs

(A–C) High-resolution X-ray photoelectron spectra for (A) C 1s, (B) N 1s, and (C) O 1s of GQDs.

in GQDs: C = 70.2%, N = 10.8%, and O = 19.0%; this indicates that the prepared GQDs are rich in oxygen-containing functional groups (Table 1). The aforementioned data, including the AFM, pXRD, Raman, FT-IR, and XPS analysis, confirm that GQDs used for the present study are composed of π-conjugated areas in their carbon cores, whereas hydroxyl, carboxyl and amine functionalities are present on their surfaces.

The UV-Vis absorption spectrum of the as-synthesized GQDs shows an absorption band around 275 nm, which is attributed to the $\pi \rightarrow \pi^*$ transitions of the conjugated C=C bonds, whereas a broad shoulder at 295–455 nm is ascribed to the $n \rightarrow \pi^*$ transitions associated with C=N and C=O bonds (Figure 3A) (Ding et al., 2016). The GQDs also exhibit a characteristic excitation-dependent photoluminescence behavior (Singh et al., 2019). As shown in Figures 3B, 3A gradual shift in the emission maximum from 490 to 610 nm is observed with an associated shift in the respective excitation wavelength from 400 to 440 nm. It should be noted that the excitation of GQDs at 420 nm results in an optimal emission having a maximum at 550 nm. The wavelength-dependent emission properties of GQDs could be attributed to the formation of various sizes of polycyclic aromatic bunches, edge defects, surface emissive traps as well as the different size distribution of GQDs (Singh et al., 2019). The absolute fluorescence quantum yield of these GQDs is evaluated as 51%. To our knowledge, this quantum yield value compares well with that of the most reported as-synthesized GQDs derived from biomass-based feedstock and GQDs without any surface treatments.

Earlier reports suggest that the presence of the unpaired electrons and surface defects of GQDs attribute to the scavenging of the free radicals (Wang et al., 2020). The efficiency of the *in vitro* radical-quenching capability of the GQDs is evaluated by examining the scavenging activity against ROS species such as $DPPH^{\bullet}$, $^{\bullet}OH$, and $^{\bullet}O^{2-}$. DPPH assay is a commonly used methodology for *in vitro* assessing of total

Table 1. XPS analysis of GQDs

Fine spectra	Energy (eV)	Species	At%
C1s	284.5	C=C, C-C, C-H	57.15
	286.1	C-N	26.34
	288.5	C-O	12.87
	290.8	O-C=O (COOH)	3.64
N1s	400.1	C-NH (Pyrrolic N)	31.93
	401.7	Graphitic N	58.33
	403.3	Oxidized N	9.74
O1s	531.6	O-C=O	58.56
	532.8	O-C=O…H	29.56
	533.5	O-C=O	11.88

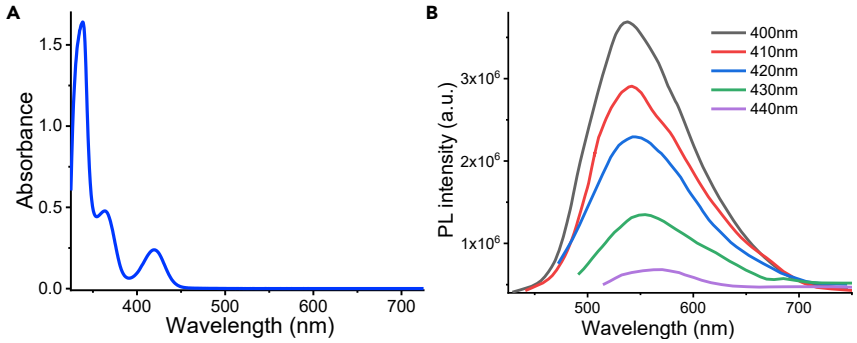

Figure 3. Optical performance of GQDs

(A and B) (A) Absorption spectrum and (B) photo illumination emission spectra of the aqueous solution of GQDs under excitation with light of different wavelengths.

antioxidant activity. GQDs show a dose-dependent scavenging effect on DPPH$^{\bullet}$; a steady decrease in the effective concentration of DPPH$^{\bullet}$ with an associated decrease in the intensity of the electronic spectral band is observed with the increase of GQDs concentration (Figure S4). Moreover, the EC_{50} of GQDs toward DPPH$^{\bullet}$ is evaluated as 0.19 mg/mL, and this suggests that GQDs at 0.55 mg/mL can eliminate approximately 95% DPPH$^{\bullet}$ (Figure S4). The scavenging efficiency of GQDs against DPPH$^{\bullet}$ is possibly ascribed to the plentiful reductive functional groups on the surface of GQDs after the hydrothermal reaction. The scavenging action of GQDs toward $^{\bullet}OH$ and $^{\bullet}O_2^-$ was checked using Fenton-reaction-based assay (the detailed experimental procedure in supporting information). As shown in Figures 4A and 4B, GQDs can effectively eliminate $^{\bullet}OH$ and $^{\bullet}O_2^-$ in a dose-dependent manner. The GQDs effectively eliminate the $^{\bullet}O^{2-}$and $^{\bullet}OH$ with respective EC_{50} value of 0.21 mg/mL and 0.25 mg/mL (Figures 4C and 4D). This dose-dependent decrease in the signal intensity and the effective concentration of $^{\bullet}OH$ or $^{\bullet}O^{2-}$ radical, evaluated using Fenton-reaction-based assay, confirms the efficient scavenging of these ROS species by GQDs.

To test the potential of these GQDs for biomedical applications, biocompatibility studies using MTT assay are performed with GQDs (see Figure S5). Results of this assay indicate that the GQDs are fully biocompatible, and this makes them brilliant candidates for the therapeutic applications.

ROS, the most critical components attributed for gastric ulceration, are induced by stress that creates oxidative injury through protein oxidation and lipid peroxidation (Bhattacharyya et al., 2014; Das et al., 1997). With an aim to deal with this specific issue, we have further investigated the function of GQDs on murine-forced swim-stress-induced oxidative injury in the stomach mucosa. The ulcer index of ~70 in gastric tissues of mice was induced by swim stress for 4 h. This time point was chosen for the rest of the experiments unless mentioned otherwise. Interestingly, in this murine model of gastric ulcer, GQDs drastically reduced swim-stress-induced gastric lesions dose dependently and showed nearly 95% inhibitions at 10 mg/kg (Figure S6A). GQDs used at low (2 mg/kg b.w.) and high (10 mg/kg b.w.) doses were chosen for the rest of the experiments for the comparative analysis between low versus high dose. Microscopic examination revealed that forced swim stress caused extreme hemorrhagic wounds all through the epithelium, whereas those wounds were not found in GQDs-pretreated group, particularly at 10 mg/kg body weight (b.w) (Figure 5). Moreover, the investigation from histology of tissue indicates that the stress causes shedding of the gastric epithelial cells, besides interruption of the epithelial-mucosal barrier (red bolt) of the stomach in contrast with that of control, and the ulcer formation is prevented in tissues that are treated with varying dosages of GQDs (Figure 5A; middle and lower panel). In addition, myeloperoxidase (MPO) assay (an inflammatory marker enzyme) shows the effects of GQDs administration at a higher dose (10 mg/kg) to control/healthy mice and swim-stressed group. We did not find any toxic inflammatory activity in only GQDs-treated mice group compared with control mice (mice received only buffer solution), emphasizing safety of GQDs even at a higher dose (Table TS1). Moreover, MPO activity was significantly elevated in murine-forced swim-stress-ulcerated mucosa and that activity per gram tissue was reduced to normal level following GQDs treatment indicating the anti-inflammatory property of GQDs. Table 2 reveals the significant antioxidant activity of GQDs in protecting gastric damage. Presumably, the antioxidant activity of GQDs is induced through blockage of stress-induced augmentation in protein oxidation and lipid peroxidation. In addition, the results of the TUNEL assay (Figure 5C) indicate that stress-induced gastric cell death while pretreatment with GQDs

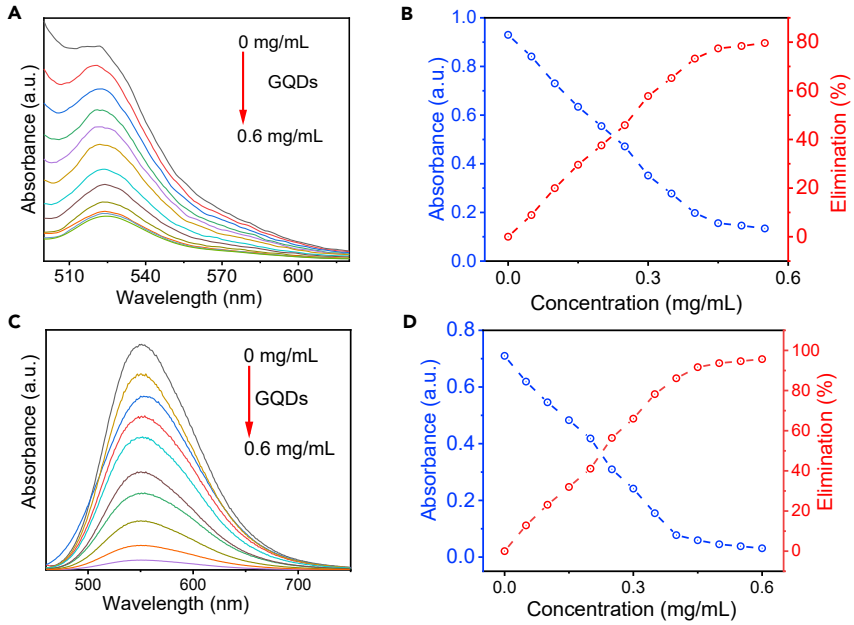

Figure 4. Demonstration of the antioxidant activity of GQDs

(A–D) (A and B) $^{\bullet}OH$ scavenging test and (C and D) $^{\bullet}O_2^-$ scavenging test as a function of varying the effective concentration of GQDs (0–0.6 mg/mL). Quantification of the $^{\bullet}OH$ and $^{\bullet}O_2^-$ radicals was achieved using a Fenton-reaction-based assay.

completely reduces that damage at a dose of 10 mg/kg b.w. Dark brown dots (Figure 5C) (black arrow) are used to indicate the end-labeling that is restricted inside the nucleus and increased DNA disintegration inside the nuclei of gastric cells after generation of forced swim stress.

Matrix metalloproteinase (MMP)-9 is well known for its inflammatory action in gastric tissues. Upon inhibition of MMP-9, pathogenesis is ameliorated; therefore, the tissues from GQDs-treated and untreated groups were processed for *in vivo* analysis of MMP-9 expression using immunofluorescence staining. Red fluorescence represents MMP-9, which is immune stained with anti-MMP-9 antibody and Texas Red conjugated secondary antibody (Figure 6A). Blue fluorescence represents DAPI-stained nuclei and documented equal fluorescence in control, stress ulcerated, and GQDs-pretreated stressed gastric tissue sections (Figure 6A). The increased expression of MMP-9 is observed in the epithelial layer and glandular regions of stress ulcerated stomach compared with control. Both low (2 mg/kg b.w.) and high (10 mg/kg b.w.) doses of GQDs-pretreated sections exhibit inhibited MMP-9 signals as evident from merging the images with corresponding DAPI-stained nuclei. Furthermore, in gelatin zymographic analysis, we found an increase in each pro and active MMP-9 activity in acute ulcerated stomach tissue extract, whereas GQDs treated at doses 2 and 10 mg/kg b.w. effectively reverse that upregulation during gastroprotection (Figure 6B). The densitometric evaluation of zymographic bands (Figure 6C) shows that stress increases the pro and active MMP-9 activity by ~60% and ~50%, respectively, in comparison with control, whereas GQDs prevent this activity and bring it almost near to control.

Furthermore, to delineate the function of GQDs in expressing secreted MMP-9, western blotting was performed using PBS extracts of control, ulcerated, and GQDs-treated tissues. Stress causes significant enhancement of MMP-9 expression in secreted form, whereas GQDs pretreatment, even at a dose of 2 mg/kg b.w, significantly reduces MMP-9 secretion during the prevention of ulceration (Figures 7A and 7B). In addition, the effect of GQDs in stress-responsive chaperone heat shock protein 70 (Hsp70) was also observed. Hsp70 expression was significantly reduced in ulcerated gastric tissue and was upregulated by GQDs (Figures 7A and 7B). The Hsps preserve cellular functional stability caused by sublethal injury and are known to induce through oxyradical, thermal, and inflammatory stress (Rafiee et al., 2006). The chaperone-denatured intracellular proteins and signal transduction proteins modulate signaling events in repetitive stress (Rafiee et al., 2006). Herein, we hypothesize GQDs-induced overexpression of anti-apoptotic

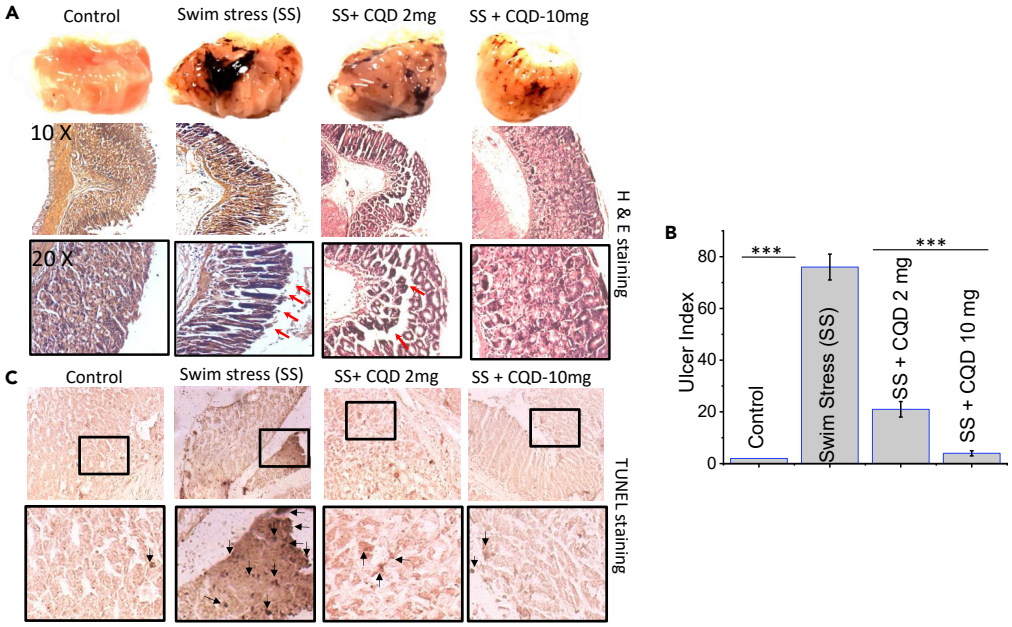

Figure 5. Protection by graphene quantum dots (GQDs) against forced swim-stress-induced gastric ulcer in mice

(A) Macroscopic observation of control, forced swim-stressed and GQDs-treated mouse stomach (upper panel). Histological representation of gastric tissue sections from different groups. The red arrow indicates disruption of the tissue layer of the stomachs from different groups (lower panel).

(B) Ulcer indices for each stomach and plotted for GQDs-treated and untreated groups (data were indicated as the mean ± SEM). Evaluation between groups was executed using one-way analysis of variance (ANOVA) after that Student–Newman–Keuls t test.

(C) TUNEL staining of gastric tissue sections from different groups. Black arrow indicates that the incidence of apoptosis was majorly concentrated in ulcerated sections.

Bcl-2 along with a sustained increased level of Hsp70 is sufficient to clear gastric damage during gastroprotection as evident from Figures 7A and 7B. However, excess and sustained accumulation of apoptotic BAX ultimately triggers BAX-dependent apoptosis and consequent caspase-3 expression (Figures 7A and 7B). Caspase-3 is one of the main initiator caspases and is linked to the mitochondrial death pathway, whereas Caspae-3 is an effector caspase (De et al., 2017). Oxidative stress damages mitochondria, which in turn results in the associated functional failure and programmed cell death. Cumulatively, GQDs significantly prevent inflammation and subsequent apoptosis in the gastric milieu even after stress by inhibiting the expression of MMP-9, BAX, and Caspase-3 and upregulating the BCL2 as evident from densitometry analysis (Figures 7A and 7B). Furthermore, to test whether GQDs could hamper the caspase signaling and lead to cell death, we have checked the caspase-9 and caspase-3 in gastric milieu by activity assay (Figure S7). The results indicate that pretreatment with GQDs significantly downregulated both caspase-9 and caspase-3 activity in a dose-dependent manner during gastroprotection (Figure S7).

Therefore, herein we report that ROS-induced MMP-9-mediated inflammation with excess mitochondrial oxidative damage and aberrant BCL2, Bax protein expressions play significant roles in swim-stress-induced gastric ulceration. Altogether, GQD acts as a double-edged sword that can promote ulcer healing via both normalizing the BCL2, Bax expression as well as by inhibition of ROS-induced MMP-9-mediated inflammation. In addition, Figure 8 shows GQDs-corrected mitochondrial dysfunction induced in swim stress. Data indicated that GQDs at 10 mg/kg prevented forced swim-stress-induced mitochondrial damage as evident from rectification of $\Delta\Psi m$ depolarization (Figure 8A), loss of dehydrogenase activity (Figure 8B), and tissue ATP depletion (Figure 8C).

Conclusion

In brief, we report a facile method for the preparation of GQDs in water from a neem bark extract. GQDs thus produced are appropriately characterized using various analytical, spectroscopic, and electron microscopic studies. Results of the XPS studies suggest the probable distribution of hydroxyl, carboxyl, and

Table 2. *In vivo* anti-oxidative activity of graphene quantum dots (GQDs) during gastroprotection

Assays	Control	Stress	Stress + GQDs 2 mg	Stress + GQDs 10 mg
Lipid peroxidation (nmol TBARS/mg protein)	0.16 ± 0.016	0.27 ± 0.028	0.241 ± 0.024	0.20 ± 0.01
Protein carbonylation (nmol/mg protein)	1.23 ± 0.049	2.68 ± 0.15	2.15 ± 0.12	1.67 ± 0.080

Lipid peroxidation and protein carbonylation were measured as described in the materials and methods. The antioxidant activity of GQDs (10 mg/kg body weight) in protecting gastric injuries through blocking of stress-induced lipid peroxidation and protein oxidation. The results were expressed as mean ± SEM.

amine functionalities on the surfaces. GQDs are found to be an effective ROS scavenger, and the efficacy of this process is evaluated through both *in vitro* and *in vivo* studies. Results reveal a remarkable elimination efficiency, as high as 99%, against toxic ROS and effective in suppressing stress-induced gastric ulcers. To mimic the stress experienced by critically ill patients, we have adopted a model of murine-forced swim-stress-induced gastric ulcer in the laboratory. The GQDs offer gastroprotection by targeting MMP-9 pathway and reducing the inflammatory burden by suppressing excessive oxidative stress. Excess and sustained accumulations of ROS generate mitochondrial dysfunction, ultimately triggering apoptosis of gastric mucosal cells. The present study confirms the high caspase activity, overproduction of Bax, down-regulation of BCL2, and TUNEL assay. In conclusion, besides its antioxidant and anti-apoptotic properties, we could establish the mechanistic pathways for effective inhibition of inflammatory MMP-9 by GDQs that are derived from neem barks.

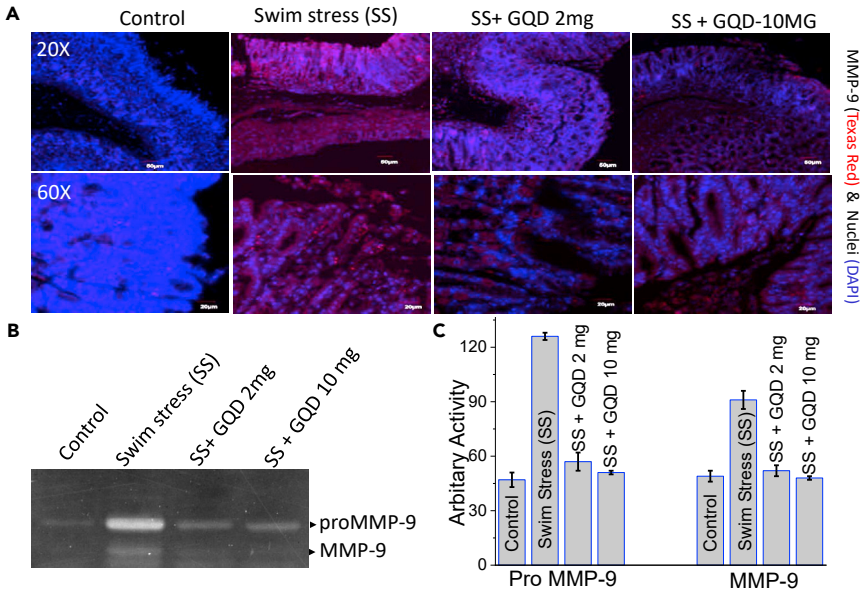

Figure 6. Gastroprotective mechanism of GQDs

(A) GQDs downregulate *in vivo* MMP-9 expression and activity in forced swim-stress-induced gastric ulcer in mice: here MMP-9 was immunostained with anti-MMP-9 antibody and Texas Red (red) conjugated secondary antibody. The nuclei were stained with 4′, 6-diamidino-2-phenylindole or DAPI (blue). Both low (2 mg/kg b.w.) and high (10 mg/kg b.w.) doses of GQDs treated tissues exhibited significant inhibition of MMP-9 signals (red) compared with stress as evident from merged images with DAPI.

(B) Gelatin zymographic representation of both pro and active MMP-9 activity in acute ulcerated stomach-tissue-extract-treated, as well as GQDs-treated, groups.

(C) Histographic representation of pro and active MMP-9 activity in control, stress ulcerated, and GQDs-treated gastric mucosa. Graph shows fold change versus both form of MMP-9 under stress (data were indicated as the mean ± SEM). Statistical evaluation was done using ANOVA after that Student–Newman–Keuls t test.

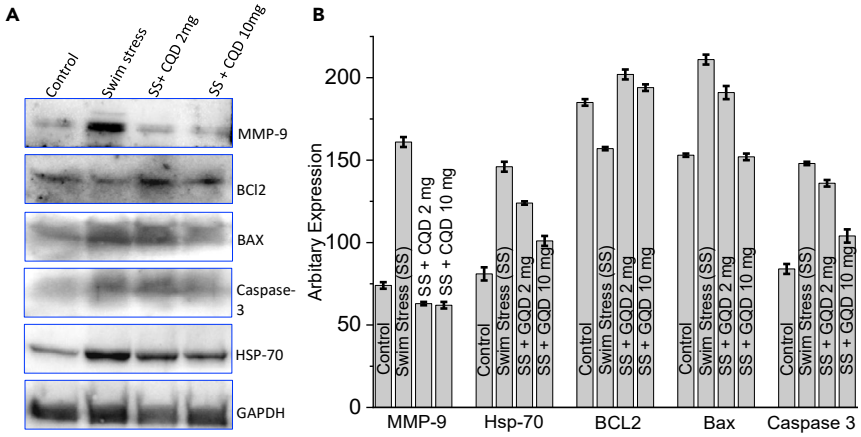

Figure 7. Anti-inflammatory and anti-apoptotic effect of GQDs during gastroprotection

(A) Effect of GQDs pretreatment (2 and 10 mg/kg b.w.) on expressions of MMP-9, BCL2, Bax, Caspase-3, Hsp70, and GAPDH (loading control) in gastric tissues after 4 h of stress as presented in respective western blots for these molecules. Each blot is representative of three independent experiments.

(B) Histographic representation shows the significance of fold changes versus expressions of MMP-9, Hsp70, BCL2, Bax, and Caspase-3 under stress and GQDs-treated conditions compared with control (data were indicated as the mean ± SEM). Statistical evaluation was performed using ANOVA after that Student–Newman–Keuls t test.

Limitations of the study

GQDs reported in this article are efficient in scavenging GI-ROS and preventing stress-induced gastric ulcers by targeting the MMP-9 pathway and correcting gut mitochondrial dysfunction. However, further internal validation points are necessary to evaluate the swim-stress model with additional environmental factors, including pH, temperature, and O_2, which could impact the healing role of GQDs after ulceration caused by swim stress.

STAR★METHODS

Detailed methods are provided in the online version of this paper and include the following:

- KEY RESOURCES TABLE
- RESOURCE AVAILABILITY
  - Lead contact
  - Materials availability
  - Data and code availability
- EXPERIMENTAL MODEL AND SUBJECT DETAILS
  - Mice (Balb/c)
- METHOD DETAILS

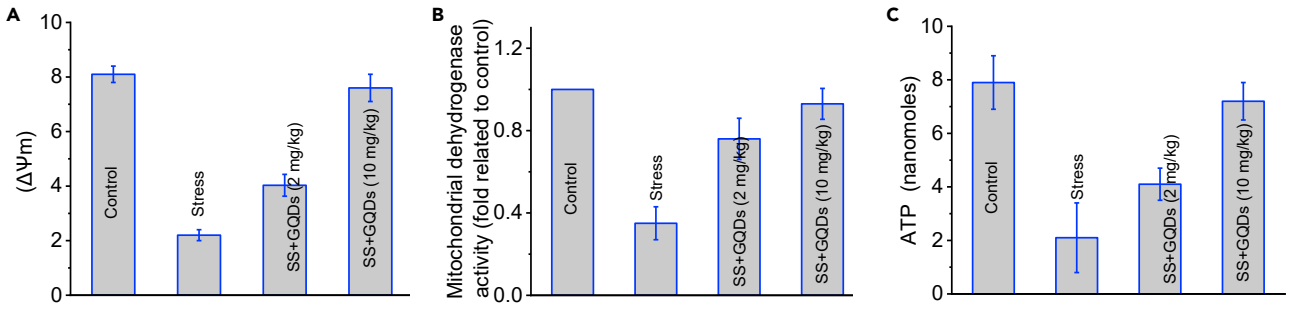

Figure 8. GQDs corrected mitochondrial dysfunction induced in swim stress

(A) Inhibition of gastric mitochondrial trans-membrane potential (ΔΨm) following forced swim stress was corrected by GQDs.

(B) Mitochondrial dehydrogenase activity in mice gastric mitochondria after forced swim stress and protective effect of GQDs thereon. (C) Gastric mucosal tissue ATP content.

SUPPLEMENTAL INFORMATION

Supplemental information can be found online at https://doi.org/10.1016/j.isci.2022.104062.

ACKNOWLEDGMENTS

A.D. acknowledges SERB (India) Grants (CRG/2020/000492 & JCB/2017/000004). A.D. and S.K.P. acknowledges DBT Grant (BT/PR22251/NNT/28/1274/2017) for supporting this research. We thank Prof. Sayan Bhattacharya of IISER Kolkata for his help with the XPS analysis. This manuscript bears a CSIR-CSMCRI PRIS No: 47/2022.

AUTHOR CONTRIBUTIONS

P.C., S.B., N.K., A.C., and D.T performed the experiments; S.S., S.C., A.D., and S.K.P. supervised. All authors conceptualized, discussed, and wrote the manuscript.

DECLARATION OF INTERESTS

The authors declare no competing interests.

Received: November 5, 2021
Revised: February 15, 2022
Accepted: March 9, 2022
Published: April 15, 2022

REFERENCES

Aviello, G., and Knaus, U.G. (2017). ROS in gastrointestinal inflammation: rescue or Sabotage? Br. J. Pharmacol. *174*, 1704–1718. https://doi.org/10.1111/bph.13428.

Aviello, G., and Knaus, U.G. (2018). NADPH oxidases and ROS signaling in the gastrointestinal tract. Mucosal Immunol. *11*, 1011–1023. https://doi.org/10.1038/s41385-018-0021-8.

Bandyopadhyay, U., Biswas, K., Chatterjee, R., Bandyopadhyay, D., Chattopadhyay, I., Ganguly, C.K., Chakraborty, T., Bhattacharya, K., and Banerjee, R.K. (2002). Gastroprotective effect of Neem (Azadirachta indica) bark extract: possible involvement of H+-K+-ATPase inhibition and scavenging of hydroxyl radical. Life Sci. *71*, 2845–2865. https://doi.org/10.1016/S0024-3205(02)02143-4.

Bandyopadhyay, U., Das, D., Bandyopadhyay, D., Bhattacharjee, M., and Banerjee, R.K. (1999). Role of reactive oxygen species in

mercaptomethylimidazole-induced gastric acid secretion and stress-induced gastric ulceration. Curr. Sci. *76*, 55–63.

Bhattacharyya, A., Chattopadhyay, R., Mitra, S., and Crowe, S.E. (2014). Oxidative stress: an essential factor in the pathogenesis of gastrointestinal mucosal diseases. Physiol. Rev. *94*, 329–354. https://doi.org/10.1152/physrev.00040.2012.

Chong, Y., Ge, C., Fang, G., Tian, X., Ma, X., Wen, T., Wamer, W.G., Chen, C., Chai, Z., and Yin, J.-J. (2016). Crossover between anti- and pro-oxidant activities of graphene quantum dots in the absence or presence of light. ACS Nano *10*, 8690–8699. https://doi.org/10.1021/acsnano.6b04061.

Das, D., Bandyopadhyay, D., Bhattacharjee, M., and Banerjee, R.K. (1997). Hydroxyl radical is the major causative factor in stress-induced gastric ulceration. Free Radic. Biol. Med. *23*, 8–18. https://doi.org/10.1016/S0891-5849(96)00547-3.

De, R., Mazumder, S., Sarkar, S., Debsharma, S., Siddiqui, A.A., Saha, S.J., Banerjee, C., Nag, S., Saha, D., and Bandyopadhyay, U. (2017). Acute mental stress induces mitochondrial bioenergetic crisis and hyper-fission along with aberrant mitophagy in the gut mucosa in rodent model of stress-related mucosal disease. Free Radic. Biol. Med. *113*, 424–438.

Ding, H., Yu, S.-B., Wei, J.-S., and Xiong, H.-M. (2016). Full-color light-emitting carbon dots with a surface-state-controlled luminescence mechanism. ACS Nano *10*, 484–491. https://doi.org/10.1021/acsnano.5b05406.

Facure, M.H.M., Schneider, R., Mercante, L.A., and Correa, D.S. (2020). A review on graphene quantum dots and their nanocomposites: from laboratory synthesis towards agricultural and environmental applications. Environ. Sci.: Nano. *7*, 3710–3734. https://doi.org/10.1039/D0EN00787K.

Islas, J.F., Acosta, E., G-Buentello, Z., Delgado-Gallegos, J.L., Moreno-Treviño, M.G., Escalante, B., and Moreno-Cuevas, J.E. (2020). An overview of Neem (Azadirachta indica) and its potential impact on health. J. Funct. Foods *74*, 104171. https://doi.org/10.1016/j.jff.2020.104171.

Kinoshita, Y., Ishimura, N., and Ishihara, S. (2018). Advantages and disadvantages of long-term proton pump inhibitor use. J. Neurogastroenterol Motil. *24*, 182–196. https://doi.org/10.5056/jnm18001.

Li, H., Yan, X., Kong, D., Jin, R., Sun, C., Du, D., Lin, Y., and Lu, G. (2020). Recent advances in carbon dots for bioimaging applications. Nanoscale Horizons *5*, 218–234. https://doi.org/10.1039/C9NH00476A.

Li, Y., Zhao, Y., Cheng, H., Hu, Y., Shi, G., Dai, L., and Qu, L. (2012). Nitrogen-doped graphene quantum dots with oxygen-rich functional groups. J. Am. Chem. Soc. *134*, 15–18.

Middha, E., and Liu, B. (2020). Nanoparticles of organic electronic materials for biomedical applications. ACS Nano *14*, 9228–9242. https://doi.org/10.1021/acsnano.0c02651.

Patel, K.D., Singh, R.K., and Kim, H.-W. (2019). Carbon-based nanomaterials as an emerging platform for theranostics. Mater. Horizons *6*, 434–469. https://doi.org/10.1039/C8MH00966J.

Patlevič, P., Vašková, J., Švorc, P., Vaško, L., and Švorc, P. (2016). Reactive oxygen species and antioxidant defense in human gastrointestinal diseases. Integr. Med. Res. *5*, 250–258. https://doi.org/10.1016/j.imr.2016.07.004.

Pérez, S., Taléns-Visconti, R., Rius-Pérez, S., Finamor, I., and Sastre, J. (2017). Redox signaling in the gastrointestinal tract. Free Radic. Biol. Med. *104*, 75–103. https://doi.org/10.1016/j.freeradbiomed.2016.12.048.

Rafiee, P., Theriot, M.E., Nelson, V.M., Heidemann, J., Kanaa, Y., Horowitz, S.A., Rogaczewski, A., Johnson, C.P., Ali, I., and Shaker, R. (2006). Human esophageal microvascular endothelial cells respond to acidic pH stress by PI3K/AKT and p38 MAPK-regulated induction of Hsp70 and Hsp27. Am. J. Physiology-Cell Physiol. *291*, C931–C945.

Ruiz, V., Yate, L., García, I., Cabanero, G., and Grande, H.-J. (2017). Tuning the antioxidant activity of graphene quantum dots: protective nanomaterials against dye decoloration. Carbon *116*, 366–374. https://doi.org/10.1016/j.carbon.2017.01.090.

Saleem, S., Muhammad, G., Hussain, M.A., and Bukhari, S.N.A. (2018). A comprehensive review of phytochemical profile, bioactives for pharmaceuticals, and pharmacological attributes of Azadirachta indica. Phytotherapy Res. *32*, 1241–1272. https://doi.org/10.1002/ptr.6076.

Saleh Al-Hashemi, Z.S., and Hossain, M.A. (2016). Biological activities of different neem leaf crude extracts used locally in Ayurvedic medicine. Pac. Sci. Rev. A: Nat. Sci. Eng. *18*, 128–131. https://doi.org/10.1016/j.psra.2016.09.013.

Sandler, S.E., Fellows, B., and Mefford, O.T. (2019). Best practices for characterization of magnetic nanoparticles for biomedical applications. Anal. Chem. *91*, 14159–14169. https://doi.org/10.1021/acs.analchem.9b03518.

Singh, H., Sreedharan, S., Tiwari, K., Green, N.H., Smythe, C., Pramanik, S.K., Thomas, J.A., and Das, A. (2019). Two photon excitable graphene quantum dots for structured illumination microscopy and imaging applications: lysosome specificity and tissue-dependent imaging. Chem. Commun. *55*, 521–524. https://doi.org/10.1039/C8CC08610A.

Strand, D.S., Kim, D., and Peura, D.A. (2017). 25 Years of proton pump inhibitors: a comprehensive review. Gut Liver *11*, 27–37. https://doi.org/10.5009/gnl15502.

Tang, Z., Xu, W., Zhou, G., Bai, Y., Li, J., Tang, X., Chen, D., Liu, Q., Ma, W., Xiong, G., et al. (2018). Patterns of plant carbon, nitrogen, and phosphorus concentration in relation to productivity in China's terrestrial ecosystems. Proc. Natl. Acad. Sci. *115*, 4033–4038. https://doi.org/10.1073/pnas.1700295114.

Taylor, C.T., and Colgan, S.P. (2017). Regulation of immunity and inflammation by hypoxia in immunological niches. Nature reviews. Immunol. *17*, 774–785. https://doi.org/10.1038/nri.2017.103.

Tian, P., Tang, L., Teng, K.S., and Lau, S.P. (2018). Graphene quantum dots from chemistry to applications. Mater. Today Chem. *10*, 221–258. https://doi.org/10.1016/j.mtchem.2018.09.007.

Ungaro, R., Mehandru, S., Allen, P.B., Peyrin-Biroulet, L., and Colombel, J.-F. (2017). Ulcerative colitis. Lancet *389*, 1756–1770. https://doi.org/10.1016/S0140-6736(16)32126-2.

Wang, B.B., Cheng, Q.J., Wang, L.H., Zheng, K., and Ostrikov, K. (2012). The effect of temperature on the mechanism of photoluminescence from plasma-nucleated, nitrogenated carbon nanotips. Carbon *50*, 3561–3571. https://doi.org/10.1016/j.carbon.2012.03.028.

Wang, L., Li, Y., Zhao, L., Qi, Z., Gou, J., Zhang, S., and Zhang, J.Z. (2020). Recent advances in ultrathin two-dimensional materials and biomedical applications for reactive oxygen species generation and scavenging. Nanoscale *12*, 19516–19535. https://doi.org/10.1039/D0NR05746K.

Wang, L., Wang, Y., Xu, T., Liao, H., Yao, C., Liu, Y., Li, Z., Chen, Z., Pan, D., Sun, L., and Wu, M. (2014). Gram-scale synthesis of single-crystalline graphene quantum dots with superior optical properties. Nat. Commun. *5*, 5357. https://doi.org/10.1038/ncomms6357.

Yan, Y., Gong, J., Chen, J., Zeng, Z., Huang, W., Pu, K., Liu, J., and Chen, P. (2019). Recent advances on graphene quantum dots: from chemistry and physics to applications. Adv. Mater. *31*, 1808283. https://doi.org/10.1002/adma.201808283.

Yang, Y., Zhang, M., Song, H., and Yu, C. (2020). Silica-based nanoparticles for biomedical applications: from nanocarriers to biomodulators. Acc. Chem. Res. *53*, 1545–1556. https://doi.org/10.1021/acs.accounts.0c00280.

Yoo, E., Okata, T., Akita, T., Kohyama, M., Nakamura, J., and Honma, I. (2009). Enhanced electrocatalytic activity of Pt subnanoclusters on graphene nanosheet surface. Nano Lett. *9*, 2255–2259. https://doi.org/10.1021/nl900397t.

Zhang, M., Bai, L., Shang, W., Xie, W., Ma, H., Fu, Y., Fang, D., Sun, H., Fan, L., Han, M., et al. (2012). Facile synthesis of water-soluble, highly fluorescent graphene quantum dots as a robust biological label for stem cells. J. Mater. Chem. *22*, 7461–7467. https://doi.org/10.1039/C2JM16835A.

Zheng, X.T., Ananthanarayanan, A., Luo, K.Q., and Chen, P. (2015). Glowing graphene quantum dots and carbon dots: properties, syntheses, and biological applications. Small *11*, 1620–1636. https://doi.org/10.1002/smll.201402648.

Zhou, J., Yang, Y., and Zhang, C.-y. (2013). A low-temperature solid-phase method to synthesize highly fluorescent carbon nitride dots with tunable emission. Chem. Commun. *49*, 8605–8607. https://doi.org/10.1039/C3CC42266F.

STAR★METHODS

KEY RESOURCES TABLE

REAGENT or RESOURCE	SOURCE	IDENTIFIER
Gelatin	Sigma-Aldrich	CAS: 9000-70-8
Protease inhibitors cocktail	Calbiochem	Cat# 539131
Protein ladder	Puregene	Cat# PG-PMT2922
Bradford	Sigma-Aldrich	Cat# B6916
Caspase-9 assay	Calbiochem	Cat# 218824
Caspase-3 assay	Millipore	Cat# CASP3C-1kit
DAPI	Sigma-Aldrich	Cat# D9564
MMP-9	Santa Cruz	Cat# SC-6841
Bcl2	Santa Cruz	Cat# SC-492
Bax	Cell Signaling	Cat# 2112S
HSP-70	Abcam	Cat# Ab- 137680
GAPDH	Santa Cruz	Cat# SC-47724
Caspase-3	Santa Cruz	Cat# SC-22140
HRP conjugated secondary	Santa Cruz	Cat# SC-2055
HRP conjugated secondary	Merck Millipore	Cat# AP-106P
HRP conjugated secondary	Santa Cruz	Cat# SC-2357
HRP Luminescent	Biorad	Cat# 1705061
Triton X-100	Sigma-Aldrich	CAS: 9036-19-5
2-4-dinitrophenyl hydrazine	Sigma-Aldrich	CAS: 119-26-6
Guanidine hydrochloride	Sigma-Aldrich	CAS: 50-01-1

RESOURCE AVAILABILITY

Lead contact

Further information and requests for resources and reagents should be directed to and will be fulfilled by the lead contact, Sumit Kumar Pramanik (sumitpramanik@csmcri.res.in).

Materials availability

This study did not generate new unique reagents.

Data and code availability

- Data: All data reported in this paper will be shared by the lead contact upon request.
- Code: This paper does not report the original code.
- Any additional information required to reanalyze the data reported in this paper is available from the lead contact upon request.

EXPERIMENTAL MODEL AND SUBJECT DETAILS

Mice (Balb/c)

Healthy Balb/c mice (20–25 g) obtained from an in-house breeding program with a "nonstress" control group (unlimited access to food and water with proper light exposure) were used for the studies. We restricted our studies to a minimum sample size, while complying with the valid statistical estimation. Ketamine (12 mg/kg b.w.) was used for anesthetizing the animals, which were then subjected to cervical dislocation. The study was discussed and approved by the ethics and animal welfare committee of the Institute of Chemical Biology (Kolkata, India), where experiments were performed.

METHOD DETAILS

Synthesis of GQDs

Neem bark extract (1 g), obtained by grinding the Neem bark into a fine powder using a commercial mixer grinder, were boiled in deionized water at 60°C for 2 h, and followed by centrifugation at 12000 *g* for 30 min to remove any remaining solids. The supernatant liquid solution was passed through a 0.22 μm filter membrane for further removal of any trace solid residues present in the solution. After that, this solution was used for the hydrothermal reaction. The hydrothermal reaction was performed in a stainless steel autoclave at a temperature of 200°C for 6 h. The obtained GQDs were a mixture of a transparent brown suspension along with black precipitates. The black precipitate was removed by centrifugation at 25000 *g* for 20 min and the supernatant was collected and washed three times with deionized water. The GQD solution was then dialyzed using a filter (cutoff 4.0 kDa) for 24 h and dried in a lyophilizer.

Quantum yield calculation

The quantum yield was calculated by using the below equation. Here both samples (GQDs) and reference were excited at a point where they have the same absorbance. Here Φ stands for quantum yield, η for refractive index, I for integrated fluorescence intensity for sample and reference.

$$\Phi_s = \Phi_{ref} \times \left(\frac{\eta_s^2}{\eta_{ref}^2}\right) \times \left(\frac{I_s}{I_{ref}}\right)$$

Powder X-ray diffraction

Powder X-ray diffraction patterns were collected in the range of 5–50° with a Philips X'pert X-ray powder diffractometer using Cu Kα (λ = 1.54178 Å) radiation.

Dynamic light scattering

The average size and size distribution of the GQDs were measured at 27°C by DLS using Brookhaven instruments Zetapals.

Fourier transform infrared spectroscopy

The FT-IR spectroscopic measurements were carried out using a PerkinElmer GX spectrophotometer. The spectra were recorded in the range 400–4000 cm−1 in KBr media.

Raman spectroscopy

Raman spectra were recorded using a Horiba LABRAM HR excited by a 514-nm laser.

Transmission electron microscopy

Transmission electron microscope images were recorded using a JEOL JEM 2100 microscope operated at 200 kV. The morphology of GQDs were obtained by placing a dilute sample on the TEM grids (lacey carbon formvar coated Cu grids (300 mesh)) using transmission electron microscopy. No additional staining was used.

DPPH$^{\cdot}$ scavenging activity

DPPH$^{\cdot}$, as stable nitrogen centered free radical (2,2-diphenyl-1-picrylhydrazyl), is usually used for quantitative estimation of antioxidant activity. The aqueous solution DPPH$^{\cdot}$ is of dark purple color and has a strong absorption peak at 520 nm. The free radical scavengers pair up with the unpaired electron of DPPH$^{\cdot}$, quenching the absorbance at 520 nm and discoloring the purple solution. The DPPH$^{\cdot}$ solution (0.125 mmol/L) was mixed with various concentrations of GQDs and with pure HEPES buffer as the control. The absorbance intensity of this solution at 520 nm was used to evaluate the DPPH$^{\cdot}$ scavenging efficiency. The elimination scavenging of GQDs toward DPPH$^{\cdot}$ was calculated by using the following equation, where Do is the absorbance at 520 nm of the control and Ds is the absorbance of the mixture of GQDs and DPPH$^{\cdot}$.

DPPH elimination efficiency = $(D_o - D_s)/D_o \times 100\%$

$^{\bullet}$OH scavenging activity

$^{\bullet}$OH radicals were produced by the traditional Fenton reaction. The $^{\bullet}$OH radical of the Fenton reaction, reacts with salicylic acid and forms 2,3-dihydroxybenzoic acid, which has an absorption peak at 520 nm. The $^{\bullet}$OH scavenging efficiency of GQDs was estimated by measuring the decrease in intensity of the absorbance peak at 520 nm. Ferrous sulfate (10.0 mmol/L), salicylic acid (10.0 mmol/L), and various concentrations of GQDs were prepared and mixed. In the control group of the experiment, the GQDs solution was replaced by HEPES buffer. After that, H_2O_2 (9.0 mmol/L) was added to the resultant solution. The $^{\bullet}$OH scavenging efficiency of GQDs was calculated from the below equation, where H_o is the absorbance at 520 nm of the control and H_S is the absorbance of the mixture of GQDs and the $^{\bullet}$OH solution.

$$^{\bullet}\text{OH scavenging efficiency} = (H_o - H_S)/H_0 \times 100\%$$

$^{\bullet}O_2^-$ scavenging activity

The scavenging of $^{\bullet}O_2^-$ was performed with a superoxide anion radical detection kit, and the principle was based on the xanthine/xanthine oxidase system. The xanthine oxidase enzyme oxidises xanthine to uric acid and $^{\bullet}O_2^-$. Then the generated $^{\bullet}O_2^-$ radical oxidizes hydroxylamine to nitrite, which has an absorption at 550 nm in the presence of a chromogenic agent. The $^{\bullet}O_2^-$ solution was mixed with various concentrations of GQDs, and in the control group, the GQDs solution was replaced by HEPES buffer. The $^{\bullet}O_2^-$ scavenging efficiency of GQDs was measured from the below equation, where S_o is the absorbance at 550 nm of the control and S_s is the absorbance of the mixture of GQDs and the $^{\bullet}O_2^-$ solution.

$$^{\bullet}O_2^- \text{ scavenging efficiency} = (S_o - S_s/S_o) \times 100\%$$

Ethics statement for animal experiment

All animals were housed in the general animal center of the institute (CSIR-Indian Institute of Chemical Biology, Kolkata). Animal experiments were carried out following the guidelines of the Institutional Animal Ethics Committee (IAEC). Experiments were designed to minimize animal suffering and to use the minimum number associated with valid statistical evaluation.

Mice model of stress-induced gastric ulcer

Balb/c mice (20–25 g) bred in-house with free access to food and water were used for all experiments. Animals were anesthetized with ketamine (12 mg/kg b.w.) followed by cervical dislocation. Control and experimental animals were allowed to fast for 6 h with free access to water before each experiment. The ulcer was induced in Balb/c male mice by stressor using forced swim stress for 4 h at 22 $\pm$ 2°C. Carbon dots at different doses (2 and 10 mg/kg b. w.) were administered orally 1 h prior to swim stress. Next, the mice were forced to swim inside a vertical cylinder (height 40 cms and diameter 20 cms) containing water up to about 20 cms height. The height of the water column is so in tune that the mice were not able to jump out of the cylinder. Following forced swim stress, animals were sacrificed after 4 h, and the stomachs of the mice were isolated for scoring the ulcer index. Gastric lesions in the fundic mucosa are scored in a blinded manner and expressed as the ulcer index as follows: 0 for no pathology; 10 for a small pinhead ulcer, and 20–50 for lesions of 2–5 mm in length according to the standard method. The sum of the total scores divided by the number of animals indicated the mean ulcer index.

Histological studies and TUNEL assay

Gastric tissues were sectioned into 2–3 mm^2 pieces. The tissue samples were fixed in 4% paraformaldehyde, dehydrated, and embedded in paraffin wax. Approximately 5 μm thick serial sections were rehydrated in descending alcohol series and stained with hematoxylin and eosin or subjected to Terminal deoxynucleotidyl transferase-mediated dUTP Nick End Labeling (TUNEL) assay by using a commercial reagent kit (Millipore). Fixation, permeabilization, and staining were carried out in exact parallel to ensure comparative significance among groups. Images were captured in Olympus microscope using Camedia software (Chicago, MI, USA) and processed using Adobe Photoshop version 7.0.

Measurement of lipid peroxidation

The cytosolic fraction from the fundic stomach homogenate was used for the measurement of lipid peroxide content as thiobarbituric acid-reactive species (TBARS). Briefly, 1 mL of the cytosolic fraction was allowed to react with 2 mL of TCA-TBA-HCl (15%TCA, 0.375%TBA and 0.25N HCl) reagent, heated

in a boiling water bath for 15 min, cooled, and centrifuged. The absorbance of the supernatant was measured for nanomoles of TBARS at 535 nm (€ = 1.5 × 10^{-5} M/cm).

Measurement of protein carbonyl content

Protein oxidation was measured as carbonyl content in the low-speed supernatant of the fundic stomach homogenate. The fundic stomachs from different groups of mice were homogenized in 50 mM sodium phosphate buffer, pH 7.4, in a Potter–Elvehjem glass homogenizer for 2 min to get 20% homogenate. After centrifugation at 600 *g* for 10 min, the proteins from 1.0 mL of the supernatant were precipitated with 10% trichloroacetic acid and allowed to react with 0.5 mL of 10 mM 2,4-dinitrophenyl hydrazine for 1 h. After precipitation with 20% trichloroacetic acid, the protein was washed thrice with a mixture of ethanol:ethyl acetate (1:1) and dissolved in 1.0 mL of a solution containing 6 M guanidine HCl in 20 mM potassium phosphate adjusted to pH 2.3 with trifluoroacetic acid followed by centrifugation. The supernatant was read for carbonyl content at 362 nm (€ = 22,000/M/cm).

Immunofluorescence

For immunofluorescence study, the gastric tissue samples were fixed in 4% paraformaldehyde solution for 48 h, dehydrated in ascending alcohol series. It was embedded in paraffin wax and sectioned at 5 μm thickness using a microtome. The tissue sections were deparaffinized with xylene followed by rehydration with descending alcohol series. Antigen retrieval was done by trypsin (0.05% trypsin, 0.1% $CaCl_2$), and blocking was performed using 5% BSA in TBS (20 mM Tris-HCl, pH 7.4 containing 150 mM NaCl) for 2 h at room temperature followed by the incubation overnight at 4°C in primary antibody solution (1:200 dilutions in TBS with 1% BSA) in a humid chamber. The tissue sections were washed four times with TBST (20 mM Tris-HCl, pH 7.4 containing 150 mM NaCl and 0.025% Triton X-100) followed by incubation with Texas red-conjugated secondary antibody (Santa Cruz Biotechnology, USA) solution (1:400 dilutions in TBS containing 1% BSA) for 2 h at room temperature. The sections were counter-stained using DAPI and images were observed in an Olympus microscope. Images at 20× and 60× magnification were captured using Camedia software (E– 20P 5.0 Megapixel) and processed under Adobe Photoshop version 7.0.

Tissue extraction

The whole stomach (including fundic, body, and pyloric parts) was washed with saline and used for extraction. The stomach except for connective tissue layer (named as gastric tissue) were suspended in 10 mM phosphate buffer saline (PBS) containing protease inhibitors, minced and incubated for 10 min at 4°C. Following centrifugation at 12,000 g for 15 min, the supernatant was collected as PBS extracts. The pellet was then extracted in lysis buffer (10 mM Tris-HCl pH 8.0, 150 mM NaCl, and 1% Triton X-100 and protease inhibitors) and centrifuged at 12,000 g for 15 min to obtain TX extracts. Both PBS and TX extracts were preserved at −80°C and used in future studies. Proteins were estimated by Lowry method.

Gelatin zymography

For the assay of MMP activities, tissue extracts (70 μg/lane) were electrophoresed in 8% SDS-polyacrylamide gel containing 1.2 mg/mL gelatin under non-reducing conditions. The gels were washed in 2.5% Triton X-100 and incubated in calcium assay buffer (40 mM Tris-HCl, pH 7.4, 0.2 M NaCl, 10 mM $CaCl_2$) for 18 h at 37°C and stained with 0.1% coomassie blue followed by destaining. The zones of gelatinolytic activity came as negative staining. Quantification of zymographic bands was performed using densitometry linked to proper software (ImageJ 1.52a).

Western blotting

PBS extract (100 μg/lane) was resolved by 10% reducing SDS-polyacrylamide gel electrophoresis and processed for Western blot. Briefly, protein was transferred to membranes, blocked in 3% BSA solution in 20 Mm Tris-HCl, pH 7.4 containing 150 Mm NaCl and 0.02% Tween 20 (TBST) and then incubated at 4°C in 1:500 dilution of the respective primary antibodies in TBST containing 0.3% BSA. The membranes were washed with TBST, incubated with HRP conjugated secondary antibody, and bands were visualized using luminol peroxide substrate solution.

Assay of Caspase-9 and Caspase-3

The activity of Caspase-9 and -3 was measured from the gastric tissue homogenates using a commercially available kit from Calbiochem and Millipore respectively, according to the manufacturer's protocol. For

both the caspase assays equal amount of gastric tissue (20 mg) was homogenized in a specific cell lysis buffer (provided with the respective kits). The homogenate was centrifuged at 16,000 × g for 15 min. The collected supernatant was quantified for protein by Bradford method and an equal amount of sample protein from different groups was used for the assays. The respective substrates for the caspases were added to the reaction mixture and incubated in the dark at 37°C for 2 h. The absorbance was taken in a spectrophotometer at 405 nm to measure the caspase activity.

Cytotoxicity study

The cytotoxicity of GQDs on human gastric epithelial cells (HGaEpC) was studied by traditional MTT assay. The cells were seeded at a density of 10^5/well plated in 96-well plates. Cells were typically grown to 60–70% confluence, rinsed in phosphate-buffered saline (PBS), and then placed into a serum-free medium for 12 h prior to treatments. After 12 h of incubation, the cells were treated with GQDs at a concentration of 5, 10, 20, 40, 60, 80, and 100 μg/mL. After 48 h, the medium was removed, and 100 μL of fresh medium was added along with 10 μL of MTT (5 mg/mL in PBS), and incubation was continued further for 4 h at 37°C. Subsequently, MTT solution was removed, and the purple crystals were solubilized in 1.0 mL of DMSO. The absorbance was recorded at a wavelength of 550 nm in the Elisa Plate Reader. The experiment was done in triplicate.

Measurement of gastric tissue ATP content

ATP was measured with an ATP determination kit [ATP Determination Kit (A22066), Molecular Probes, Inc.] following the manufacturer's instructions. Briefly, the scraped gastric mucosa from control, swim stressed, and GQD treated stressed rats were minced, homogenized in 3% sulfosalicylic acid, and subsequently centrifuged at 12000× g. The clear supernatant was used for the measurement of ATP in a luciferase-based luminometric assay. Intensity readings for the above mixtures were measured with BioTEK luminometer (at emission maximum ~560 nm).

Mitochondrial dehydrogenase assay

The mitochondrial metabolic function was estimated in terms of mitochondrial dehydrogenase activity. The principle of the assay was that mitochondrial dehydrogenases are capable of reducing MTT into purple-colored formazan dye, which upon dissolution in DMSO can be estimated spectrophotometrically at 570 nm. Briefly, isolated mitochondria were estimated by Lowry method, and subsequently equal amount of mitochondrial protein was incubated with MTT in PBS for 4 h at 37°C/5% CO_2 condition. The samples were next centrifuged, and the precipitate was dissolved in an equal amount of anhydrous DMSO. The resultant purple-color solution was measured at 570 nm in ELISA reader (BioTek Instruments, Inc., Winooski, VT, USA).

Measurement of mucosal mitochondrial trans-membrane potential ($\Delta\psi m$)

$\Delta\psi m$ was measured as in the following way. Briefly, isolated mitochondria from stomach tissues were incubated in 500 μL of 5,5′,6,6′-tetrachloro-1,1′,3,3′-tetraethyl benzimidazolyl carbocyanine iodide (JC-1) assay buffer containing 300 nM of JC-1 in the darkness for 15 min. Fluorescence was measured in an F-7000 Fluorescence Spectrophotometer (Hitachi High-Technologies Corporation) (excitation, 490 nm; emission, 530 nm for JC-1 monomer, and 590 nm for JC-1 aggregates).

Myeloperoxidase assay

Myeloperoxidase (MPO) activity in the mice gastric tissues was measured by a calorimetric assay using guaiacol as the substrate. Briefly, gastric tissue homogenate prepared in 5 mM phosphate buffer was added in 1 mL of reaction buffer containing 0.5 mM H_2O_2 and 0.4 M guaiacol in 50 mM phosphate buffer, pH 7.4. The changes in the optical density per minute for tetraguaiacol were measured at 470 nm in a Shimadzu spectrophotometer. The results were expressed in units/gram gastric tissue (ε = 26.6/mM/cm).

QUANTIFICATION AND STATISTICAL ANALYSIS

Experiments were repeated at least three times independently. The statistical analysis of the data was done using Graph Pad PRISM 5 (version 5.04) software. Comparison between groups was performed using one-way analysis of variance (ANOVA) followed by Student–Newman–Keuls T-test. Data were fitted using Graph Pad PRISM 5 (version 5.04) software represented as means ± SEM. $p < 0.05$ was accepted as level of significance; *** very highly significant $p < 0.001$, ** highly significant $p < 0.01$; * significant $p < 0.05$; NS not significant for $p > 0.05$.

An Insight into Targeted Therapy for Ovarian Cancer

Abhishek Chatterjee, Vineet Kumar Mishra, Susmita Saha, and Snehasikta Swarnakar

Contents

Abstract

Ovarian cancer (OC) is one of the most fatal gynecological malignancies in the world. Poor diagnosis and a lack of prognostic biomarkers have contributed greatly to the high mortality rate of OC. The standard treatment for OC is surgery followed by chemotherapy by a single drug or in combination with one or more drugs. Although this treatment procedure works in most early-stage patients, most women with advanced disease may experience multiple episodes of recurrent disease with gradual shorter disease-free intervals. Another major disadvantage of

Abhishek Chatterjee and Vineet Kumar Mishra contributed equally as first authors.

A. Chatterjee · V. K. Mishra · S. Saha · S. Swarnakar (✉)
Infectious Diseases and Immunology Division, CSIR-Indian Institute of Chemical Biology, Kolkata, West Bengal, India
e-mail: sikta@iicb.res.in

S. Chakraborti (ed.), *Handbook of Oxidative Stress in Cancer: Therapeutic Aspects*,
https://doi.org/10.1007/978-981-16-1247-3_230-1

standard chemotherapy is that the patients often suffer from a plethora of side effects. OC is well known as a highly heterogeneous disease at the molecular level. Therefore, molecular targeted therapy has emerged as a more effective option. At present, FDA-approved PARP inhibitors and anti-VEGF monoclonal antibodies are the most widely used targeted drugs against OC. Other promising therapeutic targets, such as immune checkpoints, folate receptor, p53, PI3K/AKT pathway, and miRNA, are going through phase II and phase III clinical trials at present. Targeted therapies were expected to deliver better outcomes with minimum toxicity. However, just like conventional chemotherapies, targeted therapies also come with their own set of limitations and newly developed resistance mechanisms in OC patients. This chapter highlights studies conducted on the most important pathways for targeted therapies associated with OC in recent times and the major loopholes and the risks associated with each one of them.

Keywords

Ovarian cancer · Targeted therapy · Immunotherapy · miRNA · PARP inhibitors · Combination therapy

Introduction

Ovarian cancer (OC) is the third most common cancer affecting women following breast and cervical cancer with 313,959 new cases in 2020 alone (Sung et al. 2021). The WHO categorizes epithelial ovarian cancer (EOC) into a number of categories based on cell morphology, namely serous carcinomas (SC), mucinous carcinomas (MC), endometrioid carcinomas (EC), and clear-cell carcinomas (CCC) (Kossai et al. 2018). SC is further categorized into high-grade serous carcinoma (HGSC) and low-grade serous carcinoma (LGSC). HGSCs comprise 70–80% of all types and subtypes of OC (Stewart et al. 2019). In many cases, diagnosis of OC is tricky until stage III or IV, making the treatment even harder. It is found that the survival rate of OC patients after 5 years is around 47% (Chien and Poole 2017). The standard treatment for OC is surgery followed mostly by chemotherapy by a single drug or in combination with one or more drugs (combination chemotherapy). Platinum drugs and taxane drugs are widely used chemotherapeutic agents for the treatment of OC, but, in most cases, patients relapse and develop chemotherapy resistance (Chandra et al. 2019). One of the major disadvantages of chemotherapy is that the drugs used cannot distinguish malignant cells from nonmalignant ones. Hence, the patient often suffers from the side effect of the treatment (Lorusso et al. 2017). In recent times, the targeted therapy has acquired significant popularity. It focuses on specific signaling pathways, which lead nonmalignant tissues towards tumor progression without causing adverse effects on surrounding tissues (Previs et al. 2019). Poly (ADP-ribose) polymerase (PARP) inhibitors are one of the biggest successes of targeted therapy. Olaparib (AstraZeneca), rucaparib (Clovis Oncology), and niraparib (Tesaro Inc.) are approved by the FDA for the treatment of platinum drug-resistant OC cases (Rose et al. 2020).

The targeted therapy has also its loopholes along with the promises it shows. If a single targeted therapy inhibitor (TTi) is unable to cure cancer with a specific genetic mutation, then a combination of TTi with other drugs/anticancer agents becomes a necessity. The possible combinations with TTi can be chemotherapeutic drugs, other TTi of the different pathways of the same cancer, radiotherapy, etc. (Keefe and Bateman 2019). However, these combinations may also carry the side effects and/or the toxicity of chemotherapy and radiotherapy. PARP inhibitors in combination with chemotherapy have shown promising results in OC patients but also along with the overlapping toxicity (Xie et al. 2020). One of the widely accepted mechanisms of developing PARP inhibitor resistance is the development of secondary BRCA mutations in the patients previously treated with chemotherapy or combination chemotherapy (Bitler et al. 2017).

Although targeted therapy side effects are less likely than chemotherapy alone, they are associated with certain toxicity and resistance towards TTi. The focus of this book chapter is to provide an overview of studies conducted on targeted therapies associated with OC in recent times and the major loopholes and the risks associated with each one of them.

Targeted Therapies

Homologous Recombination and PARP Inhibitors in OC Therapeutics

Homologous recombination (HR) comprises a network of interrelated pathways to repair double-strand DNA breaks (DSDB) caused by ionizing radiation or topoisomerase inhibitors or other physiological abnormalities. Both BRCA1 and BRCA2 proteins are involved in HR of which BRCA2 has a crucial role in repair mechanism involving Rad51 recombinase. The HR pathway along with poly [adenosine diphosphate-ribose] polymerases (PARP) plays crucial roles in repairing the DSDB in the replication fork. PARP1 in particular is vital for locating the single-strand breaks (SSB) and its repair by base excision repair mechanism.

The discovery of PARP inhibitors (PARPi) has opened therapeutic avenues for the treatment of OC. Few PARPi, such as olaparib (Lynparza), rucaparib (Rubraca), and niraparib (Zejula), have been approved by the FDA (USA) for the treatment of OC. Veliparib, IDX-1197, pamiparib (BGB-290), fluzoparib, and talazoparib are currently under phase II and III trials. Several clinical trials have indicated that PARPi in combination with other drugs may deliver a better outcome in cancer treatment. For instance, in the recent VELIA trial, 1000 women with early diagnosis of OC were treated with veliparib along with chemotherapy. The trial concluded that veliparib extended the median progression-free survival rate by 7 months (Rose et al. 2020). In the PRIMA clinical trial, niraparib along with chemotherapy was used to treat patients. An increase in the survival rate in the population was observed by 10 months.

PARPi (olaparib and niraparib) have been successful in the maintenance treatment of ovarian cancers, which has appeared as a strategy to extend the duration

between treatment and cancer relapse (McMullen et al. 2020). However, along with the platinum drug resistance in patients, PARPi resistance has also been reported in some cases. It is noteworthy that the patients on PARPi therapy more often than not maintain sensitivity to the chemotherapy drugs. Therefore, the resistance mechanisms of both PARPi and platinum drugs are complex and interrelated (McMullen et al. 2020). This issue is currently being addressed in a phase III trial named OReO (NCT03106987). Restoration of the HR mechanism is a key aspect of acquired PARPi and platinum resistance. Reactivation of HR can be achieved by additional mutations called BRCA reversion mutations leading to the restoration of the open reading frame of the BRCA gene. BRCA reversion mutations are reported in both biopsy samples and cell-free DNA samples of OC patients having PARPi resistance (Lin et al. 2019). Another mechanism of acquired PARPi resistance is the stabilization of the replication fork that delays the cell cycle progression (Lee et al. 2018). Reduced cellular availability of drugs is another mechanism of acquired resistance to PARPi and platinum drugs used for OC treatment. The copper transporters CTR1, CTR2, and ATP7A regulate the intracellular concentration of platinum by their efflux mechanism (Li et al. 2017). Moreover, overexpression of the ABCB1 gene encoding multidrug resistance protein 1 (MDR1) is reported to play a role in PARPi resistance. Upregulation of MDR1 protein has been shown in an engineered PARPi-resistant human ovarian cancer cell line (Vaidyanathan et al. 2016). Most PARPi are MDR1 substrates, which indicate that prior chemotherapy can precondition the tumors for PARPi resistance. A better understanding of the mechanism of action of each PARPi in context to the stage and progression of cancer as well as appropriate selection of patients may help to tackle these challenges.

VEGF/VEGFR-Mediated Angiogenesis

Cancer cells are known to secrete various pro-angiogenic factors like platelet-derived growth factor (PDGF), vascular endothelial growth factor (VEGF), fibroblast growth factor (FRF), and placental growth factor (PlGF). Among these growth factors, VEGF has been identified as the most potent mitogen, which not only promotes angiogenesis but can also stimulate epithelial cells to proliferate and migrate (Kabbinavar et al. 2005). VEGF-A is a major regulator of angiogenesis among the VEGF family of growth factors under both normal and disease conditions (Fig. 1). Upon binding to VEGFR-2, it leads to angiogenesis and also initiates tumorigenesis by promoting epithelial-mesenchymal transition (EMT) as well as cancer stemness (Fantozzi et al. 2014). Furthermore, VEGF and VEGFRs have been reported to be overexpressed in OC tissues, thereby making this pathway an exciting therapeutic target.

Bevacizumab (Avastin®, Genentech), a humanized anti-VEGF monoclonal antibody, became the first active targeted therapy to be approved by the FDA for treating platinum-resistant OC (Monk et al. 2016). It is the most well-studied antiangiogenic agent across different types of cancer and especially in OC. Bevacizumab was reported to be active at a dosage of 15 mg/kg (IV) for every 3 weeks, in patients

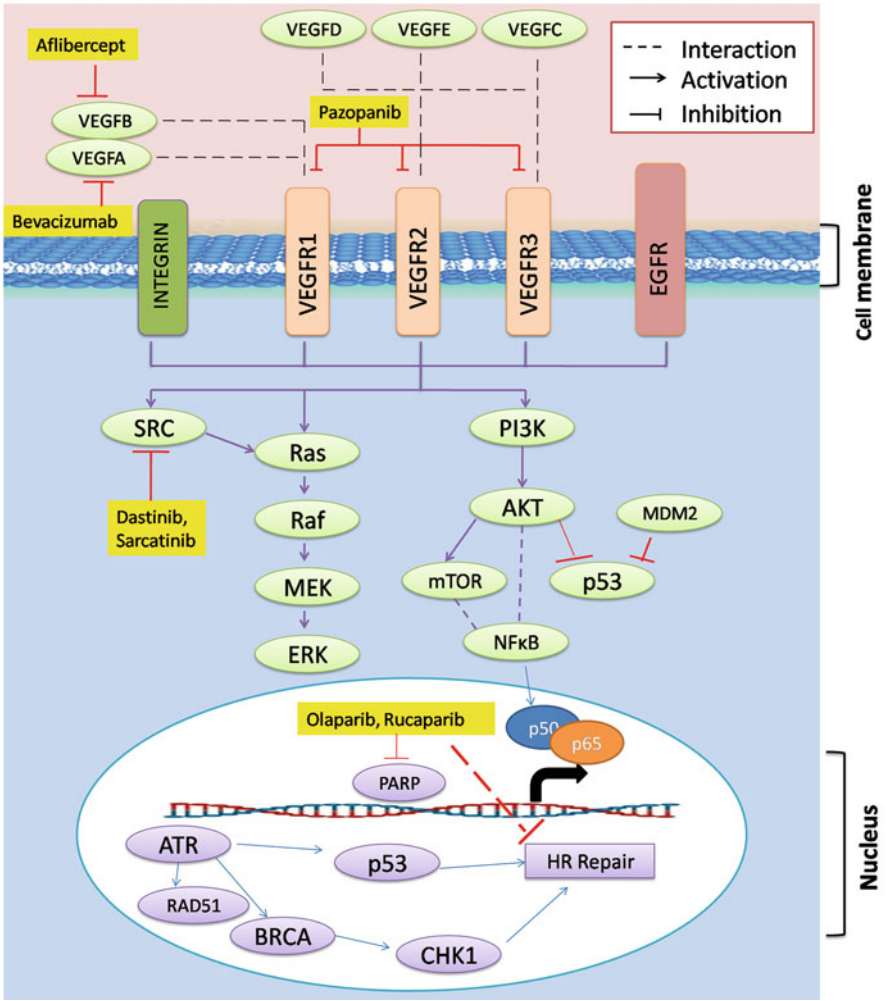

Fig. 1 Overview of the various ligands, receptors, their interactions, signaling pathways, and their respective inhibitors involved in the development of ovarian cancer

with advanced refractory epithelial OC (Monk et al. 2005). Following this discovery, four randomized phase III trials had been carried out, namely the GOG protocol 218 (Burger et al. 2011), ICON7 (Perren et al. 2011), AURELIA Trial (Pujade-Lauraine et al. 2012), and OCEANS Trial (Aghajanian et al. 2012). From the data obtained by these trials, it can be concluded that bevacizumab posed a great benefit to patients with ovarian carcinoma (Table 1). Vascular disrupting agents (VDAs) have surfaced as a better alternative to VEGF/VEGFR-targeting therapies. They target existing tumor-associated vasculatures, instead of preventing neovascularization. Interestingly, these VDAs are relatively harmless to non-

Table 1 Summarized data of the phase III trials of bevacizumab in ovarian cancer

Clinical trial	Disease setting	No. of subjects enrolled	Treatment regimen	PFS (median, months)	OS (median, months)
GOG-218 (Burger et al. 2011)	Frontline and maintenance	1873	**I**: Paclitaxel + carboplatin + placebo; placebo maintenance	10.3	39.3
			II: Paclitaxel + carboplatin + bevacizumab; placebo maintenance	11.2	38.7
			III: Paclitaxel + carboplatin + bevacizumab; bevacizumab maintenance	14.1	39.7
ICON7 (Perren et al. 2011)	Frontline and maintenance	1528	**I**: Paclitaxel + carboplatin	17.5	58.6
			II: Paclitaxel + carboplatin + bevacizumab; bevacizumab maintenance	19.98	58.0
AURELIA Trial (Pujade-Lauraine et al. 2012)	Recurrent, platinum-resistant OC	361	**I**: Chemotherapy (paclitaxel weekly, topotecan daily 5× or weekly, PLD)	3.4	13.3
			II: Chemotherapy + bevacizumab	6.7	16.6
OCEANS Trial (Aghajanian et al. 2012)	Recurrent, platinum-sensitive OC	484	**I**: Gemcitabine + carboplatin + placebo (combination and maintenance)	8.4	35.2
			II: Gemcitabine + carboplatin + bevacizumab (combination and maintenance)	12.4	33.3

Abbreviations: *PFS* progression-free survival, *PLD* pegylated liposomal doxorubicin, *OS* overall survival

tumor-associated blood vessels, due to their increased endothelial pericyte coverage (Monk et al. 2016). One such VDA is fosbretabulin, otherwise known as combretastatin A4 mono-triphosphate. Several other compounds targeting tyrosine kinase receptors (mostly VEGFR and PDGFR) have shown promise in early-phase clinical trials. Among them, nintedanib, pazopanib, and cediranib have even completed phase III clinical trials (Mahner et al. 2015).

Overall, targeting VEGF-mediated angiogenesis in ovarian cancer therapy has been quite fruitful. This is mostly because VEGF is a circulating molecule and the drug targeting it need not penetrate the tumor to elicit its activity. However, even after so many years of constant effort by researchers around the world, bevacizumab remains the only FDA-approved antiangiogenic therapy to cure OC. But the use of bevacizumab is most often accompanied by certain life-threatening adverse effects, like gastrointestinal (GI) perforation, hemorrhage, GI fistulae, hypertension, and posterior reversible encephalopathy syndrome (Hayman et al. 2012). Due to such potentially fatal adverse effects, the use of bevacizumab is being discontinued by many patients. A better alternative approach for targeting tumor vasculature remains the need of the hour.

PI3K/AKT/mTOR Pathway

The phosphatidyl-inositol-3-kinase (PI3K)/protein kinase-B (PKB or AKT)/mechanistic target of rapamycin kinase (mTOR) pathway is known to regulate essential cellular processes like cell growth, survival, proliferation, metabolism, and angiogenesis. Alterations within this pathway are common in most types of cancer, including ovarian cancer (Mabuchi et al. 2015). The canonical mechanism of activation of this signaling pathway has been briefly elucidated in Fig. 1.

The inhibitors targeting PI3K and AKT are primarily small molecules undergoing clinical trials. In a phase II study involving temsirolimus, a mTOR inhibitor, 24.1% of the 54 enrolled patients had a progression-free survival (PFS) of $\geq$6 months with only 9.3% experiencing a partial response, after receiving 25 mg IV temsirolimus weekly (Behbakht et al. 2011). Pilaralisib, a selective pan-class I PI3K inhibitor, has completed phase I studies, showing that it was well tolerated (Sarker et al. 2015). In another phase I trial, pilaralisib also had a favorable safety profile but did not show any enhanced antitumor activity when used in combination with paclitaxel and carboplatin (Wheler et al. 2017). The combination of docetaxel and an AKT inhibitor perifosine was administered in platinum-resistant ovarian cancer patients. But the PFS and overall survival (OS) of patients being low hinted towards its limited activity (Fu et al. 2012). Another combination of AKT inhibitor, GSK2110183, along with carboplatin and paclitaxel has been evaluated in a phase I/II study (Blagden et al. 2019). The overall response rate to GSK2110183 was 32%, and the median PFS of GSK2110183- and paclitaxel-treated patients was 7.1 months.

The use of PI3K/AKT/mTOR pathway inhibitors in the treatment of ovarian cancer patients seems to be a promising regimen. Since this pathway is highly complex with many feedback loops and cross-talk mechanisms with other pathways,

most of its inhibitors will achieve optimal efficacy only when they are used in combination. But, even then, most such candidate drugs fail to achieve desired patient survival rates. Those that do bring with them a plethora of hazards to the patient's quality of life, like severe nausea, vomiting, diarrhea, fatigue, neutropenia, and alopecia.

Cyclin-Dependent Kinases (CDKs)

The importance of cell cycle dysregulation in the development as well as the progression of cancer including OC is well recognized. Given that cancer usually involves dysregulation of the cell cycle, cyclins and CDKs have been the obvious targets in several types of cancers using CDK inhibitors (CKIs) (Zhou 2017). Current studies have shown that CDKs are repeatedly overexpressed in many cancer types including OC, which ultimately results in uncontrolled cell proliferation and chemoresistance (Wang et al. 2019). Hence, CDKs have turned into potential targets for anti-OC therapy. Recently, CDK-2, -4, -9, -11, and -16 have been shown to play crucial roles in OC development (Gao et al. 2017).

CDK9 was found to be highly upregulated in human OC cell lines as well as in metastatic tumor tissue. Additionally, an increase in CDK9 levels significantly correlated with the poor patient prognosis (Wang et al. 2019). CDKi-83 has been reported to inhibit CDK9 activity in nM range. Additionally, it has been reported to induce cell cycle arrest at the G2/M phase in A2780 OC cells (Liu et al. 2012). Etemadmoghadam et al. (2013) demonstrated that upregulation of CDK2 could elicit reduced sensitivity to CDK2 inhibitors when tested against OC cell lines SKOV-3, OVCAR-4, and OVCAR-3. CDK11 is known to be associated with malignant metastatic tumors in OC patients. Liu et al. (2016) demonstrated that RNAi-mediated CDK11 silencing induced apoptosis in OC cells. This also improves the cytotoxicity of paclitaxel to inhibit cell growth in OC cell lines. Furthermore, in an OC xenograft model, it was shown that systemic in vivo administration of CDK11 siRNA considerably reduced tumor growth (Liu et al. 2016).

The challenges of developing a highly selective CDKi against OC will be its specificity against targeted CDK, assessing the need to combine CDKi with other drugs and minimal toxicity. Palbociclib (PD0332991) was the first CDKi approved by FDA for ER-positive breast cancer patients in 2015 (McCain 2015). Few studies claimed that palbociclib could also prove to be effective in patients with OC (Taylor-Harding et al. 2015). Palbociclib was tested against 40 OC cell lines, and it displayed antiproliferative effects on all tested cell lines (Zhou 2017). Currently, the drug has completed phase II trials successfully as per Clinicaltrials.gov, a database of privately and publicly funded clinical trials. It remains to be seen as to how effective palbociclib is in dealing with the treatment of OC and drug resistance.

MAPK Pathway

The mitogen-activated protein kinase (MAPK) family of signaling proteins can be grouped into three subfamilies in mammals (Fig. 1). These are the extracellular signal-regulated kinases (ERKs), Jun N (amino)-terminal kinases (JNKs), and stress-activated protein kinases (SAPKs) or p38 subfamilies. Among these, the RAS/RAF/MAP kinase-ERK kinase (MEK)/ERK pathway is crucial for human cancer cell survival, proliferation, dissemination, and differentiation. Dysregulation of the MAPK/ERK pathway is a major triggering event in the development of most carcinomas, including OC (García-Gómez et al. 2018). The low-grade serous OC is characterized by mutations in various members of the MAPK/ERK cascade, often leading to its constitutive activation (Diaz-Padilla et al. 2012). This type of OC has mutations in either *KRAS* (27–36%) or *BRAF* (33–50%) (Singer et al. 2003). Mucinous carcinoma, another type I OC, is reported to have KRAS mutations in most cases (Singer et al. 2003). RAF-1 or CRAF is frequently dysregulated in OC, via either mutation or overexpression. Its dysregulation is associated with poor prognosis and reduced survival in OC patients (McPhillips et al. 2001). RAF-1 inhibition using siRNA is reported to reduce cellular proliferation and inhibits tumor cell growth in vitro and in vivo (Leng and Mixson 2005).

Inhibition of MEK1/2, a component of the MAPK/ERK pathway, by selumetinib has been evaluated in patients with recurrent low-grade serous ovarian carcinoma (Farley et al. 2013). This phase II clinical trial reported a 15% objective response rate, whereas 65% of the patients did not show any significant response (NCT00551070). Another recently completed clinical trial, the MILO study, demonstrated that treatment with binimetinib in recurrent or persistent LGSC patients yielded better results than conventional chemotherapy in terms of median overall survival (25.3 vs. 20.8 months), overall response rate (16% vs. 13%), and median duration of response (8.1 months vs. 6.7 months) (NCT01849874) (Monk et al. 2020). The authors of this study have also reported that KRAS mutation may be able to predict a patient's response to binimetinib (Monk et al. 2020).

There are also quite a few ongoing clinical trials that are investigating the effects of different MEK inhibitors in patients with OC. One such trial is investigating the combination of MEK162 with paclitaxel (NCT01649336). Another study, which has just started recruiting patients, is going to investigate the effects of olaparib and selumetinib in patients with KRAS mutations including those who have failed PARP inhibitors (NCT03162627).

SRC Family Kinases

SRC family of tyrosine kinases have long been recognized for playing a key role in initiating and regulating intracellular signaling pathways. SRC is a proto-oncogene, and its dysregulation can cause cell proliferation and invasion. In the case of OC, this pathway is reported to be frequently dysregulated (Han et al. 2006). SRC can be a target for OC therapy as miR-485-5p achieved inhibition of OC progression both

in vitro and in vivo by targeting SRC inhibition. SRC kinase activation can lead to chemoresistance and decreased survival rate of patients, whereas its inhibition has been shown to reverse the chemotherapy resistance (Wang and Fu 2016). SRC family tyrosine kinase inhibitors dasatinib and saracatinib in combination with paclitaxel and carboplatin were tested in phase I and phase II trials with recurrent OC patients. The response rate of dasatinib in phase I was 40%. However, both these drugs failed to give any positive responses in phase II trials (Wang and Fu 2016). Interestingly, SRC and MEK inhibitors saracatinib and selumetinib, respectively, displayed target kinase inhibition and combined induction of apoptosis as well as cell cycle arrest of established cell lines and primary OC cultures. Furthermore, saracatinib and selumetinib inhibited tumors in xenografts.

To date, no specific drug has been approved by the FDA that targets SRC kinase in OC treatment. However, dasatinib in combination with paclitaxel and carboplatin is undergoing phase I clinical trial for their toxicity and maximal tolerated dose (MTD) in advanced or recurrent OC patients.

Folate Receptor Alpha

The folate receptor-α (FR-α), a glycosylphosphatidylinositol (GPI)-anchored cell surface protein, is overexpressed in more than 90% of epithelial ovarian cancer cells, particularly in platinum-resistant patients, thereby making it an outstanding target for developing targeted therapies. In this regard, two major targeting approaches have been pursued.

The first approach exploits the naturally high affinity of FRs for binding with folate and its analogs. This provides a highly specific targeting mechanism via which different toxic compounds like chemotherapeutics or other cytotoxic drugs can be delivered to FR-positive ovarian cancer cells, by simply conjugating them with folate or one of its analogs. Such targeting allows these drugs to exhibit activity at a much lower dosage than their maximum tolerated dose (MTD) while reducing their harmful effects on neighboring normal cells. A novel folate conjugate with desacetylvinblastine, termed vintafolide, is undergoing clinical trials. The MTD for vintafolide was established to be 2.5 mg/kg body weight, and the most common adverse effects were constipation, nausea, vomiting, and fatigue (Lorusso et al. 2012). In a preclinical study, the antitumor effects of vintafolide in combination with some standard anticancer drugs, like pegylated liposomal doxorubicin (PLD), were found to be better than the single chemotherapeutic agent or vintafolide alone. Based on the previous preclinical study, a clinical trial, PRECEDENT, in platinum-resistant OC patients concluded that patients with 10–90% FR-positive cancer, upon treatment with vintafolide and PLD combination therapy, demonstrated an improvement over standard chemotherapy alone (Naumann et al. 2013). But patients without FR-α-positive tumor did not receive any benefit at all. Regrettably, the subsequent phase III trial (PROCEED) was terminated early, since an interim analysis showed that patients did not receive any significant benefit (NCT01170650). Another phase II clinical trial of vintafolide has recently been completed in patients with

FR-positive non-small cell lung cancer (NCT01577654). Preclinical and clinical evaluation of other folate–drug conjugates is also ongoing.

The second approach utilizes FRα-binding monoclonal antibodies to deliver anticancer activity. Farletuzumab (MORAb-003), one such humanized monoclonal antibody against FRα, is currently undergoing clinical trials. In a phase II clinical trial on patients with platinum-resistant OC, the efficacy of farletuzumab alone or in combination with carboplatin or paclitaxel was evaluated. Patients receiving the combination therapy showed a partial or complete overall response rate of 75% (Armstrong et al. 2013). In a subsequent phase III trial, two different doses of farletuzumab were evaluated for efficacy, but neither of them showed any significant difference in PFS from the placebo group (Morris et al. 2014).

The increased potency of the most recently developed FRα-directed therapy, farletuzumab, has provided hope of improvement in the clinical outcome for patients with OC. However, in a recent phase II clinical trial (NCT02289950), it has been shown that the use of farletuzumab is often associated with various treatment-emergent adverse effects, like nausea, anemia, fatigue, constipation, neutropenia, anemia, and thrombocytopenia. Five percent of the patients treated with farletuzumab developed interstitial lung disease, which is a potentially life-threatening side effect (Herzog et al. 2021). For this reason, farletuzumab (MORAb-003) will most likely not have any future in the treatment of OC, and research into an alternative has already gained pace.

p53 Pathway

p53 is one of the most studied genes involved in cancer. Several stimuli including UV-induced DNA damage, ROS, hypoxia, and mitogenic signaling have been reported to activate p53, which in turn induces cell cycle arrest and/or apoptosis depending upon the signaling cascade. Mutation in p53 is the most common alteration observed in most cases of high-grade serous ovarian cancer (HGSOC), squamous cell carcinoma, and triple-negative breast cancer (Duffy et al. 2017). However, p53 being a transcriptional factor has made it an unpopular target in the past, and few compounds have been reported only in recent times that target mutant p53. APR-246 (PRIMA-1MET) is the best-studied compound reported to reactive mutant p53 to wild-type p53. It is a methylated analog of PRIMA-1, a quinuclidine best known for restoring the wild-type function of mutant p53. Several studies in various animal models demonstrated that restoration of wild-type p53 from mutant p53 protein suppressed tumor growth depending upon the stage of cancer (Duffy et al. 2017). A clinical trial PiSARRO (NCT02098343) in patients with HGOC was carried out to evaluate the effectiveness of APR-246, PLD, and carboplatin combination chemotherapy in platinum-sensitive HGSOC patients. The trial demonstrated that APR-246 at a dose of 67.5 mg/kg along with carboplatin and PLD was approved as the recommended phase II dose (RP2D).

p53 is well known to regulate the G1 cell cycle checkpoint, while with mutant p53, the cell will be dependent upon the G2/M checkpoint. Wee-1 kinase causes

DNA damage-induced G2/M cell cycle arrest by phosphorylating and inhibiting CDK1. MK-1775 is a potent wee-1 inhibitor that has demonstrated improved anticancer activity in cancer cells with mutant p53. A randomized phase II study in patients with p53 mutant OC concluded that there was no significant difference between the MK-1775-treated and placebo groups, in terms of anticancer activity (NCT01357161). Additionally, a peptide ReACp53 was reported to inhibit the aggregation of mutant p53 and rescue its wild-type functions (Soragni et al. 2016). In vivo experiments using peptide ReACp53 in mice having OC demonstrated reduced proliferation (Duffy et al. 2017).

Despite promises shown by mutant p53 inhibitors, several issues such as their efficacy at every stage of cancer and long-term treatment side effects need to be addressed before practically using these compounds either alone or in combination for OC treatment. Moreover, the stability of p53 peptide inhibitors has remained a major question to be addressed before considering them for potential cancer treatment.

Immunotherapy

In the last few years, immunotherapy has undergone prolific growth due to encouraging results in the treatment of various types of cancer. Immunotherapy mainly focuses on priming our body's immune system to fight against cancerous cells. This effect can be brought about by various approaches, resulting in the emergence of different types of immunotherapy. The different types of anticancer immunotherapies include cancer vaccines (like Provenge and Vigil), immunomodulation (via checkpoint inhibitors and regulatory cytokines), targeted monoclonal antibodies (like bevacizumab and farletuzumab), and adoptive cell transfer therapy (like CAR-T therapy).

Recently, more attention is being directed towards newer strategies with a keen focus on combination therapy. Various types of immunotherapy are being combined with different chemotherapeutics, antiangiogenic agents, PARP inhibitors, other immunotherapy agents, and many more. Some noteworthy clinical trials on different immunotherapy agents as monotherapy or combination therapy have been briefed in Table 2.

The development of immunotherapy came as a boon to many patients suffering from certain kinds of solid tumorlike melanoma and renal cancer. However, the majority of patients with ovarian cancer did not benefit as much from immunotherapy, and a lot of issues remain to be addressed. The disease phase at which the administration of immunotherapy would be optimal is still not clear. Since ovarian cancer is a disease with high genetic instability, not all OC patients respond similarly to immunotherapy. For these reasons, the administration of immunotherapy in OC is mostly performed during clinical trials. But we can expect that the ongoing phase II and III clinical trials will be able to answer these questions, leading to great progress in OC treatment.

Table 2 Ongoing clinical trials evaluating the efficacy of different immunotherapeutics in ovarian cancer

Clinical trial	Phase of study	Immunotherapy used	Mechanism of action	Disease setting	Treatment regimen	Primary endpoint/ outcome	Status
Adoptive cell therapies and vaccines							
NCT03814447	Early phase I	Anti-mesothelin CAR-T cells	Specifically targets mesothelin expressing OC cells	Refractory-relapsed OC	Cyclophosphamide + fludarabine + anti-MESO CAR-T cells	AEs and SAEs	Recruiting
NCT02737787	Phase I; non-randomized	WT1 and NY-ESO-1 vaccines	WT1 protein is an oncogenic protein involved in tumor escape from immune surveillance NY-ESO-1 protein is associated with high-grade tumors	Recurrent OC	**I**: WT1 vaccine + nivolumab **II:** ESO-1 vaccine + nivolumab	DLT	Active
ORION-01 NCT03100006	Phase Ib/IIa	Oregovomab vaccine	Oregovomab targets the tumor-associated CA 125 antigen, which is known to promote cancer cell proliferation	Recurrent epithelial OC	Nivolumab + oregovomab	AEs, SAEs, ORR, and PFS	Terminated (interim analysis showed poor efficacy)
Immune checkpoint inhibitors							
JAVELIN Ovarian 200 NCT02580058 (Pujade-Lauraine et al. 2021)	Phase III; randomized	Avelumab	Avelumab binds to PD-L1 and prevents inhibition of immune reaction by blocking any interactions between PD-1 and PD-L1	Platinum-resistant/ refractory OC	**I**: Avelumab alone **II**: Avelumab + PLD **III**: PLD alone	**I**: PFS = 1.9; OS = 11.8 **II**: PFS = 3.7; OS = 15.7 **III**: PFS = 3.5; OS = 13.1	Active
ATALANTE NCT02891824	Phase III; randomized	Atezolizumab	Atezolizumab is an immune checkpoint inhibitor that binds with PD-L1 to stop its interaction with PD-1.	Platinum-sensitive relapsed OC	**I**: Placebo + bevacizumab + Avastin + carboplatin + gemcitabine/PLD	PFS	Active

(continued)

Table 2 (continued)

Clinical trial	Phase of study	Immunotherapy used	Mechanism of action	Disease setting	Treatment regimen	Primary endpoint/ outcome	Status
			However, it allows interaction between PD-1 and PD-L2		**II**: Atezolizumab + bevacizumab + Avastin + carboplatin + gemcitabine/PLD		
NCT03353831	Phase III; randomized	Atezolizumab		Platinum-resistant recurrent OC	**I**: Placebo + bevacizumab + paclitaxel/PLD **II**: Atezolizumab + bevacizumab + paclitaxel/PLD	PFS and OS	Recruiting
NCT02484404 (Zimmer et al. 2019)	Phase I/II; non-randomized	Durvalumab	Durvalumab blocks the interactions between PD-1 and PD-L1	Platinum-resistant recurrent OC	**I**: Durvalumab + cediranib **II**: Durvalumab + olaparib **III**: Durvalumab + olaparib + cediranib	**Phase I**: Recommended phase II dose (RP2D) for cediranib = 20 mg **Phase II**: ORR	Recruiting for phase II
ATHENA NCT03522246	Phase III; randomized	Nivolumab	Nivolumab binds to the PD-1 receptor and prevents its interaction with PD-L1 and PD-L2	Newly diagnosed stage III/IV OC	**I**: Rucaparib (oral) + nivolumab (IV) **II**: Rucaparib (oral) + placebo (IV) **III**: Placebo (oral) + nivolumab (IV) **IV**: Placebo (oral) + placebo (IV)	PFS	Active

NCT02571725	Phase I/II	Tremelimumab	Tremelimumab binds to CTLA-4 and blocks the inhibitory signal mediated by interaction of CTLA-4 and B7-1/B7-2. Thereby, it maintains T-cell activation in tumor microenvironment	BRCA -1/-2 mutant recurrent OC	Olaparib + tremelimumab	**Phase I**: RP2D **Phase II**: ORR	Active
KEYLYNK-001 NCT03740165	Phase III; randomized	Pembrolizumab	Pembrolizumab binds to the PD-1 receptor, thereby preventing the activation of PD-L1 and PD-L2	BRCA non-mutated advanced epithelial OC	**I**: Pembrolizumab + olaparib **II**: Pembrolizumab + placebo **III**: Placebo + placebo	PFS	Active
NCT02498600	Phase II; randomized	Ipilimumab	Ipilimumab binds to CTLA-4 and rescues immune system from downregulation	Persistent or recurrent epithelial OC	**I**: Nivolumab **II**: Nivolumab + ipilimumab	Objective tumor response	Active
FIRST NCT03602859	Phase III; randomized	Dostarlimab	Dostarlimab inhibits any interactions between PD-1 and PD-L1	Stage III/IV non-mucinous epithelial OC	**I**: Carboplatin + paclitaxel + bevacizumab + placebo **II**: Carboplatin + paclitaxel + bevacizumab + niraparib **III**: Carboplatin + paclitaxel + bevacizumab + dostarlimab	PFS	Active

Abbreviations: *AEs* adverse events, *DLT* dose-limiting toxicity, *OC* ovarian cancer, *ORR* overall response rate, *OS* overall survival, *PFS* progression-free survival, *PLD* pegylated liposomal doxorubicin, *SAEs* serious adverse events

MicroRNA-Based Therapeutics

MicroRNAs (miRNAs) are small, noncoding, single-stranded RNAs, of around 19–25 nucleotides, cleaved from hairpin pre-miRNA precursors. In recent years, altered expression of miRNAs was identified in several studies on the invasion and metastasis of OC. The progression of EMT is also established to be strongly related to tumor progression and metastasis. A number of miRNAs associated with OC have been reported to modulate EMT by regulating the expression of transcription factors such as the SNAIL family, TWIST family, and ZEB family. Several miRNAs, such as miR-16, miR-34a, miR-137, miR-340, and miR-506, have similar roles in EMT (Ghafouri-Farda et al. 2020).

One of the important aspects of studying miRNA associated with OC is to provide solutions for chemotherapy resistance, which affects both the prognosis and treatment of the disease. miR-214 and miR-21 are associated with chemoresistance in OC. miR-214 induces cisplatin resistance and cell survival by binding to the 3′-untranslated region (UTR) of PTEN, thereby causing its down-regulation and induction of the AKT pathway. PTEN is a well-known tumor-suppressor gene that regulates the cell cycle, and mutations in this gene cause development of many types of cancer. Inhibition of AKT pathway using specific AKT inhibitors such as API-2/triciribine can prevent miR-214-induced cell survival. This suggests that miR-214 plays an important role in OC and can be used as a possible target to overcome chemoprevention (Yang et al. 2008). miR-552 also regulates PTEN expression through interaction with its 3′-UTR and promotes OC proliferation and metastasis (Zhao et al. 2019). miRNA-regulated pathways can be relevant targets for a new therapeutic opportunity in OC patients. Recently, newly identified miRNAs let-7109 and ATP11B biomarkers were found to be associated with platinum drug resistance cases (Chandra et al. 2019). miRNAs can alter the expression of a number of pathways related to OC, including PI3K/AKT/mTOR, Wnt/β-catenin, FOXP1/ATG14, MAPK, PTEN, and EGFR and AKT pathways (Zhao et al. 2019). miR-506 is a tumor suppressor, which targets CDK4/6 and inhibits the CDK4/6-FOXM1 pathway, which is otherwise activated in most cases of OC. Downregulation of miR-506 leads to overexpression of these CDKs, which in turn phosphorylates and thereby activates FOXM1 (Liu et al. 2019). Production of FOXM1 causes upregulation of catalase and SOD, which in turn inhibits senescence in tumor cells by decreasing ROS levels (Ghafouri-Farda et al. 2020). Further studies and clinical trials are required to assess the efficacy of delivery methods in order to successfully apply therapeutic miRs to OC.

Combination Therapy

As discussed previously, multiple therapeutic drugs have been developed to target different pathways related to carcinogenesis. But a vast majority of these targeted therapies include cytostatic agents, which inhibit cell growth and division of both cancerous and noncancerous cells. For this reason, their effectiveness as

monotherapy is greatly limited. Therefore, such targeted therapies are usually administered in combination with other targeted therapies. Such combination therapies have been proven to be most effective in terms of anticancer effects. This superior effectivity of combination therapy stems from its ability to target multiple pathways at the same time. It also minimizes any chance for drug resistance, as cancer cells cannot adapt to the simultaneous toxicity of two or more therapeutic agents (Zimmermann et al. 2007).

Drug combinations that are frequently used by physicians to treat OC include bleomycin–etoposide phosphate–cisplatin, carboplatin–paclitaxel, gemcitabine hydrochloride–cisplatin, carboplatin–etoposide phosphate–bleomycin, vincristine sulfate–dactinomycin–cyclophosphamide, and vinblastine sulfate–ifosfamide–cisplatin. In the case of recurrent disease, topotecan and PLD are used in most countries (Gordon et al. 2004). Following the FDA approval of bevacizumab, the first targeted therapy for OC, combinations of different chemotherapeutics with bevacizumab have been evaluated in patients. Due to the cross talk between PI3K/AKT and MAPK/ERK pathways, the effects of a combination of trametinib, a MEK inhibitor, and buparlisib, a PI3K inhibitor, were tested on OC patients in a phase Ib clinical trial (Bedard et al. 2015). The drug combination showed promising antitumor activity for patients with KRAS-mutant OC (Bedard et al. 2015). Another ongoing phase II/III trial is comparing trametinib to standard treatment with either letrozole, paclitaxel, PLD, tamoxifen citrate, or topotecan. The preliminary results obtained from this study prove that trametinib is indeed a better alternative to standard therapy in treating patients with OC (NCT02101788). Temsirolimus is another drug that is being evaluated for its anticancer activity. Temsirolimus in combination with carboplatin and paclitaxel was used to treat patients in a phase II clinical trial. But no statistically significant result was obtained from this study (Farley et al. 2016).

Many ongoing clinical trials are currently investigating the efficacies of various combinations of different targeted therapies. But the overall common goal of all these studies is to better understand the interactions between these anticancer agents, in order to produce the maximum effect with least toxicity. Many anticancer agents can be combined to potentially result in significant therapeutic efficacy, but they have not yet undergone proper investigation. Therefore, the search for more effective combination therapies will go on.

Conclusion

OC remains a highly lethal disease among women throughout the world. The standard treatment procedure of OC includes surgery followed by platinum- and taxane-based chemotherapy. Even though a majority of patients respond well to platinum chemotherapy initially, most of them develop resistance towards them after one or more relapses. Besides, platinum-based chemotherapy shows a poor response to second-line chemotherapy. Recent advances in OC research leading to an enhanced understanding of molecular networks in the tumor microenvironment

have expanded the prospects for OC patients, causing a plodding shift from standard chemotherapy approaches to targeted therapy.

Targeted therapy showed promise by the nontoxic nature of TTis and early breakthroughs by exploiting several molecular pathways in the tumor microenvironment, but it was soon followed by reports of the development of acquired resistance in OC patients against some of these TTis. PARPi, olaparib, rucaparib, and niraparib have demonstrated their efficacy successfully in maintenance therapy in OC patients. However, PARPi resistance has been reported in some cases, with the most common mechanism of resistance being the restoration of BRCA1 or BRCA2 protein functionality due to secondary mutations. Similarly, the antiangiogenic agent bevacizumab has serious adverse effects in OC patients, like GI perforation, proteinuria, hypertension inflammation of skin, and possibility of stroke. AKT/mTOR inhibitors and p53 inhibitors are still in phase II and III clinical trials, and their long-term side effects are yet to be discovered. There is growing interest in restoring the abnormal miRNA expression to normal levels in the tumor site by efficient delivery of miRNAs. However, stability, safety, and cell permeability are the major limitations of targeted delivery in vivo. Generally, RNA is unstable and is prone to degradation by serum ribonucleases. Hence, chemical modifications are required to stabilize the oligonucleotides for in vivo delivery. Inorganic materials, including gold nanoparticles (Au-NPs), mesoporous silicon adenovirus, and retrovirus-based delivery approaches, have also been reported in several studies. More recently, a study showed miRNA replacement therapy as a treatment for OC. Treatment with synthesized miR-199a-3p-loaded-exosomes (miR-199a-3p-Exo) drastically increased the tumor suppressor miR-199a-3p level in OC cell lines and thus inhibited cell proliferation and invasion. The research on miRNA regulation of their target genes concerning OC progression is still in its early years, and more studies are needed to practically realize the possibility of miRNA therapeutics. In recent years, combination therapy has also made inroads to tackle the resistance developed in OC patients. However, to date, the full potential of these combinations has not been completely understood. The use of a proper evidence-based selection of targeted inhibitors upon a defined patient population will allow better treatment of OC in the near future.

Acknowledgments Abhishek Chatterjee and Susmita Saha would like to acknowledge the University Grants Commission (UGC) for financial support. Vineet Kumar Mishra acknowledges DBT-RA Program in Biotechnology and Life Sciences for financial support.

References

Aghajanian C, Blank SV, Goff BA, Judson PL, Teneriello MG, Husain A, Sovak MA et al (2012) OCEANS: a randomized, double-blind, placebo-controlled phase III trial of chemotherapy with or without bevacizumab in patients with platinum-sensitive recurrent epithelial ovarian, primary peritoneal, or fallopian tube cancer. J Clin Oncol 30(17):2039–2045

Armstrong DK, White AJ, Weil SC, Phillips M, Coleman RL (2013) Farletuzumab (a monoclonal antibody against folate receptor alpha) in relapsed platinum-sensitive ovarian cancer. Gynecol Oncol 129(3):452–458

Bedard PL, Tabernero J, Janku F, Wainberg ZA, Paz-Ares L, Vansteenkiste J, Van Cutsem E et al (2015) A phase Ib dose-escalation study of the oral pan-PI3K inhibitor buparlisib (BKM120) in combination with the oral MEK1/2 inhibitor trametinib (GSK1120212) in patients with selected advanced solid tumors. Clin Cancer Res 21(4):730–738

Behbakht K, Sill MW, Darcy KM, Rubin SC, Mannel RS, Waggoner S, Schilder RJ et al (2011) Phase II trial of the mTOR inhibitor, temsirolimus and evaluation of circulating tumor cells and tumor biomarkers in persistent and recurrent epithelial ovarian and primary peritoneal malignancies: a Gynecologic Oncology Group study. Gynecol Oncol 123(1):19–26

Bitler BG, Watson ZL, Wheeler LJ, Behbakht K (2017) PARP inhibitors: clinical utility and possibilities of overcoming resistance. Gynecol Oncol 147:695–704

Blagden SP, Hamilton AL, Mileshkin L, Wong S, Michael A, Hall M, Goh JC et al (2019) Phase IB dose escalation and expansion study of AKT inhibitor afuresertib with carboplatin and paclitaxel in recurrent platinum-resistant ovarian cancer. Clin Cancer Res 25(5):1472–1478

Burger RA, Brady MF, Bookman MA, Fleming GF, Monk BJ, Huang H, Mannel RS et al (2011) Incorporation of bevacizumab in the primary treatment of ovarian cancer. N Engl J Med 365 (26):2473–2483

Chandra A, Pius C, Nabeel M, Nair M, Vishwanatha JK, Ahmad S, Basha R (2019) Ovarian cancer: current status and strategies for improving therapeutic outcomes. Cancer Med 8:7018–7031

Chien J, Poole E (2017) Ovarian cancer prevention, screening and early detection: report from the 11th biennial ovarian cancer research symposium. Int J Gynecol Cancer 27:S20–S22

Diaz-Padilla I, Malpica AL, Minig L, Chiva LM, Gershenson DM, Gonzalez-Martin A (2012) Ovarian low-grade serous carcinoma: a comprehensive update. Gynecol Oncol 126(2):279–285

Duffy MJ, Synnott NC, Crown J (2017) Mutant p53 as a target for cancer treatment. Eur J Cancer 83:258–265

Etemadmoghadam D, Au-Yeung G, Wall M, Mitchell C, Kansara M, Loehrer E, Batzios C et al (2013) Resistance to CDK2 inhibitors is associated with selection of polyploid cells in CCNE1-amplified ovarian cancer. Clin Cancer Res 19:5960–5971

Fantozzi A, Gruber DC, Pisarsky L, Heck C, Kunita A, Yilmaz M, Meyer-Schaller N et al (2014) VEGF-mediated angiogenesis links EMT-induced cancer stemness to tumor initiation. Cancer Res 74(5):1566–1575

Farley J, Brady WE, Vathipadiekal V, Lankes HA, Coleman R, Morgan MA, Mannel R et al (2013) Selumetinib in women with recurrent low-grade serous carcinoma of the ovary or peritoneum: an open-label, single-arm, phase 2 study. Lancet Oncol 14(2):134–140

Farley JH, Brady WE, Fujiwara K, Nomura H, Yunokawa M, Tokunaga H, Saitou M et al (2016) A phase II evaluation of temsirolimus in combination with carboplatin and paclitaxel followed by temsirolimus consolidation as first-line therapy in the treatment of stage III–IV clear cell carcinoma of the ovary. J Clin Oncol 34(15_Suppl):55315531

Fu S, Hennessy BT, Ng CS, Ju Z, Coombes KR, Wolf JK, Sood AK et al (2012) Perifosine plus docetaxel in patients with platinum and taxane resistant or refractory high-grade epithelial ovarian cancer. Gynecol Oncol 126(1):47–53

Gao Y, Shen J, Choy E, Mankin H, Hornicek F, Duan Z (2017) Inhibition of CDK4 sensitizes multidrug resistant ovarian cancer cells to paclitaxel by increasing apoptosis. Cell Oncol 40: 209–218

García-Gómez R, Bustelo XR, Crespo P (2018) Protein-protein interactions: emerging oncotargets in the RAS-ERK pathway. Trends Cancer 4(9):616–633

Ghafouri-Farda S, Shooreib H, Taheric M (2020) miRNA profile in ovarian cancer. Exp Mol Pathol 113:104381

Gordon AN, Tonda M, Sun S, Rackoff W et al (2004) Long-term survival advantage for women treated with pegylated liposomal doxorubicin compared with topotecan in a phase 3 randomized study of recurrent and refractory epithelial ovarian cancer. Gynecol Oncol 95(1):1–8

Han LY, Landen CN, Trevino JG, Halder J, Lin YG, Kamat AA, Kim TJ et al (2006) Antiangiogenic and antitumor effects of SRC inhibition in ovarian carcinoma. Cancer Res 66(17):8633–8639

Hayman SR, Leung N, Grande JP, Garovic VD (2012) VEGF inhibition, hypertension, and renal toxicity. Curr Oncol Rep 14(4):285–294

Herzog T, Pignata S, Ghamande S, Rubio MJ, Fujiwara K, Vulsteke C, Armstrong D et al (2021) A randomized, double-blind, placebo-controlled, phase II study to assess the efficacy/safety of farletuzumab in combination with carboplatin plus paclitaxel or carboplatin plus pegylated liposomal doxorubicin (PLD) in women with low CA-125 platinum-sensitive ovarian cancer. Gynecol Oncol 162(1):S38–S39

Kabbinavar FF, Hambleton J, Mass RD, Hurwitz HI, Bergsland E, Sarkar S (2005) Combined analysis of efficacy: the addition of bevacizumab to fluorouracil/leucovorin improves survival for patients with metastatic colorectal cancer. J Clin Oncol 23(16):3706–3712

Keefe DMK, Bateman EH (2019) Potential successes and challenges of targeted cancer therapies. J Natl Cancer Inst Monogr 53:lgz008

Kossai M, Leary A, Scoazec JY, Genestie C (2018) Ovarian cancer: a heterogeneous disease. Pathobiology 85:41–49

Lee SB, Segura-Bayona S, Villamor-Payà M, Saredi G, Todd MA, Attolini CSO, Chang TY et al (2018) Tousled-like kinases stabilize replication forks and show synthetic lethality with checkpoint and PARP inhibitors. Sci Adv 4(8):eaat4985

Leng Q, Mixson AJ (2005) Small interfering RNA targeting Raf-1 inhibits tumor growth in vitro and in vivo. Cancer Gene Ther 12(8):682–690

Li T, Peng J, Zeng F, Hang K, Liu J, Li X, Ouyang Q et al (2017) Association between polymorphisms in CTR1, CTR2, ATP7A, and ATP7B and platinum resistance in epithelial ovarian cancer. Int J Clin Pharmacol Ther 55:774–780

Lin KK, Harrell MI, Oza AM, Oaknin A, Ray-Coquard I, Tinker AV, Helman E et al (2019) BRCA reversion mutations in circulating tumor DNA predict primary and acquired resistance to the PARP inhibitor Rucaparib in high-grade ovarian carcinoma. Cancer Discov 9:210–219

Liu X, Lam F, Shi S, Fischer PM, Wang S (2012) *In vitro* antitumor mechanism of a novel cyclin-dependent kinase inhibitor cdki-83. Investig New Drugs 30:889–897

Liu X, Gao Y, Shen J, Yang W, Choy E, Mankin H, Hornicek FJ, Duan Z (2016) Cyclin-dependent kinase 11 (CDK11) is required for ovarian cancer cell growth *in vitro* and *in vivo*, and its inhibition causes apoptosis and sensitizes cells to Paclitaxel. Mol Cancer Ther 15(7):1691–1701

Liu G, Sun Y, Ji P, Li X, Cogdell D, Yang D, Parker BJ et al (2019) MiR-506 suppresses proliferation and induces senescence by directly targeting the CDK4/6–FOXM1 axis in ovarian cancer. J Pathol 249:268–268

Lorusso PM, Edelman MJ, Bever SL, Forman KM, Pilat M, Quinn MF, Li J et al (2012) Phase I study of folate conjugate EC145 (Vintafolide) in patients with refractory solid tumors. J Clin Oncol 30(32):4011–4016

Lorusso D, Bria E, Costantini A, Di Maio M, Rosti G, Mancuso A (2017) Patients' perception of chemotherapy side effects: expectations, doctor–patient communication and impact on quality of life - an Italian survey. Eur J Cancer Care 26:e12618

Mabuchi S, Kuroda H, Takahashi R, Sasano T (2015) The PI3K/AKT/mTOR pathway as a therapeutic target in ovarian cancer. Gynecol Oncol 137(1):173–179

Mahner S, Woelber L, Mueller V, Witzel I, Prieske K, Grimm D, Keller V, Amsberg G et al (2015) Beyond bevacizumab: an outlook to new anti-angiogenics for the treatment of ovarian cancer. Front Oncol 5(211):1–6

McCain J (2015) First-in-class CDK4/6 inhibitor Palbociclib could usher in a new wave of combination therapies for HR+, HER2− breast cancer. P T 40:511–520

McMullen M, Karakasis K, Madariaga A, Oza AM (2020) Overcoming platinum and PARP-inhibitor resistance in ovarian cancer. Cancers (Basel) 12:1607

McPhillips F, Mullen P, Monia BP, Ritchie AA, Dorr FA, Smyth JF, Langdon SP (2001) Association of c-Raf expression with survival and its targeting with antisense oligonucleotides in ovarian cancer. Br J Cancer 85(11):1753–1758

Monk BJ, Choi DC, Pugmire G, Burger RA (2005) Activity of bevacizumab (rhuMAB VEGF) in advanced refractory epithelial ovarian cancer. Gynecol Oncol 96(3):902–905

Monk BJ, Minion LE, Coleman RL (2016) Anti-angiogenic agents in ovarian cancer: past, present, and future. Ann Oncol 27(Suppl 1):i33–i39

Monk BJ, Grisham RN, Banerjee S, Kalbacher E, Mirza MR, Romero I, Vuylsteke P et al (2020) MILO/ENGOT-ov11: binimetinib versus physician's choice chemotherapy in recurrent or persistent low-grade serous carcinomas of the ovary, fallopian tube, or primary peritoneum. J Clin Oncol 38(32):3753–3762

Morris RT, Joyrich RN, Naumann RW, Shah NP, Maurer AH, Strauss HW, Uszler JM et al (2014) Phase II study of treatment of advanced ovarian cancer with folate-receptor-targeted therapeutic (vintafolide) and companion SPECT-based imaging agent (99mTc-etarfolatide). Ann Oncol 25 (4):852–858

Naumann RW, Coleman RL, Burger RA, Sausville EA, Kutarska E, Ghamande SA, Gabrail NY et al (2013) PRECEDENT: a randomized phase II trial comparing vintafolide (EC145) and pegylated liposomal doxorubicin (PLD) in combination versus PLD alone in patients with platinum-resistant ovarian cancer. J Clin Oncol 31(35):4400–4406

Perren TJ, Swart AM, Pfisterer J, Ledermann JA, Pujade-Lauraine E, Kristensen G, Carey MS et al (2011) A phase 3 trial of bevacizumab in ovarian cancer. N Engl J Med 365(26):2484–2496

Previs RA, Mills GB, Westin SN (2019) Novel therapeutic approaches and targets for ovarian cancer. In: Leung PCK, Adashi EY (eds) The ovary, 3rd edn. Academic Press, Cambridge, MA

Pujade-Lauraine E, Hilpert F, Weber B, Reuss A, Poveda A, Kristensen G, Sorio R et al (2012) Aurelia: a randomized phase III trial evaluating bevacizumab (BEV) plus chemotherapy (CT) for platinum (pt)-resistant recurrent ovarian cancer (OC). J Clin Oncol 30(18_Suppl): LBA5002LBA5002

Pujade-Lauraine E, Fujiwara K, Ledermann JA, Oza AM, Kristeleit R, Ray-Coquard IL, Richardson GE et al (2021) Avelumab alone or in combination with chemotherapy versus chemotherapy alone in platinum-resistant or platinum-refractory ovarian cancer (JAVELIN Ovarian 200): an open-label, three-arm, randomised, phase 3 study. Lancet Oncol 22(7):1034–1046

Rose M, Burgess JT, O'Byrne K, Richard DJ, Bolderson E (2020) PARP inhibitors: clinical relevance, mechanisms of action and tumor resistance. Front Cell Dev Biol 8:564601

Sarker D, Ang JE, Baird R, Kristeleit R, Shah K, Moreno V, Clarke PA et al (2015) First-in-human phase I study of pictilisib (GDC-0941), a potent pan-class I phosphatidylinositol-3-kinase (PI3K) inhibitor, in patients with advanced solid tumors. Clin Cancer Res 21(1):77–86

Singer G, Oldt R III, Cohen Y, Wang BG, Sidransky D, Kurman RJ, Shih I (2003) Mutations in BRAF and KRAS characterize the development of low-grade ovarian serous carcinoma. J Natl Cancer Inst 95(6):484–486

Soragni A, Janzen DM, Johnson LM, Lindgren AG, Thai-Quynh Nguyen A, Tiourin E et al (2016) A designed inhibitor of p53 aggregation rescues p53 tumor suppression in ovarian carcinomas. Cancer Cell 29:90–103

Stewart C, Ralyea C, Lockwood S (2019) Ovarian cancer: an integrated review. Semin Oncol 35: 151–156

Sung H, Ferlay J, Siegel RL, Laversanne M, Soerjomataram I, Jemal A, Bray F (2021) Global cancer statistics 2020: GLOBOCAN estimates of incidence and mortality worldwide for 36 cancers in 185 countries. CA Cancer J Clin 71:209–249

Taylor-Harding B, Aspuria PJ, Agadjanian H, Cheon DJ, Mizuno T, Greenberg D, Allen GR et al (2015) Cycline 1 and RTK/RAS signaling drive CDK inhibitor resistance via activation of E2F and ETS. Oncotarget 6:696–714

Vaidyanathan A, Sawers L, Gannon AL, Chakravarty P, Scott AL, Bray SE, Ferguson MJ et al (2016) ABCB1 (MDR1) induction defines a common resistance mechanism in paclitaxel- and olaparib-resistant ovarian cancer cells. Br J Cancer 115:431–441

Wang Z, Fu S (2016) An overview of tyrosine kinase inhibitors for the treatment of epithelial ovarian cancer. Expert Opin Investig Drugs 25:15–30

Wang J, Dean DC, Hornicek FJ, Shi H, Duan Z (2019) Cyclin-dependent kinase 9 (CDK9) is a novel prognostic marker and therapeutic target in ovarian cancer. FASEB J 33:5990–6000

Wheler J, Mutch D, Lager J, Castell C, Liu L, Jiang J, Traynor AM (2017) Phase I dose-escalation study of pilaralisib (SAR245408, XL147) in combination with paclitaxel and carboplatin in patients with solid tumors. Oncologist 22(4):377–e37

Xie H, Wang W, Xiaa B, Jin W, Loua G (2020) Therapeutic applications of PARP inhibitors in ovarian cancer. Biomed Pharmacother 127:1–13

Yang H, Kong W, He L, Zhao JJ, O'Donnell JD, Wang J, Wenham RM et al (2008) MicroRNA expression profiling in human ovarian cancer: miR-214 induces cell survival and cisplatin resistance by targeting PTEN. Cancer Res 68:425–433

Zhao W, Han T, Li B, Ma Q, Yang P, Li H (2019) miR-552 promotes ovarian cancer progression by regulating PTEN pathway. J Ovarian Res 12(121):1–10

Zhou Q (2017) Targeting cyclin-dependent kinases in ovarian cancer. Cancer Investig 35:367–376

Zimmer AS, Nichols E, Cimino-Mathews A, Peer C, Cao L, Lee MJ, Kohn EC et al (2019) A phase I study of the PD-L1 inhibitor, durvalumab, in combination with a PARP inhibitor, olaparib, and a VEGFR1-3 inhibitor, cediranib, in recurrent women's cancers with biomarker analyses. J Immunother Cancer 7(1):197

Zimmermann GR, Lehár J, Keith CT (2007) Multi-target therapeutics: when the whole is greater than the sum of the parts. Drug Discov Today 12(1–2):34–42

LIST OF POSTER & ORAL PRESENTATIONS

Poster Presentations

1. **Chatterjee, A.**, Roy, T., & Swarnakar, S. Hyperglycemia-induced transcriptional upregulation of Matrix Metalloproteinase-9 (MMP-9) in gastric cancer cells: Role of AP-1 transcription factor. Presented at the **SNU-BioTalk 2025** held during 16-17th January 2025 at the Sister Nivedita University, Kolkata.
2. **Chatterjee, A.**, Roy, T., & Swarnakar, S. Hyperglycemia-induced Matrix Metalloproteinase-9 (MMP-9) upregulation via AP-1 binding drives gastric cancer progression: Insights for targeted therapeutics. Presented at the3rd NCRI International ONCO Summit (**NIOS 2025**) held during 11-12th January 2025 at the ITC Sonar Hotel, Kolkata.
3. **Chatterjee, A.**, Roy, T., Jyothi, D., Mishra, V. K., Singh, U. P., & Swarnakar, S. Melatonin reverses hyperglycemia induced gastric cancer cell proliferation. Presented at the 91st Annual Meeting of the Society of Biological Chemists (India) **SBC-2022** held during 8-11th December 2022 at the Biswa Bangla Convention Centre, Kolkata.

Oral Presentations

4. **Chatterjee, A.**, Roy, T., Jyothi, D., Singh, U. P., & Swarnakar, S. Excess proliferation of gastric cancer cells in an induced hyperglycemic environment: Alleviation by melatonin. Presented at the North Zone 2024 conference of the Indian Academy of Biomedical Sciences (**IABS-NZ 2024**) held during 5-6th August 2024 at the JLN Auditorium, AIIMS, New Delhi.
5. **Chatterjee, A.**, Roy, T., Jyothi, D., Singh, U. P., & Swarnakar, S. Melatonin alters hyperglycemia induced gastric cancer cell proliferation and MMP-9/TIMP-1 expression. Presented at the 3rd International Conference **BIONEXT 2023** held during 4-6th October 2023 at Adamas University, Kolkata.

CERTIFICATE OF RECOGNITION

SNU-Bio Talk 2025

International Conference on
"Symphony of Cellular Signals in Metabolism and Immune Response"

This is to certify that **Abhishek Chatterjee, CSIR IICB**

Participated/Presented (oral/poster/model) in the Conference held on **16th-17th January, 2025** organized by Dept. of Microbiology, Dept. of Biotechnology & Dept. of Applied Nutrition and Dietetics, Sister Nivedita University, Kolkata, India

Dr. Sudipta Saha Convener	**Dr. Amit Sarkar** Convener	**Dr. Anindita Banerjee** Co-Convener	**Dr. Moumita Das** Co-Convener

NIOS

3rd NCRI International ONCO Summit

NETAJI SUBHAS CHANDRA BOSE CANCER HOSPITAL

CERTIFICATE

OF PARTICIPATION

ABHISEK CHATTERJEE

Has participated as Poster Presenter in NIOS 2025 held on 11th & 12th January 2025 at ITC SONAR Hotel

Dr. Soma Mukhopadhyay
Patron

Dr. Soumen Das
President

Dr. Anupam Datta
Organising Secretary

Dr. Poulomi Basu
Organising Secretary

Dr. Rahul Agarwal
Organising Secretary

Dr. C.K Bose
Scientific Committee
Chairman

IABS NORTH ZONE 2024

AIIMS- New Delhi, 5-6 August 2024

CERTIFICATE

This is to certify that

Abhishek Chatterjee

has presented **oral presentation** on Excess proliferation of gastric cancer cells in an induced hyperglycemic environment: Alleviation by melatonin in the North Zone 2024 conference of the Indian Academy of Biomedical Sciences (IABS-NZ 2024), with a theme on ***Artificial Intelligence and Translational Research in Human Health,*** organized by the Department of Laboratory Medicine, AIIMS New Delhi.

Dr Hari S Sharma **Dr.Abbas Ali Mahdi** **Dr.B S S Rao** **Dr. Shyam Prakash**

ADAMAS UNIVERSITY KOLKATA
PURSUE EXCELLENCE

INSTITUTION'S INNOVATION COUNCIL
(Ministry of HRD Initiative)

SOCIETY OF BIOLOGICAL CHEMISTS

BIONEXT 2023

3rd International Conference on
Translational Research toward attaining
"Good Health & Well Being"

Organized by
School of Life Science and Biotechnology, Adamas University
In collaboration with
The Society of Biological Chemists (I), Kolkata Chapter & Microbiologists Society, India (MBSI)

CERTIFICATE OF APPRECIATION

This is to certify that Prof./ Dr. / Mr. /Ms. Abhishek Chatterjee participated /delivered an invited lecture / oral presentation / poster presentation / chaired a session in the 3rd International Conference **BIONEXT 2023** held during 4-6th October 2023 at Adamas University Kolkata.

.....
Prof. Rudra Prasad Saha
(Convener & Dean, SOLB)

.....
(Member, Organizing committee)

Society of Biological Chemists (India) presents this

Certificate

to

Abhishek Chatterjee

in appreciation of participation/poster presentation/~~delivering lecture~~/~~chairing session~~

at

91st Annual Meeting of the Society of Biological Chemists (India)

on

"Life at the Confluence of Biology & Chemistry"

Jointly organised by Bose Institute, CSIR-IICB, NIBMG and SNU

Held at the Biswa Bangla Convention Centre, New Town, Kolkata

December 08-11, 2022

President	Jt. Secretary	Jt. Secretary

AWARDS

&

ACHIEVEMENTS

IABS NORTH ZONE 2024

AIIMS- New Delhi, 5-6 August 2024

CERTIFICATE

This is to certify that

ABHISHEK CHATTERJEE

is **appreciated for best participation** in the North Zone 2024 conference of the Indian Academy of Biomedical Sciences (IABS-NZ 2024), with a theme on ***Artificial Intelligence and Translational Research in Human Health***, organized by the Department of Laboratory Medicine, AIIMS New Delhi.

Dr Hari S Sharma **Dr.Abbas Ali Mahdi** **Dr.B S S Rao** **Dr. Shyam Prakash**

ADAMAS UNIVERSITY KOLKATA
PURSUE EXCELLENCE

INSTITUTION'S INNOVATION COUNCIL
(Ministry of HRD Initiative)

SOCIETY OF BIOLOGICAL CHEMISTS

BIONEXT 2023

3rd International Conference on
Translational Research toward attaining
"Good Health & Well Being"

Organized by
School of Life Science and Biotechnology, Adamas University
In collaboration with
The Society of Biological Chemists (I), Kolkata Chapter & Microbiologists Society, India (MBSI)

CERTIFICATE OF AWARD

This certificate is presented to Dr. / Mr. /Ms. ..ABHISHEK CHATTERJEE..... for securing....SECOND POSITION..... In poster presentation / oral presentation in the 3rd International Conference **BIONEXT 2023** held during 4-6th October 2023 at Adamas University Kolkata.

.....
Prof. Rudra Prasad Saha
(Convener & Dean, SOLB)

.....
(Member, Organizing committee)

Dr. Surender Singh
Joint Secretary
Ph.: 011-24115419, Telefax: 011-24112276
Email: ssingh.ugc@nic.in

UNIVERSITY GRANTS COMMISSION
(Ministry of Human Resource Development)
NET Bureau, University of Delhi, South Campus,
Benito Juarez Marg, New Delhi-110021

Joint CSIR-UGC Test
JRF AWARD LETTER

17 JAN 2019

F.No. 16-6(DEC. 2017)/2018(NET/CSIR)

UGC-Ref. No.: 766/(CSIR-UGC NET DEC. 2017)

ABHISHEK CHATTERJEE
S/O SOMNATH CHATTERJEE
3/41A, BIJOYGARH, JADAVPUR, KOLKATA
WEST BENGAL 700032

Roll No.: 354303 Subject: LIFE SCIENCES

Dear Candidate,

I am pleased to inform you that you have qualified for Junior Research Fellowship (JRF) and Eligibility for Assistant Professor in the Joint CSIR-UGC Test conducted on 17th December, 2017. The tenure of fellowship is five years and it commences from the date of declaration of NET result, i.e., 9th May 2018 (or) from the date of admission under M.Phil/Ph.D. (or) from the date of joining M.Phil./Ph.D. programme, whichever is later. The summary of financial assistance offered under the scheme is mentioned at **Annexure I** available on www.ugc.ac.in/netjrf along with other Annexures.

The Awardee is required to get admission and registration for regular and full time **M.Phil/Ph.D.** course in a University/Institution/College recognized by UGC at the first available opportunity **but not later than three years** from the date of issue of this award letter. University/Institution/College is requested to process for award of JRF based on this letter, in accordance with procedure available on www.ugc.ac.in/netjrf.

It may be noted that the fellowship amount shall be disbursed through Canara Bank to bank account of the Awardee (any bank) directly. UGC has developed a dedicated web portal (https://scholarship.canarabank.in/AdminLogin.aspx) for capturing data of the awardee. The Universities/ Colleges/ Institutions will submit the master data of the awardee on the portal with a unique user profile of the University/ Institution/ College (user name and password already provided to the University/ Institution/ College). The Universities/Institutions/ Colleges shall **update** the information in the master data (regarding continuation, HRA, up-gradation, resignation etc.) of the beneficiaries on **quarterly** basis. Based on the master data received from the concerned Universities/Institutions/Colleges, the payment of the fellowship will be made to the beneficiaries.

It may also be noted that UGC has proposed to link "**AADHAAR**" with bank account of students so that there can be direct cash transfer and effective disbursal of fellowship into bank account of the student. In this regard, Secretary, UGC had requested the universities to help students in Aadhaar enrolment vide D.O. No. F.14-34/2011 (CPP-II) dated 11.01.2013.

It may please be noted that the award is liable to be cancelled by Implementing/Awarding agency and it will also attract legal action against the Awardee in the following cases:

(i) If the awardee is found to be ineligible to receive the award at any point during the entire duration of fellowship,
(ii) Misconduct of Awardee,
(iii) Unsatisfactory progress of research work,
(iv) Failure in any examination related to M.Phil/ Ph.D,
(v) In case, any other fellowship is drawn from other source(s),
(vi) Concealment of facts.

The E-certificate of Eligibility for Assistant Professor has already been uploaded on www.ugcnetonline.in. The eligibility of the candidate is to be ensured by the concerned institution/appointing authority. The category in which the candidate had appeared may be verified from UGC.

With best wishes,

Surendra

(Surender Singh)

COUNCIL OF SCIENTIFIC & INDUSTRIAL RESEARCH
HUMAN RESOURCE DEVELOPMENT GROUP
CSIR Complex, Library Avenue
Pusa, New Delhi - 110 012, India

The date of declaration of result of **Joint CSIR-UGC Junior Research Fellowship & Eligibility for Lecturership (NET) Exam** held on 17th December, 2017 is 09/05/2018

Marks Statement

Roll Number : **354303**
Name : **ABHISHEK CHATTERJEE**
Subject : Life Science
Applied For : **JRF-LECTURERSHIP**

Marks obtained	
Part A	10.5
Part B	35
Part C	64
Total Marks	109.5
Percentage	54.75%
Rank	67
Result	JRF(NET)-UGC

PENDING THE FINAL OUTCOME OF THE JUDGMENT OF HON'BLE HIGH COURT OF PUNJAB AND HARYANA IN LPA 2243/2017 AND ISSUANCE OF FORMAL JRF/NET QUALIFYING CERTIFICATE, MARKS STATEMENT OF THE QUALIFIED CANDIDATES MAY BE TREATED AS PROOF OF THEIR QUALIFYING THE SAID EXAM PROVISIONALLY SUBJECT TO THEIR FULFILLING THE ELIGIBILITY CRITERIA AS PER THE NOTIFICATION

CSIR HRDG is not responsible for any inadvertent error that may have crept in the result being published on internet.

Electronic Certificate No.: 172000766

University Grants Commission
NATIONAL EDUCATIONAL TESTING BUREAU

ज्ञान-विज्ञानं विमुक्तये

JOINT CSIR-UGC TEST

NATIONAL ELIGIBILITY TEST FOR ASSISTANT PROFESSOR

UGC Ref. No.: 766/(CSIR-UGC NET DEC. 2017)

Roll No.: 354303

Certified that ABHISHEK CHATTERJEE

Son/Daughter of SOMNATH CHATTERJEE has qualified the Joint CSIR-UGC Test for Eligibility for Assistant Professor held on 17-12-2017 in the Subject LIFE SCIENCES

As per the information provided by the candidate, he/she had completed his/her Master's degree or equivalent examination at the time of applying for this test.

The date of Eligibility for Assistant Professor is the date of declaration of NET result, i.e., 9th May 2018, OR the date of completion of Master's degree or equivalent examination with required percentage of marks within two years from the date of declaration of NET result, i.e., by 8th May 2020, whichever is later.

This is an electronic certificate only. Its authenticity and category in which the candidate had appeared should be verified from UGC by the institution/appointing authority. This electronic certificate can also be verified by scanning QR Bar Code printed on the electronic certificate.

Validity of this electronic certificate is forever.

Date of Issue: 01-01-2019

Surender

Head
NET Bureau

Note: UGC has issued the electronic certificate on the basis of information provided by the candidate in his/her Application Form. The appointing authority should verify the original records/certificates of the candidate while considering him/her for appointment, as the Commission is not responsible for the same. The candidate must fulfil the minimum eligibility conditions for NET as laid down in the notification for Joint CSIR-UGC Test.

GATE 2018 Scorecard
Graduate Aptitude Test in Engineering

Candidate's Details

Name

ABHISHEK CHATTERJEE

Registration Number

EY18S16063218

Examination Paper

Ecology and Evolution (EY)

Abhishek Chatterjee

(Candidate's Signature)

Performance

Marks out of 100*	71.0			
Qualifying Marks**	49.3	44.3	32.8	
	General	OBC (NCL)	SC/ST/PwD	
GATE Score	735			

Valid from March 17, 2018 to March 16, 2021

All India Rank in this paper	26
Number of Candidates Appeared in this paper	1110

* Normalized marks for multi-session papers

** A candidate is considered qualified if the marks secured are greater than or equal to the qualifying marks mentioned for the category for which valid category certificate, if applicable, is produced along with this scorecard

Digital Fingerprint: 1d0f59df550df54f3756494a26c35584

G. Pugazhenthi

Prof. G. Pugazhenthi
Organizing Chairman, GATE 2018
(on behalf of NCB – GATE, for MHRD)

March 17, 2018

The GATE 2018 score is calculated using the formula

$$GATE\ Score = S_q + (S_t - S_q)\frac{(M - M_q)}{(\overline{M}_t - M_q)}$$

where,
M is the marks obtained by the candidate in the paper, mentioned on this GATE 2018 scorecard
M_q is the qualifying marks for general category candidate in the paper
$\overline{M}_t$ is the mean of marks of top 0.1% or top 10 (whichever is larger) of the candidates who appeared in the paper (in case of multi-session papers including all sessions)
S_q = 350, is the score assigned to M_q
S_t = 900, is the score assigned to $\overline{M}_t$

In the GATE 2018 score formula, M_q is 25 marks (out of 100) or $\mu + \sigma$, whichever is greater. Here μ is the mean and σ is the standard deviation of marks of all the candidates who appeared in the paper.

Qualifying in GATE 2018 does not guarantee either an admission to a post-graduate program or a scholarship/assistantship. Admitting institutes may conduct further tests and interviews for final selection.

Codes for XE and XL Paper Sections (compulsory section and any other two sections)

XE: Engineering Sciences
A – Engineering Mathematics (compulsory)
B – Fluid Mechanics
C – Materials Science
D – Solid Mechanics
E – Thermodynamics
F – Polymer Science and Engineering
G – Food Technology
H – Atmospheric and Oceanic Sciences

XL: Life Sciences
P – Chemistry (compulsory)
Q – Biochemistry
R – Botany
S – Microbiology
T – Zoology
U – Food Technology

Graduate Aptitude Test in Engineering (GATE) 2018 was organized by Indian Institute of Technology Guwahati on behalf of the National Coordination Board (NCB) – GATE for the Department of Higher Education, Ministry of Human Resource Development (MHRD), Government of India.